Interactions entre les Cyclones Tropicaux et l'Océan : de l'échelle synoptique à l'échelle climatique

Emmanuel M. Vincent

To cite this version:

Emmanuel M. Vincent. Interactions entre les Cyclones Tropicaux et l'Océan : de l'échelle synoptique à l'échelle climatique. Océan, Atmosphère. Université Pierre et Marie Curie - Paris VI, 2011. Français. NNT : . tel-00721714

HAL Id: tel-00721714
https://theses.hal.science/tel-00721714v1
Submitted on 30 Jul 2012

Thèse présentée pour obtenir le grade de

DOCTEUR
DE L'UNIVERSITE PIERRE ET MARIE CURIE

Specialité : OCÉANOGRAPHIE & CLIMAT

(Ecole doctorale 129 : Sciences de l'Environnement d'Ile de France)

par
Emmanuel VINCENT

Interactions entre les Cyclones Tropicaux et l'Océan : de l'échelle synoptique à l'échelle climatique

(*Interactions between Tropical Cyclones and the Ocean : linking event scale processes to climate scale consequences*)

soutenue le 02 Décembre 2011 devant le jury composé de :

M^{me} Pascale BOURUET-AUBERTOT (Professeur UPMC)	*Présidente du jury*
M. Christophe CASSOU (CR CNRS)	*Examinateur*
M^{me} Pascale DELECLUSE (DR Météo–France)	*Examinateur*
M. Hervé GIORDANI (Ingénieur Météo–France)	*Rapporteur*
M. Frank ROUX (Professeur UPS)	*Rapporteur*
M. Jérôme VIALARD (CR IRD)	*Invité*
M. Gurvan MADEC (DR CNRS)	*Directeur de Thèse*
M. Matthieu LENGAIGNE (CR IRD)	*co-directeur de Thèse*

Thèse préparée au sein du *Laboratoire d'Océanographie et du Climat – Expérimentations et Approches Numériques*

« *The sea does not belong to despots. Upon its surface men can still exercise unjust laws, fight, tear one another to pieces, and be carried away with terrestrial horrors. But at thirty feet below its level, their reign ceases, their influence is quenched, and their power disappears. Ah ! sir, live--live in the bosom of the waters ! There only is independence ! There I recognise no masters ! There I am free !* »

Captain NEMO *in Twenty Thousand Leagues Under the Sea*

Introduction générale

Top !

4 En 1274 et 1281, j'ai détruit plus de 5,000 navires de guerre portant environ 180,000 hommes et ai ainsi empêché à deux reprises les flottes mongoles de Kublai Kahn d'envahir le Japon, me valant l'appellation de *kamikaze* ou « vent divin ».

D'une puissance instantanée de 10^{12}W environ, je dissipe autant d'énergie cinétique en une heure que la France ne consomme d'énergie électrique en 1 jour. 3

2 Pour m'identifier, les prévisionnistes ont souvent utilisé des prénoms féminins depuis le 18e siècle, mais la parité avec des prénoms masculins a été adoptée en 1979, suite à des protestations de mouvements féministes.

Système de basse pression non–frontal à cœur chaud, je suis caractérisé par des vents organisés en un tourbillon cyclonique d'échelle synoptique ; je me forme au–dessus des mers chaudes tropicales et me nourris des flux de chaleur et d'humidité que j'extraie de l'océan. 1

Je suis, je suis. . . ? Un cyclone tropical, bien sûr.

Les cyclones tropicaux (TCs) sont des phénomènes plus fréquents que ne le laisse supposer ce que l'on en entend au journal télévisé. Il s'en produit environ 90 par an[1] et chacun dure environ 8 jours ; ce qui fait 720 TC.jours par an. On peut donc dire qu'en ce moment, il y a statistiquement 2 cyclones tropicaux quelque part sur la Terre. . .sur l'océan pour être plus précis.

Les TCs atteignent parfois la terre et y provoquent des pertes humaines et matérielles colossales : plus de 300,000 morts au Bangladesh en 1970 suite au passage du TC Bhola et environ 100 milliards de $ de dégâts associés au passage du TC Katrina, la catastrophe naturelle la plus coûteuse de l'histoire des Etats–Unis. Pour s'adapter à leurs conséquences, il est nécessaire de prévoir leur trajectoire et leur intensité. Cet exercice requiert, entre autres, une bonne compréhension de leur interaction avec l'océan.

Le cyclone tropical fonctionne en effet comme une immense machine thermique atmosphérique qui extrait son énergie de l'océan de surface sous forme de vapeur

---

[1] En incluant les dépressions et tempêtes tropicales.

d'eau et la convertit en énergie cinétique. Les vents du cyclone exercent une friction à la surface de l'océan et y injectent en retour une quantité importante d'énergie cinétique. Cette énergie permet de détruire la stratification verticale de l'océan et de mélanger les eaux chaudes de surface avec les eaux plus froides sous–jacentes. Le refroidissement de surface qui en résulte limite l'évaporation et constitue une rétroaction négative sur l'intensité du cyclone.

Afin de mieux comprendre cette rétroaction à l'échelle du cyclone, il est nécessaire de caractériser les processus contrôlant le refroidissement de surface. Les observations directes de l'océan sous ces tempêtes étant rares et chères, une approche numérique de la réponse océanique aux cyclones est proposée dans cette thèse. Le dispositif expérimental permet d'étudier les processus du refroidissement de surface et de comprendre ses dépendances aux caractéristiques du TC et de l'océan.

En raison du mélange qu'ils induisent, les TCs injectent de la chaleur sous la surface et pourraient ainsi influencer le climat en modifiant le transport de chaleur océanique. Bien qu'extrêmement puissants, les TCs sont caractérisés par des échelles spatiales et temporelles limitées et il convient de remonter de l'échelle locale de ces processus extrêmes à leurs conséquences à l'échelle globale *via* une méthodologie appropriée. En reproduisant la réponse océanique aux TCs dans un modèle de circulation océanique mondial, cette thèse propose un cadre permettant de lier les processus à l'échelle du cyclone à leurs conséquences sur le climat.

Ce n'est que récemment que l'on a supposé une influence des TCs sur le climat ; en revanche, le contrôle de l'activité cyclonique par la variabilité climatique est un fait largement reconnu. Comprendre l'influence du changement climatique sur les TCs est aujourd'hui un objectif crucial, dont l'exercice reste délicat. Il s'agit, cette fois, d'opérer une descente d'échelle pour comprendre comment l'état de l'atmosphère et de l'océan contrôle l'activité de ces évènements sporadiques. Ce contrôle climatique sera illustré dans le Pacifique Sud–Ouest, une région où l'activité cyclonique est relativement peu étudiée.

Il serait exagéré de dire que les processus atmosphériques contrôlant les TCs sont entièrement compris, mais l'importance de l'océan a certainement été sous–estimée. Cette thèse explore les influences réciproques entre les TCs et le climat présent, avec une attention particulière pour le rôle de l'océan. Les processus de l'interaction cyclone–océan à l'échelle de l'événement sont décrits dans la première partie de la thèse et les interactions entre les TCs et le système climatique sont ensuite abordées dans la deuxième partie. Afin de comprendre les interactions qui lient les TCs à leur environnement océanique et atmosphérique, nous nous intéressons tout d'abord à leurs caractéristiques principales et à leur fonctionnement dans le chapitre 1 ; un plan plus détaillé de la thèse conclura ce chapitre.

Remerciements

Quand j'étais gosse, je rêvais d'être un scientifique... Ah non ! c'est vrai, quand j'étais gosse je voulais être cuisto (cf mon cahier de Français du CM2).

Reprenons. Quand j'étais ado, rebelle et voix muante, je rêvais (secrètement) de devenir un scientifique, et surtout d'écrire un article du genre *Une nouvelle théorie de l'univers* dans Sciences et Avenir : LA revue scientifique de référence internationale. Cette thèse constitue une première étape vers l'accomplissement de mon rêve de gosse mais aussi la fin du long cheminement de mes études. Je ne peux conclure cette dernière longue traversée sans remercier l'éducation nationale française de m'avoir permis d'étudier, de me passionner pour la science et par–dessus tout de développer mon propre raisonnement scientifique.

Cette thèse a été une longue traversée, disais–je, mais heureusement pas en solitaire. Je tiens à remercier tout particulièrement mes encadrants de thèse pour leur disponibilité, leurs qualités humaines et scientifiques, ainsi que pour leur présence et leur suivi resserré même à quelques milliers de km de distance.

La traversée a souvent été agrémentée de plongées en eaux troubles lors des discussions avec Gurvan dont la passion contagieuse communique l'envie d'explorer la science en profondeur. Ces plongées m'ont emmené jusque dans des abysses obscurs peuplés de concepts dont il est difficile de déchiffrer le sens, d'hydres à cinq équations de la mécanique des fluides et de monstres marins thermodynamiques... Merci donc au capitaine pour m'avoir révélé quelques–unes de ses clés pour survivre dans ces profondeurs hostiles.

Mais un tel engouement aurait pu entraîner le frêle esquif à la poursuite de chants de sirènes si Matthieu n'avait été là pour larguer du leste (dans les parties Modèles & Méthode) et tenir ferme la barre droit vers l'objectif, sabrant même un pan de la thèse en dernière minute pour sauver le reste de la cargaison... Merci donc à Mat' d'avoir tenu le cap même au plus fort de la tempête.

En mer, on n'est à l'abri de rien, pas même de l'assaut d'un pirate navigant sur les eaux tropicales. C'est à peu près ainsi que Jérôme a abordé le navire, heureusement avec sa longue–vue et une bonne dose d'optimisme. Merci donc à Jeev pour m'avoir encouragé à creuser un peu plus : on ne sait jamais où se cache le trésor.

Pour avoir regardé par–dessus mon épaule, mis du vent dans les voiles et montré une direction, même si votre jeune mousse n'a pas toujours été à la hauteur de votre légendaire soif de rhum, je vous remercie chaleureusement.

Je tiens aussi à remercier les nombreux compagnons de route pour les discussions scientifiques que nous avons partagées, que ce soit au sein de "la *team* des *riders*" sur une île grecque avec Nicolas Jourdain et Fabrice Chauvin, autour d'une piña–colada sur une plage goannaise avec Guillaume Samson et Marina Lévy, dans un bar à kava avec Patrick Marchesiello et Christophe Eugène Menkes ou sur le pont du Marion-Dufresne avec Ariane Koch-Larrouy et Christophe Cassou pendant la campagne INDOMIX. Saluons leur professionnalisme pour ce travail mené toujours avec rigueur même dans les pires conditions qu'offrent les tropiques.

Merci aux membres de l'équipe NEMO : Rachid, Christian, Simona pour avoir été présent quand le *run* plante et que libIGCM se contente d'un sobre "*error* 441–*segmentation fault*". Il serait préférable que les futurs thésards au LOCEAN ne lisent pas les quelques lignes qui suivent, mon remerciement à Sébastien Masson pourrait en effet se transformer en cadeau empoisonné pour lui. Ils apprendraient par exemple qu'il est capable de répondre à n'importe quelle question d'un thésard perdu, allant de la gestion des *meshmask* dans IDL aux options cachées de la fonction *initncdf* dans SAXO en passant par les fichiers de sortie *corelight* sur Vargas... Merci donc pour ton aide sur les secrets des outils nco, cdo, du bash et de X11 sous Mac, entre autre.

Merci à l'équipe de direction et aux membres de l'équipe du secrétariat du LOCEAN pour leur disponibilité, leur accueil souriant et les éclairages nécessaires pour remplir toutes les formalités administratives pré–mission, post–mission, anté–missions et per–mission.

Je tiens à remercier les membres de mon jury de thèse pour avoir accepté de corriger ce manuscript et m'avoir accompagné jusqu'au rite initiatique de la soutenance.

Merci à ma famille : 'Pa pour le goût de la science, de la nature et de la météo, Mam' pour ton attention permanente et ton soutien inconditionnel, Philou pour m'avoir tapé dessus comme tout bon grand frère qui se respecte entre deux parties de pêche sur l'Orb et Marie pour ta présence et la force de tes idéaux.

Merci à mes amis pour leur soutien, aux procto de Normalesup' et au Ker du Lycée du Parc. Merci Rudy, pour nos longues parties de *Heroes of Might and Magic* qui m'ont permis de presque devenir un crack en informatique. Merci Manus pour ta précieuse amitié.

Glossaire

- **Abréviations** :

Voici une liste des acronymes incontournables utilisés dans cette thèse. La forme anglaise des acronymes est conservée tout au long de la thèse dans un soucis d'homogénéité entre les articles, rédigés en anglais, et le reste du texte, rédigé en français.

CI : *Cooling Inhibition index* — Indice d'inhibition au refroidissement
L'indice CI proposé dans cette thèse mesure l'énergie potentielle qu'il faut apporter à une colonne d'océan afin d'obtenir un refroidissement de surface élémentaire par un mélange vertical pénétrant conservant la chaleur. Le CI mesure la stabilité de la stratification verticale en densité et donc la difficulté de refroidir la surface pour un cyclone ; il permet de prévoir le refroidissement qu'un cyclone est susceptible d'engendrer en fonction des caractéristiques de l'océan sur lequel il se déplace (voir chap. 4).

CW : *Cold Wake* — Sillage froid
La CW désigne le refroidissement océanique de surface que les cyclones tropicaux laissent dans leur sillage. Ce refroidissement, d'une échelle de la centaine de km, constitue une rétroaction négative sur l'intensité du cyclone. Il provient en partie de l'extraction d'énergie thermique par les vents cycloniques et en partie du mélange vertical induit dans l'océan (voir chap. 3).

MLD : *Mixed Layer Depth* — Profondeur de la couche mélangée
Le soleil chauffe les couches superficielles de l'océan par le haut créant une forte stratification thermique verticale près de la surface, plusieurs mécanismes (principalement le transfert d'énergie des vents aux courants océaniques) conduisent à homogénéiser les couches superficielles jusqu'à une profondeur appelée MLD. Cette profondeur détermine la capacité thermique de la couche d'océan interagissant avec l'atmosphère. La couche mélangée est largement approfondie lors du passage d'un cyclone.

MHT : *Meridional Heat Transport* — Transport méridien de chaleur
Le MHT mesure la quantité d'énergie transportée par l'océan depuis les tropiques vers les hautes latitudes terrestres. Les surfaces tropicales reçoivent plus d'énergie du soleil qu'elles n'en émettent vers l'espace ; ce surplus d'énergie est transporté vers les hautes latitudes par la circulation atmosphérique et par la circulation océanique. Le MHT joue donc un rôle majeur dans la répartition des climats terrestres. Récemment, il a été suggéré que le mélange induit par les cyclones tropicaux pourrait modifier le MHT (voir chap. 5).

NEMO : *Nucleus for European Modeling of the Ocean* —
1. NEMO est le modèle océanique que j'ai utilisé dans ma thèse (voir chapitre 2).
2. Le point NEMO désigne aussi le pôle maritime d'inaccessibilité, c'est–à–dire le point de l'océan le plus éloigné de toute terre émergée. Ce point est situé dans l'océan Pacifique Sud, par 48°50'S / 123°20'W. Les terres émergées les plus proches sont :
- l'île Ducie, membre des îles Pitcairn, à 2 688 km au Nord ;
- au Nord–Est, Motu Nui, membre de l'archipel de l'île de Pâques ;
- au Sud, l'île Maher, au large de l'île Siple et de la terre Marie Byrd, en Antarctique ;
- à l'Ouest, l'île Chatham ;
- à l'Est, le Sud du Chili.

3. NEMO est aussi le nom du capitaine du Nautilus dans le roman de Jules Verne *20 000 lieues sous les mers.*
4. Enfin, plus récemment, cet acronyme a aussi été signalé pour désigner le Dr Gurvan Madec, j'en veux pour preuve l'affiche placardée sur la porte de son bureau au LOCEAN…

OHC : *Ocean Heat Content* — Contenu thermique de l'océan
Dans sa version couramment utilisée sous les tropiques, l'OHC mesure la quantité d'énergie thermique contenue dans les couches océaniques superficielles (au–dessus de 26°C) : $\text{OHC} = \int_{z=0}^{z(T=26°C)} \rho \, C_p \, (T - 26°C) \; dz$. Utilisée en prévision opérationnelle des cyclones depuis $\sim$10 ans, cette variable n'a apporté que de maigres améliorations car elle ne prend pas en compte les processus induisant un refroidissement sous les cyclones (à savoir : le mélange vertical plutôt que les flux de chaleur de surface).

PD : *Power Dissipated* — Puissance dissipée
La PD mesure la puissance dissipée par friction à l'interface air–mer sous un cyclone tropical $\text{PD} = \int \rho_{air} \, C_D |V|^3 \, dt$. Cette friction constitue la principale perte d'énergie pour le système cyclonique.

SPCZ : *South Pacific Convergence Zone* – Zone de convergence du Pac. Sud
La SPCZ est une des zones de convergence inter–tropicales (ITCZ) ; elle est marquée par une bande nuageuse de plusieurs milliers de km s'étirant de la Papouasie Nouvelle–Guinée au Nord–Ouest vers la Polynésie Française au Sud-Est. La variabilité de sa position en lien avec le phénomène *El Niño* entraine de larges modifications du climat dans le Pacifique Sud et dans la géographie de la cyclogenèse (voir chap. 6).

TD(s) : *Tropical Depression(s)* — Dépression(s) Tropicale(s)
Le terme dépression tropicale désigne un système de basses pressions d'échelle sy-

noptique situé au–dessus des mers tropicales ou subtropicales présentant une convection organisée et une circulation cyclonique de surface bien définie. On parle de dépression tropicale dès l'instant où l'on observe une chute de pression en surface d'au moins 2 hPa par rapport à l'environnement.

TS(s) : *Tropical Storm(s)* — Tempête(s) Tropicale(s)
On parle de tempête tropicale lorsque le vent maximum en surface moyenné sur 10 minutes atteint 17 m/s au sein d'une dépression tropicale. À ce stade d'intensité, le système est baptisé pour faciliter la communication entre les prévisionnistes et le public dans les bulletins de prévision et d'alerte.

TC(s) : *Tropical Cyclone(s)* — Cyclone(s) Tropi-cal(-caux)
On parle de cyclone tropical lorsque le vent maximum en surface moyenné sur 10 minutes atteint 33 m/s au sein d'une tempête tropicale. Une définition plus ludique du TC sera trouvée en introduction générale (page v). Le terme de "Cyclone" sera aussi utilisé pour "TC" puisque –dans cette thèse– tout se passe sous les tropiques.

$\mathbf{V}_{\max}$: *Maximum surface wind speed* — Vitesse max. des vents de surface
$V_{\max}$ mesure le maximum de la vitesse des vents de surface mesurés à 10 m autour d'un système cyclonique. Cette variable est largement utilisée pour refléter la force d'un TC dans les différentes classifications d'intensité des cyclones (voir 1.1.2.2). Il est mesuré en moyennant les vents en un point sur une période de 1 minute (standard américain) ou de 10 minutes (standard de l'Organisation Météorologique Mondiale).

WPi : *Wind Power index* — Indice de puissance des vents
Le WPi est défini en un point donné comme la racine cubique de l'intégrale temporelle de la puissance dissipée (PD) normalisée : WPi = $(\mathrm{PD}/\mathrm{PD}_0)^{1/3}$, où $\mathrm{PD}_0 = \int \rho_{air}\, C_D |V_0|^3\, dt$ intègre la puissance dissipée d'une tempête tropicale. Alors que $V_{\max}$ est utilisé pour refléter les dégâts potentiels d'un TC, le WPi a été développé dans cette thèse pour décrire le refroidissement océanique qu'engendre un TC.

- **Lexique** :

Définitions des termes non–usuels dans le discours quotidien et autres barbarismes anglophoniques rencontrés dans cette thèse.

Activité cyclonique — Dans la thèse, ce terme est utilisé pour décrire les caractéristiques générales de l'activité cyclonique affectant une région donnée, à savoir : le nombre et la position géographique des évènements de cyclogenèse, la fréquence de passage de cyclones autour d'un point, les régions de propagations préférentielles des cyclones ainsi que l'intensité moyenne ou intégrée des cyclones (vitesses maximales des vents, puissance dissipée…).

Cyclogenèse — La cyclogenèse désigne l'instant et le lieu où les vents dans un système cyclonique atteignent une vitesse maximale en surface de 15 m/s (moyennés sur 10 minutes). L'évènement de cyclogenèse n'est retenu que si le système s'intensifie par la suite et persiste plus de deux jours.

Cyclonique — Un mouvement de rotation est qualifié de cyclonique lorsqu'il s'effectue dans le même sens que le mouvement local de rotation terrestre. Vue du dessus, une rotation cyclonique "tourne" dans le sens des aiguilles d'une montre dans l'hémisphère Sud et dans le sens anti-horaire dans l'hémisphère Nord.

Enthalpie — L'enthalpie (k) est couramment utilisée pour mesurer la quantité de chaleur contenue dans l'air de basse altitude dans un cyclone tropical. Elle s'exprime comme $k = [C_p\,(1-q) + C_l\,q]\,T + L_v\,q$, où q est l'humidité spécifique, L_v est la chaleur latente de vaporisation, et C_p et C_l sont les capacités thermiques de l'air sec et de l'eau respectivement. Le flux de chaleur (d'enthalpie) extrait par les vents cycloniques à l'océan de surface est la somme des flux de chaleur sensible et de chaleur latente.

Ouragan (*Hurricane*) — Synonyme de cyclone tropical, terme utilisé principalement aux Etats–Unis.

Synoptique — En météorologie et océanographie, le terme synoptique désigne des systèmes d'une échelle du millier de km de diamètre, et durant plusieurs jours.

Thermocline — La thermocline est la zone de fort gradient vertical de température séparant les eaux chaudes de surface des eaux plus froides du fond océanique. Elle est particulièrement marquée sous les tropiques et confère une stabilité verticale à la colonne d'eau.

Typhon (*Typhoon*) — Synonyme de cyclone tropical, terme utilisé principalement au Japon.

Upwelling — Un *upwelling* désigne une remontée d'eaux océaniques profondes forcée par les vents, comme c'est le cas sous un cyclone tropical.

Table des matières

II Deuxième partie : Interactions entre les cyclones et le climat 109

CHAPITRE 1

Introduction Scientifique : Les Cyclones Tropicaux et leurs interactions avec le climat

1.1 Observation et description des Cyclones Tropicaux (TCs)

1.1.1 Caractéristiques d'un TC

Afin d'illustrer les caractéristiques d'un TC, le cyclone DORA est préférentiellement choisi comme exemple. Sa genèse a eu lieu début Février 2007 dans l'Océan Indien Sud et a été observée de près pendant la campagne VASCO-CIRENE ; il a été étudié par plusieurs équipes françaises, notamment au LOCEAN (*e.g.* [Vialard *et al.* 2009], [Le Vaillant *et al.* 2012], [Duvel *et al.* 2008]).

1.1.1.1 Propriétés thermodynamiques

La figure 1.1 illustre la nébulosité observée par le satellite METEOSAT–7 le 03 Février 2007 pendant le passage du cyclone DORA dans l'océan Indien Sud. Comme tous les cyclones, il se caractérise avant tout par une masse nuageuse d'échelle synoptique (taille caractéristique du millier de kilomètres). Les nuages convectifs sont organisés en spirales s'enroulant autour d'un point central appelé l'œil du cyclone. Ces spirales, d'une largeur de 5 à 40 km, s'entrelacent avec des spirales de ciel clair où l'air est en subsidence. De l'extérieur vers le centre, les spirales décrivent un mouvement de rotation cyclonique : dans le sens des aiguilles d'une montre dans l'hémisphère sud et le sens inverse dans l'hémisphère nord.

Autour de l'œil, qui est calme et libre de nuage, se trouve un anneau de convection très intense de 10 à 50 km de largeur que l'on appelle le mur de l'œil. D'énormes cumulonimbus y atteignent le haut de la troposphère, soit une altitude d'environ 15 km sous les tropiques. L'altitude importante du sommet des nuages se traduit par une température d'émission infra–rouge très basse (Fig. 1.2).

La chaleur latente libérée par l'intense convection a pour effet de réchauffer fortement l'air dans le mur de l'œil. Les taux de chauffage instantanés peuvent y

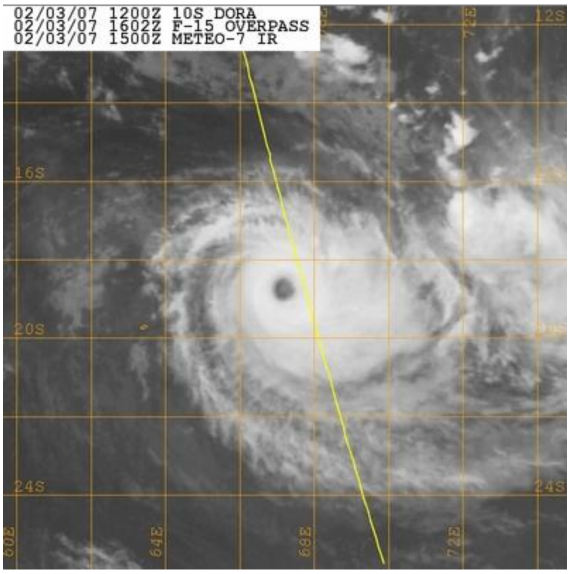

Figure 1.1 – Image satellite du cylcone DORA prise le 03 Février 2007 par METEOSAT–7 (canal visible) dans l'océan Indien Sud.

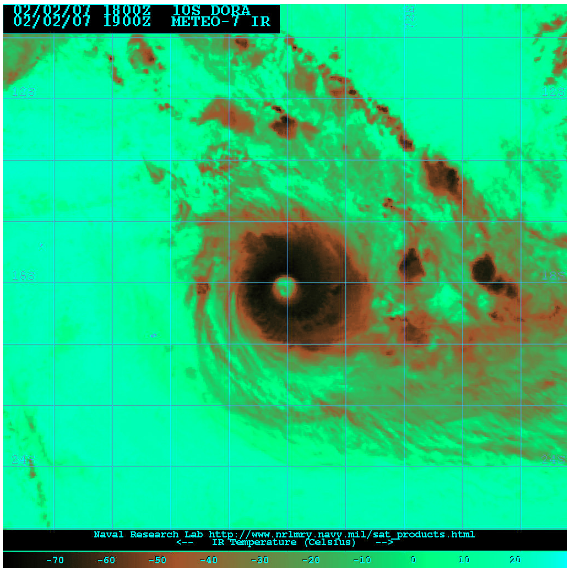

Figure 1.2 – Température infra–rouge du cylcone DORA prise le 02 Février 2007 par METEOSAT–7 (canal infra-rouge). La température d'émission atteint $-80°$C.

atteindre 60°C/h ; et l'anomalie de température au cœur de l'œil est typiquement de 5 à 10 °C (Fig. 1.3). L'élévation de la température entraîne une diminution de la densité de la colonne d'air et crée une dépression en surface par le simple effet de l'équilibre hydrostatique. La différence de pression entre le cœur de l'œil et l'environnement génère des vents violents dirigés vers la dépression et s'enroulant autour de celle–ci sous l'effet de la force de Coriolis (Fig. 1.4). Dans le cas du cyclone DORA, la vitesse des vents atteint plus de 40 m/s (70 nœuds) dans le mur de l'œil. L'intense zone de précipitation est ainsi alimentée par une convergence des masses d'air dans la couche limite atmosphérique (CLA) qui se chargent en humidité au contact de l'océan.

Figure 1.3 – Coupe radiale–verticale d'anomalies de température (à un niveau de pression donné par rapport à l'environnement distant) dans un cyclone.

Extrait de [Hawkins & Imbembo 1976]

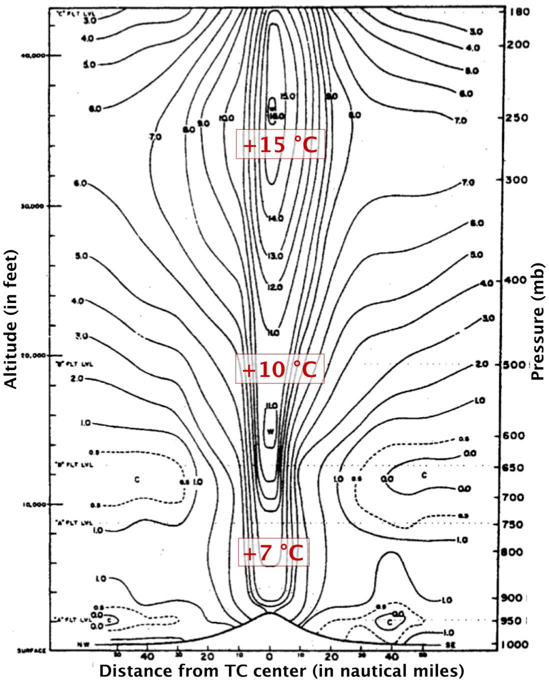

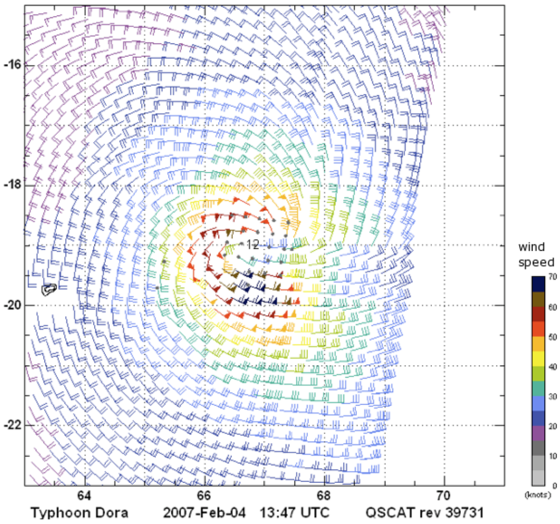

Figure 1.4 – Vents de surface du cyclone DORA observés le 04 Février 2007 par le satellite Quick–Scat.

1.1.1.2 Le champ de vent associé

En première approximation, le vent associé à un cyclone peut être décrit comme un vortex axisymétrique. La vitesse des vents tangentiels augmente rapidement lorsque l'on s'éloigne du centre et atteint son maximum autour de 30 à 100 km du centre, dans le mur de l'œil : c'est le rayon de vent maximum (RMW pour *Radius of Maximum Winds*). Ces vents tangentiels présentent une valeur maximale près de la surface, à environ 500 m d'altitude (Fig. 1.5).

La composante radiale des vents est convergente en basse couche et divergente en haute troposphère (Fig. 1.5). Elle peut atteindre une amplitude de 10 m/s en basse couche et plusieurs dizaines de m/s dans les jets divergents anticycloniques en haute troposphère. Cette convergence au centre du cyclone est associée à des vitesses verticales pouvant atteindre plusieurs m/s. L'air ascendant sature et la vapeur d'eau se condense en créant d'intenses précipitations et des cumulonimbus qui s'étendent sur toute la troposphère dans l'anneau du mur de l'œil. Par contraste, l'intérieur de l'œil est libre de nuage et l'air y est en subsidence lente (∼5–10 cm/s). De même, à quelques centaines de km du centre du cyclone, l'air est en subsidence marquée et empêche la formation des cumulus d'alizés. Quelques heures avant l'arrivée du cyclone, il est donc fréquent d'observer un ciel parfaitement bleu : le fameux calme avant la tempête.

L'organisation tri–dimensionnelle de la circulation des vents au sein du cyclone que nous venons brièvement de décrire est schématisée sur la figure 1.6.

Extrait de [Beucher 2010]

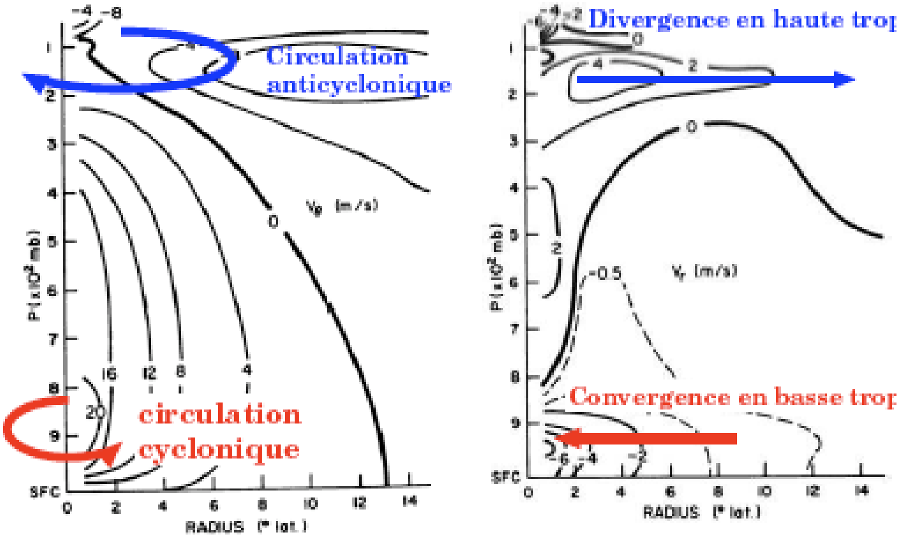

Figure 1.5 – Coupe verticale-radiale du vent dans un cyclone. Les composantes tangentielle (*à gauche*) et radiale (*à droite*) de la force du vent sont indiquées en m/s.

Extrait de [Gray & Emanuel 2010]

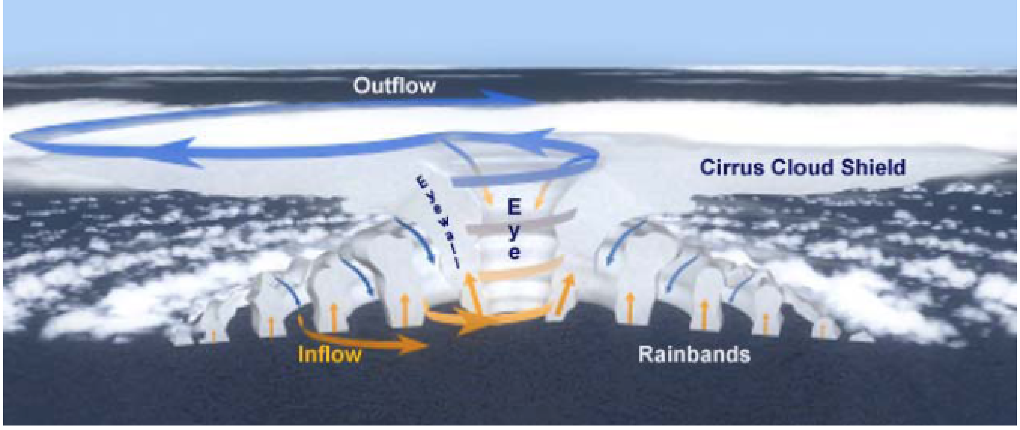

Figure 1.6 – Représentation schématique de la circulation tri–dimensionnelle dans un cyclone vu en coupe.

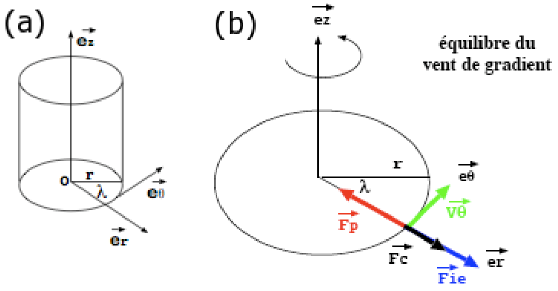

Figure 1.7 – (**a**) Repère cylindrique, (**b**) Equilibre des forces définissant le vent gradient. Cet équilibre est vérifié à l'extérieur du mur de l'œil.

Extrait de [Beucher 2010]

• Equilibre dynamique

Circulation primaire La composante axisymétrique des vents (circulation primaire) résulte d'un équilibre entre les forces de pression, de Coriolis et la force centrifuge qualifié d'équilibre du vent gradient (Fig. 1.7). En l'absence de frottements (au sommet de la CLA), l'évolution du vent radial (V_r) s'exprime :

$$\frac{\partial V_r}{\partial t} = \frac{V_\theta^2}{r} + fV_\theta - \frac{1}{\rho_a}\frac{\partial p}{\partial r} \tag{1.1}$$

donnant le champ de vent tangentiel $V_\theta(r)$ en état stationnaire où p est la pression, r la distance au centre du TC et ρ_a la masse volumique de l'air. Dans le mur de l'œil, la force de Coriolis f devient négligeable devant les autres termes et le gradient de pression est alors équilibré par la force centrifuge : on parle d'équilibre cyclostrophique où $\frac{V_\theta^2}{r} = \frac{1}{\rho_a}\frac{\partial p}{\partial r}$. Loin de l'œil, c'est la force centrifuge qui est négligeable : le mouvement des parcelles est alors régi par l'équilibre géostrophique $fV_\theta = \frac{1}{\rho_a}\frac{\partial p}{\partial r}$. Le profil de vent typique résultant est illustré sur la figure 1.8.

En première approximation, l'équilibre hydrostatique ($\partial_z p = -\rho_a g$) est vérifié hors du mur de l'œil, ce qui permet d'étendre le champ de vent sur la verticale par

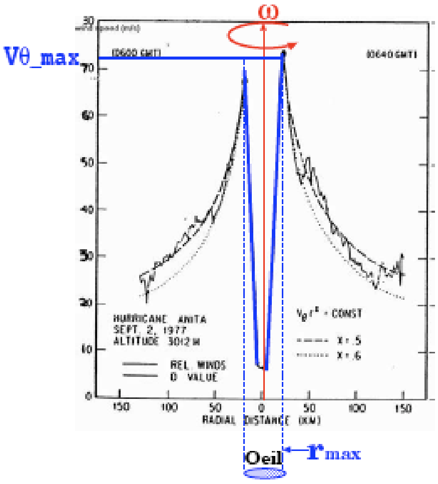

Figure 1.8 – Profil radial du vent tangentiel d'un cyclone (en m/s).

Extrait de [Beucher 2010]

l'équilibre du vent thermique qui relie les gradients verticaux de vent aux gradients horizontaux de température :

$$\left(\frac{2V}{r} + f\right) \frac{\partial V}{\partial \log(p)} = -R \frac{\partial T}{\partial r} \tag{1.2}$$

où R est la constante des gaz parfaits pour l'air et V le module du vent. Le cœur chaud du cyclone est donc associé à des vents décroissants avec l'altitude au–dessus de la CLA.

Circulation secondaire La composante radiale et verticale (circulation secondaire) se caractérise par une convergence en basses couches, un mouvement ascendant dans le mur de l'œil et une divergence en altitude (Fig. 1.5.b). Dans la CLA, la force de friction joue un rôle en plus des trois forces évoquées précédemment. Les forces de Coriolis et centrifuge ne compensent plus entièrement le gradient de pression et d'après l'équation 1.1, $\partial_t V_r \leqslant 0$ correspondant à une vitesse radiale vers le centre. Ajoutée à la rotation du vent, cette composante donne aux parcelles de fluides de la CLA des trajectoires en spirales (Fig. 1.9). L'angle que fait le vecteur vitesse avec les isobares (*inflow*) est typiquement de 15 à 20°.

• **Représentation paramétrique** Une représentation paramétrique du champ de vent de surface exprime celui–ci en fonction d'un nombre réduit de paramètres. L'avantage est de pouvoir reconstruire un champ de vent complet lorsque l'on dispose de données parcellaires. Ceci a des applications en prévision opérationnelle des TCs (en particulier pour l'évaluation des marées de tempêtes), mais aussi potentiellement en modélisation pour forcer l'océan comme nous le verrons dans le cœur de cette thèse. Deux principales représentations ont été proposées, l'une basée sur la dynamique, l'autre sur des observations aéroportées de vent dans des cyclones.

Sur la base de champs de pression observés dans des cyclones, [Holland 1980] propose d'approximer le profil radial de pression dans un cyclone par $p(r) = p_{\text{eye}} +$

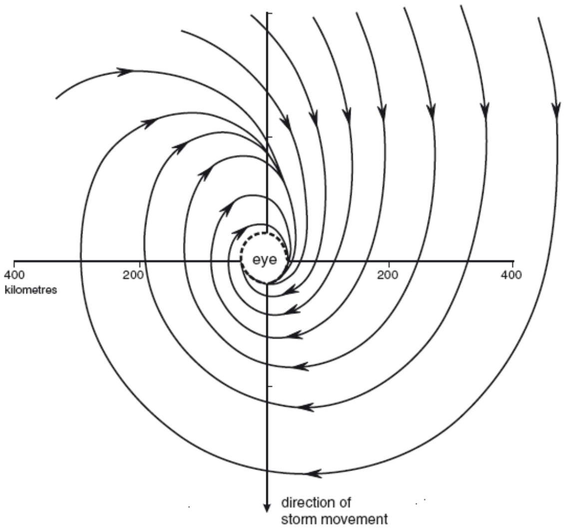

Figure 1.9 – Lignes de courant du vent de surface pour un cyclone de l'hémisphère Sud.

Extrait de [Terry 2007]

$(p_{\text{env}} - p_{\text{eye}}) \exp\left(-\left({}^{r_m}\!/_{r}\right)^b\right)$ où p_{eye} est la pression dans l'œil, p_{env} la pression dans l'environnement loin de l'œil, r_m est le rayon de vent maximum ($v_{\max}$) et b est un paramètre de forme. Connaissant le vent maximum ($v_{\max}$), l'équation du vent gradient permet d'en déduire un profil radial du module du vent :

$$V(r) = V_{\max}\sqrt{\left({}^{r_m}\!/_{r}\right)^b \exp\left(1 - \left({}^{r_m}\!/_{r}\right)^b\right)} \tag{1.3}$$

Pour reconstituer les vents de surface, on applique simplement une composante d'*inflow* de ∼15–20°.

Le vortex de Holland présente plusieurs biais importants par rapport aux observations. Il sur–estime notamment la largeur des vents maximum, sous–estime la valeur des vents très près de l'œil et induit une décroissance trop rapide des vents hors du RMW. Une nouvelle représentation paramétrique des vents basée sur un *fit* statistique à des observations aéroportées dans $sim500$ cyclones a donc été proposée par [Willoughby *et al.* 2006]. La comparaison aux observations s'avère meilleure (Fig. 1.10) mais l'inconvénient est que cette représentation paramétrique fait appel à un nombre de paramètres plus importants :

$$V(r) = \begin{cases} V_{\text{in}} = V_{\max}\left({}^{r}\!/_{r_m}\right)^n & r \leqslant R_1 \\ V_{\text{out}} = V_{\max}\left((1-A)\exp\left(-\left(\frac{r-r_m}{X_1}\right)\right) + A\exp\left(-\left(\frac{r-r_m}{X_2}\right)\right)\right) & r \geqslant R_2 \\ V_{\text{wall}} = (1-w)\,V_{\text{out}} + w\,V_{\text{in}} & R_1 \leqslant r \leqslant R_2 \end{cases} \tag{1.4}$$

où $n \sim 1$ décrit la croissance des vents dans l'œil ; les paramètres A, X_1 et X_2 définissent la décroissance des vents près et loin du mur de l'œil et w est une fonction permettant le raccord lisse entre les vents dans et hors de l'œil.

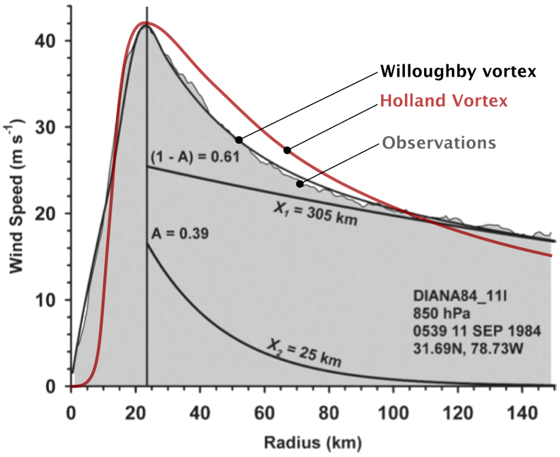

Figure 1.10 – Profil paramétrique de Willoughby (*ligne noire*) et comparaison aux observations (*surface grisée*).

Adapté de [Willoughby *et al.* 2006]

1.1.1.3 Cycle de vie

• **Genèse** La genèse d'un cyclone est définie par les centres opérationnels de prévisions lorsque les vents de surface[1] atteignent 15 m/s (soit 54 km/h ou 28 nœuds) et que le système présente un potentiel pour continuer à s'intensifier, *i.e.* que la perturbation est capable de s'auto–alimenter par les flux de chaleur qu'elle génère en surface. La cyclogenèse se définit donc par le développement d'un vortex à cœur chaud d'ampleur suffisante pour générer une convergence d'humidité alimentant la convection dans le mur de l'œil.

L'initiation d'un TC est en général précédée de la formation d'un noyau de convection concentré appelé *cluster*. En l'absence d'une concentration de la convection, la convergence de grande échelle ne peut se mettre en place. De plus, dans un système désorganisé, des régions de subsidence (*downdrafts*) se développent autour des zones d'ascendance convective, alimentant la couche de surface en air froid et limitant l'humidification de la CLA. Le *cluster* convectif permet aussi d'humidifier l'ensemble de la troposphère, ce qui est un prérequis à l'intensification du système. Lorsque le *cluster* commence à générer de forts vents de surface (> 15 m/s), on parle de dépression tropicale (TD pour *Tropical Disturbance*)[2].

Il existe plusieurs phénomènes permettant la formation d'un *cluster* : développement barocline classique, interaction d'ondes d'Est avec des perturbations tropicales de haute troposphère, fusion de plusieurs vortex cycloniques associés à des systèmes convectifs initialement séparés… Les ondes proche–équatoriales qui se propagent zonalement dans les tropiques peuvent favoriser la cyclogenèse en permettant la concentration de la convection, ou en augmentant localement la vorticité. Parmi les ondes identifiées comme précurseurs potentiels de la cyclogenèse, on peut citer : les ondes d'Est africaines (*African Easterly Waves*), les ondes de Rossby, les ondes mixtes Rossby-gravité… Enfin, en l'absence de telles ondes, des TCs peuvent

---

[1] moyenné sur 10 minute selon les règles de l'Organisation Météorologiques Mondiales

[2] selon la terminologie utilisée par Météo–France

se former par déstabilisation des zones de convergence inter–tropicales (ITCZ) qui peuvent alors se fractionner en plusieurs cyclones (Fig. 1.11).

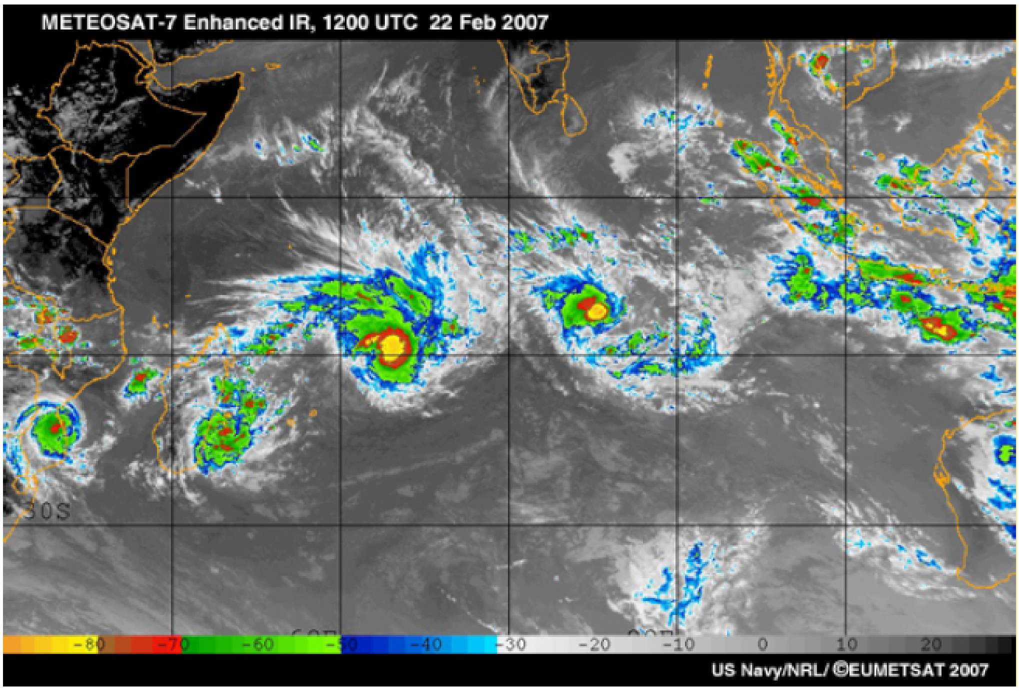

Figure 1.11 – Formation de 4 cyclones tropicaux par déstabilisation de l'ITCZ (*ITCZ breakdown*) quelques jours après le passage du cyclone DORA au cours de la très active saison cyclonique 2006–2007 dans l'Océan Indien Sud.

• **Développement** Si les conditions environnementales sont favorables, le noyau de convection peut se développer en tempête tropicale (TS pour *Tropical Storm*). A ce stade, la tempête tire son énergie de l'évaporation qu'engendrent ses propres vents (> 18 m/s), et des conditions environnementales favorables ne sont donc plus une condition nécessaire à l'intensification du cyclone. La tempête tropicale peut alors évoluer en cyclone tropical (TC pour *Tropical Cyclone*), caractérisé par une structure axisymétrique, un œil clairement défini et des vents de surface dépassant les 33 m/s. Enfin, quelques systèmes, rencontrant des conditions particulièrement favorables, s'intensifient jusqu'à devenir des cyclones tropicaux majeurs (*major hurricane* pour les américains, *super–typhoon* pour les japonais) dont les vents maximum dépassent $\sim$50 m/s.

Au cours de la vie du TC, le mur de l'œil a tendance à se contracter. Lorsqu'il atteint une taille critique de l'ordre d'une vingtaine de km, il se dissipe (le TC perd alors en intensité) et peut être remplacé par un nouvel œil qui se forme par enroulement des spirales nuageuses et qui converge à son tour vers le centre du TC.

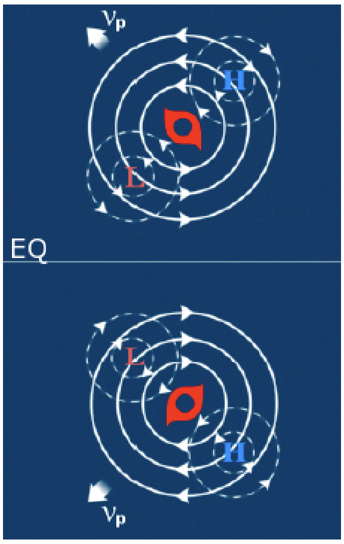

Figure 1.12 – Schéma des gyres–β crées par un cyclone dans l'hémisphère Nord ou Sud. Du fait de l'existence d'un gradient équateur–pôle de vorticité planétaire, la rotation cyclonique advecte vers le pôle un air ayant une anomalie anticyclonique du côté Est du cyclone et un air ayant une anomalie cyclonique du côté Ouest du cyclone. Le cyclone se déplace donc toujours vers l'Ouest et le pôle par rapport aux vents environnants.

• **Trajectoire** Les TCs se déplacent en général vers l'Ouest et les pôles au début de leur vie et vers l'Est et le pôle en fin de vie (Fig. 1.27b) ; deux phénomènes principaux contrôlent la trajectoire des TCs.

Les TCs sont en première approximation advectés par les vents moyens dans la troposphère libre ($\sim$850–200 hPa) qui soufflent vers l'Est entre 5° et $\sim$15° (vents alizés) et vers l'Ouest entre 30° et 50°.

En plus de cette advection par la circulation grande échelle, le cyclone se crée un mouvement propre par l'advection de vorticité planétaire de ses vents appelé l'effet–β. Les 'vents' de la gyre–β produisent un flux net au travers du centre du TC vers le Nord–Ouest en hémisphère Nord et vers le Sud–Ouest en hémisphère Sud (Fig. 1.12). Cet effet correspond à des vitesses de translation typiquement de l'ordre de quelques m/s et est donc secondaire par rapport à l'effet de l'advection.

• **Déclin** Le déclin du TC, et éventuellement sa mort, peut subvenir de différentes manières.

Si un TC se déplace sur les terres, sa source d'énergie provenant de l'océan disparaît et le système perd en intensité faute de "carburant" ; de plus la friction plus élevée que sur l'océan accélère les pertes d'énergie cinétique et participe au déclin.

La plupart des TCs finissent leur course aux moyennes latitudes (du fait de la dérive–β). La température des eaux de surface diminuant, l'évaporation n'est plus capable de fournir une énergie suffisante au TC qui s'affaiblit. Il est toutefois possible que la dépression tropicale à cœur chaud se transforme en système à cœur froid aux moyennes latitudes et que le système s'intensifie à nouveau sous forme de dépression extra–tropicale. Celle-ci peut alors générer des vents forts et des précipitations importantes comme dans le cas des ouragans Florence et Igor qui ont touché St Pierre et Miquelon en Septembre 2006 et 2010 respectivement.

Enfin, des conditions environnementales défavorables peuvent aussi être responsables du déclin d'un TC au–dessus des océans tropicaux (voir section 1.4, p 30).

1.1.2 Observations et prévisions de l'intensité des TCs

1.1.2.1 Méthodes d'observation

Les observations satellitaires sont la principale source des données existantes sur les TCs. Les conditions extrêmes et la faible densité du réseau d'observations rendent en effet difficile l'obtention de données *in situ*. Depuis les années 1970s, les satellites orbitant autour de la Terre sont en nombre suffisant pour permettre la détection de tous les TCs. Cependant la fréquence de passage des satellites défilants ne donne accès qu'à une résolution temporelle de l'ordre de la journée, et il faut attendre la fin des années 1980s (et une couverture globale par des satellites géostationnaires) pour avoir une fréquence d'observation horaire de tous les TCs à l'échelle globale. Bien que des radiomètres comme Quick-Scat donnent des informations sur les vents de surface (Fig. 1.4), ils ne permettent pas d'obtenir une mesure fiable des vents les plus intenses et n'ont une fréquence d'observation que de l'ordre de la journée (satellite défilant). Les observations dans le visible et l'infra–rouge (provenant de satellites géostationnaires) sont donc communément utilisées pour évaluer l'intensité des TCs. La technique de [Dvorak 1975] estime l'intensité d'un cyclone à partir d'interprétation de la structure des nuages. L'estimation des vents maximum en surface ($V_{\max}$) reste approximative et présente une marge d'erreur d'au moins 10% (marge d'erreur de 5–10 m/s pour des $V_{\max}$ de l'ordre de 50 m/s).

Il existe aujourd'hui de nombreuses observations complémentaires de la structure tridimensionnelle des TCs : en plus des satellites micro–ondes et des radars côtiers, des informations précises sur la structure et l'intensité des TCs sont récoltées par des mesures aéroportées qui permettent aussi de déployer des sondes de vent (*GPS drop wind sondes*) à l'intérieur du TC. Cependant les vols de reconnaissance de routine ne sont pratiqués qu'en Atlantique.

Avant l'ère satellitaire, les trajectoires de TCs contenues dans les bases de données proviennent principalement d'observations effectuées par des navires en mer et des régions côtières. [Vecchi & Knutson 2008] notent que « dans l'Atlantique, la majeure partie des TCs qui se sont développés depuis les années 1900s sont répertoriés dans les bases de données » ; la probabilité que les nombreux navires en mer ne croisent pas un cyclone donné étant faible. Cependant les données récoltées avant l'ère satellitaire sont très parcellaires et les TCs observés ne l'ont été que sur une partie restreinte de leur trajectoire. Dans tous les autres bassins, une grande partie des TCs est absente des bases de données avant les années 1970s.

La variabilité de l'activité des TCs à l'échelle globale peut donc être étudiée à partir de données d'observations directes sur une période d'environs 40 ans (1970–2010). Dans cette thèse, j'utilise la base de données IBTrACS (*International Best*

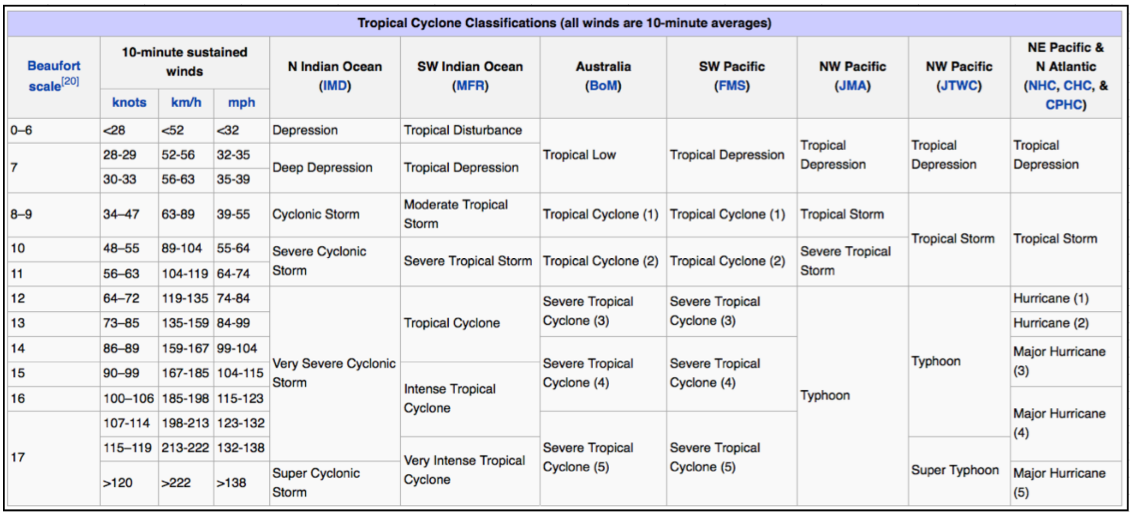

Tropical Cyclone Classifications (all winds are 10-minute averages)										
Beaufort scale[20]	10-minute sustained winds			N Indian Ocean (IMD)	SW Indian Ocean (MFR)	Australia (BoM)	SW Pacific (FMS)	NW Pacific (JMA)	NW Pacific (JTWC)	NE Pacific & N Atlantic (NHC, CHC, & CPHC)
	knots	km/h	mph							
0–6	<28	<52	<32	Depression	Tropical Disturbance	Tropical Low	Tropical Depression	Tropical Depression	Tropical Depression	Tropical Depression
7	28-29	52-56	32-35	Deep Depression	Tropical Depression					
	30-33	56-63	35-39							
8–9	34–47	63-89	39-55	Cyclonic Storm	Moderate Tropical Storm	Tropical Cyclone (1)	Tropical Cyclone (1)	Tropical Storm	Tropical Storm	Tropical Storm
10	48–55	89-104	55-64	Severe Cyclonic Storm	Severe Tropical Storm	Tropical Cyclone (2)	Tropical Cyclone (2)	Severe Tropical Storm		
11	56–63	104-119	64-74							
12	64–72	119-135	74-84	Very Severe Cyclonic Storm	Tropical Cyclone	Severe Tropical Cyclone (3)	Severe Tropical Cyclone (3)	Typhoon	Typhoon	Hurricane (1)
13	73–85	135-159	84-99							Hurricane (2)
14	86–89	159-167	99-104			Severe Tropical Cyclone (4)	Severe Tropical Cyclone (4)			Major Hurricane (3)
15	90–99	167-185	104-115		Intense Tropical Cyclone					
16	100–106	185-198	115-123							Major Hurricane (4)
17	107-114	198-213	123-132			Severe Tropical Cyclone (5)	Severe Tropical Cyclone (5)			
	115–119	213-222	132-138		Very Intense Tropical Cyclone				Super Typhoon	
	>120	>222	>138	Super Cyclonic Storm						Major Hurricane (5)

Table 1.1 – Les différentes classifications des TCs en fonction de l'intensité des vents comparées à l'échelle historique de Beaufort.

Track Archive for Climate Stewardship)[3] qui regroupent les données mondiales de trajectoires et d'intensités estimées toutes les 6 heures par les différents centres de prévisions opérationnels.

1.1.2.2 Classification des TCs

Plusieurs échelles de classification d'intensité des TCs ont été proposées dans les différents bassins (Tab. 1.1). Toutes ces classifications sont basées sur la vitesse des vents maximum mesurés à 10 m (V_{max} où max reflète un maximum spatial) ou, de manière équivalente, sur l'amplitude de la dépression dans l'œil.

L'objectif de ces échelles était à l'origine de fournir une information simple et représentative des dégâts potentiels, afin d'alerter les populations vivant sur les côtes. Cependant, il est aujourd'hui reconnu que les dégâts ne sont pas uniquement corrélés à la vitesse maximale des vents mais aussi à la taille du cyclone, à la durée de l'exposition (donc à la vitesse de translation du TC), à l'ampleur des précipitations, ainsi qu'à l'état de la mer que le TC génère. Il existe donc de nombreuses critiques sur l'utilisation de ces échelles et il semble nécessaire d'en définir de plus pertinentes. Il a par exemple été proposé d'intégrer la quantité d'énergie perdue par friction [Emanuel 2005] ou l'énergie cinétique des vents [Powell & Reinhold 2007].

1.1.2.3 Prévision opérationnelle de l'intensité des TCs

Les enjeux humains et économiques d'une prévision fiable des caractéristiques des TCs sont énormes. Au Bengladesh, par exemple, le bilan humain suite au passage du cyclone Bhola (le 12 Novembre 1970) est estimé entre 300 000 et 500 000

---

[3] description du jeu de données sur `http://www.ncdc.noaa.gov/oa/ibtracs/`

morts. Par contraste, suite au cyclone Sidr du 15 Novembre 2007, d'une intensité comparable, seules 3 000 pertes humaines ont été à déplorer, entre autres grâce à une meilleure prévision et à l'évacuation de plusieurs millions d'habitants de la côte.

Les prévisions de trajectoire et d'intensité d'un TC vont de pair. En effet, l'intensité est susceptible d'être modulée différemment selon les régions traversées par le cyclone tandis que l'effet–β est d'autant plus important que le TC est intense et grand.
Du fait de la relative simplicité des contrôles de la trajectoire d'un TC (décrits en 1.1.1.3), on est aujourd'hui capable de prévoir la position d'un TC 24h à l'avance avec une erreur de 90 km en moyenne. La prévision de la trajectoire des cyclones s'est continuellement améliorée au cours des 30 dernières années (Fig. 1.13.a) : l'erreur de prévision de position des TCs a été divisée par ∼3 en 40 ans. Par contraste, l'amélioration de la prévision de l'intensité des TCs est bien plus modeste (Fig. 1.13.b).

Il existe des méthodes de prévision d'intensité dynamique et statistiques qui ont à peu près les mêmes scores de prévisions.

Les prévisions dynamiques s'appuient sur une simulation du cyclone par des modèles de circulation atmosphérique régionaux. Le modèle est initialisé avec les variables observées (température de surface, humidité, vents...) et un précurseur de cyclone (*bogus*, noyau de vorticité cyclonique par exemple) est introduit dans l'état initial. Le modèle est alors lancé pour prévoir l'évolution future de l'état de l'atmosphère et du cyclone. C'est par exemple le cas du modèle ALADIN (modèle numérique à Aire Limitée Adaptation dynamique Développement InterNational) utilisé par Météo–France pour la prévision opérationnelle dans la région de la Réunion.

Les modèles statistiques utilisent des régressions linéaires multiples (cas de SHIPS : *Statistical Hurricane Intensity Prediction Scheme* [DeMaria & Kaplan 1994]) ou une équation logistique de croissance (cas de LGEM : Logistic Growth Equation Model [DeMaria 2009]) afin de lier l'évolution d'intensité des TCs avec les paramètres environnementaux dans lequel il se trouve.

• **Pistes pour l'amélioration des prévisions** La rétroaction de l'océan sur le cyclone figure parmi les mécanismes les plus mal représentés du contrôle de leur intensité [Marks & Shay 1998]. Une meilleure compréhension de l'interaction cyclone–océan est donc susceptible d'améliorer les prévisions opérationnelles de leur intensité.

Pour les prévisions dynamiques, cela nécessite une représentation du couplage air–mer et une modélisation explicite de l'océan à haute résolution, une solution particulièrement coûteuse.

Pour les modèles statistiques, il s'agit d'identifier les mécanismes par lesquels l'océan influe sur l'intensité d'un TC et d'intégrer des variables pertinentes comme prédicteurs supplémentaires. La prise en compte du contenu thermique océanique (OHC pour *Ocean Heat Content*) dans le modèle SHIPS a permis une modeste amé-

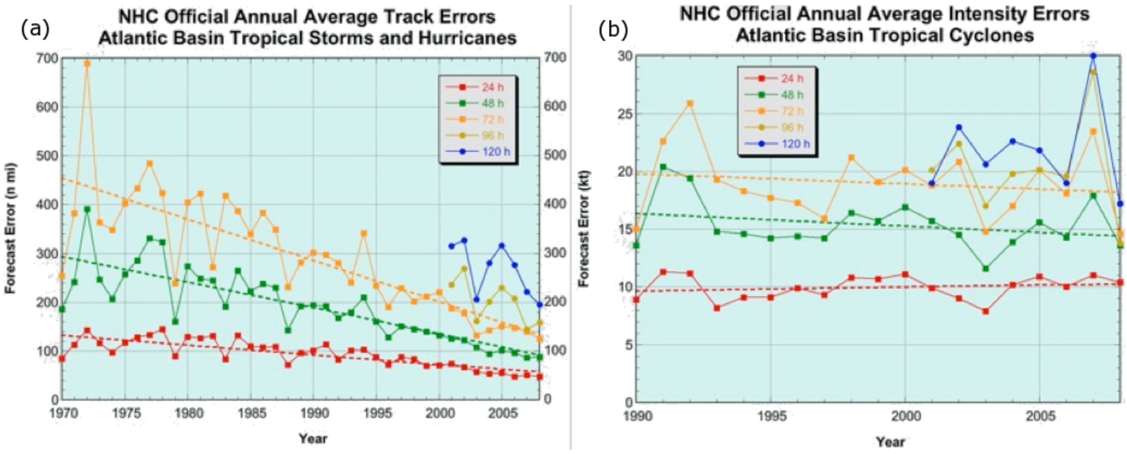

Figure 1.13 – Evolution de l'erreur de prévision (**a**) de la position (en miles nautiques) et (**b**) de l'intensité (en nœuds) des TCs de l'Atlantique concernant la prévision opérationnelle officielle du *National Hurricane Center* aux Etats–Unis.

lioration des prévisions d'intensité (environ 5% pour quelques cas de cyclones forts). Cependant l'OHC n'est pas la variable océanique qui se corrèle le mieux à l'évolution d'intensité d'un TC. Le contenu thermique de la couche mélangée semble un meilleur indicateur selon [Goni *et al.* 2009]. D'autre part, [Cione & Uhlhorn 2003] ont souligné que la température de l'océan sous l'œil du cyclone est d'une importance cruciale pour déterminer les flux de chaleur latente nourrissant le cyclone, Il faudrait donc mesurer cette température, ou bien, la prévoir.

Mieux identifier et quantifier le rôle de l'océan dans l'évolution d'un TC reste donc un enjeu majeur pour améliorer leur prévision et cela passe, entre autres, par la définition d'une métrique caractérisant l'état de l'océan et sa propension à rétroagir sur l'intensité du cyclone.

1.2 Energétique du Cyclone Tropical et Intensité Potentielle

Dans la section précédente, nous avons vu que la connaissance de ses vents maximum (ou de sa dépression centrale) suffit à décrire la force du TC au premier ordre. Cette section décrit de manière simple le fonctionnement énergétique des TCs et présente une théorie de leur intensité.

1.2.1 Théorie CISK de l'intensité potentielle

Une première théorie de l'intensité des TCs a été développée par [Miller 1958] et complétée par [Holland 1997]. Cette théorie relie l'énergie du TC à la quantité d'énergie potentielle disponible pour la convection atmosphérique (CAPE pour

Convective Available Potential Energy). La température et l'humidité en basse couche sont utilisées pour calculer le profil vertical de température (par conservation de la température pseudo–potentielle équivalente θ_e) et donc la baisse de pression hydrostatique en surface caractérisant la force du cyclone.

Cette conception est en accord avec le modèle de l'instabilité conditionnelle du deuxième type (instabilité–CISK pour *Conditionnal Instability of the Second Kind* ; [Charney & Eliassen 1964]). L'instabilité–CISK s'appuie sur une rétroaction entre anomalie grande échelle et convection locale. Une perturbation de pression initiale génère de la convergence (par friction à l'interface air–mer) qui alimente la CLA en chaleur et humidité (la CAPE augmente). Aidée par le pompage d'Ekman, la convection se met en place. La chaleur latente libérée par la convection réduit la pression dans les basses couches renforçant la perturbation initiale. Selon cette théorie, c'est donc la convergence induite par la friction des vents à la surface de l'océan qui force mécaniquement le mouvement ascendant au centre du système. Et c'est la convergence d'air chaud et humide dans la CLA qui, en augmentant la CAPE, détermine la quantité de chaleur latente qui sera libérée lors de la convection et donc l'énergie mécanique du cyclone. L'intensité du vortex ne dépend ainsi que de la convergence en basses couches et nécessite que l'atmosphère soit conditionnellement instable.

1.2.2 Théorie WISHE de l'intensité potentielle

1.2.2.1 Principe

Il existe de nombreuses observations de convection soutenue sans qu'il y ait convergence nette en basse couche et sans que la CAPE soit particulièrement élevée [Emanuel 1986]. De plus, des observations (*e.g.* [Craig & Gray 1996]) montrent que l'intensification d'un TC est plus corrélée à l'intensité des flux de chaleur mer–air qu'à celle des forces de frottement et donc à la convergence de basses couches comme le suppose la théorie CISK. [Emanuel *et al.* 1994] proposent un mécanisme de rétroaction entre la grande échelle et la convection pilotée par les flux de chaleur induits par les vents (théorie baptisée WISHE pour *Wind–Induced Surface Heat Exchange*). On parle d'instabilité–WISHE lorsque la convection s'auto–alimente en énergie thermique par l'intermédiaire des vents qu'elle génère en basse couche.

L'instabilité–WISHE suppose que l'intensité du cyclone est directement liée aux flux de chaleur extraits de l'océan. Selon ce modèle, un TC peut exister même dans une atmosphère convectivement neutre (de CAPE nulle) contrairement à ce que prévoit l'instabilité–CISK. Il est toutefois probable que les deux types d'instabilité agissent conjointement dans le développement d'une dépression tropicale.

[Emanuel 1986] base sa théorie de l'intensité des TCs sur cette approche selon laquelle l'énergie thermique (enthalpie) extraite à l'océan par les vents est convertie en énergie mécanique. Ce dernier évalue l'intensité potentielle d'un TC en effectuant un bilan énergétique de son cycle thermodynamique, considérant le TC comme un système isolé fonctionnant comme un moteur de Carnot.

1.2.2.2 Description du cycle thermodynamique

Le TC est ici décrit par sa circulation secondaire (dans le plan radial–vertical). Les hypothèses d'[Emanuel 1986] sur la nature des transformations thermodynamiques affectant les parcelles d'air lors de ce cycle de convergence-ascendance-divergence-subsidence sont décrites par analogie avec les transformations ayant lieu dans un cycle de Carnot (Fig. 1.14).

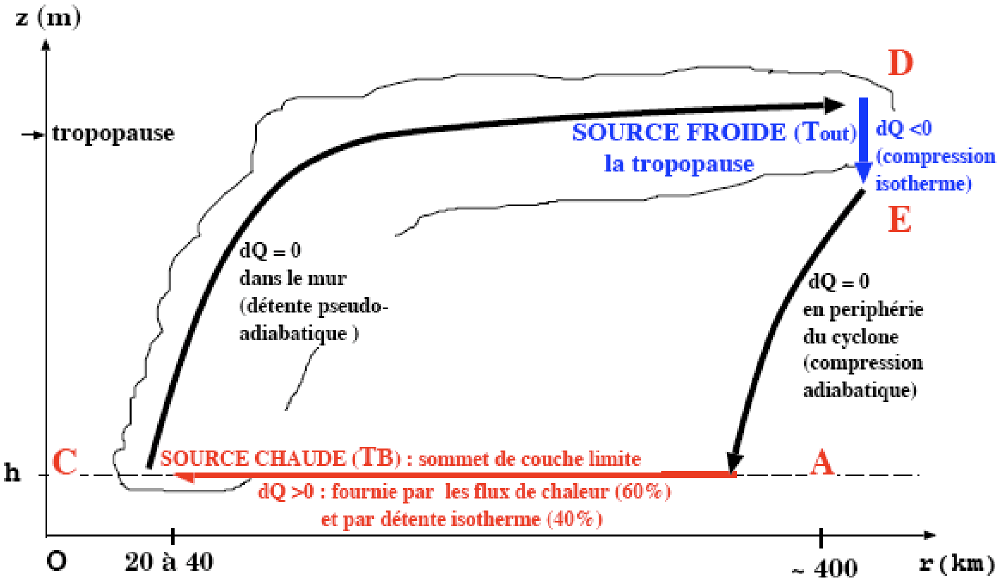

Extrait de [Beucher 2010]

Figure 1.14 – Représentation schématique du cycle thermodynamique dans un TC assimilé à un cycle de Carnot. Le sommet de la CLA (z=h) représente la source chaude du cycle ($\delta Q > 0$) et la tropopause représente la source froide ($\delta Q < 0$).

Branche A–C Lorsque l'air converge dans la CLA, il s'approche de l'œil où la pression est faible et subit une détente qui est supposée isotherme. Deux mécanismes permettent d'assurer le caractère isotherme en compensant le refroidissement dû à l'expansion adiabatique : i) les flux de chaleur sensible qui rappellent la température de l'air vers la SST et ii) la dissipation d'énergie cinétique par turbulence qui génère de la chaleur (*dissipative heating* ; [Bister & Emanuel 1998]). Au cours de la détente isotherme, l'air gagne de l'énergie au détriment de la source chaude qui est ici l'océan. L'énergie de l'air augmente aussi du fait du transfert de chaleur latente sous forme d'évaporation.

Branche C–D Au niveau du mur de l'œil, l'air entame une ascension supposée pseudo–adiabatique (θ_e conservée) et à moment angulaire M constant. L'affaiblissement des vents avec l'altitude (vent thermique) est compensé par un mouvement vers l'extérieur des parcelles pour conserver M, d'où la forme en amphithéâtre du mur de l'œil.

Branche D–E En haute troposphère, l'air diverge et subside à température constante. Sa pression augmente donc, mais le chauffage généré par la compression est compensé par une perte d'énergie par rayonnement électromagnétique vers l'espace assurant une température constante. L'énergie qu'avaient gagnée les parcelles en basse couche est perdue ici ; la tropopause peut donc être assimilée à la source froide du moteur.

Branche E–A Lorsque le chauffage par compression l'emporte sur la perte par rayonnement, on peut supposer que la descente des particules se fait le long d'une adiabatique sèche. [Emanuel 1986] a proposé de fermer le cycle en supposant une branche descendante de compression adiabatique conservant le moment angulaire même s'il est impossible de mettre en évidence cette branche dans les observations.

1.2.2.3 Intensité maximale du Cyclone

Un bilan énergétique du cycle permet de lier le travail utilisable (*i.e.* l'énergie cinétique) à l'énergie thermique fournie par la source chaude.

• **Dérivation de l'expression** Les gains et pertes d'énergie de ce cycle ont lieu principalement au niveau de l'interface air–mer. Le flux F_m de quantité de mouvement ($\rho_a V$) perdu par le cyclone s'exprime :

$$\vec{F_m} = -\rho_a C_D \, |V| \, \vec{V} \tag{1.5}$$

Le flux de chaleur F_k gagnée par le cyclone s'exprime :

$$F_k = \rho_a C_k \, |V| \, (k_S^* - k) \tag{1.6}$$

où V est le vent à 10 m, ρ_a la masse volumique de l'air ; C_D et C_k sont respectivement les coefficients adimensionnels de transfert de quantité de mouvement et d'enthalpie. Le flux de chaleur est exprimé en terme d'enthalpie ($k = C_p T + L_v q$ où C_p est la capacité calorifique de l'air, T est sa température, L_v est la chaleur de vaporisation de l'eau et q est l'humidité relative). k représente l'enthalpie massique de l'air à 10 m et k_S^* l'enthalpie de l'air en contact avec l'océan supposé saturé en vapeur d'eau à la température de surface de la mer ; c'est ce différentiel d'énergie $\Delta k = (k_S^* - k)$ qui permet le transfert de chaleur de l'océan à l'atmosphère.

En appelant T_S la température de surface de la mer et T_0 la température au sommet de la troposphère (les températures respectives des branches isothermes du cycle) ; par analogie avec le cycle de Carnot, la production nette d'énergie mécanique P du cycle s'exprime :

$$P = 2\pi \frac{T_S - T_0}{T_S} \int_A^C \left[\rho_a C_k \left| V \right| (k_S^* - k) \right] r \, dr \tag{1.7}$$

La perte nette d'énergie mécanique du cyclone est dominée par la friction à l'interface air–mer :

$$D = 2\pi \iint \rho_a C_D V^3 \, r \, dr \, d\lambda \tag{1.8}$$

En état stationnaire, production P et pertes D d'énergie mécanique sont égales, et les équations 1.7 et 1.8 permettent de donner une approximation de la vitesse maximale des vents que peut soutenir le cycle :

$$\left| V_{\max} \right|^2 = \frac{C_k}{C_D} \frac{T_S - T_0}{T_S} (k_S^* - k) \tag{1.9}$$

- **Dépendance de $V_{\max}$ à l'environnement du TC** Cette expression 1.9 souligne la dépendance intrinsèque de l'intensité du TC à son environnement atmosphérique et océanique ainsi qu'aux flux de chaleur mer–air. Elle permet de relier l'intensité à la température de l'océan de surface, la température au sommet de la troposphère et le déséquilibre thermodynamique Δk entre l'océan et l'atmosphère. L'intensité du TC est fonction du rendement du cycle de Carnot $\epsilon = \frac{T_S - T_0}{T_S}$; elle est d'autant plus importante que la différence de température entre la surface de l'océan et la tropopause est élevée.

- **Recyclage d'énergie dissipée par friction** Le travail qui est libéré par ce cycle l'est principalement sous forme de vent. Une partie de cette énergie mécanique réintègre le cycle au niveau de la branche A–C où la dissipation turbulente augmente l'énergie de l'air. [Bister & Emanuel 1998] proposent de modifier la production d'énergie dans la branche A–C pour prendre en compte ce chauffage ; l'équation 1.7 devient :

$$P = 2\pi \frac{T_S - T_0}{T_S} \int_A^C \left[\rho_a C_k \left| V \right| (k_S^* - k) + \rho C_D V^3 \right] r \, dr \tag{1.10}$$

et l'équation 1.9 s'écrit alors :

$$\left| V_{\max} \right|^2 = \frac{C_k}{C_D} \frac{T_S - T_0}{T_0} (k_S^* - k) \tag{1.11}$$

La seule différence avec l'équation 1.9 est que T_0 apparaît au dénominateur au lieu de T_S, ce qui accroit $V_{\max}$; l'efficacité du cycle est augmentée par ce recyclage d'énergie cinétique en chaleur dans la CLA.

• **Limites de la théorie WISHE de l'intensité potentielle** Le cycle thermodynamique est hautement idéalisé : i) il considère le TC comme un système fermé, ii) il est impossible de mettre en évidence la branche E–A, iii) la branche A–C (au contact de l'océan) est supposée isotherme mais ceci n'est pas supporté par les observations [Cione *et al.* 2000].

L'intensité maximale dépend du ratio des coefficients de transferts d'enthalpie et de quantité de mouvement qui sont fonction de la vitesse des vents. Leur expression exacte est mal connue aujourd'hui (plus de détails dans la section 1.3.2.1) ; on utilise communément un ratio $\frac{C_k}{C_D} = 1$.

Bien qu'approximative, l'estimation d'intensité potentielle de l'équation 1.11 permet de décrire l'intensité des cyclones, ou plutôt leur limite supérieure, comme le montre la section suivante.

1.2.3 Intensité observée versus intensité potentielle

A partir de l'équation 1.11 il est aisé de calculer la valeur de l'intensité potentielle (PI pour *Potential Intensity*) à partir de champs observés. La figure 1.15 présente la PI atteignable par un TC dans différentes régions du globe. La *Warm Pool* du Pacifique Ouest est la région où les cyclones les plus forts peuvent être soutenus, avec des vents pouvant atteindre théoriquement les 90 m/s.

Les valeurs de PI, calculées à partir de champs saisonniers sur la figure 1.15, peuvent aussi être calculées à l'aide de données quotidiennes de réanalyses. L'intensité d'un cyclone que l'on observe un jour donné peut alors être comparée à la PI théorique. La figure 1.16 compare la $V_{\max}$ observée au PI théorique pour tous les TCs du Pacifique Nord–Ouest et de l'Atlantique [Emanuel 2000]. Les cyclones n'atteignent que rarement l'intensité potentielle maximale permise par leur environnement (intensité normalisée de 1) mais ont une probabilité égale d'avoir une intensité normalisée entre 0.2 (le seuil de définition d'un TC) et 1 comme le montre la loi uniforme que suit la distribution. Cette observation peut être interprétée simplement comme le fait que les cyclones sont sous l'influence d'autres contraintes qui limitent leur intensité. Ces contraintes de l'environnement océanique et atmosphérique du TC (non prises en compte dans la théorie du PI) sont détaillées dans les sections suivantes.

1.3 Rétroaction de l'océan sur l'intensité des cyclones

1.3.1 Influence de la température de l'océan sur le cyclone

• **Température de surface** La température de surface de la mer (SST pour *Sea Surface Temperature*) de grande échelle joue un rôle important dans l'établis-

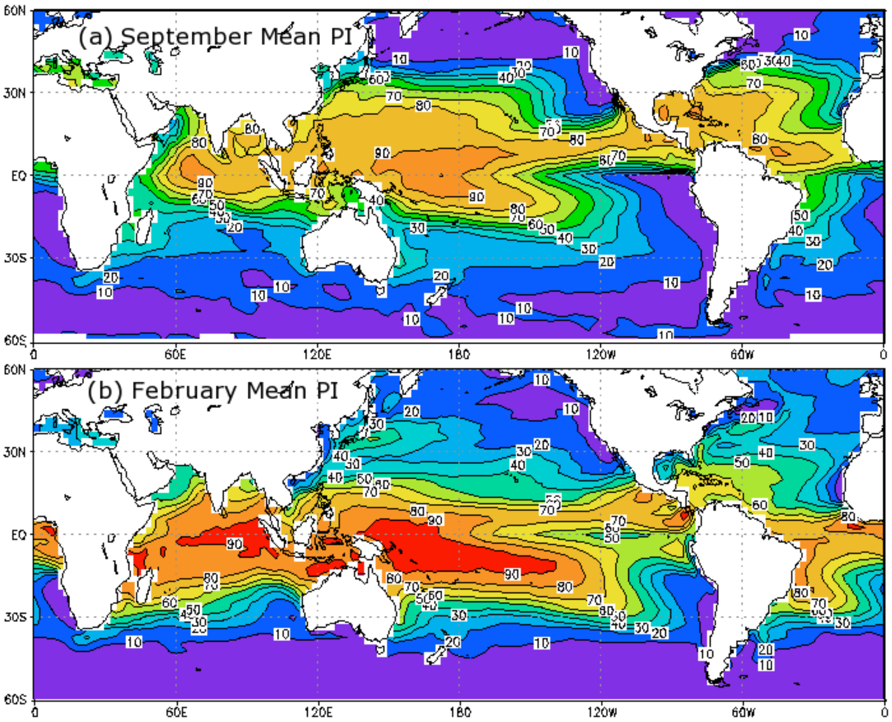

Figure 1.15 – Intensité potentielle calculée à partir de l'équation 1.11 pour les mois de (**a**) Septembre (pic de la saison cyclonique de l'hémisphère Nord) et (**b**) Février (pic de la saison cyclonique de l'hémisphère Sud). (V_{max} est ici donné en m/s moyenné sur 1 minute, un facteur 0.88 doit être appliqué pour retrouver un équivalent de vent moyenné sur 10 minute, comme dans le reste de la thèse.)

Extrait de [Emanuel 2000]

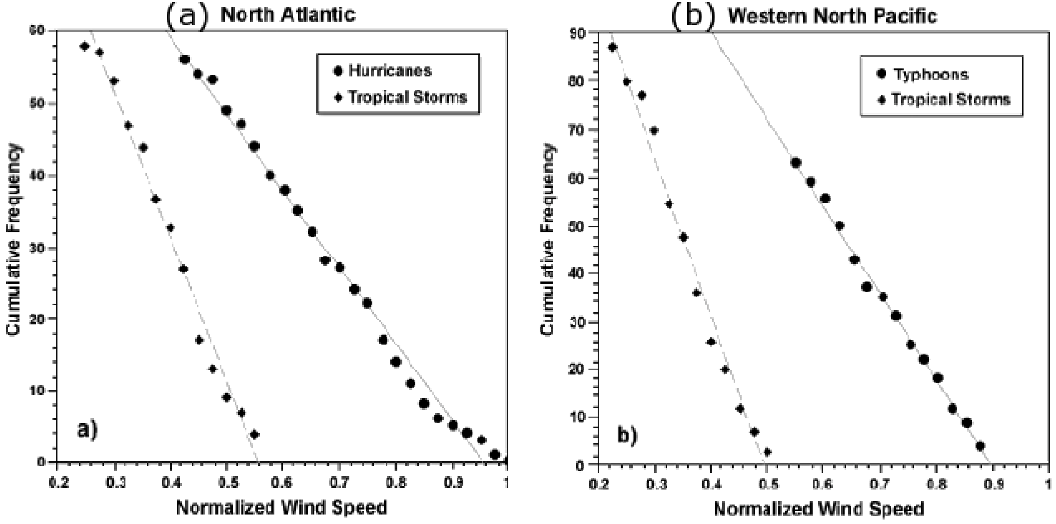

Figure 1.16 – Fonctions de densité cumulative des intensités normalisées (V_{max} observé / V_{max} potentiel) pour les cyclones (**a**) de l'Atlantique et (**b**) du Pacifique Nord–Ouest.

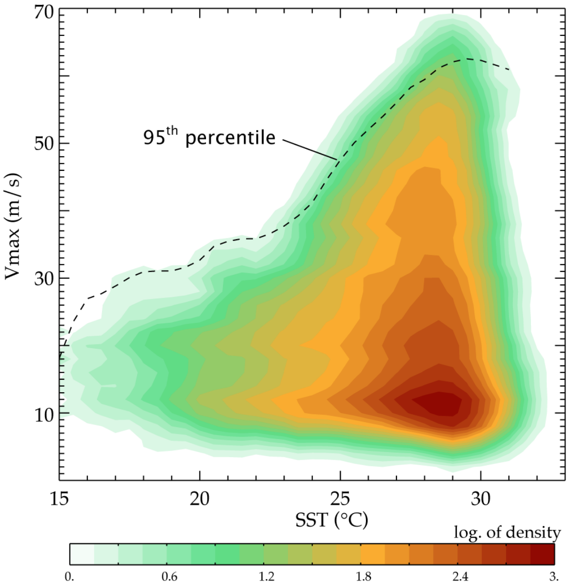

Figure 1.17 – Densité de probabilité de l'intensité des TCs (V_{max}) en fonction de la SST quelques jours avant le passage du cyclone.

sement d'un environnement favorable aux TCs. Les SSTs élevées sont notamment associées à des zones de convergence et de vorticité cyclonique des vents en basse couche et déterminent l'intensité potentielle sur de vastes régions, comme l'illustre la figure 1.15. Plus localement, la SST joue aussi un rôle déterminant en contrôlant les flux de chaleur mer–air. L'amplitude des flux de vapeur d'eau, première source d'énergie du cyclone, est fortement associée à la force des vents et est donc particulièrement élevée dans un rayon de 200 km autour du centre du TC ; on y observe des flux de chaleur latente de l'ordre de 1 000 W.m^{-2}. Les flux de chaleur sensible sont en général plus faibles, de l'ordre de 100 W.m^{-2}.

L'intensité maximale que peut atteindre un TC est une fonction croissante de la SST (Fig. 1.17) ; ce qui révèle que la PI est en fait largement déterminée par la SST.

• **Température tridimensionnelle** La SST est un prédicteur central dans les méthodes statistiques de prévision comme SHIPS [DeMaria *et al.* 2005] , mais il a été montré par [Mainelli *et al.* 2008] qu'un indicateur du contenu thermique océanique apporte une information complémentaire et permet de mieux prévoir les cyclones intenses. Depuis son introduction par [Leipper & Volgenau 1972], l'indice le plus couramment utilisé dans les études sur l'interaction cyclone–océan est le contenu thermique océanique (OHC pour *Ocean Heat Content*) défini comme OHC= $\int_0^{z_{26}} \rho\, C_p \,(T(z) - 26°\text{C})\ dz$. L'utilisation de cette variable repose sur l'hypothèse que l'énergie disponible pour le cyclone est directement reliée au contenu thermique de l'océan.

[Lin *et al.* 2008] ont montré que les cyclones les plus intenses dans le Pacifique Nord–Ouest (*SuperTyphoon*, *i.e.* TCs de catégorie 5) se sont développés sur des régions océaniques présentant un contenu thermique particulièrement élevé. Ce lien a aussi été mis en évidence dans l'Atlantique pour les cyclones Katrina et Rita (figure 1.18) : ces derniers ont en effet atteint la catégorie 5 de Saffir–Simpson au moment de leur passage sur un tourbillon chaud. La pression au cœur du cyclone est anti–corrélée à l'OHC alors que la SST est à peu près constante (Fig. 1.18.bd).

Extrait de [Shay 2010]

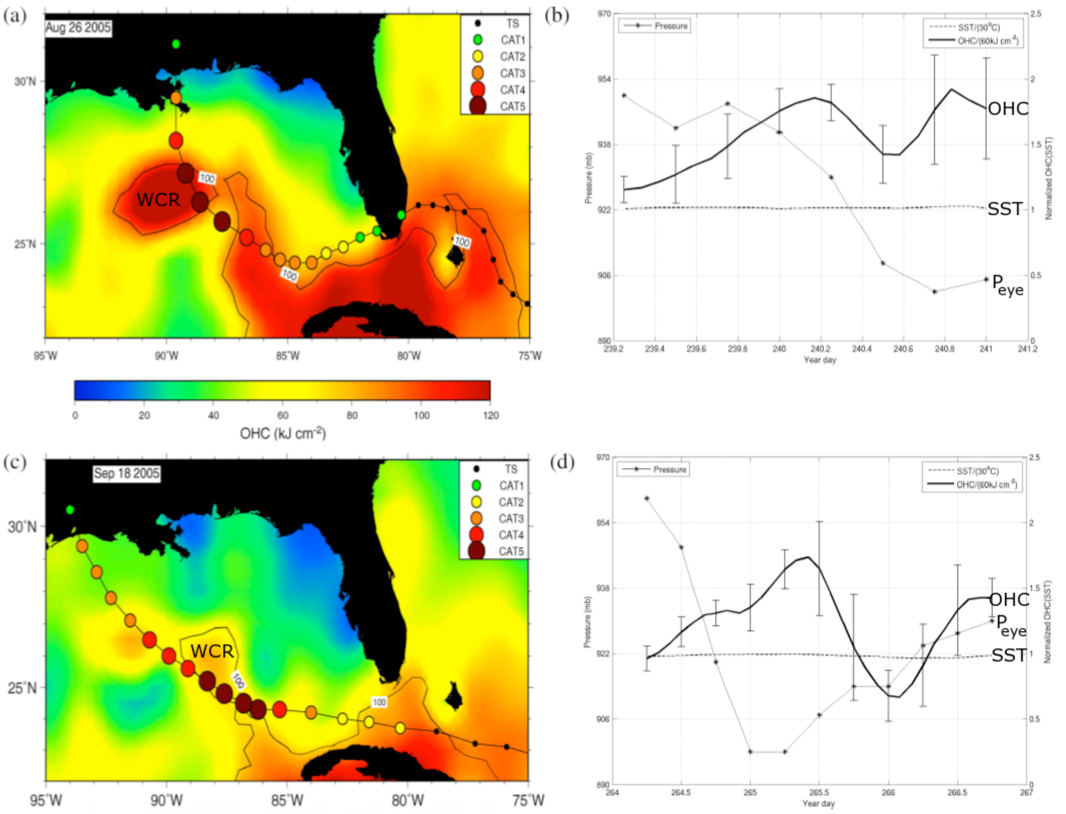

Figure 1.18 – *à gauche :* OHC pré–cyclonique et trajectoires des cyclones Katrina (**haut**) et Rita (**bas**) ; les *cercles* indiquent la catégorie de Saffir–Simpson, *WCR* (*Warm Core Ring*) indique un tourbillon chaud. *à droite :* Séries temporelles de pression dans l'œil (*ligne fine*), OHC (*ligne épaisse*) et SST (*ligne pointillé*).

Cette dépendance de l'intensité du TC à la structure tri–dimensionnelle de l'océan s'explique par l'influence de la sub-surface océanique sur l'intensité du refroidissement de surface (CW pour *Cold Wake*) associé au passage du cyclone.

1.3.2 Rétroaction de la *Cold Wake* et importance de l'océan de sub–surface

Dès les années 1960s, il a été mis en évidence que les TCs refroidissent intensément l'océan de surface, modifient la profondeur de la couche de mélange et influencent les courants océaniques jusqu'à des profondeurs de ∼200 m [Leipper 1967].

Extrait de [Shay 2010]

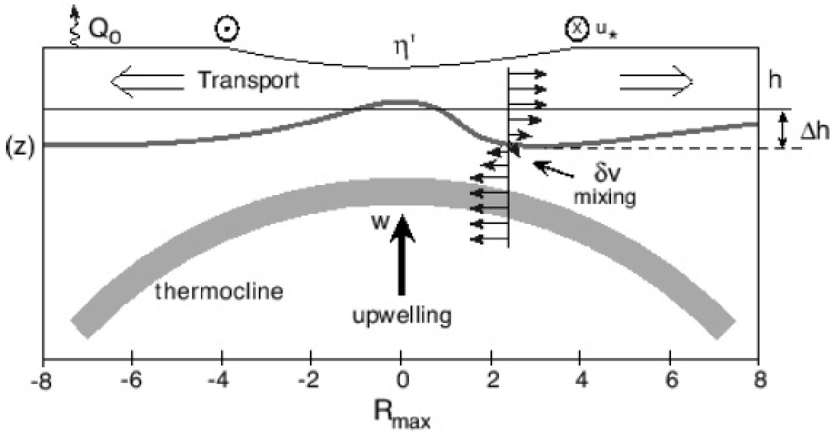

Figure 1.19 – Schéma des processus physiques affectant la température océanique lors du passage d'un TC. Q_0 représente les flux de surface, w l'upwelling et δv le cisaillement de courant à la base de la couche mélangée ; Δh est la modification de la profondeur de la couche mélangée par rapport à la profondeur initiale h.

Les vents intenses du cyclone engendrent une évaporation importante qui participe à refroidir la surface. Le forçage cyclonique engendre également une divergence du transport d'Ekman associée à une remontée d'eau froide sous le cyclone d'autant plus marquée que le cyclone se déplace lentement (Fig. 1.19). Ces deux mécanismes participent à refroidir la surface de l'océan, mais de nombreuses études suggèrent que la majeure partie du refroidissement de surface (70–80%) est associée à l'entraînement dans la couche mélangée d'eaux froides de la thermocline [Price 1981].

Cette sous–section décrit le forçage de surface (flux de chaleur et de quantité de mouvement) associé à un cyclone et détaille les conséquences des processus évoqués ci–dessus sur l'évolution des couches de surface de l'océan.

1.3.2.1 Forçage de surface

• Flux de quantité de mouvement et de chaleur Les vents du cyclone ont pour effet de créer des transferts intenses de quantité de mouvement (transfert d'énergie cinétique des vents aux vagues et aux courants de surface), ainsi que de chaleur sensible et latente (humidité) à l'interface air–mer. Les flux verticaux turbulents de quantité de mouvement et de chaleur s'expriment en fonction des corrélations entre les fluctuations turbulentes de vitesse verticale et les fluctuations turbulentes du vent horizontal, de la température et de l'humidité. Les fluctuations turbulentes de vitesse (notamment la vitesse verticale) sont difficiles à estimer expérimentalement et ne sont pas résolues par les modèles de circulation atmosphérique. Les formules aéronomiques de masse (*bulk formulas*) constituent une simplification de cette formulation et permettent de lier les flux turbulents aux profils verticaux

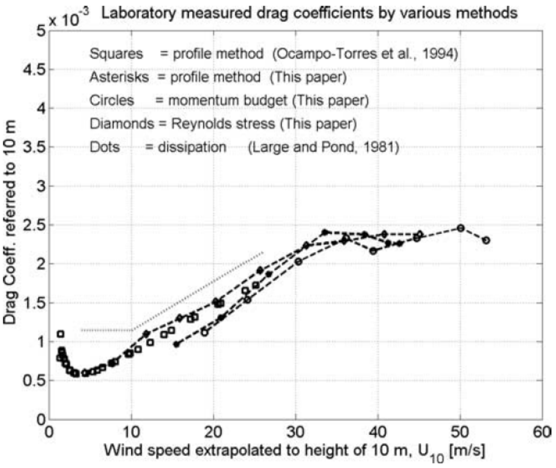

Figure 1.20 – Coefficient de transfert de quantité de mouvement en fonction de la vitesse du vent à 10 m mesuré dans une expérience de laboratoire.

Extrait de [Donelan *et al.* 2004]

de vent, température et humidité :

$$\vec{\tau} = C_D \left(\vec{V} - \vec{V_S}\right) \left(\vec{V} - \vec{v}_{oce}\right) \rho_a \tag{1.12}$$

$$F_H = C_H \left(V - V_S\right) \left(T - T_S\right) \rho_a C_p \tag{1.13}$$

$$F_{LE} = C_E \left(V - V_S\right) \left(q - q_S\right) \rho_a L_v \tag{1.14}$$

où C_D, C_H et C_E sont les coefficients de transfert de quantité de mouvement, de température et d'humidité respectivement.

Ces coefficients de transferts ne sont pas des constantes. C_D augmente avec l'intensité du vent ; l'état de la mer (vagues) permettant un meilleur transfert d'énergie aux vents forts. Il y a peu de mesures directes permettant d'estimer ces coefficients pour des vents supérieurs à $\sim$30 m/s (le seuil de vents définissant un TC). Quelques études montrent que ce coefficient de transfert sature au–delà de cette limite (Fig. 1.20 ; [Black *et al.* 2007] ; [Donelan *et al.* 2004]). Cette saturation est probablement liée au déferlement du champ de vague qui détériore le transfert d'énergie cinétique des vents aux courants.

Alors que les flux de chaleur fournissent au cyclone de l'énergie extraite de l'océan, les flux de quantité de mouvement constituent une perte d'énergie pour le cyclone. Une meilleure connaissance de ces flux, et des coefficients de transferts associés, est donc cruciale pour mieux appréhender l'énergétique d'un cyclone. Avant sa mise en évidence expérimentale, [Emanuel 1995] avait suggéré que la saturation de C_D était nécessaire pour expliquer l'existence des TCs intenses. En effet, si C_D n'était pas borné aux vents forts, les TCs perdraient trop d'énergie cinétique par friction à l'interface air–mer et ne pourraient s'intensifier.

Dans le cas des cyclones, on regroupe souvent les flux de chaleur sensible et latent dans le terme d'enthalpie (k). Le modèle d'Emanuel implique que le ratio entre C_k et C_D (contraignant le rapport énergie gagnée / énergie perdue par le cyclone) soit compris entre 0.75 et 1.5 et devienne constant aux vents forts. Les mesures les plus récentes [Zhang 2007] montrent que le ratio devient effectivement

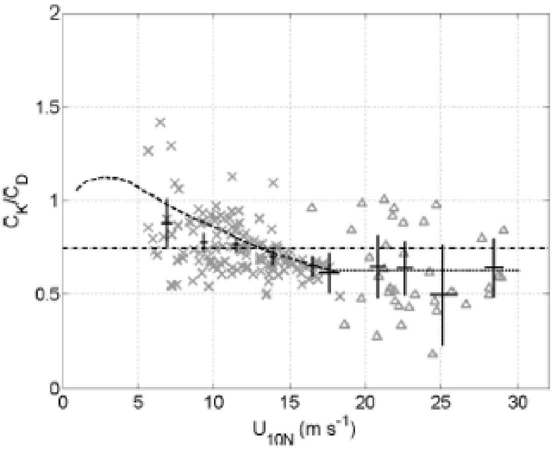

Figure 1.21 – Ratio des coefficients de transfert d'enthalpie C_k et de quantité de mouvement C_D déterminé par des mesures aéroportées dans un cyclone.

Extrait de [Zhang 2007]

constant au–delà de ∼15 m/s (Fig. 1.21), mais se stabilise autour d'une valeur de 0.7, en deçà de la suggestion d'Emanuel.

A noter que l'utilisation d'un unique coefficient de transfert de chaleur C_k est sujet à critiques ; en effet, le coefficient n'est pas uniquement fonction du vent mais dépend aussi de la température [Andreas 2011]. De même, on utilise généralement une seule fonction du vent pour C_D alors que le transfert d'énergie cinétique varie aussi en fonction de l'orientation relative du vent et des vagues et donc potentiellement de la position par rapport au centre du cyclone.

• **Précipitation** Les TCs sont associés à des précipitations intenses (∼0,3 m en cumulé) près de l'œil. On s'attend à ce que ce flux d'eau douce (de flottabilité élevée) en surface stabilise la colonne d'eau et inhibe le mélange. [Jacob & Koblinsky 2007] montrent cependant que cet effet est négligeable sur la modification de la SST par le cyclone.

Si les précipitations cycloniques ont un effet négligeable sur la dynamique, leur effet sur l'évolution de la salinité de surface est potentiellement important. Les données du satellite SMOS devraient permettre d'observer une modification de salinité dans le sillage des cyclones, mais il n'existe pas d'étude sur ce sujet à ce jour.

• **Dépression atmosphérique** La dépression de ∼50–100 hPa dans l'œil du cyclone induit une élévation du niveau de la mer de 0,5–1 m par simple effet du baromètre inverse. Cet effet est très important pour déterminer l'impact des cyclones et participe aux inondations côtières. L'invasion des terres par l'eau de mer s'explique aussi par les vents qui poussent l'eau vers les terres (*wind surge*) au moment de "l'atterrissage" (*landfall*).

L'élévation du niveau de la mer sous le cyclone induit aussi une circulation géostrophique barotrope, mais ce point a reçu peu d'attention à ce jour.

1.3.2.2 Réponse dynamique de l'océan

Les vents transfèrent de l'énergie aux vagues et au courant. Le déferlement des vagues fournit de l'énergie cinétique turbulente (ECT) en surface et les cisaillements verticaux de courants créent des instabilités qui fournissent de l'ECT à l'intérieur de l'océan. La majeure partie de l'énergie transmise à l'océan par les vents cycloniques fini donc sous forme de turbulence donc une partie est dissipée sous forme de chaleur à l'échelle moléculaire et une partie participe à homogénéiser verticalement l'océan.

• **Oscillations proche–inertielles** Le vent de surface représente une source majeure d'énergie cinétique pour l'océan. Lorsqu'un courant de surface est initié, il se met à osciller sous l'effet des forces de Coriolis et de gravité en un mouvement appelé inertiel.

Observations Plusieurs profileurs autonomes ont été déployés par avion avant le passage du cyclone Frances (SS-cat 4) en Septembre 2004 [Sanford *et al.* 2007]. Par des aller–retour entre la surface et 200 m de profondeur, ces bouées donnent des informations détaillées sur les profils verticaux de température, de salinité et de courants. Dans le sillage du cyclone, des oscillations de courant d'amplitude ∼1 m/s sont observées pendant plusieurs jours (Fig. 1.22.cd). Ces oscillations sont associées à d'importants cisaillements verticaux ($S = |\partial_z \vec{v}|$) pouvant conduire à un état instable du profil pendant plusieurs périodes d'inerties (IP pour *Inertial Period*). Le mélange vertical survient quand le cisaillement devient suffisamment important par rapport à la stabilité de la stratification (*i.e.* quand le cisaillement réduit est positif $S^2 - 4N^2 > 0$ où N^2 est la fréquence de Brunt–Väisälä). La figure 1.22.e montre que le critère d'instabilité est atteint au moment du passage du cyclone, la couche mélangée (ML pour *Mixed Layer*) s'approfondit. La salinité finale de la ML (∼36.6 PSU) résulte du mélange des eaux peu salées de surface (∼36 PSU) et des eaux plus salées de la thermocline (∼37 PSU) (Fig. 1.22.b). Le mélange refroidit aussi la couche de surface de ∼2°C et réchauffe la sub–surface (+1°C à 100m de profondeur par exemple) (Fig. 1.22.a).

Propagation verticale Les oscillations de courants horizontaux sont associées à des divergences/convergences et donc à des mouvements verticaux. Lors du passage d'un cyclone, une divergence est observée pendant la première moitié du cycle inertiel (1/2 IP), créant un *upwelling* sous l'œil du TC. Pendant la deuxième moitié de la première période d'inertie, les courants s'inversent et convergent pour engendrer un *downwelling*. Les oscillations de la thermocline, et les variations des gradients de pression associés, forcent des ondes de gravité à une fréquence proche de la fréquence inertielle. Ces ondes permettent une propagation vers le bas de l'énergie (en grande partie de l'énergie cinétique) et sont des sources de mouvements proche-inertiels dans l'océan profond. Elles peuvent induire du mélange diapycnal dans les

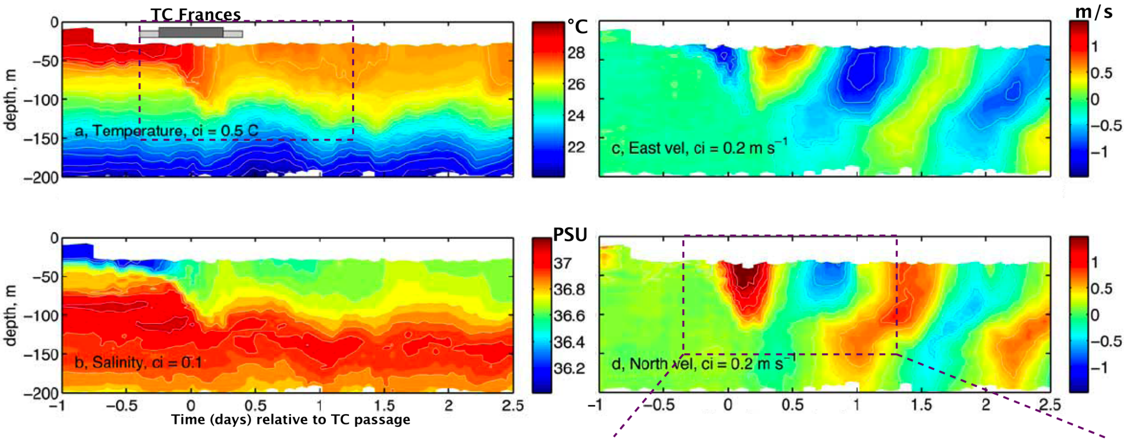

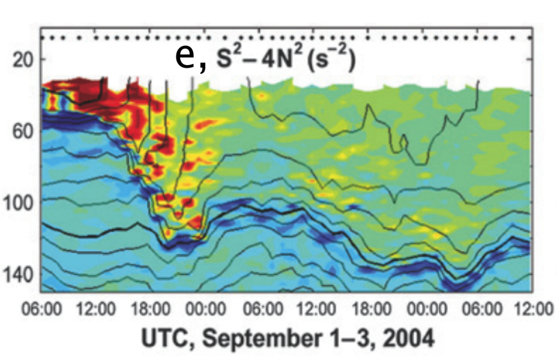

Figure 1.22 –
Observations *in situ* à 55 km à droite de la trajectoire du TC Frances des (**a**) Température, (**b**) Salinité, (**c**) courant zonal, (**d**) courant méridien et (**e**) cisaillement réduit.

Extrait de [Sanford *et al.* 2007]

zones de faible stratification ou en interagissant avec la bathymétrie. Les sites de dissipation de cette énergie injectée dans l'océan profond sous forme d'ondes interne par les cyclones sont encore mal connues.

Résonance En un point donné de l'océan, les vents cycloniques ont une amplitude et une direction qui varie au cours du temps en fonction du déplacement du TC. Selon le côté de la trajectoire où le point considéré se trouve, le sens de rotation local des vents de surface est inversé (Fig. 1.23). Pour un cyclone de l'hémisphère Nord, la rotation des vents est anti–cyclonique à droite de la trajectoire et cyclonique à gauche (l'inverse en hémisphère Sud). Les courants inertiels libres sont caractérisés par une rotation dans le sens anti–cyclonique. Les vents restent donc potentiellement plus alignés avec les courants inertiels du côté droit ce qui permet un transfert d'énergie optimal : c'est la résonance [Samson *et al.* 2009]. Les courants étant plus intenses du côté inertiel, le mélange vertical y est accru ; ce qui explique la fameuse asymétrie du refroidissement induit par le cyclone [Price 1981]. Le refroidissement observé dans le sillage d'un cyclone est en effet maximal à gauche de la trajectoire (dans l'hémisphère Sud) (Fig. 1.24).

Du fait de la dimension spatiale et de la vitesse de translation typique des TCs, la rotation des vents en un point d'océan se fait souvent avec une fréquence proche–inertielle. Les TCs sont donc de bonnes sources de courants inertiels ; cependant, quand le cyclone est très rapide ou très lent, ces ondes sont moins excitées.

Extrait de [Samson 2009]

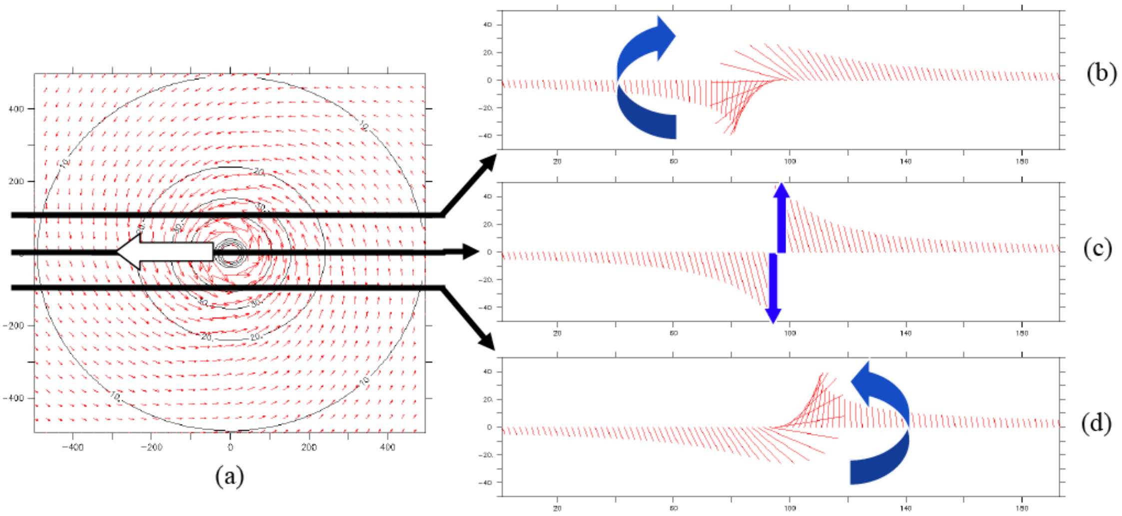

Figure 1.23 – Vent de surface d'un cyclone idéalisé de l'hémisphère Nord (**a**) et séries temporelles du vent vu en différents points fixes de l'océan : (**b**) à droite, (**c**) au centre et (**d**) à gauche de la trajectoire. Les *flèches bleues* soulignent le sens de rotation : anticyclonique à droite de la trajectoire et cyclonique à gauche.

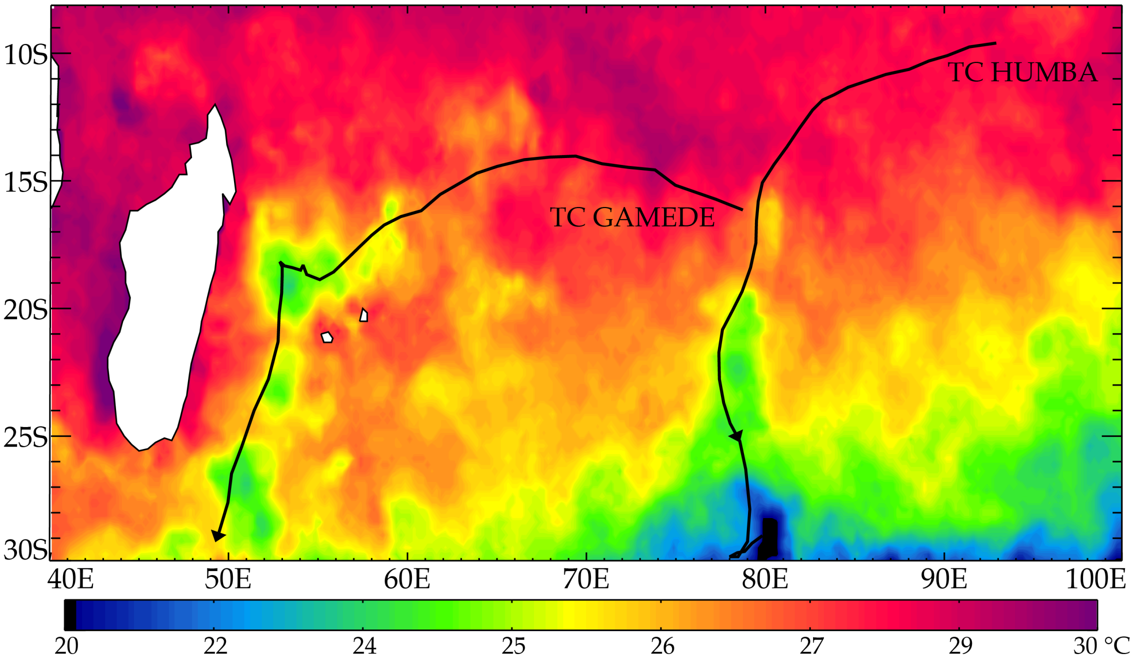

Figure 1.24 – Température de surface de la mer vue par satellite (TMI-AMSRe) lors du passage des TCs Gamede et Humba (au 05 Mars 2007). L'anomalie de température atteint $\sim -5°$C avec une valeur maximale à gauche de la trajectoire (les TCs se déplacent vers le Sud).

Figure 1.25 – Pompage d'Ekman intégré (du 25 Janvier au 14 Février 2007) induit par le cyclone DORA. La figure est obtenue en échantillonnant le forçage du cyclone reproduit avec le vortex de Willoughby sur une grille au 12^{e} de degré et en calculant analytiquement le pompage.

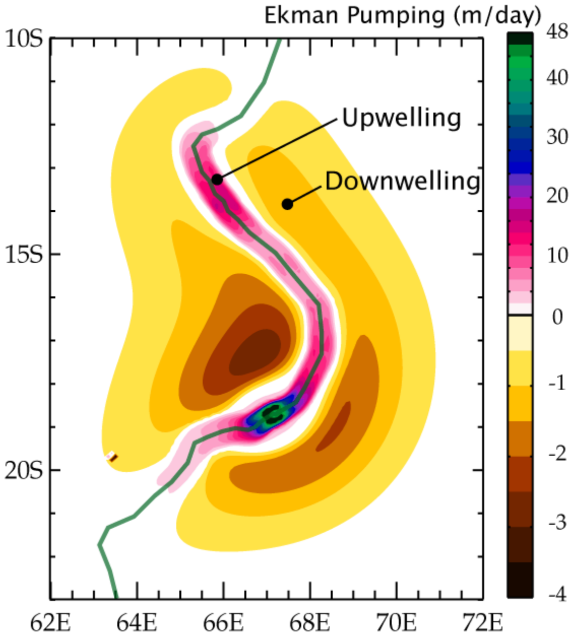

• **Courants d'Ekman** Lorsqu'un vent souffle en surface, une couche limite se crée dans l'océan ; sa profondeur augmente avec la force du vent. Sous l'effet des forces de Coriolis et de friction, les courants dans cette couche forment une spirale dont l'amplitude décroît exponentiellement avec la profondeur. Le cisaillement des courants de la spirale d'Ekman est une source majeure de mélange vertical induit par les TCs. La profondeur de la couche d'Ekman est de ∼30 à 300 m typiquement, mais la décroissance exponentielle fait que l'énergie cinétique disponible pour le mélange est maximale près de la surface.

L'effet refroidissant du mélange dépend de manière cruciale de la stratification thermique de l'océan. Une spirale d'Ekman dans une couche de température homogène n'a aucun effet sur le refroidissement de surface ; par contre s'il y a une forte stratification en sub–surface, des eaux de températures différentes peuvent être mélangées. Les mouvements verticaux sous le cyclone sont importants pour modifier la stratification de l'océan. Un *upwelling*, par exemple, augmente les gradient verticaux de température ; il affine aussi la ML et diminue donc sa capacité thermique (le changement de température sera plus important pour un forçage donné). Sous un cyclone, l'intégrale des courants d'Ekman sur la verticale donne un transport divergent, associé à un *upwelling*.

Les mouvements inertiels participent à modifier la stratification thermique mais ils ne créent pas de mouvement vertical net une fois le cyclone passé. Par contre, la composante d'Ekman du courant laisse dans le sillage du cyclone une région d'*upwelling* net le long de la trajectoire du TC (dans un rayon de 1 RMW) et un *downwelling* net au–delà (Fig. 1.25).

1.3.2.3 Importance de la CW pour le TC

L'intensité du cyclone dépend de modifications de la température de surface surtout par le biais du flux de chaleur Δk (équation 1.11). Avant le passage du cyclone, le déséquilibre énergétique entre la mer et l'air permet le transfert de chaleur de l'océan vers l'atmosphère ; le refroidissement induit par le cyclone peut détruire ce déséquilibre énergétique et ainsi empêcher les flux de chaleur de fournir de l'énergie au cyclone. [Emanuel 1999] montre qu'une réduction de SST de 2.5°C suffit à annuler Δk. Si un tel refroidissement se produit sous l'œil du cyclone (où les flux de chaleur sont maximum), le cyclone décline rapidement. On comprend ici que la connaissance du refroidissement sous l'œil induit par le cyclone apporte une information supplémentaire à la connaissance de la SST. Afin d'améliorer les prévisions d'intensité des cyclones, je pense qu'il ne suffit pas de remplacer la SST pré–cyclonique par la SST sous l'œil mais de prendre en compte les deux informations : la SST pré–cyclonique (ou la SST sous l'œil) comme déterminant du rendement du moteur de Carnot et le ΔSST comme altération du déséquilibre Δk par rapport à l'état non–perturbé.

Prévoir l'intensification d'un cyclone nécessite donc de prévoir le ΔSST qu'il engendre. Les paragraphes précédents ont illustré que le processus dominant ce refroidissement est le mélange vertical qui dépend largement de la stratification thermique de l'océan. Malgré l'importance cruciale qu'a le refroidissement induit par le cyclone sur sa propre intensité, la dépendance de son amplitude aux caractéristiques du cyclone et de l'océan de sub–surface est trop peu connue.

1.4 Influence de l'environnement sur l'activité cyclonique

La section précédente a illustré de manière détaillée comment les caractéristiques de l'océan peuvent influencer l'intensité d'un TC. Les autres caractéristiques environnementales connues pour contraindre l'intensité des TCs sont présentées dans cette section.

1.4.1 Les paramètres environnementaux de grande échelle influençant le cyclone

1.4.1.1 Les conditions nécessaires à la cyclogenèse

Bien qu'il n'existe à ce jour aucune théorie physique décrivant (et permettant de prédire) la cyclogenèse, les conditions nécessaires à la formation d'un TC sont connues depuis plusieurs décennies. Selon [Gray 1968], la cyclogenèse se produit quand les conditions suivantes sont réunies :

i une température de la mer dépassant 26°C sur les 60 premiers mètres de l'océan ;
ii une humidité relative élevée en milieu de troposphère (∼700 hPa) ;
iii une atmosphère instable pour la convection (instabilité conditionnelle) ;
iv un faible cisaillement vertical des vents horizontaux dans la troposphère ;
v une vorticité fortement cyclonique des vents en basses couches.

Les 2 derniers critères décrivent les aspects dynamiques favorables à la cyclogenèse alors que les 3 premiers sont de nature thermodynamique : ils mesurent la capacité de l'océan et de l'atmosphère à soutenir la convection profonde.

Ces conditions sont nécessaires mais non suffisantes pour la cyclogenèse et ne permettent donc pas de prédire le développement d'un TC. Il existe un large consensus sur leur caractère nécessaire à l'exception du point (iii) car la convection est possible même dans une atmosphère convectivement neutre [Emanuel 1986]. Outre ces conditions, la force de Coriolis doit être suffisamment forte, d'où le fait que l'on n'observe pas de TCs à moins de 5° de l'équateur (à quelques exceptions près, les *midget* : TCs de petite taille).

La divergence en haute troposphère est également essentielle car elle permet d'entretenir la basse pression de surface en exportant de la masse hors de la colonne centrale.

1.4.1.2 Mécanismes de l'influence des paramètres environnementaux

Ce paragraphe illustre comment les paramètres environnementaux influencent la cyclogènese à partir de deux exemples : la vorticité et le cisaillement.

• **Cisaillement** Nous avons vu en 1.1.1.3 qu'un pré–requis au développement d'un cyclone est la formation d'une colonne d'air presque saturée d'une dimension de l'ordre de ∼100 km de diamètre de sorte que la convection qui s'y produit exclue en son sein les subsidences d'air froid (*downdrafts*). Tout mécanisme prévenant la formation d'une telle colonne va donc empêcher la cyclogenèse. C'est le cas, par exemple, du cisaillement de vent qui apporte de l'air froid et sec depuis la haute troposphère jusqu'en milieu de troposphère par mélange (phénomène de ventilation). Outre l'apport d'air de haute altitude, le cisaillement déforme la structure barotrope du TC et déconnecte la convergence de basse couche de la divergence d'altitude [Pielke & Pielke Jr 1997]. Au–dessus de l'océan, l'arrivée de cyclones dans une région de fort cisaillement explique souvent leur déclin.

• **Vorticité** Une vorticité absolue cyclonique en basse couche permet de concentrer le chauffage convectif en réduisant le rayon de déformation de Rossby local $L_R = {}^{HN}/_{(\zeta+f)}$ (où H est la hauteur du système convectif, N la fréquence de Brunt–Väisäla, ζ la vorticité relative et f le paramètre de Coriolis). Si la dimension spatiale L d'une perturbation de convection est plus grande que $2\pi L_R$, cette dernière peut être ajustée par équilibre géostrophique et persister, sinon elle se dissipe. $L_R \sim 10^4$ km dans l'atmosphère tropicale si la vorticité relative est nulle ; il est difficile de créer une perturbation d'une telle taille. Une vorticité cyclonique (du même signe que f) importante, peut diminuer suffisamment L_R (donc la dimension requise) ; la perturbation peut alors être ajustée et perdurer pendant plusieurs jours.

1.4.2 Indices de cyclogenèse

Afin d'améliorer la compréhension de l'influence des variables grande–échelle sur la cyclogenèse et sa variabilité, des indices réunissant toutes les variables en un seul indicateur ont été développés. Bien qu'ils ne permettent pas d'expliquer le nombre de genèse de cyclones, ils sont utiles pour expliquer qualitativement la saisonnalité de l'activité cyclonique et dans une certaine mesure sa variabilité interannuelle.
Les 4 principaux indices utilisés sont décrits ci-après :

- **Indice YGP (*Yearly Genesis Potential*)** Le premier indice de cyclogenèse (YGP) a été développé par [Gray 1968] afin d'expliquer la distribution spatiale de la cyclogenèse à l'échelle annuelle et saisonnière. La définition du YGP reprend les conditions classiques nécessaires à la cyclogenèse décrites au paragraphe 1.4.1.1. Le calcul est un simple produit des paramètres dynamiques (vorticité I_ζ, cisaillement I_S) et thermodynamique (OHC noté E, instabilité convective I_θ et humidité en milieu de troposphère I_{RH}) :

$$\mathrm{YGP} = \underbrace{|f|\, I_\zeta\, I_S}_{dynamic}\; \underbrace{E\, I_\theta\, I_{\mathrm{RH}}}_{thermal} \tag{1.15}$$

avec f le paramètre de Coriolis, $I_\zeta = \left(\zeta_r \frac{f}{|f|} + 5\right)$ où ζ_r est la vorticité relative à 925 hPa, $I_S = \left(\left|\frac{\delta V}{\delta P}\right| + 3\right)^{-1}$ où $\frac{\delta V}{\delta P}$ est le cisaillement de vent entre 925 hPa et 200 hPa, $E = \int_0^{60m} \rho\, C_p\, (T - 26)\, dz$ est l'OHC dans les 60 premiers mètres d'océan, $I_\theta = \left(\left|\frac{\delta \theta_e}{\delta P}\right| + 5\right)$ mesure l'instabilité convective et $I_{\mathrm{RH}} = \max\left(\min\left(\frac{\mathrm{RH}-40}{30}\right), 0\right)$ mesure l'humidité relative entre 700 hPa et 500 hPa.

- **Indice CYGP (*Convective Yearly Genesis Potential*)** Afin de pouvoir utiliser l'indice de Gray dans des simulations de changement climatique, il est nécessaire de s'affranchir des seuils parfois utilisés dans les termes composant les indices (comme le seuil à 26°C dans l'OHC). [Royer *et al.* 1998] proposent une simplification de l'indice YGP en remplaçant la partie thermodynamique de l'indice par les précipitations convectives (censées constituer une grandeur intégrée du terme thermodynamique), cet indice n'inclue donc plus directement de mesure océanique :

$$\mathrm{CYGP} = \underbrace{|f|\, I_\zeta\, I_S}_{dynamic}\; \underbrace{\kappa\, (P_c - P_0)}_{thermal} \tag{1.16}$$

où κ est une constante arbitraire permettant d'ajuster le nombre de genèse au modèle considéré, P_c le terme de précipitation convective et P_0 un seuil de précipitation dépendant du modèle considéré.

• **Indice GPI (*Genesis Potential Index*)** [Emanuel & Nolan 2004] ont proposé de modifier le terme thermodynamique en utilisant l'intensité potentielle :

$$\mathrm{GPI} = \underbrace{\left|10^5\eta\right|^{3/2}\,(1+0.1V_{\mathrm{shear}})^{-2}}_{\textit{dynamic}}\underbrace{\left(\frac{H}{50}\right)^3\left(\frac{V_{\mathrm{pot}}}{70}\right)^3}_{\textit{thermal}} \tag{1.17}$$

où η est la vorticité absolue à 850 hPa (en s^{-1}), H est l'humidité relative à 600 hPa, V_{pot} est l'intensité potentielle et V_{shear} est l'amplitude du cisaillement de vent entre 850 hPa et 200 hPa (en m.s^{-1}). Cet indice contient donc une information sur la température de surface mais pas sur la sub–surface océanique.

• **Indice de TCS (Tippett, Camargo & Sobel)** Enfin, [Tippett *et al.* 2010] ont défini un nouvel indice basé sur les variables du GPI (seul V_{pot} est remplacé par un indice de SST) utilisant une méthode plus objective d'attribution du poids relatif des différentes variables :

$$\mathrm{TCS} = \cos\varphi \times \exp a \times \underbrace{\exp\left(b\eta + cV_{\mathrm{shear}}\right)}_{\textit{dynamic}} \times \underbrace{\exp\left(dH + e\mathcal{T}\right)}_{\textit{thermal}} \tag{1.18}$$

où $\mathcal{T} = SST - \overline{SST}^{[20^\circ\text{S-}20^\circ\text{N}]}$, $\eta = \min(\eta, 3.7)$, φ est la latitude et a–e sont des constantes déterminées par une régression de Poisson.

Une étude menée en collaboration avec Christophe Menkes [Menkes *et al.* 2011] compare ces 4 indices quant à leur capacité à expliquer la répartition globale et la variabilité de la cyclogenèse. L'article complet peut être trouvé Annexes (E). L'intérêt des indices pour comprendre comment l'environnement grande–échelle contraint l'activité cyclonique est illustré dans la sous–section suivante.

1.4.3 Distribution régionale et saisonnière

1.4.3.1 Régions de développement

Une centaine de TCs se forment chaque année sur le globe. Les principales régions de genèse et de propagation sont représentées sur la figure 1.27. Les TCs se forment préférentiellement entre 5° et 20° de latitude de part et d'autre de l'équateur dans les zones de convergence inter-tropicales (ITCZ pour *Intertropical Convergence Zone*). Ces régions sont caractérisées par une convergence des vents en basses couches, une nébulosité importante et de haute altitude marquant la convection profonde qui y a lieu (Fig. 1.28).

Extrait de [Menkes *et al.* 2011]

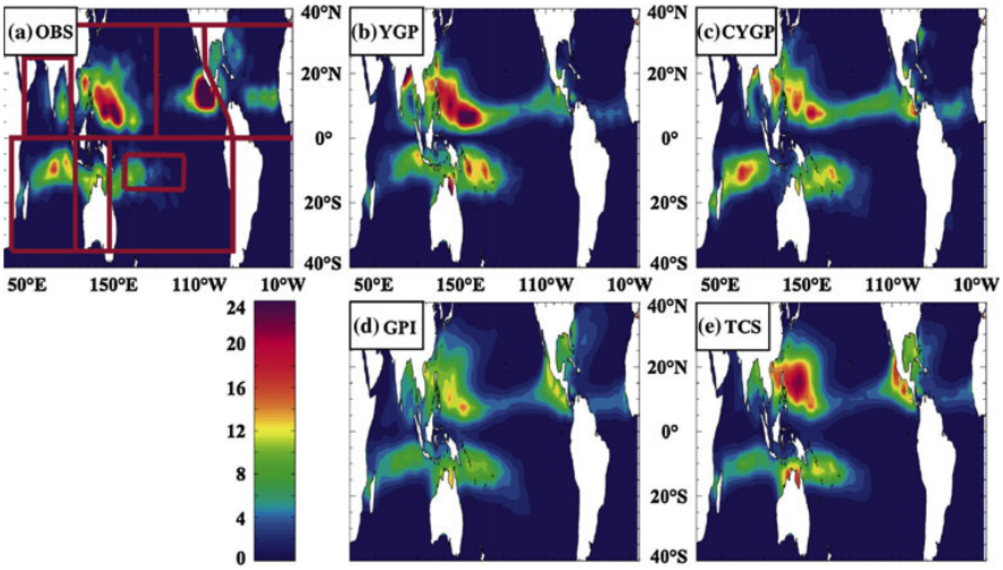

Figure 1.26 – Nombre moyen de cyclogenèse par 20 ans et par boites de $5° \times 5°$ dans les observations (**a**) et prévu par les différents indices de cyclogenèse : (**b**) YGP, (**c**) CYGP, (**d**) GPI, (**e**) TCS .

La source d'énergie des TCs étant la vapeur d'eau provenant de la surface de l'océan, ils se forment préférentiellement au–dessus des océans chauds des régions tropicales. Un certain nombre de bassins se délimitent naturellement i) par la présence des continents (au–dessus desquels les TCs ne peuvent subsister) et ii) par la présence d'eaux de surface relativement froides ; l'isotherme 26°C est souvent admise comme limite inférieure à la cyclogenèse. En plus de la température de l'océan, les différentes variables favorables à la cyclogenèse se combinent pour n'autoriser la formation de cyclones que dans des régions bien définies. Les indices de cyclogenèse permettent de décrire qualitativement ces régions comme le montre la figure 1.26. Les bassins du Pacifique Sud–Est et de l'Atlantique Sud sont caractérisés par l'absence de cyclogenèse. Cette observation s'explique par leur climat : vorticité relative anticyclonique ou faiblement cyclonique, cisaillement de vent élevé et précipitations convectives très faibles.

6 principaux bassins peuvent être définis autour des régions de maximum d'activité cyclonique (Fig. 1.27). Le bassin Pacifique Nord–Ouest (NWPac) est le siège du développement des TCs les plus nombreux et les plus puissants (Tab. 1.2 et Fig. 1.27). Les cyclones des bassins NWPac et Atlantique ont en général les trajectoires les plus longues. Dans les autres bassins, les trajectoires sont limitées par la présence de continents (Indien Nord), par la température de l'océan (en Pacifique Nord–Est) ou par la position du jet sub–tropical dans l'hémisphère Sud.

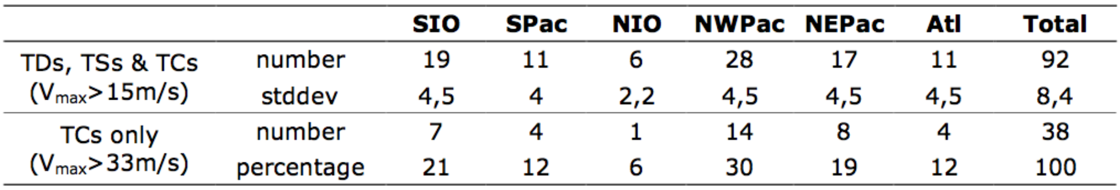

		SIO	SPac	NIO	NWPac	NEPac	Atl	Total
TDs, TSs & TCs (V_{max}>15m/s)	number	19	11	6	28	17	11	92
	stddev	4,5	4	2,2	4,5	4,5	4,5	8,4
TCs only (V_{max}>33m/s)	number	7	4	1	14	8	4	38
	percentage	21	12	6	30	19	12	100

Table 1.2 – Nombre de dépressions tropicales (TDs), tempêtes tropicales (TSs) et de cyclones tropicaux (TCs) par bassin sur la période 1980–2008. La déviation standard du nombre de genèse par saisons cycloniques est indiquée ainsi que le pourcentage des TCs de chaque bassin par rapport au total sur le globe.

- **Des cyclones en France ?** La France métropolitaine n'est *a priori* jamais affectée par les TCs ; si ce n'est, potentiellement, par des systèmes se transformant en tempête extra–tropicale. En revanche plusieurs DOM et TOM français se situent dans des régions cycloniques. C'est le cas de La Réunion, Mayotte, la Polynésie Française, la Nouvelle–Calédonie, Wallis et Futuna ainsi que la Guadeloupe et la Martinique. La plupart des régions françaises affectées par les TCs se trouvent dans l'hémisphère Sud, dans les bassins Indien Sud et Pacifique Sud–Ouest. Ces bassins sont relativement peu étudiés par la communauté de chercheurs dans le domaine des cyclones, qui est principalement concentrée aux Etats–Unis et au Japon et s'intéresse avant tout aux bassins Atlantique et Pacifique Nord. Les bassins de l'hémisphère Sud reçoivent une attention plus particulière de la communauté française, particulièrement l'Océan Indien Sud–Ouest pour lequel le « Centre Régional Météorologique Spécialisé » de la Réunion est chargé des prévisions opérationnelles. Les résultats de cette thèse sont illustrés préférentiellement dans ces bassins de l'hémisphère Sud.

1.4.3.2 Saisonnalité

La plupart des TCs se développent pendant une saison spécifique de l'année que l'on nomme la saison cyclonique (Fig. 1.29). Dans l'hémisphère Nord, la saison dure de Juin à Novembre avec un pic d'activité en Septembre. Le bassin indien Nord fait exception avec une saison cyclonique divisée en deux périodes actives avant et après la mousson. Pendant la mousson, le fort cisaillement de vent entre le bas et le haut de la troposphère empêche l'intensification des dépressions. Dans l'hémisphère Sud, la saison cyclonique s'étend des mois de Novembre à Avril. Le pic de la saison cyclonique (en Janvier–Février) est atteint au moment où l'ITCZ de l'hémisphère Sud est la plus développée et atteint sa position la plus méridionale.

Les indices de cyclogenèse parviennent relativement bien à décrire cette saisonnalité (Fig. 1.30). Globalement, l'indice TCS est le plus proche des observations.

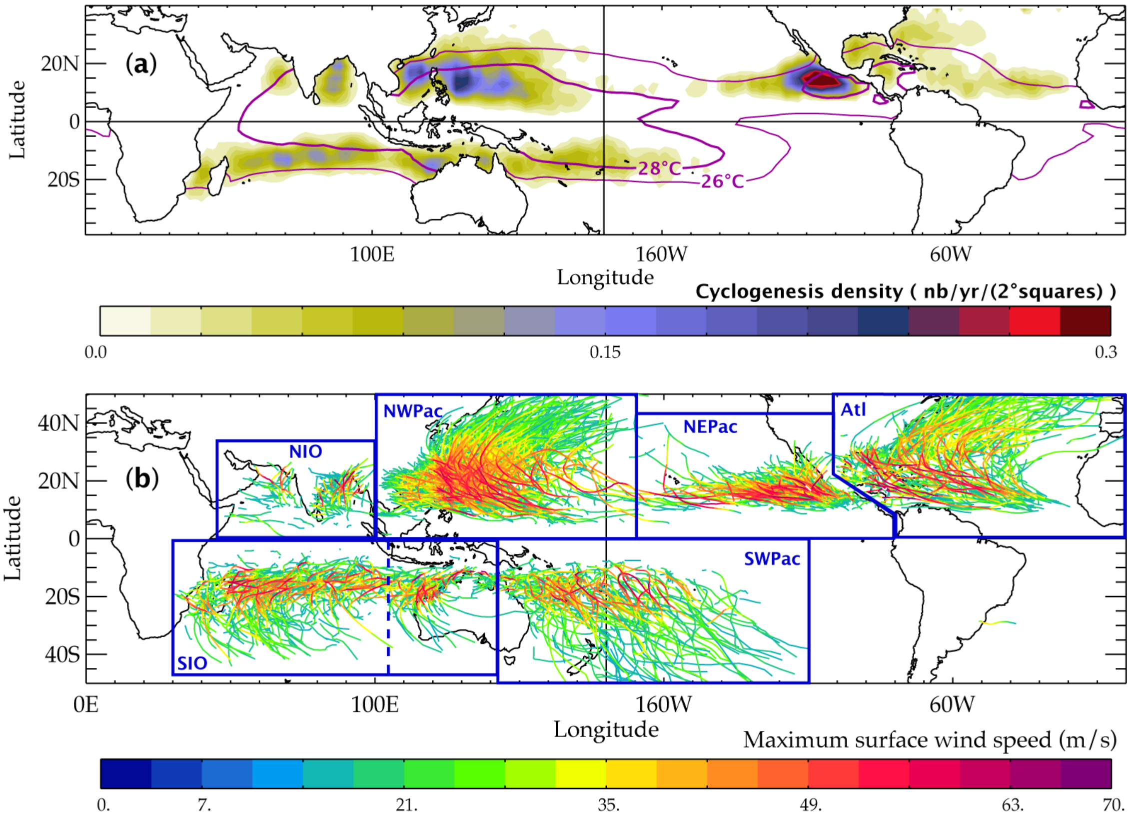

Figure 1.27 – (**a**) Densité de cyclogenèse et (**b**) Intensités le long des trajectoires de tous les cyclones sur la période 1978–2009 dans la base de données IBTrACS. Les *courbes violettes* marquent la position moyenne des isothermes 26°C et 28°C (données Had–iSST) ; les *cadres bleus* délimitent les principaux bassins cycloniques utilisés par la suite : SIO — *South Indian Ocean*, SWPac — *South–West Pacific*, NIO — *North Indian Ocean*, NWPac — *North–West Pacific*, NEPac — *North–East Pacific*, Atl — *Atlantic*

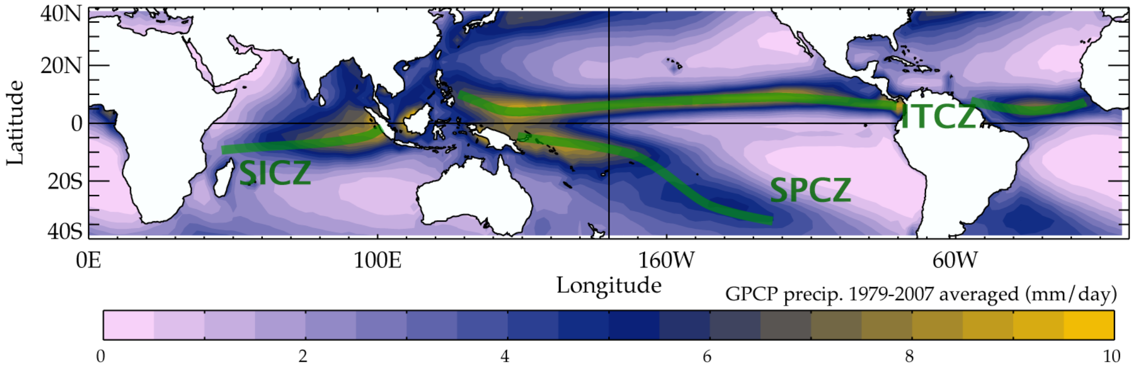

Figure 1.28 – Moyenne des précipitations dans les tropiques sur la période 1979–2007 à partir du jeu de données GPCP (*Global Precipitation Climatology Project*). Les *courbes vertes* soulignent les positions moyennes des différentes zones de convergence : SICZ : *South Indian Convergence Zone*, SPCZ : *South Pacific Convergence Zone*, ITCZ : *Intertropical Convergence Zone*.

1.5 Variabilité du climat et influence sur l'activité cyclonique

Comme l'ont illustré les deux sections précédentes, les cyclones sont sensibles aux conditions océaniques et atmosphériques de grande–échelle. Etant donné que les variables océaniques et atmosphériques importantes pour l'activité cyclonique présentent une forte variabilité à diverses échelles de temps, il est raisonnable de supposer une influence de la variabilité climatique sur l'activité cyclonique.

• **Mesure de l'activité cyclonique** Plusieurs caractéristiques de l'activité cyclonique sont susceptibles de varier : la géographie de la cyclogenèse et des trajectoires de TCs, l'intensité maximale des TCs… Une vision intégrée de l'ampleur de l'activité cyclonique d'une région pendant une saison donnée a été proposée par [Emanuel 2005]. Le PD (pour *Power Dissipated*) mesure la puissance totale des TCs et est défini par l'intégrale temporelle et spatiale de l'énergie dissipée par friction à l'interface air–mer :

$$\mathrm{PD} = 2\pi \int_0^{\tau} \int_0^{\infty} \rho_a C_D \left|V\right|^3 r \, dr \, dt \tag{1.19}$$

où τ est la durée de vie du TC. Les données complètes du champ de vent d'un cyclone sont rarement accessibles ; une valeur approchée, le PDi (*Power Dissipation index*), peut être calculée plus simplement en sommant les vents maximum au cours de la vie du TC (sans intégrer spatialement) :

$$\mathrm{PDi} = \int_0^{\tau} \left|V_{\max}\right|^3 dt \tag{1.20}$$

Extrait de [Gray & Emanuel 2010]

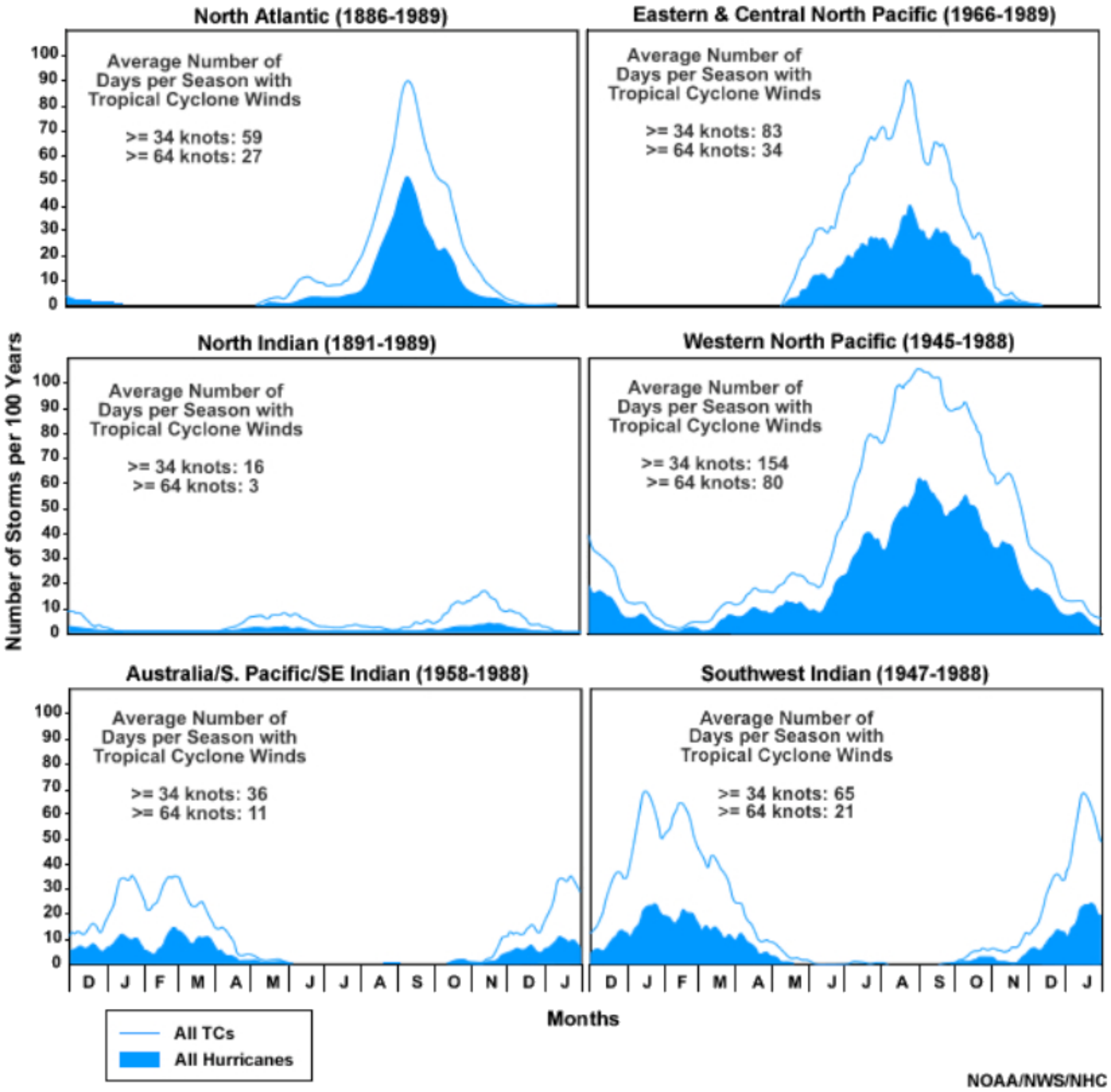

Figure 1.29 – Cycle saisonnier du nombre moyen de TCs par bassin (exprimé en nombre / 100 ans). La *ligne bleue* représente le nombre total de tempêtes tropicales (Vmax $\geqslant$ 15 m/s) ; la *surface bleue* représente le nombre total de cyclones tropicaux (Vmax $\geqslant$ 30 m/s)

Extrait de [Menkes *et al.* 2011]

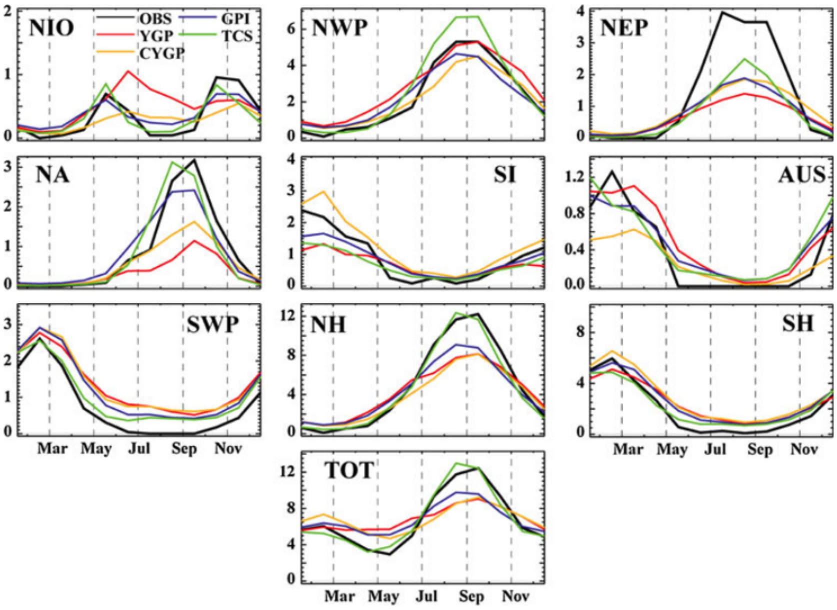

Figure 1.30 – Saisonalité de la cyclogenèse par bassin dans les observations et prévu par les différents indices de cyclogenèse.

Afin d'étudier la variabilité de l'activité cyclonique sur la période la plus longue possible, un indice encore plus simplifié est proposé par [Emanuel 2008] : "maxPD" ; il s'agit d'approcher le PD du TC par le produit de sa durée de vie et du maximum d'intensité qu'il a atteint au cube. Comme le suggèrent [Vecchi & Knutson 2008], ces deux quantités sont estimées de manière fiable depuis plus d'une centaine d'années en Atlantique ; cette approche permet de proposer une série temporelle représentant l'activité cyclonique sur près de 150 ans (Fig. 1.31). L'activité cyclonique et la température de surface sont fortement corrélées sur cette période (r^2=0.86). Une analyse des fréquences révèle des pics spectraux à 3–5 ans, 10 ans et une tendance à long terme.

Dans cette section, nous allons décrire ce que l'on connaît de l'influence de la variabilité climatique sur l'activité cyclonique pour différentes échelles de temps, de l'échelle interannuelle aux variations multi–decénnales, ainsi que les changements observés ou prévus associés au changement climatique.

1.5.1 Variabilité intrasaisonnière

La saison cyclonique est prise comme plus petite entité de variabilité tout au long de cette thèse, ce qui se justifie lorsque l'on étudie l'activité cyclonique à l'échelle interannuelle à décennale. Cependant l'activité cyclonique n'est pas homogène au sein de chaque saison cyclonique. La figure 1.32 l'illustre en montrant l'effet de la phase de l'oscillation de Madden–Julian (MJO) sur la géographie de la cycloge-

Extrait de [Emanuel 2008]

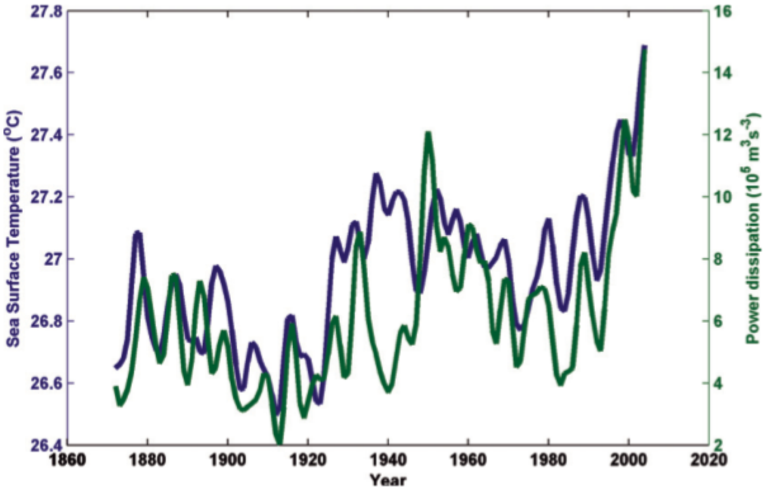

Figure 1.31 – Séries temporelles de SST (Had–iSST moyenné entre Août et Octobre dans 20°–60°W / 6°–18°N) *en bleu* et de "maxPD" (durée de vie × maximum d'intensité du cyclone au cube) *en vert* ; les séries ont subi un filtre 1-3-4-3-1.

Extrait de [Leroy & Wheeler 2008]

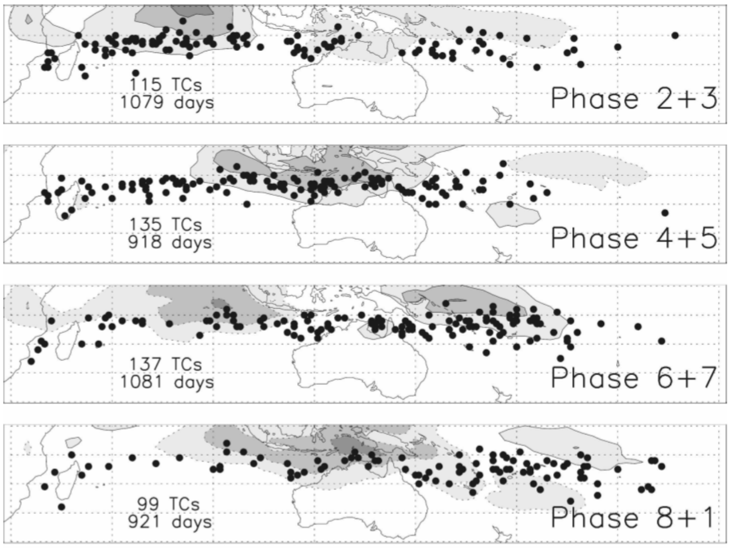

Figure 1.32 – Cartes composites de l'OLR et points de cyclogenèse (*cercles noir*) en fonction de l'évolution de l'oscillation de Madden–Julian (MJO). Les composites sont réalisés selon la classification de [Wheeler & Hendon 2004].

nèse de l'hémisphère Sud. Lors d'une phase active de MJO, la convection profonde organisée permet d'humidifier la troposphère et génère des anomalies de vorticité cyclonique en basse couche ; une augmentation du nombre de genèse de TCs est alors observée.

Extrait de [Menkes *et al.* 2011]

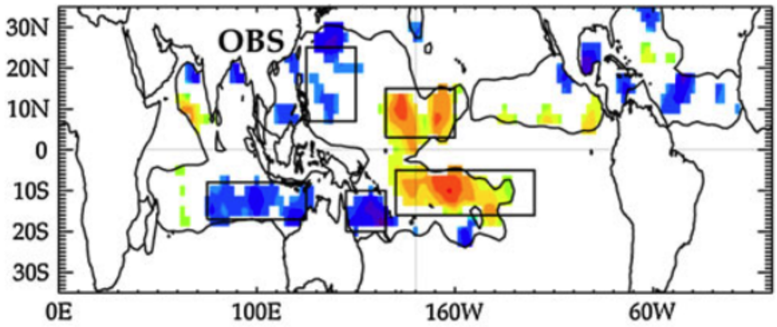

Figure 1.33 – Carte de corrélation entre le nombre de cyclogenèse et l'indice *Niño* 3.4. Seules les corrélations significatives à 90% sont montrées, dans les régions où la déviation standard du nombre de genèse est supérieure à 1 (*contour noir*).

1.5.2 Variabilité interannuelle

ENSO (*El Niño Southern Oscillation*) est le mode de variabilité le plus énergétique dans les tropiques aux échelles de temps interannuelles et module l'activité cyclonique dans les trois océans tropicaux. Ce phénomène présente un pic spectral entre 3 et 7 ans. Les phases positives (*El Niño*) et négatives (*La Niña*) sont associées entre autres à des modifications de SST, de circulation atmosphérique et de convection principalement dans le Pacifique mais les phases d'ENSO induisent des modifications du climat pratiquement partout sur le globe via des téléconnexions. Les téléconnections sont différentes dans chaque bassin cyclonique. La SST augmente dans le centre du bassin Pacifique et dans le bassin Indien pendant *El Niño* alors qu'elle diminue dans l'Ouest du Pacifique par exemple.

Bien que les indices de genèse aient été développés pour décrire la cyclogenèse à l'échelle saisonnière, ils sont aussi utilisés pour comprendre comment la variabilité interannuelle des variables grande–échelle expliquent les variations interannuelles de l'activité cyclonique. L'étude de [Menkes *et al.* 2011] montre que les indices sous–estiment l'amplitude de la variabilité interannuelle du nombre de TCs. Il convient donc de s'abstenir de les utiliser pour quantifier la variabilité des TCs. Cependant, ils reproduisent de manière acceptable le phasage de la variabilité de la cyclogenèse associée au phénomène ENSO. Les indices permettent donc l'étude qualitative des variables grande–échelle modulant la cyclogenèse en lien avec ENSO. La figure 1.33 illustre l'influence variée d'ENSO dans les différents bassins cycloniques. Alors que la cyclogenèse augmente dans le centre du Pacifique pendant les années *El Niño*, elle diminue dans la plupart des autres bassins.

L'étude de la variabilité interannuelle de l'activité cyclonique a débuté en Atlantique. [Gray 1984] a mis en évidence la modulation du nombre de cyclones dans cette région en fonction de la phase du cycle ENSO ainsi que de la phase de la QBO (*Quasi–Biennial Oscillation*). Ces modes de variabilité climatique sont en effet associés à des modifications du cisaillement vertical de vent qui est plus (moins) fort pendant les années *El Niño* (*La Niña*) [Goldenberg & Shapiro 1996]. Ces modifications passent par des téléconnexions associées à ENSO : la modification du cisaillement est liée à une modulation de la circulation de Walker par ENSO.

L'Atlantique est le bassin où l'activité cyclonique et sa variabilité sont les plus étudiées. Les bassins Pacifique Nord–Est et Pacifique Nord–Ouest reçoivent aussi une attention particulière du fait de l'intérêt et des moyens des chercheurs américains et japonais. L'Océan Indien et le Pacifique Sud restent moins étudiés malgré un intérêt croissant.

Dans l'Océan Indien Nord, [Singh *et al.* 2000] note une réduction de l'activité cyclonique pendant les années *El Niño*.

Le Pacifique Sud–Ouest se trouve dans la zone d'influence directe d'ENSO. Sur la côte Est australienne, l'activité cyclonique est plus corrélée à ENSO qu'aux SST locales [Ramsay *et al.* 2008], ce qui signifie que l'organisation des variables favorables à la cyclogenèse par le biais de téléconnexions peut–être plus importante que l'influence locale de la température de la mer.

Dans l'Océan Indien Sud, [Kuleshov *et al.* 2009] observent une augmentation du nombre de TCs à l'Est de 70°E pendant *La Niña* ; [Ho *et al.* 2006] commentent aussi ce déplacement vers l'Est de la genèse pendant *La Niña* et l'expliquent par la modification de la circulation de Walker.

Le dipôle de l'Océan Indien (IOD pour *Indian Ocean Dipole*) est un mode de variabilité important [Saji *et al.* 1999] possédant également des téléconnexions dans le Pacifique [Izumo *et al.* 2010]. Pourtant, à ce jour, aucune étude ne s'est intéressé au lien potentiel que l'IOD peut avoir avec l'activité cyclonique.

1.5.3 Variabilité décennale

Il existe une variabilité de la circulation thermohaline globale aux échelles décennales à pluri-décennales. La 4^{e} EOF de SST globale (dont la tendance linéaire a été retirée) est caractérisée par une échelle de temps décennale et un maximum d'amplitude en Atlantique Nord. [Goldenberg *et al.* 2001] ont mis en évidence une variabilité de l'activité cyclonique en lien avec cette oscillation atlantique multi–décennale (AMO pour *Atlantic Multi-decadal Oscillation*). Ce mode de variabilité (mis en évidence par une approche statistique) s'explique par des rétroactions couplées océan–atmosphère. [Vimont & Kossin 2007] montrent qu'il est associé à la position de l'ITCZ, elle-même modulée par l'intensité du gradient méridien de SST et l'intensité des vents cross–équatoriaux ; ils nomment ce mode couplé AMM (*Atlantic Meridional Mode*). [Kossin & Vimont 2007] voient l'AMM comme un organisateur des variables favorables aux cyclones (SST, cisaillement, vorticité, instabilité statique) et expliquent donc la variabilité basse fréquence de l'activité cyclonique en Atlantique en étudiant la variabilité de l'AMM. L'AMM est excité par divers forçages externes, dont les forçages thermohalins liés à l'AMO, à l'échelle décennale

Extrait de [Kossin & Vimont 2007]

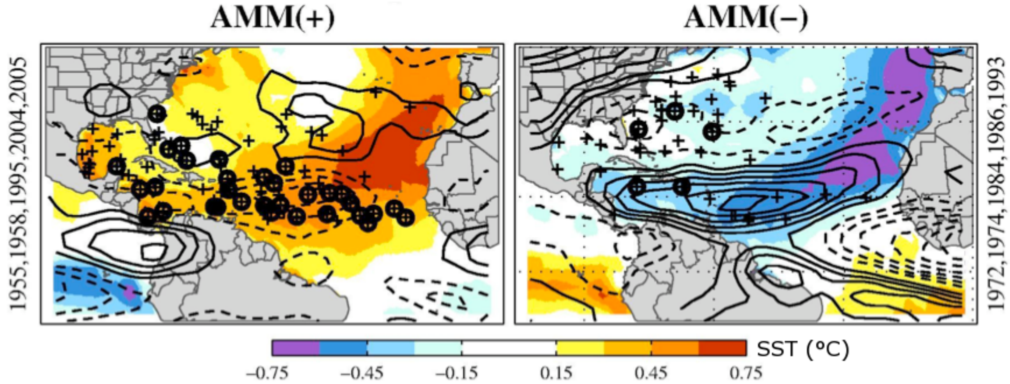

Figure 1.34 – Composites de SST (*couleur*), cisaillement vertical dans la troposphère (*contours*), et points de cyclogenèse (+ ; un cercle entoure les lieux de genèses des cyclones majeurs) pour les 5 plus fortes/faibles années AMM.

ce qui expliquerait la périodicité décennale de "maxPD" visible sur la figure 1.31. L'influence de l'AMM sur la géographie des cyclones est illustrée sur la figure 1.34.

Une limitation forte de toute étude de l'activité cyclonique à l'échelle décennale réside dans la disponibilité des données de cyclones dont la fiabilité diminue lorsque l'on remonte dans le temps ainsi que du caractère limité de la période instrumentée qui ne permet d'observer que quelques oscillations d'un quelconque cycle pluri–décennal. L'interprétation de la variabilité récente de l'activité cyclonique en Atlantique ne fait pas consensus. [Mann & Emanuel 2006] plaident pour un contrôle de l'activité cyclonique pilotée avant tout par la SST sous l'influence des forçages radiatifs (modulés par les gaz à effet de serre et les aérosols). Cette interprétation suggère que c'est le changement climatique actuel qui module l'activité cyclonique, plutôt qu'une variabilité naturelle pluri–décennale.

1.5.4 Changement climatique et activité cyclonique

Le réchauffement climatique actuel est dû à l'effet de serre provoqué par les gaz à effet de serre additionnels d'origine anthropique. L'effet de serre autorise moins de rayonnement infra–rouge à s'échapper vers l'espace et réchauffe les basses couches tout en refroidissant la haute troposphère. $T_S - T_0$ augmente, ce qui permet aux cyclones d'être potentiellement plus intenses d'après l'équation 1.11 ; avec une sensibilité de 3.5 m.s^{-1} par °C de réchauffement de surface. L'augmentation potentielle d'intensité via ce mécanisme est donc limitée et difficilement observable avec la précision des mesures existantes sur l'intensité des cyclones.

Le réchauffement climatique actuel a également pour effet d'augmenter la température de l'océan sur les 50–100 premiers mètres [Barnett *et al.* 2005]. La modi-

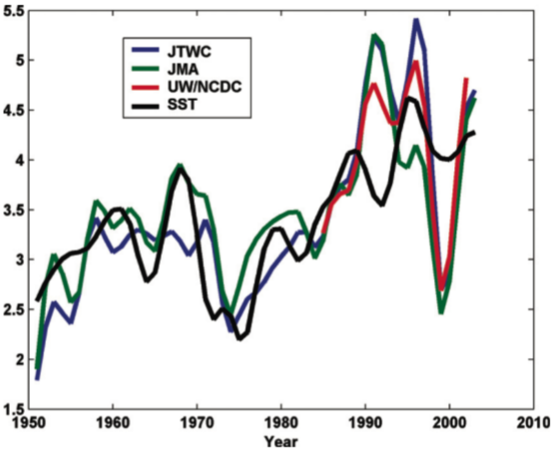

Figure 1.35 – Séries temporelles de SST (Had–iSST *en noir*), et du PDi calculé à partir de différents jeux de données (JTWC *en vert*, JMA *en bleu*, [Kossin *et al.* 2007] *en rouge*) dans le Pacifique Nord–Ouest. Les séries ont subi un filtre 1-3-4-3-1.

Extrait de [Emanuel 2008]

fication de contenu thermique et de stratification qui en résulte est certainement importante pour les cyclones mais aucune étude à ce jour n'a abordé ce thème.

1.5.4.1 Tendance de l'activité cyclonique sur la période instrumentale

Deux études [Emanuel 2005, Webster *et al.* 2005] ont suggéré récemment que le changement climatique est déjà responsable d'une modification détectable de l'activité cyclonique. Elles sont toutefois controversées.

[Emanuel 2005] montre une tendance à la hausse de la puissance des cyclones en Atlantique (Fig. 1.31) et Pacifique Nord–Ouest (Fig. 1.35) particulièrement marquée sur les 30 dernières années. L'augmentation de ∼60% de PD sur cette période peut être expliquée par une variation de ∼10% du PI (comme montré par [Emanuel 2006]) due à l'augmentation de SST et à la diminution de la température de la tropopause. [Webster *et al.* 2005] montrent que la proportion des cyclones les plus forts (catégories 4 et 5) augmente, avec un quasi–doublement entre les années 1970s et 2000s (Fig. 1.36). De même, dans l'hémisphère Sud, le nombre de jours de TCs les plus intenses (« *severe TCs days* », *i.e.* $P_{\mathrm{eye}} < 945\ hPa$) a quasiment doublé entre 1980 et 2006 [Kuleshov *et al.* 2008].

Du fait des incertitudes sur la qualité et l'homogénéité des données utilisées, certains scientifiques mettent en doute les résultats de ces études. [Landsea 2005] suggère que la majorité de l'augmentation des TCs de catégories 4–5 peut être attribuée à une évolution des pratiques d'estimation d'intensité des TCs à partir des images satellites permettant de mieux détecter les TCs les plus forts aujourd'hui. Une révision des comptes de TCs de catégories 4 et 5 annule la tendance à l'augmentation observée par [Webster *et al.* 2005] dans l'Océan Indien et réduit celle observée dans le Pacifique Nord–Ouest. Afin de palier aux problèmes d'homogénéité des données, [Kossin *et al.* 2007] ont réalisé une réanalyse objective des forces de TCs sur la période récente où des mesures satellites IR sont disponibles (1986–2005) . Ces nouvelles données illustrent la fragilité des tendances observées dans l'Océan Indien et l'hémisphère Sud, mais confirment les tendances à la hausse

Extrait de [Webster *et al.* 2005]

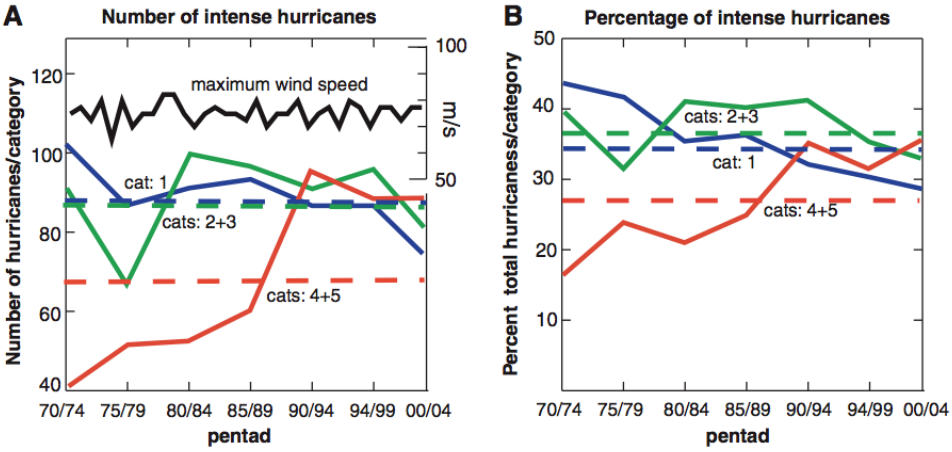

Figure 1.36 – Séries temporelles (**A**) du nombre total et (**B**) de la proportion de TCs selon la catégorie de Saffir–Simpson par périodes de 5 ans. La *ligne noire* représente l'intensité du cyclone le plus fort observé chaque année ; les *lignes pointillées* montrent la valeur moyenne sur toute la période.

en Atlantique et Pacifique Nord–Ouest (Fig. 1.37). A partir de ce jeu de données, [Elsner *et al.* 2008] approfondissent l'étude séminale de [Webster *et al.* 2005] en séparant l'analyse de tendances par quantiles de force de vent. La figure 1.38 montre que les TCs les plus forts sont caractérisés par des tendances haussières plus prononcées que les TCs modérés (ces tendances globales sont dominées par les TCs des bassins Atlantique et Indien).

1.5.4.2 L'activité cyclonique dans un climat plus chaud

La tendance des émissions mondiales de GES n'étant pas à la baisse, le changement climatique s'amplifiera très probablement dans le futur [4]. Il est donc essentiel d'étudier l'influence que pourrait avoir le changement climatique futur sur les caractéristiques de l'activité cyclonique (modification de la fréquence, force, géographie...). Etant donné qu'aucune observation n'est disponible, le recours à des méthodes indirectes est nécessaire pour évaluer l'influence d'un climat plus chaud sur les cyclones.

Méthodes de modélisation explicite des TCs Les modèles de circulation générale couplés (CGCMs) utilisés pour prévoir les changements climatiques futurs (*e.g.* les modèles utilisés pour les rapports du GIEC) présentent une faible résolution atmosphérique qui ne permet de simuler que des cyclones de faible intensité (TCLVs pour *TC–Like Vortices*). Il est possible d'étudier l'évolution des caractéristiques de

---

[4] L'éventualité d'une élévation future des température est jugée « pratiquement certaine » selon la terminologie du GIEC, *i.e.* a une probabilité d'occurrence $> 99\%$

Extrait de [Kossin *et al.* 2007]

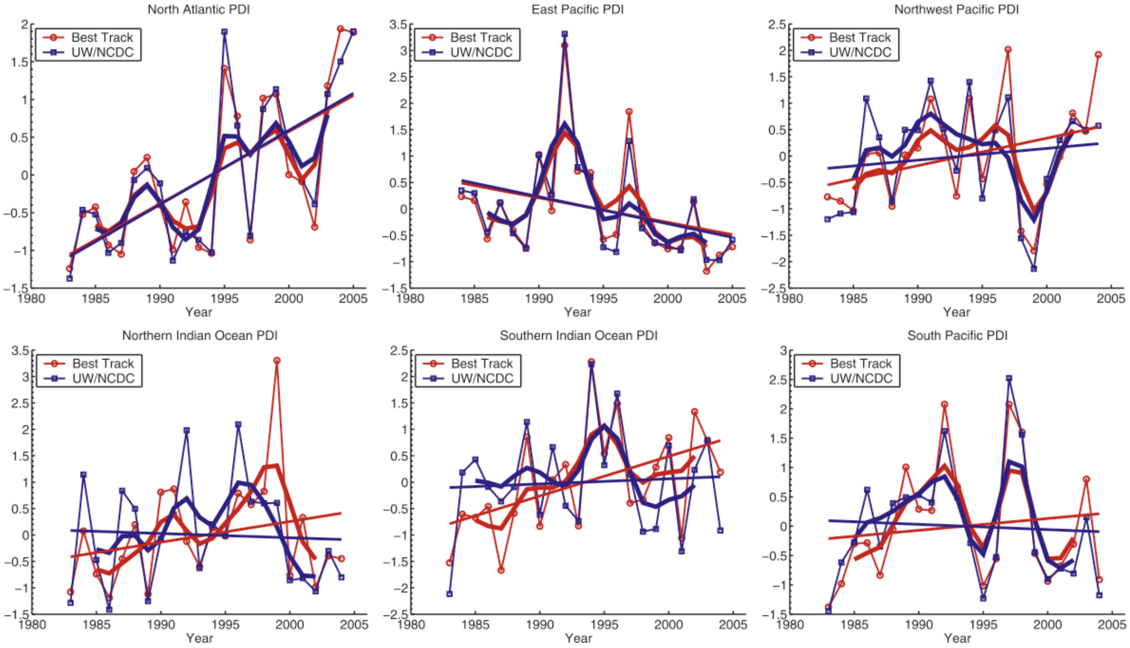

Figure 1.37 – Séries temporelles de PDi par bassin utilisant les données du JTWC (*en rouge*) et de la réanalyse de [Kossin *et al.* 2007] (*en bleu*). Contrairement aux données du JTWC, les données réanalysées ne supportent pas l'hypothèse d'une augmentation de la puissance totale des TCs dans l'Océan Indien et l'hémisphère Sud.

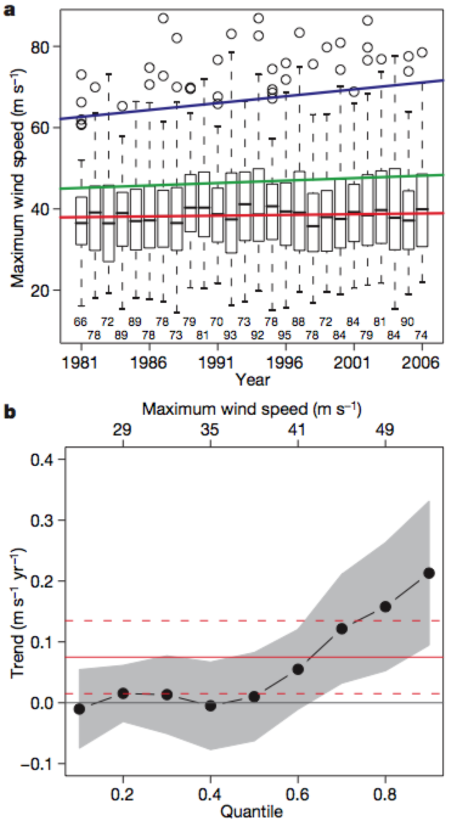

Figure 1.38 – (**a**) Séries temporelles des valeurs annuelles de l'intensité maximale atteinte par chaque cyclone au cours de sa vie où *les boites* montrent les quartiles, les *traits gras* montrent la médiane, *les cercles* montrent le décile supérieur et *les barres verticales pointillés* montrent l'interquartile×1.5.
(**b**) Tendance de l'intensité calculée pour chaque décile d'intensité (*points noirs*) et pour l'ensemble des intensités (*ligne rouge*) et intervale de confiance à 90% (en *gris* et *lignes pointillés rouges* respectivement).

Extrait de [Elsner *et al.* 2008]

ces TCLVs (fréquence, durée, distribution spatiale) en réponse au changement climatique, mais le manque de réalisme de leur intensité simulée rend hasardeuse toute conclusion sur une éventuelle modification de leur force [Bengtsson *et al.* 2007].

Les études discutant l'influence du réchauffement climatique sur l'évolution du nombre de TCs à partir de l'analyse de différents modèles sont pour le moment contradictoires [Grossmann & Morgan 2008]. Cette approche est aujourd'hui limitée mais l'augmentation de résolution des modèles ouvre des perspectives intéressantes.

Afin d'accroître la résolution (avec une maille typiquement de l'ordre de la dizaine de km) tout en restant dans les puissances de calcul disponibles aujourd'hui, il est commun de faire tourner des configurations régionales à haute résolution en les forçant aux frontières par un modèle à plus basse résolution. En forçant un modèle régional par des données de réanalyses et d'observations, une telle stratégie a permis à [Knutson *et al.* 2007] de simuler l'activité cyclonique du bassin Atlantique de manière très réaliste (Fig. 1.39). En appliquant cette fois un forçage aux frontières issu de scénarios de changement climatique, [Knutson *et al.* 2008] trouvent une diminution de la fréquence future des TCs de 27% et des TSs de 18% (à la fin du 21^{e} siècle dans le scénario A1B de l'ensemble multi–modèle CMIP3). Par une approche similaire autour de l'Australie, [Walsh *et al.* 2004] observe une augmentation du nombre des TCs les plus forts dans un scénario de triplement de CO_2 sans modification de la fréquence des TCs.

Extrait de [Knutson *et al.* 2007]

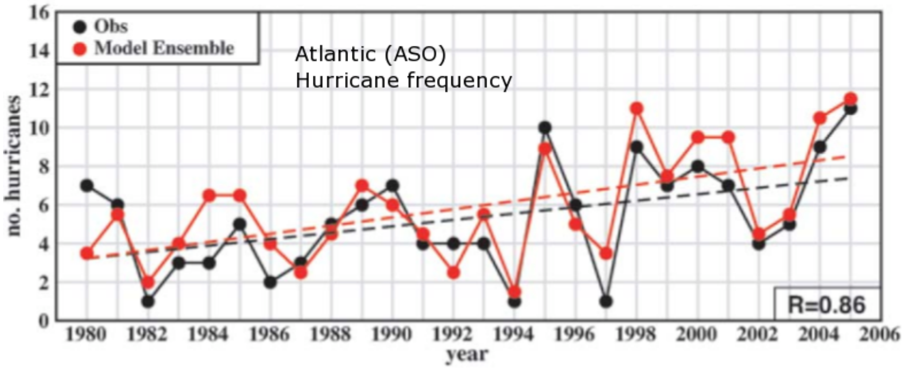

Figure 1.39 – Séries temporelles du nombre total de TCs par saison cyclonique de l'Atlantique (Août–Octobre) dans les observations (*en noir*) et dans la moyenne d'ensemble des simulations haute résolution du modèle régional WRF (*en rouge*). L'accord entre les deux est stupéfiant (corrélation de 0.86).

Méthodes d'étude des variables favorables aux TCs Si l'on peut douter de la capacité des CGCM à simuler des TCs suffisamment réalistes, ces derniers représentent par contre les variables grande échelle avec beaucoup plus de fidélité. Une approche alternative est donc d'étudier les variables favorables aux cyclones, celles constituant les indices de cyclogenèse par exemple (décrites en section 1.4.2). En utilisant l'indice de [Royer *et al.* 1998], [Caron & Jones 2008] montrent que les modifications attendues du nombre de cyclogenèse sont faibles dans la plupart des bassins à l'exception du Pacifique central où la cyclogenèse pourrait augmenter significativement à la fin du siècle selon les scénarios A1B et A2 du GIEC.

[Vecchi & Soden 2007b] étudient les modifications des variables favorables dans les runs multi-modèles CMIP3. En Atlantique, ils observent que la plupart des variables de cyclogenèse deviennent moins favorables en changement climatique : le cisaillement vertical augmente, l'humidité relative en moyenne troposphère et la PI diminuent. Ils interprètent cette modification par une évolution du système climatique vers un état moyen ressemblant plus aux conditions d'*El Niño*, défavorable à la cyclogenèse Atlantique. Au contraire, dans les bassins Indien et Pacifique central, les variables deviennent plus favorables et pourraient soutenir une activité cyclonique accrue.

Méthodes hybrides Afin de tirer parti des avantages des deux méthodes décrites ci–dessus, [Emanuel 2006] propose une méthode qui consiste à « semer » des précurseurs de cyclones (*seeds i.e.* noyaux à cœur chaud ayant des vents initiaux de 12 m.s^{-1}) dans des sorties de modèles et de simuler leur trajectoire et intensité dans des modèles séparés. Cette technique permet de bénéficier à la fois de la qualité des variables grande–échelle simulées par les CGCMs et de la capacité de simuler l'intensité du cyclone dans un modèle haute–résolution couplé à un océan uni–colonne. Ces modèles, très peu coûteux en temps de calcul, sont "nourris" par les variables (profils de température atmosphérique et océanique, d'humidité, cisaillement. . .) du GCM. L'avantage est qu'il est possible de simuler le comportement de plusieurs milliers de TCs alors qu'il ne s'en produit naturellement qu'une centaine par an, ce qui augmente la significativité statistique des résultats.

[Emanuel 2006] montre que cette technique parvient à reproduire de manière réaliste la climatologie et la variabilité interannuelle du nombre de TCs à l'échelle globale sur les 50 dernières années en créant les cyclones synthétiques à partir des données de réanalyses.

En semant maintenant les noyaux de TCs dans le climat tel que simulé par les CGCMs pour le scénario A1B, [Emanuel 2008] conclut que la puissance totale des cyclones augmente dans le Pacifique Ouest et diminue dans l'Océan Indien (Fig. 1.40.a). Pour les bassins Atlantique et Pacifique Est, les différents modèles ne donnent pas des résultats cohérents, ce qui illustre l'incertitude encore élevée provenant des différences inter–modèles. Cette augmentation de puissance totale résulte d'une augmentation de l'intensité des cyclones (d'environ 10% à l'échelle globale) alors que leur fréquence diminue globalement (Fig. 1.40.bc).

Concernant la géographie de la cyclogenèse, les résultats d'[Emanuel 2008] sont cohérents avec ceux de [Caron & Jones 2008] montrant une augmentation dans le Pacifique central et une diminution légère dans la plupart des autres bassins.

Paléo–tempestologie Enfin il est possible d'étudier des enregistrements géologiques pour comprendre le lien entre l'activité cyclonique et le climat ; la discipline de la paléo–tempestologie connaît aujourd'hui un essor et pourrait permettre de comprendre la dépendance des TCs au climat sur des échelles de temps longues (de la centaine d'années au milliers d'années).

En étudiant les dépôts de sable grossier (*storm–surge overwash deposits*) dans les étangs proches des côtes, [Liu & Fearn 2000] ont obtenu une série d'enregistrement des atterrissages (*landfall*) des cyclones forts de la région Alabama–Floride sur plus de 3 000 ans. Les résultats montrent un fort lien de l'activité cyclonique à ENSO (confirmant la diminution de TCs observée en période *El Niño* aujourd'hui) ainsi qu'une recrudescence d'activité dans les 250 dernières années.

Il est aussi possible d'utiliser le contenu isotopique en oxygène atypique dans les précipitations cycloniques enregistré dans les cernes des arbres ou dans les spéléothèmes[5] [Frappier *et al.* 2007].

---

[5] stalagtites et stalagmites

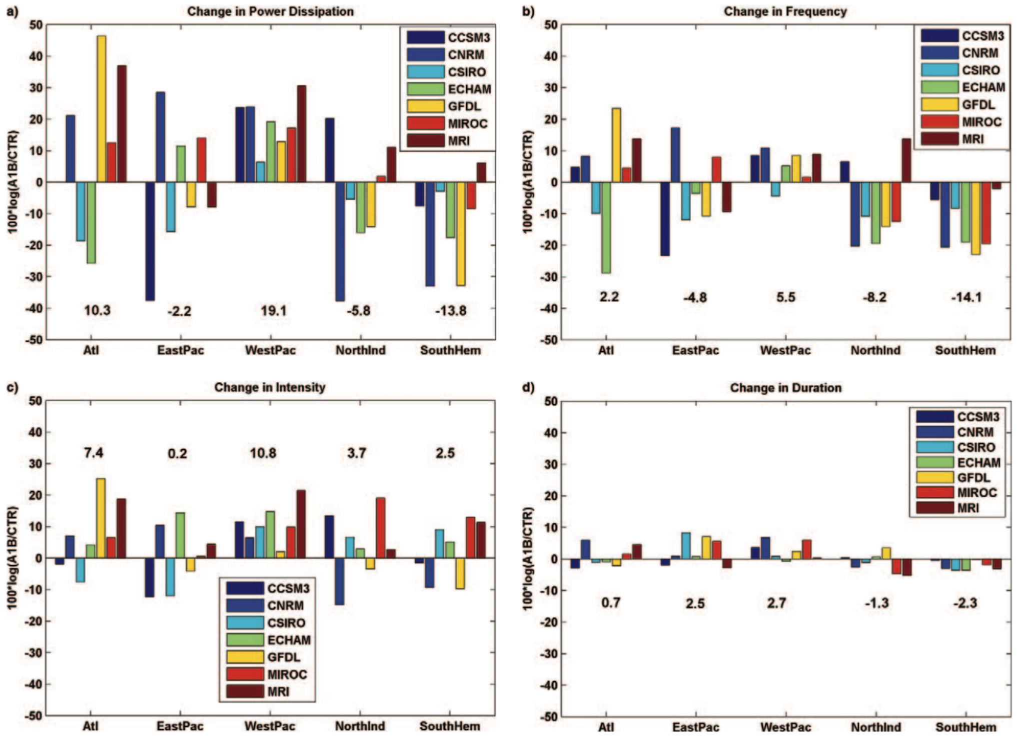

Extrait de [Emanuel 2008]

Figure 1.40 – Changements des caractéristiques des TCs par bassin pour le climat du scénario A1B par rapport à l'actuel pour (**a**) le PDi cumulé sur 20 ans, (**b**) le nombre de cyclogenèse, (**c**) l'intensité, (**d**) la durée de vie des TCs. La comparaison est faite pour le climat de 2080–2100 par rapport au climat de 1980–2000 en simulant 2 000 TCs synthétiques dans chaque bassin pour plusieurs simulations des modèles du 4^{e} rapport du GIEC (*couleurs*).

Adapté de [Wada & Chan 2008]

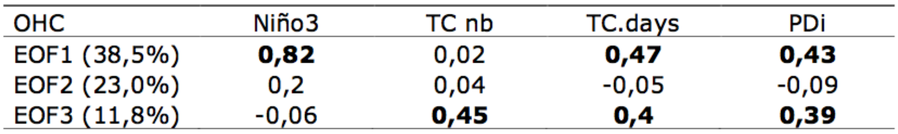

OHC	Niño3	TC nb	TC.days	PDi
EOF1 (38,5%)	**0,82**	0,02	**0,47**	**0,43**
EOF2 (23,0%)	0,2	0,04	-0,05	-0,09
EOF3 (11,8%)	-0,06	**0,45**	**0,4**	**0,39**

Table 1.3 – Coefficients de corrélation entre les 3 premières EOFs de l'OHC dans le Pacifique, l'indice niño.3, et plusieurs indices de l'activité cyclonique du Pacifique Nord–Ouest : nombre de TCs (*TC nb*), nombre de jours de TCs (*TC.days*) et PDi. Les valeurs en gras sont significatives à 99%.

1.5.5 Variabilité de l'océan et activité cyclonique

Cette section a montré que l'activité cyclonique est intimement liée à la température de surface de la mer. La section 1.3 a aussi souligné l'importance de l'océan de sub–surface qui module la *Cold Wake*. Il est donc légitime de supposer une importance de la variabilité de l'océan de sub–surface pour l'activité cyclonique.

Une des seules études reliant la variabilité interannuelle de l'état de l'océan à l'activité cyclonique a été menée par [Wada & Chan 2008]. Ils montrent que la variabilité interannuelle de l'OHC dans le Pacifique est dominée par 3 modes : la première EOF est associée à ENSO ($r = 0.82$; Tab. 1.3), la seconde EOF concerne tout le bassin (probablement liée au réchauffement climatique) et la troisième EOF est dominée par les anomalies d'OHC du Pacifique centre–équatorial. La 1$^{\text{re}}$ et la 3$^{\text{e}}$ EOF de l'OHC sont corrélées, faiblement mais significativement, à l'activité cyclonique du Pacifique Nord–Ouest (Tab. 1.3).

L'amplitude de la variabilité de l'OHC par rapport à sa valeur moyenne est faible dans le Pacifique Ouest. Par contraste, la région du dôme de thermocline (TRIO *Thermocline Ridge of the Indian Ocean*) est caractérisée par une forte variabilité des températures de sub–surface [Vialard *et al.* 2009]. [Xie *et al.* 2002] ont suggéré que la profondeur du dôme de thermocline module l'activité cyclonique dans le Sud–Ouest de l'Océan Indien. La figure 1.41 montre en effet que pendant les années où la TRIO est profonde, le nombre de trajectoires de TCs observées au sud de la TRIO est anormalement élevé. Cela suggère que la variabilité interannuelle de l'océan de sub–surface dans la région permet d'expliquer une part de la variabilité de l'activité cyclonique.

Toutes les études sur l'influence de la variabilité climatique sur les TCs qui ont été présentées font intervenir l'océan, ne serait–ce que par son rôle dans les modes de variabilité couplés (ENSO, AMM...). Cependant un faisceau d'arguments suggère que la variabilité de l'océan apporte une information complémentaire à celle de la variabilité atmosphérique. La mise en évidence claire de la part de variabilité de l'activité cyclonique qui peut être attribuée à l'océan de sub–surface ainsi que des mécanismes par lesquels cette influence s'opère reste à réaliser.

Extrait de [Xie *et al.* 2002]

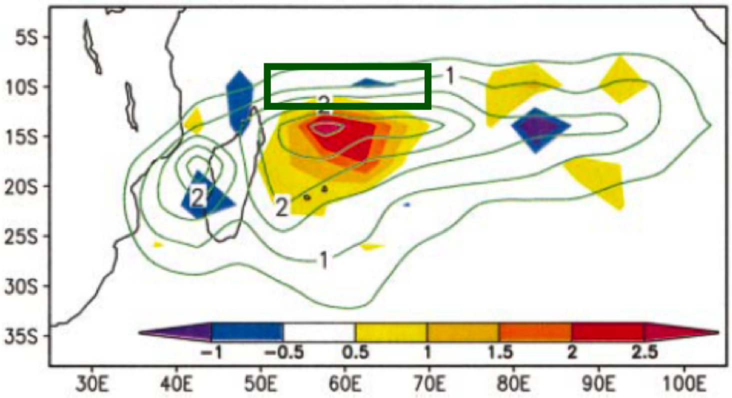

Figure 1.41 – Moyenne climatologique du nombre de TC×jours sur Dec–Avril (*contours verts*) et différences de TC×jours entre les années où la thermocline dans le *cadre vert* est plus-moins profonde que la moyenne (*plages de couleur*).

1.6 Influence des Cyclones Tropicaux sur le climat

Nous avons considéré jusqu'à présent que les TCs sont affectés par le climat de manière passive. Pourtant, certaines études suggèrent une rétroaction des TCs sur le climat.

Parmi les influences potentielles, on peut noter le refroidissement de surface de l'océan par l'accroissement des flux de chaleur sensible et latente. Le taux global de refroidissement de l'océan exercé par les TCs est estimé à ~1 $W.m^{-2}$ [Trenberth & Fasullo 2007]. Les TCs sont aussi des systèmes précipitants très efficaces qui laissent dans leur sillage une atmosphère appauvrie en vapeur d'eau sur de vastes régions ; la diminution de l'effet de serre qui s'en suit participe encore à refroidir l'océan de surface [Emanuel & Khairoutdinov 2011].

Les TCs génèrent aussi un flux de chaleur depuis l'océan vers l'atmosphère en évaporant à la surface et en relâchant la chaleur latente dans l'atmosphère tropicale ; une partie de cette énergie sera perdue par radiation vers l'espace et le reste sera transporté dans la circulation atmosphérique.

Enfin, [Emanuel 2001] a suggéré que les TCs pouvaient être des acteurs majeurs du transport de chaleur vers les pôles et a provoqué une vague de recherche sur ce sujet.

1.6.1 Injection de chaleur dans l'océan par les TCs

Le refroidissement de surface dans le sillage des TCs est principalement dû au mélange pénétrant causé par le cisaillement vertical de courant (1.3.2 p22). Un tel mélange contribue à réchauffer l'océan de sub–surface en même temps qu'il refroidit la couche mélangée (Fig. 1.42.a). Si l'anomalie froide de la couche mélangée est comblée par les flux de surface, ce processus est associé à un chauffage net de la colonne d'eau (Fig. 1.42.b). Etant donné que les bassins cycloniques ont une température océanique stable d'année en année, [Emanuel 2001] suggère qu'un flux de chaleur latéral doit intervenir dans l'océan pour maintenir le bilan fermé.

La quantité de chaleur de l'anomalie négative peut être évaluée en observant la différence de SST avant/après le passage du TC et en faisant des hypothèses simples sur la profondeur du mélange. Par égalité des anomalies de chaleur négative et positive, il est donc possible de calculer la quantité de chaleur « pompée vers l'océan intérieur » (*ocean heat pump*). En extrapolant à partir de la valeur trouvée sous un cyclone, [Emanuel 2001] évalue à 1.4±0.7 PW le flux d'énergie vers l'océan intérieur induit par tous les cyclones, ce qui est du même ordre de grandeur que le total du transport de chaleur océanique (OHT pour *Oceanic Heat Transport*) par l'océan. De là à suggérer que les TCs sont des acteurs majeurs de la circulation thermohaline, il n'y avait qu'un pas.

Extrait de [Emanuel 2001]

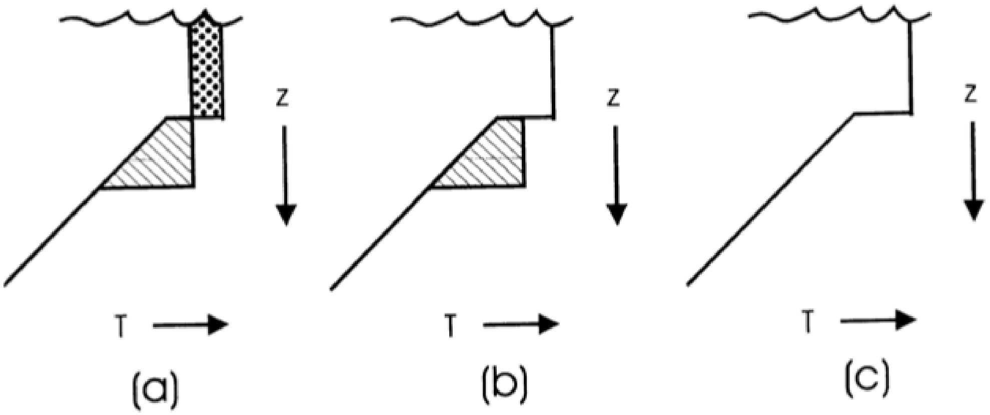

Figure 1.42 – Représentation schématique de l'effet des TCs sur le mélange océanique. (**a**) le mélange pénétrant approfondie la couche mélangée initiale et crée une anomalie froide en surface (*zone pointillée*) et chaude en sub–surface (*zone hachurée*) ; (**b**) l'anomalie froide de surface est "comblée" par les flux de surface ; (**c**) l'anomalie chaude de sub–surface est advectée vers d'autres régions par la circulation océanique.

1.6.2 Influence des TCs sur le transport méridien de chaleur

Plusieurs études se sont appuyées sur cette hypothèse pour en étudier les implications et/ou pour tenter de la valider. Afin de confirmer l'ordre de grandeur donné par Emanuel, [Sriver *et al.* 2008] utilisent les données satellitaires de SST afin d'évaluer l'amplitude du refroidissement induit pour les TCs à l'échelle globale. En répétant l'hypothèse d'Emanuel selon laquelle le refroidissement de surface égale le réchauffement de sub–surface, ils ré-estiment le flux de chaleur entrant dans l'océan dans le sillage des TCs à 0.48±0.1 PW.

L'importance climatique de ce flux de chaleur induit par le mélange cyclonique a été principalement représentée par l'augmentation du coefficient de mélange dans des modèles de circulation océanique. Cette approche s'avère être très sensible à la durée du mélange appliqué [Sriver *et al.* 2010], à sa profondeur [Fedorov *et al.* 2010], à son amplitude [Sriver & Huber 2010] et à l'extension spatiale où le mélange est appliqué [Jansen & Ferrari 2009]. Les estimations de modification du transport méridien de chaleur évalué dans ces diverses études varient de 0.05 à 0.4 PW, et il existe peu d'observations permettant de valider les hypothèses faites, notamment en ce qui concerne la profondeur et l'amplitude du coefficient de mélange.

L'estimation la plus extrême a été proposée par [Fedorov *et al.* 2010] qui incorporent une paramétrisation du mélange vertical dans un modèle couplé avec une intensité (×10), une profondeur (200 m) et une couverture géographique (la totalité des bandes tropicales 8°–40°) largement exagérées afin de simuler une activité cyclonique accrue. Ils montrent qu'une telle modification dans l'océan réchauffe l'upwelling du Pacifique Est de plusieurs °C et pourrait expliquer l'*El Niño* permanent qui a pu exister au Pliocène. Ils suggèrent donc que la modification d'activité cyclonique par le changement climatique futur pourrait en retour modifier le climat.

Deux défauts principaux de ces études doivent être signalés.
i) L'approche par une simple modification du coefficient de mélange est énergétiquement inconsistante : l'énergie potentielle injectée par un mélange dépend du coefficient de viscosité dynamique et de la stratification ; elle est donnée par $K_z N^2$; c'est cette énergie qui devrait être imposée et non K_z.
ii) La plupart de ces études appliquent un coefficient de mélange annuel, ce qui injecte de la chaleur en sub–surface tout au long de l'année. [Jansen *et al.* 2010] ont cependant suggéré récemment que seule une faible partie de la chaleur injectée en sub–surface par les TCs peut en fait être exportée vers d'autres latitudes. En effet, l'approfondissement de la couche mélangée en hiver ré–entraînerait les anomalies chaudes injectées en été. Ils estiment qu'$^1/_4$ seulement de la chaleur pompée vers le bas persiste après l'hiver mais donnent une fourche(tte) d'erreur de 100% à leur estimation de pompage de chaleur dans l'océan.

L'hypothèse d'un impact majeur des cyclones sur le OHT est donc controversée. Seules des approches théoriques ou de paramétrisation dans des modèles d'océan ont été entreprises pour aborder la question et donnent des estimations très diverses de la modification de l'OHT par les TCs. Pour aller plus loin, une prise en compte explicite de l'effet des cyclones sur l'océan est requise.

Plan de la thèse

L'objectif principal de cette thèse est de détailler les processus de l'interaction entre les cyclones tropicaux et l'océan afin de mieux en comprendre les conséquences. Celles–ci s'articulent autour de 2 enjeux : i) le contrôle de l'intensité d'un TC par l'océan et ii) l'influence des TCs sur l'océan. Le premier enjeu est abordé au niveau de l'événement cyclonique dans la première partie tandis que l'importance climatique des processus dynamiques et thermodynamiques induits par les TCs dans l'océan est traitée dans la deuxième partie. Une approche numérique est utilisée afin d'analyser la réponse océanique aux TCs ; la méthodologie développée permet de répondre aux questions posées à ces deux échelles.

Les prévisions opérationnelles de l'intensité des cyclones tropicaux (TCs) n'ont pas significativement progressé au cours des vingt dernières années. Une voie privilégiée pour les améliorer est de mieux comprendre le couplage cyclone–océan. La rétroaction de l'océan sur un TC s'opère via le refroidissement qui est généré en surface sous l'œil et dans le sillage de chaque TC : la *Cold Wake* (CW).

La première partie de cette thèse s'intéresse aux contrôles de l'amplitude des CWs. Du fait des conditions météorologiques extrêmes qui règnent dans les TCs et de leur localisation géographique, il est très difficile d'utiliser des observations *in situ* pour étudier les CWs. Le chapitre 2 présente l'approche numérique développée dans ma thèse permettant de simuler de manière réaliste les CWs de tous les cyclones qui ont été observés sur les 30 dernières années. Une validation exhaustive des caractéristiques des CWs simulées ainsi qu'une description des processus de la couche mélangée expliquant le refroidissement de surface sont présentées dans le chapitre 3. Le chapitre 4 décrit la dépendance de l'amplitude de la CW aux caractéristiques du TC et de l'océan sur lequel il se déplace ; ce chapitre décrit le contrôle crucial qu'exerce la stratification de l'océan superficiel sur le refroidissement et donc sur le cyclone.

Au cours de leur déplacement, les TCs apportent à l'océan une grande quantité d'énergie cinétique, ce qui leur confère un rôle potentiellement important pour la circulation océanique et le climat.

La deuxième partie de la thèse s'intéresse aux interactions entre les cyclones, l'océan et l'atmosphère à l'échelle climatique. La méthode de modélisation détaillée au chapitre 2 a l'avantage de représenter directement le forçage des TCs à la surface d'un modèle de circulation océanique mondial. L'effet des TCs peut donc y être étudié sans avoir recours à une paramétrisation du mélange. L'influence controversée des TCs sur l'océan à l'échelle climatique est revisitée au chapitre 5. La question de l'influence réciproque, celle de la variabilité océanique sur les TCs, se pose ici naturellement. Celle–ci s'opère indirectement, *via* la variabilité du système couplé et directement *via* une modification des caractéristiques de l'océan influençant les

TCs. Le phénomène *El Niño* est caractérisé par des modifications interannuelles de l'environnement atmosphérique et océanique pouvant renforcer ou détruire les TCs. Son influence sur l'activité cyclonique est illustrée dans la région peu étudiée du Pacifique Sud–Ouest au chapitre 6. L'influence directe de la variabilité de la stratification océanique sur les TCs n'a été abordée que marginalement dans cette thèse, faute de temps, mais ce thème en constitue une perspective majeure.

Première partie

Couplage air–mer à l'échelle du cyclone

Chapitre 2

Modélisation de la réponse océanique aux cyclones

Le chapitre introductif a souligné l'importance pour le cyclone des flux de chaleur de surface et leur altération par la réponse océanique au cyclone. Afin d'étudier ses dépendances tant aux caractéristiques du cyclone qu'à celles de l'océan, il est nécessaire de modéliser de manière réaliste l'amplitude du refroidissement de surface sous un nombre important de cyclones. Le spectre des phénomènes induits par les vents cycloniques est large et leur modélisation requiert, pour certains, des modèles complexes et représentant des échelles fines. Ce chapitre décrit comment la réponse de surface peut être modélisée de manière réaliste à l'aide d'un modèle de résolution modérée.

2.1 Les modélisations forcées de la réponse océanique aux TCs

2.1.1 Comment forcer le modèle d'océan en surface ?

La modélisation de la réponse de l'océan à un TC requiert en premier lieu une représentation la plus réaliste possible du forçage en vent.

Les données satellites de vents QSCAT donnent une structure spatiale réaliste des vents de surface mais sous–estiment systématiquement le maximum de vent dans le mur de l'œil[1]. De plus la fréquence de passage au–dessus de chaque point d'océan est de l'ordre de la journée. Ce type de vent a été utilisé par [Sriver & Huber 2010] pour forcer un modèle d'océan global. Afin de palier à la sous–estimation associée à ces mesures satellitaires, ils ont arbitrairement multiplié les vents QSCAT par 2, ce qui a des conséquences dramatiques pour le réalisme de la réponse océanique : l'amplitude des vents maximum est corrigée, mais les vents sont largement sur–estimés loin de l'œil.

Les observations directes (aéroportées principalement) sont très rares. Il existe un produit de réanalyse (HWIND [Powell *et al.* 1998]) donnant des champs de vent réalistes pour un nombre limité de TCs pour lesquels des données ont été récoltées.

---

[1] D'une part, les précipitations cycloniques perturbent le signal micro–ondes ; et d'autre part, les vents sont évalués à partir de l'état de la mer par QSCAT, or la relation entre vitesse du vent et état de la mer n'est pas calibrée pour les vents les plus intenses.

Ce produit ne décrit que certains TCs dans l'Atlantique et est utilisé couramment pour des études de cas (*e.g.* [Sanford *et al.* 2007]). Ces champs de vent sont assez réalistes, mais ce type de produit ne permet pas de couvrir le large spectre des caractéristiques des TCs et des conditions océaniques sur lesquelles ils se déplacent.

Les réanalyses atmosphériques représentent la plupart des dépressions tropicales sous la forme de faibles TCLVs (*i.e. Tropical Cyclone–Like Vortices*) mais ont une résolution horizontale trop lâche pour simuler correctement l'amplitude des TCs, notamment autour de l'œil. Les réanalyses sur–estiment la dimension du cyclone (~100% pour le RMW) et sous–estiment de plus de ~50% l'intensité maximale des vents, en particulier pour les cyclones intenses. Le refroidissement de surface simulé avec un modèle océanique forcé par des vents issus de réanalyse est largement sous–estimé [Halliwell Jr *et al.* 2010]. L'augmentation de la puissance de calcul dans les années à venir (et donc potentiellement de la résolution horizontale des réanalyses) offre des perspectives intéressantes pour permettre d'améliorer le réalisme des TCLVs représentés par les réanalyses mais la résolution reste insuffisante à ce jour.

Enfin, il est possible de reconstruire les champs de vent des cyclones en connaissant leur position, taille et intensité et en utilisant des vortex paramétriques (1.1.1.2). Cette approche a permis à [Liu *et al.* 2008] d'estimer l'énergie mécanique transférée à l'échelle globale par les TCs.

2.1.2 Modèles de circulation océanique utilisés précédemment

• **Modèle 1D ou 3D ?** La plupart des études de modélisation de réponse océanique aux TCs ont été réalisée dans des modèles régionaux permettant l'utilisation d'une résolution horizontale très fine (~1/10 °). [Sanford *et al.* 2007] ont simulé la réponse de l'océan au passage du TC Frances à l'aide d'un modèle régional tri–dimensionnel de circulation océanique à très haute résolution (10 m sur la verticale, 5 km sur l'horizontale). Le champ de vent de surface est issu de la réanalyse HWIND. Ce modèle permet de reproduire de manière très réaliste les oscillations de courants et leur propagation sur la verticale ainsi que la réponse thermique de l'océan au cyclone (figure 2.1 à comparer à la figure 1.22).

Parallèlement aux modèles tri–dimensionnels résolvant les équations primitives, des modèles uni–colonne extrêmement simple ont aussi été utilisés pour simuler la réponse en SST au forçage cyclonique. Partant du constat que le mélange vertical domine la réponse en SST, [Emanuel *et al.* 2004] a ainsi couplé un modèle atmosphérique axisymétrique de cyclone à un modèle uni–dimensionnel d'océan où le mélange vertical est paramétrisé en fonction de l'intensité des vents. Cette approche est raisonnable en première approximation car le couplage améliore considérablement le réalisme des intensités de cyclone prévu par le modèle.

Extrait de [Sanford *et al.* 2007]

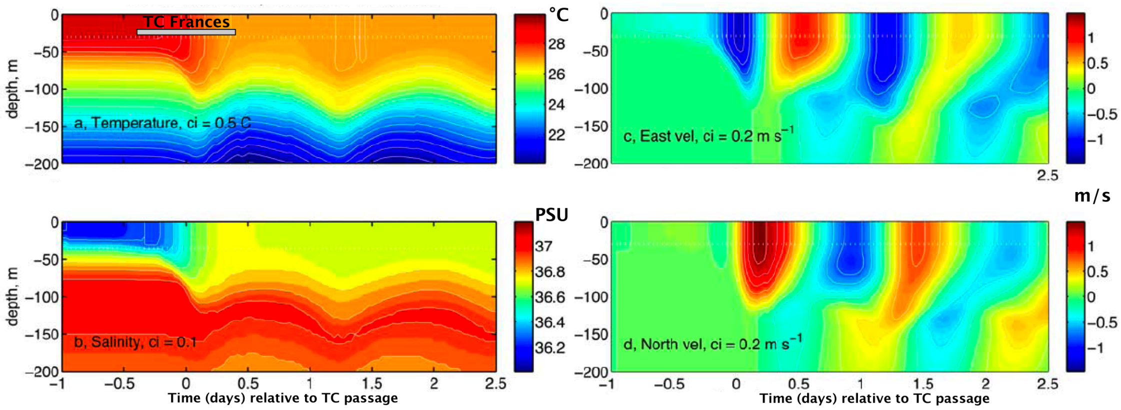

Figure 2.1 – Modélisation des propriétés océaniques à 55 km à droite de la trajectoire du TC Frances des (**a**) Température, (**b**) Salinité, (**c**) courant zonal et (**d**) courant méridien. Ces résultats de modélisation sont à comparer aux observations de la figure 1.22.

La prépondérance du mélange vertical ne signifie pas que les autres processus n'ont pas un rôle dans la réponse océanique. [Yablonsky & Ginis 2009] montrent que l'advection verticale permet d'augmenter l'effet refroidissant du mélange, et ce d'autant plus que la vitesse de translation du TC est faible (Fig. 2.2).
Il convient donc de prendre en compte l'advection verticale lorsque l'on veut simuler précisément le refroidissement de surface. La simulation de l'advection verticale requiert un modèle tri–dimensionnel simulant correctement les courants induits par le TC et les convergences/divergences associées. Il est envisageable d'utiliser un modèle 1D dans lequel le pompage d'Ekman est paramétrisé pour prendre en compte la non–linéarité pompage–mélange, mais ce type de modèle ne permet pas de simuler l'importance éventuelle de l'advection sur l'océan à plus long terme.

• **La paramétrisation du mélange vertical** Le mélange vertical sous les cyclones provient principalement de la tension de vent de surface (en amont du TC) et du cisaillement de courant (sous et dans le sillage des TCs) [Jacob & Shay 2003]. Ces processus ne sont pas résolus pour des modèles de résolutions couramment utilisées en océanographie et doivent donc être paramétrisés. Il existe différentes manières de paramétriser le mélange dans les modèles de circulation océanique ; une bibliographie pléthorique existe sur le sujet ([Large *et al.* 1994] en font une bonne revue). Une description exhaustive de la physique contrôlant le mélange et de sa modélisation est au–delà du champ de cette thèse, seules les paramétisations les plus couramment utilisées dans des cas de modélisation de l'océan sous des cyclones sont évoquées ci–dessous. [Jacob & Koblinsky 2007] testent la sensibilité de l'amplitude de la CW simulée sous un cyclone idéalisé en utilisant les 5 paramétri-

Extrait de [Yablonsky & Ginis 2009]

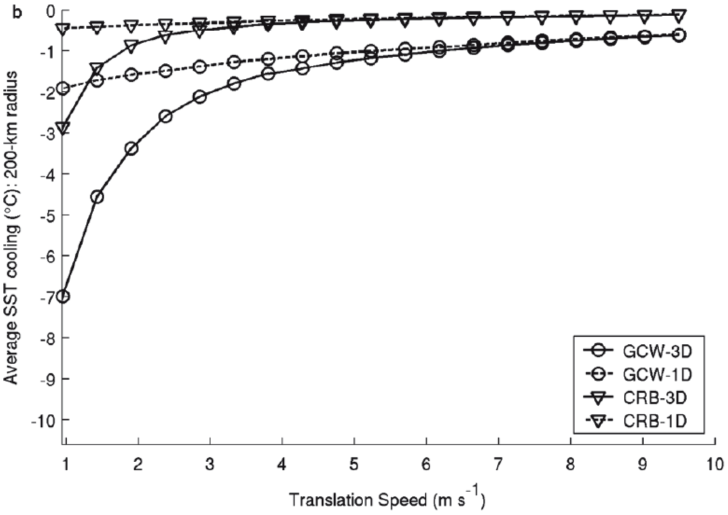

Figure 2.2 – Refroidissement moyen dans un rayon de 200 km de l'œil obtenus avec un modèle 3D (*lignes continues*) et avec un modèle 1D (*lignes pointillées*) forçant un océan à stratification thermique prononcée typique du Golfe du Mexique (GCW *cercles*) ou à faible stratification typique des Caraïbes (CRB *triangles*).

sations du mélange vertical disponible dans le modèle HYCOM (Fig. 2.3).
Nous pouvons regrouper ces paramétrisations en 3 familles :

i les modèles intégraux de couche de mélange (PWP [Price *et al.* 1986] ; *Gaspar* [Gaspar 1988] ;

ii la fermeture *KPP* (*K-profile parameterization*) [Large *et al.* 1994] qui est totalement diagnostique ;

iii les paramétrisations basées sur des fermetures en énergie cinétique turbulente : *MY* [Mellor & Yamada 1982] et *GISS* (du *Goddard Institute of Space Studies* [Canuto *et al.* 2001]).

Les différentes paramétrisations donnent des amplitudes de CW peu différentes, à l'exception des modèles intégraux. MY, GISS et KPP sont les plus réalistes selon [Jacob & Shay 2003].

• **Modèle régional ou global ?** Les modèles idéalisés ou régionaux à très haute résolution couramment utilisés en prévision opérationnelle ne permettent pas de généraliser la dépendance de l'amplitude de la CW à la variété des cyclones existants et de l'état de l'océan sur lequel ils se déplacent.

D'autre part, pour étudier les interactions entre les TCs et le climat, des modèles très simple (*e.g.* modèle à $2^1/_2$ couches dans [Liu *et al.* 2008]) ou des modèles globaux de circulation océanique (*e.g.* [Fedorov *et al.* 2010], [Jansen & Ferrari 2009], Extrait de [Jacob & Koblinsky 2007]

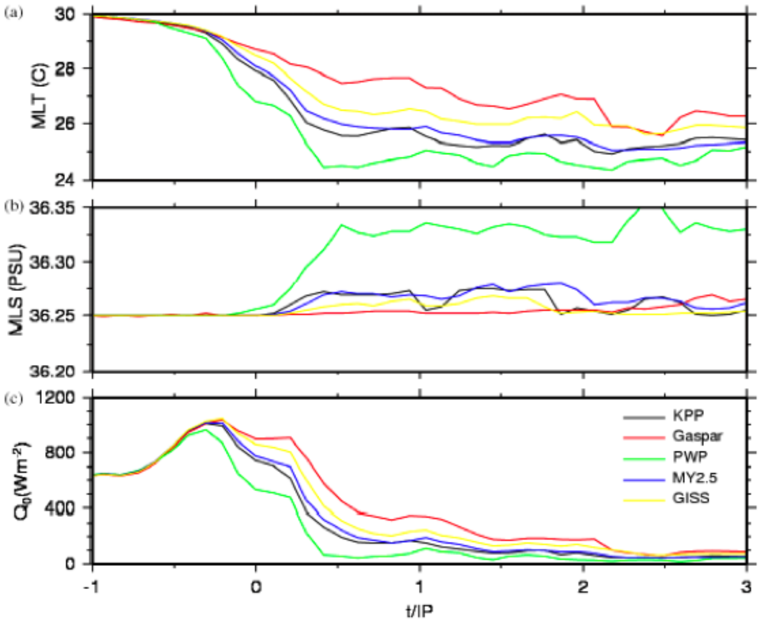

Figure 2.3 – Séries temporelles de température (**a**) et salinité (**b**) dans la couche mélangée et de flux de surface (**c**) sous un TC idéalisé en utilisant les 5 paramétrisations du mélange vertical du modèle HYCOM.

[Korty *et al.* 2008]) ont été utilisés. Dans ces dernières études, la résolution utilisée est très basse (∼3–4°) et l'effet des TCs est représenté par un mélange vertical additionnel dont les caractéristiques sont hautement idéalisées.

La section suivante décrit l'approche expérimentale développée pour combler le fossé entre ces deux approches.

2.2 Description du protocole expérimental

Cette section décrit "l'esprit" de l'approche expérimentale suivie et sa particularité par rapport aux autres études existantes. Une description détaillée des différentes expériences réalisées et la validation des résultats par rapport aux observations peut être trouvée dans le chapitre 3.

[Halliwell Jr *et al.* 2010] donnent un bon aperçu de l'importance respective des ingrédients nécessaires pour réaliser une simulation réaliste de l'océan forcé par un cyclone. Cette référence est utilisée pour valider (rétrospectivement) la plupart des choix du protocole expérimental.

2.2.1 Forçage de l'océan

• **Vents cycloniques** Les données IBTrACS donnent des positions et $V_{\max}$ à 6h fiables pour tous les TCs du globe sur les 30 dernières années environ. Le vortex de Willoughby (1.1.1.2) est utilisé pour reconstruire le champ de vent de surface autour des trajectoires. Les avantages d'utiliser un vortex paramétrique sont que :

i le forçage en vent décrit explicitement les vents intenses du mur de l'œil ;

ii il est possible de reconstruire le champ de vent au pas de temps du modèle océanique et ainsi d'éviter l'étalement de la structure fine du TC par interpolation spatiale[2] ;

iii l'expression du champ de vent est peu coûteuse en mémoire (il n'est pas nécessaire de sauvegarder de lourds champs 2D de forçage à haute fréquence temporelle) ;

iv d'utiliser un nombre réduit d'information pour chaque TC autorisant de reconstituer le forçage de plus de 3000 cyclones.

Un inconvénient est que le vortex est basé sur le champ de vent moyenné sur de nombreux TCs ; il est donc possible de faire des études statistiques sur de nombreux TCs, mais, pris individuellement, chaque cyclone diffère des observations.

• **Fréquence de forçage** Un cyclone est un événement haute–fréquence associé à d'importantes variations du vent (intensité et direction) en un point en l'espace de quelques heures. De telles variations temporelles du forçage engendre une réponse proche–inertielle de l'océan susceptible d'influencer tant l'intensité que la structure spatiale (asymétrie) de la CW. La fréquence d'application du forçage est donc capitale pour fournir à l'océan la bonne quantité d'énergie, une périodicité de reconstruction du vortex de l'ordre de l'heure ou moins est donc nécessaire. Avec un intervalle de forçage à 6h par exemple, le TC peut se déplacer de ∼100km, ce qui correspond à la dimension spatiale de retournement des vents ; la rotation ne sera pas bien capturée par le modèle d'océan.

• **Flux de surface** Afin de rendre compte de l'augmentation des flux de surface associée aux vents des cyclones, le vent à 10m du vortex cyclonique est ajouté au vent de la réanalyse CORE. Les TCLVs de CORE ont été préalablement filtrés afin d'éviter de sur–estimer la quantité de mouvement transmise à l'océan (une expérience sans filtrage montre des CWs d'amplitudes sur–estimées).

Concernant les flux de chaleur, le vent total sous le cyclone a été utilisé dans les *bulk*, permettant de prendre en compte l'effet du module du vent sur les flux. Cependant, en toute rigueur, l'humidité, la température de l'air, le flux solaire. . . doivent

---

[2] La position et le vent max à 6h sont interpolés au pas de temps du modèle (36 min) ; le vortex est alors reconstruit avec ces informations.

être aussi modifiés en accord avec les caractéristiques du cyclone, ce qui influencerait aussi le flux de chaleur. Très peu de données décrivent les profils d'anomalies de température et d'humidité de l'air dans la CLA des cyclones. Faute de solution adaptée, ces anomalies n'ont pas été prises en compte dans le calcul des *bulk*.

Enfin les précipitations associées aux TCs n'ont pas été intégrées dans les expériences présentées dans cette thèse. Sur la base de considérations théoriques et d'observations, une étude de [Jourdain *et al.* 2012] montre que l'effet stabilisant des précipitations (comme leur apport de chaleur) peut être négligé en ce qui concerne l'amplitude de la CW. Par contre, une étude de modélisation couplée océan–atmosphère de [Hu & Meehl 2009] suggère que les précipitations cycloniques pourraient influencer le transport méridien de chaleur en Atlantique.

• **Coefficients de transferts** On a vu en introduction que les coefficients de transferts sont paramétrisés. De la formulation précise du coefficient de transfert dépendent l'énergie transmise à l'océan, l'amplitude des courants, leur cisaillement et donc le mélange ainsi que le pompage d'Ekman. La saturation de C_D aux vents forts est cruciale ; ne pas la prendre en compte, conduit à une large sur–estimation des CWs pour les cyclones forts [Halliwell Jr *et al.* 2010]. Certaines études (*e.g.* [Jarosz *et al.* 2007]) suggèrent même que C_D diminue au–delà de ∼40 m/s de vent. Les incertitudes sur la formulation exacte de C_D restent élevées. Nous utilisons la formulation de COARE [Large & Yeager 2009] dont les coefficients de transfert de chaleur et de quantité de mouvement saturent au–delà de 33 m/s (comme observé par [Donelan *et al.* 2004]) ; cette formulation donne des résultats réalistes [Halliwell Jr *et al.* 2010].

Remarque : [Liu *et al.* 2008] n'ont pas pris en compte la saturation de C_D dans leur étude globale de l'énergie transférée à l'océan par les cyclones ; leur estimation du transfert d'énergie des TCs à l'océan est donc vraisemblablement sur–estimée.

2.2.2 Le modèle d'océan NEMO

• **Résolution** Les expériences sont réalisées en forçant le modèle global de circulation océanique NEMO (*Nucleus for European Modeling of the Ocean*) configuré au $^1/_2$° de résolution horizontale. Le pas de temps associé est de 36 minutes, ce qui est suffisant pour capturer les variations temporelle du vent pour les vitesses de translation typiques des TCs.

La configuration possède 46 niveaux verticaux, avec une résolution verticale de 10 m près de la surface (et 250 m en profondeur). Une résolution verticale de 10 m est suffisante selon [Halliwell Jr *et al.* 2010]. L'article préconise aussi une résolution de 10 km sur l'horizontale, ce qui est nettement supérieur à notre configuration. Notre résolution n'est certainement pas suffisante pour reproduire la propagation vers l'océan profond des ondes internes d'inertie–gravité par exemple. Notre résolu-

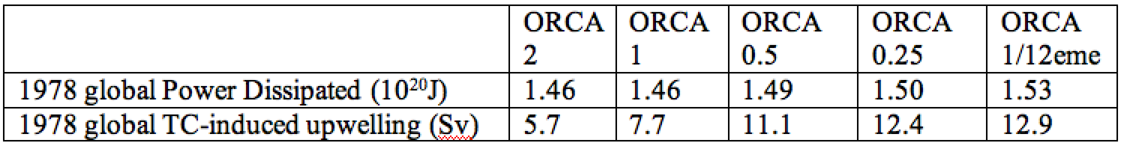

	ORCA 2	ORCA 1	ORCA 0.5	ORCA 0.25	ORCA 1/12eme
1978 global Power Dissipated (10^{20}J)	1.46	1.46	1.49	1.50	1.53
1978 global TC-induced upwelling (Sv)	5.7	7.7	11.1	12.4	12.9

Table 2.1 – Comparaison de la Puissance dissipée et du Pompage d'Ekman associés à tous les TCs de l'année 1978 pour des grilles de résolutions croissantes.

tion de $^1/_2$° ne permet pas de reproduire certains des phénomènes de fine échelle[3]. Elle reste cependant ∼8 fois plus élevée que celle utilisée dans les autres approches globales de l'effet des TCs sur l'océan. Toutefois, un des problèmes majeur d'une résolution insuffisante est que les modèles d'océan sont souvent forcés par des données atmosphériques à une résolution spatiale similaire et à une résolution temporelle lâche. Une résolution du $^1/_2$° ne permet pas de représenter correctement la structure du cyclone. L'utilisation d'un vortex paramétrique nous permet d'éviter ce problème ; techniquement, un point d'océan peut voir passer le cyclone avec une amplitude, une variation temporelle et une orientation des vents réalistes. La question qui demeure est de savoir comment le modèle d'océan, et la grille associée, capture ce forçage atmosphérique (*i.e.* l'effet du sous–échantillonnage spatial). La figure 2.4 illustre la puissance dissipée (PD, un proxy de l'énergie disponible pour l'océan) et le pompage d'Ekman forçant l'océan en utilisant des grilles de résolution croissante. Le PD est très bien échantillonné par une grille au $^1/_2$° ; le pompage, lui, est très bien résolu à partir du $^1/_4$° dans le cas de ce cyclone particulièrement intense. Le tableau 2.1, qui compare ces mêmes grandeurs cumulées sur tous les TCs du globe, montre que la quantité totale d'énergie dissipée par les cyclones en une année est similaire à toutes les résolutions testées (avec une sous–estimation atteignant 5% pour le 2° par rapport au $^1/_{12}$°). Pour le pompage d'Ekman cumulé, le $^1/_2$° sous–estime le $^1/_{12}$° de ∼15% alors que le 2° sous–estime de moitié.

Nous utilisons une simulation au $^1/_2$° qui offre un compromis intéressant entre la précision du forçage et le coût numérique.

• **Paramétrisation du mélange vertical** La paramétrisation du mélange utilisée est basée sur une fermeture en énergie cinétique turbulente (TKE pour *Turbulent Kinetic Energy*. Cette fermeture repose sur une équation d'évolution temporelle de TKE régie principalement par un terme source lié au cisaillement vertical de courant, un terme de destruction par la stratification, et un terme puit de dissipation à l'échelle moléculaire (cascade de Kolmogorov). La longueur de mélange est évaluée en convertissant la TKE en énergie potentielle. Elle a été initialement développée dans les modèles d'atmosphère ([Bougeault & Lacarrere 1989]), adaptée à

---

[3] Par exemple la propagation des ondes de gravité proche–inertielles qui se propagent dans l'océan intérieur (d'une échelle de 80 à 250 km) ou encore les interactions entre le cyclone et les structures méso–échelle océaniques (tourbillons/filaments).

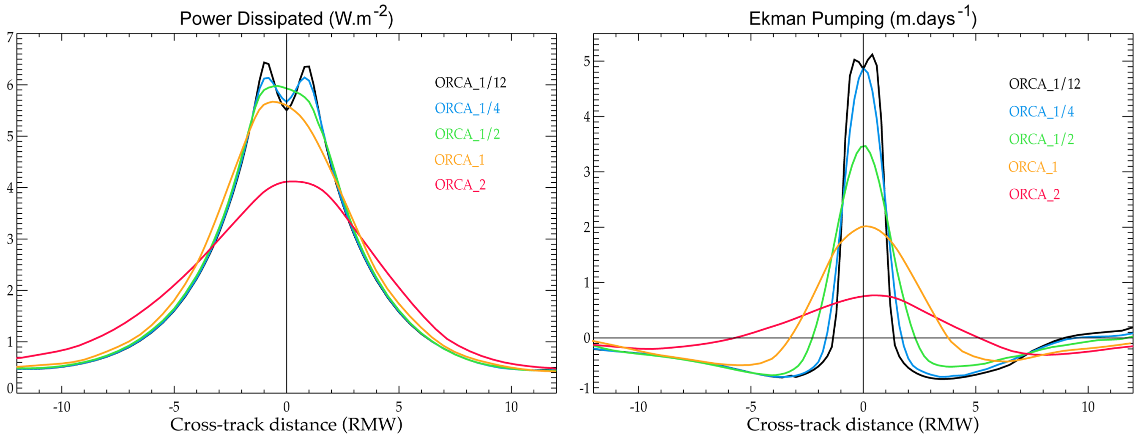

Figure 2.4 – Comparaison de la Puissance dissipée (a) et du Pompage d'Ekman (b) reproduisant le forçage du TC DORA (du 25 Jan. au 7 Fév. 2007) pour des grilles de résolutions croissantes. Les sections sont des moyennes des sections réalisées à chaque position du cyclone (toutes les 6h) dans les champs de PD et pompage d'Ekman moyennés sur la durée de vie du TC.

l'océan par [Gaspar *et al.* 1990] et incorporée dans OPA (l'ancêtre de NEMO) par [Blanke & Delecluse 1993]. La dernière version, celle que j'ai utilisé dans ma thèse, comporte les améliorations suivantes [Madec 2008] :

i l'ajout d'une paramétrisation de l'effet des cellules de Langmuir ([Axell 2002] ; qui, pour l'essentiel, permet de maintenir une couche de mélange profonde en période de chauffage) ;

ii l'ajout d'une paramétrisation de l'effet des vagues (qui renforce substantiellement (× 60) la valeur de TKE en surface et augmente la profondeur de mélange [Mellor & Blumberg 2004]) ;

iii l'introduction d'un changement de la discrétisation spatiale et temporelle des termes de l'équation de TKE. Ceci permet d'assurer que l'énergie cinétique de grande échelle dissipée par cisaillement équilibre exactement le terme source de TKE et que l'énergie potentielle injectée à grande échelle équilibre le terme de destruction de TKE [Burchard 2002, Marsaleix *et al.* 2008]. Le gain en stabilité numérique ainsi obtenu permet de se débarrasser de la procédure de moyenne horizontale (sur 9 points) introduite par [Blanke & Delecluse 1993].

Ce type de fermeture s'est avéré performant pour reproduire l'amplitude des refroidissements induits par les TCs [Jacob & Koblinsky 2007].

• **Réalisme de la structure 3D du champ de température** L'amplitude du refroidissement de surface induit par un mélange dépend de la stratification thermique de l'océan. En prévision opérationnelle, une initialisation correcte de la structure 3D du champ de température est donc cruciale (*e.g.* [Halliwell Jr *et al.* 2010]).

Dans notre cas, cette condition se traduit par la nécessité que les TCs soient placés sur un océan reproduisant correctement la profondeur de la ML, de la thermocline... Le modèle NEMO forcé par les vents CORE reproduit des structures climatologiques de température et de salinité réalistes. Cependant, la variabilité haute–fréquence du modèle d'océan ne correspond pas exactement à la variabilité observée. D'un point de vue statistique, les cyclones rencontrent des profils océaniques réalistes, mais on ne peut attendre que chaque CW corresponde à celle observée.

Remarque : La réponse tri–dimensionnelle de l'océan décrite dans cette thèse est très proche de celle décrite dans l'article de [Jullien *et al.* 2012]. L'utilisation de 2 modèles différents (NEMO $1/2°$ vs ROMS $1/3°$), 2 paramétrisations différentes du mélange vertical (TKE vs KPP), donne confiance sur la faible sensibilité des résultats obtenus à ces choix.

Chapitre 3

Processus du refroidissement dans la couche mélangée

Ce chapitre est basé sur l'article [Vincent *et al.* 2012a].

Depuis les travaux de [Price 1981], il est communément admis que le mélange vertical est le processus dominant le refroidissement de surface dans le sillage des cyclones tropicaux. Les autres processus sont i) l'advection verticale/horizontale qui redistribue spatialement les anomalies de température (ce processus ayant été très peu étudié [Huang *et al.* 2009]) et ii) les flux de chaleur en surface qui refroidissent l'océan, principalement par évaporation [Trenberth & Fasullo 2007]. Dans la suite ces 3 processus dominants sont notés MIX (pour le mélange), FOR (pour les flux de surface) et ADV (pour l'advection).

Jusqu'à présent, ces processus ont été étudiés principalement à partir d'études de cas avec une attention particulière pour les cyclones les plus intenses et les processus se déroulant près de la trajectoire du TC [D'Asaro *et al.* 2007]. L'article qui suit détaille l'importance relative des différents processus en fonction de la distance au centre du cyclone, de la puissance du TC et de l'état de stratification de l'océan. Pour caractériser la puissance du cyclone et la stratification océanique, nous utilisons deux métriques définies dans l'article [Vincent *et al.* 2012c]. Le WPi (pour *Wind Power index*) intègre l'énergie dissipée par friction à l'interface air–mer sous un cyclone. L'intégration permet de prendre en compte la vitesse maximale des vents, la vitesse de translation et la taille du cyclone dans un index atmosphérique unique. Le CI (pour *Cooling Inhibition index*) est un indice mesurant la résistance de la stratification océanique à générer un refroidissement de surface par mélange. La description détaillée de ces deux indices ainsi qu'une étude approfondie de leur pertinence sont données dans le chapitre suivant (4).

Synthèse de l'article

Afin de valider la capacité de notre dispositif expérimental à reproduire de manière réaliste la réponse océanique aux TCs, l'article présente une comparaison détaillée des caractéristiques des CWs simulées (amplitude, extensions spatiale et temporelle) par rapport aux observations satellites. En moyenne, l'amplitude du refroidissement moyen dans un rayon de 200 km autour de chaque point de trajectoire est de 1°C dans le modèle et les observations. La comparaison de l'amplitude de chacun des refroidissements individuels simulés et observés est raisonnable (corrélation de 0.71). On ne peut s'attendre à une correspondance parfaite entre les refroidissements individuels simulés et observés ; en effet, le vortex analytique ne correspond pas exactement à la structure de chaque cyclone et la variabilité interne océanique de fine échelle diffère entre le modèle et les observations. La dépendance de l'amplitude de la CW à la force du cyclone est aussi correctement reproduite. L'amplitude du refroidissement augmente avec V_{max} jusqu'à $\sim$40 m/s puis sature pour les vents plus élevés en accord avec les résultats de [Lloyd & Vecchi 2010]. Par contraste, l'amplitude du refroidissement augmente linéairement avec la puissance du cyclone (WPi). Le modèle sur–estime l'amplitude du refroidissement induit par les cyclones les plus puissants, mais les refroidissements les plus intenses sont aussi ceux qui sont le plus probablement sous–estimés dans les observations, étant associés à des cyclones lents qui ne permettent pas une mesure fiable de la signature en température de surface par les satellites. En moyenne l'évolution temporelle du refroidissement simulé reproduit fidèlement les observations : le minimum de température est atteint 1 à 2 jours après le passage du TC et la CW se dissipe avec un temps caractéristique de $\sim$15 jours, principalement sous l'effet des flux de chaleur en surface. L'extension spatiale est légèrement sous–estimée, probablement du fait de la forme du vortex analytique. Le refroidissement dépasse les -0.5°C typiquement sur une distance de 4–5 rayons de vent maximum, soit environ 200 km. Le très bon accord général entre les CWs modélisées et les observations permet d'utiliser avec confiance le modèle pour décrire les contributions relatives des différents processus au refroidissement de surface.

Nous retrouvons l'effet prépondérant du mélange vertical dans le refroidissement induit près de la trajectoire. Cependant l'importance de chacun des processus impliqués dans le refroidissement est modulée par la puissance du cyclone, la distance à la trajectoire, ainsi que la stratification océanique. Pour les TCs les plus puissants, MIX explique effectivement 80% du refroidissement, mais ce chiffre passe à 30% pour les TCs faibles. L'augmentation linéaire de l'amplitude du refroidissement avec le WPi est expliquée par l'augmentation du terme de mélange. Les flux de surface jouent un rôle relatif important sous les cyclones faibles, mais le terme sature pour les cyclones de puissance modérée à forte. La faible valeur absolue du refroidissement dû aux flux de chaleur (latent principalement) ne doit pas mener à en sous–estimer l'importance. Loin de l'œil, ce processus explique $\sim$50% du refroidissement sur des superficies très importantes. Il est donc erroné d'attribuer la totalité du refroidissement au terme de mélange lorsque l'on s'intéresse aux grandes échelles spatiales.

La dépendance de l'amplitude du refroidissement à la stratification de l'océan est principalement liée à la modulation du terme MIX. Alors que la valeur absolue du refroidissement par les flux de chaleur et l'advection est peu modifiée, l'amplitude du refroidissement par mélange est ~5 fois plus forte dans les cas de fortes stratifications océaniques que de faibles stratifications (à puissance de TC constante). La part relative du mélange dans le refroidissement total varie en conséquence : elle approche les 60% pour les faibles stratifications contre 85% pour les fortes stratifications. Une inhibition élevée (fort CI) peut être associée à une couche mélangée (ML) profonde et/ou un faible gradient vertical de température à sa base. Dans ces conditions, un mélange entraîne peu de modifications de SST car une ML profonde a une capacité thermique élevée et un faible $\partial_z T$ ne permet pas d'incorporer des eaux froides dans la ML.

L'advection horizontale a généralement un rôle plus limité, mais les courants d'Ekman peuvent expliquer jusqu'à 15% du refroidissement sous les TCs les plus puissants en chassant les eaux chaudes superficielles vers l'extérieur du TC. L'article met aussi en évidence le rôle prépondérant de l'advection dans l'asymétrie de la CW pour les TCs les plus puissants. La résonance des courants inertiels sur le côté droit[1] de la trajectoire (donc le terme MIX) explique l'essentiel de l'asymétrie pour les TCs de puissance modérée. Cependant, les courants géostrophiques (en rotation cyclonique) induits par le TC participent aussi à l'asymétrie de la CW. Sur un axe perpendiculaire à la direction de propagation du TC, ils advectent de l'eau froide de la CW vers l'avant du côté inertiel, alors qu'ils advectent de l'eau relativement chaude vers l'arrière de l'autre côté de la trajectoire. Bien que plus anecdotique pour le couplage cyclone–océan, ce résultat est difficilement observable dans des études de cas et apparaît grâce au grand nombre de réalisations que nous avons mené dans l'expérience.

Article

---

[1] gauche en hémisphère Sud

JOURNAL OF GEOPHYSICAL RESEARCH, VOL. 117, C02020, doi:10.1029/2011JC007396, 2012

Processes setting the characteristics of sea surface cooling induced by tropical cyclones

Emmanuel M. Vincent,[1] Matthieu Lengaigne,[1] Gurvan Madec,[1,2] Jérôme Vialard,[1]
Guillaume Samson,[1] Nicolas C. Jourdain,[3] Christophe E. Menkes,[1,4] and Swen Jullien[5]

Received 23 June 2011; revised 21 November 2011; accepted 22 November 2011; published 9 February 2012.

[1] A 1/2° resolution global ocean general circulation model is used to investigate the processes controlling sea surface cooling in the wake of tropical cyclones (TCs). Wind forcing related to more than 3000 TCs occurring during the 1978–2007 period is blended with the CORE II interannual forcing, using an idealized TC wind pattern with observed magnitude and track. The amplitude and spatial characteristics of the TC-induced cooling are consistent with satellite observations, with an average cooling of ∼1°C that typically extends over 5 radii of maximum wind. A Wind power index (*WPi*) is used to discriminate cooling processes under TCs with high-energy transfer to the upper ocean (strong and/or slow cyclones) from the others (weak and/or fast cyclones). Surface heat fluxes contribute to ∼50 to 80% of the cooling for weak *WPi* as well as away from the cyclone track. Within 200 km of the track, mixing-induced cooling increases linearly with *WPi*, explaining ∼30% of the cooling for weak *WPi*s and up to ∼80% for large ones. Mixing-induced cooling is strongly modulated by pre-storm oceanic conditions. For a given *WPi*, vertical processes can induce up to 8 times more cooling for shallow mixed layer and steep temperature stratification than for a deep mixed layer. Vertical mixing is the main source of rightward bias of the cold wake for weak and moderate *WPi*, but along-track advection becomes the main contributor to the asymmetry for the largest *WPi*s.

Citation: Vincent, E. M., M. Lengaigne, G. Madec, J. Vialard, G. Samson, N. C. Jourdain, C. E. Menkes, and S. Jullien (2012), Processes setting the characteristics of sea surface cooling induced by tropical cyclones, *J. Geophys. Res.*, *117*, C02020, doi:10.1029/2011JC007396.

1. Introduction

[2] The ocean surface can cool by up to 10°C in the wake of tropical cyclones [*Chiang et al.*, 2011]. Such cooling was until recently mostly documented from ship measurements [*Leipper*, 1967], bathythermographs [*Shay et al.*, 1992] and buoy arrays [*Cione et al.*, 2000; *D'Asaro*, 2003]. The availability of satellite microwave sea surface temperature (SST) measurements, which are less sensitive to masking by clouds than infrared measurements [*Wentz et al.*, 2000], now allows a more extensive description of the SST response in several TC case studies [e.g., *Lin et al.*, 2005; *Chiang et al.*, 2011]. *Lloyd and Vecchi* [2011] describe TC-induced cooling at the global scale for the entire microwave satellite period. Their study reveals that the cold wake amplitude increases monotonically with the cyclone intensity up to category 2 but saturates for larger TC wind forcing. This result led the authors to assume that oceanic feedbacks could inhibit intensification of cyclones.

[3] Because TCs draw their energy from evaporation at the ocean surface [*Emanuel*, 1986, 2003], sea surface temperature (SST) changes under the storm's eye can negatively feed back on cyclone intensification, as suggested by observational [*Cione and Uhlhorn*, 2003; *Kaplan and DeMaria*, 2003] and modeling results [*Schade and Emanuel*, 1999; *Bender and Ginis*, 2000; *Shen and Ginis*, 2003; *Schade*, 2000]. Among other influences–such as the storm's inner core dynamics or the structure of the synoptic-scale environment–processes that control the upper-ocean temperature under the TC remain one of the major uncertainties for improving TC intensity forecasts [*Marks et al.*, 1998].

[4] Dominant processes in the oceanic response to TCs have mainly been discussed through cases studies in both observations [*Sanford et al.*, 1987; *D'Asaro*, 2003; *D'Asaro et al.*, 2007] and models [*Price*, 1981; *Morey et al.*, 2006; *Chiang et al.*, 2011; *Huang et al.*, 2009; *Chen et al.*, 2010]. These studies show that three main processes control SST fluctuations under TCs: oceanic vertical mixing, advection and air-sea heat exchange. The upper ocean cooling is primarily controlled by the entrainment of cold water from the thermocline into the mixed layer through vertical mixing,

---

[1] LOCEAN, IRD/CNRS/UPMC/MNHN, Paris, France.
[2] NOC, Southampton, UK.
[3] LEGI, CNRS/UJF/INPG, Grenoble, France.
[4] IRD, Noumea, New Caledonia.
[5] LEGOS, IRD/CNRS/UPS, Toulouse, France.

0148-0227/12/2011JC007396

principally generated by the vertical shear of horizontal currents [*Pollard et al.*, 1973; *Price*, 1981; *Huang et al.*, 2009]. This entrainment mixing accounts for about 80% of the SST drop in TCs wakes [*Price*, 1981; *Sanford et al.*, 1987; *Shay et al.*, 1992; *Huang et al.*, 2009], but its contribution to the total cooling varies depending on the case study considered, from 70% in the case of TC Gilbert [*Jacob et al.*, 2000] to more than 90% in the case of TC Frances [*D'Asaro et al.*, 2007] or TC Gloria [*Bender et al.*, 1993]. Vertical mixing also seems to be responsible for the asymmetry of the cold anomaly with respect to the TC translation direction. Most intense inertial oscillations (and associated vertical shear) are indeed generated to the right (left) of the track in the Northern (Southern) Hemisphere, where TC winds rotate in the same direction as inertial currents, thus increasing the energy transfer to these currents [e.g., *Price*, 1981].

[5] Although of secondary importance, enhanced surface heat fluxes and advection processes also contribute to the TC-induced cooling. Evaporation (latent heat) dominates TC-related heat fluxes, while sensible, shortwave, longwave and precipitation-related fluxes play a lesser role [*Jacob et al.*, 2000; *Huang et al.*, 2009]. A coupled simulation of Hurricane Dennis revealed that air-sea heat exchanges were responsible for a widespread cooling of the sea surface and largely contributed to the total cooling far from the TC track for this cyclone [*Morey et al.*, 2006]. While cyclone-induced vertical suction cools the subsurface ocean near the cyclone track (S. Jullien et al., Impact of tropical cyclones on the South Pacific Ocean heat budget, submitted to *Journal of Physical Oceanography*, 2011), the effect of water advection on the structure of surface temperature anomalies requires further description. Indeed, horizontal advection has been shown to be locally important and it is suggested that it modulates the spatial pattern of the cold wake [*Huang et al.*, 2009; *Chen et al.*, 2010] as well as its asymmetry [*Greatbatch*, 1983].

[6] Most of the aforementioned studies investigate the mechanisms controlling the cold wake characteristics for case studies of individual or a limited number of TCs. Although vertical mixing was identified as the major contributor to the cooling around the TC eye, the respective contribution of each process to the observed cooling is shown to vary from one cyclone to another. The heat balance has also generally been examined in the region of maximum cooling or at a few points sampled by moored instrumentation of drifting buoys, while the cyclone-induced cooling often extends over hundreds of kilometers. A systematic study of the processes controlling the SST anomaly off the cyclone core region is however still missing [*D'Asaro et al.*, 2007].

[7] Past case studies have illustrated the influence of subsurface oceanic background conditions on the TC-induced SST signature [*Shay et al.*, 2000; *Cione and Uhlhorn*, 2003; *Jacob and Shay*, 2003; *Shay and Brewster*, 2010]. Further support for sub-surface oceanic control of the amplitude of the TC-induced cooling has recently been provided on a global scale [*Lloyd and Vecchi*, 2011; E. M. Vincent et al., Assessing the oceanic control on the amplitude of sea surface cooling induced by tropical cyclones, submitted to *Journal of Geophysical Research*, 2011]. Vincent et al. (submitted manuscript, 2011) show that the widely varying characteristics of upper-ocean pre-cyclone stratification can modulate the amplitude of TC-induced cooling by up to an order of magnitude for a given level of TC wind energy input to the upper ocean, but processes responsible for this modulation still need to be assessed.

[8] Because detailed observations under TCs are scarce, modeling offers a promising alternative to perform such an investigation. A few modeling studies [*Liu et al.*, 2008; *Sriver and Huber*, 2010; *Scoccimarro et al.*, 2011] have already performed global ocean simulations including TCs forcing. Using a simplified four layer ocean model forced by idealized hurricane wind forcing, *Liu et al.* [2008] estimated the rate of mechanical energy input to the world ocean induced by TCs. *Sriver and Huber* [2010] evaluated the influence of TCs on the mean ocean state and poleward heat transport from a global ocean general circulation model simulation in which they prescribe TC winds estimated from high resolution satellite wind data. None of these studies, however, investigated the processes involved in TC-induced cooling.

[9] The aim of this study is to characterize surface temperature response to TCs at a global scale, and to quantify how the related processes depend on TCs characteristics and oceanic background conditions. To that end, we forced a global ocean model with a modified version of CORE II forcing [*Large and Yeager*, 2009] including an analytic formulation of two-dimensional TC winds along observed TC tracks between 1978 and 2007. High-resolution data from satellite scatterometers do not provide reliable estimates for wind larger than 50 m s^{-1} and are only available from 2000 onward [*Brennan et al.*, 2009]. Our approach has the advantage of covering the entire range of TC intensities over a 30 years period, hence providing a large database of simulated ocean responses to more than 3000 TCs, with the caveat being that wind spatial structure for each individual cyclone is less accurate than satellites estimates.

[10] The paper is structured as follows. Section 2 describes the observed data set used in this study, the model configuration and the proposed modeling strategy to account for TC wind forcing. Section 3 validates our numerical experiment from statistical comparison of the simulated cold wakes to satellite estimates. The main processes that control the cooling, as well as their dependency to the cyclone wind power, distance to the track and oceanic background state are discussed in section 4. Section 5 provides a summary of our results as well as a discussion of their implications.

2. Data Sets and Methods

2.1. Observed Data Sets

2.1.1. Ocean Sub-Surface Temperature

[11] The depth of the mixed layer (ML) and the upper ocean thermohaline stratification are two important parameters controlling the response of near-surface ocean to the atmospheric forcing [*Jacob and Shay*, 2003; Vincent et al., submitted manuscript, 2011]. We use the recently updated mixed layer depth climatology of *de Boyer Montégut et al.* [2004], which includes ARGO profiles to September 2008 and temperature and salinity of the World Ocean Atlas 2009 climatology (WOA09) [*Locarnini et al.*, 2010] to validate the model climatology.

2.1.2. Sea Surface Temperature (SST)

[12] We use a blend of Tropical Rainfall Measuring Mission (TRMM) Microwave Imager (TMI) and Advanced Microwave Scanning Radiometer AMSR-E SST daily data set (http://www.ssmi.com/sst/microwave_oi_sst_data_description.html) to characterize the observed SST response to TCs over the 1998–2007 period. Despite its inability to retrieve SST data under heavy precipitation [*Wentz et al.*, 2000], TMI and AMSR-E offer the advantage of being insensitive to atmospheric water vapor and provide accurate observations of SST beneath clouds, a few days before and after TC passage. The inner-core cooling (i.e., cooling under the eye) cannot be assessed confidently with TMI-AMSR; data are most of the time missing in a 400 km radius around the current TC position. This data set however provides a reliable estimate of the cooling in the TCs wake, data being typically available 1 to 2 days after TC passage. It has however to be noted that the cooling amplitude in the TCs' wake may not be fully captured by this data set, especially for slow moving TCs.

2.1.3. Tropical Cyclone Position and Strength

[13] Observed TC position and strength are derived from the International Best Track Archive for Climate Stewardship (IBTrACS) [*Knapp et al.*, 2010]. In this study, we focus on the 1978–2007 period, over which worldwide satellite coverage provides the position and estimated maximum wind speed every 6 h for more than 3000 TCs. The maximum wind speed value characterizing the TC strength is taken as the 10-minute averaged wind at 10 meters.

2.2. Methodology to Monitor the Ocean Response to TCs

[14] To characterize the ocean response to TCs, the mean seasonal cycle of each field collocated to TC tracks is first subtracted from model and observations; TC track locations, available at 6-h intervals, are then used to retrieve the ocean response to TCs through these fields (SST, ML currents and ML heat budget terms). Those data are projected along and across track axes, with cross-translation axis oriented to the right (left) of the moving TC in the Northern (Southern) Hemisphere. A fixed radius of 200 km (about 3–4 RMW) around each TC-track position is used to characterize the maximum cooling amplitude. This region encompasses a crucial area where SST is known to influence TC intensity [*Cione and Uhlhorn*, 2003; *Schade*, 2000].

[15] The reference unperturbed pre-storm SST conditions (SST_0) is defined as the 7-day average from 10 to 3 days before the TC passage. The inner-core SST (SST_{eye}) is defined as the daily average 12 hours before to 12 hours after the storm passage. The SST in the wake of the TC (SST_{CW}) is defined as the 3-day average starting 24 hours after the storm passage. The amplitude of the SST response is characterized by the cooling amplitude in the cold wake (CW) as $\Delta T_{CW} = SST_{CW} - SST_0$ and the cooling amplitude in the inner-core region as $\Delta T_{eye} = SST_{eye} - SST_0$. We will see in section 3 that these choices for spatial and temporal averaging are justified by the observations and modeling results. Because satellite observations do not offer reliable estimates for SST_{eye}, only ΔT_{CW} is validated against satellite estimates. However, results for ΔT_{eye} in the model will also be discussed owing to the importance of temperature right under the TC eye on cyclone intensity [*Cione and Uhlhorn*, 2003]. Note that while the definitions above are generally reasonable for most storms, they may induce some errors for very slow (where our definition of SST_0 or SST_{CW} may capture some of the eye signal) or very fast moving storms.

[16] Following Vincent et al. (submitted manuscript, 2011), two variables are used in this study to diagnose the amplitude of the TC atmospheric forcing and the subsurface oceanic background conditions. The Wind Power index (*WPi*) characterizes the strength of the TC forcing. This index integrates in a single measure several parameters known to influence the cold wake amplitude: storm size, maximum winds and translation speed of the TC. The *WPi* builds on the Power Dissipated by friction at the air-sea interface (*PD*) [*Emanuel*, 2005] that is a good proxy of the kinetic energy transferred from the winds to the ocean surface currents (Vincent et al., submitted manuscript, 2011). The *PD* is calculated for each cyclone track position as

$$PD = \int_{t_o}^{t_c} \rho\, C_D \mathbf{V}^3\, dt,$$

and the *WPi* writes as follows:

$$WPi = [PD/PD_0]^{1/3},$$

where $|\mathbf{V}|$ is the local magnitude of surface wind, C_D the dimensionless surface drag coefficient, ρ the surface air density, t_o the time when a cyclone starts influencing the considered location and t_c the current time; $PD_0 = \int_{to}^{tc} \rho C_D |\mathbf{V}_0|^3 dt$ is a normalization constant corresponding to a weak storm with a translation speed of 7 $m.s^{-1}$ (25 $km.h^{-1}$) and a maximum 10-minute averaged wind speed of 15 $m.s^{-1}$ (the wind speed defining a Tropical Depression: the weakest cyclonic system classified).

[17] *WPi* is a proxy of the amount of kinetic energy available for mixing under the storm (Vincent et al., submitted manuscript, 2011). As the cooling mainly results from mixing induced by vertical shear of oceanic currents [*Price*, 1981], this is a pertinent variable to describe the resulting ocean cooling. We use the term 'power' to refer to a TC's *WPi* while the term 'intensity' is kept to comment the maximum wind speed ($V_{\max}$) for consistency with most previous studies.

[18] The magnitude of the cooling also depends on the ocean background conditions (i.e., shallow and steep or deep and diffuse thermocline). We use the Cooling Inhibition index (CI) introduced by Vincent et al. (submitted manuscript, 2011) to describe that effect. The definition of the CI is based on the physical process responsible for the cooling: conversion of kinetic energy to potential energy by vertical mixing. Vincent et al. (submitted manuscript, 2011) show that the amplitude of the cooling is proportional to the cube root of the potential energy change. CI is hence defined as the cube root of the potential energy necessary to produce a 2°C cooling via a heat-conserving vertical mixing. This quantity can easily be computed from any available pre-storm temperature and salinity profiles. It measures the inhibition of mixing-induced ocean surface cooling by the ocean background state. Vincent et al. (submitted manuscript, 2011) showed that TC-induced variations in our simulation are largely a function of *WPi* and CI, with CI modulating the cooling amplitude by up to an order of magnitude for a given *WPi*.

2.3. Model Setup

2.3.1. Model Configuration

[19] The model configuration used here is built from the "Nucleus for European Modeling of the Ocean" ocean/sea-ice numerical framework (NEMO v3.2) [*Madec*, 2008]. This configuration (known as ORCA05) uses a tripolar, quasi-isotropic grid with a nominal resolution of 1/2° (i.e., cell size ~50 km in the tropics). It has 46 vertical levels, with 10 levels in the upper 100 m and 250 m resolution at depth. Partial filling of the deepest cells is allowed [*Bernard et al.*, 2006; *Barnier et al.*, 2009]. Such a configuration has been shown to successfully reproduce tropical ocean variability at time scales ranging from intra-seasonal to inter-annual [*Penduff et al.*, 2010].

[20] The mixed layer dynamics is parameterized using an improved Turbulent Kinetic Energy (TKE) closure scheme [*Madec*, 2008] with a Langmuir cell [*Axell*, 2002], a surface wave breaking parameterization [*Mellor and Blumberg*, 2004] and an energetically consistent time and space discretization [*Burchard*, 2002; *Marsaleix et al.*, 2008]. Additional subgrid-scale mixing parameterizations include a bi-Laplacian viscosity and an iso-neutral Laplacian diffusivity. For tracer advection, a total variance dissipation scheme —a second-order, two-step monotonic scheme with moderate numerical diffusion— is used [*Lévy et al.*, 2001].

[21] In this configuration, the mixed layer depth is defined as the depth where the vertical density is 0.01 kg m^{-3} higher than the surface density. The different terms contributing to the heat budget in the ocean mixed layer (ML) are calculated online and stored. As with *Vialard et al.* [2001], the ML temperature evolution equation reads

$$\partial_t \bar{T} = -\underbrace{\langle u\partial_x T + v\partial_y T + w\partial_z T\rangle}_{(a)} + \underbrace{\langle D_l(T)\rangle}_{(b)} - \underbrace{\frac{1}{h}\frac{\partial h}{\partial t}\left(\bar{T} - T|_{z=h}\right)}_{(c)} + \underbrace{\frac{(\kappa\partial_z T)|_{z=h}}{h}}_{(d)} + \underbrace{\frac{Q^* + Q_s(1 - F(z=h))}{\rho_o C_p h}}_{(e)}, \qquad (1)$$

where $\bar{T} = \langle T\rangle \approx SST$ is the mean temperature in the ML, T the temperature, (u, v, w) the three components of ocean currents, $D_l(T)$ the lateral diffusion operator, κ is the vertical diffusion coefficient, h the time varying MLD, $C_p = 4.10^3\ J.\ K^{-1}.\ kg^{-1}$ is the specific heat of seawater, and ρ_o is a reference density. Brackets denote the vertical average over h. Term a is the advection, term b is the lateral diffusion, term c is the entrainment/detrainment at the ML base, term d is the vertical diffusion flux at the ML base and term e is heat flux storage in the ML (with Q_s the solar heat flux and Q^* the non-solar heat fluxes: sensible, latent, radiative heat fluxes; $F(z = h)$ is the fraction of surface solar irradiance that penetrates below the mixed layer.

[22] We will use this heat budget calculation to infer the respective contribution of these processes to the amplitude of the TCs-induced cooling. The term b for lateral diffusion is negligible in the wake of TCs. In the following, term b is neglected, terms c and d are grouped together in a vertical processes term and referred to as MIX; term e is the surface forcing term is referred to as FOR; term a is the advection term is referred to as ADV. In fact ADV is almost only the horizontal advection term, the vertical one being always negligible. Indeed, the temperature equation (1) is a budget over the time varying ML (defined on a density criterion), the base of which is a surface moving up and down with vertical currents. In this Lagrangian framework, it is largely the MIX term that operates for exchanging heat between the ML and subsurface layers. The Eulerian vertical advection is known to be an important contributor to the ocean cooling under TCs [*Greatbatch*, 1985; *Yablonsky and Ginis*, 2009; Jullien et al., submitted manuscript, 2011], but its effect on ML temperature only appears indirectly in (1): it contributes to term d by both reducing the MLD (thus increasing shear-induced mixing and so κ), and tightening the stratification at the base of the ML (thus increasing $\partial_z T$).

[23] To quantify the relative contribution of all processes to the cooling magnitude, each term of the ML heat budget is integrated starting 10 days prior to TC passage. The cooling magnitude ΔT_{CW} and ΔT_{eye} associated with each term are then calculated as explained in part 2.2.

2.3.2. Model Surface Boundary Conditions

[24] The three simulations performed in this paper use the atmospheric data sets and formulations proposed by *Large and Yeager* [2009] as surface boundary conditions. This approach was developed in the design of the "coordinated ocean-ice reference experiments (COREs)" program [*Griffies et al.*, 2009] and is referred to as COREII forcing. The forcing data sets presented by *Large and Yeager* [2009] are based on NCEP/NCAR reanalysis products over the 1958–2007 period combined with various satellite data sets. Turbulent fluxes are computed from bulk formulae as a function of the prescribed atmospheric state and the simulated ocean surface state (SST and surface currents). Data are provided at six-hourly (wind speed, humidity and atmospheric temperature), daily (short- and long-wave radiation) and monthly (precipitation) resolution, with inter-annual variability over the 1978–2007 period, except for river runoff that remains climatological. To avoid an artificial model drift, the sea surface salinity is damped towards monthly-mean climatological values with a piston velocity of 50 m per 300 days [*Griffies et al.*, 2009]. It must be noted that the *Large and Yeager* [2009] formulation of the forcing accounts for the observed saturation at strong winds [*Donelan et al.*, 2004], the dimensionless surface drag coefficient (C_D) is bounded to a value of 2.34×10^{-3} for winds greater than 33 m s^{-1}. The use of a threshold on the surface drag coefficient C_D also implies a similar bound on the latent heat exchange C_E and sensible heat exchange C_H coefficients (calculated from C_D following *Large and Yeager* [2009, equations 9 and 11]).

[25] The model starts from an ocean at rest initialized with temperature and salinity fields from the World Ocean Atlas 2005 [*Locarnini et al.*, 2010]. It is then spun up for a 30-year period using the interannual 1948–1977 COREII forcing. The final state is then used to start the simulations described below (which are run over 1978–2007). The first of these experiments simply continues with the original COREII forcing, and will be referred to as COREII. As illustrated in Figure 1a, the COREII wind forcing contains weaker-than-observed TC wind signatures (TC-like vortices). These residual TCs signatures have been filtered out by applying a 11-day running mean to the zonal and meridional wind components of the original COREII wind forcing, within 600 km around each cyclone track position, with a linear

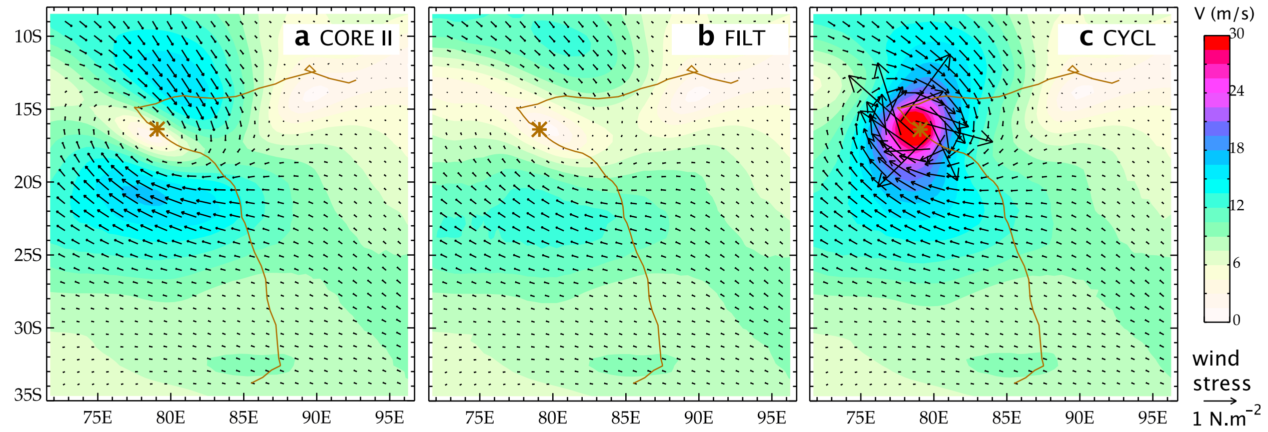

Figure 1. Wind module (shading) associated to the passage of TC Francesca at the position noted by a star (5 February 2002) in (a) CORE II, (b) FILT and (c) CYCL experiments. Black arrows are for the 1-day averaged wind stress magnitude.

transition from filtered to unfiltered winds between 600 and 1200 km. In this simulation (FILT), most of the TC-like vortex is suppressed (Figure 1b). It will therefore be our reference simulation for ocean response without TC.

[26] The third simulation, which is the main focus of this paper, is obtained by adding idealized TC wind forcing along cyclone tracks to the filtered COREII forcing. TC wind patterns are computed using the *Willoughby et al.* [2006] idealized vortex, which is based on a statistical fit to observed TC winds [*Willoughby and Rahn*, 2004]. This idealized wind pattern is computed at each model time step (36 min) using interpolated position and maximum wind speed of each cyclone from the 6-hourly IBTrACs database. This strategy ensures that both temporal evolution and spatial structure of the TC wind forcing are properly captured in the simulation. This procedure results in a simulation (CYCL) where TC wind magnitude is realistic (Figure 1c). Note that we chose not to take into account the translation speed of the storm in the wind vortex we added. Indeed, even if it is known to affect the wind asymmetry, *Samson et al.* [2009] have shown that it has a limited effect on the CW asymmetry and can be neglected. The validity of our methodology for simulating the ocean response to TCs will be further illustrated in the next section.

2.3.3. Model Resolution

[27] The 1/2° horizontal resolution employed in the present study may seem rather coarse compared to previous case studies simulating the ocean response to single TCs [e.g., *Yablonsky and Ginis*, 2009; *Halliwell et al.*, 2011]. Our strategy is to perform long-term global simulations that allow analyzing the ocean response to a large variety of TCs. This does not allow us to use eddy permitting ocean model due to computing cost limitations. A major requirement for realistic simulation of ocean response to TC is that the surface wind forcing accurately captures the maximum winds of the TC eyewall [*Halliwell et al.*, 2011]. We stress that the use of an analytic TC vortex allows us to avoid the pitfall of low atmospheric resolution that would smooth out the maximum winds. The remaining question is thus how the spatial sampling on the ocean grid will capture the TC surface forcing. We provide here a simple quantification of how horizontal resolution may affect our results by analyzing two crucial processes of the ocean response to a cyclone wind forcing: vertical mixing and wind-induced upwelling [*Yablonsky and Ginis*, 2009]. The ability to force the former can be evaluated by considering the power dissipated (PD: a good proxy of the energy input to the ocean (Vincent et al., submitted manuscript, 2011) to which the shear-induced mixing is roughly proportional) while for the later, the Ekman pumping can be used as a mean proxy (vertical motion is an Ekman solution with a superimposed inertial oscillation; in the text, we use the term Ekman suction when explicitly referring to upward vertical motion). Figure 2 provides a comparison of these two quantities for a selected strong tropical cyclone (TC DORA; SS-Cat. 4; in the southwestern Indian Ocean in early 2007 [*Vialard et al.*, 2009]) computed for various grid resolutions ranging from 2° to 1/12°. The 1/2° resolution model used in our study is sufficient to provide a reasonable estimate of these two quantities and thus appears to be a good compromise between computational cost and accuracy. Compared to the 1/12°, it provides very similar results in terms of power dissipated. However, it underestimates the maximum upwelling amplitude near the cyclone's eye by about 30%. We will come back to this point in the discussion.

3. Characteristics of Modeled and Observed Cold Wakes

3.1. Validation of the Model Background State

[28] The mixed layer depth (MLD) and the Cooling Inhibition index (CI) are two important parameters involved in the amplitude of the SST response to TCs. The CI characterizes the efficiency of vertical mixing in cooling the ocean surface (Vincent et al., submitted manuscript, 2011) while the MLD controls the amplitude of the SST response to a given atmospheric heat flux forcing. Figure 3 shows these parameters for model and observations during the peak cyclonic season for both hemispheres (DJF for Southern Hemisphere and JJA for Northern Hemisphere). The model reproduces qualitatively the main features of both observed estimates of MLD and CI (Figure 3). The highest values of CI are found in the west Pacific warm pool where the thermocline is deep, while upwelling regions such as the eastern

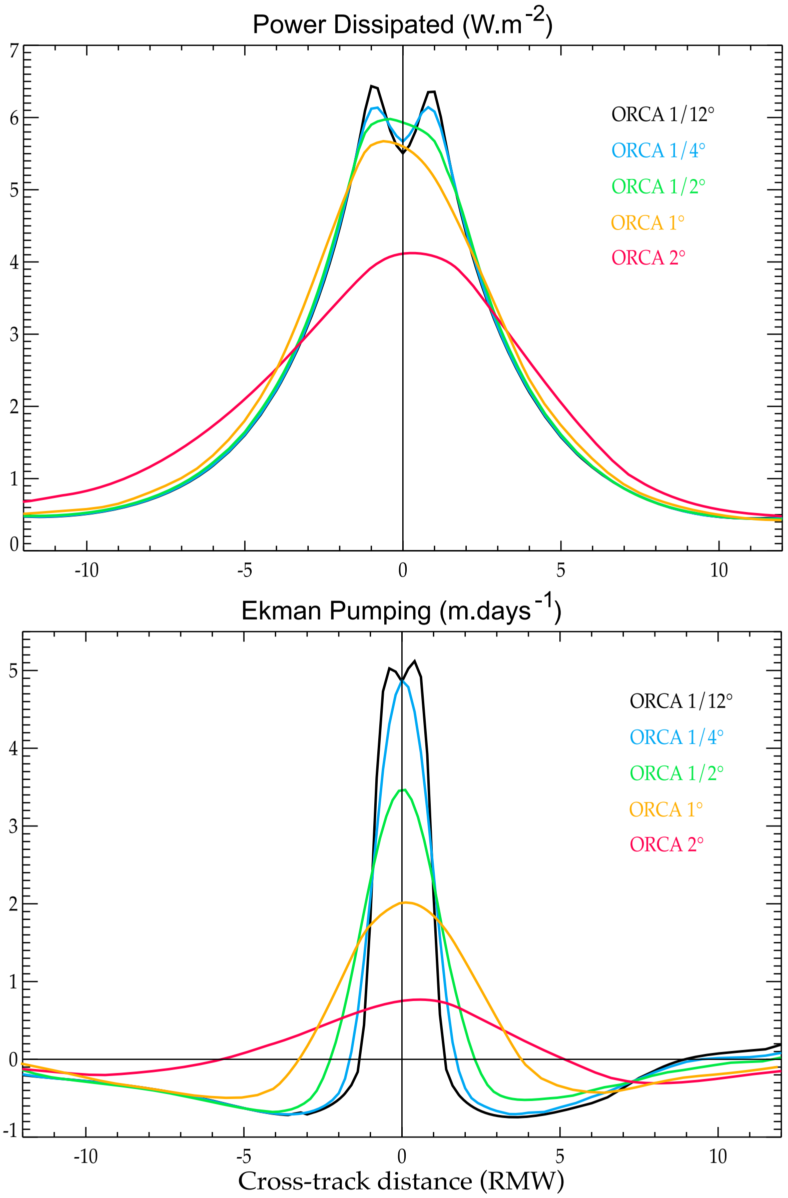

Figure 2. Comparison of average (a) power dissipated (W m^{-2}) and (b) Ekman pumping (m d^{-1}) for grids of increasing resolution (1/12°, black; 1/4°, blue; 1/2°, green; 1°, orange; 2°, red). These figures were obtained from reproducing category 4 TC DORA surface forcing (from 25 January to 7 February 2007) over different ocean grids. Cross section are averages of all cross sections for each 6-h track-position made in the averaged PD and cumulated Ekman pumping fields over the storm's lifetime.

equatorial Pacific or the Seychelles-Chagos thermocline ridge [e.g., *Vialard et al.*, 2009] are characterized by low CI. The model generally tends to underestimate CI, most notably in three cyclonic basins: northeastern and southwestern Pacific, northern Indian Ocean. This may lead to overestimated cooling response in those regions, especially in the northeastern Pacific where the mean CI value is rather low. Similarly, in those three regions, the mixed layer depth tends to be underestimated.

3.2. Amplitude of TC-Induced Ocean Response

[29] The efficiency of our experimental design to account for a realistic TC wind forcing is illustrated on Figure 4. The figure displays a scatter plot of the amplitude of modeled against observed TC-induced cold wake amplitude (ΔT_{CW}) at individual locations for the three experiments discussed in section 2.4. The original COREII forcing contains weaker than observed TC-like vortices along the observed TC tracks, triggering weaker than observed sea surface cooling that saturate around $-1°C$ (Figure 4a). Filtering these vortices (FILT experiment) allows suppressing most of those weak cooling events (Figure 4b); further applying idealized TC wind along the observed tracks (CYCL experiment) allows a realistic simulation of the cold wake (CW) amplitude. In CYCL, there is a 0.71 correlation between modeled and observed TC-induced cooling magnitude at individual

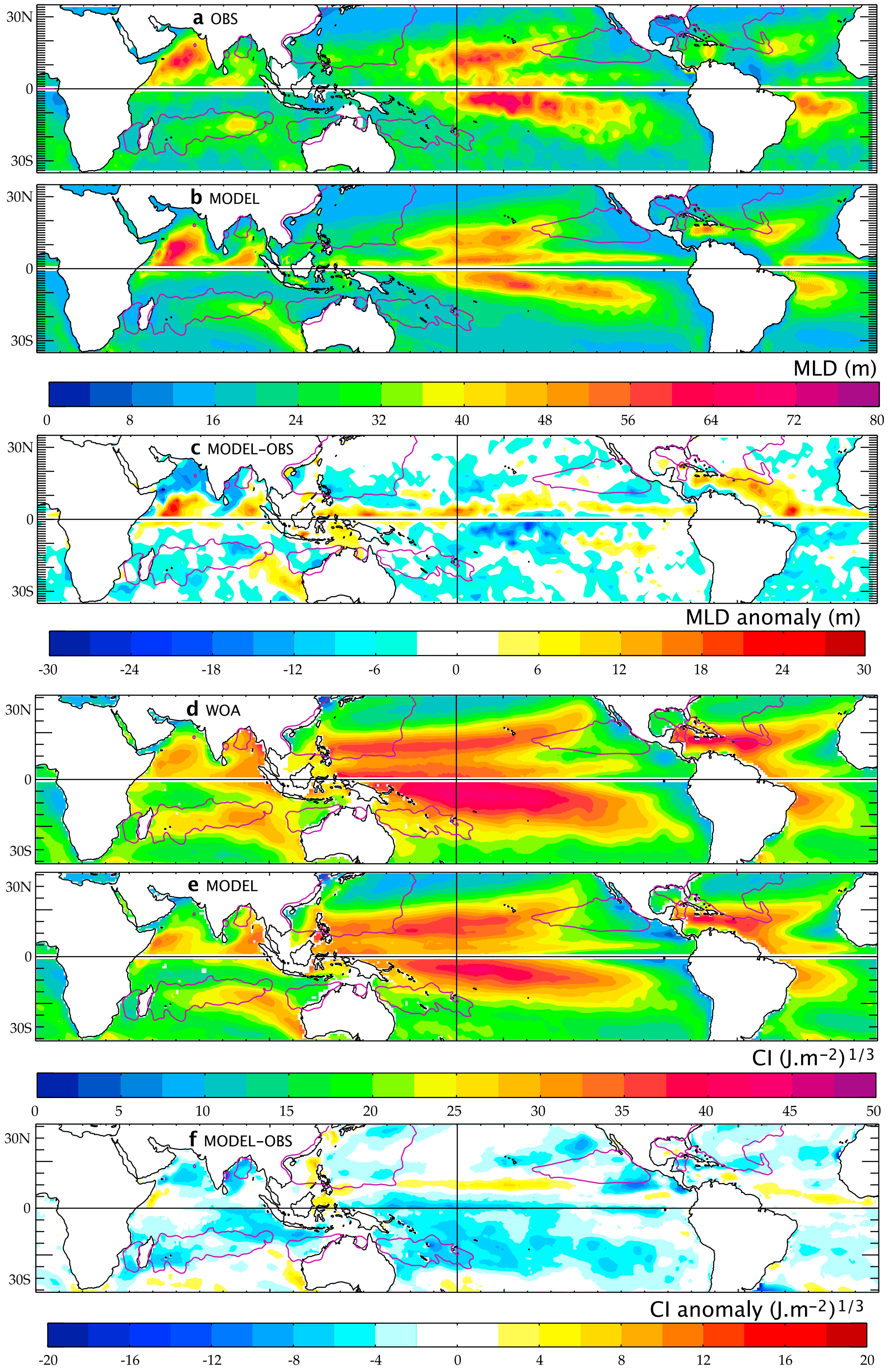

Figure 3. Climatological values for "cyclonic season" (DJF for the Southern Hemisphere and JJA for the Northern Hemisphere) of the mixed layer depth (a) observed [*de Boyer Montégut et al.*, 2004], (b) modeled in CYCL experiment and (c) difference between modeled and observed. (d–f) Same as Figures 3a–3c but for the cooling inhibition index (*CI*) (Vincent et al., submitted manuscript, 2011); in Figure 3d "observation" is from WOA09 database [*Locarnini et al.*, 2010]. The purple line reminds the regions of intense TC activity (average 1978–2007 *WPi* > 1).

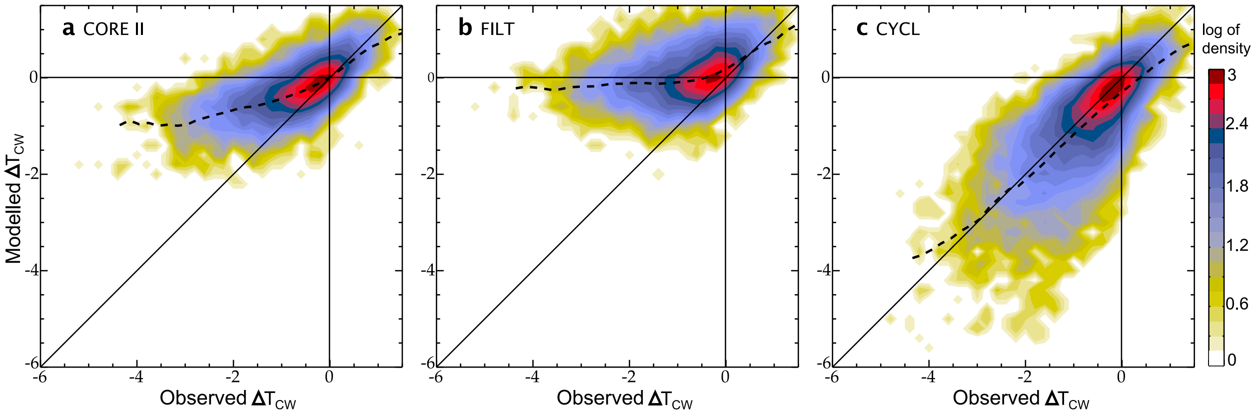

Figure 4. Probability density function of simulated versus observed cold wake amplitude averaged within 200 km of any cyclone position over the 1998–2007 period for (a) CORE II, (b) FILT and (c) CYCL experiments. ΔT_{CW} is calculated as the difference between the post-storm SST (averaged from 1 to 4 days after TC passage) minus the pre-storm SST (averaged from 10 days prior to 3 days prior TC passage). Dashed lines indicate the mean modeled cooling as a function of the observed one.

locations (Figure 4c), indicating that this simulation realistically samples the ocean response to TCs. Because the analytic cyclone wind field formulation is fitted to an average of observed cyclone wind radial profiles [*Willoughby and Rahn*, 2004], and because the underlying ocean state does not exactly match the observed one (biases, misplaced or missing oceanic eddies…), we however do not expect every simulated cold wake to perfectly match the corresponding observed one as indicated by the rather large spread observed on Figure 4c.

[30] The model also successfully reproduces the observed spatial distribution of the TC-induced cooling (Figure 5): the average cooling within TC-active regions is about 1°C in most basins, with maximum amplitude of about 2°C in the northwest Pacific region where most of the strongest TCs occur. The main model deficiency lies in the northeast Pacific basin where modeled average cooling is overestimated by almost 1°C. This bias may be attributed to a shallower than observed thermocline in this region. As a result, the modeled CI underestimates the value from the World Ocean Atlas (Figure 3) in a region where its value is the lowest of all TC basins (CI value in JJA of 12 in the model against 18 $(\mathrm{J\ m^{-2}})^{1/3}$ in observations in the region 120°W–80°W/5°N–20°N). The statistical model of Vincent et al. (submitted manuscript, 2011), that links the cooling amplitude to the CI and *WPi* suggests that such CI bias explains the ~1°C cooling bias in this region.

[31] In observations, the cooling magnitude monotonically increases with wind intensity up to TC category 2 of the Saffir-Simpson scale and then saturates from category 2 to 5 (Figure 6a), as discussed by *Lloyd and Vecchi* [2011]. The model reproduces reasonably well this feature, despite a slight overestimation of the cooling for the strongest cyclones with winds greater than 45 m $\mathrm{s^{-1}}$ (~0.3°C on

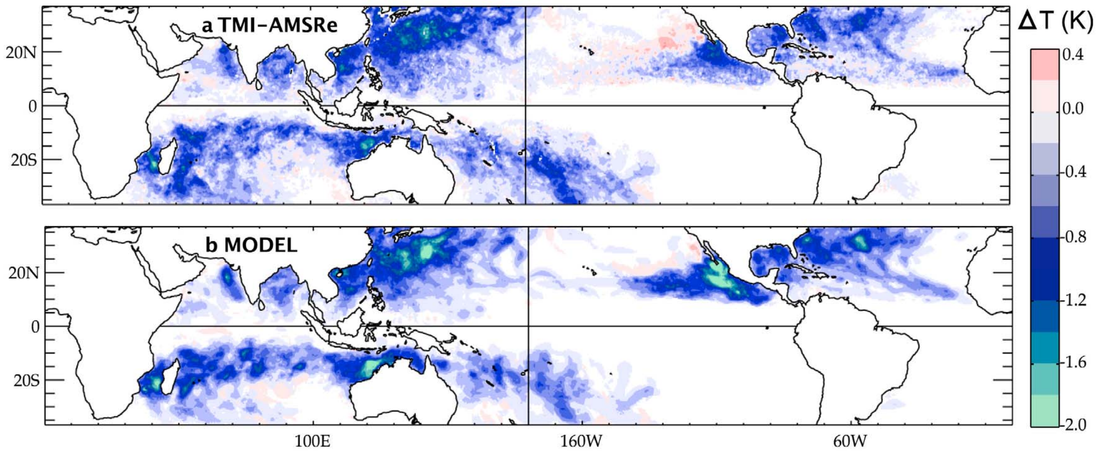

Figure 5. Spatial map of average cold wake amplitude over 1998–2007 for (a) TMI-AMSRe observations and (b) CYCL experiment. These maps are produced as follows: the maximum amplitude of ΔT_{CW} reached during a TC passage over each grid point within 200 km of each TC position are averaged for all TCs passing over the same grid point within the same TC season; these seasonal maps are then averaged over the 1998–2007 period.

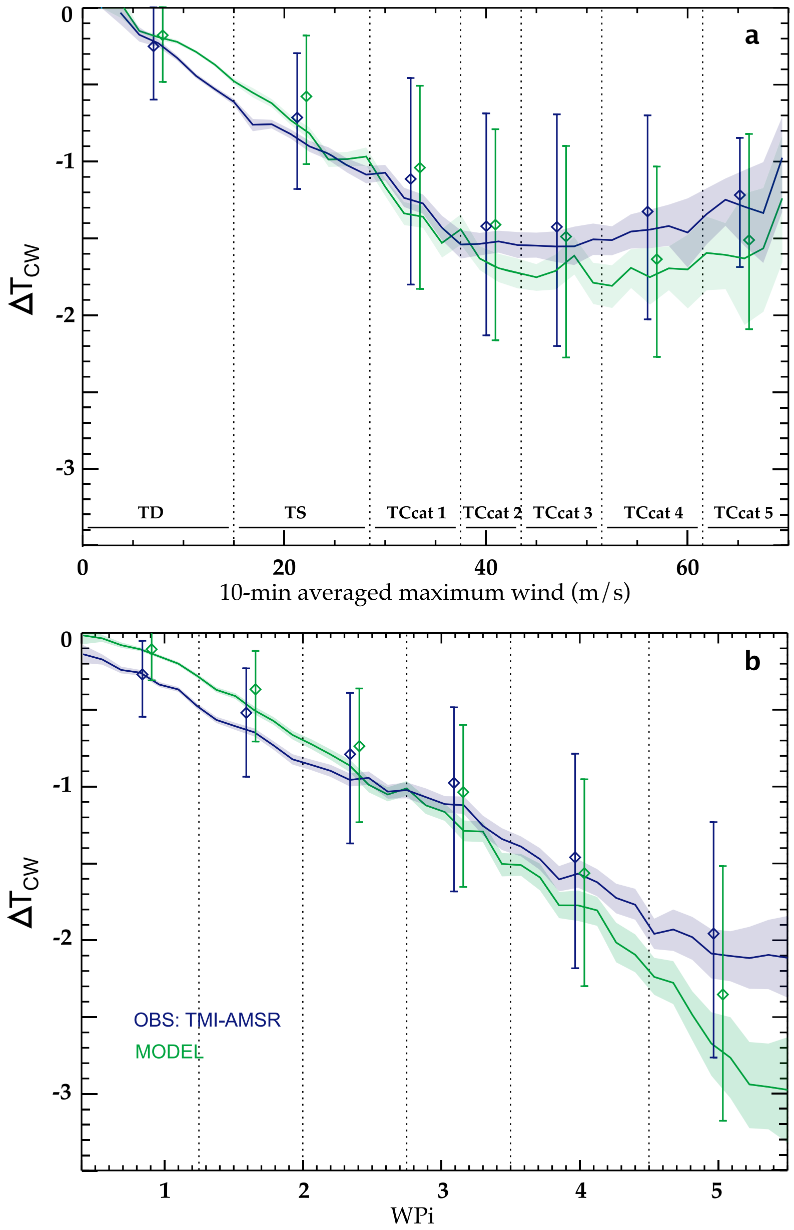

Figure 6. Mean observed and simulated cooling (a) as a function of 10-min averaged maximum wind speed (Saffir Simpson scale is reminded by the horizontal bars) and (b) as a function of the wind power index (*WPi*). Comparison is made for all TCs occurring during the 1998–2007 period. Shading indicates the 95% confidence level from a bootstrap test for the calculation of the average ΔT. Diamonds are for the median cooling per bin and vertical bar indicates the dispersion between the lower and upper quartiles per bin.

average). *Lloyd and Vecchi* [2011] interpreted this saturation as evidence of the ocean control on TCs: they suggest that, on average, the strongest observed cyclones are those for which pre-storm oceanic conditions do not allow large cooling.

[32] As discussed by Vincent et al. (submitted manuscript, 2011), the *WPi* is a proxy of the kinetic energy transferred to the upper ocean by the cyclone and is thus a better predictor of the cooling than the maximum wind of a TC. When displayed as a function of *WPi*, the mean cooling increases almost linearly and hardly saturates for the most intense wind power (Figure 6b). The model also reproduces the observed linear increase of the cooling with the *WPi*, but with a clear overestimation (~0.8°C) of the cooling for the highest range of *WPi* (>5). The modeled overestimation is partly related to the CI bias in the northeast Pacific that promotes stronger cooling than observed. Excluding the northeast Pacific basin in Figure 6b results in a 40% reduction of the cooling bias observed for $WPi > 5$ (bias of 0.5°C instead of 0.8°C). Another reason for this bias may also stem from data limitations: the highest *WPi* can only be reached for slow moving storms (typically translating at about 1.5 m s^{-1} for *WPi* above 5 (Vincent et al., submitted manuscript, 2011)); in this

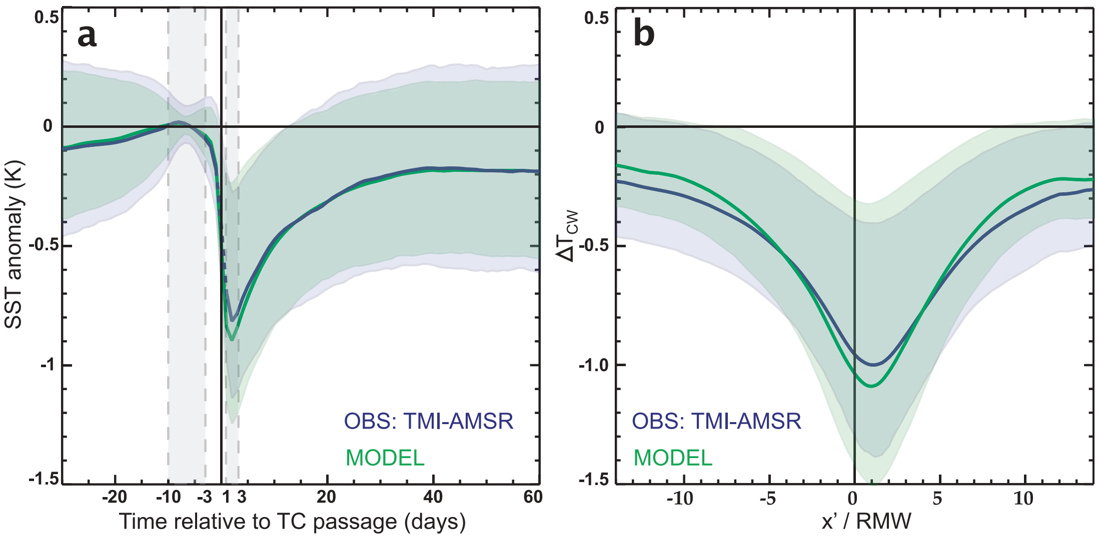

Figure 7. (a) Temporal evolution of the TC-induced cooling for model and observations. (b) Cross-track section of the cold wake. SST anomalies are calculated with respect to pre-storm SST (day-10 to day-3) and averaged for all TCs during the period 1998–2007. For Figure 7a, SST anomalies are averaged within 200 km radius of any TC track position. For Figure 7b, SST anomalies are averaged from 1 to 3 days after the cyclone passes and the x′ axis is normalized by the RMW value of the corresponding storm (the average RMW value for all TCs is 48 km). The x′ axis points to the right (left) of the track in the Northern (Southern) Hemisphere. Shading indicates the spread around the mean value, evaluated from the lower and upper quartiles.

case the TC covers ~250 km in 2 days and part of the 200 km area over which the cooling is evaluated is still affected by precipitation: the cooling amplitude ΔT_{CW} is thus very likely underestimated by satellite observations. Excluding the slowest TCs (translation speed < 2.5 m s^{-1} (10 km h^{-1})) from Figure 6b and the northeast Pacific basin, the model overestimation for *WPi* > 5 is reduced by 75% (bias of 0.2°C instead of 0.8°C). The overestimation of modeled cooling to the strongest TCs may thus be linked to sampling issues rather than to inaccurate model representation of the ocean response.

3.3. Temporal Evolution and Spatial Extent of TC-Induced Ocean Response

[33] The CYCL experiment also captures accurately the temporal evolution of the average observed TC-induced cooling (Figure 7a). In both model and observation, SST averaged over a 200 km radius starts decreasing a few days before the TC reaches a given location (Day0) and maximum cooling occurs after the TC passage. Although maximum cooling appears to occur 1 to 2 days after the TC passage on Figure 7a for both model and observations, the exact timing of the maximum cooling after the TC passage cannot be confidently validated due to numerous missing satellite SST data around the time of TC passage. Figure 7a however illustrates that the decaying time scale of the cooling is accurately simulated, with about 40 days for the SST signal to disappear although the SST remains on average 0.2°C colder than pre-storm SSTs, as previously discussed by *Lloyd and Vecchi* [2011].

[34] The cold wake cross-track extent is also reasonably well simulated, despite a tendency to overestimate (underestimate) the cooling close (far) of the TC-track position (Figure 7b). On average, the maximum cooling is shifted by one RMW on the inertial side (right for Northern Hemisphere, left for Southern Hemisphere in the frame of the moving TC) with respect to the TC-

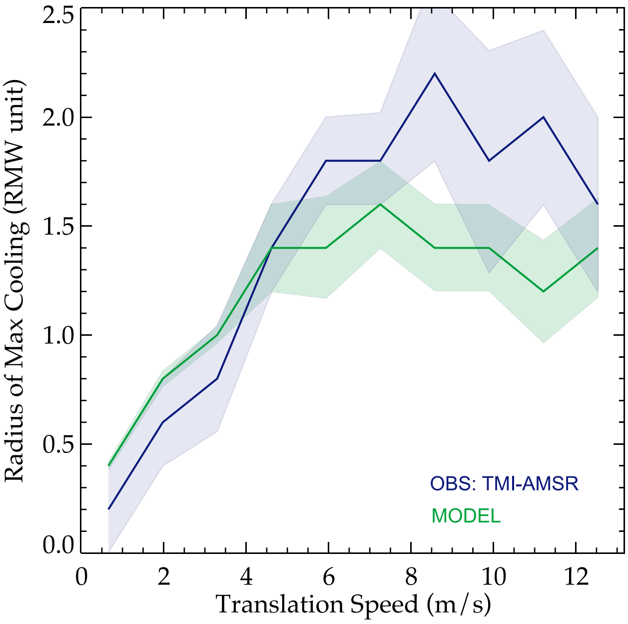

Figure 8. Cross-track distance between maximum cooling and the TC track in the wake of TCs as a function of storm translation speed. SST anomalies are calculated as the difference between the post-storm SST (averaged from 1 to 3 days after TC passage) minus the pre-storm SST (averaged from 10 days prior to 3 days prior TC passage).

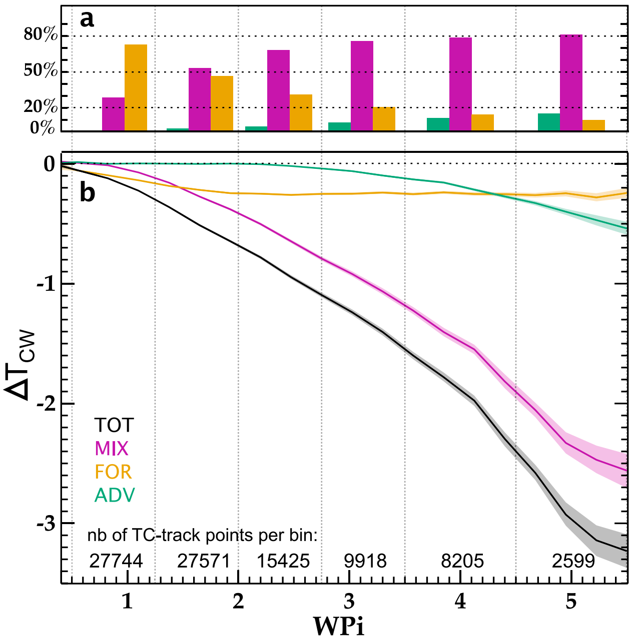

Figure 9. Mean amplitude of modeled cold wake ΔT_{CW} and respective contribution of vertical mixing (MIX), heat fluxes (FOR) and advection (ADV) to the total cooling as a function of the wind power index (*WPi*). (b) The absolute values and (a) the relative contribution of each process to the total cooling for 6 bins of increasing *WPi* are shown. The number of observations for each bin is indicated.

track position. Previous studies estimated this shift to be of 1 to 2 RMW [*Shay and Brewster*, 2010]. In both model and observations, the shift depends upon the translation speed of the storm (Figure 8), with slow moving storms triggering more symmetric CWs in agreement with previous results [*Price*, 1981; *Samson et al.*, 2009]. *Price* [1981] attributed the more symmetric CWs to the effect of enhanced upwelling induced by slow moving storms that is centered under the TC track. This upwelling would allow entrainment to cool the ML more efficiently under the TC track that on the sides. The CW asymmetry is underestimated for fast moving cyclones in our simulation (Figure 8). Previous studies [*Greatbatch*, 1983; *Price et al.*, 1994; *Samson et al.*, 2009] suggest that the surface wind asymmetry due to the translation speed of the storm is of secondary importance to explain the asymmetric ocean response to TC forcing. The reason for the model biais may more likely be attributed to spatial/temporal grid sampling issues. Cyclone forcing is increasingly under-sampled by the model time-step (36 minutes) and spatial resolution at increasing translation speed: this may explain why the resonance mechanism is less well resolved for fast-moving storms.

[35] In the CYCL simulation, the amplitude of TC-induced ocean response, its temporal evolution, spatial extent and asymmetry with respect to the center of the track agree well with observed estimates. In the next section, we therefore use the model with some confidence to investigate the main oceanic and atmospheric processes controlling the characteristics of the TC-induced cooling. In the following, the analysis is extended to the full temporal coverage of the simulations (1978–2007) and the SST response is calculated from the difference between the CYCL and FILT simulations. This strategy, not applicable when comparing to observations, allows suppressing most of the variability unrelated to TCs (with the exception of the internal oceanic variability).

4. Oceanic and Atmospheric Processes Controlling the TC-Induced Cooling

4.1. Processes Controlling the Cooling Amplitude

[36] In agreement with previous studies, mixing at the base of the ML is the main process responsible for the

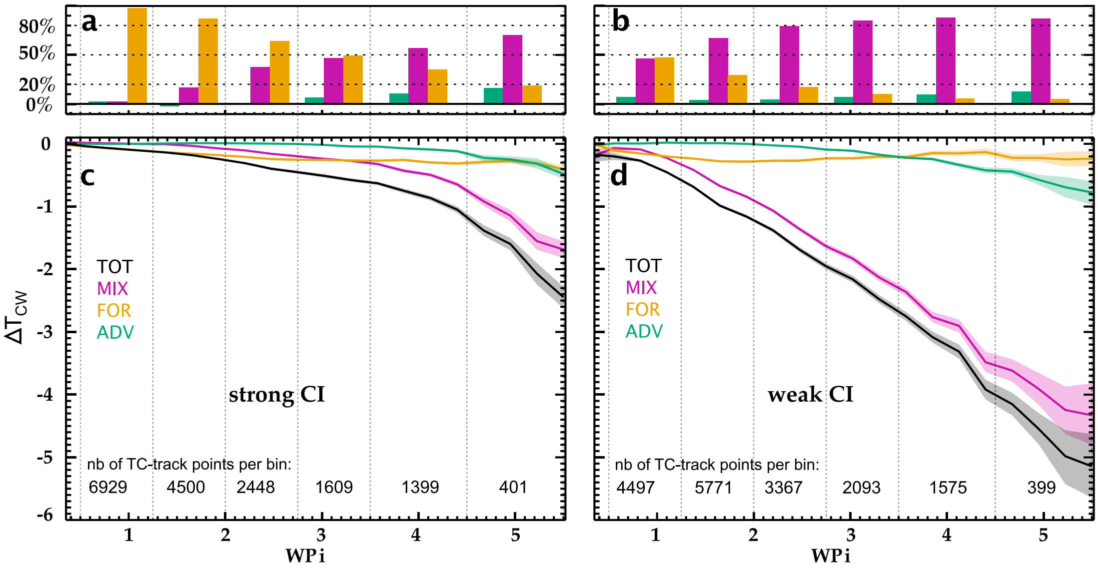

Figure 10. Same as Figure 9 but (a and c) for oceanic conditions that do not favor a strong cooling (strong cooling inhibition *CI* > 30) and (b and d) for oceanic conditions favorable to strong cooling (*CI* < 16).

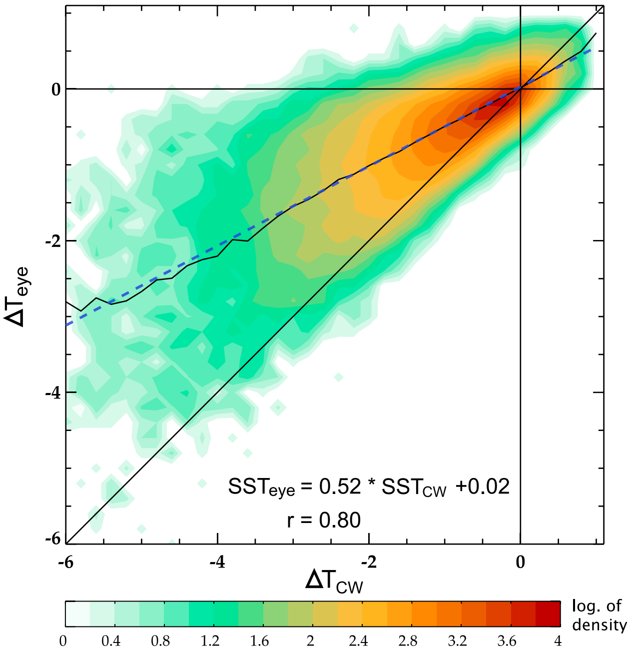

Figure 11. Probability density function of inner core cooling ΔT_{eye} versus cold wake ΔT_{CW} averaged within 200 km of any cyclone position. The plain line indicates the mean ΔT_{eye} as a function of ΔT_{CW}, while the dashed blue line is the linear fit of ΔT_{eye} onto ΔT_{CW}. The corresponding regression and correlation coefficients are provided.

TC-induced cooling, accounting for 56% of the SST signal within 200 km of the TC track on average for all TCs, while heat fluxes explain the largest part of the remaining signal (43%). The relative contribution of each term however strongly varies depending on the TC power (Figure 9). The relative contribution of mixing is shown to increase with *WPi*, evolving from $\sim$30% of the total cooling for the weakest *WPi*s (*WPi* ≈ 1, i.e., weak and/or fast TCs) to 80% for the largest one (*WPi* ≥ 3, i.e., strong and/or slow TCs). This estimation of the mixing contribution for strong cyclonic forcing (i.e., slow and/or intense cyclones) is in broad agreement with previous estimates [*Shay et al.*, 1992; *Price*, 1981] that mainly investigated the SST response in the wake of intense TCs [*Jansen et al.*, 2010]. For low *WPi*, the weaker cooling is to a large extent explained ($\sim$70%) by enhanced surface fluxes associated with cyclone winds. The cooling amplitude induced by surface heat fluxes saturates around -0.25°C for *WPi* larger than 2, resulting in a decrease of the heat flux relative contribution to SST cooling for the strongest TCs (10%). Three main processes may explain this feature: (1) the saturation of heat exchange coefficients for the strongest winds, (2) the strong deepening of the mixed layer induced for the largest TC wind forcing (not shown) and (3) the limitation of latent heat flux by the increasingly cold SST anomaly in the wake of TCs of increasing power. Although of secondary importance, our analysis also reveals that advection, dominated by its horizontal component, significantly contributes to the cooling amplitude for the largest wind forcing (*WPi* > 3.5), accounting for more than 10% of the total cooling. As we

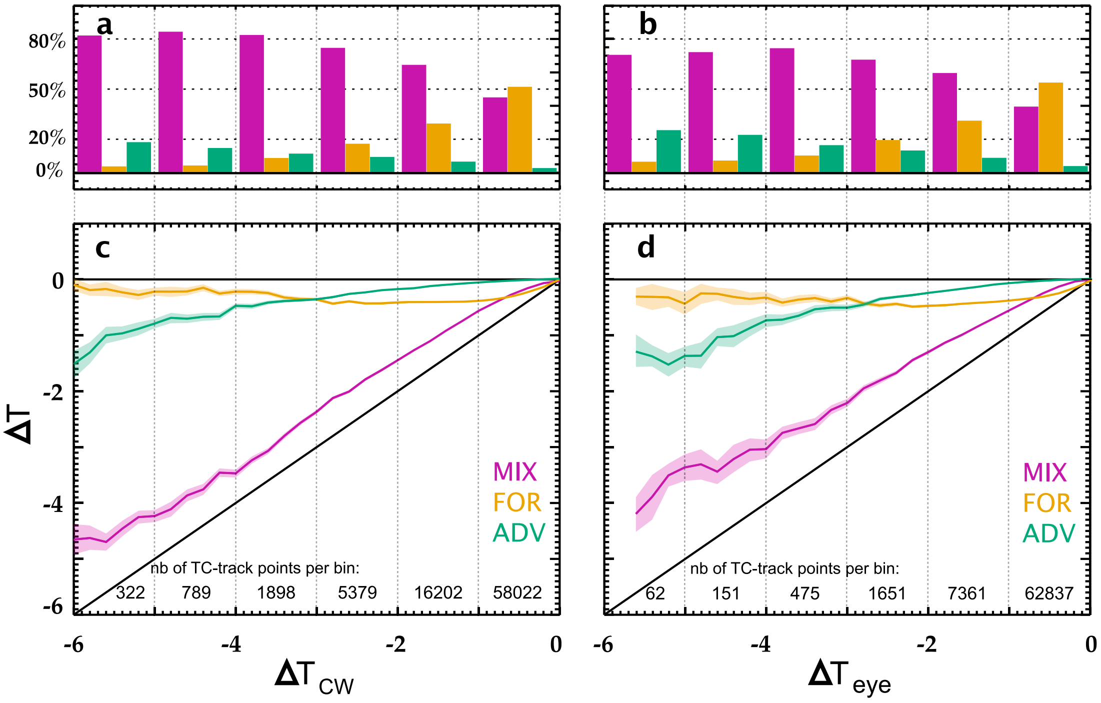

Figure 12. Respective contribution of vertical mixing (MIX), heat fluxes (FOR) and advection (ADV) as a function of the total cooling amplitude for (a and c) cold wake ΔT_{CW} and (b and d) inner core cooling ΔT_{eye}. Figures 12c and 12 d display absolute values, while Figures 12a and 12b display the relative contribution of each process to the total cooling for 6 bins of increasing cooling amplitude.

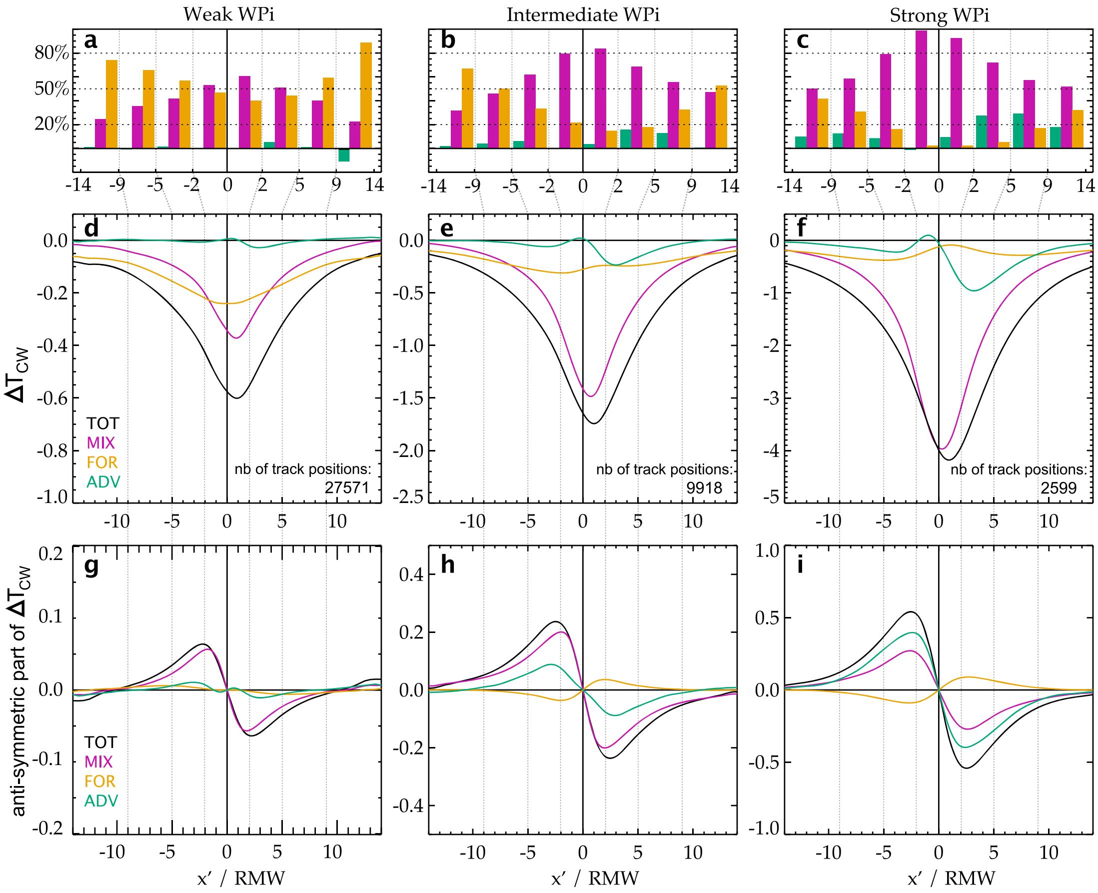

Figure 13. Cross-track sections of amplitude of modeled cold wake ΔT_{CW} and respective contribution of vertical mixing (MIX), heat fluxes (FOR) and advection (ADV) to the total cooling for three wind forcing categories: (a, d, and g) weak *WPi* ($1.25 < WPi < 2$), (b, e, and h) moderate *WPi* ($2.75 < WPi < 3.5$) and (c, f, and i) strong *WPi* ($WPi > 4.5$). Figures 13a–13c display the relative contribution of each process to the total cooling. Figures 13d–13f display absolute values, while Figures 13g–13i show the asymmetric part of the cooling. The x′ axis points to the right (left) of the track in the Northern (Southern) Hemisphere.

explained in section 2.3, vertical advection has a nearly negligible direct contribution to surface cooling in our Lagrangian framework (the bottom of the mixed layer is defined with a density criterion, and moves vertically with the vertical currents).

[37] The influence of subsurface oceanic conditions on the processes controlling the cooling is illustrated on Figure 10. As previously discussed by Vincent et al. (submitted manuscript, 2011), for a given wind power input, the cooling is greater for TCs occurring over oceanic conditions favorable for a strong cooling (low CI) than for those occurring over high CI. For *WPi* above 4.5, the cooling reaches 5°C for weak CI while it only reaches 2.5°C for large CI. This difference is mainly explained by the sensitivity of the mixing term to CI, while surface fluxes and advection have similar absolute contributions in both cases. Favorable oceanic conditions (i.e., shallow MLD and strong stratification below the mixed layer) increase the efficiency of vertical mixing in cooling the surface layers. For moderate *WPi* ($2 < WPi < 3.5$), mixing-induced cooling is on average −0.2°C (~50% of the total) in the case of large CI, while it is 8 times larger for weak CI with a −1.6°C cooling (~80% of the total). As expected, a strong CI hence prevents the wind-induced mixing to entrain cold water into the ML except for the strongest and/or slowest TCs ($WPi > 4.5$).

[38] Investigating the processes responsible for the inner-core cooling is of great interest because this cooling is known to feedback onto the TC intensity [*Cione and Uhlhorn*, 2003]. In addition, this inner-core cooling is easily accessible in our model, while it is poorly sampled by observations (satellites being strongly affected by masking by clouds and intense rain). The amplitude of the inner-core cooling is on average half the amplitude of the cold wake (consistent with observations of *Cione and Uhlhorn* [2003]) but their respective amplitude are strongly correlated (0.8; Figure 11). The respective contribution of the processes explaining the inner core and cold wake are also globally similar (Figure 12). Surface fluxes and vertical mixing equally contribute to the weakest cooling in both the TC inner core and its wake. Mixing dominates the cooling greater than 3°C below the TC inner core, although its contribution is slightly weaker compared to cold wake cooling (70% against 80%). Lateral advection has on

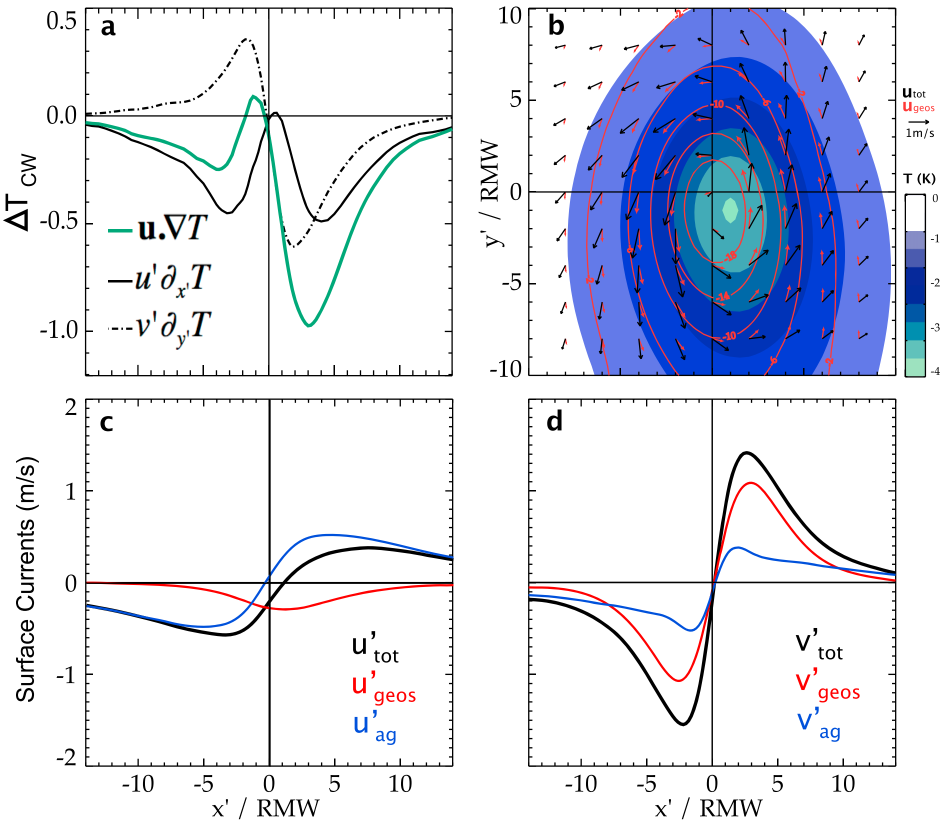

Figure 14. (a) Cross-track section of the contributions of total advection (green), advection by along track currents (dashed black) and cross track currents (plain black) to the total ML heat budget for strong *WPi* (*WPi* > 4.5). (b) Composite of CYCL-FILT SST (shading) SSH (red contours, in cm) surface currents (black arrows) and geostrophic currents (red arrows) in the frame of the moving TC averaged over day-1 to day + 3. Total, geostrophic and ageostrophic currents for the (c) cross-track components and (d) along-track components projected onto the cross-track direction axis x′. Ageostrophic component (blue) is simply calculated as the difference between total (black) and geostrophic (red) currents. Currents are averaged over the forced-stage period of the ocean response to the TC forcing (from day-1 to day + 3). The set of TCs used for this figure (*WPi* > 4.5) have an average translation speed of 2.6 m s^{-1}.

average a slightly larger relative contribution to the inner-core cooling than to the cold wake.

4.2. Processes Controlling the Cooling Spatial Extent

[39] We have so far investigated processes controlling the cooling averaged within 200 km of the TC track. This section investigates processes controlling the cooling away from the cyclone track, and its asymmetry with respect to the track.

[40] Irrespective of the cyclone power, the relative importance of mixing increases toward the eye, whereas the contribution of surface fluxes decreases (Figure 13). For the strongest wind power input, mixing induced cooling accounts for more than 80% of the total cooling within 2 RMW of the TC position, and dominates the cooling amplitude all along the cross track section (Figures 13c and 13f). For the weakest *WPi*s, mixing and heat flux induced cooling have a similar contribution near the cyclone track while heat fluxes dominate the cooling outside 2 RMW, explaining up to 80% of the cooling outside 9 RMW (Figures 13a and 13d).

[41] For strong *WPi*s, advection accounts for up to 30% of the total cooling at 2 to 5 RMW to the right of the TC track. Advection-induced cooling is increasingly asymmetric with increasing TC power (Figures 13g–13i). This asymmetry in advection is primarily associated to horizontal advection while vertical advection effect is symmetrical about the storm center (Ekman suction). Cold Wake asymmetry has been so far mainly attributed to the resonant regime between wind forcing and near-inertial current oscillations on the right side of the track [*Price*, 1981; *Samson et al.*, 2009]. Mixing-induced cooling is indeed the main contributor to the cooling asymmetry for weak and intermediate *WPi* categories (Figures 13g and 13h). For the strongest *WPi* category, mixing-induced cooling asymmetry is however not as prominent, essentially because strong *WPi*s are usually associated with slow TCs, which trigger more symmetric CWs (Figure 8). For the strongest *WPi* category, advection explains most of the asymmetric pattern (~70%; Figures 13f and 13i), and this is true for both slow and fast moving storms (not shown). In this case, mixing is not the only contributor to the cooling asymmetry.

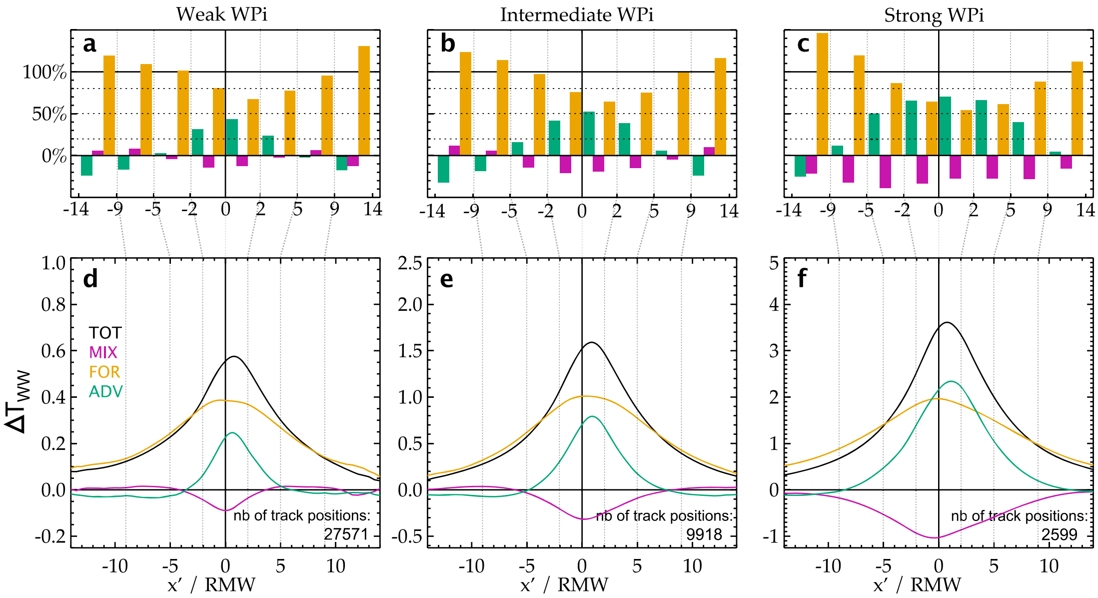

Figure 15. Same as Figures 13a–13f but for the wake warming phase ΔT_{WW} (difference between T_{WW} temperature averaged from day + 3 to day + 63 and T_{CW} in the time integral of each ML heat budget term).

[42] The role of horizontal advection on the CW asymmetry has so far been poorly documented [*Chen et al.*, 2010]. Figure 14a displays separately the along and cross-track advection terms in the frame of the moving TC ($v'\partial_{y'}T$ and $u'\partial_{x'}T$, respectively, with u/x′ the cross-track surface current/axis, and v/y′ the along-track current and axis) for the largest wind forcing. This analysis reveals that asymmetry related to the heat advection mainly results from the along-track component. A two dimensional composite of horizontal currents in the TC-moving frame (Figure 14b) allows understanding this feature. Figure 14 corresponds to a 4-day average, so that near-inertial currents triggered by the TC forcing are largely smoothed (and their residual, i.e., the stationary Ekman flow, is contained in the ageostrophic component). Surface currents anomalies are primarily related to the geostrophic response to the TC-induced negative SSH anomaly under the track (Figure 14b). The negative SSH anomaly centered on the TC position is associated with a cyclonic geostrophic surface circulation (Figure 14b). The ageostrophic part of the current is largely consistent with the stationary Ekman transport response to cyclonic wind forcing (veered to the right of the surface wind stress, Figure 14b).

[43] Along the cross-track axis, geostrophic currents dominate along-track currents (Figure 14d), with forward (backward) currents to the right (left) of the track. This current asymmetry combines with the cold wake asymmetry, with coldest anomalies in the rear-right quadrant (Figure 14b). Along-track currents advect water from the cold wake forward to the right of the track, while they advect relatively warmer water backward on the left side. This explains why along-track currents are a strong source of asymmetry (Figure 14a). As indicated above, cross track currents are dominated by the divergent stationary surface Ekman flow, which is symmetric with respect to the TC-track (Figure 14c). The cross-track component advects cold water from the wake away from the cyclone track, hence cooling both sides in roughly equal proportions (Figure 14a). Asymmetric effect of the cooling for strong cyclones is hence largely due to forward advection of the cold wake by geostrophic currents to the right of the track.

4.3. Processes Controlling the Cold Wake Damping

[44] The good agreement between the modeled and observed SST during the cold wake dissipation (Figure 7a) suggests that our simulation is able to describe the first-order processes that lead to the CW recovery. Based on the averaged time-series, the value of the e-folding time (time for the cold anomaly to be reduced by a factor *e*) is 15 days, in broad agreement with e-folding scales estimated by *Price et al.* [2008] (5 days for TC Fabian and 20 days for TC Frances). About 60 days after the TC passage, the cold anomaly is almost entirely restored to background conditions. Figure 15 shows the integral of the ML temperature budget terms during the warming phase, averaged over a 60-day period starting 3 days after the storm passage. As expected, air-sea heat flux forcing appears as the main process responsible for the CW damping, explaining more than 80% of the ML warming for weak and intermediate strength *WPi* (Figures 15a and 15b). Lateral advection plays a non-negligible role close to the TC track where it explains more than 30% of the warming (and up to 70% for the strongest and or slowest cyclones, Figures 15c and 15f).

5. Conclusion

5.1. Summary

[45] This paper investigates the processes controlling the sea surface cooling induced by Tropical Cyclones (TCs). To that end, we use an ocean general circulation model forced from reconstructed wind perturbations associated with more than 3000 observed TCs over the 1978–2007 period. Reanalysis products usually used to force ocean models

strongly underestimate the amplitude of TCs wind forcing and the resulting TC-induced cooling. We developed an original methodology that allows realistic TC wind forcing based on an idealized vortex [*Willoughby et al.*, 2006] to be included, constrained by observed TC characteristics (location, amplitude) and applied at each ocean model time step.

[46] The statistics of the simulated ocean surface temperature response to TC compare reasonably well to satellite estimates. Average surface temperature anomaly is ~1°C and extends typically over 5 radii of maximum wind (RMW). The modeled cold anomaly amplitude also agrees well with observations at individual locations (0.71 correlation), although the model tends to overestimate cold wakes associated with the strongest and slowest TCs. Overall, the good agreement between the model and observations allows us to estimate the contribution of various oceanic processes to TC cooling for a very diverse sample of observed cyclones over 1978–2007, providing a more general insight than case studies.

[47] The amplitude of the TC-induced cooling depends on the strength of the TC forcing. Following Vincent et al. (submitted manuscript, 2011), we use the wind power index (*WPi*) as an integrated measure of the cyclone's wind forcing. *WPi* is a proxy of kinetic energy transferred to the upper ocean by the cyclone, and integrates important parameters for the cold wake amplitude (cyclone size, intensity and translation speed). TC-induced cooling within 200 km of the TC eye increases linearly with *WPi*: vertical mixing at the base of the mixed layer explains from ~30% of the cooling for weak *WPi* up to ~80% for large *WPi* (above 2.75). Surface heat fluxes however overcome the mixing contribution for lowest *WPi*s (for $WPi < 2$, surface fluxes contribute to ~50%–70% of the cold wake). Away from the cyclone's eye, latent heat fluxes contribute increasingly to the cooling: surface fluxes explain 50 to 80% of the weak cooling further than ~250 km away from the track.

[48] Lateral advection plays a modest role compared to mixing and surface fluxes. For the strongest and/or slowest cyclones, it can however explain up to 30% of the cooling to the right of the TC track. While mixing dominates the cold-wake asymmetry for weak and intermediate *WPi*s, our results suggest that the anti-symmetric pattern of along-track currents is the main contributor to the cooling asymmetry for the most intense cyclones ($WPi > 4.5$). This asymmetry is primarily related to the forward advection of cold wake water by geostrophic currents on the right side of the TC. While heat fluxes control to a large extent the damping of the CW in the months following the TC passage, our analysis also reveals that advective processes play a non-negligible role, contributing to as much as 70% close to the TC track for the strongest TC wind forcing.

[49] The pre-storm ocean state also modulates the amplitude of the TC-induced cooling. The Cooling Inhibition index (CI) is a measure of the ocean "resistance" to cooling by the TC (measured as the amount of potential energy required to cool the ocean surface by 2°C (Vincent et al., submitted manuscript, 2011)). Using this measure, Vincent et al. (submitted manuscript, 2011) showed that ocean background state can modulate the cooling amplitude by up to an order of magnitude for a given cyclone wind power input. We show here that this modulation is related to the increasing efficiency of mixing to cool the ocean surface when CI decreases. In the case of strong CI, the surface current kinetic energy is dissipated to produce vertical mixing but in this case, little cold water is entrained into the ML. In contrast, weak CI is usually associated to a shallow ML and/or steep temperature stratification below the ML before the TC passage, allowing mixing to efficiently incorporate cold water into the ML.

5.2. Limitations of the Present Study

[50] Although the model response to TCs agrees well with observations, we believe that our modeling strategy can be further improved. An inherent limitation to our study is that we rely on analytical formulations for the RMW and surface wind field of TCs. The latest version of the IBTrACS database provide radius estimations for some cyclones, which could be a first step in defining the geometry of the cyclone better. Using satellite observations of surface TC wind from QSCAT would provide more accurate wind pattern but satellites do not provide accurate estimates of the strongest winds. *Sriver and Huber* [2010] used QSCAT surface winds extracted around observed TC tracks to force an ocean general circulation model; they noted that this method underestimates the observed cooling and had to multiply the wind amplitude by a factor 2 to yield realistic cooling amplitude. By contrast, our strategy is based on observed TCs amplitudes and allows us to accurately represent the amplitude of TC-induced cooling in spite of the rather low resolution of the ocean model. This may be due to the fact that we resolve better temporal variations of the cyclone winds, and hence energy transfers to the upper ocean. We indeed apply wind perturbations every time-step (36 minutes) using an interpolated cyclone position, while QSCAT temporal sampling is at best daily, and a cyclone typically travels over ~400 km in 1 day.

[51] We have shown that our 1/2° resolution model simulates reasonably the CW magnitude and spatial extent. The simple analysis of Figure 2 indeed suggests that the 1/2° resolution is enough to capture the transfer of cyclone kinetic energy to the upper ocean, which is the main driver of mixing, a dominant process in the cold wake formation. Figure 2 however suggests that Ekman suction maximum amplitude is probably underestimated by ~30% near the cyclone eye. As demonstrated by several studies [*Greatbatch*, 1985; *Yablonsky and Ginis*, 2009; Jullien et al., submitted manuscript, 2011], Ekman suction can promote increased cooling by shallowing the thermocline near the eye, thus making mixing more efficient. Higher resolution experiments (at least 1/4°) may hence be needed to strengthen the present results. But again, the relatively good agreement between the simulated cold wake and available observations suggest that the current study probably resolves most of the dominant processes.

[52] The wind forcing asymmetry due to the translation speed of TCs has been designated as a secondary order process in regulating the asymmetry of the SST response to TCs [*Price et al.*, 1994; *Samson et al.*, 2009]. We confirm the secondary order importance of this process as the simulation produces asymmetric cold wakes without this effect. We however believe that including this effect may improve characteristics of the simulated CW asymmetry, in particular for fast cyclones.

[53] Cloudiness, precipitation, temperature and humidity anomalies associated to TCs are poorly accounted for in our experimental design. We indeed rely on COREII forcing (i.e., a crude resolution re-analysis) to provide the air temperature and humidity perturbations associated with cyclones, and neglect TC rainfall. Strong uncertainties thus remain on surface fluxes because of air temperature, humidity, and cloud cover perturbations associated with the cyclone. We did not take into account the strong precipitation associated to TC passage either, neglecting the stabilizing effect they may have on the water column and hence potentially overestimate the mixing induced by TCs associated with heavy precipitation.

[54] Finally, mesoscale eddies are known to modulate the ocean response to TCs [*Jacob and Shay*, 2003] and the most intense TCs are often developing over warm core eddies [*Lin et al.*, 2005, 2008] where SST cooling is inhibited. Because our model does not include data assimilation, the position of such eddies in our model is uncorrelated to the observed one. This explains in part why the correlation between simulated and observed cold wakes is "only" 0.71. Moreover, the most intense TCs occur randomly over warm or cold core eddies in our simulation while they tend to occur preferentially over warm core eddies in reality. This sampling discrepancy may be responsible for the overestimation of the average modeled cooling for intense TCs.

5.3. Perspectives

[55] Results described in this paper have practical consequences for statistical operational forecasts of TC intensity. For strongest TC forcing, cooling under the eye is to a large extent controlled by vertical entrainment and mixing. Including an index describing the ocean sub-surface stratification as proposed by Vincent et al. (submitted manuscript, 2011) or *Lloyd and Vecchi* [2011] could hence greatly benefit to cyclone intensity statistical forecast schemes [*DeMaria et al.*, 2005; *Mainelli et al.*, 2008]. However, for weaker cyclones, the effect of surface fluxes cannot be neglected and alternative indices should be proposed to account for their effect on TC-induced cooling.

[56] These results can also be interpreted in the light of the potential impacts of TCs on the ocean at climatic timescales [*Emanuel*, 2001; *Sriver and Huber*, 2010; *Scoccimarro et al.*, 2011]. TC-induced mixing warms water under the ML at the same time as it cools the ML temperature. If surface cold anomaly is entirely damped by surface fluxes, a net warming of the water column results and has to be equilibrated by lateral heat transport [*Emanuel*, 2001]. *Sriver et al.* [2008] argued that TCs significantly modify the poleward heat transport out of the tropics assuming that the observed surface cooling is entirely due to vertical mixing within a 6° footprint around the cyclone. This assumption presumably led the authors to overestimate the amount of heat pumped downward: mixing indeed only explains 52% of the total cooling within 6° of the TC track in our simulation.

[57] Finally, because cooling by surface fluxes affect large areas, we argue that any attempt to diagnose the effects of TCs on the ocean heat budget at the climatic timescale should account for the influence of surface heat fluxes. Further studies are required to investigate the relative effects of mixing and surface fluxes induced by TCs, and their related impacts on the ocean at climatic timescale.

[58] **Acknowledgments.** Experiments were conducted at the Institut du Développement et des Ressources en Informatique Scientifique (IDRIS) Paris, France. We thank the Nucleus for European Modelling of the Ocean (NEMO) Team for its technical support and particularly Simona Flavoni and Christian Ethé for their technical assistance. The analysis was supported by the project Les Enveloppes Fluides et l'Environnement (LEFE) CYCLOCEAN AO2010-538863 and European MyOcean project EU FP7. TMI/AMSR-E data are produced by Remote Sensing Systems and sponsored by the NASA Earth Science MEaSUREs DISCOVER Project. We thank Daniel Nethery for useful comments.

References

Axell, L. B. (2002), Wind-driven internal waves and Langmuir circulations in a numerical ocean model of the southern Baltic Sea, *J. Geophys. Res.*, *107*(C11), 3204, doi:10.1029/2001JC000922.

Barnier, B., et al. (2009), Erratum: Impact of partial steps and momentum advection schemes in a global ocean circulation model at eddy-permitting resolution, *Ocean Dyn.*, *59*, 537, doi:10.1007/s10236-009-0180-y.

Bender, M. A., and I. Ginis (2000), Real-case simulations of hurricane-ocean interaction using a high-resolution coupled model: Effects on hurricane intensity, *Mon. Weather Rev.*, *128*, 917–946, doi:10.1175/1520-0493(2000)128<0917:RCSOHO>2.0.CO;2.

Bender, M. A., I. Ginis, and Y. Kurihara (1993), Numerical simulations of tropical cyclone-ocean interaction with a high-resolution coupled model, *J. Geophys. Res.*, *98*(23), 245–263.

Bernard, B., et al. (2006), Impact of partial steps and momentum advection schemes in a global ocean circulation model at eddy-permitting resolution, *Ocean Dyn.*, *56*, 543–567, doi:10.1007/s10236-006-0082-1.

Brennan, M. J., C. C. Hennon, and R. D. Knabb (2009), The operational use of QuikSCAT ocean surface vector winds at the National Hurricane Center, *Weather Forecasting*, *24*(3), 621–645, doi:10.1175/2008WAF2222188.1.

Burchard, H. (2002), Energy-conserving discretisation of turbulent shear and buoyancy production, *Ocean Modell.*, *4*, 347–361, doi:10.1016/S1463-5003(02)00009-4.

Chen, S., T. J. Campbell, H. Jin, S. Gaberšek, R. M. Hodur, and P. Martin (2010), Effect of two-way air–sea coupling in high and low wind speed regimes, *Mon. Weather Rev.*, *138*, 3579–3602, doi:10.1175/2009MWR3119.1.

Chiang, T. L., C. R. Wu, and L. Y. Oey (2011), Typhoon Kai-Tak: An ocean's perfect storm, *J. Phys. Oceanogr.*, *41*, 221–233, doi:10.1175/2010JPO4518.1.

Cione, J. J., and E. W. Uhlhorn (2003), Sea surface temperature variability in hurricanes: Implications with respect to intensity change, *Mon. Weather Rev.*, *131*, 1783–1796, doi:10.1175//2562.1.

Cione, J. J., P. G. Black, and S. H. Houston (2000), Surface observations in the hurricane environment, *Mon. Weather Rev.*, *128*, 1550–1561, doi:10.1175/1520-0493(2000)128<1550:SOITHE>2.0.CO;2.

D'Asaro, E. A. (2003), The ocean boundary layer below Hurricane Dennis, *J. Phys. Oceanogr.*, *33*, 561–579, doi:10.1175/1520-0485(2003)033<0561:TOBLBH>2.0.CO;2.

D'Asaro, E. A., T. B. Sanford, P. P. Niiler, and E. J. Terrill (2007), Cold wake of Hurricane Frances, *Geophys. Res. Lett.*, *34*, L15609, doi:10.1029/2007GL030160.

de Boyer Montégut, C., G. Madec, A. S. Fischer, A. Lazar, and D. Iudicone (2004), Mixed layer depth over the global ocean: An examination of profile data and a profile-based climatology, *J. Geophys. Res.*, *109*, C12003, doi:10.1029/2004JC002378.

DeMaria, M., M. Mainelli, L. K. Shay, J. A. Knaff, and J. Kaplan (2005), Further improvements to the statistical hurricane intensity prediction scheme (SHIPS), *Weather Forecast.*, *20*, 531–543, doi:10.1175/WAF862.1.

Donelan, M. A., B. K. Haus, N. Reul, W. J. Plant, M. Stiassnie, H. C. Graber, O. B. Brown, and E. S. Saltzman (2004), On the limiting aerodynamic roughness of the ocean in very strong winds, *Geophys. Res. Lett.*, *31*, L18306, doi:10.1029/2004GL019460.

Emanuel, K. A. (1986), An air-sea interaction theory for tropical cyclones. Part I: Steady-state maintenance, *J. Atmos. Sci.*, *43*, 585–605, doi:10.1175/1520-0469(1986)043<0585:AASITF>2.0.CO;2.

Emanuel, K. A. (2001), Contribution of tropical cyclones to meridional heat transport by the oceans, *J. Geophys. Res.*, *106*, 14,771–14,781, doi:10.1029/2000JD900641.

Emanuel, K. A. (2003), Tropical cyclones, *Annu. Rev. Earth Planet. Sci.*, *31*, 75–104, doi:10.1146/annurev.earth.31.100901.141259.

Emanuel, K. A. (2005), Increasing destructiveness of tropical cyclones over the past 30 years, *Nature*, *436*, 686–688, doi:10.1038/nature03906.

Greatbatch, R. J. (1983), On the response of the ocean to a moving storm: The nonlinear dynamics, *J. Phys. Oceanogr.*, *13*, 357–367, doi:10.1175/1520-0485(1983)013<0357:OTROTO>2.0.CO;2.

Greatbatch, R. J. (1985), On the role played by upwelling of water in lowering sea surface temperatures during the passage of a storm, *J. Geophys. Res.*, *90*, 11,751–11,755, doi:10.1029/JC090iC06p11751.

Griffies, S., et al. (2009), Coordinated ocean-ice reference experiments (COREs), *Ocean Modell.*, *26*, 1–46, doi:10.1016/j.ocemod.2008.08.007.

Halliwell, G. R., L. K. Shay, J. K. Brewster, and W. J. Teague (2011), Evaluation and sensitivity analysis of an ocean model response to Hurricane Ivan, *Mon. Weather Rev.*, *139*, 921–945, doi:10.1175/2010MWR3104.1.

Huang, P., T. B. Sanford, and J. Imberger (2009), Heat and turbulent kinetic energy budgets for surface layer cooling induced by the passage of Hurricane Frances (2004), *J. Geophys. Res.*, *114*, C12023, doi:10.1029/2009JC005603.

Jacob, S. D., and L. K. Shay (2003), The role of oceanic mesoscale features on the tropical cyclone-induced mixed layer response: A case study, *J. Phys. Oceanogr.*, *33*, 649–676, doi:10.1175/1520-0485(2003)33<649:TROOMF>2.0.CO;2.

Jacob, S. D., L. K. Shay, A. J. Mariano, and P. G. Black (2000), The 3D oceanic mixed layer response to Hurricane Gilbert, *J. Phys. Oceanogr.*, *30*, 1407–1429, doi:10.1175/1520-0485(2000)030<1407:TOMLRT>2.0.CO;2.

Jansen, M. F., R. Ferrari, and T. A. Mooring (2010), Seasonal versus permanent thermocline warming by tropical cyclones, *Geophys. Res. Lett.*, *37*, L03602, doi:10.1029/2009GL041808.

Kaplan, J., and M. DeMaria (2003), Large-scale characteristics of rapidly intensifying tropical cyclones in the North Atlantic Basin, *Weather Forecasting*, *18*, 1093–1108.

Knapp, K. R., M. C. Kruk, D. H. Levinson, H. J. Diamond, and C. J. Neumann (2010), The International Best Track Archive for Climate Stewardship (IBTrACS): Unifying tropical cyclone data, *Bull. Am. Meteorol. Soc.*, *91*, 363–376, doi:10.1175/2009BAMS2755.1.

Large, W., and S. Yeager (2009), The global climatology of an interannually varying air–sea flux data set, *Clim. Dyn.*, *33*, 341–364, doi:10.1007/s00382-008-0441-3.

Leipper, D. F. (1967), Observed ocean conditions and Hurricane Hilda, 1964, *J. Atmos. Sci.*, *24*, 182–186, doi:10.1175/1520-0469(1967)024<0182:OOCAHH>2.0.CO;2.

Lévy, M., A. Estublier, and G. Madec (2001), Choice of an advection scheme for biogeochemical models, *Geophys. Res. Lett.*, *28*(19), 3725–3728, doi:10.1029/2001GL012947.

Lin, I. I., C. C. Wu, K. A. Emanuel, I. H. Lee, C. R. Wu, and I. F. Pun (2005), The interaction of Supertyphoon Maemi (2003) with a warm ocean eddy, *Mon. Weather Rev.*, *133*, 2635–2649, doi:10.1175/MWR3005.1.

Lin, I. I., C. C. Wu, I. F. Pun, and D. S. Ko (2008), Upper-ocean thermal structure and the western North Pacific category 5 typhoons. Part I: Ocean features and the category 5 typhoons' intensification, *Mon. Weather Rev.*, *136*, 3288–3306, doi:10.1175/2008MWR2277.1.

Liu, L. L., W. Wang, and R. X. Huang (2008), The mechanical energy input to the ocean induced by tropical cyclones, *J. Phys. Oceanogr.*, *38*, 1253–1266, doi:10.1175/2007JPO3786.1.

Lloyd, I. D., and G. A. Vecchi (2011), Observational evidence of oceanic controls on hurricane intensity, *J. Clim.*, *24*, 1138–1153, doi:10.1175/2010JCLI3763.1.

Locarnini, R. A., et al. (2010), *World Ocean Atlas 2009*, vol. 1, *Temperature*, *NOAA Atlas NESDIS*, vol. 68, edited by S. Levitus, NOAA, Silver Spring, Md.

Madec, G. (2008), NEMO ocean engine, *Note Pôle Modél. 27*, Inst. Pierre-Simon Laplace, Paris.

Mainelli, M., M. DeMaria, L. K. Shay, and G. Goni (2008), Application of oceanic heat content estimation to operational forecasting of recent Atlantic category 5 hurricanes, *Weather Forecasting*, *23*, 3–16, doi:10.1175/2007WAF2006111.1.

Marks, F., et al. (1998), Landfalling tropical cyclones: Forecast problems and associated research opportunities, *Bull. Am. Meteorol. Soc.*, *79*, 305–323.

Marsaleix, P., et al. (2008), Energy conservation issues in sigma-coordinate free-surface ocean models, *Ocean Modell.*, *20*, 61–89, doi:10.1016/j.ocemod.2007.07.005.

Mellor, G., and A. Blumberg (2004), Wave breaking and ocean surface layer thermal response, *J. Phys. Oceanogr.*, *34*(3), 693–698, doi:10.1175/2517.1.

Morey, S. L., M. A. Bourassa, D. S. Dukhovskoy, and J. J. O'brien (2006), Modeling studies of the upper ocean response to a tropical cyclone, *Ocean Dyn.*, *56*, 594–606, doi:10.1007/s10236-006-0085-y.

Penduff, T., et al. (2010), Impact of global ocean model resolution on sea-level variability with emphasis on interannual time scales, *Ocean Sci.*, *6*, 269–284, doi:10.5194/os-6-269-2010.

Pollard, R., P. Rhines, and R. Thompson (1973), The deepening of the wind-mixed layer, *Geophys. Fluid Dyn.*, *3*, 381–404.

Price, J. F. (1981), Upper ocean response to a hurricane, *J. Phys. Oceanogr.*, *11*, 153–175, doi:10.1175/1520-0485(1981)011<0153:UORTAH>2.0.CO;2.

Price, J. F., T. B. Sanford, and G. Z. Forristall (1994), Forced stage response to a moving hurricane, *J. Phys. Oceanogr.*, *24*, 233–260, doi:10.1175/1520-0485(1994)024<0233:FSRTAM>2.0.CO;2.

Price, J. F., J. Morzel, and P. P. Niiler (2008), Warming of SST in the cool wake of a moving hurricane, *J. Geophys. Res.*, *113*, C07010, doi:10.1029/2007JC004393.

Samson, G., H. Giordani, G. Caniaux, and F. Roux (2009), Numerical investigation of an oceanic resonant regime induced by hurricane winds, *Ocean Dyn.*, *59*, 565–586, doi:10.1007/s10236-009-0203-8.

Sanford, B., et al. (1987), Ocean response to a hurricane. Part I: Observations, *J. Phys. Oceanogr.*, *17*, 2065–2083, doi:10.1175/1520-0485(1987)017<2065:ORTAHP>2.0.CO;2.

Schade, L. R. (2000), Tropical cyclone intensity and sea surface temperature, *J. Atmos. Sci.*, *57*, 3122–3130, doi:10.1175/1520-0469(2000)057<3122:TCIASS>2.0.CO;2.

Schade, L. R., and K. A. Emanuel (1999), The ocean's effect on the intensity of tropical cyclones: Results from a simple coupled atmosphere–ocean model, *J. Atmos. Sci.*, *56*, 642–651, doi:10.1175/1520-0469(1999)056<0642:TOSEOT>2.0.CO;2.

Scoccimarro, E., S. Gualdi, A. Bellucci, A. Sanna, P. G. Fogli, E. Manzini, M. Vichi, P. Oddo, and A. Navarra (2011), Effects of tropical cyclones on ocean heat transport in a high resolution coupled general circulation model, *J. Clim.*, *24*, 4368–4384, doi:10.1175/2011JCLI4104.1.

Shay, L. K., and J. K. Brewster (2010), Oceanic heat content variability in the eastern Pacific Ocean for hurricane intensity forecasting, *Mon. Weather Rev.*, *138*, 2110–2131, doi:10.1175/2010MWR3189.1.

Shay, L. K., P. Black, A. Mariano, J. Hawkins, and R. Elsberry (1992), Upper ocean response to Hurricane Gilbert, *J. Geophys. Res.*, *97*(20), 227–248.

Shay, L. K., G. J. Goni, and P. G. Black (2000), Effects of a warm oceanic feature on Hurricane Opal, *Mon. Weather Rev.*, *128*, 1366–1383, doi:10.1175/1520-0493(2000)128<1366:EOAWOF>2.0.CO;2.

Shen, W., and I. Ginis (2003), Effects of surface heat flux-induced sea surface temperature changes on tropical cyclone intensity, *Geophys. Res. Lett.*, *30*(18), 1933, doi:10.1029/2003GL017878.

Sriver, R. L., and M. Huber (2010), Modeled sensitivity of upper thermocline properties to tropical cyclone winds and possible feedbacks on the Hadley circulation, *Geophys. Res. Lett.*, *37*, L08704, doi:10.1029/2010GL042836.

Sriver, R. L., M. Huber, and J. Nusbaumer (2008), Investigating tropical cyclone-climate feedbacks using the TRMM Microwave Imager and the Quick Scatterometer, *Geochem. Geophys. Geosyst.*, *9*, Q09V11, doi:10.1029/2007GC001842.

Vialard, J., C. E. Menkes, J.-P. Boulanger, P. Delecluse, and E. Guilyardi (2001), A model study of oceanic mechanisms affecting equatorial Pacific sea surface temperature during the 1997–98 El Niño, *J. Phys. Oceanogr.*, *31*, 1649–1675, doi:10.1175/1520-0485(2001)031<1649:AMSOOM>2.0.CO;2.

Vialard, J., et al. (2009), Cirene: Air sea interactions in the Seychelles-Chagos thermocline ridge region, *Bull. Am. Meteorol. Soc.*, *90*, 45–61, doi:10.1175/2008BAMS2499.1.

Wentz, F. J., C. Gentemann, D. Smith, and D. Chelton (2000), Satellite measurements of sea surface temperature through clouds, *Science*, *288*, 847–850, doi:10.1126/science.288.5467.847.

Willoughby, H. E., and M. E. Rahn (2004), Parametric representation of the primary hurricane vortex. Part I: Observations and evaluation of the Holland (1980) Model, *Mon. Weather Rev.*, *132*, 3033–3048, doi:10.1175/MWR2831.1.

Willoughby, H. E., R. W. R. Darling, and M. E. Rahn (2006), Parametric representation of the primary hurricane vortex. Part II: A new family of sectionally continuous profiles, *Mon. Weather Rev.*, *134*, 1102–1120, doi:10.1175/MWR3106.1.

Yablonsky, R. M., and I. Ginis (2009), Limitation of one-dimensional ocean models for coupled hurricane-ocean model forecasts, *Mon. Weather Rev.*, *137*, 4410–4419, doi:10.1175/2009MWR2863.1.

N. C. Jourdain, LEGI, CNRS/UJF/INPG, BP 53, Grenoble F-38401 CEDEX 09, France.

S. Jullien, LEGOS, IRD/CNRS/UPS, 18, Ave. Edouard Belin, Toulouse F-31401 CEDEX 09, France.

M. Lengaigne, G. Madec, G. Samson, J. Vialard, and E. M. Vincent, LOCEAN, IRD/CNRS/UPMC/MNHN, Tour 45-55 4ème 4, Place Jussieu, Paris F-75252 CEDEX 05, France. (emvincent@phare.normalesup.org)

C. E. Menkes, IRD, 101 Promenade Roger Laroque, BP A5, 98848 Noumea, New Caledonia.

CHAPITRE 4

Contrôle océanique du couplage air-mer sous les TCs

Ce chapitre est basé sur l'article [Vincent *et al.* 2012c].

Les travaux de [Greatbatch 1983, Greatbatch 1984] établissent la dépendance de la réponse océanique aux caractéristiques du cyclone, notamment leur dimension et vitesse de translation. Une dépendance de l'amplitude de la *Cold Wake* (CW) à l'intensité du cyclone semble aller de soit mais la relation à la vitesse maximale des vents du TC n'est pas évidente [Lloyd & Vecchi 2010]. Plusieurs études de cas (*e.g.* [Jacob & Shay 2003]) ont montré que le refroidissement dépend aussi de la structure tri–dimensionnelle du champ de température océanique, mais l'ampleur de cette dépendance n'a pas été quantifiée.

Cet article détaille la dépendance de l'amplitude de la CW aux caractéristiques du TC et de l'océan et propose deux métriques pour en rendre compte.

Synthèse de l'article

Comme le démontre le chapitre précédent, le refroidissement de surface autour de l'oeil du cyclone est dominé par le mélange vertical et il convient donc d'utiliser des métriques du TC et de l'océan pertinentes au regard de ce processus.

Concernant la dépendance atmosphérique, la vitesse maximale des vents n'est pas la meilleure variable explicative de la CW. En effet, l'amplitude du refroidissement sature rapidement pour des vents d'intensité croissante [Lloyd & Vecchi 2010]. Le mélange dépend du transfert d'énergie cinétique des vents aux courants de surface ($W = \int_{t_0}^{t} \vec{\tau}.\vec{u}_{\mathrm{oce}} dt'$) dont le calcul ne peut être réalisé simplement à partir des observations. L'article montre que la puissance dissipée (PD pour *Power Dissipated* ; [Emanuel 2005]) est fortement corrélée à W. PD présente l'intérêt d'intégrer l'énergie dans le temps, incorporant ainsi V_{max}, la vitesse de translation et la taille du cyclone en un seul indice. Un raisonnement théorique simple montre que le refroidissement de surface doit être proportionnel à la racine cubique de l'énergie transférée à l'océan. Un indice de puissance des vents (WPi pour *Wind Power index*) est donc proposé comme la racine cubique de PD normalisé. Le refroidissement de surface augmente linéairement avec WPi ; il est donc possible de prédire un refroidissement avec WPi alors que ce n'est pas le cas avec V_{max} (plusieurs V_{max} étant associé au même refroidissement).

Concernant l'océan, une métrique pertinente doit refléter la propension de l'océan à créer un refroidissement de la température de surface de la mer (SST) sous l'effet d'un mélange vertical. Au cours d'un mélange vertical, l'énergie potentielle de la colonne d'océan augmente lorsque des eaux froides et denses sont déplacées vers le haut. L'article propose de qualifier l'état de l'océan pré–cyclonique par la quantité d'énergie potentielle requise pour conduire à un refroidissement élémentaire en surface. Le même raisonnement que précédemment montre, dans un cas idéalisé, que le refroidissement dépend de la racine cubique de cette augmentation d'énergie potentielle (que l'on a supposée proportionnelle à W en première approche). Un indice d'inhibition au refroidissement par la stratification océanique (CI pour *Cooling Inhibition*) est donc défini par CI= $(\Delta E_{\mathrm{pot}}\,(-2°\mathrm{C}))^{1/3}$ où ΔE_{pot} est l'énergie potentielle à fournir à l'océan pour qu'un mélange pénétrant résulte en un refroidissement de surface de 2°C.

Bien que le refroidissement moyen augmente avec WPi, il existe une très forte dispersion de l'amplitude du refroidissement pour un WPi donné, cette amplitude pouvant varier d'un ordre de grandeur. Par exemple, pour un WPi de 4, le refroidissement du 5$^{\mathrm{e}}$ percentile est -0,5°C alors qu'il est de -5°C pour le 95$^{\mathrm{e}}$ percentile (Fig. 7). Le résultat principal de l'article est de montrer que la majeure partie de cette dispersion est expliquée par l'état de l'océan pré–cyclonique. Lorsqu'il se déplace sur un océan de fort CI (*i.e.* $\sim$45 $(\mathrm{J.m}^{-2})^{1/3}$), un cyclone de WPi=4 engendre en moyenne un refroidissement de -0,5°C alors qu'il engendre un refroidissement de -5°C en moyenne sur un océan de faible CI (*i.e.* $\sim$5 $(\mathrm{J.m}^{-2})^{1/3}$).

Le refroidissement est largement une fonction de WPi et CI ; ces deux indices permettent d'expliquer $\sim$60% de la variance de l'amplitude de la CW. Connaissant les caractéristiques du cyclone et de l'océan, il est donc envisageable de prévoir le refroidissement. En utilisant le WPi seul, un modèle statistique simple est capable de prévoir le refroidissement avec environ 50% d'erreur : un refroidissement de 2°C, par exemple, est prédit avec une erreur de ±1°C. La prise en compte du CI dans le modèle statistique permet de diminuer cette erreur de 40% environ : l'erreur est réduite à ±0.6°C.

Pour décrire le couplage cyclone–océan, la métrique la plus utilisée au cours des 20 dernières années est le contenu thermique océanique (OHC). Plusieurs constats ont participé à la prise de conscience que cette métrique n'est pas la plus pertinente. Alors que l'OHC décrit l'énergie thermique disponible pour le cyclone, celui–ci n'en utilise en général pas plus de 10%. L'utilisation du seuil à 26°C n'est pas fondé sur la physique de l'intensité des TCs, il ne permet pas d'étudier l'interaction TC–océan dans les régions où l'océan y est plus froid et n'autorise pas de l'utiliser dans un contexte de réchauffement climatique. [Price 2009] a récemment proposé d'utiliser « la température moyenne sur les 100 premiers mètres d'océan, la profondeur moyenne de mélange d'un cyclone de catégorie 3 ». [Lloyd & Vecchi 2010] ont quant à eux utilisé la profondeur de l'isotherme SST-2°C (h_2) comme proxy de la stratification de sub–surface. [Goni *et al.* 2009] rappelle la nécessité d'une réflexion approfondie sur le sujet et d'une comparaison des métriques existantes. Etant donné que la SST est connue avant le passage de tout cyclone mais ne peut être observée sous les précipitations intenses de l'œil, une métrique intéressante doit être en mesure de prévoir le ΔSST induit par le cyclone. L'article compare les performances des diverses métriques en ce sens. CI s'avère être la variable la plus pertinente pour prévoir l'amplitude de la CW. h_2 et CI sont très fortement corrélées, mais, contrairement à h_2, CI permet de prendre en compte les effets de la stratification haline qui peut influencer le refroidissement dans certaines régions comme la baie du Bengale.

Remarque : La stratification thermique ($\partial_z T$) a deux effets contradictoire sur l'amplitude du refroidissement de surface : i) elle diminue le mélange en stabilisant la colonne, et ii) elle autorise un mélange à incorporer des eaux plus froides dans la couche mélangée. En s'appuyant sur le point i), [Shay & Brewster 2010] proposent de corriger l'OHC en l'augmentant de la stratification N^2 (« *highly stratified water will act as a barrier to strong shear–induced mixing* »). L'étude de [Jourdain *et al.* 2012] montre que N^2 apparaît à la fois au numérateur et au dénominateur dans CI ; cependant, l'effet ii) l'emporte sur i). La correction proposée pour l'OHC ne va donc pas dans la "bonne" direction. Un $\partial_z T$ plus important permet d'obtenir un refroidissement de surface supérieur pour un coefficient de mélange K_z donné ; une réflexion sur l'énergie, plutôt que sur la valeur du coefficient de mélange, serait plus appropriée.

Article

JOURNAL OF GEOPHYSICAL RESEARCH, VOL. 117, C05023, doi:10.1029/2011JC007705, 2012

Assessing the oceanic control on the amplitude of sea surface cooling induced by tropical cyclones

Emmanuel M. Vincent,[1] Matthieu Lengaigne,[1] Jérôme Vialard,[1] Gurvan Madec,[1,2]
Nicolas C. Jourdain,[3] and Sébastien Masson[1]

Received 24 October 2011; revised 28 March 2012; accepted 30 March 2012; published 15 May 2012.

[1] Tropical cyclones (TCs) induce sea surface cooling that feeds back negatively on their intensity. Previous studies indicate that the cooling magnitude depends on oceanic conditions as well as TC characteristics, but this oceanic control has been poorly documented. We investigate the oceanic influence on TC-induced cooling using a global ocean model experiment that realistically samples the ocean response to more than 3,000 TCs over the last 30 years. We derive a physically grounded oceanic parameter, the Cooling Inhibition index (CI), which measures the potential energy input required to cool the ocean surface through vertical mixing, and hence accounts for the pre-storm upper-ocean stratification resistance to TC-induced cooling. The atmospheric control is described using the wind power index (*WPi*), a proxy of the kinetic energy transferred to the ocean by a TC, which accounts for both the effects of maximum winds and translation speed. The cooling amplitude increases almost linearly with *WPi.* For a given *WPi*, the cooling amplitude can however vary by an order of magnitude: a strong wind energy input can either result in a 0.5°C or 5°C cooling, depending on oceanic background state. Using an oceanic parameter such as CI in addition to wind energy input improves statistical hindcasts of the cold wake amplitude by ~40%. Deriving an oceanic parameter based on the potential energy required to cool the ocean surface through vertical mixing is thus a promising way to better account for ocean characteristics in TCs studies.

Citation: Vincent, E. M., M. Lengaigne, J. Vialard, G. Madec, N. C. Jourdain, and S. Masson (2012), Assessing the oceanic control on the amplitude of sea surface cooling induced by tropical cyclones, *J. Geophys. Res.*, *117*, C05023, doi:10.1029/2011JC007705.

1. Introduction

[2] Tropical cyclones (TCs) are one of the most destructive natural disasters known to man. Accurately forecasting their intensity is a key to mitigating their huge human and financial costs. Most of the kinetic energy lost by TCs is dissipated by friction at the air-sea interface [*Emanuel*, 2003]. This friction is a source of kinetic energy for the ocean and drives strong upper-layer currents. The resulting oceanic vertical shear triggers instabilities that mix warm surface water with colder water below. This is by far the dominant mechanism contributing to the sea surface temperature (SST) cooling observed in the wake of TCs. By contrast, air-sea heat fluxes play a much smaller role [*Price*, 1981; *Jacob et al.*, 2000; *Vincent et al.*, 2012]. TCs primarily draw their energy from evaporation at the surface of the ocean [*Riehl*, 1950]. While higher ambient SSTs provide the potential for stronger tropical cyclones, the SST cooling under the storm eye is the oceanic parameter to which cyclone intensity is most sensitive [*Schade*, 2000]. TC-induced cooling limits evaporation, thereby resulting in a negative air-sea feedback [*Cione and Uhlhorn*, 2003]. For instance, a modest 1°C cooling can lead to a ~40% decrease in surface enthalpy fluxes [*Cione and Uhlhorn*, 2003], while a 2.5°C decrease seems sufficient to shut down energy production entirely [*Emanuel*, 1999]. *Emanuel et al.* [2004] demonstrated that coupling a single-column ocean model to a simple axisymmetric hurricane model did clearly improve intensity forecasts of a few selected storms, suggesting that further improvement in operational TC intensity forecasts may be achieved by taking the surface cooling feedback into account. Using a coupled hurricane-ocean model, *Schade and Emanuel* [1999] showed that the surface cooling feedback can reduce TC intensity by more than 50%; the intensity of this feedback depending on the storm translation speed and oceanic parameters such as the mixed layer depth and upper ocean stratification.

[3] Past case studies have illustrated the influence of subsurface oceanic background conditions onto the amplitude of the TC-induced cooling and related TCs intensification [e.g., *Cione and Uhlhorn*, 2003; *Jacob and Shay*, 2003; *Shay and Brewster*, 2010; *Lloyd and Vecchi*, 2011]. These studies

---

[1] LOCEAN, IRD/CNRS/UPMC/MNHN, Paris, France.
[2] NOC, Southampton, UK.
[3] LEGI, CNRS/UJF/INPG, Grenoble, France.

Corresponding author: E. M. Vincent, LOCEAN, IRD/CNRS/UPMC/MNHN, Tour 45-55 4ème 4, Place Jussieu, Paris F-75252 CEDEX 05, France. (emvincent@phare.normalesup.org)

0148-0227/12/2011JC007705

indeed suggest that the TC-induced mixing is particularly efficient in cooling the ocean surface when the mixed layer is shallow and/or the upper temperature profile is strongly stratified. These conditions often results in a small Ocean Heat Content (OHC) [*Leipper and Volgenau*, 1972], a commonly used metric of TC sensitivity to the ocean subsurface calculated as the temperature integral from the surface down to the 26°C isotherm depth. Further support for oceanic control on TC-induced cooling arises from observations of TCs intensification over the passage of a warm loop current or warm core ring allowing an increase of the ocean to atmosphere enthalpy flux [e.g., *Jacob and Shay*, 2003; *Ali et al.*, 2007]. A well-documented example of the oceanic impact onto TC intensity is the Hurricane Opal (1995) that rapidly intensified as it crossed a warm core ring in the Gulf of Mexico, unexpectedly increasing from Category 1 to Category 4 in 14 h [*Shay et al.*, 2000; *Bosart et al.*, 2000; *Hong et al.*, 2000]. *Lloyd and Vecchi* [2011] illustrated this influence of the upper-ocean stratification on the TCs' intensity evolution on a global basis. *Lloyd et al.* [2011] further showed that the performance of an operational hurricane forecasting system can be improved by a better representation of the horizontal structure of upper-ocean stratification. These findings are also confirmed by the improvements in statistical intensity forecasting resulting from the simple inclusion of OHC as a supplementary predictor [*DeMaria et al.*, 2005; *Mainelli et al.*, 2008]. However, these improvements are still modest, reducing the intensity forecast errors by ~5%, on average. In a recent review, *Goni et al.* [2009] underlined the need to adequately investigate and quantify the role of the upper ocean in TC intensification and to improve oceanic metrics of cyclone air-sea interactions. *Cione and Uhlhorn* [2003] underlined that under most TCs conditions, the upper-ocean heat content is at least an order of magnitude greater than the energy actually extracted by the storm, suggesting that OHC may not be the most appropriate parameter to account for the upper-ocean effect on TC intensity. *Price* [2009] also suggested that a metric based on a vertical average of temperature would be more relevant for cyclone-ocean interaction studies than a metric based on vertically integrated temperature (such as OHC) as it better reflects the way TCs interact with the ocean.

[4] The ocean influences TCs through changes in SST. *Schade* [2000] argued that the SST effect can be split into two distinct contributions: the ambient SSTs ahead of the storm and the SST cooling induced by the storm under the eyewall. Satellite observations accurately capture the ambient SST ahead of the storm but do not provide reliable estimates of inner-core SST due to intense rainfall [*Wentz et al.*, 2000]. The usefulness of a metric of the oceanic influence on the TC should therefore be measured through its ability to quantify the amplitude of the storm-induced cooling. While idealized studies (such as *Schade and Emanuel*, 1999) already demonstrated that oceanic conditions can modulate the amplitude of the negative air-sea feedback on TCs, they did not propose an integrated oceanic parameter that accounts for this control. Our goal in this paper is hence to derive a simple, physically based measure of the control of oceanic vertical stratification on the surface cooling under TCs conditions and to assess by how much the oceanic vertical stratification modulates the CW magnitude.

[5] The limited number of sub-surface observations under TCs (especially in the inner core region) prevents a direct and precise quantification of the influence of the upper ocean structure on the TC-induced cooling at a global scale from observations alone. While dedicated field campaigns [*Chen et al.*, 2007] and autonomous profilers [*Roemmich et al.*, 2009] now provide access to ocean sub-surface data in the cyclone's vicinity, they do not sample the widely varied oceanic conditions over which TCs transit. As suggested by *Goni et al.* [2009], numerical modeling can provide a useful indirect methodology to investigate the oceanic control of the amplitude of the TC-induced cooling. In this paper, we use an Ocean General Circulation Model (OGCM) driven by TC wind-forcing from an historical TC database, that samples the ocean response to more than 3000 TCs over the last 30 years. The realism of the simulated TC-induced cooling in this data set has been extensively validated in a companion paper [*Vincent et al.*, 2012]. This simulation hence provides a comprehensive data set, allowing in-depth analysis of the influence of a wide spectrum of realistic oceanic stratifications on TC-induced cooling.

[6] The paper is organized as follow. Section 2 presents our strategy to include TC wind-forcing in our OGCM. In section 3, we lay out the physical concept and idealized analytical approach that justify two simple (one oceanic and one atmospheric) parameters that account for the amplitude of the TC-induced cooling. Based on the use of these indices, section 4 quantifies the role of the ocean stratification in modulating the cooling amplitude. This section further describes the improvement brought by accounting for the CI index in predicting the cooling and compares this index to other recently suggested alternatives to the OHC [*Price*, 2009; *Buarque et al.*, 2009; *Lloyd and Vecchi*, 2011]. Section 5 provides a summary of our results as well as a discussion of their implications.

2. Methods

2.1. Data

[7] Observed TCs positions and intensities are derived from the International Best Track Archive for Climate Stewardship (IBTrACS) [*Knapp et al.*, 2010]. The observed SST response to tropical cyclones (TCs) is characterized using the optimally interpolated blend of Tropical Rainfall Measuring Mission (TRMM) Microwave Imager (TMI) and Advanced Microwave Scanning Radiometer AMSR-E SST daily data set over 1998–2007. Despite its inability to provide SST data under heavy precipitation, TMI and AMSR-E provide observations of SST beneath clouds a few days before and after a TC's passage.

2.2. Experimental Design and Model Validation

[8] The model configuration, strategy to include the TC wind-forcing and the experiments analyzed in the present paper have been extensively described and validated in *Vincent et al.* [2012]. The following section provides a short summary of this modeling framework and of the validation of TC-induced cooling.

[9] We use an OGCM configuration built from the NEMO framework [*Madec*, 2008], with 1/2° horizontal resolution and 46 levels (10 m resolution in the upper 100 m). The mixed layer dynamics are represented by an improved Turbulent Kinetic Energy (TKE) closure scheme [*Madec*, 2008]. This configuration successfully reproduces tropical

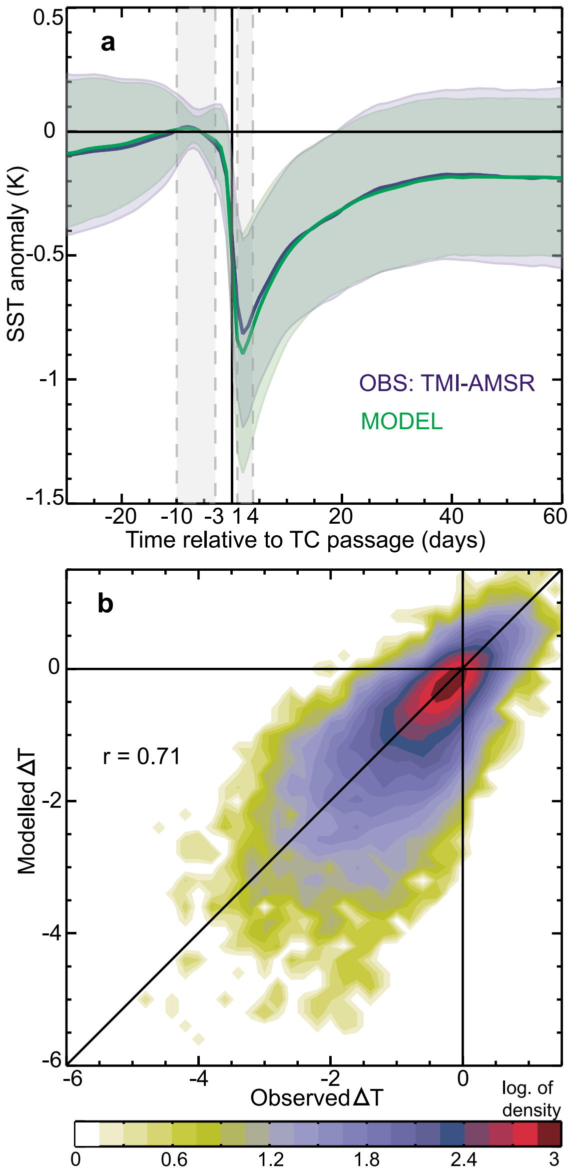

Figure 1. (a) Composite SST evolution averaged under all TCs in observations (blue) and in the model (green). Anomalies are calculated with respect to average pre-storm SST time (days −10 to −3) over a 200 km radius from the TC's position. Day 0 refers to the time when the TC reaches the track position. Color shading shows the ±1/2 standard deviation around the mean composite value. (b) Probability density function of modeled versus observed ΔT due to the passage of the TC: SST averaged over day +1 to day +4 less the SST averaged over day −10 to day −3. The validation samples 1100 storms over the 1998–2007 period (both figures are from *Vincent et al.* [2012]).

ocean variability at intraseasonal to interannual time scales [*Penduff et al.*, 2010; *Lengaigne et al.*, 2012], and is able to simulate TC-induced cooling reasonably well [*Vincent et al.*, 2012]. *Vincent et al.* [2012] show in particular that the 1/2° resolution is a good compromise between accuracy and numerical cost for a realistic global simulation of the ocean response to TCs, thanks to the high temporal resolution of the wind-forcing that allows each grid point to properly sample the wind sequence during TC passage.

[10] The model starts from an ocean at rest, initialized with temperature and salinity fields from the World Ocean Atlas 2005 [*Locarnini et al.*, 2006]. It is then spun up for a 30-year period using the CORE-II bulk formulae and interannual forcing data set (1948–1977) [*Large and Yeager*, 2009; *Griffies et al.*, 2009]. The final state is then used to start the simulations described below, which are run over 1978–2007.

[11] The CORE-II forcing data set does not resolve intense winds associated with tropical cyclones, but contains weaker than observed TC wind signatures. The cyclone free simulation (FILT) is forced by the original interannual CORE forcing from which TC-like vortices are filtered out by applying an 11-day running mean to the wind within 600 km of each cyclone track position (a smooth transition zone, between 600 km and 1,200 km, is also prescribed). The cyclone simulation (CYCL) is forced by realistic TC-wind signatures superimposed to FILT forcing. The 6-hourly cyclone position and strength of the 3,000 named TC between 1978 and 2007 from IBTrACS database [*Knapp et al.*, 2010] are interpolated to the model time step (i.e., every 36 min). This information is used to reconstruct the 10-m wind vector from an idealized TC wind vortex fitted to observations [*Willoughby et al.*, 2006]. A more detailed description of this forcing strategy can be found in *Vincent et al.* [2012].

[12] Our model reproduces the average observed cooling within 200 km of TC tracks quite realistically (Figure 1a). The average maximum cooling for all observed cyclones between 1998 and 2007 is about 1°C in both model and observations. SST starts cooling 3 days prior to the TC passage, and the maximum cooling occurs in its wake of the TC after the passage of the eye. Hereafter, we define the cold wake amplitude ΔT_{CW} as the difference between the wake (days 1 to 3) and the pre-storm (days −10 to −3) SST average values (Figure 1a). We also define the cooling under the eye ΔT_{eye}, as the difference between the eye (12 h before to 12 h after the cyclone passage) and the pre-storm SST (days −10 to −3) average values.

[13] There is a 0.71 correlation between modeled and observed ΔT_{CW} at individual locations (Figure 1b), indicating that our simulation realistically samples the ocean response to the wide spectrum of TC characteristics. The model also successfully reproduces the observed spatial distribution of the cold wake amplitude (see *Vincent et al.* [2012] for more details about the model validation).

3. Introducing a Metric of Oceanic Control of TC-Induced Cooling

[14] In this section, we introduce the basic physical concepts behind our approach. We derive two indices, using analytical calculations from a highly idealized case, to describe the expected dependence of the cooling amplitude to the TC and ocean characteristics.

3.1. Physical Basis

[15] Cooling under TCs largely results from mixing, i.e., from the conversion of kinetic energy to potential energy [*Price*, 1981]. The kinetic energy transferred to the ocean results from the work of surface wind stress on ocean

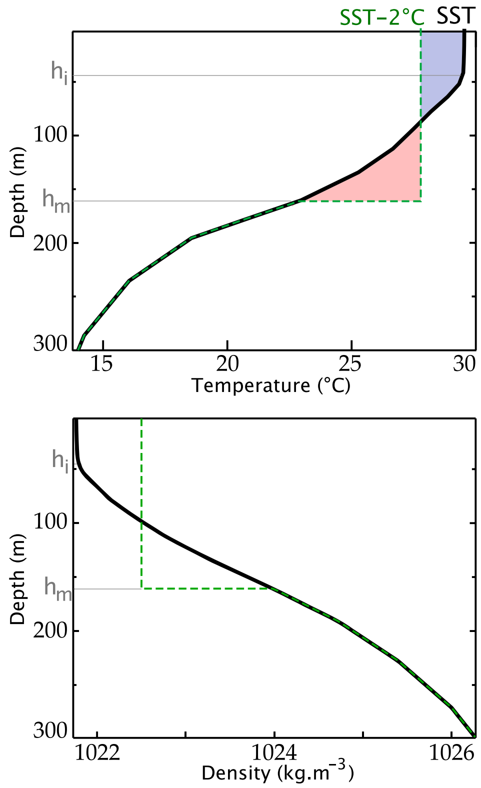

Figure 2. Typical tropical temperature and density profiles before the storm passage (black) and after an idealized heat and mass conserving mixing (dashed green line) used for calculation of the Cooling Inhibition.

currents. The strong resulting currents are driving mixing through strong vertical shear that promotes instabilities. Most of the energy transferred to the ocean radiates away in the surface waves field but a fraction of the kinetic energy is converted into potential energy [*Liu et al.*, 2008]. Warm, light particles are indeed displaced downward while cold, denser particles are displaced upward leading to an increase of the water column potential energy. Based on these simple considerations, a simple relation between the cooling and change in potential energy is derived as follows.

[16] Let us consider an ocean with a linear equation of state depending on temperature only: $\rho(z) = \rho_0(1 - \alpha\, T(z))$. We present here a very simple case with constant stratification N^2, all the way up to the surface. The temperature profile is $T(z) = T_i + \frac{N^2}{\alpha g} z$. Let us now assume that the surface layer has been homogeneously mixed down to the depth h_m, at the temperature T_f.

[17] Conservation of heat yields an equation linking h_m with the surface cooling ΔT

$$h_m + 2\frac{\alpha g}{N^2}\Delta T = 0. \tag{1}$$

The potential energy difference between the initial and final profile (ΔE_p) provides an equation linking h_m, ΔT and ΔE_p

$$h_m^3 + \frac{3}{2}\frac{\alpha g}{N^2}\Delta T\, h_m^2 = 3\frac{\Delta E_p}{\rho_0 N^2}. \tag{2}$$

By combining equations (1) and (2), we obtain an equation linking the cooling and the increase of potential energy of the water column

$$\Delta T = -\frac{1}{\alpha g}\left(\frac{3\,N^4}{2\,\rho_0}\Delta E_p\right)^{1/3}. \tag{3}$$

[18] In the idealized framework above, the surface cooling ΔT is associated to an increase of the water column potential energy ΔE_p and ΔT scales as the cube root of this potential energy increase. Calculations using a more realistic temperature profile that includes a mixed layer are provided in section A1. These calculations show that the relationship found in the simple case above (where the initial mixed layer depth vanishes) remains valid when the initial mixed layer is shallower than a characteristic mixing length. For deeper initial mixed layer, ΔT scales linearly with the potential energy increase ΔE_p. In our simulation, we found that the mixed layer before the cyclone passage is shallower than the characteristic mixing length in ~80% of the cases (Figure A2). This motivates the definition of an oceanic metric based on the cube root of a potential energy change in the next paragraph.

3.2. A Metric of Oceanic Control of TC-Induced Cooling

[19] Given a pre-storm upper-ocean density profile, one can calculate the potential energy increase $\Delta E_p(\Delta T)$ necessary to produce a given ΔT cooling assuming heat conservation and a perfectly homogeneous mixed layer after the mixing (as we did in the idealized case of section 3.1, but this time with the actual profile before the storm). The larger this ΔE_p, the more energy has to be injected into the ocean to produce this cooling. The idea is thus to characterize the propensity of the pre-storm ocean state to yield a weak or strong surface cooling in response to a surface kinetic energy input.

[20] The mixing depth h_m that is necessary to produce a cooling ΔT is first computed from the equation of conservation of heat (see the example with a model profile, for a ΔT of −2°C, on Figure 2). The associated potential energy increase is then computed as

$$\Delta E_p(\Delta T) = \int_{h_m}^{0}\left(\rho_f - \rho_i(z)\right) g z\, dz, \tag{4}$$

where ρ_i is the initial unperturbed profile of density, g is the acceleration of gravity, z is ocean depth, ρ_f is the homogeneous final density profile. After the mixing, temperature T is assumed to be constant and equal to $SST + \Delta T$ within the mixed layer (Figure 2, top). Similarly, salinity S is assumed to be constant within the mixed layer and its value is computed from conservation of salt. Density ρ_f can then be obtained using these (T,S) values. $\Delta E_p(\Delta T)$ is finally computed from the density difference between the initial and final profiles, using equation (4). This computation of $\Delta E_p(\Delta T)$ hence only requires knowledge of the temperature and salinity profiles before the cyclone passage.

[21] In the following, we define the cooling inhibition (CI) as the cube root of the necessary potential energy to induce a 2°C SST cooling:

$$CI = [\Delta E_p(-2°\mathrm{C})]^{1/3}. \tag{5}$$

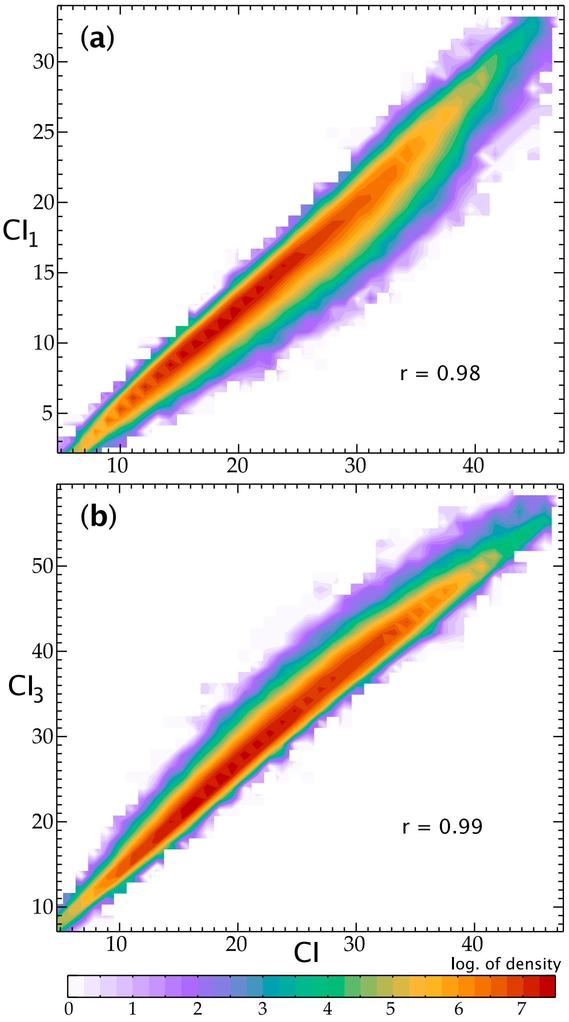

Figure 3. Probability density functions of (a) Cooling Inhibition calculated using a 1°C threshold (CI_1) versus a 2°C threshold (CI) and (b) Cooling Inhibition calculated using a 3°C threshold (CI_3) versus a 2°C threshold (CI). Correlations between these indices are, respectively, 0.98 and 0.99. Units are in $(J.m^{-2})^{1/3}$.

CI is defined as a cube root on the basis of the idealized analysis of section 3.1, which suggested that the cooling should scale as the cube root of a potential energy. The analysis preformed in Section 4 will provide further evidence of the relevance of this scaling. We compute cooling inhibition CI from a cooling of −2°C, a rather typical value under a tropical cyclone. The typical variations of CI over the cyclone-affected regions are anyway relatively insensitive to a choice of 1°C (CI_1), 2°C (CI) or 3°C (CI_3) (Figure 3): CI_1 and CI_3 are highly correlated (0.98 and 0.99) to CI.

[22] We call this index "Cooling Inhibition" (CI) because it measures the resistance of the ocean to surface cooling through mixing. CI is a useful metric to describe the oceanic inhibition to a wind-induced cooling because it integrates two relevant parameters for the cooling amplitude: the initial mixed layer depth and the strength of the stratification just below it. Indeed, the deeper the initial mixed layer, the more kinetic energy is required to produce mixing at its base. And the deeper the initial mixed layer, the greater the thermal capacity of the surface layer: for a given entrainment cooling, a thicker layer cools less. The stratification at the base of the mixed layer is another relevant parameter because it sets the temperature of water that can be entrained into the mixed layer. Figure 4a shows that CI accounts for both these parameters: it increases with the mixed layer depth (h_i) and decreases with the stratification at its base (N). Largest CI are only found when the mixed layer is deep and the stratification at its base is weak. We will show in the following that CI accurately describes the ocean propensity to mitigate

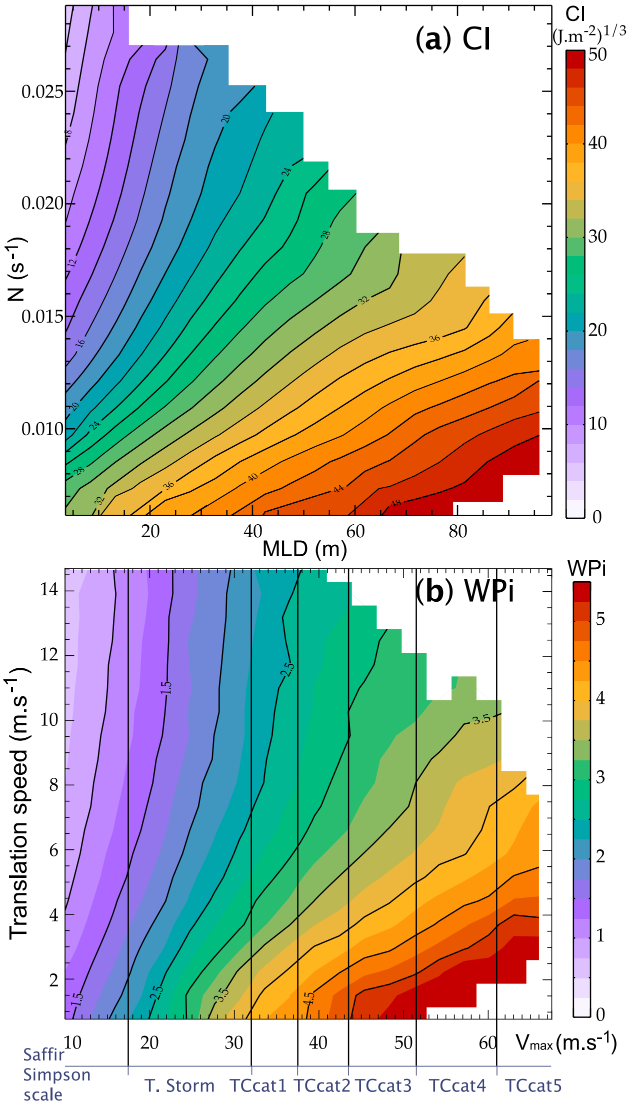

Figure 4. (a) Average CI values as a function of the mixed layer depth (MLD) and the stratification at its base (N) evaluated as $N^2 = \alpha g \frac{T_{ML}-2^{\circ}C}{h_2-h_i}$, where h_2 is the depth of the isotherm "T_{ML}-2°C" and h_i the mixed layer depth. (b) Average $WPi = [PD/PD_0]^{1/3}$ as a function of the maximum 10-min sustained wind (V_{max}) and TC translation speed. For representativeness, the mean is limited to regions with 6 samples or more. Saffir–Simpson tropical cyclone scale is reminded for reference.

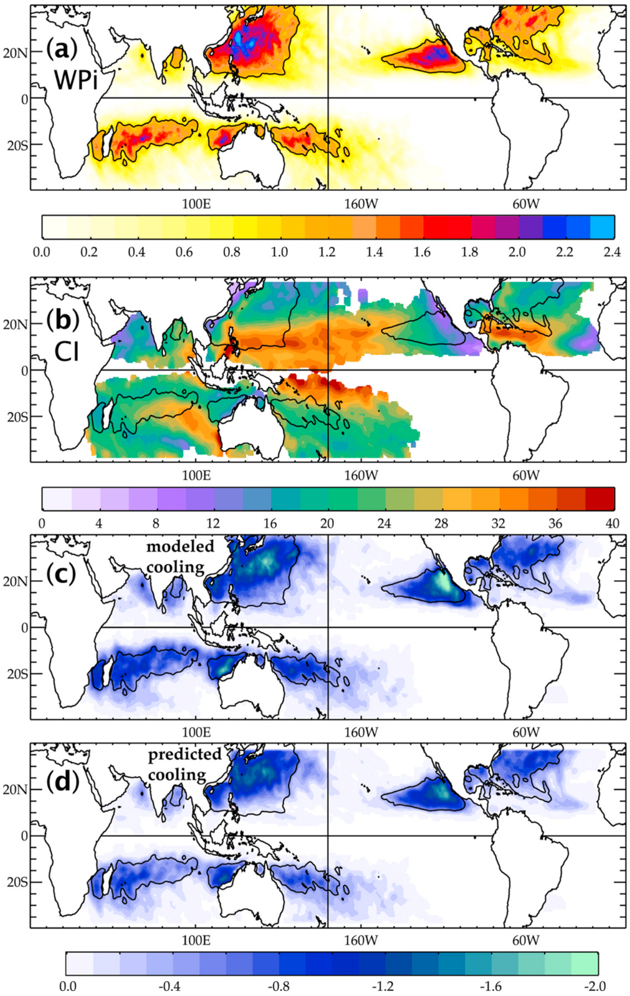

Figure 5. Maps over 1978–2007 of average (a) wind power index, (b) CI (in $(\mathrm{J.m^{-2}})^{1/3}$), (c) TC-induced cooling in the ocean model and (d) cooling predicted with the bivariate fit on *WPi* and CI (in °C). For each cyclonic season, a map is obtained by first recording the integrated-*WPi*, CI or ΔT_{CW} within 200 km of each TC position and averaging for all TCs of the season. Figure 5 shows the 30-years average of these seasonal maps. Isoline "*WPi* = 1" is repeated over each panel for reference.

the SST response to a cyclone. In the rest of the paper, we compute CI in our simulation based on the pre-storm ocean column density (averaged over 10 to 3 days before TC passage, and within 200 km from the TC track position). Figure 5b illustrates the average CI value under all TCs track in our simulation, for all pre-cyclone oceanic profiles during 1978–2007 (this figure does not strongly differ from the figure of the CI computed from the oceanic climatological state during the cyclonic season in *Vincent et al.* [2012, Figure 3e]). This map partially reflects the depth of the thermocline (larger energy is required to bring cold water parcels to the surface when the thermocline is deep), with large CI values in the western Pacific warm Pool or in the Northwestern Tropical Atlantic. CI does not only reflect thermal stratification, but also haline stratification: CI is larger in the Bay of Bengal than in the Arabian Sea, partly due to the very strong river runoffs and resulting haline stratification in the Bay, that prevents vertical mixing [*Sengupta et al.*, 2008; M. Neetu et al., Influence of upper ocean stratification on tropical cyclones-induced surface cooling in the Bay of Bengal, unpublished manuscript, 2012].

3.3. A Metric of the Atmospheric Control of TC-Induced Cooling

[23] The kinetic energy transferred by the storm to the upper ocean can be computed from the work W of surface wind stress on the ocean $W = \int_{t_o}^{t_c} \boldsymbol{\tau}\cdot\mathbf{u}_{oce}\,dt$ where $\boldsymbol{\tau}$ is the surface wind stress, $\mathbf{u}_{oce}$ the surface ocean current, t_o the time when the storm starts influencing a certain point and t_c the current time. In this paper, t_o is set to day -3 (3 days before a TC reaches a given ocean point). Taking t_o equal to day -5 or day -10 however yields very similar results, as most of the energy transferred to the ocean occurs within a couple of days before and after the cyclone reaches a given location. t_c is taken as day +3 to integrate the wind-forcing over the full period during which the TC influences the ocean column and relate it to the cooling occurring in the wake of the TC.

[24] While W can easily be calculated in our simulation, it is not available in observations due to the lack of reliable high-frequency estimates of observed surface currents. A more easily computable quantity is the power dissipated by friction at the air-sea interface. *Bister and Emanuel* [1998] showed that, in a hurricane, dissipation occurs mostly in the atmospheric surface layer, with a dissipation rate per unit area, D, given by: $D = \rho C_D |V|^3$. In our simulation, we find that the time integral of this dissipation (Power Dissipation (PD)) [*Emanuel*, 2005] is highly related to W (correlation of 0.9) as shown on Figure 6. It can hence be used as a proxy to estimate the kinetic energy transferred to the ocean W. Because it is more easily estimated from observations and

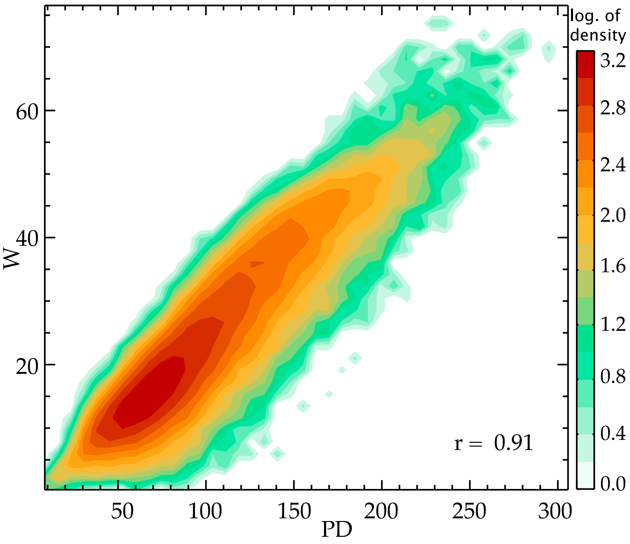

Figure 6. Probability density function of the wind work on surface currents (W) versus the Power Dissipated (PD) averaged within 200 km of each TC track position. Correlation between these two quantities is 0.91. Units are in $(\mathrm{J.m^{-2}})^{1/3}$.

can be used for future studies, we will hereafter use *PD*, calculated at every point along cyclone tracks as

$$PD = \int_{t_o}^{t_c} \rho\, C_D |\mathbf{V}|^3\, dt, \qquad (6)$$

where $|\mathbf{V}|$ is the local magnitude of surface wind, C_D the dimensionless surface drag coefficient [*Large and Yeager*, 2009] and ρ the surface air density.

[25] The cooling amplitude can be related to TC wind-forcing by the very crude assumption that the kinetic energy input *W* (approximated by PD) linearly relates to the potential energy increase in the ocean. Using the idealized approach of section 3.1 and equation (3), this leads to a ΔT that should be proportional to $W^{1/3}$ for cases where the initial mixed layer is shallow (~80% of the TC cases). It is however far from being obvious that the fraction of kinetic energy transformed into potential energy is constant as it is likely to depend for instance on the relative ML depth and wind-induced mixing depth. A similar dependence of ΔT to $W^{1/3}$ can also be derived using a different framework that directly relates surface cooling to wind-forcing such as the one developed in the appendix of *Korty et al.* [2008]. Using this framework based on the *Price* [1979] assumption that the bulk Richardson number remains constant during TC mixing, one can demonstrate that the temperature change scales as the cube root of the wind power input for shallow MLDs. This provides further theoretical justification for the choice of the scaling for the index proposed below.

[26] We hence define a dimensionless "wind power index" as

$$WPi = [PD/PD_0]^{1/3}, \qquad (7)$$

where $PD_0 = \int_{t_o}^{t_c} \rho\, C_D\, |\mathbf{V}_0|^3\, dt$ is a normalization constant corresponding to a typical weak storm with a translation speed of 7 m.s^{-1} (25 km.h^{-1}) and maximum 10-min averaged wind speed of 15 m.s^{-1} (the wind speed defining a Tropical Depression: the weakest cyclonic system classified). *PD* is computed using the same choices for t_0 and t_c as for *W*. The almost linear relationship between average ΔT and WP_i (that will be shown later in the paper) illustrates the first order validity of this simple approach for the scaling definition.

[27] Previous studies have underlined that not only cyclone intensity, but also translation speed influences the amplitude of the cold wake, slower cyclones being associated with intense cooling [*Greatbatch*, 1984; *Lloyd and Vecchi*, 2011]. Figure 4b shows that *WPi* gathers information about these two factors. *WPi* increases (decreases) monotonically with storm intensity (translation speed), and reaches its highest values (~5) for TCs that are both strong and slow (Category 4 or more on the Saffir-Simpson scale and translation speed <4 m/s). Bigger storms are also characterized by a longer influence of strong wind-forcing at a given point; WP_i also naturally integrates the storm size effect.

[28] Figure 5a shows the average *WPi* by basin. It underlines familiar regions of TC occurrence. Most powerful TCs occur in the northeast and northwest tropical Pacific. There is also a high averaged wind power North of Australia (both on the Indian ocean and Pacific sides), and in the Southwestern Indian Ocean. The Caribbean and Northern Indian Ocean display the weakest averaged wind power. In the following section, we will discuss the upper-ocean cooling, in response to this forcing.

4. Dependence of the Cold Wake Magnitude to TC and Ocean Characteristics

[29] Using the two metrics described above, the following section quantifies the dependency of the cooling amplitude on the oceanic background state. The improvement brought by including this oceanic metric in the CW intensity hindcast is then assessed. The efficiency of CI against other proposed oceanic metrics is finally discussed.

4.1. Surface Cooling as a Function of *WPi* and CI

[30] The average cooling under TCs largely reflects the spatial distribution of *WPi* (Figures 5a and 5c), but a closer inspection reveals that maximum cooling are in general not collocated with maximum *WPi.* For example, the maximum cooling occurs poleward of the maximum energy input in the northwestern Pacific as less energy is required to cool the ocean there (low CI values; Figure 5b). The maximum cooling intensity in the Southwestern Indian Ocean is similarly shifted to the west (e.g., into the Mozambique channel) of the *WPi* maximum. The spatial distribution of the average TC cooling (Figure 5c) is hence a consensus between the energy input (Figure 5a) and the cooling inhibition by ocean stratification (Figure 5b).

[31] Figure 7a shows a probability distribution of the cooling as a function of *WPi.* The mean cooling increases with *WPi*, as suggested by the idealized approach in section 3. This increase is almost linear for *WPi* <4, justifying a posteriori the relevance of *WPi* formulation and scaling to estimate the cold wake amplitude. The slope of ΔT versus *WPi* however increases for *WPi* larger than 4. This nonlinearity probably arises from the fact that Figure 7 accounts for all simulated cooling, including cases of deep initial mixed layer (~20% of the cases) for which the scaling between ΔT and ΔE_p (and hence PD) is different (see section A1). In addition, it is likely that the ratio of potential energy increase (ΔE_p) to the wind energy transferred to the ocean (*W*) depends on the initial ML depth relative to the TC-induced mixing length, thus being dependent on *W* itself. The simple cube root scaling used for the *WPi* definition is thus a first order approach that may be further improved. The proposed *WPi* variable however fulfills our main objective, which was to define a metric that condenses the main TC parameters that affect the cooling into a single explanative variable, from which ΔT is a monotonically increasing function. This is not the case for the widely used $V_{\max}$ (TC maximum winds) variable [*Lloyd and Vecchi*, 2011]). Although the mean cooling increases with *WPi* (Figure 7a), there is a large scatter of the cooling amplitude around this mean value. For a given wind energy, the cooling of the 5th and 95th percentile of events differs by one order of magnitude. For instance, a *WPi* of 4 results in a cooling ranging from 0.5°C to 5°C. We will show below that this scatter of the cooling magnitude can be largely explained by the influence of the oceanic background state, as measured by the CI parameter.

[32] Figure 8a shows that the average cooling increases as a function of *WPi* and decreases as a function of *CI.* Very large cooling (up to 5°C) only occur when powerful TCs (*WPi* > 4) travel over a very stratified upper ocean (low CI).

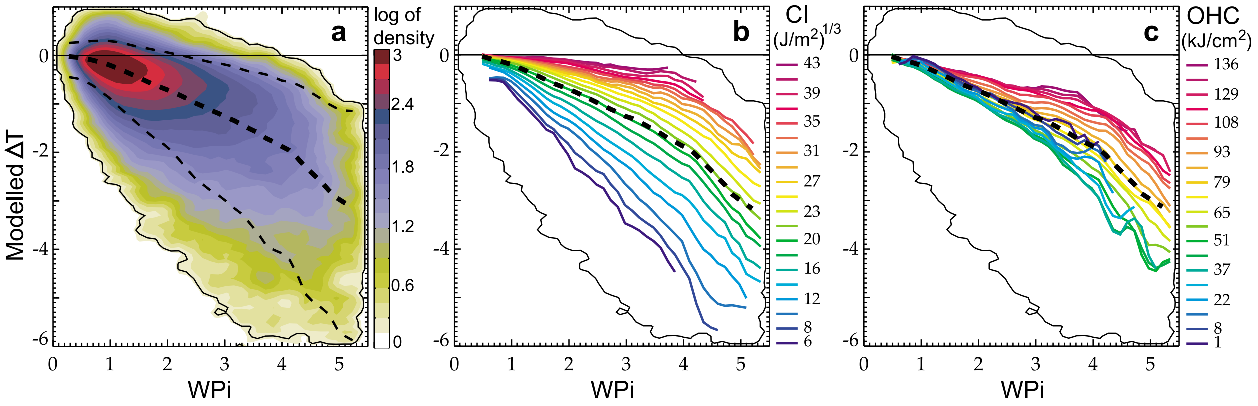

Figure 7. (a) Probability density function of storm-induced cooling ΔT versus wind power index *WPi.* The thick dashed line indicates the average cooling as a function of *WPi* while the thin dashed lines represent the highest and lowest 5% of the distribution. (b) Average cooling as a function of *WPi* for 20 regularly spaced values of Cooling Inhibition (CI). (c) Same as Figure 7b but for the Ocean Heat Content (OHC). Contour of 0.1 probability density isoline from Figure 7a is reported on Figures 7b and 7c (thin plain line) as well as the average cooling as a function of *WPi* (dashed line).

Figure 7b further displays the average cooling as a function of *WPi* binned by *CI* values (the dark blue curves corresponding to low values of *CI* and the purple curves to high values of *CI*). Taking *CI* into account allows one to explain the wide range of possible TC cooling amplitudes for a given wind power input (Figure 7b). For a large *CI*, the cooling is about an order of magnitude smaller than for a weak *CI.* For example, the average cooling for a *CI* of ~40 $(\mathrm{J.m^{-2}})^{1/3}$ never exceeds 0.5°C, while it can reach up to 5°C for a *CI* of ~10 $(\mathrm{J.m^{-2}})^{1/3}$. This demonstrates that oceanic stratification is a major factor controlling the SST response to a TC.

[33] This control of the surface cooling magnitude by the oceanic background state is further quantified by comparing cooling prediction skills of hindcasts based on the atmospheric metric alone (*WPi*) or on *WPi* along with *CI.* Simple bivariate statistical models of ΔT are constructed based on *WPi* and *CI* from a least squares fit of the surface $\Delta T = f(WPi, CI)$ of Figure 8a in the form

$$\Delta T_{predicted} = c_0 + c_1 \times WPi + c_2 \times CI + c_3 \times WPi \times CI. \quad (8)$$

[34] The performance of this model can be qualitatively assessed by comparing the spatial distribution of the average predicted cooling against the actually simulated cooling (Figures 5c and 5d). Despite an underestimation of the extrema, Figure 5d shows that the bivariate model is able to describe the average cooling distribution from *CI* and *WPi.*

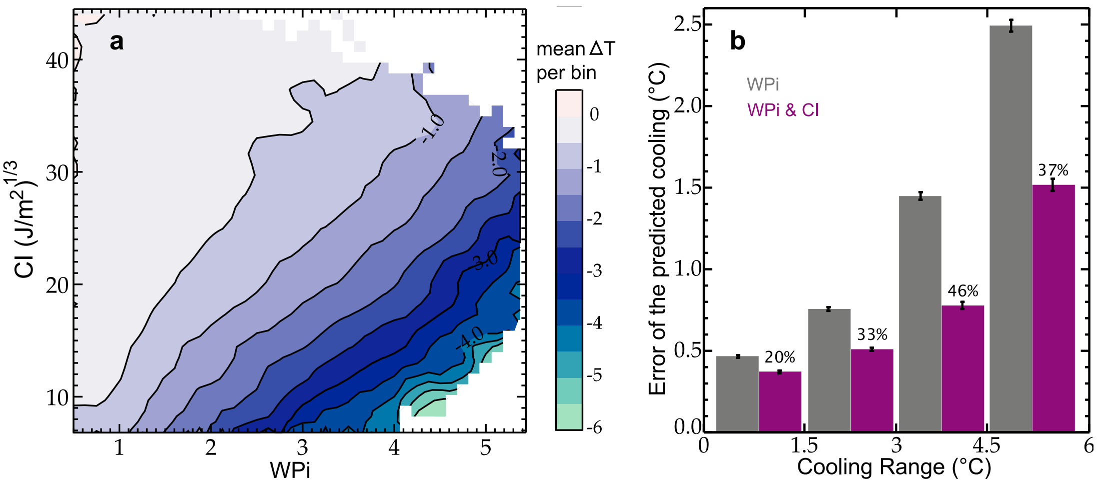

Figure 8. (a) Average cooling for any couple of WPI and CI. The mean cooling is shown here for 40 regularly spaced bins of *WPi* and 40 bins of CI. For representativeness, the mean is limited to regions with 6 samples or more. (b) Mean absolute error of a linear prediction of the simulated cooling using *WPi* as a single predictor (gray) and *WPi* and CI as a couple of predictors (purple). The percentage of improvement with respect to using *WPi* alone is indicated over each bar. Error bars give the 90% confidence interval estimated from a bootstrap technique (as explained in section A2).

Table 1. Percentage of Improvement in The Mean Absolute Error of the Predicted Cooling Brought by the Use of Both CI and *WPi* With Respect to *WPi* Alone[a]

Cooling Range (°C)	MOD ΔT_{CW}	MOD ΔT_{eye}	OBS ΔT_{CW}
0–1.5	20	13	9
1.5–3	33	35	16
3–4.5	46	31	16
4.5–6	37	18	14

[a] MOD ΔT_{CW}, MOD ΔT_{eye}, OBS ΔT_{CW}, respectively, corresponds to the hindcast improvement for modeled wake cooling (as in Figure 8b), the modeled inner-core cooling and the observed wake cooling from TMI-AMSRe. For the hindcast of the inner-core cooling (ΔT_{eye}), end time for integration (t_c) is taken as day +0 in the *WPi* calculation.

More quantitatively, using both *CI* and *WPi* clearly reduces the error of the predicted cooling compared to using *WPi* alone. Using *WPi* alone yields a ~50% relative error on the cooling prediction for all range of cooling magnitude. Using *WPi* and CI allows to reduce this relative error to an average of ~30%. For instance, while the prediction error is 1.4°C for a 3°C cooling using *WPi* alone, this error is reduced to 0.8°C when using both CI and *WPi*. The improvement of the relative error is larger for the most intense cooling, ranging from 33% to 46% for cooling between 1.5°C and 6°C (Figure 8b). The relative improvement brought by the inclusion of CI is weaker for weak cooling (20%). This may be related to the larger contribution of surface heat fluxes to the total cooling for weakest cooling [*Vincent et al.*, 2012] that are not expected to be sensitive to sub-surface stratification.

[35] The above results discuss the modeled cyclone cold wake ΔT_{CW} (i.e., cooling after the cyclone passage). The relevant parameter to investigate ocean influence on TC intensity is not cooling in the cyclone wake ΔT_{CW}, but inner-core cooling ΔT_{eye} (cooling under the storm eye) [*Cione and Uhlhorn*, 2003; *Schade*, 2000] for which satellite observations are not reliable. In our model, however, we can estimate the ability of the various metrics to predict the inner-core cooling ΔT_{eye}. Inner-core cooling and cold wake are in fact highly correlated in our simulation (correlation coefficient of 0.8, as discussed by *Vincent et al.* [2012]). *CI* also improves the predictive skills of *WPi* for the inner-core cooling, most substantially for intermediate cooling intensities (improvement of more than 30% for cooling between 1.5°C and 4.5°C) (Table 1). Finally, using *CI* (calculated from model outputs) also improves estimates of the *observed* ΔT_{CW} cooling (from TMI-AMSRE) by up to 16% compared to atmospheric information alone (Table 1). This weaker skill compared to the modeled cooling prediction is easily understandable. Our model without data assimilation does not realistically simulate locations of oceanic mesoscale structures, and suffers from systematic bias in some regions. The improvement above would hence arguably be better with a model properly constrained by observations through data assimilation [e.g., *Drevillon et al.*, 2008]. This result however suggests that *CI* not only allows predicting the TC-cooling in the model world, but is also helpful to improve the prediction of observed cooling under TCs.

4.2. Comparison of CI to Other Metrics

[36] This paper proposes a physically based metric to account for the influence of the upper ocean stratification onto TC-induced cooling. Aside from OHC, recent papers have proposed other alternatives to quantify the effect of oceanic background state on TCs. These alternatives include T100 (temperature averaged in the upper 100 m, the typical mixing depth of a strong TC) [*Price*, 2009] the Interacting Tropical Cyclone Heat Content (ITCHC, the heat content in the mixed layer) [*Buarque et al.*, 2009], or the depth of the mixed layer temperature isotherm minus 2°C, hereafter h_2 [*Lloyd and Vecchi*, 2011]. In this subsection, we gauge all these metrics by their ability to estimate the TC-induced cooling globally, over the last 30 years.

[37] OHC is the most popular index of oceanic control of air-sea interactions below cyclones. However, unlike *CI*, OHC only explains a small fraction of the wide range in TC-induced cooling amplitudes for a given wind power (Figure 7c): the lowest values of OHC are shown to be unable to describe the most intense cooling events, in contrast to *CI*. The relation between OHC and the cooling is also not monotonous: for weak OHC, the cooling first increases and then decreases with OHC. A measure of the thermal energy of the upper ocean hence only partially describes the CW dependence to ocean characteristics.

[38] A more quantitative comparison is provided by comparing the improvement brought by each ocean metric to hindcast the cooling magnitude using the bivariate model described above. Metrics based on a thermal energy definition (OHC, ITCHC, T100) do not perform as well (only up to 20% improvement) compared to CI and h_2. These two variables both induce up to ~45% improvement to the predicted cooling. They display a similar performance, except for the weakest cooling range (<1.5°C) for which CI allows a significantly greater improvement. The modest performance of the measures based on thermal energy (OHC, ITCHC, T100) is related to the use of the absolute temperature in those metrics, which is useful to predict the absolute temperature after the cyclone, but not the cooling magnitude. Modifying T100 by subtracting the SST to it (*SST-T100*) indeed results in a considerable improvement of the prediction skills (Figure 9), with the largest improvement (~43%) for the strongest cooling range (>4.5°C). A measure such as *SST-T100* is indeed appropriate to describe a surface cooling associated to a deep mixing (100 m is a typical mixing depth for a category 3 hurricane [*Price*, 2009]).

[39] While not explicitly taking physical processes of the cooling into account, h_2 performs as well as *CI*. This metric is highly correlated to *CI* (correlation coefficient of 0.94) and basically measures the same information as *CI* does: namely the depth of the ML and the importance of the temperature stratification at its base. h_2 can actually be expressed in a similar way as *CI* if we assume that density is proportional to temperature. In the simple case where $h_i = 0$ (presented in section 3.1), h_2 can be written as $h_2 = \left(\frac{3}{2}\frac{\Delta E_p}{\rho_0 N^2}\right)^{1/3}$, hence h_2 is expected to scale as *CI* (see Annex A1 for the calculation). In our global analysis, h_2 skills are very similar to *CI* and its definition is somehow simpler. However, the h_2 definition does not account for the effect of salinity on stratification. This effect can be important in some regions, for example in the Bay of Bengal where haline stratification can reduce the amplitude of TC-induced cooling after the monsoon [*Sengupta et al.*, 2008; Neetu et al., unpublished manuscript, 2012]. *CI* brings a larger improvement than h_2 for cooling predictions over the Bay of Bengal (Table 2). This is an

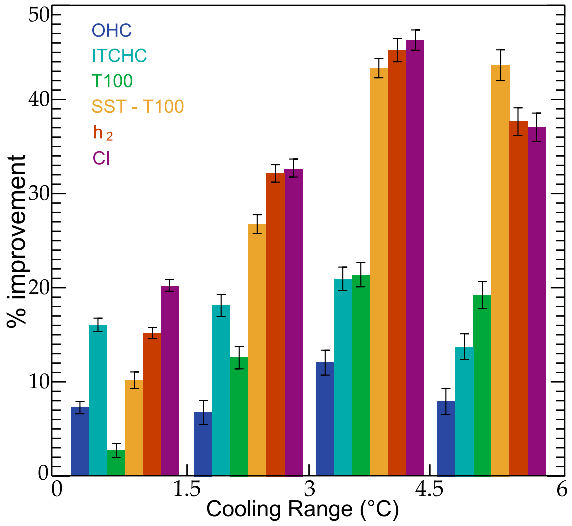

Figure 9. Percentage of improvement in the mean absolute error of the predicted cooling brought by the inclusion of various ocean metric in addition to *WPi* in the predictors (as in Figure 8b): OHC (dark blue), ITCHC (light blue), T100 (green), SST-T100 (yellow), h_2 (red), and CI (purple). Error bars give the 90% confidence interval estimated from a bootstrap technique (as explained in section A2).

illustration that, although h_2 is generally a good indicator of the cooling, the integration of salinity effects into the CI index makes it appropriate for a wider range of oceanic conditions.

5. Conclusion

[40] Sea surface temperature (SST) influences tropical cyclones (TCs) intensity through two mechanisms: (1) ambient SST that sets the maximum potential intensity for TCs and (2) the negative feedback associated with the cooling under the TC eye. TCs intensity is more sensitive to the feedback associated with the cooling than to the ambient SST [*Schade*, 2000]. *Lloyd and Vecchi* [2011] further demonstrated that the TC intensity evolution is linked to the observed cooling magnitude in the wake of TCs, and suggested that the ocean sub-surface temperature stratification is a key parameter in controlling the TC intensity evolution through its modulation of the SST feedback.

[41] This paper provides a comprehensive and global quantification of the sensitivity of TC-induced cooling amplitude to pre-storm ocean state. In order to overcome limited availability of ocean in situ data below tropical cyclones, we use an ocean general circulation model experiment that realistically samples the ocean response to more than 3,000 TCs. As cooling largely results from mixing, i.e., a conversion of mechanical into potential energy, we propose to describe the ocean effect on the TC-induced cooling by two metrics: a wind power index (*WPi*) and a Cooling Inhibition index (CI). *WPi* is a proxy of the kinetic energy provided to the ocean by a TC, which triggers upper-ocean mixing. It integrates the effects of various TC parameters (maximum winds, translation speed, size) that affect the TC-induced cooling. CI is a measure of the input of potential energy required to cool the surface ocean by 2°C through vertical mixing. It thus accounts for the pre-storm upper ocean stratification and its resistance to surface cooling via mixing.

[42] We show that these two simple metrics are relevant to explain the wide TC-induced cooling amplitude distribution. While average cooling increases with *WPi*, a given *WPi* (i.e., a given kinetic energy deposit in the ocean) can be associated to a wide range of cooling. Our results demonstrate that contrasts in upper ocean stratification, as measured by CI, explain most of this range. Ocean pre-storm stratification modulates the cooling magnitude by up to an order of magnitude for a given wind energy input. For example, for high *WPi*, the cooling amplitude varies from 0.5°C to 5°C depending on CI (a high CI resulting in a small cooling). Upper ocean stratification is thus a key factor for the CW magnitude.

[43] We further show that using CI in addition to *WPi* improves statistical hindcasts of the cold wake amplitude by ~40% (for cooling larger than 1.5°C). Previously proposed metrics that are based on a fixed threshold and/or absolute temperature (i.e., OHC, T100, ITCHC) do not predict accurately the CW magnitude. In contrast, metrics that account for both mixed layer depth and the steepness of the stratification at its base (e.g., h_2, SST-T100) display comparable hindcast skills to CI. The main interest of CI is however to rely on the physical mechanism responsible for the oceanic control of the CW namely the amount of potential energy required to yield a given surface cooling. Still, our results suggest that CI is a better alternative than previously proposed metrics of cyclone-ocean interactions in regions where haline stratification plays an important role in controlling the surface cooling, like the Bay of Bengal [*Sengupta et al.*, 2008; Neetu et al., unpublished manuscript, 2012].

[44] We think that this work may have practical consequences for cyclone intensity forecasts. While OHC only brought modest ~5% improvement to TC intensity statistical forecast schemes [*DeMaria et al.*, 2005; *Mainelli et al.*, 2008], a metric like CI, which properly captures the ocean propensity to modulate TC-induced surface cooling (and hence the storm growth rate), could be tested in TC intensity forecast schemes. CI calculation requires both salinity and temperature profiles in front of the storm track and is thus harder to compute operationally than metrics based on temperature profile alone. Temperature and salinity data are provided by ARGO measurements, but their spatial and temporal coverage is not sufficient to sample all pre-cyclones oceanic conditions. Even though salinity stratification partly controls the surface cooling in some regions such as the Bay of Bengal, a first approach could be to calculate CI

Table 2. Percentage of Improvement in the Mean Absolute Error of the Predicted Cooling Brought by the Inclusion of Various Ocean Metrics in Addition to *WPi* for the Bay of Bengal

Cooling Range (°C)	Percent Improvement for Bay of Bengal MOD ΔT_{CW}					
	OHC	ITCHC	T100	SST-T100	h_2	CI
0–1	3	14	4	10	12	20
1–2	2	6	4	20	23	32
>2	10	8	10	26	37	45

with temperature stratification only, which can be reconstructed from altimetry measurements in the same manner as OHC [*Shay et al.*, 2000]. Alternatively, CI could also be computed from currently available operational oceanography products constrained by oceanic observations [e.g., *Drevillon et al.*, 2008].

[45] Although CI rather accurately captures the upper ocean propensity to modulate the amplitude of TC-induced cooling, we believe that our approach can be further improved. The scaling used to define both CI and *WPi* are based on rather crude assumptions. For instance, we hypothesized a linear relationship between the energy input from the wind and the potential energy increase in the ocean to derive the cube root scaling of *WPi.* It is however likely that the fraction of kinetic energy transformed into potential energy depends on oceanic parameters such as the mixed layer depth and the wind-induced mixing depth. A careful investigation of the mechanical energy budget under TCs is required to shed light on the energy transfer from surface winds to surface currents and quantify the respective amount of energy that is locally converted to potential energy or radiated away in the form of internal waves.

[46] Our aim in this paper was to quantify the influence of the oceanic stratification on TC-induced cooling globally, not to include all the physically relevant processes into an analytic prediction of the TC-induced cooling. In a way similar to *Schade and Emanuel* [1999], a potential route for a more accurate prediction of TC-induced cooling would be to include other relevant parameters of the TC-ocean interaction. An inherent limitation to the CI definition is indeed to only account for the TC-induced cooling driven by penetrative vertical mixing. Mixing generally dominates surface cooling for moderate to high wind power but cooling by air-sea fluxes also plays a significant role for weak TCs [*Vincent et al.*, 2012]. The surface cooling also depends on the amplitude of the upwelling induced by the TC that alters the thermal stratification [*Yablonsky and Ginis*, 2009]. Accounting for these processes (surface fluxes and advection) may further improve the forecast skills of the TC-induced cooling. In addition, while our results allow us to illustrate the strong impact of the oceanic background conditions on the amplitude of the TC-induced surface cooling, we did not directly assess the influence of the oceanic background conditions of the cyclone intensification itself. As demonstrated by *Schade and Emanuel* [1999], the effect of a given cooling on a TC also depends on characteristics of the TC itself such as its intensity and translation speed. A statistical forecasting technique of TC intensity including the parameters proposed in the present study should allow to address this issue.

[47] Finally, some studies suggest that ocean eddies [e.g., *Jacob and Shay*, 2003] or low frequency climate variations [e.g., *Xie et al.*, 2002] impact tropical cyclones activity through modification of the TC-induced cooling magnitude. Our approach offers potential for quantifying the extent to which ocean stratification changes linked to natural ocean variability can mitigate cyclone intensity. Changes in the atmospheric background state driven by anthropogenic forcing could also alter cyclone distributions in present and future climate [*Knutson et al.*, 2008]. Our approach may also allow to estimate the potential influence of upper-ocean stratification changes driven by climate change on future TCs cooling amplitude and ultimately on TCs intensification. In contrast to OHC, T100 or ITCHC, CI is suited to perform such an investigation, as its definition does neither depend on absolute temperature nor on fixed thresholds representative of the present-day climate [*Royer et al.*, 1998].

Appendix A

A1. Idealized Framework to Illustrate Surface Cooling Scaling

[48] The purpose of this appendix is to develop the approach in section 3.1 to the more realistic case where a mixed layer is present (i.e., the ocean is not linearly stratified all the way up to the surface). Depending on the mixed layer depth, two forms of solutions can be derived for the scaling between surface cooling and potential energy input associated to vertical mixing.

[49] Let us consider an ocean with constant stratification N^2 under a ML of initial depth h_i as illustrated on Figure A1a, and a linear equation of state with density depending on temperature only: $\rho(z) = \rho_0(1 - \alpha\, T(z))$. The temperature profile is $T(z) = \begin{cases} T_i & ,z > -h_i \\ T_i + \Gamma(z + h_i) & ,z < -h_i \end{cases}$ with $N^2 = -\frac{g}{\rho_0}\frac{\partial \rho}{\partial z} = \alpha g \frac{\partial T}{\partial z} = \alpha g \Gamma$. α is the coefficient for thermal expansion of seawater, ρ_0 is a reference density and Γ is the temperature gradient under the ML.

[50] Let us now assume that after the ‘passage of the cyclone;’ the surface layer has been homogeneously mixed down to the depth h_m, at the temperature T_f (Figure A1a).

[51] Conservation of heat yields an equation linking h_m with the surface cooling $\Delta T = T_f - T_i$

$$\int_{-h_m}^{0} \rho_o C_P (T_f - T_i(z))dz = 0. \tag{A1}$$

Assuming constant C_P and ρ_o ($\rho \approx \rho_o$ at the first order in $\rho \times T$) and $h_m \neq 0$ yields:

$$h_m^2 - 2h_2 h_m + h_i^2 = 0, \tag{A2}$$

where $h_2 = h_i - \frac{\alpha g}{N^2}\Delta T$ (as defined on Figure A1a is the variable discussed by *Lloyd and Vecchi* [2011] when $\Delta T = -2°\mathrm{C}$).

[52] The potential energy difference between the initial and final profile is

$$\Delta E_p = \int_{-h_m}^{0} \left(\rho_f - \rho_i\right) g z dz, \tag{A3}$$

providing an equation linking h_m, ΔT and ΔE_p

$$h_m^3 - \frac{3}{2} h_2 h_m^2 + \frac{h_i^3}{2} = H^3, \tag{A4}$$

with $H \equiv \left(\frac{3\Delta E_p}{\rho_0 N^2}\right)^{1/3}$. H can be seen as a characteristic mixing length associated to a potential energy input ΔE_p.

[53] From (A2) and (A4), it is possible to derive the dependence of the surface cooling ΔT to the potential

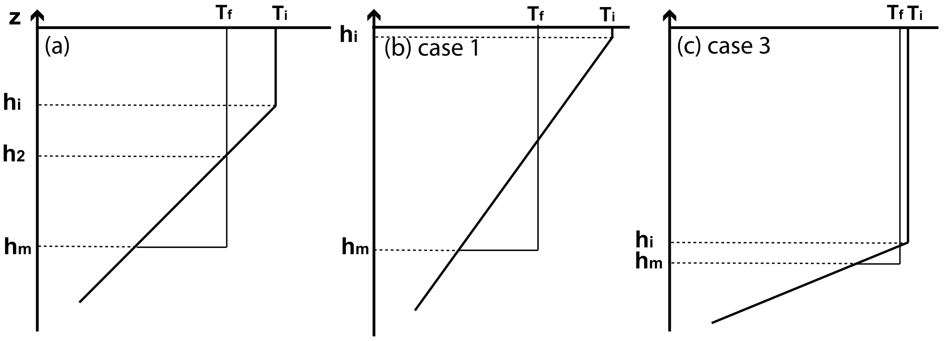

Figure A1. Temperature profile (a) with "normal" ML, (b) with shallow ML and (c) with "deep" ML corresponding to the different cases used in the calculation of the scaling between the surface cooling and the associated potential energy increase of the water column.

energy increase of the water column ΔE_p. Substituting (A2) into (A4) yields

$$h_m^3 - 3h_i^2 h_m + 2(h_i^3 - 2H^3) = 0 \tag{A5}$$

that can be set in the reduced Cardan's form $h_m^3 + 3ph_m + 2q = 0$ (with $p = -\, h_i^2$ and $q = h_i^3 - 2H^3$).

[54] The resolution of (A5) is conditioned to the sign of $\Lambda \equiv p^3 + q^2$ and the different cases lead to different scaling of the surface cooling versus the energy input:

[55] *Case 1.* If $\Lambda > 0 \Leftrightarrow h_i < H$ (i.e., the initial MLD is shallower than the typical mixing length), then there is one solution $h_m = \sqrt[3]{-q - \sqrt{\Lambda}} + \sqrt[3]{-\mathrm{q} + \sqrt{\Lambda}}$. In the limit $h_i \rightarrow 0$, $h_m \approx 4^{1/3} H$ and $\Delta T \approx -\frac{1}{\alpha g}\left(\frac{3}{2}\frac{N^4}{\rho_0}\Delta E_p\right)^{1/3}$; in this case (presented in the part 3.1 of the paper), there is a cube root scaling between the surface cooling and the potential energy increase.

[56] *Case 2.* If $\Lambda = 0 \Leftrightarrow h_i = H$ (i.e., the initial MLD equals the typical mixing length), there is one positive solution for h_m: $h_m = 2h_i$, and $\Delta T = \frac{-N^2 h_i}{4\alpha g} = \frac{-1}{4\alpha g}\left(\frac{3N^4}{\rho_0}\Delta E_p\right)^{1/3}$. We note that this intermediate case occurs when the final mixed layer depth is twice the initial one.

[57] *Case 3.* If $\Lambda < 0 \Leftrightarrow h_i > H$ (i.e., the initial MLD is deeper than the typical mixing length) there are 3 solutions for h_m but only one real positive: $h_m = 2h_i \cos\left(\frac{1}{3}\arccos\left(\frac{2H^3}{h_i^3} - 1\right)\right)$. (1) In the limit when $h_i = H$, $h_m = 2h_i$, the cube root scaling still applies as in case 2. (2) In the limit when $h_i \gg H$, then $h_m \approx h_i\left(1 + 2\sqrt{\frac{H^3}{3h_i^3}}\right)$ and $\Delta T \approx -\frac{2}{\alpha g \rho_0 h_i^2}\Delta E_p$; in this case the scaling between surface cooling and energy input is linear.

[58] Figure A2 illustrates the frequency with which case 1 and case 3 occur in our numerical experiment. Case 1 appears to occur more often: 80% of the time under systems of tropical cyclones strength. One would remark that the upwelling induced by TCs under their track further participates in reducing the mixed layer depth, favoring the occurrence of case 1 scaling. Based on this analysis, we chose to use a cube root scaling in the definition of the cooling inhibition index although it may not reflect the scaling for all cases.

A2. Confidence Interval for Figures 8b and 9

[59] The confidence interval for the Mean Absolute Error of predicted TC-induced cooling is estimated using a bootstrap technique (Figures 8b and 9). We consider three distinct ranges of cooling amplitude ([0,2], [2,4], [4,6]°C). In each range, the N observations of the absolute difference

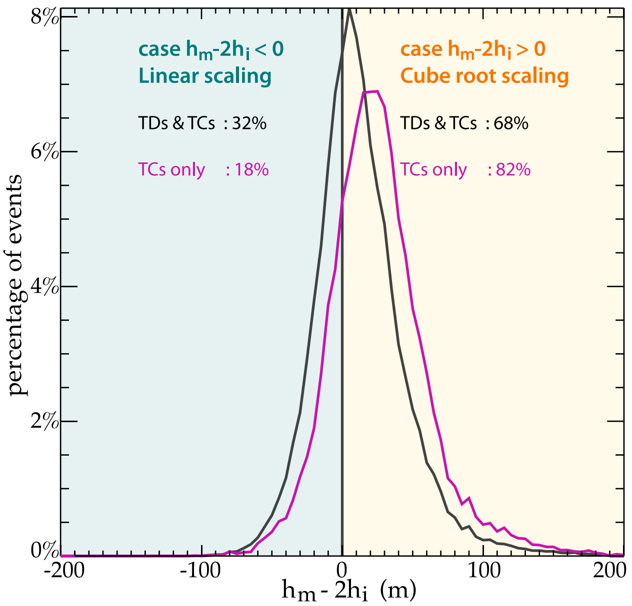

Figure A2. Histogram of the percentage of TC events associated to h_m-$2h_i$ values; according to the resolution of equation (A5), surface cooling scales linearly with ΔE_p when h_m-$2h_i$ $\ll$0 and scales as the cube root of ΔE_p when h_m-$2h_i$ > 0. h_i is the MLD measured one week before TC passage and averaged within 200 km of each TC track position and h_m (the mixing depth) is calculated to obtain the modeled surface cooling by a heat conserving mixing. The black curve for both Tropical Depressions (TDs) and TCs shows the histogram for all systems with 10-min averaged winds greater than 15 m/s, the purple curve for TCs only shows systems with winds greater than 33 m/s.

between the predicted cooling $\Delta T_{predicted}$ and the actual cooling ΔT are called events. We randomly select N events from the total number of events in each range. Overlapping selection is allowed, meaning that one event can be selected more than once. From the selected N events, we calculate the average absolute error. By repeating this process 1,000 times, we obtain 1,000 values for the MAE. The upper and lower limit of each error bar (in Figures 8b and 9) represents the 5% and 95% percentile of the probability distribution function. If the MAE value using *WPi* and *CI* lies outside the error bar of the *WPi* alone, the improvement is significant at the 90% confidence level.

[60] **Acknowledgments.** Experiments were conducted at the Institut du Développement et des Ressources en Informatique Scientifique (IDRIS) Paris, France. We thank the Nucleus for European Modeling of the Ocean (NEMO) Team for its technical support. The analysis was supported by the project CYCLOCEAN from Les Enveloppes Fluides et l'Environnement (LEFE) AO2010-538863. We thank Daniel Nethery for useful comments. We thank Kerry Emanuel and an anonymous reviewer for their useful comments that led to improve the present manuscript.

References

Ali, M. M., P. S. V. Jagadeesh, and S. Jain (2007), Effect of eddies on the Bay of Bengal cyclone intensity, *Eos Trans. AGU*, *88*, 93, doi:10.1029/2007EO080001.

Bister, M., and K. A. Emanuel (1998), Dissipative heating and hurricane intensity, *Meteorol. Atmos. Phys.*, *65*, 233–240, doi:10.1007/BF01030791.

Bosart, L. F., W. E. Bracken, J. D. Molinari, C. S. Velden, and P. G. Black (2000), Environmental influences on the rapid intensification of Hurricane Opal (1995) over the Gulf of Mexico, *Mon. Weather Rev.*, *128*, 322–352, doi:10.1175/1520-0493(2000)128<0322:EIOTRI>2.0.CO;2.

Buarque, S. R., C. Vanroyen, and C. Agier (2009), Tropical cyclone heat potential index revisited, *Mercator Ocean Q. Newsl.*, *33*, 24–30.

Chen, S., W. Zhao, and M. A. Donelan (2007), The CBLAST-Hurricane program and the next-generation fully coupled atmosphere-wave-ocean models for hurricane research and prediction, *Bull. Am. Meteorol. Soc.*, *88*, 311–317, doi:10.1175/BAMS-88-3-311.

Cione, J. J., and E. W. Uhlhorn (2003), Sea surface temperature variability in hurricanes: Implications with respect to intensity change, *Mon. Weather Rev.*, *131*, 1783–1796, doi:10.1175//2562.1.

DeMaria, M., M. Mainelli, L. K. Shay, J. A. Knaff, and J. Kaplan (2005), Further improvements to the Statistical Hurricane Intensity Prediction Scheme (SHIPS), *Weather Forecasting*, *20*, 531–543, doi:10.1175/WAF862.1.

Drevillon, M., et al. (2008), The GODAE/Mercator-Ocean global ocean forecasting system: Results, applications and prospects, *J. Oper. Oceanogr.*, *1*, 51–57.

Emanuel, K. A. (1999), Thermodynamic control of hurricane intensity, *Nature*, *401*, 665–669, doi:10.1038/44326.

Emanuel, K. A. (2003), Tropical cyclones, *Annu. Rev. Earth Planet. Sci.*, *31*, 75–104, doi:10.1146/annurev.earth.31.100901.141259.

Emanuel, K. A. (2005), Increasing destructiveness of tropical cyclones over the past 30 years, *Nature*, *436*, 686–688, doi:10.1038/nature03906.

Emanuel, K. A., C. DesAutels, C. Holloway, and R. Korty (2004), Environmental control of tropical cyclone intensity, *J. Atmos. Sci.*, *61*, 843–858, doi:10.1175/1520-0469(2004)061<0843:ECOTCI>2.0.CO;2.

Goni, G., et al. (2009), Applications of satellite-derived ocean measurements to tropical cyclone intensity forecasting, *Oceanography*, *22*, 190–197, doi:10.5670/oceanog.2009.78.

Greatbatch, R. J. (1984), On the response of the ocean to a moving storm: Parameters and scales, *J. Phys. Oceanogr.*, *14*, 59–78, doi:10.1175/1520-0485(1984)014<0059:OTROTO>2.0.CO;2.

Griffies, S., et al. (2009), Coordinated Ocean-ice Reference Experiments (COREs), *Ocean Modell.*, *26*, 1–46, doi:10.1016/j.ocemod.2008.08.007.

Hong, X., S. W. Chang, S. Raman, L. K. Shay, and R. Hodur (2000), The interaction between Hurricane Opal (1995) and a warm core ring in the Gulf of Mexico, *Mon. Weather Rev.*, *128*, 1347–1365, doi:10.1175/1520-0493(2000)128<1347:TIBHOA>2.0.CO;2.

Jacob, S. D., and L. K. Shay (2003), The role of oceanic mesoscale features on the tropical cyclone-induced mixed layer response: A case study, *J. Phys. Oceanogr.*, *33*, 649–676, doi:10.1175/1520-0485(2003)33<649:TROOMF>2.0.CO;2.

Jacob, S. D., L. K. Shay, A. J. Mariano, and P. G. Black (2000), The 3D oceanic mixed layer response to Hurricane Gilbert, *J. Phys. Oceanogr.*, *30*, 1407–1429, doi:10.1175/1520-0485(2000)030<1407:TOMLRT>2.0.CO;2.

Knapp, K. R., M. C. Kruk, D. H. Levinson, H. J. Diamond, and C. J. Neumann (2010), The International Best Track Archive for Climate Stewardship (IBTrACS): Unifying tropical cyclone data, *Bull. Am. Meteor. Soc.*, *91*, 363–376.

Knutson, T. R., J. J. Sirutis, S. T. Garner, G. A. Vecchi, and I. M. Held (2008), Simulated reduction in Atlantic hurricane frequency under twenty-first-century warming conditions, *Nat. Geosci.*, *1*, 359–364, doi:10.1038/ngeo202.

Korty, R. L., K. A. Emanuel, and J. R. Scott (2008), Tropical cyclone-induced upper-ocean mixing and climate: Application to equable climates, *J. Clim.*, *21*, 638–654.

Large, W., and S. Yeager (2009), The global climatology of an interannually varying air-sea flux data set, *Clim. Dyn.*, *33*, 341–364, doi:10.1007/s00382-008-0441-3.

Leipper, D. F., and D. Volgenau (1972), Hurricane heat potential of the Gulf of Mexico, *J. Phys. Oceanogr.*, *2*, 218–224, doi:10.1175/1520-0485(1972)002<0218:HHPOTG>2.0.CO;2.

Lengaigne, M., U. Haussman, G. Madec, C. Menkes, J. Vialard, and J. M. Molines (2012), Mechanisms controlling warm water volume interannual variations in the equatorial Pacific: Diabatic versus adiabatic processes, *Clim. Dyn.*, *38*, 1031–1046.

Liu, L. L., W. Wang, and R. X. Huang (2008), The mechanical energy input to the ocean induced by tropical cyclones, *J. Phys. Oceanogr.*, *38*, 1253–1266, doi:10.1175/2007JPO3786.1.

Lloyd, I. D., and G. A. Vecchi (2011), Observational evidence of oceanic controls on hurricane intensity, *J. Clim.*, *24*, 1138–1153, doi:10.1175/2010JCLI3763.1.

Lloyd, I. D., T. Marchok, and G. A. Vecchi (2011), Diagnostics comparing sea surface temperature feedbacks from operational hurricane forecasts to observations, *J. Adv. Model. Earth Syst.*, *3*, M11002, doi:10.1029/2011MS000075.

Locarnini, R. A., A. V. Mishonov, J. I. Antonov, T. P. Boyer, and H. E. Garcia (2006), *World Ocean Atlas 2005*, vol. 1, *Temperature*, *NOAA Atlas NESDIS*, vol. 61, edited by S. Levitus, 182 pp., NOAA, Silver Spring, Md.

Madec, G. (2008), NEMO ocean engine, *Note Pôle Modél. 27*, Inst. Pierre-Simon Laplace, Paris.

Mainelli, M., M. DeMaria, L. K. Shay, and G. Goni (2008), Application of oceanic heat content estimation to operational forecasting of recent Atlantic category 5 hurricanes, *Weather Forecasting*, *23*, 3–16, doi:10.1175/2007WAF2006111.1.

Penduff, T., M. Juza, L. Brodeau, G. C. Smith, B. Barnier, J.-M. Molines, A.-M. Treguier, and G. Madec (2010), Impact of global ocean model resolution on sea-level variability with emphasis on interannual time scales, *Ocean Sci.*, *6*, 269–284, doi:10.5194/os-6-269-2010.

Price, J. F. (1979), On the scaling of stress-driven entrainment experiments, *J. Fluid Mech.*, *90*(3), 509–529, doi:10.1017/S0022112079002366.

Price, J. F. (1981), Upper ocean response to a hurricane, *J. Phys. Oceanogr.*, *11*, 153–175, doi:10.1175/1520-0485(1981)011<0153:UORTAH>2.0.CO;2.

Price, J. F. (2009), Metrics of hurricane-ocean interaction: Vertically integrated or vertically averaged ocean temperature?, *Ocean Sci.*, *5*, 351–368, doi:10.5194/os-5-351-2009.

Riehl, H. (1950), A model of hurricane formation, *J. Appl. Phys.*, *21*, 917–925, doi:10.1063/1.1699784.

Roemmich, D., G. C. Johnson, S. Riser, R. Davis, J. Gilson, W. B. Owens, S. L. Garzoli, C. Schmid, and M. Ignaszewski (2009), The Argo program: Observing the global ocean with profiling floats, *Oceanography*, *22*, 34–43, doi:10.5670/oceanog.2009.36.

Royer, J. F., F. Chauvin, B. Timbal, P. Araspin, and D. Grimal (1998), A GCM study of the impact of greenhouse gas increase on the frequency of occurrence of tropical cyclones, *Clim. Change*, *38*, 307–343, doi:10.1023/A:1005386312622.

Schade, L. R. (2000), Tropical cyclone intensity and sea surface temperature, *J. Atmos. Sci.*, *57*, 3122–3130, doi:10.1175/1520-0469(2000)057<3122:TCIASS>2.0.CO;2.

Schade, L. R., and K. A. Emanuel (1999), The ocean's effect on the intensity of tropical cyclones: Results from a simple coupled atmosphere-ocean model, *J. Atmos. Sci.*, *56*, 642–651, doi:10.1175/1520-0469(1999)056<0642:TOSEOT>2.0.CO;2.

Sengupta, D., B. R. Goddalehundi, and D. S. Anitha (2008), Cyclone-induced mixing does not cool SST in the post-monsoon north Bay of Bengal, *Atmos. Sci. Lett.*, *9*, 1–6, doi:10.1002/asl.162.

Shay, L. K., and J. K. Brewster (2010), Oceanic heat content variability in the eastern Pacific Ocean for hurricane intensity forecasting, *Mon. Weather Rev.*, *138*, 2110–2131, doi:10.1175/2010MWR3189.1.

Shay, L. K., G. J. Goni, and P. G. Black (2000), Effects of a warm oceanic feature on Hurricane Opal, *Mon. Weather Rev.*, *128*, 1366–1383, doi:10.1175/1520-0493(2000)128<1366:EOAWOF>2.0.CO;2.

Vincent, E. M., M. Lengaigne, G. Madec, J. Vialard, G. Samson, N. C. Jourdain, C. E. Menkes, and S. Jullien (2012), Processes setting the characteristics of sea surface cooling induced by tropical cyclones, *J. Geophys. Res.*, *117*, C02020, doi:10.1029/2011JC007396.

Wentz, F. J., C. Gentemann, D. Smith, and D. Chelton (2000), Satellite measurements of sea surface temperature through clouds, *Science*, *288*, 847–850, doi:10.1126/science.288.5467.847.

Willoughby, H. E., R. W. R. Darling, and M. E. Rahn (2006), Parametric representation of the primary hurricane vortex. Part II: A new family of sectionally continuous profiles, *Mon. Weather Rev.*, *134*, 1102–1120, doi:10.1175/MWR3106.1.

Xie, S. P., H. Annamalai, F. A. Schott, and J. P. McCreary (2002), Structure and mechanisms of South Indian Ocean climate variability, *J. Clim.*, *15*(8), 864–878, doi:10.1175/1520-0442(2002)015<0864:SAMOSI>2.0.CO;2.

Yablonsky, R. M., and I. Ginis (2009), Limitation of one-dimensional ocean models for coupled hurricane-ocean model forecasts, *Mon. Weather Rev.*, *137*, 4410–4419, doi:10.1175/2009MWR2863.1.

Deuxième partie

Interactions entre les cyclones et le climat

Chapitre 5

Influence des Cyclones Tropicaux sur l'océan

Ce chapitre est basé sur l'article [Vincent *et al.* 2012b].

Contrairement à l'atmosphère, l'océan est opaque au rayonnement visible et est donc chauffé par le haut. Ceci lui confère une stratification thermique stable –avec les eaux chaudes et peu denses en surface– particulièrement marquée sous les tropiques. Les mouvements verticaux, associés à la circulation thermohaline par exemple, doivent ainsi "lutter" contre l'énergie potentielle que représente la stratification. La tension de vent en surface et les dissipations de courants de marée sont les deux sources d'énergie mécanique principales permettant de maintenir la circulation océanique générale qui tempère les écarts de température sur le globe. Les événements extrêmes ont traditionnellement été "oubliés" des calculs de transfert d'énergie à l'océan [Liu *et al.* 2008] ; l'intense mélange vertical induit par les cyclones tropicaux (TCs) pourrait cependant ne pas être négligeable et participer à maintenir la circulation thermohaline [Emanuel 2001]. L'évaluation de l'importance des TCs sur la circulation océanique a jusqu'ici été abordée par des études théoriques et de modélisation en paramétrisant dans l'océan l'effet de leur mélange. Il reste toutefois difficile de valider par des observations les hypothèses sur la profondeur et l'amplitude du mélange qui ont été choisies dans les études précédentes.

Le dispositif expérimental de la thèse simule de manière réaliste la réponse de l'océan aux TCs directement dans un modèle global de circulation océanique. Il permet d'étudier le devenir des anomalies thermiques générées par les TCs et donc leur impact aux échelles de temps climatiques.

Synthèse de l'article

Ce chapitre décrit l'influence des cyclones tropicaux sur l'état moyen de l'océan. En contradiction des résultats précédents, nous montrons que les TCs ne modifient que de manière anecdotique le transport méridien de chaleur océanique (OHT pour *Ocean Heat Transport*). En effet, la majeure partie des anomalies chaudes injectées en sub-surface par le mélange durant la saison cyclonique (en été local) sont ramenées à la surface durant l'hiver suivant. De plus, l'influence des TCs sur l'océan ne peut être réduit au seul effet du mélange (comme cela a été fait dans les études précédentes). Les autres processus impliqués dans la réponse de l'océan aux TCs (advection, flux de chaleur) jouent un rôle qui est loin d'être négligeable.

L'article présente une méthodologie originale permettant de réaliser des expériences de sensibilité isolant l'effet de chaque processus physique induit par les cyclones sur la réponse de l'océan. Les simulations représentant uniquement l'effet du mélange, de la dynamique ou des flux de chaleur en surface sont notées CMIX, CDYN et CFLX respectivement. La non–linéarité entre les 3 processus est faible ; ces trois expériences peuvent donc être utilisées pour décomposer le signal observé dans la simulation comportant le forçage total des TCs (CYCL) par rapport à la simulation de référence (FILT).

Les principales modifications induites par les TCs sur l'état moyen de l'océan sont : i) un refroidissement de surface, ii) un réchauffement de sub–surface et iii) un refroidissement profond sous le cœur des bassins cycloniques.

En moyenne annuelle, les cyclones sont responsables d'un refroidissement de 0.1 à 0.5°C dans les bassins cycloniques. Ce refroidissement est principalement attribuable à l'augmentation des flux de chaleur sensible et latent par les forts vents des cyclones. Un réchauffement de sub–surface de ∼0.3°C, principalement attribuable au mélange vertical, est aussi observé dans les bassins cycloniques. La vision canonique "classique" de l'effet des TCs (résultant d'un mélange vertical) se cantonne à cette structure dipolaire des anomalies de température : chaudes en sub–surface / froides en surface. La simulation CYCL présente pourtant aussi des anomalies froides profondes (∼100–400 m) au cœur des bassins cycloniques qui ne peuvent être expliquées par le mélange vertical. La simulation CDYN permet d'attribuer ces anomalies à l'effet résiduel de l'advection qui a été très peu discuté dans la littérature. Ce résultat peut surprendre ; il est en effet admis que le transport vertical intégré induit par un cyclone est nul : l'*upwelling* intense autour de la trajectoire est compensé par un *downwelling* de faible amplitude, mais affectant une large région, loin de la trajectoire (Fig. 1.25). L'*upwelling* dominant dans le centre des bassins cycloniques, la thermocline y est remontée de ∼10 m/an, alors que le *downwelling* domine en périphérie des bassins cycloniques. L'émission d'ondes de Rossby dans le sillage des TCs permet de propager vers l'Ouest ces anomalies de profondeur de la thermocline. Ces ondes planétaires propagent les *upwelling* induits par les cyclones expliquant les anomalies froides profondes que notre simulation met en évidence.

Les modifications de l'état moyen océanique sont dominées par les anomalies générées pendant les saisons cycloniques (été local). La présence de TCs engendre un refroidissement au cœur des bassins cycloniques jusqu'à ∼1.5°C en été alors que la température de surface de la mer (SST) est légèrement réchauffée en hiver (jusqu'à ∼0.5°C localement). L'amplitude du cycle saisonnier de SST est ainsi réduite de ∼10% dans les bassins cycloniques ! L'anomalie chaude hivernale est liée à l'entraînement dans la couche mélangée des anomalies chaudes de sub–surface placées dans la thermocline saisonnière par le mélange pendant la saison cyclonique. La profondeur des anomalies chaudes est donc cruciale ; seules les anomalies chaudes localisées dans la thermocline permanente ne sont pas remises en contact avec l'atmosphère localement, et peuvent induire un transport de chaleur méridien. Ainsi s'explique le rôle marginal des TCs dans le transport océanique de chaleur.

Les études précédentes ([Emanuel 2001], [Sriver *et al.* 2008], [Fedorov *et al.* 2010], [Jansen & Ferrari 2009]) ont supposé i) que les anomalies froides de surface égalent les anomalies chaudes de sub–surface et ii) que les flux de chaleur comblent entièrement l'anomalie froide en surface. Dans ce cas, la quantification des anomalies froides de surface suffit à calculer le flux de chaleur entrant dans l'océan dans le sillage des TCs : l'estimation la plus réaliste étant de 580 TW [Jansen *et al.* 2010]. Dans l'expérience CYCL, nous retrouvons une anomalie de flux de chaleur entrant dans l'océan après le passage des TCs de ∼500 TW, mais une part non–négligeable de ce flux sert en fait à compenser la chaleur perdue durant le passage des TCs et seuls ∼300 TW sont injectés en sub–surface (voir le schéma bilan de la figure 5.12). Parmi eux, les $3/5^{\mathrm{e}}$ retournent à l'atmosphère durant l'hiver à l'endroit même où ils ont été injectés, ne laissant que ∼120 TW disponible pour un éventuel transport latéral de chaleur (OHT) ; un ordre de grandeur inférieur à l'évaluation de [Emanuel 2001]. Il est par conséquent conclu que le rôle des TCs n'est pas de modifier profondément le transport méridien de chaleur terrestre mais de jouer un rôle de lissage des températures de surface : en transférant à l'hiver de l'énergie thermique stockée en sub–surface pendant les mois d'été…

Article

Climate Dynamics

Influence of Tropical Cyclones on sea surface temperature seasonal cycle and ocean heat transport

Emmanuel M. Vincent · Gurvan Madec · Matthieu Lengaigne · Jérôme Vialard · Ariane Koch–Larrouy

Abstract :
Recent studies suggested that tropical cyclones (TCs) contribute significantly to the meridional oceanic heat transport by injecting heat into the subsurface through mixing. Here, we estimate the long-term oceanic impact of TCs by inserting realistic wind vortices along observed TCs tracks in a $\frac{1}{2}^{\circ}$ resolution ocean general circulation model over the 1978–2007 period. Warming of TCs' cold wakes results in a positive heat flux into the ocean (oceanic heat uptake; OHU) of ∼480 TW, consistent with most recent estimates. However, ∼2/5 of this OHU only compensates the heat extraction by the TCs winds during their passage. Another ∼2/5 of this OHU is injected in the seasonal thermocline and hence released back to the atmosphere during the following winter. Because of zonal compensations and equatorward transport, only one–tenth of the OHU is actually exported poleward (46 TW), resulting in a marginal maximum contribution of TCs to the poleward ocean heat transport. Other usually neglected TC–related processes however impact the ocean mean state. The residual Ekman pumping associated with TCs results in a sea–level drop (rise) in the core (northern and southern flanks) of TC–basins that expand westward into the whole basin as a result of planetary wave propagation. More importantly, TC-induced mixing and air–sea fluxes cool the surface in TC–basins during summer, while the re-emergence of subsurface warm anomalies warms it during winter. This leads to a ∼10% reduction of the sea surface temperature seasonal cycle within TCs basins, which may impact the climate system.

Emmanuel Vincent
4, place Jussieu
75005 Paris
Tel.: +33-1-44274157
E-mail: emvincent@nsup.org

Keywords Tropical Cyclones · Ocean Heat Transport · SST · Seasonal Cycle

1 Introduction

Intense winds associated with Tropical Cyclones (TCs) cause vigorous upper–ocean vertical mixing. This mixing cools the ocean upper layers, while injecting warm surface waters downward. Because surface fluxes act to restore cold surface anomalies to background conditions, this results in a net warming of the tropical ocean at the end of the TC season. Emanuel (2001) argued that this net ocean heat uptake (OHU) in the tropics has to be equilibrated by a net ocean heat transport (OHT) out of the tropics, implying that TCs may significantly contribute to the poleward ocean heat transport. Using a one–dimensional ocean model, Emmanuel (2001) estimated the yearly averaged TC-induced OHU to be ∼1.4 ±0.7 PW (1 PW=10^{15} W). Sriver et al. (2008) repeated the calculation using a more extensive data set, but a somewhat cruder model, and found a yearly averaged TC–induced OHU of 0.48 PW. Jansen et al. (2010) revisited the calculation and end up with a slightly larger estimate (0.58 PW). The order of magnitude of the total heat transported out of the tropics by the ocean being approximately 2.9 PW (Fasullo and Trenberth 2008), those studies hence advocate for a significant role of TCs on the climate system through their influence on OHT.

Modeling studies (Korty et al. 2008; Jansen and Ferrari 2009; Sriver et al. 2010) have then attempted to quantify the TCs' impact on the OHT. Results from these studies however reveal a large sensitivity to the numerical design of the experiments, with a TC contribution to local heat transport at 20° ranging from 0.05 to 0.4 PW depending on the considered study. The aforementioned studies parameterized TC–induced mixing effect by enhancing vertical diffusivity in the tropical regions. This simplified approach is however very sensitive to the latitudinal (Jansen and Ferrari 2009) and longitudinal (Sriver et al. 2010) extents of TC–induced mixing. The oceanic response to these parameterizations also relies on several strong assumptions regarding the depth over which TC–induced mixing is applied (usually set to a few hundred meters), its magnitude, and the period over which this additional mixing is applied (Manucharyan et al. 2011).

The TC–induced OHU may also be overestimated in the observation–based studies (Emmanuel 2001; Sriver et al. 2008) because most of them assumed that all the heat injected below the mixed layer during the summer cyclonic season remains in the ocean. The analysis by Jansen et al. (2010) however estimates that only one quarter of the TC–induced OHU remains in the permanent thermocline after winter. This study suggests that the mixed layer deepening in winter re–entrains most of the warm sub–surface anomalies generated during the cyclonic season, thus preventing the bulk of the warm anomalies from being advected poleward. Accounting for this seasonality, they re–evaluated the influence of TCs on the OHT to 0.15 PW (±100%). Jansen and Ferrari (2009) also pointed out that a substantial part of the OHU is advected equatorward by the wind–driven circulation and hence does not contribute to the poleward export.

The aforementioned studies assumed that the entire TC–induced surface cooling is attributable to vertical mixing. This may also lead to an overestimation of the TC–induced heat injection into the ocean. Indeed, observational (Park et al. 2011; Trenberth and Fasullo 2007) and modeling studies (Vincent et al. 2012a) indicate that a substantial part of the surface cooling may be related to enthalpy fluxes, especially for weak storms and/or a few hundreds of kilometers away from the storm.

Trenberth and Fasullo (2007) further suggested that these fluxes might as well influence the tropical sea surface temperature (SST) climatology. Hart (2011) hypothesized that TC–induced processes during summer season might affect the subsequent winter climate by modifying the meridional heat flux. TC–induced dynamical processes may as well impact the long–term oceanic state: the strong upwelling generated by TC winds near the cyclone track results in a westward radiating negative sea level anomaly (Jansen et al. 2010). Jullien et al. (2012) and Scoccimarro et al. (2011) suggested that the TC–winds strengthen the wind stress curl at the center of TC basins and contribute to background Ekman pumping. The climatic effect of TCs through their impact on surface heat fluxes and ocean dynamical processes hence deserves further investigation.

Previous global numerical studies investigating TCs climatological impacts used ocean models with rather coarse resolution (∼2° to 4° horizontal resolution), and most of them accounted for TCs influence by enhancing upper–ocean vertical diffusivity. The aim of the present paper is to investigate the climatological ocean response to TCs using a higher resolution model that allows an explicit representation of TC forcing. We analyze a set of $\frac{1}{2}^\circ$ global ocean model simulations that include TC–wind forcing at the ocean surface over a 30–year period (1978–2007). TC wind forcing is applied along observed TC–tracks using the Willoughby et al. (2006) analytical vortex, with maximum winds amplitude and TC position derived from observations. This strategy captures the TC–induced surface cooling reasonably well (Vincent et al. 2012a) and allows accounting for TC–induced mixing, but also for the potential impacts of TC–induced dynamical response and surface heat fluxes.

The paper is organized as follow. Section 2 summarizes our numerical framework and describes the experiments designed for separating the respective influence of mixing, advective processes and surface heat fluxes on the TC–induced ocean response. Section 3 describes the ocean response associated with each of these processes at the storm scale. Section 4 then discusses the contribution of these processes to the climatological TC–induced oceanic response and quantifies the TCs importance on the oceanic heat budget and transport. Section 5 provides a summary of our conclusions and their implications.

2 Numerical strategy

Vincent et al. (2012a) describe the model configuration, the strategy to include TC forcing and two of the experiments analyzed in this study. The following section provides a short summary of this modeling framework and details three additional sensitivity experiments specifically designed for this study that allow separating the respective contribution of mixing, dynamical response and surface heat fluxes in the ocean response to TCs.

2.1 Ocean model and additional TC-forcing

We use a $\frac{1}{2}^\circ$ global ocean model configuration (known as ORCA05; Biastoch et al. 2008) built from the NEMO (Nucleus of European Model of the Ocean, version 3.2; Madec 2008). This version uses a Turbulent Kinetic Energy (TKE) closure scheme Blanke and Delecluse (1993) improved by including the effect of Langmuir cells (Axell 2002), a surface wave breaking parameterization (Mellor and Blumberg 2004) and an energetically consistent time and space discretization (Burchard 2002; Marsaleix et al. 2008). This configuration successfully reproduces tropical ocean variability at intra–seasonal to inter–annual time scales (Penduff et al. 2010; Lengaigne et al. 2012; Keerthi et al. 2012) as well as the local SST response to TC winds forcing (Vincent et al. 2012a; Neetu et al. 2012). The experiment starts from an ocean at rest, initialized with temperature and salinity fields from the World Ocean Atlas 2005 (Locarnini et al. 2010). It is then spun up for a 30–year period (1948–1977) using the COREII bulk formulae and interannual forcing dataset (Large and Yeager 2009; Griffies et al. 2010). This final state is then used to start the simulations described hereafter, which cover the 1978–2007 period.

The cyclone–free simulation (FILT) is forced by the interannual CORE forcing. The CORE forcing strongly underestimates the intensity of observed cyclones (Vincent et al. 2012a). We filter out these underestimated TC–like vortices by applying an 11–day running mean to the wind components within 600 km of each cyclone track position (with a linear transition zone to unfiltered winds between 600 km and 1,200 km of the cyclone tracks).

The cyclone simulation (CYCL) is forced by realistic TC winds superimposed to the FILT forcing. The 6–hourly cyclone position and maximum winds of the 3,000 named TCs from the IBTrACS database (Knapp et al. 2010) are temporally interpolated to the model timestep (i.e. every 36 minutes). This information is used to reconstruct the 10m–wind vector from an idealized TC wind vortex fitted to observations (Willoughby et al. 2006). A more detailed description of this forcing strategy and of the model validation can be found in Vincent et al. (2012a).

In the following, we computed TC–induced ocean mean state changes as the 1983–2007 (25 years) average difference between CYCL and FILT experiments. We exclude the first 5 years of the experiments, which display a transient adjustment of the upper 400 m to TC forcing.

2.2 Sensitivity of TC surface forcing to horizontal resolution

The $\frac{1}{2}^{\circ}$ horizontal resolution used in the present study may seem rather coarse compared to previous case studies simulating the ocean response to single TCs (e.g. Halliwell et al. 2011). Our forcing strategy is however a good compromise between accuracy and numerical cost for a realistic simulation of the climatological global ocean response to TCs. Indeed, a major requirement for a realistic ocean response to TC forcing is to accurately capture the maximum winds of the TC eyewall in the atmospheric forcing (Halliwell et al. 2011). The use of an analytic TC vortex fitted to observed TCs characteristics allows fulfilling such a requirement. It is then crucial that the spatio–temporal sampling of the ocean grid allows capturing accurately the key processes involved in the ocean response to TC wind forcing, such as vertical mixing and upwelling. The ability of the ocean grid to capture the TC–induced mixing can be evaluated by calculating the TC Power Dissipation (PD): PD = $\int \rho_a C_D \left|\mathbf{V}\right|^3 dt$ where C_D is the surface drag coefficient, ρ_a the surface air density, and **V** the magnitude of the TC 10 m winds. The PD is indeed a good proxy of the energy transferred by TCs to surface currents (Vincent et al. 2012b), thus indicating the amount of energy available for ocean mixing. Ekman pumping can be used as a proxy of TC–induced vertical motions. Even though traditional Ekman pumping solution is not valid at the time scale of a TC passage, the thermocline displacement in the aftermath of the storm is similar to the Ekman solution, but with a superimposed inertial oscillation (Gill 1982).

Table 1 Global mean Power Dissipation and Ekman upwelling transport of Tropical Cyclones averaged over the 1983–2007 period as function of model resolution. These values were computed from the Willoughby et al. (2006) analytical TC wind vortex, applied using IBTrACS TC positions and maximum wind. The space and time sum of TCs upwelling transport is calculated over upward pumping, in order to only cumulate the upwelling induced by each cyclone. Note that the downwelling part calculated in the same way has the same magnitude, so that Ekman pumping cancels out both for a single storm and global mean.

ORCA mesh resolution	2°	1°	1/2°	1/4°	1/12°
global mean PD (TW)	4.48	4.47	4.49	4.50	4.62
global TC-induced upwelling	5.7	7.6	10.6	11.8	12.3

The spatial distribution of the power dissipation and Ekman pumping averaged over the 1983–2007 period are shown in Figure 1 for the $\frac{1}{2}^{\circ}$ resolution used in the present study. The largest PD values are found in the Northwest Pacific (38% of the global cumulated PD), where the most numerous (30% of worldwide number) and strongest (34% of all cyclones of Category 4-5 on the Saffir–Simpson scale) TCs develop. A relatively large PD also characterizes the North East Pacific and South Indian Ocean, with each representing 17% of the globally cumulated PD. A comparatively smaller amount of TC energy is available in the Southwest Pacific, North Atlantic and Northern Indian Ocean.

The wind structure of an individual TC forces a strong and localised upwelling along its track (within 1 RMW) compensated by a more modest and widespread downwelling on both sides of the TC inner–core footprint (Vincent et al. 2012a, see their Fig. 2b). When averaged annually, the spatial distribution of TC tracks results in a residual Ekman suction (upwelling) in the core of TCs basins and a residual Ekman pumping (downwelling) along

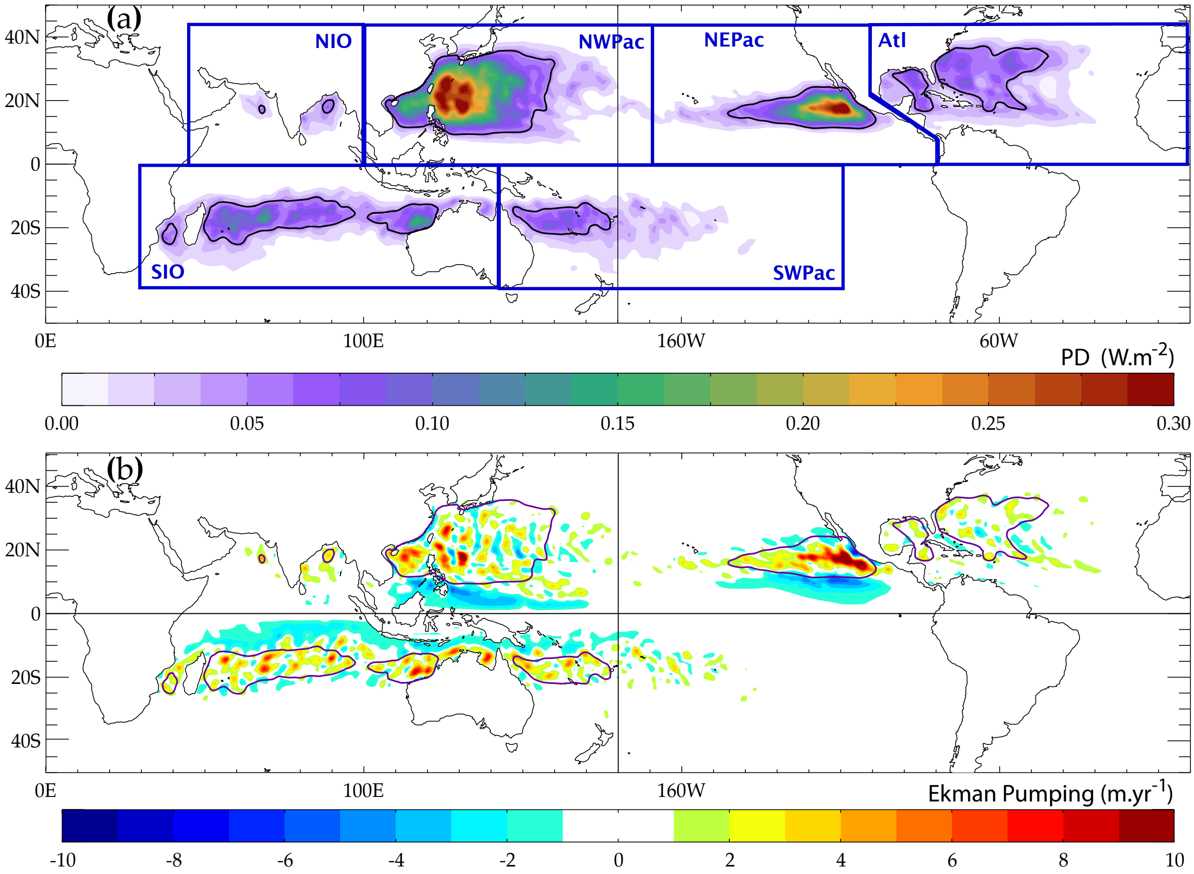

Fig. 1 Mean 1983–2007 Tropical Cyclone induced (**a**) Power dissipation (W.m^{-2}), and (**b**) Ekman pumping (m.year^{-1}); the superimposed contour is PD=0.05 W/m^2. These values are computed on the $\frac{1}{2}^\circ$ global ORCA mesh, and a 1° filter is applied in order to highlight the large–scale structure of the curl.

their northern and southern flanks (these regions being mainly affected by winds outside the TCs inner–core, Fig. 1b). The residual downwelling signal is also larger on the equatorward side of TC–basins because of the equatorward decrease of the Coriolis parameter. When averaged globally the upward and downward mass transports cancel out, as it is the case for a single storm.

Table 1 provides the global annual mean TC–induced PD and upwelling (i.e. the spatial integral of positive values of Ekman transport) over the 1983–2007 period computed for increasing horizontal grid resolutions ranging from 2° to 1/12° (with an identical 36 minutes temporal resolution in all cases). This table clearly illustrates that a $\frac{1}{2}^\circ$ resolution is sufficient to provide a reasonable estimate of these two quantities and thus appears to be a good compromise between computational cost and accuracy for a global simulation: compared to the 1/12°, it provides very similar results in terms of power dissipation (3% weaker) while slightly underestimating the mean wind–driven vertical transport by 14%.

2.3 Sensitivity experiments

Our numerical strategy incorporates TCs wind forcing by adding idealized vortices to the 10 m–wind field used in CORE bulk formulae. Such additional forcing results in an ocean response mainly driven by three processes. First, the kinetic energy transferred by the wind stress to surface currents enhances the upper–ocean vertical shear that, in turn, increases *vertical mixing*. This mixing acts to cool the surface and warm the subsurface waters. Second, the TC wind forcing induces vertical motions (upwelling within 1 RMW of the track and downwelling outside), which modify the water column thermal structure through purely adiabatic *dynamical processes*. Third, the TC wind forcing enhances the *surface heat fluxes* (mainly through latent heat flux) and thus cools the ocean mixed layer. In order to separate the respective influence of these processes on the TC–induced ocean response, three sensitivity experiments that simulate separately each of these three processes are performed.

To that end, two modifications are introduced online in the three–dimensional (3-D) ocean model: (i) a twin computation of the momentum and heat surface fluxes, so that net forcing accounting or not for TCs wind forcing are simultaneously available (τ_{TC}, HF_{TC} and τ_{noTC}, HF_{noTC}) where τ is the surface wind stress and HF stands for the surface heat fluxes); (ii) a twin computation of the vertical mixing coefficients so that two set of mixing coefficients are available, including or not the TC-induced mixing (κ_{TC} and κ_{noTC}). While obtaining a second set for (i) is straightforward, (ii) requires a more detailed explanation. We introduced a 1-D model that solves, for each ocean column of the 3-D ocean model, the following linear momentum equation:

$$\frac{\partial \mathbf{u}_{1D}}{\partial t} = -f\,\mathbf{k}\times\mathbf{u}_{1D} + \frac{\partial}{\partial z}\left(\kappa\frac{\partial \mathbf{u}_{1D}}{\partial z}\right) + \left.\frac{\tau}{\rho_o \Delta z}\right|_{surface} \qquad (1)$$

where $\mathbf{u}_{1D}$ is the horizontal velocity and f the Coriolis parameter. τ is the surface wind stress with or without the TC wind forcing. Finally, a vertical mixing coefficient κ, is computed from a duplication of the TKE turbulent closure. In the TKE equation itself, the surface boundary condition is computed from τ_{TC} or τ_{noTC} resulting in a vertical mixing coefficient κ_{TC} or κ_{noTC}. The shear TKE production term uses $\mathbf{u}_{1D}$ and the destruction by stratification term is computed using the 3-D model stratification.

With respect to FILT and CYCL experiments (described in section 2a), the three sensitivity experiments can be described as follows. The CMIX experiment only accounts for the TC–induced vertical mixing. For this experiment, the 3-D model is forced by τ_{noTC} and HF_{noTC} (i.e. FILT wind forcing) but uses the vertical mixing coefficients provided by the 1-D model forced by CYCL wind forcing (κ_{TC}) under the TC footprint. The CDYN experiment only accounts for the TC–induced ocean dynamical response. In this case, the 3-D model is forced by τ_{TC} and HF_{noTC} but uses κ_{noTC} as vertical mixing coefficients along the TC footprints. Finally, CFLX experiment only accounts for the TC–induced heat fluxes. The 3-D model is forced by FILT wind forcing (τ_{noTC}) but uses HF_{TC} under the TC footprints.

3 Ocean response at the storm scale

The purpose of this section is to detail the surface and 3-D processes triggered by TCs under their track before addressing their long–term and large–scale oceanic impact in section 4.

3.1 3-dimensional ocean response

Using FILT and CYCL experiments, Vincent et al. (2012a) investigated the mixed layer processes responsible for the characteristics of TC–induced surface cooling. They show that CYCL reproduces the observed TC cold wake characteristics (amplitude, asymmetry, extent, duration) reasonably well. Since the model also accurately simulates the tropical ocean mean state and variability (Penduff et al. 2010; Lengaigne et al. 2012), this strongly suggests that the mixed layer depth reached during TC passage is reasonably well simulated. The purpose in this subsection is thus not to validate the model against observations, but to illustrate the ability of our numerical strategy to separate the effect of the three main processes (mixing, dynamical response and surface heat fluxes) acting on the ocean thermal structure under a TC.

To that purpose, a composite evolution of the vertical profiles of TC–induced temperature anomalies is computed as the temperature difference between CYCL and FILT experiments underneath TC track positions (Fig. 2). These composites are performed in the vicinity of the TC center (defined as the cross–track average within ±2 Radius of Maximum Wind (RMW)) and on TC sides (cross–track average between 2 and 8 RMW on both sides of the TC track). The composite is built from every position (at a 6–hour resolution) along the tracks of all TCs over the 1983–2007 period.

The largest oceanic signature underneath TCs center appears as a cold anomaly throughout the water column that last ~30 days following the TC passage (Fig. 2a). The ocean response on TC sides exhibits a surface cooling overlying a warm anomaly between 30 and 80 m, with no prominent signal at depth (Fig. 2a). The surface cooling disappears within~2 months after the TC passage and is replaced by warm anomalies in the top 100 m both along the TC–track and on the TC sides (Fig. 2a).

The structure and magnitude of these responses can be easily understood in the light of the three sensitivity experiments described in the previous section (Fig. 2b-d). As illustrated on Figure 2, the total TC–induced ocean response (CYCL experiment) can be largely described as the sum of the TC–induced mixing (CMIX experiment), dynamical processes (CDYN experiment) and heat fluxes (CFLX experiment). Non–linearities are indeed weak, except below TCs in the top 100 m for about 20 days where they can reach 25% of the total signal (Fig. 2e vs. Fig. 2a). This non–linearity near the surface is likely to result from the overestimation of cooling induced by heat fluxes in CFLX experiment: surface fluxes under TCs are enhanced in this experiment compared to CYCL because it does not include the cooling induced by mixing and advection. These weak non–linearities suggest that our modeling strategy allows identifying unambiguously the first–order contribution of each process to the model ocean response.

Both TC–induced heat fluxes (Fig. 2b) and vertical mixing (Fig. 2d) strongly contribute to the surface cool-

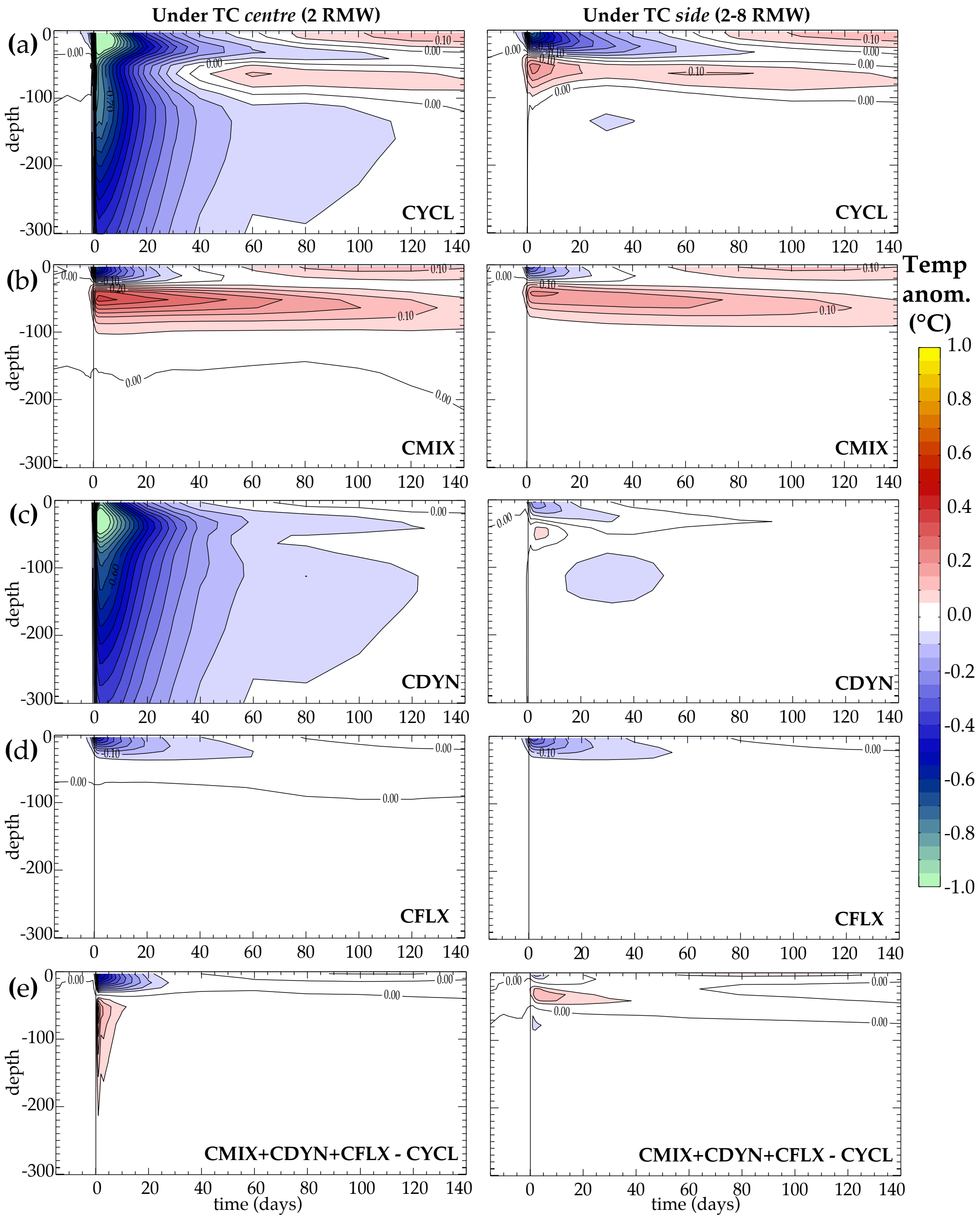

Fig. 2 Depth–time composite of temperature anomalies relative to the FILT experiment for experiments (**a**) CYCL (total effect of the TC), (**b**) CMIX (TC–induced mixing), (**c**) CDYN (TC–induced dynamical response), (**d**) CFLX (TC–induced fluxes), and (**e**) the difference (CMIX+CDYN+CFLX) - CYCL (non–linearities), (Left) within 2 Radii of Maximum Wind (RMW) of the TC–center and (right) on the TC–sides (within 2 to 8 RMW of the cyclone track). The composite encompasses all TCs with 10-min sustained wind speed greater than 15 m.s^{-1} during the 1983–2007 period.

ing simulated both under and further away from TC track, in agreement with Vincent et al. (2012a). This large–scale cooling disappears in ∼40 days after the TC passage for both experiments. In CFLX, the surface cooling is damped by atmospheric heat fluxes. In CMIX, as TC–induced mixing warms the 30 to 100 m sub–surface layer (Fig. 2b), both entrainment of these mixing–induced warm sub–surface anomalies into the mixed layer and heat fluxes contribute to damp the surface cooling. The entrainment of these warm subsurface anomalies further results in a slight SST warming after ∼60 days that persists beyond 100 days after the cyclone passage. Finally, TC–induced upwelling (Fig. 2c) dominates the large cooling signal simulated at depth under the TC track (Fig. 2a).

Another remarkable feature of the local response to TCs, first described by Jansen et al. (2010) from observed sea level anomaly (SLA; their Fig. 2), is the westward propagation of TC–induced thermocline depth anomalies. Replicating Jansen et al. (2010) analysis allows validating this propagating feature in the model. As shown on Figure 3, the model reproduces the main characteristics of this propagation of TC–induced SLA. The residual TC–induced upwelling results in a sea level anomaly that propagates westward at a speed of 0.1°/day (≃0.1m/s) in both datasets. While the SLA amplitude closely agrees 1 month after TC passage, it is larger in the model than in observations one week after the TC passage. Although model deficiencies cannot be discarded, we argue that satellite observation's poor spatial and temporal sampling of the TC response may partly explain this mismatch for the fast evolving anomalies under the TC. Conversely, the 'long–lived' residual large scale SLA signal one month after TC passage could be more accurately captured by satellite observations. We will show that this westward SLA propagation is important to explain the TC–induced impact on the ocean climatology discussed in section 4a.

3.2 Surface ocean response

The purpose of this subsection is to describe the SST, MLD and heat flux evolution beneath the TC, not only during the TC passage but also later in their wake, a necessary step to explain the climatic impact of TCs in the next section.

As a TC translates over a given ocean location, the SST drops as a result of the three main processes presented in the previous section. The maximum cooling (∼1.4°C) is observed 1-2 days after the TC passage (Fig. 4a) in conjunction with a mixed layer deepening (Fig. 4b). During this period (about days -4 to days +2), TC winds *extract* heat from the ocean through enhanced enthalpy fluxes used to fuel the TC heat–engine (Emanuel 1986) (Fig. 4c).

The cold surface temperature anomaly left in the TCs' wake is then damped by atmospheric fluxes in the months following the TC passage, inducing an oceanic heat *uptake* (i.e. a net surface heat transfer into the ocean) from a few days after to ∼80 days after the TC passage (Fig. 4c). As noticed by Park et al. (2011) in their analysis of ARGO profilers data, the oceanic heat uptake lasts slightly longer than the typical surface temperature anomaly decay time scale found in satellite observations (Price et al. 2008) and in the CYCL experiment (Vincent et al. 2012a). The mixed layer depth evolution allows explaining this feature. The storm passage induces a deepening of the mixed layer (Fig. 4b)

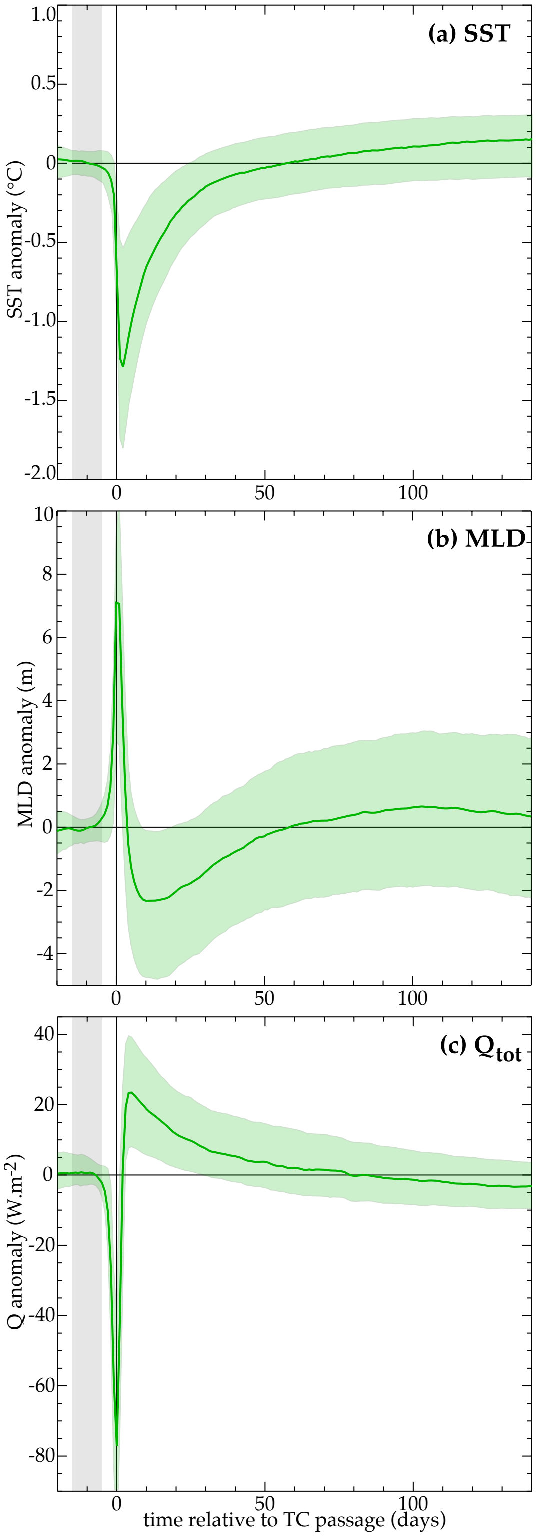

Fig. 4 Composite time series of (**a**) sea surface temperature (SST; in °C), (**b**) mixed layer depth (MLD; in m) and (**c**) total surface flux (Q_{tot}; in W.m^{-2}) anomalies generated by TCs in the CYCL experiment relative to FILT. MLD and SST anomalies are averaged within 200 km of the center of the storms and Q_{tot} is averaged within 600 km of the center of the storms. The composite gathers all TCs with 10-min sustained wind speed greater than 15 m.s^{-1} over the 1983–2007 period. Shading indicates the spread around the mean value, evaluated from the lower and upper quartiles.

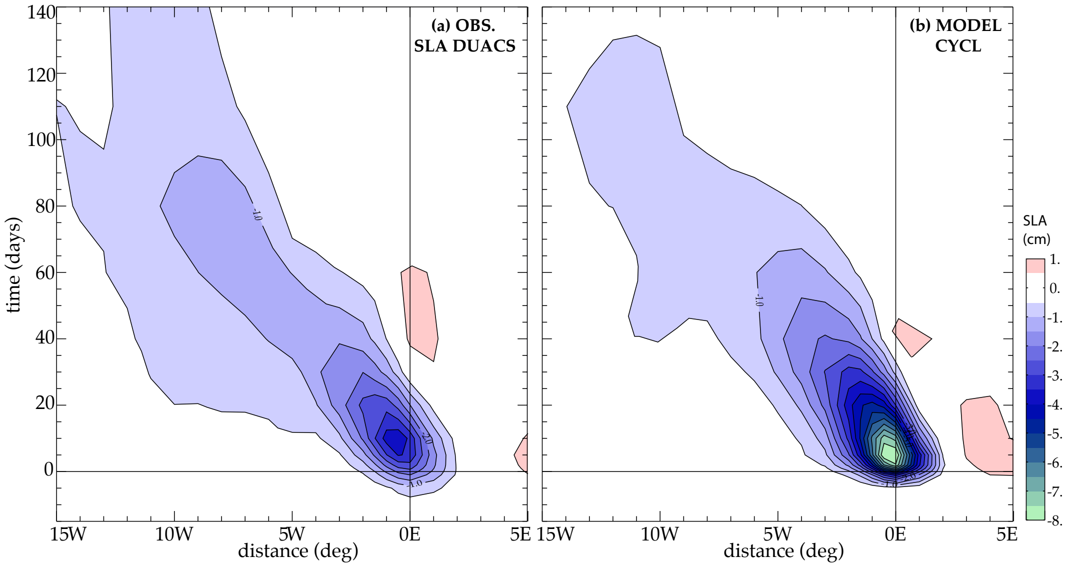

Fig. 3 Composite hovmöller diagram (longitude–time) of the sea level anomaly (cm) response to the tropical cyclone passage. The composite gathers all poleward–propagating TCs with maximum 10-min sustained winds exceeding 15 m.s^{-1} for the time period 1998 to 2006. Anomalies are calculated relative to the values before the passage of the storm (day -15 to day -5) and the seasonal cycle is removed. (**a**) Observed SLA from AVISO weekly 1/3° product, and (**b**) CYCL weekly averaged SLA fields.

and a strong cooling in the top 40 m (Figs. 2a and 4a). Just after the TC passage, the ocean quickly restratifies and the mixed layer shallows (Fig. 4b) so that cold surface anomalies vanish quicker than cold anomalies just below the mixed layer (Fig. 2a). Then, after ~60 days, as the mixed layer deepens in fall, remnant cold anomalies left just below the mixed layer from the TC passage are re–entrained in the mixed layer. The resulting ML cooling induces compensating heat fluxes into the ocean, explaining the long–lasting ocean heat uptake displayed on Fig. 4c. Finally, as ML continues to deepen in fall, sub–surface warm anomalies are further entrained into the ML and the SST becomes warmer in the CYCL run than in FILT (Fig. 4a). As a result, heat flux anomalies become negative again after ~80 days when heat stored in the sub–surface layers is *released* back to the atmosphere.

4 Climatological impact of TCs on the Ocean

4.1 Annual mean oceanic response to Tropical Cyclones

Figure 5 shows TC–induced long–term mean temperature changes averaged over three oceanic layers (0-10m, 30-100 m and 100-400 m), selected on the basis of the vertical extents of the TC–response in Figure 2.

TCs result in a climatological cooling of the upper–oceanic layer in TC–prone regions (i.e. where PD is large, see Fig. 5a) with a magnitude roughly proportional to the mean TC wind power (Vincent et al. 2012b). The largest cooling is found in the Northwest and Northeast Pacific basins (-0.5°C). The TC–induced climatological cooling hardly reaches -0.2°C in the South Indian Ocean, and -0.1°C in the Southwest Pacific and Atlantic basins. Modest warm anomalies (< 0.1°C) are also found poleward of the main TC–basins as well as in the eastern equatorial Pacific. A local strong warming (~0.7°C) occurs along the California coast and will be discussed later on.

All TC–basins exhibit a subsurface warm anomaly shifted poleward of the regions of maximum TC activity in the intermediate layer (30 to 100 m) (Fig. 5b). Strongest warming are found in the North Pacific Ocean (up to 1°C in the Northeast Pacific and 0.7°C in the Northwest Pacific) while those warm anomalies do not exceed 0.2°C in other TC–basins. The equatorial strip is characterized by a 0.1°C warming in the Indian Ocean and eastern Pacific Ocean, and a stronger 0.5°C warming just south of the Northeast Pacific TC–basin. Finally, the deeper layer (100–400 m) is characterized by zonally distributed anomalies of alternating signs, with cooling in the core of TC basins and warming on their poleward and equatorward flanks (except in South Indian Ocean where a deep cold anomaly is observed around the equator).

Figures 6 and 7 display respectively the TC–induced climatological sea surface height (SSH) and sea surface temperature (SST) changes and the relative contribution of cyclone–induced mixing, surface fluxes and dynamical response to the total anomalies. Figure 8 shows corresponding temperature latitude–depth sections across the

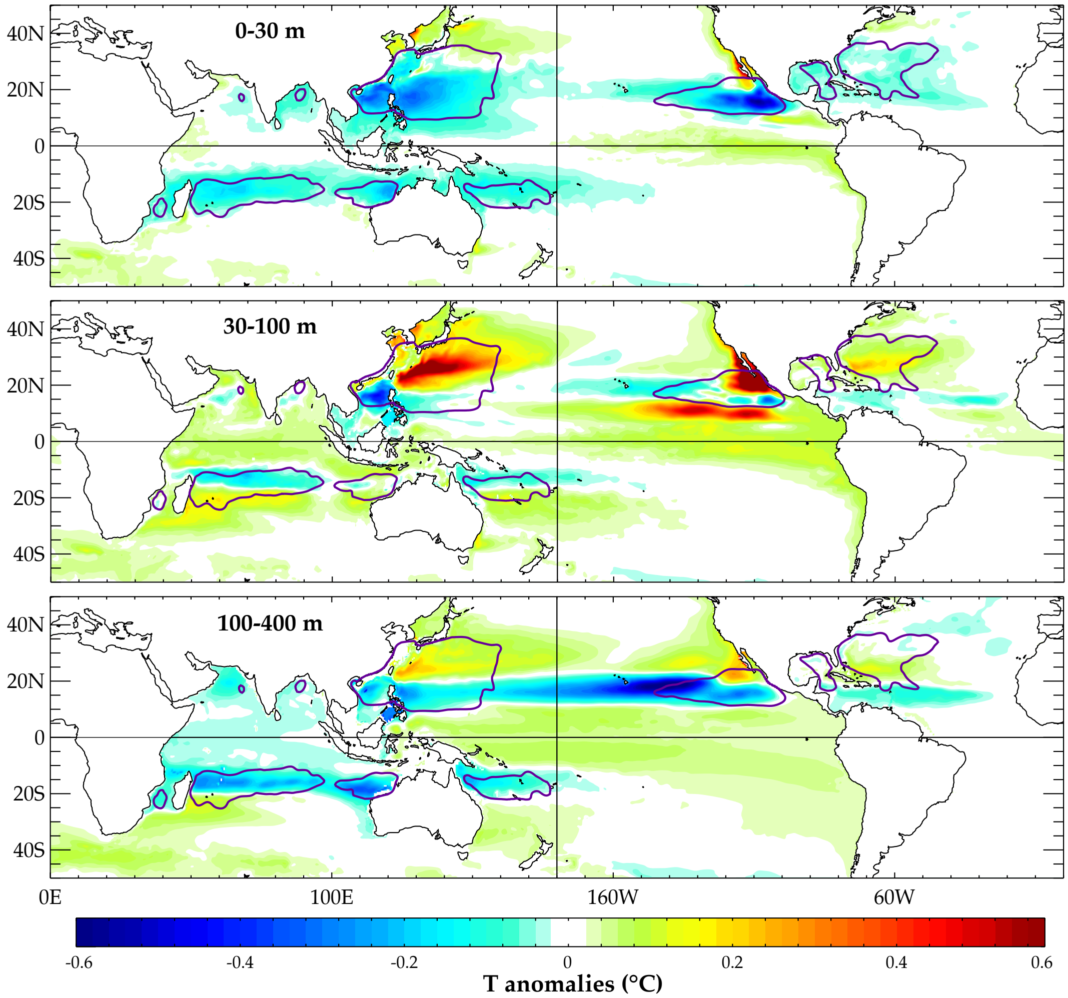

Fig. 5 Mean 1983–2007 TC–induced temperature anomalies (°C) averaged over (**a**) the surface layer (0–30 m), (**b**) the 30–100 m layer, and (**c**) the 100–400 m layer. The purple contour delineates regions of intense TC activity (PD=0.05 W/m^2, see Fig. 1).

Northwest Pacific and South Indian Ocean basins. As for the local response to TCs, non–linearities are negligible everywhere, except in regions of strongest SST cooling (Fig. 6e and 7e). As discussed in section 3.1, this feature results from the overestimation of the heat fluxes extracted under TCs in CFLX experiment, due to the absence of surface cooling by mixing and upwelling.

SSH anomalies shown on Figure 6 integrate the signature of the three oceanic layers depicted in Figure 5. TC–induced upwelling and downwelling signals driven by the dynamical response isolated in CDYN experiment dominates the climatological SSH response (Fig. 6c). In the Northeast Pacific, the residual climatological TC–induced Ekman upwelling around ∼15°N (Fig. 1b) shifts the thermocline upward, resulting in a negative SSH anomaly in this region. The opposite occurs on the northern and southern flanks of TC basins where residual climatological TC–induced Ekman downwelling dominates (Fig. 1b), resulting in a positive SSH anomaly. These thermocline anomalies then propagate westward as a result of planetary wave dynamics (Fig. 3; Jansen et al. 2010) and hence expand zonally to affect the entire North Pacific. These SSH anomalies signals are reinforced in the western part of the basin due to local Ekman pumping in the Northwest Pacific. The other TC–prone basins exhibit similar zonally oriented structures of negative SSH anomalies in the latitude bands of maximum cyclonic activity (Fig. 6c). TC–induced dynamical ocean response is also largely responsible for the sea level rise in the equatorial eastern Pacific and the associated warm surface and sub-surface equatorial anomaly seen on Figure 5. TC–induced vertical mixing is the second largest contributor to TC–induced SSH anomalies. Mixing injects warm water down below the mixed layer in TC–prone regions while surface cooling is cancelled by surface fluxes, resulting in a positive SSH anomaly. This rise is largest in the Northwest (0.9 cm) and Northeast

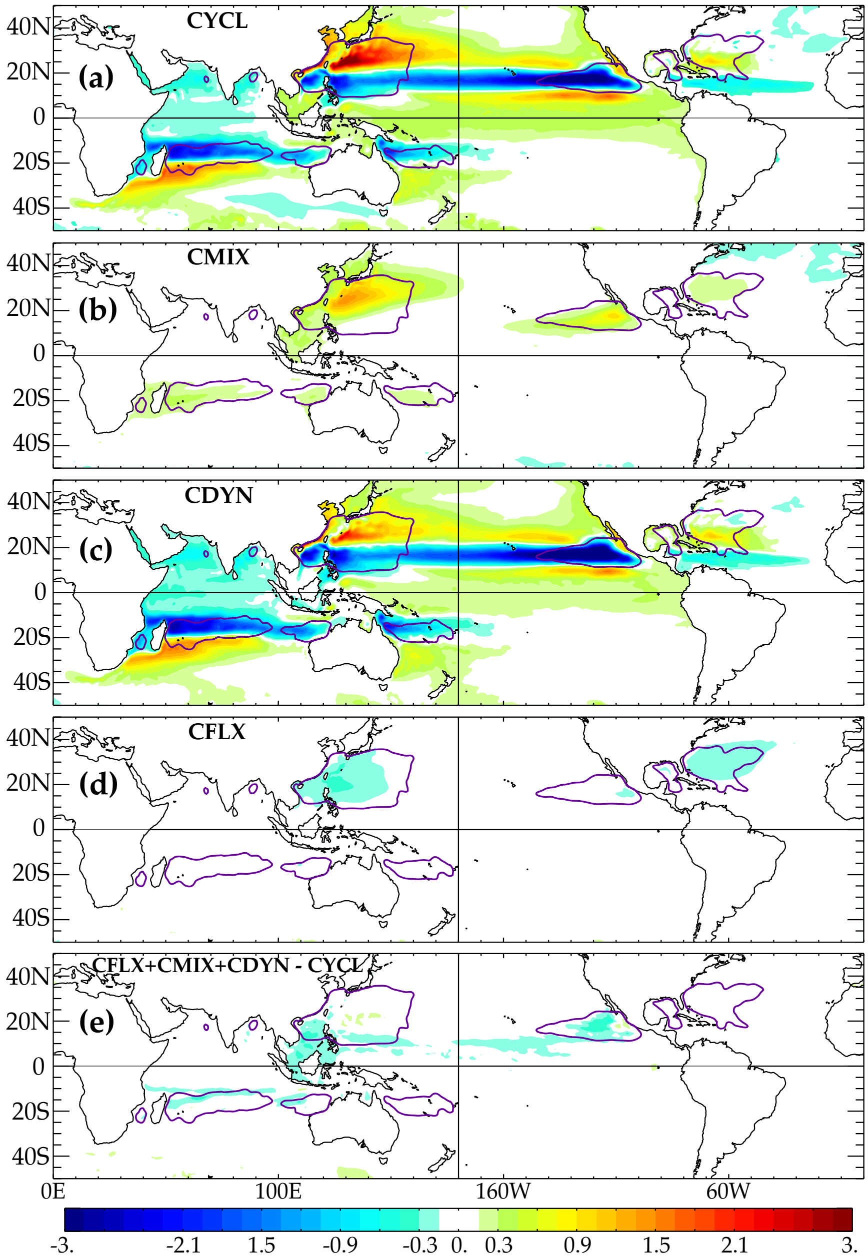

Fig. 6 Mean 1983–2007 sea surface height anomalies (cm) relative to FILT experiment for (**a**) CYCL (total effect of the TC), (**b**) CMIX (TC–induced mixing), (**c**) CDYN (TC–induced dynamical response), (**d**) CFLX (TC induced fluxes), and (**e**) the difference (CMIX+CDYN+CFLX) - CYCL (non–linearities). Purple contour reminds the regions of intense TC activity (PD=0.05 W/m^2).

Pacific (0.6 cm) while it only reaches ~0.1 cm in other TCs basins.

In contrast to sea level, TC–induced heat fluxes are the major contributor to the basin–wide sea surface cooling (Fig. 7). TC–induced vertical mixing (Fig. 7b) cools the ocean surface in the core of TC basins. TC dynamical response (Fig. 7c) slightly cools the SST in TC–induced upwelling areas (by ~0.1°C), except in the Northeast Pacific where the shallow thermocline allows a larger surface cooling (~0.3°C), comparable to the effect of TC–induced air–sea fluxes and mixing. The TC–induced dynamical response also warms the ocean surface on the poleward flank of TC–basins by deepening the thermocline, hence reducing surface cooling by entrainment. The strong warming along the California coast is driven by the TC–induced dynamical response (Fig. 7c). In this region, tropical storms are known to be a major driver of SLA intraseasonal variability (Enfield and Allen 1983). In this region, TCs usually travel northward along the coast, favoring a large coastal downwelling signal and

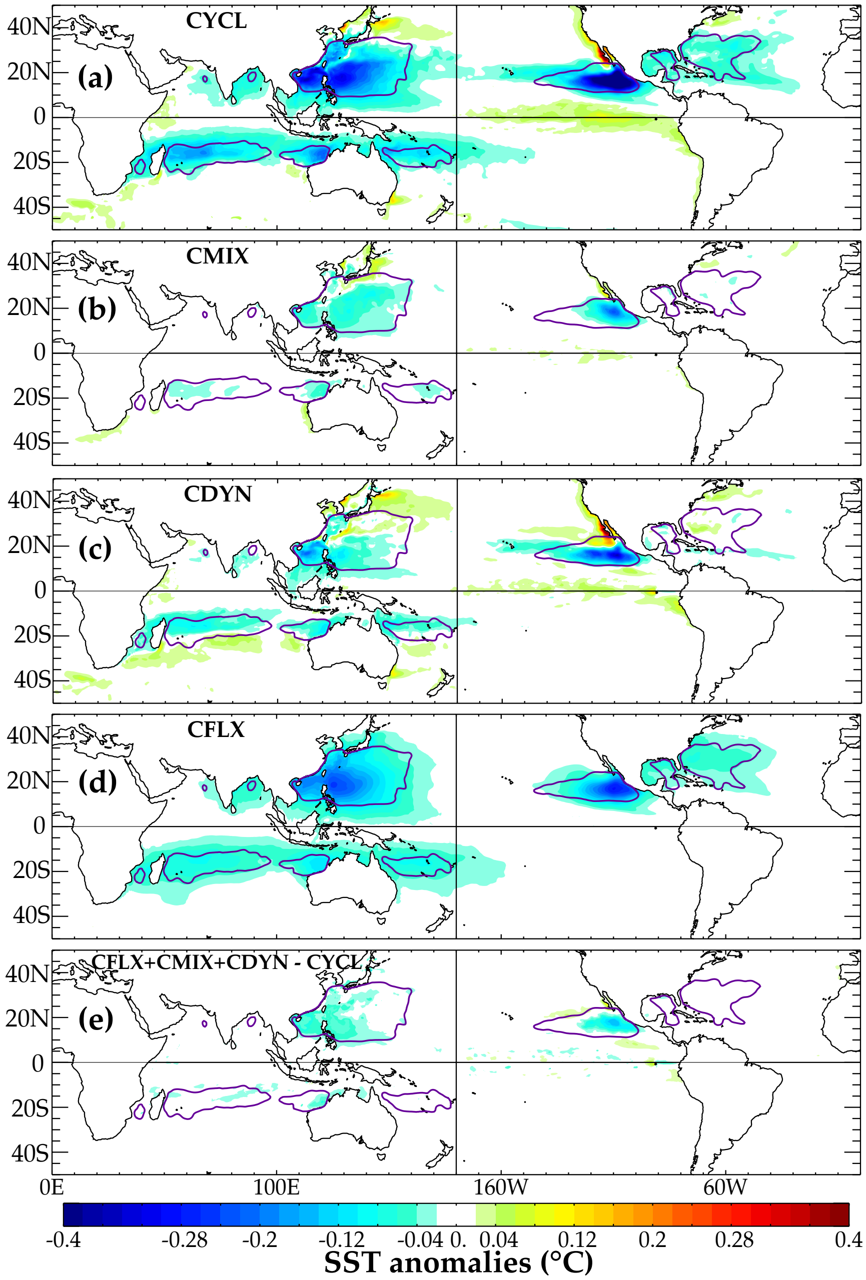

Fig. 7 Mean 1983–2007 sea surface temperature anomalies (°C) relative to FILT experiment for (**a**) CYCL (total effect of the TC), (**b**) CMIX (TC–induced mixing), (**c**) CDYN (TC–induced dynamical response), (**d**) CFLX (TC induced fluxes), and (**e**) the difference (CMIX+CDYN+CFLX) - CYCL (non–linearities). Purple contour reminds the regions of intense TC activity (PD=0.05 W/m^2).

resulting in positive SSH anomalies. These anomalies then propagate northward as coastally trapped Kelvin Waves, and warm the ocean surface.

Finally, meridional temperature sections shown on Figure 8 allow summarizing the salient features of the mean vertical ocean response to TCs forcing. TCs forcing is responsible for:

(i) an intense subsurface warming around 20-30°: this warming is maximum at 50 m depth, reaching 0.4°C in the Northwest Pacific. At this depth, warming largely results from TC–induced mixing. From 50 m down to 300 m, TC–induced downwelling also contributes to this warming.

(ii) an intense cooling of the whole water column centered around 15°: TC–induced upwelling is largely responsible for this cooling at depth while mixing–induced warming and upwelling–induced cooling almost entirely cancel each other around 100 m depth. In the surface lay-

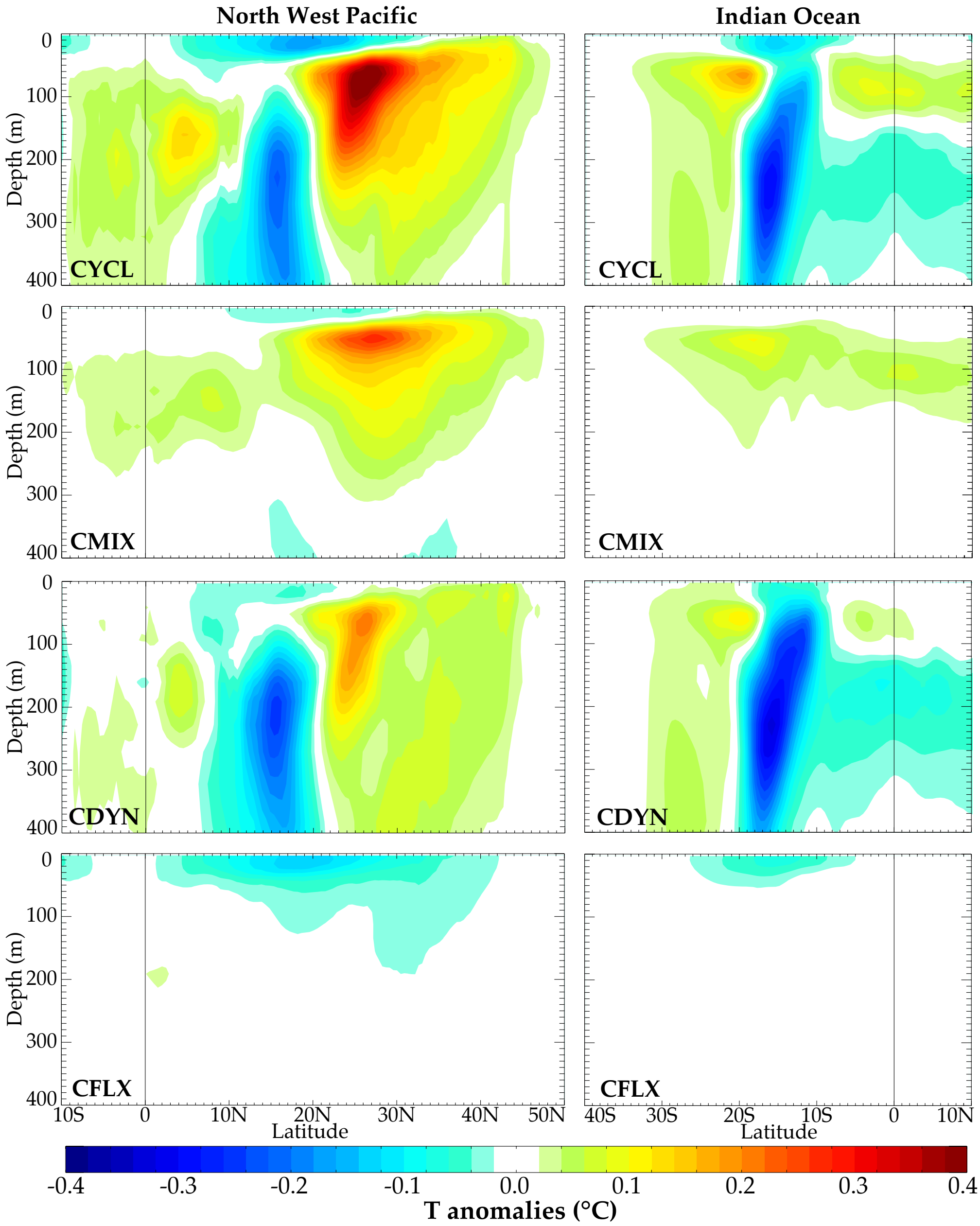

Fig. 8 Latitude–depth zonal averaged 1983–2007 temperature anomalies (°C) relative to FILT experiment for (left) Northwest Pacific and (right) Indian Ocean basins. From top to bottom: CYCL (total effect of the TC), CMIX (TC-induced mixing), CDYN (TC-induced dynamical response), CFLX (TC induced fluxes). These sections are zonally averaged between 120°E and 170°E for the NW Pacific basin and between 50°E and 100°E for the Indian Ocean basin. The difference (CMIX+CDYN+CFLX) - CYCL (non linearities) is very weak and thus not shown.

ers, the three processes work together to produce a persistent surface cooling, with TC–induced air–sea fluxes being the dominant process.

(*iii*) a warming in the equatorial (∼10°S-10°N) thermocline due to TCs wind: two third of this signal results from TC–induced downwelling. The remaining part is explained by subsurface equatorward advection of mixing–induced warm anomalies.

4.2 Seasonality of ocean response to TCs

The annual mean values discussed in the previous subsection mask the contrasted seasonal impact of TCs. TCs are indeed mainly active during local summer, with a maximum activity between July and October in the northern hemisphere and December to March in the southern hemisphere. Figure 9 displays a depth–latitude section of TC–induced temperature anomalies in the Northwest

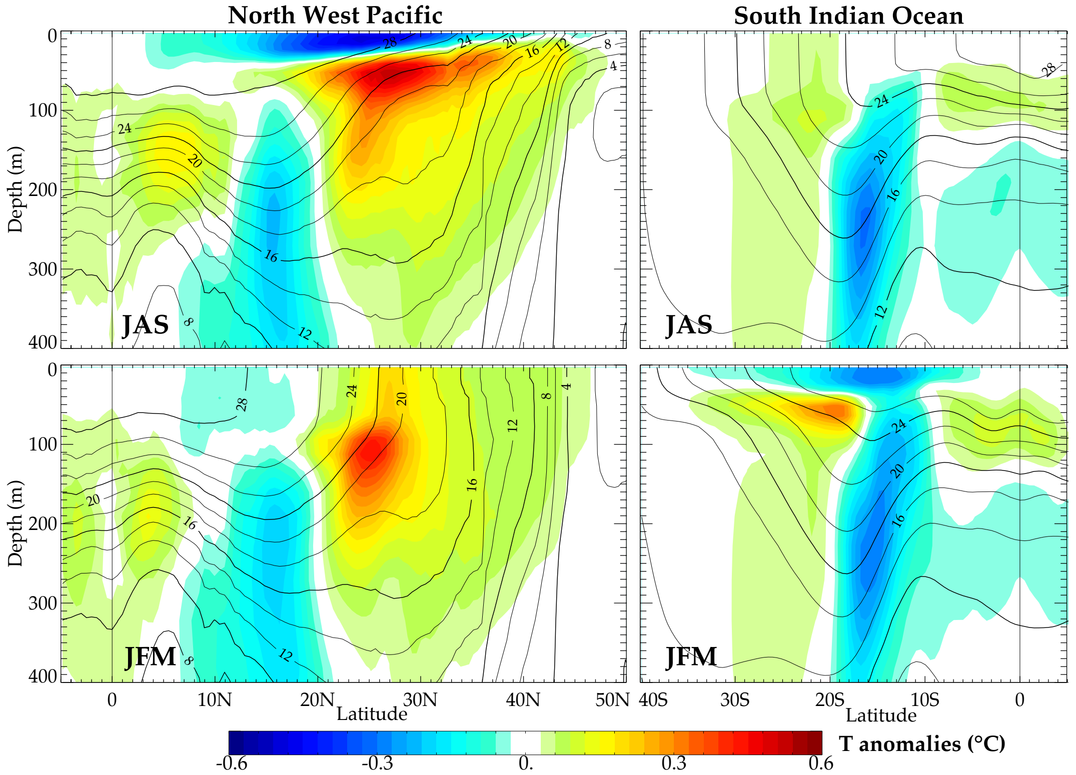

Fig. 9 Mean 1983–2007 temperature (°C; contour) and temperature anomalies (°C; shading) in (left) Northwest Pacific and (right) Indian Ocean basins during (top) the Northern Hemisphere cyclonic season (July to September) and (bottom) during the Southern Hemisphere cyclonic season (January to March). These sections are zonally averaged between 120°E and 170°E for the NW Pacific basin and between 50°E and 100°E for the Indian Ocean basin. Note that the maximum sub–surface warm anomalies during TC seasons are located in the seasonal thermocline.

Pacific and South Indian Ocean basins during these two seasons. In both basins, cold surface and warm sub–surface TC–induced anomalies are twice stronger during cyclonic seasons than on annual average (Fig. 9 and Fig. 8), with largest warm sub–surface anomalies located in the seasonal thermocline. During local winter, most of the surface layer cooling vanishes, while the warm subsurface anomaly considerably weakens and extends up to the surface. Anomalies located deeper than the seasonal thermocline persist all year long.

This seasonal behavior can be understood as follows. TCs primarily occur during summer and early fall, when the ocean mixed layer is generally shallow and lies above a seasonal thermocline. TC–related mixing hence acts to cool the ocean surface and warm the seasonal thermocline. As the mixed layer deepens the following winter, most of the heat anomalies deposited within the seasonal thermocline during the TC–season are re–entrained into the mixed layer. This results in a SST warming in the heart of TC–basins during the TC–inactive season (local winter), when heat is released back to the atmosphere. Only the deepest part of the warm anomalies deposited in the main thermocline during the TC–season is able to persist through winter.

This seasonal TC–induced buffering effect has a significant impact on the amplitude of the SST seasonal cycle. TC–induced SST anomalies during TC–seasons in each hemisphere are displayed on Figure 10. Summer seasons are characterized by widespread cooling in TC–prone regions while winter seasons mainly exhibit warm anomalies. These surface anomalies are particularly large in regions where TCs are most frequent (Northwest and Northeast Pacific; compare Figs. 1 and 10). For instance, the Northwest Pacific SST anomaly reaches -0.7°C during summer and becomes positive during winter, reaching +0.4°C in regions of maximum subsurface warming (Figs. 5b and 10b). The effect of TCs is to cool the ocean surface during summer and to slightly warm it during winter, and thus TCs act to reduce the SST seasonal cycle.

The seasonal cycle amplitude can be diagnosed as the SST difference between the warmest and coldest months in the monthly mean seasonal cycle (Fig. 11a). The TC–induced reduction of the SST seasonal cycle can then be computed as the difference of this seasonal cycle amplitude in the CYCL and FILT experiments (Fig. 11b). TCs act to reduce the seasonal cycle equatorward of 30° in both hemispheres. This reduction reaches ~0.5°C

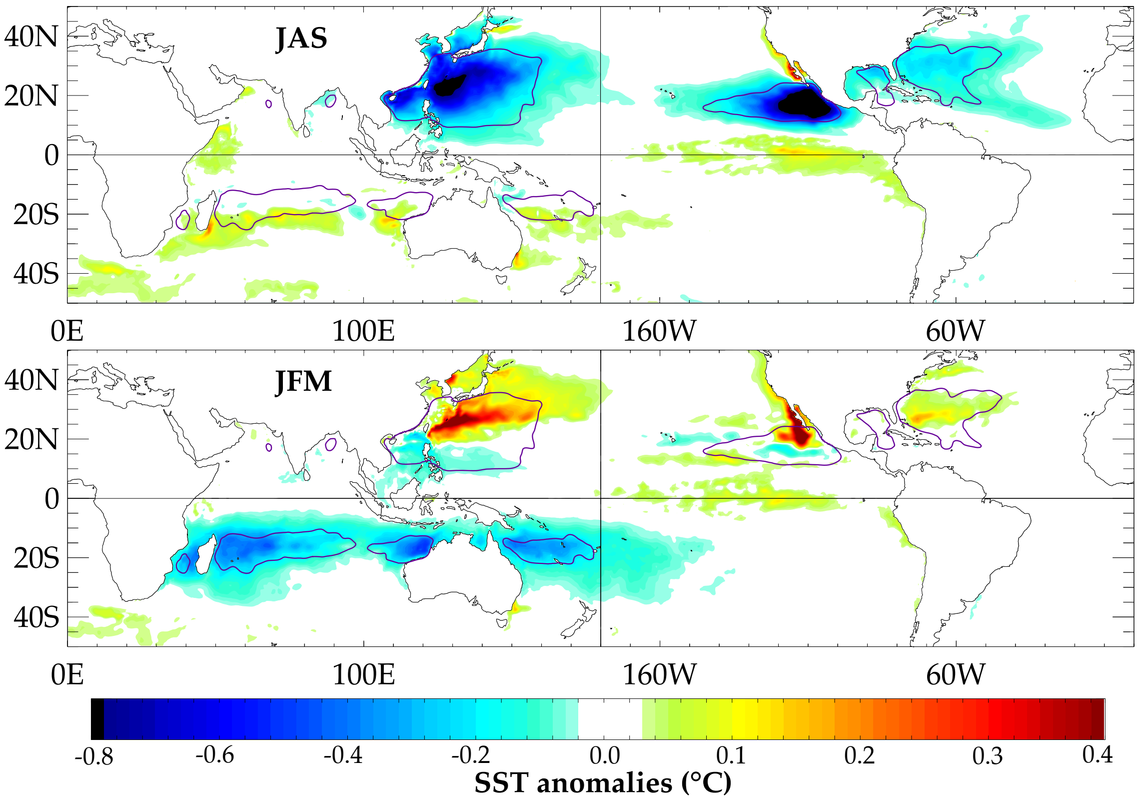

Fig. 10 Mean 1983–2007 CYCL SST anomalies (°C) relative to the FILT experiment for (**a**) the northern and (**b**) the southern hemisphere TC–seasons (July to September and January to March, respectively).

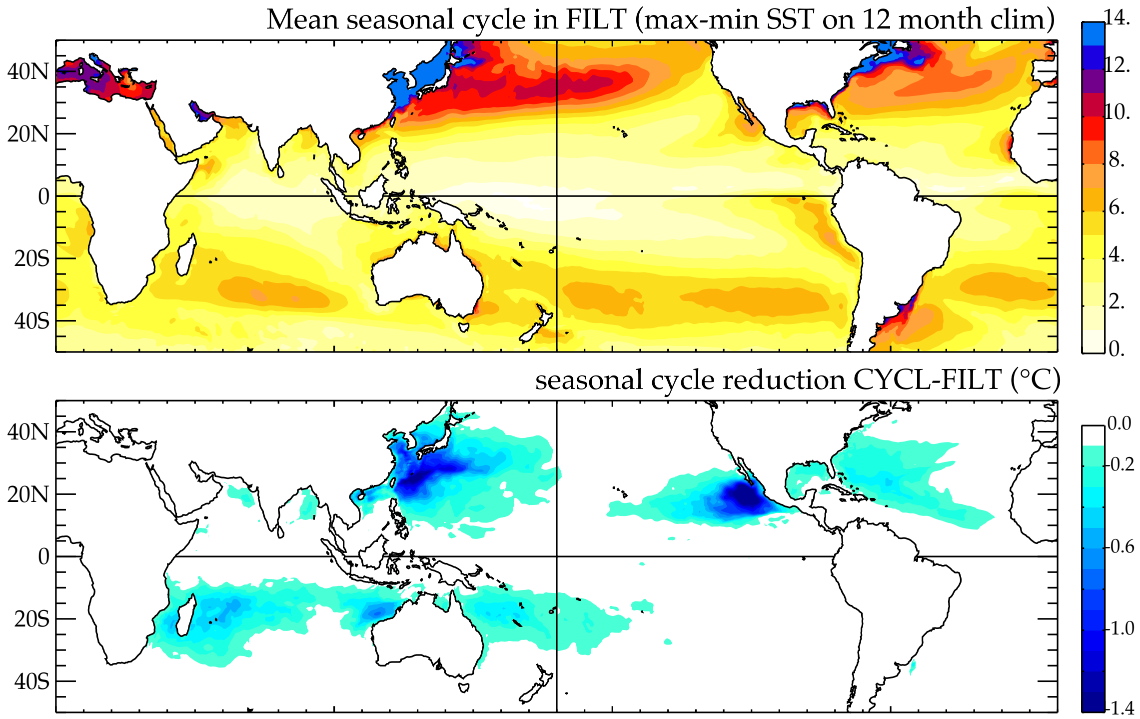

Fig. 11 (**a**) Mean 1983–2007 CYCL SST (°C) seasonal cycle amplitude (max-min on 12–month SST) and (**b**) its anomalies relative to FILT experiment.

in the Southern hemisphere and more than 1°C in the Northern hemisphere and corresponds to a 5 to 15% decrease of the seasonal cycle amplitude in most of the TC basins, except in the Northeast Pacific where it reaches up to 30%.

4.3 TC-induced Ocean Heat Uptake and Transport

This subsection aims at quantifying and understanding the TC–induced change in surface fluxes and the associated oceanic heat transport required to balance them. As discussed in section 3.2, there are three typical phases associated with a cyclone passage (Fig. 12a): a strong *ocean heat extraction* (OHE, purple area on Fig. 12a) during the cyclone passage (i.e. the strong enthalpy fluxes under the TC associated to its intense winds), followed by an *ocean heat uptake* (OHU, red area on Fig. 12a) i.e., positive heat fluxes into the ocean in response to the cold SST in the TC wake, and finally an *ocean heat release* (OHR, blue area on Fig. 12a) associated with the re-emergence of the subsurface warm anomalies during the following fall/winter and associated positive heat flux toward the atmosphere.

Note that this definition of the Ocean Heat Uptake (OHU) is identical to the one used by previous authors (e.g. Emanuel 2001; Sriver et al. 2008; Jansen et al. 2010). While some authors (Jansen et al. 2010) took into account the fact that the OHU was partially canceled by the OHR (i.e. the heat released back to the atmosphere during the next season), no study took the OHE into account, i.e. the fact that the amount of heat flux toward the atmosphere extracted during the TC passage partially compensates the OHU. Below, we explain how we estimate all these quantities.

OHE corresponds to the integral of the negative part (i.e. heat flux toward the atmosphere) of the surface heat flux difference between CYCL and FILT experiment at every timestep over the TCs duration and extent. OHE can hence be computed at each location as

$$\mathrm{OHE} = \iint \min\left(Q', 0\right)\, dS\, d\tau \tag{2}$$

where the double integral is done over all elementary surfaces dS and elementary durations $d\tau$ within TCs footprint (within a 1200 km radius of a TC track position). OHE represents the total amount of heat extracted from the ocean during the passage of TCs. The annual average global OHE over the 1983–2007 period estimated from our simulations is 178 TW (1 TW=10^{12} W).

Cold anomalies in the TCs' wake induce a positive heat flux into the ocean, i.e. a gain of heat for the ocean, the Ocean Heat Uptake (OHU). OHU is computed as the integral of the positive part of daily heat fluxes difference between CYCL and FILT experiments in all cyclonic basins over the 1983–2007 period

$$\mathrm{OHU} = \iiint \max\left(Q', 0\right)\, dx\, dy\, dt \tag{3}$$

Contrarily to the OHE calculation, the values are not cumulated only during TC passage (duration $d\tau$ and surface dS): any heat flux into the ocean (used to dissipate the TC cold wake) is accounted for. The long–term average of this heat uptake estimated from our simulations is 483 TW. This value can directly be compared to OHU estimates by Emanuel (2001): 1 400 TW, Sriver et al. (2008): 480 TW and Jansen et al. (2010): 580 TW. Our model estimate is in good agreement with these two most recent observation–based studies.

None of the previous studies accounted for the reduction of the OHU by the heat fluxes extracted during the TC passage (OHE). We define the *net* OHU as OHU minus OHE. The *net* OHU estimated from our simulations is 305 TW. This means that ∼2/5 of the heat flux entering the ocean in the wake of TCs only compensates the heat extracted to the ocean during TC passage (Fig. 12). Only the remaining ∼3/5 (the *net* OHU of 305 TW) actually induces a net warming of the ocean that may affect the ocean heat transport. Figure 13a shows the spatial distribution of the *net* OHU. A net total heat uptake of 185 TW (resp. 120 TW) penetrates the ocean seasonal and main thermocline in the northern hemisphere (resp. southern hemisphere) in TC–prone regions.

The re–emergence of subsurface warm anomalies in the months following the cyclonic season induce a long–term SST warming, and hence a heat loss to the atmosphere (ocean heat release, or OHR, Fig. 12a). The total ocean heat loss is obtained as the integral of the *negative* part of the daily surface fluxes difference between CYCL and FILT experiments within TC basins over the 1983–2007 period. OHR is then computed as the difference between this total ocean heat loss and OHE to exclude from the calculation the heat lost directly under TCs and only account for the heat released well after TCs' passage (blue area on Fig. 12a). The spatial pattern of the long–term averaged OHR is shown on Figure 13b. This heat is released back to the atmosphere in slightly different regions than where they were injected (compare Figs. 13a and 13b). The heat injected into the subsurface ocean during the TC season is indeed advected by the subtropical gyre and equatorial circulations, before being re–entrained in the mixed layer and released back to the atmosphere.

The average TC–induced heat flux anomaly between the CYCL and FILT simulations (equivalently obtained from the difference between the net heat uptake and heat released displayed in Fig.13a and 13b) is shown in Figure

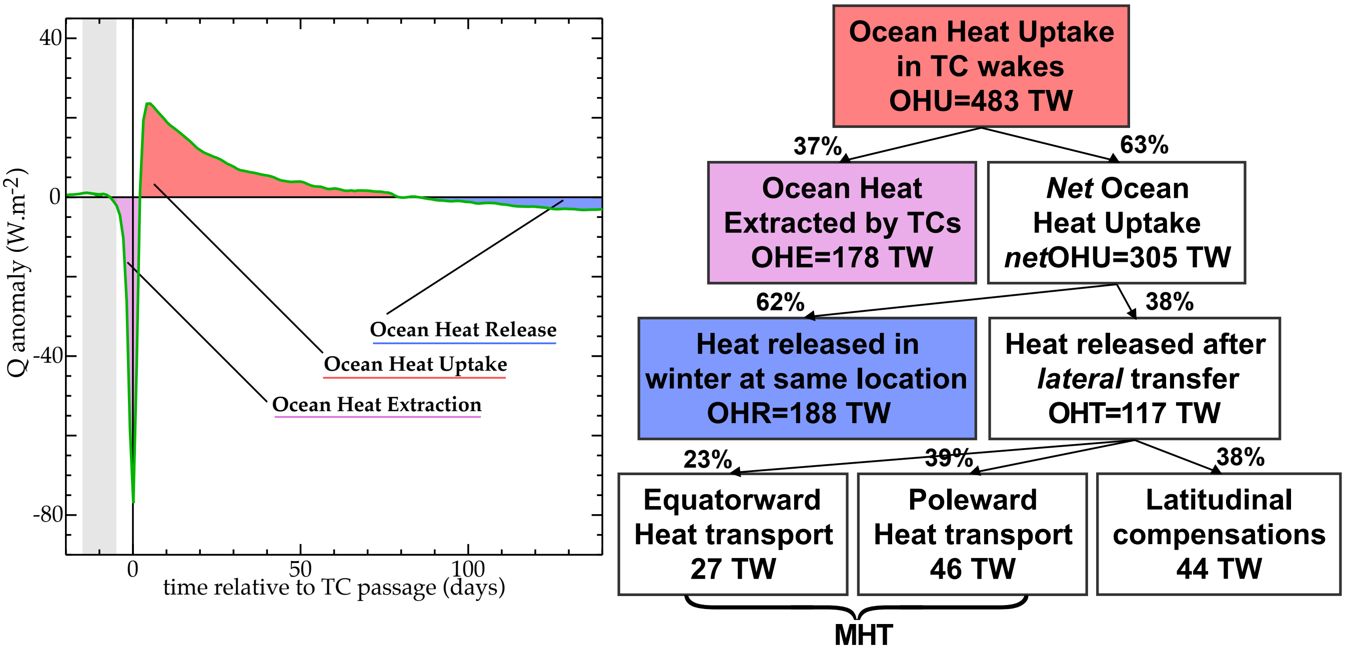

Fig. 12 Summarizing sketch: (**a**) Composite time series of TC–induced total surface flux anomalies within 600 km of TC–tracks (same curve as Figure 4a) with annotations indicating our naming conventions for the different heat transfers induced by TCs. The ocean heat extraction (OHE) corresponds to the TC–induced enthalpy fluxes to the atmosphere during the cyclone passage. The ocean heat uptake (OHU) is defined in the same way to other authors as the heat input from the atmosphere that is needed to dissipate the cold wake (i.e. the heat input to the ocean due in TCs' wake). Once the cold wake has been dissipated, subsurface anomalies re–emerge during the next winter and are associated with a delayed ocean heat release (OHR) to the atmosphere. Finally, a part of these subsurface anomalies is also transported laterally at the same latitude (and hence does not contribute to meridional heat transport) before re–emerging: this is the OHT or Ocean Heat Transport. (**b**) Total heat uptake by the ocean (OHU) in the wake of TCs and its partition into various components: OHE, OHR and OHT.

13c. At equilibrium, this mean surface heat flux anomaly has to be balanced by an horizontal oceanic heat transport, carrying heat from regions of TC–induced fluxes into the ocean (positive values on Fig. 13c) to regions of TC–induced fluxes out of the ocean (negative values on Fig. 13c). The TC–induced ocean heat transport can hence be computed as

$$\mathrm{OHT} = \iint \max\left(\overline{Q'}, 0\right)\, dx\, dy \qquad (4)$$

where the overbar signifies temporal averaging, i.e. $\overline{Q'}$ corresponds to Figure 13c. The resulting TC–induced OHT amounts to 117 TW. This is about 1/3 of the *net* TC–induced OHU (i.e. about 2/3 of the heat injected in the subsurface at a given point is later released to the atmosphere locally, because of the re–emergence of subsurface warm anomalies; Fig. 12).

A relevant quantity for earth's climate is the ocean Meridional Heat Transport (MHT), which can be obtained from zonal averaging of the OHT. At a given latitude, there is a partial compensation between positive and negative heat fluxes (Fig. 13c), so that only 2/3 of the OHT results in a MHT. The total model MHT and anomalies induced by TCs are displayed on Figure 14. The TC–induced MHT anomalies show a poleward heat export at 20°S and 25°N and an equatorward heat convergence between 10°N and 10°S. This structure is very similar to the one displayed in Jansen and Ferrari (2009). Overall, TCs result in an injection of 73 TW in TC basins of which 27 TW is released in the equatorial band and 46 TW is released poleward (18 TW in the Northern hemisphere and 28 TW in the Southern hemisphere). The overall TC–induced MHT change ends up being very small with respect to the total MHT of the model (Fig. 14): moreover, this MHT anomaly is largely driven by dynamical processes rather than vertical mixing (see Appendix).

Figure 12b summarizes how compensations finally reduce the 483 TW OHU to a very modest ~30-50 TW change of equatorward/poleward heat transport by the meridional oceanic circulation. The largest compensations occur because of heat extraction by TC winds (178 TW) and release of TC–induced subsurface heat storage during winter (188 TW), with latitudinal compensation playing a lesser role (44 TW).

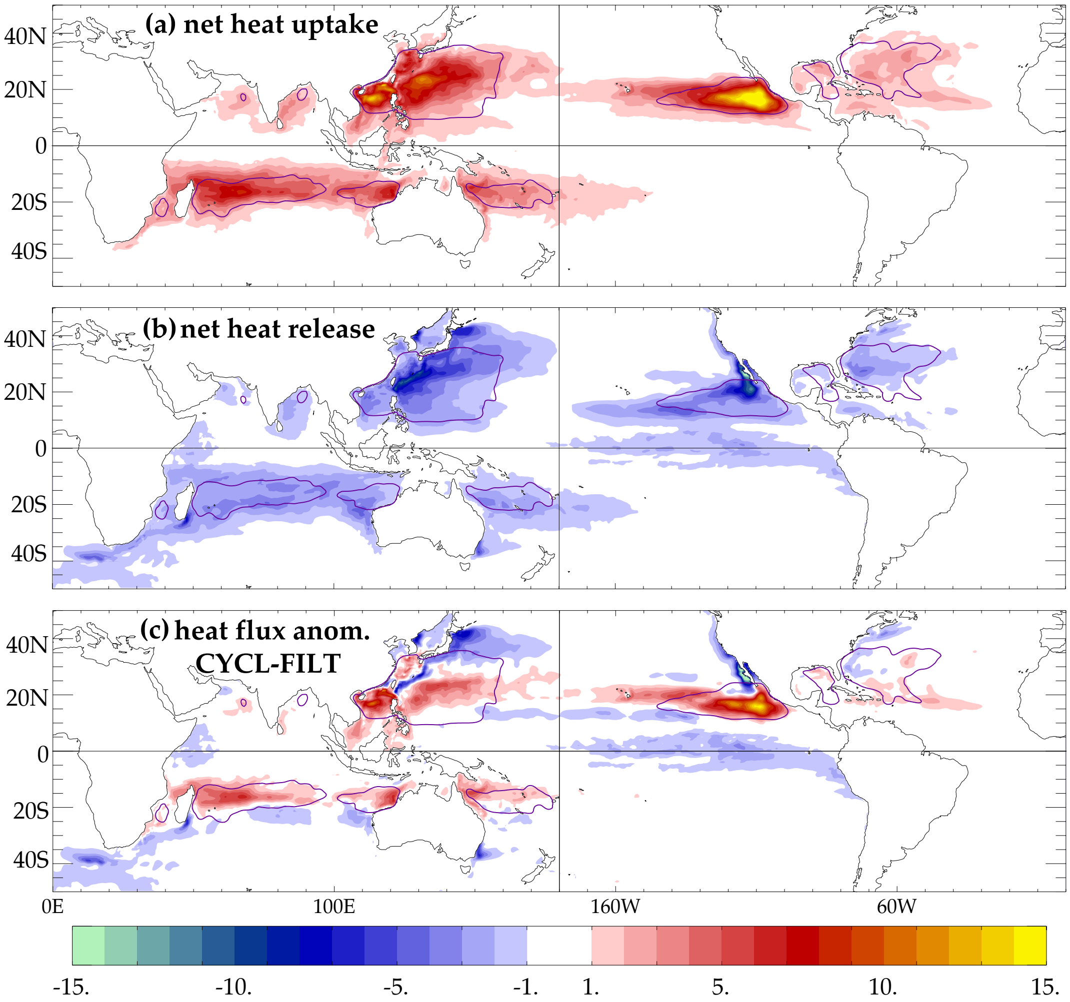

Fig. 13 Average 1983–2007 (**a**) Net TC–induced ocean heat uptake (>0, W/m^2). The net heat uptake is the extra heat entering the ocean after the TCs passage (as the result of the cold wake; OHU) minus the heat extracted from the ocean to the atmosphere during TCs passage (OHE, the enthalpy flux to the atmosphere that fuels the cyclone heat engine). (**b**) Net TC–induced ocean heat release (<0, W/m^2; OHR). The net heat release is the long–term TC–induced heat loss to the atmosphere that results from the re–emergence of subsurface warm mixing–induced anomalies after the end of the cyclonic season. (**c**) CYCL surface heat flux anomaly relative to FILT (W/m^2); it is also the sum of the two fields shown in panel (a) and represents the total effect of TCs on surface heat fluxes, that has to be equilibrated by a change in ocean heat transport (OHT).

5 Conclusion

5.1 Summary

Past studies investigating TCs impact on the ocean mean state and heat transport have focused on the effect of vigorous vertical mixing under TCs. Most of these studies crudely incorporated this effect by enhancing the vertical diffusivity coefficients in rather coarse ocean circulation models. Here, we adopt an alternative approach that also allows taking TC–induced surface fluxes and advection into account. We use an ocean general circulation model at $\frac{1}{2}^{\circ}$ resolution, forced from reconstructed wind perturbations associated with more than 3,000 observed TCs over 1978–2007. Vincent et al. (2012a) show that this forcing strategy allows simulating the TC–induced surface cooling reasonably well. Here, we focus on the climatological impact of the oceanic response to TC passages and perform sensitivity experiments that allow quantifying the respective contributions of TC–induced mixing, advective processes and surface heat fluxes.

All three processes significantly impact the ocean climatology, and have weak nonlinear interactions. TCs wind–driven heat fluxes dominate the large–scale surface cooling that affect the upper 30 m in all TC–basins. TC–induced mixing warms the sub–surface ocean down to 300 m depth by injecting warm surface waters into the thermocline. Our analysis also reveals that TC–induced dynamical processes have a global scale impact on the ocean thermal structure at depth. The wind pattern as-

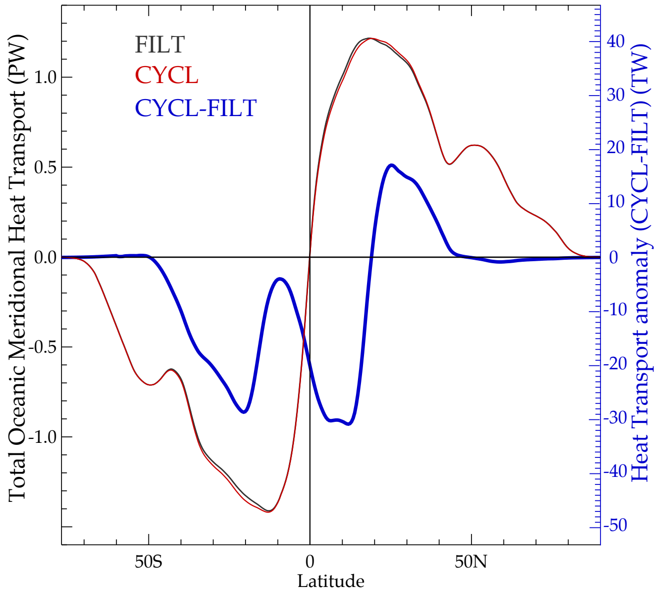

Fig. 14 Total oceanic Meridional Heat Transport in the model in the CYCL and FILT experiment and Meridional Heat Transport anomaly for TC forcing experiment (CYCL) relative to FILT (vertical scale for the anomaly indicated on the right).

sociated with individual TCs indeed results in a strong upwelling along their track compensated by downwelling on both sides of the eyewall. When averaged over the TC season, these signals induce a residual Ekman pumping with a well–defined spatial pattern: upwelling and a sea–level drop in the heart of TC–basins and downwelling and a sea level rise on the northern and southern flanks of these basins. Those sea–level signals expand westward to fill the entire basin as the result of planetary wave propagation.

The salient features of the resulting long–term mean oceanic response to these TC–induced processes are:
(i) a large cooling of the ocean surface in all TC–basins with maximum amplitude in the North Pacific (about -0.4°C). All three processes contribute to this cooling, the TC–induced heat flux being dominant.
(ii) a subsurface warming over 10° latitude bands centered around 25°N and 25°S and maximum in the Northwest Pacific (~0.4°C). The warming is largely due to TC-induced mixing at 30 m to 200 m depth while TC–induced downwelling signals are responsible for the weak deeper warming signal.
(iii) a subsurface cooling over 10° latitude bands centered around 15°N and 15°S. TC–induced upwelling in the heart of the TC–basins is largely responsible for this cooling at depth (mixing induced warming and upwelling induced cooling almost cancel each other around ~100 m depth).
(iv) a weak warming of the equatorial thermocline (0.1°C): two third of this signal arise from near equator TC related downwelling signals. The remaining part is explained by sub–surface equatorward advection of mixing induced warm anomalies.

The TCs impact on the ocean is strongly modulated at seasonal timescale. The summer TC–induced surface cooling does not persist during winter as it is damped within ~2 months. The TC–induced sub–surface warming mostly occurs in the seasonal thermocline. It is therefore largely re–entrained into the mixed layer and released back to the atmosphere during the following winter, as a result of seasonal mixed layer deepening. The TC–induced cooling in summer and warming in winter result in a ~10% reduction of the SST seasonal cycle in TC–prone regions.

Because of the cold surface anomalies left in their wake, TCs induce a large ocean heat uptake of 483 TW (OHU, as estimated by previous studies), but several compensations explain the resulting very modest ~50 TW Poleward Heat Transport (see the summarizing sketch of Fig. 12b). About 2/5 of the 483 TW injected into the ocean in the wake of TCs simply compensate the heat extracted by the TC during its passage (178 TW), so that the heat injection rate to the ocean due to TCs is only 305 TW. As a consequence of the mixed layer depth seasonality, another ~2/5 of the OHU (188 TW) are re–entrained into the mixed layer and released back to the atmosphere in the same region during winter. Only 117 TW hence contribute to the ocean heat transport. When zonally averaged, only 73 TW remain for meridional heat transport, because of latitudinal compensations. 27 TW is transported equatorward and 46 TW is transported poleward. This TC–induced poleward heat transport is very weak compared to the total ocean heat transport in our simulation.

5.2 Discussion

Our results are consistent with most recent studies evaluating the TC–induced ocean heat uptake (OHU) from satellite observations. Sriver et al. (2008) and Jansen et al. (2010) estimated an OHU of 480 and 580 TW, respectively. Nevertheless, over the entire storm footprint, about half of the SST cooling is due to surface latent heat loss at the TC passage (Vincent et al. 2012a), which thus has to be deduced from the OHU to yield the net ocean heat uptake. In their study, Jansen et al. (2010, see their auxiliary material) also estimate the contribution to OHT. They note that TCs occur primarily during summer and early fall, when the mixed layer is generally shallow. As the mixed layer deepens in the following winter, any warm anomaly deposited within the thermocline will be reabsorbed by the mixed layer and lost to the atmosphere. They suggest that only 150 TW (±100%) are injected deep enough (i.e. into the permanent thermocline) to contribute to OHT, in agreement the 117 TW found in the present study.

All the results presented here (and in previous papers) heavily depend upon the maximum depth to which TCs mixing penetrates. If warm sub–surface anomalies are located within the seasonal thermocline, these anomalies cannot efficiently contribute to the ocean heat transport as they are released back to the atmosphere during the following winter. Only temperature anomalies residing in the permanent thermocline can really alter the OHT. There is a clear lack of observational data and modeling studies to allow for an accurate quantification of the TC–induced mixing depths. We however argue that our model results are realistic as the simulated TCs cold wake intensity compares well with observations (Vincent et al. 2012a). Given that this cold wake mainly results from penetrative mixing, a correct mean thermal structure and correct surface cooling amplitude in the model implies that cold water has been entrained from the right depth and that the model mixing depth under TCs is reasonable.

Shallow sub–surface processes may however not be the only way through which TCs impact the ocean. Near–inertial waves generated in the wake of TCs propagate in the thermocline and below and induce deep mixing (e.g. Le Vaillant et al. 2012). Our simulation does not properly resolve such small–scale phenomena. In addition, even if the order of magnitude of TC–induced upwelling is correct in our simulation, increased resolution may yield more realistic TC–induced upwelling/downwelling. Additional experiments at higher resolution are therefore required to confirm the present results and explore further impacts that TCs may have on the ocean and climate.

The present study suggests that TCs do not significantly impact the poleward ocean heat transport. It however suggests that TCs strongly impact the amplitude of the SST seasonal cycle in convective TC–prone regions. The use of a forced model does not allow us to assess the importance of this seasonal TC–related heat flux on the coupled climate system but one can speculate that this seasonal cycle buffering effect may affect the climate system in coupled mode. A methodology to account for this impact of TCs in a coupled system is currently being developed to further investigate this impact.

Acknowledgements Experiments were conducted at the *Institut du Développement et des Ressources en Informatique Scientifique* (IDRIS) Paris, France. We thank the Nucleus for European Modelling of the Ocean (NEMO) Team for its technical support. The analysis was supported by the project *Les enveloppes fluides et l'environnement* (LEFE) CYCLOCEAN AO2010-538863 and European MyOcean project EU FP7.

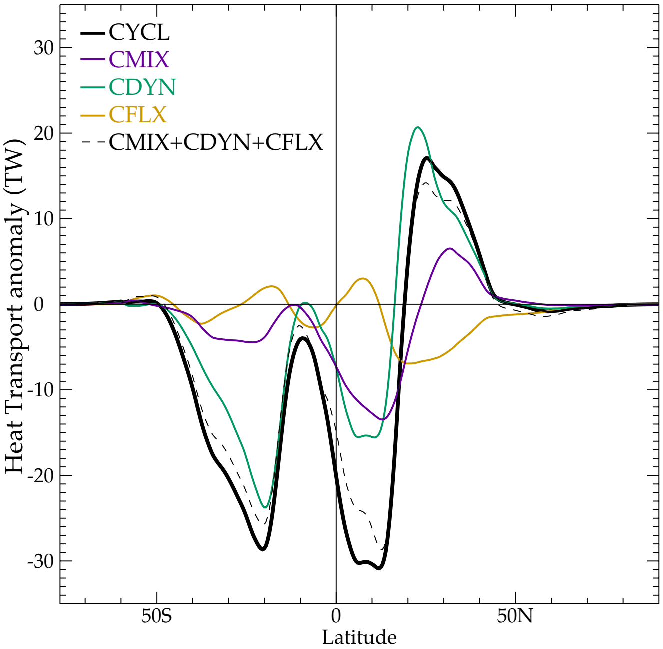

Fig. 15 Meridional Heat Transport anomalies relative to FILT, for TC forcing experiment (CYCL: thick black curve is the same as the blue curve in Fig. 13), TC forcing acting on vertical mixing only (CMIX), on advection only (CDYN) and on surface heat fluxes only (CFLX).

Appendix: Contribution of each process to the MHT anomaly

The linear approximation to separate the respective contribution of the three main TC–induced processes (mixing, dynamical response and surface heat flux) also appears reasonable for heat transport anomalies. The sum of the 3 processes only underestimate CYCL MHT anomalies by ∼10%. The three processes play a significant role in driving TC–induced MHT changes (Fig. 15). The effect of TC–induced mixing is in agreement with previous studies (Emanuel 2001; Sriver et al. 2008; Korty et al. 2008; Jansen and Ferrari 2009). Vigorous vertical mixing below TCs acts to inject heat downward. This heat stored in subsurface is then exported both poleward and equatorward by the oceanic circulation (Jansen and Ferrari 2009).

Our analysis also reveals a poorly discussed contribution of TC–induced dynamical response (Scoccimarro et al. 2011). The mean upwelling generated by TCs induces a surface cooling, even in the absence of TC–induced mixing (Fig. 7c). This cooling is compensated by a net surface heat flux into the ocean, and hence a heat transport change. On poleward and equatorward flanks of TC–basins, the opposite effect occurs: the residual TC–induced downwelling induces a net heat loss. This results in a MHT change that has a similar shape but a much larger magnitude than the one due to TC–induced vertical mixing (Fig. 15). This contribution of TC–induced dynamical processes to the MHT is in agreement with previous results by Scoccimaro et al (2011) who argued that TCs slightly modify the mean ocean circulation with impacts on the MHT.

The contribution of surface heat fluxes acts in opposition to the two previous effects. At the TC passage, surface heat fluxes cool the mixed layer. The subsequent fast warming restores the SST back to its background value, but this warming occurs over a shallower mixed layer, leaving behind a cold anomaly just below it. This cold anomaly is advected poleward and equatorward by the oceanic circulation before being re–entrained in the mixed layer the following winter. The related net surface fluxes are then negative in the re–emergence regions. Their effect on MHT therefore opposes the one related to mixing and advection.

References

1. Axell, L.: Wind-driven internal waves and langmuir circulations in a numerical ocean model of the southern baltic sea. Journal of Geophysical Research **107**, 3204 (2002)
2. Biastoch, A., Böning, C., Lutjeharms, J.: Agulhas leakage dynamics affects decadal variability in atlantic overturning circulation. Nature **456**(7221), 489–492 (2008)
3. Blanke, B., Delecluse, P.: Variability of the tropical atlantic ocean simulated by a general circulation model with two different mixed-layer physics. Journal of Physical Oceanography **23**(7), 1363–1388 (1993)
4. Burchard, H.: Energy-conserving discretisation of turbulent shear and buoyancy production. Ocean Modelling **4**(3-4), 347–361 (2002)
5. Emanuel, K.: Contribution of tropical cyclones to meridional heat transport by the oceans. Journal of Geophysical Research **106**, 14 (2001)
6. Enfield, D., Allen, J.: The generation and propagation of sea level variability along the pacific coast of mexico. Journal of Physical Oceanography **13**, 1012–1033 (1983)
7. Fasullo, J., Trenberth, K.: The annual cycle of the energy budget. part ii: Meridional structures and poleward transports. Journal of Climate **21**, 2314–2326 (2008)
8. Griffies, S., Biastoch, A., Böning, C., Bryan, F., Danabasoglu, G., Chassignet, E., England, M., Gerdes, R., Haak, H., Hallberg, R., et al.: Coordinated ocean-ice reference experiments (cores). Ocean Modelling **26**(1-2), 1–46 (2009)
9. Halliwell Jr, G., Shay, L., Brewster, J., Teague, W.: Evaluation and sensitivity analysis of an ocean model response to hurricane ivan. Monthly Weather Review **139**, 921–945 (2010)
10. Hart, R.: An inverse relationship between aggregate northern hemisphere tropical cyclone activity and subsequent winter climate. Geophysical Research Letters **38**(L01705) (2011)
11. Huang, P., Sanford, T., Imberger, J.: Heat and turbulent kinetic energy budgets for surface layer cooling induced by the passage of hurricane frances (2004). Journal of Geophysical Research **114**(C12023) (2009). DOI 10.1029/2009JC005603
12. Jansen, M., Ferrari, R.: Impact of the latitudinal distribution of tropical cyclones on ocean heat transport. Geophysical Research Letters **36**(L06604) (2009)
13. Jansen, M., Ferrari, R., Mooring, T.: Seasonal versus permanent thermocline warming by tropical cyclones. Geophysical Research Letters **37**(L03602) (2010). DOI 10.1029/2009GL041808
14. Korty, R., Emanuel, K., Scott, J.: Tropical cyclone-induced upper-ocean mixing and climate: Application to equable climates. Journal of Climate **21**(4), 638–654 (2008)
15. Large, W., Yeager, S.: The global climatology of an interannually varying air–sea flux data set. Climate Dynamics **33**, 341–364 (2009)
16. Le Vaillant, X., Cuypers, Y., Bouruet-Aubertot, P., Vialard, J., McPhaden, M.: Tropical storm-induced near-inertial internal waves during the cirene experiment: energy fluxes and impact on vertical mixing. Journal of Geophysical Research (submitted 2012)
17. Madec, G.: NEMO Ocean Engine. Institut Pierre-Simon Laplace (IPSL) (2008)
18. Manucharyan, G., Brierley, C., Fedorov, A.: Climate impacts of intermittent upper ocean mixing induced by tropical cyclones. Journal of Geophysical Research **116**(C11038) (2011)
19. Marsaleix, P., Auclair, F., Floor, J., Herrmann, M., Estournel, C., Pairaud, I., Ulses, C.: Energy conservation issues in sigma-coordinate free-surface ocean models. Ocean Modelling **20**(1), 61–89 (2008)
20. Mellor, G., Blumberg, A.: Wave breaking and ocean surface layer thermal response. Journal of Physical Oceanography **34**, 693–698 (2004)
21. Park, J., Park, K., Kim, K., Youn, Y.: Statistical analysis of upper ocean temperature response to typhoons from argo floats and satellite data. In: Geoscience and Remote Sensing Symposium, 2005. IGARSS'05. Proceedings. 2005 IEEE International, vol. 4, pp. 2564–2567. IEEE (2005)
22. Price, J., Morzel, J., Niiler, P.: Warming of sst in the cool wake of a moving hurricane. Journal of Geophysical Research **113**(C7), C07,010 (2008). DOI 10.1029/2007JC004393
23. Scoccimarro, E., Gualdi, S., Bellucci, A., Sanna, A., Fogli, P.G., Manzini, E., Vichi, M., Oddo, P., Navarra, A.: Effects of tropical cyclones on ocean heat transport in a high resolution coupled general circulation model. J. Climate p. 110322084303027 (2011). DOI 10.1175/2011JCLI4104.1
24. Sriver, R., Goes, M., Mann, M., Keller, K.: Climate response to tropical cyclone-induced ocean mixing in an earth system model of intermediate complexity. Journal of Geophysical Research **115** (2010)
25. Sriver, R.L., Huber, M., Nusbaumer, J.: Investigating tropical cyclone-climate feedbacks using the trmm microwave imager and the quick scatterometer. Geochemistry, Geophysics, Geosystems **9** (2008). DOI 10.1029/2007GC001842
26. Trenberth, K., Fasullo, J.: Water and energy budgets of hurricanes and implications for climate change. Journal of Geophysical Research **112**(D23107) (2007)
27. Vincent, E., Lengaigne, M., Madec, G., Vialard, J., Samson, G., et al.: Processes setting the characteristics of sea surface cooling induced by tropical cyclones. Journal of Geophysical Research **117**(C02020) (2012)
28. Vincent, E., Vialard, J., Lengaigne, M., Madec, G., Masson, S., et al.: Assessing the oceanic control on the amplitude of sea surface cooling induced by tropical cyclones. Journal of Geophysical Research **117**(C05023) (2012)
29. Willoughby, H., Darling, R., Rahn, M.: Parametric representation of the primary hurricane vortex. part ii: A new family of sectionally continuous profiles. Monthly Weather Review **134**(4), 1102–1120 (2006)

Résultats complémentaires

L'étude précédente s'intéresse aux influences dynamiques des TCs sur l'océan mais les TCs peuvent aussi influencer significativement la biogéochimie marine [Bates *et al.* 1998]. La solubilité du CO_2 diminue avec la température ; le refroidissement de surface dans le sillage des TCs permet donc à l'océan d'absorber plus de CO_2 qu'en temps normal. En extrapolant les anomalies de flux air–mer observées sous plusieurs cyclones, quelques études suggèrent que les TCs pourraient avoir une influence importante sur le pompage global de CO_2 par l'océan (e.g. [Bates *et al.* 1998], [Huang & Imberger 2010]).

En forçant le modèle de circulation océanique NEMO couplé au modèle de biogéochimie marine PISCES, la méthodologie mise en place dans ma thèse permet d'étudier l'influence des TCs sur le flux global de CO_2. L'article de [Levy *et al.* 2012] constitue la première étude globale du flux de CO_2 induit par les TCs qui ne s'appuie pas sur des hypothèses pour passer de l'échelle locale à l'échelle globale. Alors que les estimations de flux de CO_2 sous les TCs pris individuellement sont cohérentes avec les observations disponibles, nous concluons que le flux de CO_2 global est 1 à 2 ordres de grandeur inférieur aux estimations précédentes. Deux mécanismes de compensation expliquent en grande partie ce constat (Fig. 5.1). D'une part, les vents du TC au moment de son passage peuvent amener l'océan aussi bien à capter qu'à dégazer du CO_2 en fonction de sa saturation relative par rapport à l'atmosphère. L'effet des TCs dépend donc de la région étudiée ; ils permettent de capter du CO_2 dans les régions où l'océan est sous–saturé et d'en dégazer dans les régions sur–saturées. D'autre part, après le passage du TC, le sillage froid accroit toujours l'anomalie de flux vers l'océan. Cet effet peut s'ajouter à l'effet des vents dans les régions sous–saturées ou compenser l'effet de dégazage associé au vent du TC dans le cas d'un océan sur–saturé en CO_2.

Pour plus de détails, l'article complet peut être trouvé en Annexe D.

Outre leur effet sur les flux de CO_2, des observations satellites montrent que les TCs sont associés à des développements soudains de phytoplancton (*blooms*) modifiant la couleur de l'eau (*e.g.* [Hanshaw *et al.* 2008], [Walker *et al.* 2005] ; Fig. 5.2). Dans l'océan tropical, la stratification thermique empêche les échanges verticaux. Les organismes photosynthétiques vivant près de la surface, où l'énergie solaire est disponible, consomment rapidement les nutriments présents dans l'eau. Les eaux de surface sont donc pauvres en nutriments (et le développement des micro-organismes y est limité) alors que les eaux plus profondes sont riches en nutriments. Par l'*upwelling* et le mélange qu'ils engendrent, les cyclones tropicaux ramènent des nutriments près de la surface et créent de véritables oasis de vie dans leur sillage. Une étude globale de l'influence des TCs sur la biologie est envisagée en utilisant des observations satellitaires (type SeaWiffs) ainsi que le modèle NEMO/PISCES (étude menée par M. Lévy et M. Lengaigne). L'*upwelling* jouant un rôle important

Extrait de [Levy *et al.* 2012]

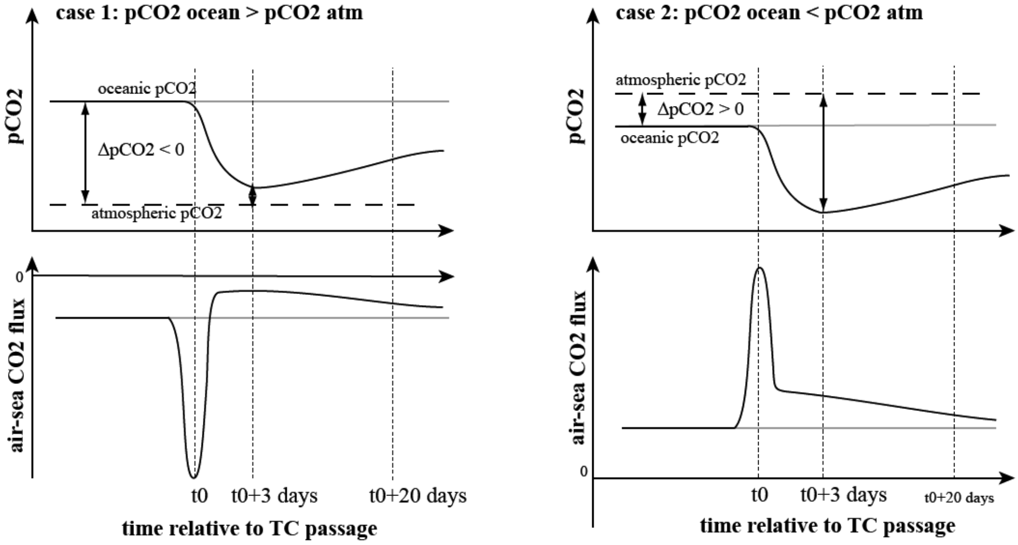

Figure 5.1 – Représentation schématique de l'impact des TCs sur les flux de CO_2 air–mer dans le cas où l'océan est sur–saturé (à gauche) ou sous–saturé (à droite). Les séries temporelles du haut correspondent au ΔpCO_2 air-mer au moment du passage du TC et celles du bas correspondent au flux net de CO_2 (positif vers l'océan).

Extrait de [Walker *et al.* 2005]

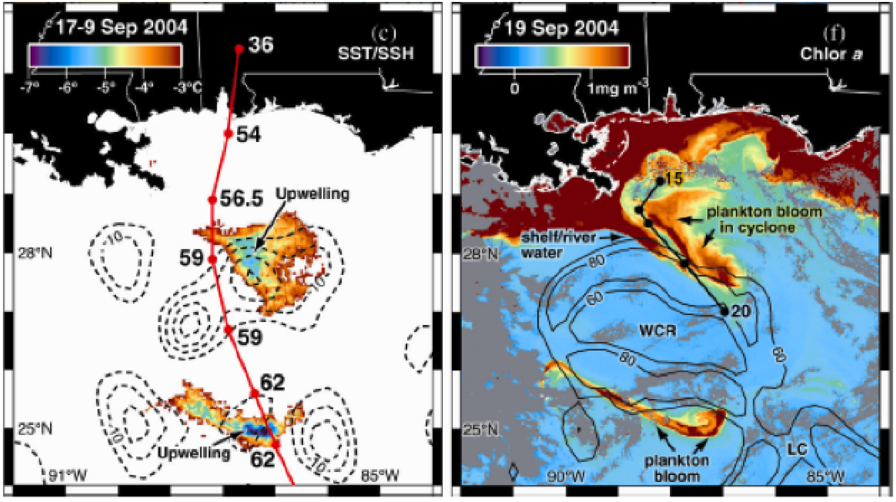

Figure 5.2 – Observations d'anomalie de température et d'altimétrie de surface de la mer (à gauche) entre le 17 et le 9 Sept. ; et de concentration en chlorophylle–a (à droite) après le passage du TC Ivan, le 17 Septembre.

dans cette réponse biologique, un modèle au $^1/_4°$ de résolution devrait être utilisé idéalement. Cependant, le modèle de biogéochimie PISCES étant très gourmand en temps de calcul, le $^1/_2°$ sera utilisé dans un premier temps.

Chapitre 6

Variabilité interannuelle de la Zone de Convergence du Pacifique Sud et implications pour la cyclogenèse

Ce chapitre est basé sur l'article [Vincent *et al.* 2009a].

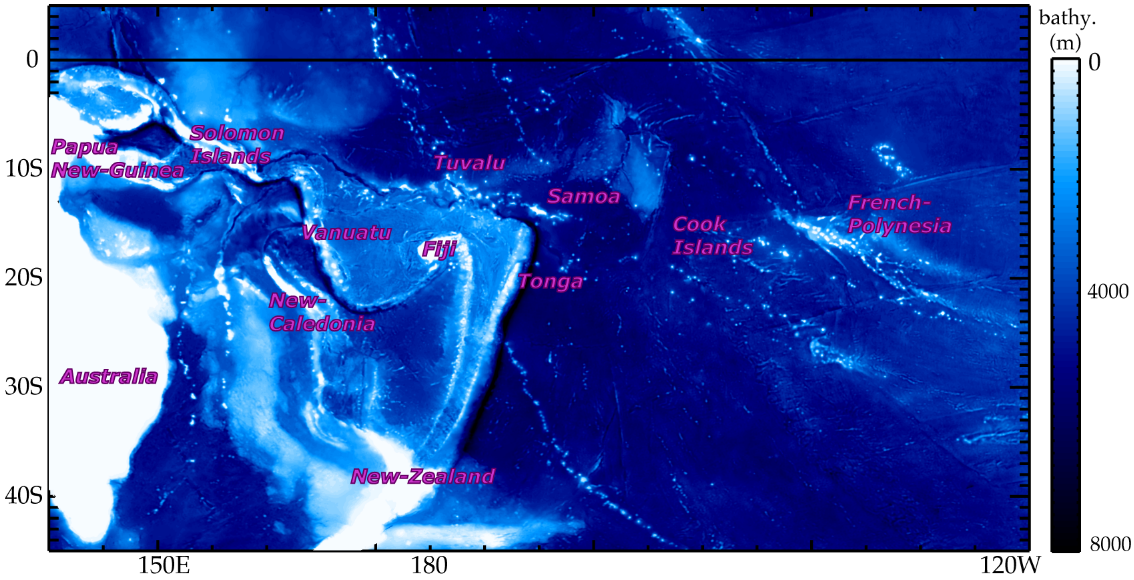

Figure 6.1 – Bathymétrie et principales îles de la région d'étude.

Le chapitre précédent a mis en évidence que les TCs sont susceptibles d'influencer le climat, notamment par l'intermédiaire de leurs interactions avec l'océan. Il est aussi reconnu que le climat et sa variabilité influence les caractéristiques de l'activité cyclonique (1.4.1.1). Par le biais de téléconnexions, le phénomène *El Niño* modifie les variables favorables aux TCs et déplace les régions d'activité cyclonique à l'échelle globale, comme illustré en introduction (1.5.2). Le bassin Pacifique Sud–Ouest se trouve dans la zone d'influence directe d'ENSO. L'activité cyclonique de ce bassin représente ∼12% de l'activité globale et influence les nombreuses îles de la région (Polynésie française, Nouvelle–Calédonie, Fiji, Vanuatu. . .) ainsi que la côte Est australienne (Fig. 6.1). Il existe une littérature abondante concernant l'influence du climat sur les caractéristiques des TCs dans les bassins Nord Atlantique et Nord

Pacifique. La variabilité des TCs dans le Pacifique Sud–Ouest a été moins étudiée malgré un intérêt croissant au cours des dernières années. La variabilité interannuelle de l'activité cyclonique dans la région est particulièrement affectée par ENSO ([Revell & Goulter 1986], [Basher & Zheng 1995], [Kuleshov *et al.* 2009]). La région de cyclogenèse se déplace vers le Nord–Est / Sud–Ouest durant les phases *El Niño / La Niña* (Fig. 6.2). Des études locales et régionales ont permis de détailler l'influence d'ENSO sur la fréquence, l'intensité, et les caractéristiques des trajectoires des TCs. Pendant les années *El Niño*, l'activité cyclonique est largement réduite au large des côtes Est australiennes (Queensland) alors que leur changement de trajectoires amènent plus de TCs sur la côte Nord de l'Australie [Evans & Allan 1992]. Par contraste, les TCs se forment préférentiellement dans la région de Tuvalu et ont des trajectoires plus méridiennes pendant les années *El Niño* ; la région de Fiji est donc plus particulièrement affectée [Chand & Walsh 2009]. La variabilité des TCs dans la région de Fiji est particulièrement favorisée lorsque la vorticité relative est fortement cyclonique ($< -4 \times 10^{-6}$ s^{-1}), la divergence en haute troposphère est élevée ($> 2 \times 10^{-6}$ s^{-1}) et le cisaillement vertical des vents est faible (< 8 $m.s^{-1}$) [Chand & Walsh 2009]. Sur l'ensemble du Pacifique Sud–Ouest, les modifications de vorticité et d'humidité liées à ENSO sont les principaux responsables des modifications interannuelles de l'activité cyclonique, suivies du cisaillement vertical et de la SST [Kuleshov *et al.* 2009]. La SST dans le centre du Pacifique (l'indice Niño 3.4) en début de saison cyclonique est un meilleur prédicteur de l'activité cyclonique sur la côte Australienne que toute autre variable de cyclogenèse locale [Ramsay *et al.* 2008]. L'activité cyclonique dans le bassin est donc pilotée par l'organisation des variables favorables à la cyclogenèse, elle–même largement modulée par ENSO.

Le mouvement de la zone de convergence du Pacifique Sud (SPCZ pour *South Pacific Convergence Zone*) en lien avec ENSO présente une similarité avec celui de la région de cyclogenèse. La zone de convergence est en effet déplacée vers le Nord–Est / Sud–Ouest durant les phases *El Niño / La Niña* à l'échelle interannuelle et est aussi influencée par la variabilité inter–décennale du Pacifique (Fig. 6.3) [Folland *et al.* 2002]. La SPCZ exerce une influence majeure sur les caractéristiques du climat de la région Pacifique Sud–Ouest [Vincent 1994]. Nous faisons donc l'hypothèse que l'étude des caractéristiques de la SPCZ et de sa variabilité est une entrée intéressante pour décrire l'activité cyclonique de la région.

Synthèse de l'article

L'objectif de l'article est de mieux identifier les principaux forçages grande–échelle contrôlant la variabilité interannuelle de l'activité cyclonique dans le Pacifique Sud–Ouest. Dans un premier temps, l'étude décrit l'organisation spatiale des variables favorables à la cyclogenèse autour de la zone de convergence du Paci-

Extrait de [Kuleshov *et al.* 2009]

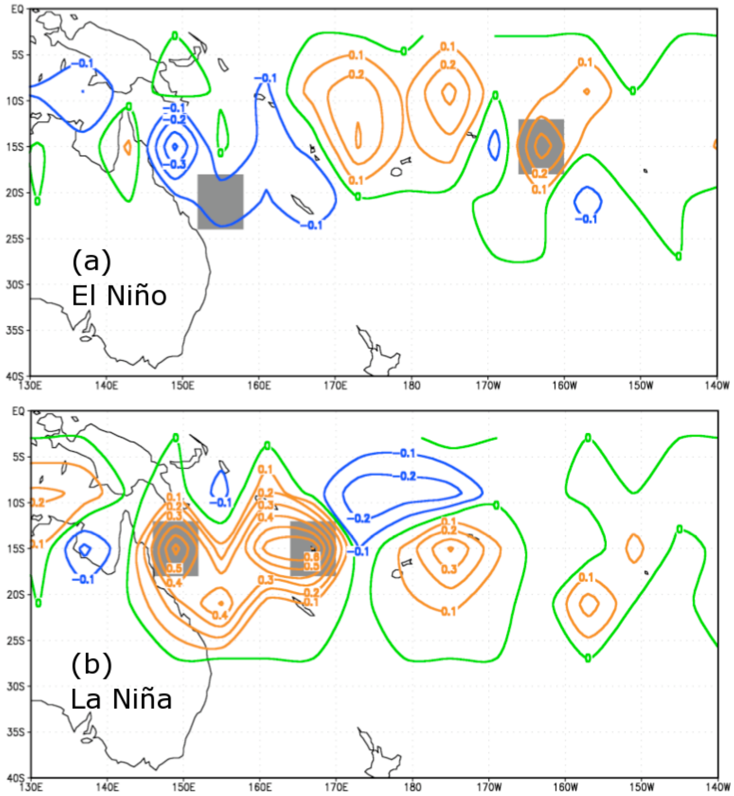

Figure 6.2 – Composites d'anomalies de densité de cyclogenèse annuelles dans des boites de $6° \times 6°$ pendant les années *El Niño* (**a**) et *La Niña* (**b**).

Extrait de [Folland *et al.* 2002]

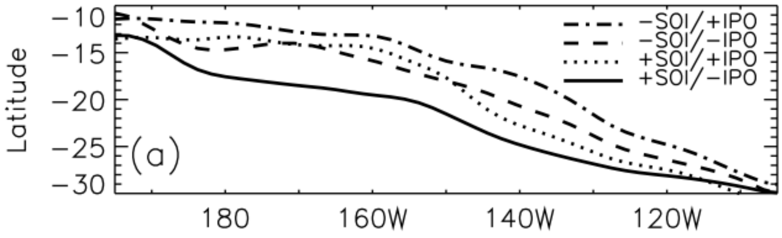

Figure 6.3 – Position moyenne de la SPCZ en fonction des phases d'ENSO (SOI *Southern Oscillation Index*) et de la IPO (*Interdecadal Pacific Oscillation*).

fique Sud (SPCZ). Sa variabilité interannuelle est ensuite étudiée afin de décrire la variabilité de l'activité cyclonique sans présupposer un lien avec ENSO.

La SPCZ est définie par une convection atmosphérique intense qui s'étend de l'équateur au–dessus de la piscine d'eaux chaudes du Pacifique Ouest (*Warm Pool*) jusqu'au centre du Pacifique (140°W) à 30°S. L'activité convective dans la SPCZ persiste tout au long de l'année, mais est particulièrement marquée pendant l'été austral (Décembre–Mars). A l'Ouest de la ligne de changement de date, la zone de convergence est située à la confluence des vents alizés et des vents de la mousson australienne. Le cisaillement horizontal entre les vents de mousson (dirigés vers l'Est) et les alizés (dirigés vers l'Ouest) crée une région de vorticité cyclonique bornée au Nord par la position de la SPCZ (définie ici par son maximum de précipitation) et maximum 6° au Sud de cette position. La SPCZ est une des branches ascendantes de la circulation de Hadley–Walker ; elle correspond donc à un maximum d'humidité troposphérique et à un minimum de cisaillement vertical. L'ensemble de ces caractéristiques fait de la position de la SPCZ un bon résumé des conditions dynamiques et thermodynamiques favorables à l'activité des TCs.

L'étude montre que cette organisation des variables de cyclogenèse autour de la SPCZ est robuste d'une année sur l'autre. Les déplacements interannuels de sa position sont associés à un déplacement cohérent des régions de vorticité cyclonique, de faible cisaillement et de convection profonde. Les variations interannuelles de la position de la SPCZ se révèlent donc être un excellent proxy des variations spatiales des conditions favorables aux TCs.

La densité de cyclogenèse présente en effet un maximum localisé ∼10° au Sud de la SPCZ et la région de genèse reste, d'années en années, bornée au Nord par la position de la SPCZ. Un indice de cyclogenèse (le CYGP) est utilisé pour discuter les mécanismes pilotant cette variabilité. Les modifications de vorticité sont principalement responsables de la modulation interannuelle de la cyclogenèse, particulièrement dans la région de Tuvalu et de la Polynésie française. La partie thermodynamique de l'indice est plus importante dans la région de Fiji et à l'Est de l'Australie.

Cette étude montre que les variations interannuelles de la SPCZ sont principalement associées à la variabilité d'ENSO, conformément aux résultats obtenus par [Folland *et al.* 2002] : ses déplacements méridiens vers le Nord (resp. Sud) sont en général associées aux événements *El Niño* (resp. *La Niña*). Ses déplacements permettent ainsi d'expliquer la variabilité de la cyclogenèse le long des côtes australiennes [Evans & Allan 1992] et dans la région de Fiji [Chand & Walsh 2009]. Notre étude révèle pourtant que les évènements *El Niño* les plus intenses se démarquent de cette description canonique et sont caractérisés par une orientation zonale de la SPCZ. Les cyclones tropicaux se générant dans la région de la Polynésie française ne sont en fait associés qu'aux évènements de zonalisation de la SPCZ (cette observation étant auparavant attribuée au phénomène ENSO en général).

La position de la SPCZ, pilotée par la convergence d'humidité, est principalement influencée par les variations de SST dans le centre du bassin Pacifique. Bien que d'intensité modérée, l'événement *El Niño* de 1991–92, est caractérisé par une position zonale de la SPCZ comme les événements extrêmes (1982–83 et 1997–98) associé à un fort réchauffement du Pacifique central. De même, [Kim *et al.* 2009] ont montré dans un article paru dans Science que les réchauffements dans le Pacifique central et dans le Pacifique Est ont des conséquences différentes sur la cyclogenèse de l'Atlantique. Lors d'études d'impact régionales, il est donc essentiel d'utiliser des méthodes permettant de prendre en compte la diversité des téléconnexions associées à différents types d'ENSO.

Article

Clim Dyn (2011) 36:1881–1896
DOI 10.1007/s00382-009-0716-3

Interannual variability of the South Pacific Convergence Zone and implications for tropical cyclone genesis

**Emmanuel M. Vincent · Matthieu Lengaigne ·
Christophe E. Menkes · Nicolas C. Jourdain ·
Patrick Marchesiello · Gurvan Madec**

Received: 2 October 2009 / Accepted: 26 November 2009 / Published online: 15 December 2009

Abstract The interannual variability of the South Pacific Convergence Zone (SPCZ) and its influence on tropical cyclone (TC) genesis in the South Pacific are investigated using observations and ERA40 reanalysis over the 1979–2002 period. In austral summer, the SPCZ displays four typical structures at interannual timescales. The first three are characterized by a diagonal orientation of the SPCZ and account for 85% of the summer seasons. One is close to climatology and the other two exhibit a 3° northward or southward departure from the SPCZ climatological position. In contrast, the fourth one, that only encompasses three austral summer seasons (the extreme 1982/1983 and 1997/1998 El Niño events and the moderate 1991/1992 El Niño event), displays very peculiar behaviour where the SPCZ largely departs from its climatological position and is zonally oriented. Variability of the western/central Pacific equatorial sea surface temperature (SST) is shown to modulate moisture transport south of the equator, thereby strongly constraining the location of the SPCZ. The SPCZ location is also shown to strongly modulate the atmospheric circulation variability in the South Pacific with specific patterns for each class. However, independently of its wide year-to-year excursions, the SPCZ is always collocated with the zero relative vorticity at low levels while the maximum vorticity axis lies 6° to the south of the SPCZ position. This coherent atmospheric organisation in the SPCZ region is shown to constrain tropical cyclogenesis to occur preferentially within 10° south of the SPCZ location as this region combines all the large-scale atmospheric conditions that favour the breeding of TCs. This analysis also reveals that cyclogenesis in the central Pacific (in the vicinity of French Polynesia) only occurs when the SPCZ displays a zonal orientation while this observation was previously attributed to El Niño years in general. Different characteristics of El Niño Southern Oscillation (ENSO)-related Pacific equatorial warming are shown to impact differently on the SPCZ position, suggesting that for regional scales, such as the South Pacific, the SPCZ classification is more appropriate than a simple ENSO index to characterize TC interannual variability. These findings suggest that forecasting the strength of El Niño through SST variations in the eastern Pacific may not be sufficient to accurately predict cyclogenesis in the South Pacific, especially east of the dateline.

Keywords South Pacific Convergence Zone · Interannual variability · Tropical cyclone · El Niño Southern Oscillation

---

E. M. Vincent · M. Lengaigne · C. E. Menkes · G. Madec
Laboratoire d'Océanographie et du Climat: Expérimentation et Approches Numériques (LOCEAN), IRD/UPMC/CNRS/MNHN, Paris, France

M. Lengaigne
National Institute of Oceanography, Goa, India

C. E. Menkes · N. C. Jourdain · P. Marchesiello
Institut de Recherche pour le Développement, Nouméa, New Caledonia

P. Marchesiello
Laboratoire d'Etudes en Géophysique et Océanographie Spatiale (LEGOS), CNES/CNRS/UPS/IRD, Toulouse, France

G. Madec
National Oceanographic Centre, Southampton, UK

E. M. Vincent (✉)
LOCEAN/IPSL, UPMC, Boîte 100, 4, place Jussieu,
75252 Paris Cedex 05, France
e-mail: emmanuel.vincent@locean-ipsl.upmc.fr

1 Introduction

The South Pacific Convergence Zone (SPCZ) is characterized by a band of high cloudiness, strong convective precipitation and low-level convergence extending from the west Pacific warm pool south-eastward towards French Polynesia (Fig. 1; see review by Vincent 1994). It is the only intertropical convergence zone (ITCZ) of the southern hemisphere present all year round, although it is best developed during austral summer. It has been suggested that the summertime SPCZ consists of a zonal portion located over the western Pacific warm-pool region and a diagonal portion oriented along a northwest-southeast axis east of 170°E (Vincent 1994). The climatological characteristics of its eastern portion have been thought to rely on the interactions with higher latitude depressions (Kiladis et al. 1989) and on the existence of a dry zone in the south-eastern Pacific, controlled by the presence of the Andes (Takahashi and Battisti 2007). On higher frequency time-scales (daily to weekly) the zonal dry air inflow associated with trade wind strength has been shown to control the position of the SPCZ eastern margin (Lintner and Neelin 2008). On the other hand, the climatological characteristics and position of its western portion is likely to be influenced by both the underlying sea surface temperature (SST) gradients and the land–ocean distribution (Kiladis et al. 1989). The western part of the SPCZ is strongly influenced by the vast monsoon system that affects the Indian Ocean and Australian region, with monsoon winds extending eastward until the dateline in the SPCZ region (Fig. 1).

The SPCZ plays a significant role in global climate and is one of the major features of the southern hemisphere climate (Kiladis et al. 1989; Vincent 1994). Because the gradients of precipitation in the vicinity of the SPCZ are very strong, small displacements in its mean position can imply drastic changes in precipitation regimes for islands in the region (Gouriou and Delcroix 2002). Its location not only strongly constrains the hydrological cycle but is also the breeding ground of tropical cyclones (TCs) in the South Pacific. Despite the SPCZ's significance to tropical climate, its characteristics, dynamics and variability have attracted relatively little attention. The interannual variability of the SPCZ location and TC activity in the Australian/western Pacific have been investigated mainly with respect to their relationship with El Niño Southern Oscillation (ENSO). It has been shown that El Niño (La Niña) events tend to occur accordingly with a north-eastward (south-westward) displacement of the SPCZ (Trenberth 1976; Folland et al. 2002) and of a similar displacement of the TC genesis region in the south-western Pacific (Revell and Goulter 1986; Hastings 1990; Basher and Zheng 1995; Kuleshov et al. 2008), while decreasing (increasing) TC activity near Australia (Nicholls 1985; Holland et al. 1988; Evans and Allan 1992; Ramsay et al. 2008). Although the SPCZ and the region of TC activity in the southwest Pacific are displaced in a similar fashion during ENSO events, the detailed mechanisms and the extent to which SPCZ controls the large scale environment favouring cyclonic activity have not yet been investigated. In addition, the characteristics of El Niño events vary widely from one event to another, and the influence of this diversity on the SPCZ location and TC activity has been overlooked in the aforementioned studies. Differentiating extreme cases (1982/1983 and 1997/1998 events) from other El Nino events has been shown to be critical since the two types of event display contrasted predictability, spatial patterns and mechanisms (Vecchi 2006; Lengaigne and Vecchi 2009). In addition, the location of the maximum equatorial warming has been also shown to strongly modulate the atmospheric teleconnections (Ashok et al. 2007; Trenberth and Smith 2006) and to have different impacts on cyclonic activity in the Atlantic basin (Kim et al. 2009). Evidently, El Niño strength classification is subjective and is usually based on simple indices such as the southern oscillation

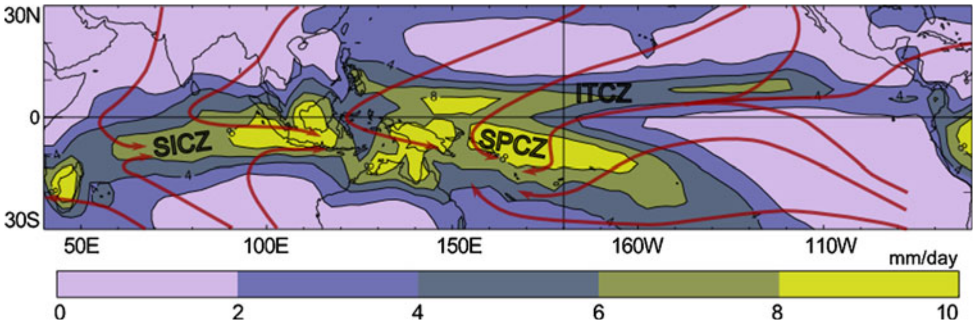

Fig. 1 Indo-Pacific climatology of December–January–February (DJF) precipitation (GPCP). Convergence zone positions are shown: InterTropical Convergence Zone (*ITCZ*), South Pacific Convergence Zone (*SPCZ*), South Indian Convergence Zone (*SICZ*). *Dark red arrows* are a few streamlines extracted from the ERA40 DJF-mean surface winds in the region; we outline the vast monsoon system affecting the Indian Ocean, Australia and western part of the SPCZ

index (SOI) or eastern equatorial Pacific SST anomalies, and a large number of thresholds have been used to account for the definition and strength of El Niño while the spatial patterns of warming are rarely taken into account (Ashok et al. 2007). Alternatively, El Niño strength can be defined by the characteristics of its regional impacts. Redefining regional indices accounting for the local effect of ENSO is shown to be appropriate for regional studies as illustrated by Wang and Hendon (2007). Our study investigates the influence of ENSO on TC activity in the South Pacific through its regional influence on the SPCZ. It will allow a better understanding and description of interannual cyclogenesis variability in the region.

The objectives of this study are therefore (1) to provide a detailed description of the interannual variability of the SPCZ (without presupposing a link with ENSO), (2) to understand the extent to which the SPCZ location modulates cyclogenesis activity and (3) to differentiate changes in TC activity in the South Pacific region depending on El Niño characteristics. The paper is structured as follows: Sect. 2 describes the data and methods used to describe the SPCZ. Section 3 focuses on the description of SPCZ interannual variability, i.e., the variability of its position and dynamical structure and the forcings driving this variability. The implications of the SPCZ displacement and related dynamical variables on the genesis of TCs are investigated in Sect. 4. A summary and discussion are given in the last section.

2 Characterization of the SPCZ: data and methods

Although the SPCZ can be seen throughout the year, it is only fully developed from November to April. In December, January and February (DJF), the SPCZ reaches its maximum extension and the climatological precipitation field shows little month-to-month variability in magnitude and geographical pattern. DJF composites of precipitation fields are therefore used to characterise the austral summer SPCZ of year $n/n+1$ and to examine its interannual variability.

2.1 Localization of the SPCZ

To define the position of the SPCZ, we seek to select observations that are homogeneous (satellite acquired) and span a period long enough to encompass the largest number of El Niño/La Niña events. In previous studies, the SPCZ has been defined by the maximum of cloud cover or minimum in outgoing longwave radiation (OLR) using satellite-based observations, or by surface wind convergence using global atmospheric reanalysis. Observed surface convergence can be obtained using the European Remote Sensing Satellite (ERS-1) scatterometer and the NASA Quick Scatterometer (QuickSCAT) but this combined satellite wind field is only available from 1993 onwards, which is too short a period for the purpose of this study. Cloudiness or precipitation products are available at least from 1984 onwards and can be used to locate the SPCZ. Cloud cover is available from the International Satellite Cloud Climatology Project data set (ISCCP) or through OLR data (a proxy for deep convection) from NOAA. Precipitation is available in the data set from the Global Precipitation Climatology Project version 2 (GPCP; Adler et al. 2003) or the Climate Prediction Center Merged Analysis of Precipitation (CMAP; Xie and Arkin 1997).

Estimations of the climatological location of the SPCZ using the various cloud and precipitation data set give very similar results between 160°E and 160°W (Fig. 2a), but display differences east of 155°W between cloud cover and precipitation based estimations. The discrepancies may be due to the larger sensitivity of total cloud cover and OLR to low level clouds in the extra-tropical south-eastern end of the SPCZ. We carry out further analysis using the precipitation maximum definition in the rest of this study because the two available datasets (GPCP and CMAP) allow us to assess the degree of confidence in the data describing the SPCZ. GPCP will be used as our reference dataset as it has been shown to give more realistic tropical precipitation magnitudes over the ocean (Yin et al. 2004). However, the main results of this study remain valid when cloud cover and OLR data are used to define the SPCZ position.

For each DJF season, the mean SPCZ position at each longitude is taken as the position of the maximum precipitation between the equator and 30°S. The line obtained by joining the latitude of the SPCZ at each longitude is referred to as the SPCZ position. The SPCZ region is

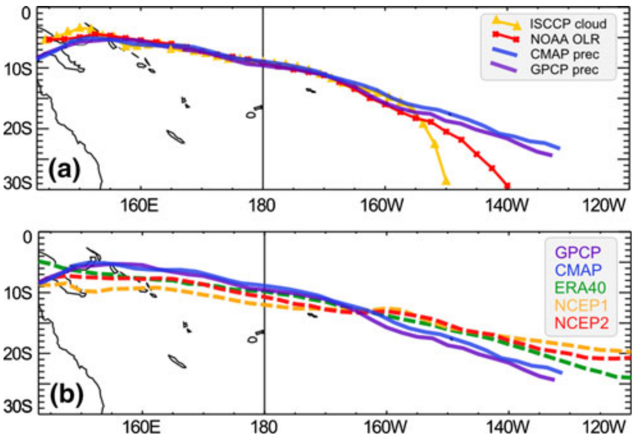

Fig. 2 **a** Mean position of the SPCZ as determined by different proxies for the period 1979–2002 (except for ISCCP on 1984–2002 period). **b** Comparison of SPCZ position in reanalyses and observations. In this figure, the SPCZ location is defined as the position of the maximum of the corresponding field (minimum for the OLR field) between the equator and 30°S

Table 1 SPCZ mean latitude in its central region and mean slope (as determined from a linear fit to the SPCZ position). Standard deviation of the latitude of the SPCZ in its central region. Correlations of the averaged latitude and slope of the SPCZ of each reanalysis to GPCP on the 1979–2002 DJF seasons

	GPCP	CMAP	ERA40	NCEP1	NCEP2
SPCZ mean latitude in 160°E–140°W (°S)	12.2	11.9	11.3	12.5	12.3
SPCZ mean slope (°S/°E)	0.27	0.26	0.2	0.14	0.17
SPCZ standard deviation (in 160°E–140°W)	3.2	3.1	2.3	1.6	2.4
Correlation with GPCP of					
Lat of the SPCZ (160°E–140°W)	1	0.98	0.89	0.83	0.79
Slope of the SPCZ	1	0.81	0.75	0.17	0.54

defined as the area where DJF mean precipitation is higher than 6 mm/day. Points where precipitation is lower than this threshold are not included in the SPCZ line.

2.2 Choice of the reanalysis

We rely on atmospheric reanalysis products to describe the dynamical structure of the SPCZ as they are available over extended periods (from at least 1979) and provide a dynamically consistent view of the large-scale convergence zone and its variability.

The climatological characteristics of the SPCZ location given by the precipitation fields of the two reanalyses NCEP1 and NCEP2 from NCEP/NCAR (National Center for Environmental Prediction/National Center for Atmospheric Research) and by the reanalysis ERA40 from EC-MWF (European Center for Medium-range Weather Forecasts) are displayed in Fig. 2b and summarized in Table 1. The mean latitude of the SPCZ in its central region is found to be close to the observed one for all reanalyses. All reanalysis products, however, underestimate the SPCZ slope determined from satellite data (Table 1). This "zonal bias" is less pronounced in ERA40 compared to NCEP1 and NCEP2, and NCEP1 and NCEP2 display a spurious "double-ITCZ" pattern in the eastern Pacific, especially in 1983/1984, 1984/1985, 1987/1988, 1998/1999 (not shown).

The interannual meridional displacement of the SPCZ in these datasets is compared to GPCP by correlating its zonal mean latitude between 160°E and 140°W (Table 1). CMAP and GPCP display very coherent temporal variability in phase and amplitude. In comparison, all reanalysis products underestimate the amplitude of the SPCZ position interannual variability by about 30% (Table 1). However, the variability of the SPCZ position and slope is better reproduced in ERA40 than in NCEP reanalyses (Table 1). Based on these findings, ERA40 is chosen in the following to illustrate the dynamical organisation of the SPCZ (part 3.3). The period used for the whole study will span the years 1979–2002 as it is the common period of precipitation observations and ERA40 availability.

3 Interannual variability of the SPCZ

3.1 Precipitation variability in the Southwest Pacific

The main modes of interannual variability affecting the SPCZ are extracted by applying a rotated Empirical Orthogonal Function analysis (using the varimax method described in Reyment and Jörekog 1993) to the austral summer precipitation in the South Pacific region (155°E–80°W/0–30°S).[1] Results are shown for GPCP in Fig. 3. Very similar modes are obtained using CMAP or ERA40 as illustrated by the high correlation of their first two principal components (PCs) to GPCP (Table 2). The first and second EOFs represent, respectively, 52 and 17% of the total variance in observations (with all other modes lower than 7%). Both EOF1 and EOF2 display opposite variability on each side of the mean SPCZ position with largest amplitude, respectively, in the western and eastern parts of the SPCZ (Fig. 3a, b). As seen in Fig. 3c, most years only project onto the first EOF, implying that the precipitation variability is mostly characterised by a north–south movement of the SPCZ in the 160°W–160°E region. Three years only (1982/1983, 1991/1992 and 1997/1998) have positive contributions to both PC1 and PC2. The resulting precipitation pattern is characterized by strong positive precipitation anomalies extending throughout the equatorial Pacific. This EOF analysis therefore reveals that the interannual variability of the SPCZ position differs in its western and eastern portions (described, respectively, by EOF1 and EOF2). To specify the longitude of the transition between these western and eastern behaviours, an EOF analysis on the latitude of the SPCZ at each longitude is performed. It displays a first mode characterising the north–south displacement of the SPCZ and a second mode opposing the variability of the SPCZ location east and west of 175°W (not shown). Describing the SPCZ movement using a single index will hence mainly capture the vari-

---

[1] The same analysis performed with the eastern boundary at 120°W and 140°W yields very similar results.

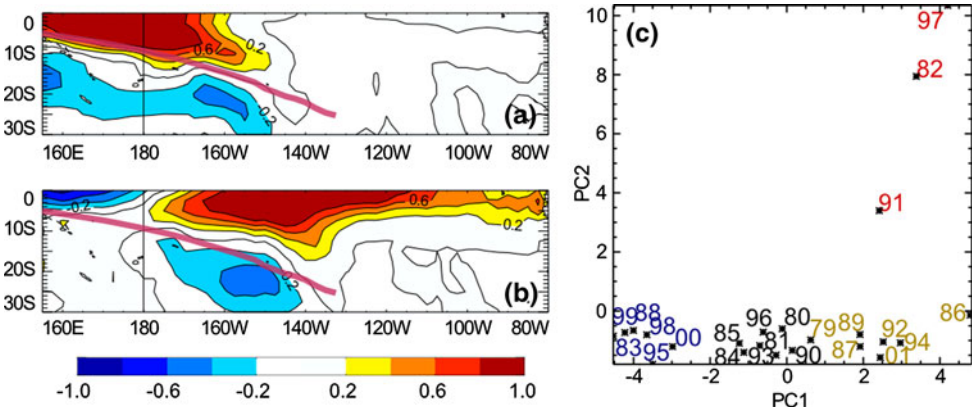

Fig. 3 **a**, **b** First and second EOFs of GPCP DJF precipitation on the period 1979–2002, the *thick purple line* indicates the mean position of the SPCZ, and **c** coordinates of each year on these two-first modes (*colors* show the class to which each season belongs, see Fig. 4); year *n* stands for the DJF season Dec. year *n* to Feb. year *n* + 1

Table 2 Percent variance of the two-first EOFs for ERA40 reanalysis and observations, correlation of the two-first PCs coordinates with respect to GPCP ones

	GPCP	CMAP	ERA40
EOF1 (% variance)	52	53.6	53.5
EOF2 (% variance)	17.2	15	15.6
PC1 correlation	1	0.97	0.97
PC2 correlation	1	0.96	0.92

All correlations significant at the 95% level with respect to a two-tailed Student's *t* test

ability related to the first EOF. To account for the information contained in both first and second EOFs, we define two indices describing eastern and western regions: latW is the SPCZ latitude averaged between 160°E and 180° and latE is the SPCZ latitude averaged between 170°W and 150°W).

A classification using an ascendant hierarchical clustering (AHC; Ward 1963) method applied to these two variables (latW and latE) is then used to summarize the interannual variability of the SPCZ position. The AHC computes a hierarchical clustering of SPCZ characteristics for the 23 austral summer seasons considered in the analysis. At the first step, there are 23 clusters; then, at each step, the two closest clusters are aggregated according to the Ward criterion with Euclidean distances as the dissimilarity measure. This method ensures a classification in which the elements of a given cluster are as close as possible to each other and as far as possible to elements of other clusters. The resulting dendrogram (or classification tree) shown on Fig. 4a depicts the partitioning from 23 clusters at the bottom of the tree to a unique cluster at the top of it. Each leaf of the tree is a subset of the 23 seasons; each node represents the conjunction of two clusters, the height of its branch being representative of the distance between two clusters. The last important jump of inter-cluster distance as the number of classes increases is seen for a division into four clusters (Fig. 4b). Seasons associated to each of these four classes are highlighted by different colours in Figs. 3c and 4a. Clusters determined by this method do also show up in the PC1–PC2 plane (Fig. 3c) thereby giving confidence that our classification is robust. This observation also confirms that the SPCZ location (on which the classification is performed) accurately summarizes the large-scale precipitation variability in the tropical South Pacific (on which the EOFs are constructed). The same AHC applied to PC1–PC2 coordinates instead of latW–latE indices gives indeed similar clusters. In the following, we will refer to the classification based on latW–latE indices that are, by construction, more representative of the SPCZ location than the EOF analysis (as the EOF analysis also accounts for variations in precipitation intensity within the SPCZ and at the equator). This classification is stable when using CMAP or ERA40 datasets, as well as when the boundaries of the western and eastern boxes are slightly changed.

The SPCZ location for each of the 4 classes is displayed on Fig. 5a. The "negative", "neutral" and "positive" classes are similar to the composites described in Folland et al. (2002). Within these classes, the SPCZ location is shifted in latitude with little change in its slope. In contrast, the "asymmetric" class has never been investigated in detail and is characterized by the SPCZ becoming almost zonal from 150°E to 140°W and merging with the ITCZ that is no longer observed in the North Pacific, west of 160°W (not shown). The corresponding cluster contains only three seasons (1982/1983, 1991/1992, 1997/1998) and its specificity will be discussed in detail in the following section.

Changes in the position of the SPCZ are also associated with modifications of total precipitation fluxes in the SPCZ region. As seen on Fig. 5b, there is a clear increase of the total precipitation flux from "neutral" to "positive" and "asymmetric" years with 50% more precipitation during

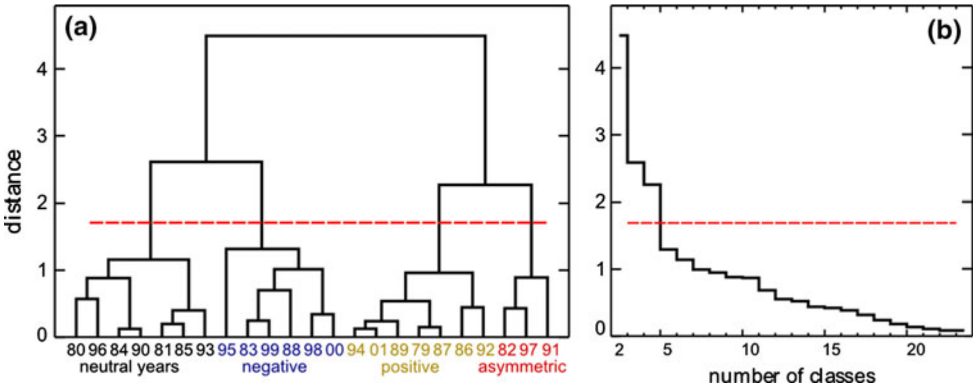

Fig. 4 **a** Dendrogram resulting from the ascendant hierarchical classification (*AHC*) performed on the two variables: latW and latE. **b** Inter-cluster distance (in the centred and normalized space of coordinates on the two variables) as a function of the number of classes. *Red dashed line* indicates the cutting level; four clusters are identified

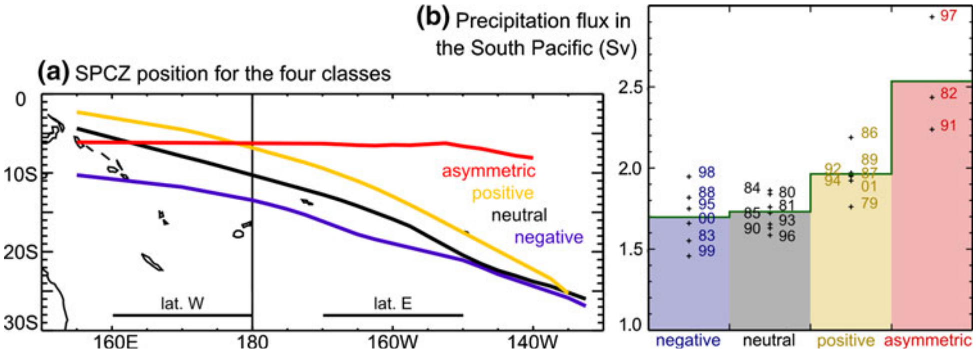

Fig. 5 **a** Positions of the SPCZ from GPCP for each class. *Red* "asymmetric", *orange* "positive", *black* "neutral" and *blue* "negative" years. **b** Total precipitation flux (in Sverdrup) in the SPCZ region (143°E–120°W/0–30°S)

the latter with respect to "neutral" conditions, while "negative" years show little difference from the "neutral" case. The increase of total precipitation is mainly due to the greater extension of the precipitating area (the SPCZ region) rather than an intensification of it. Indeed the area receiving a flux >6 mm/day shows a similar 50% increase between "asymmetric" and "neutral" years while the precipitation rate within the SPCZ varies by <10% between classes.

3.2 SST forcing of SPCZ interannual variability

In the previous section, a description of the SPCZ interannual variability has been conducted outside of any consideration of ENSO. In this section, we investigate the relation to ENSO and associated SST forcing of SPCZ displacements.

The high value of the correlation coefficients between the SPCZ latitude and the Niño 3 or Niño 3.4 index (Table 3) confirms that SPCZ interannual variability is primarily related to ENSO. However, the SPCZ position in latW is not as well correlated with the classical Niño indices (Niño 3 and Niño 3.4) as in latE (Table 3), mainly because the three "asymmetric" events strongly degrade the correlation. Indeed, in contrast to the "neutral" to "positive" tendency, the SPCZ in latW moves toward the south for these years and is found around 6°S (Figs. 5a, 6a) contributing to the zonal orientation of the SPCZ. When discarding these three years from the calculation, the correlation between latW and Niño 3 (Niño 3.4) SST increases to 0.74 (0.81). In agreement with Folland et al. (2002), El Niño (La Niña) years are generally found to drive a northward (southward) displacement of the SPCZ (Table 4). However, SPCZ displacements during El Niño events are more diverse than previously thought: El Niño years separate into two distinct clusters, displaying either a northward shift or a zonal alignment of the SPCZ position. In addition, this relationship is not systematic: three neutral ENSO years display a northward excursion of the SPCZ (1992/1993, 1989/1990 and 2001/2002), which is usually

Table 3 DJF correlation coefficients between Niño 3, Niño 3.4 and Niño 4 indexes (HadiSST) and SPCZ position proxies: latW and latE (GPCP); the fourth and fifth rows present the correlations of SPCZ latitude with SST indices that were found to yield the highest correlations (in bold in the table, see text) with the SPCZ indices in latW and latE, respectively

corr coef	latW	latE
Niño 3	0.56	0.81
Niño 3.4	0.71	0.83
Niño 4	0.84	0.70
SST in 170°E–170°W/5°N–5°S	**0.87**	0.60
Warm Pool eastern margin	0.64	**0.92**

All correlations significant at the 95% level with respect to a two-tailed Student's *t* test

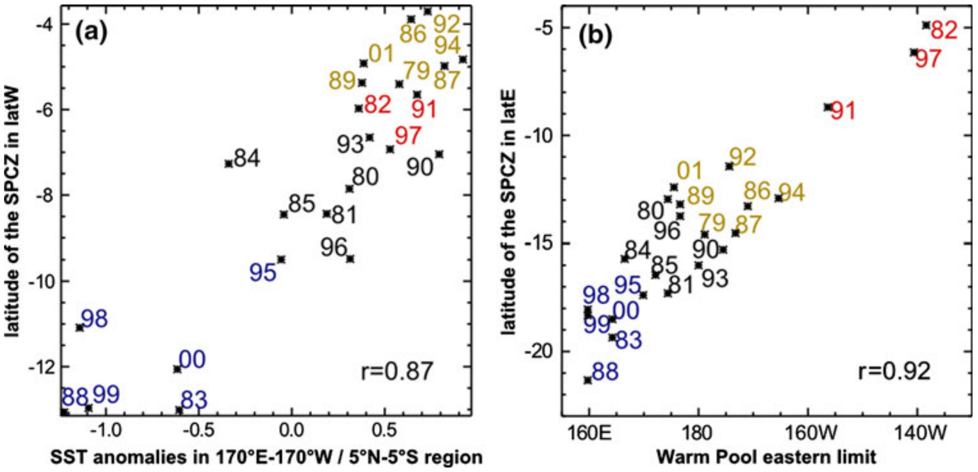

Fig. 6 Scatter plot of DJF latitude of the SPCZ **a** in latW versus SST anomalies in the 170°E–170°W/5°N–5°S region and **b** in latE versus easternmost extension of the Warm Pool at the equator (as marked by the 29°C SST isotherm in HadiSST dataset). These two SST indices are chosen as they are the ones that yield the highest correlations with latW and latE indexes

Table 4 Comparison of years belonging to the classes formed by the classification on SPCZ position (left) and on the Niño 3.4 index (right)

SPCZ position classification	ENSO classification
"Asymmetric" years	Niño years
1982/1983, 1991/1992, 1997/1998	1982/1983, 1997/1998, 1991/1992, 1986/1987, 1994/1995, 1987/1988, 1979/1980
"Positive" years	Neutral ENSO years
1992/1993, 1986/1987, 1994/1995, 2001/2002, 1987/1988, 1989/1990, 1979/1980	1992/1993, 1990/1991, 1989/1990, 1993/1994, 1981/1982, 2001/2002, 1980/1981, 1996/1997, 1985/1986
"Neutral" years	Niña years
1980/1981, 1984/1985, 1990/1991, 1996/1997, 1985/1986, 1981/1982, 1993/1994	1995/1996, 1983/1984, 2000/2001, 1984/1985, 1998/1999, 1999/2000, 1988/1989
"Negative" years	
1995/1996, 1998/1999, 2000/2001, 1999/2000, 1983/1984, 1988/1989	

Years are ordered by the amplitude of the mean SPCZ displacement (left) and by the amplitude of Niño 3.4 SST anomaly (right)

The monthly temperature averaged over the Niño 3.4 region 5°S–5°N, 170°W–120°W is used to characterize the El Niño–La Niña phenomenon. El Niño (La Niña) years are defined as those when the DJF Niño 3.4 SST anomaly is greater than (lower than) ½°C as defined by NOAA in http://www.cpc.noaa.gov/products/analysis_monitoring/ensostuff/ensoyears.shtml

typical of El Niño years, while one La Niña event (1984/1985) corresponds to a "neutral" SPCZ season, with a SPCZ close to the climatological position (Table 4).

LatW and latE are both strongly correlated to the equatorial SST variability but the location of SST with which the strongest correlations are found differs between the two indices. While for latW the strongest correlations are found around the dateline (170°E–170°W/5°N–5°S; Table 3; Fig. 6a), latE displays the strongest positive correlations with SSTs in the central Pacific (170°W–120°W/5°N–5°S, i.e., Niño 3.4 region; see Table 3). This latter region experiences large fluctuations of the eastern edge of the warm pool during the ENSO cycle. The eastern edge of the warm pool at the equator (here defined by the longitude of the 29°C isotherm) arises as a better predictor of eastern SPCZ latitude (latE) than Niño 3 or Niño 3.4 indices (Table 3; Fig. 6b).

In Fig. 7c, we note that the SPCZ is located over a tongue of warm water extending from the warm pool south-eastward into the South Pacific. Associated with SPCZ variability, the SST pattern is deeply modified (Fig. 7a, b, d). SST anomalies have two major impacts of interest in the definition of the SPCZ: they drive surface wind anomalies, and they modulate the amount of humidity available in the lower layers of the troposphere. Because tropical convective regions are primarily forced by moisture convergence, analysing the changes in wind patterns and moisture convergence in relation to the SPCZ variability allow us to better understand the mechanism of SST forcings driving the variations of SPCZ location. For the "positive" cluster, the slight eastward shift of the warm pool eastern boundary results in maximum SST anomalies around 160°W driving low level wind anomalies in the western Pacific west of 160°W that are maximum just

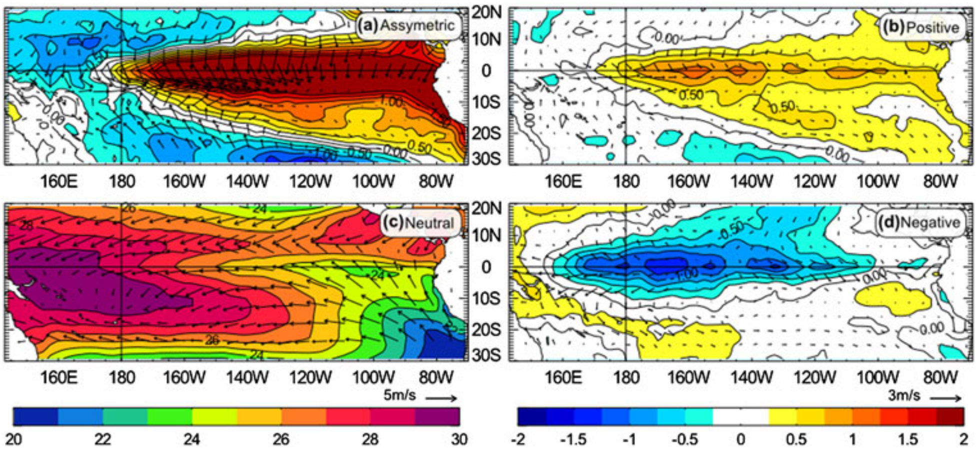

Fig. 7 Sea surface temperature (*SST*) for **c** the “neutral” class and **a**, **b**, **d** SST anomalies with respect to the “neutral” class of the “asymmetric”, “positive”, and “negative” classes, respectively. *Black arrows* are winds on the 850 hPa level in (**b**) and anomalies from the “neutral” winds on other panels

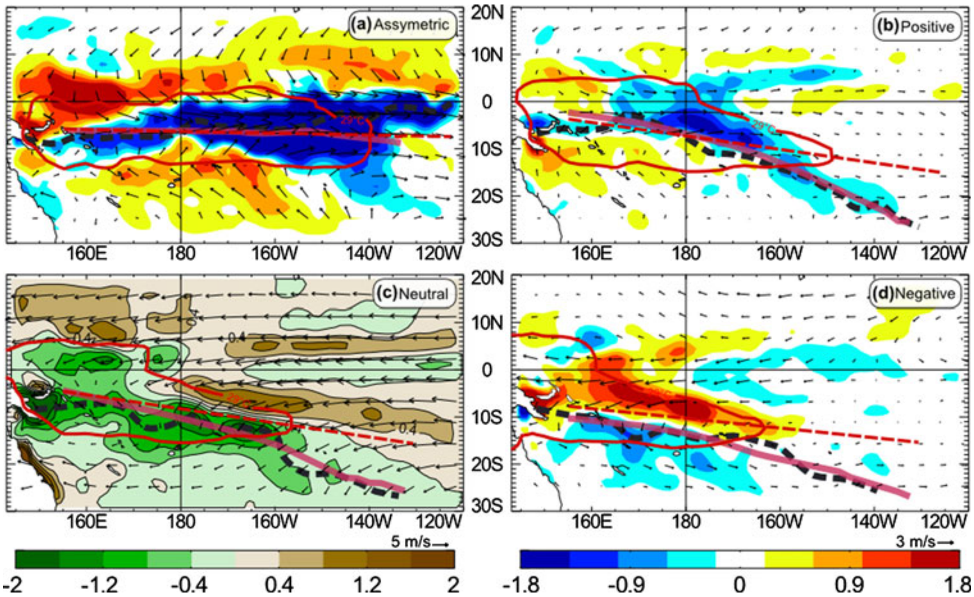

Fig. 8 Moisture divergence at 850 hPa $\vec{\nabla}(q.\vec{v})$ (in g kg^{-1} day^{-1}; with q specific humidity and $\vec{v}$ winds from ERA40 on the 850 hPa level) for **c** the “neutral” class and **a**, **b**, **d** moisture divergence anomalies with respect to the “neutral” class of the “asymmetric”, “positive”, and “negative” classes, respectively. The *red line* is the 29°C isotherm, *purple line* is the SPCZ position, *red dashed line* is the maximum SST axis, the *thick dashed black line* points the maximum moisture convergence location and *black arrows* are winds on the 850 hPa level in (**b**) and anomalies from the “neutral” winds on other panels

south of the equator (Fig. 7b). This southward shift of the wind response to the equatorially centred SST anomalies is a robust feature of El Niño years in austral summer (Larkin and Harrison 2002) and has been suggested to be fundamentally tied to the annual cycle of insolation through the non-linear response of convective anomalies to the warmest SST migrating south of the equator during austral summer (Spencer 2004; Harrison and Vecchi 1999; Lengaigne et al. 2006). This wind pattern acts to slightly increase wind convergence just north of the mean SPCZ position on both sides of the dateline, resulting in a slight northward shift of the maximum moisture convergence and a subsequent SPCZ shift of about 3° to the north (Fig. 8b). A similar argument may explain the SPCZ displacement in the “negative” class. In this case, the westward shift of the warm pool associated with the cold SST anomaly (whose maximum is found between 170°E and 150°W, Fig. 7d) generates wind anomalies that increase the divergence north of the mean SPCZ position, displacing the maximum moisture convergence and precipitation axis about 3° southward (Fig. 8d).

The SPCZ behaviour for the “asymmetric” class is more peculiar. While the SPCZ location east of the dateline is considerably shifted northward, it remains close to its climatological location in its western portion. In addition, even though this cluster contains the two strongest El Niños of the century (1982/1983 and 1997/1998), it also contains the 1991/1992 El Niño, which is considered as a rather moderate event based on the amplitude of its eastern Pacific SST anomalies. The eastern Pacific warming observed for the “asymmetric” class (Fig. 7a) is dominated by the 1982/1983 and 1997/1998 events, however, the 1991/1992 event does share one characteristic of its equatorial warming with the two strongest El Niño: the three seasons display the largest eastward extension of the warm pool, reaching longitudes east of 160°W (Fig. 6b).

Compared to the “positive” cluster, this larger warm pool expansion of the “asymmetric” cluster results in much stronger and eastward-shifted low-level wind anomalies which are maximum east of the dateline, just south of the equator (Fig. 8a). These anomalies increase considerably the moisture convergence in this region, allowing a displacement of the maximum moisture convergence and precipitation axis of about 10° to the north.

West of the dateline, the SPCZ is not shifted northward as in the “positive” cluster but remains close to its mean position. During “asymmetric” events, a cold SST anomaly is observed in the north-west Pacific (Fig. 7a). This leads to decreased humidity levels and a strong divergence anomaly that together generate a net divergence of humidity in the north-western ITCZ and around the equator (Fig. 8a), inhibiting precipitation and preventing a northward shift of the SPCZ west of the dateline.

The zonal orientation of the SPCZ therefore occurs when the warm pool also presents a zonal shape being moved southward in the west and eastward around the equator due to the disappearance of the equatorial upwelling in the central part of the basin. During “asymmetric” events, the maximum SST axis is zonally oriented and the maximum precipitation is collocated with it. In the other clusters, the western portion of the SPCZ is anchored to the warmest water while the SPCZ is located slightly poleward of this axis of maximum SST in its eastern end (and on its full length in the “negative” class; Fig. 8). This finding supports the idea that the SPCZ is mainly controlled by SST forcing when it is close to the equator, but also to some extent by interactions with the extra-tropical circulation when it is positioned further from the equator (Kiladis et al. 1989).

Previous studies have shown the importance of distinguishing Niño extremes from other events as they have different physical lifecycles (Lengaigne and Vecchi 2009) and yield different impacts on TC activity (Kim et al. 2009). Here we confirm these studies by showing that different ENSO-related central pacific warming impact differently on the SPCZ position. However, the moderate strength El Niño of 1991/1992 appears in our classification at the side of the two strongest El Niño events illustrating the need to define local indices for regional studies rather than apply a general ENSO index.

3.3 Relationship between surface wind and SPCZ variability

The SPCZ location is not only strongly associated with large-scale precipitation, SST and moisture convergence, but also with the dynamical fields. This is illustrated in Fig. 9 by applying a rotated EOF analysis to the surface wind curl (low-level vorticity), in a similar way as for the precipitation (see Fig. 3). The first mode (39% of the total variance) opposes regions north and south of the mean maximum vorticity axis west of 160°W (Fig. 9a), while the second mode (13% of the total variance) displays a strong cyclonic anomaly east of 170°W (Fig. 9b). The PC1–PC2 distribution is also similar to the precipitation one (compare Figs. 3c, 9c) with a first mode opposing “negative” and “positive” years and a second mode dominated by the three “asymmetric” events. The interannual variability of low-level vorticity is therefore intimately tied to precipitation variability in the South Pacific (correlation of PC1s from precipitation and vorticity is 0.95). The same analysis applied to the surface wind, the surface wind divergence or 500 hPa vertical velocity gives very similar results (not shown), suggesting more generally that the dynamical fields are strongly tied to the SPCZ variability in this region.

Figure 10 displays the surface wind patterns in the South Pacific for each of the four classes arising from the SPCZ classification. We begin with the ‘neutral’ class, as it presents a wind structure close to the climatological one in the South Pacific (Fig. 10c). Convective precipitation in the SPCZ region is essentially tied to surface wind convergence. This convergence arises from the confluence of the trade winds in the eastern SPCZ, while, in its western part, it results from the convergence of Australian monsoon winds (north of the SPCZ) and the trade winds (south of it). The transition between these two different dynamical regimes within the SPCZ is represented by the confluence point (CP), defined as the easternmost point at any latitude reached by monsoon westerlies in the South Pacific (adapting the original definition that Chan and Evans (2002) used in the Northwest Pacific ITCZ). Interestingly, the CP defined in this way is, for all DJF seasons, located on the SPCZ line. The monsoon trough, defined as the region of minimum surface pressure, is characterised by “moist, southwest monsoon flows on its equatorward side and easterly trades on its poleward side” (Chu 2004). Within the monsoon trough region is found the monsoon shear line (MSL) where the maximum cyclonic vorticity is found as the encounter between the eastward monsoon winds and westward trade winds results in strong meridional wind shear. East of the CP, cyclonic vorticity is associated with curving trade winds and is weaker: the CP longitude thus marks the eastern boundary of the MSL. The CP also appears to be a good proxy for the strength of the MSL since the intensity of the vorticity averaged along the axis of the MSL is strongly correlated with the CP longitude (0.89). In contrast to the north-west Pacific ITCZ where the maximum cyclonic vorticity is found to be collocated with the maximum of precipitation and as been used to defined the ITCZ axis (Chan and Evans 2002), the maximum cyclonic vorticity in the SPCZ lies 6° south of

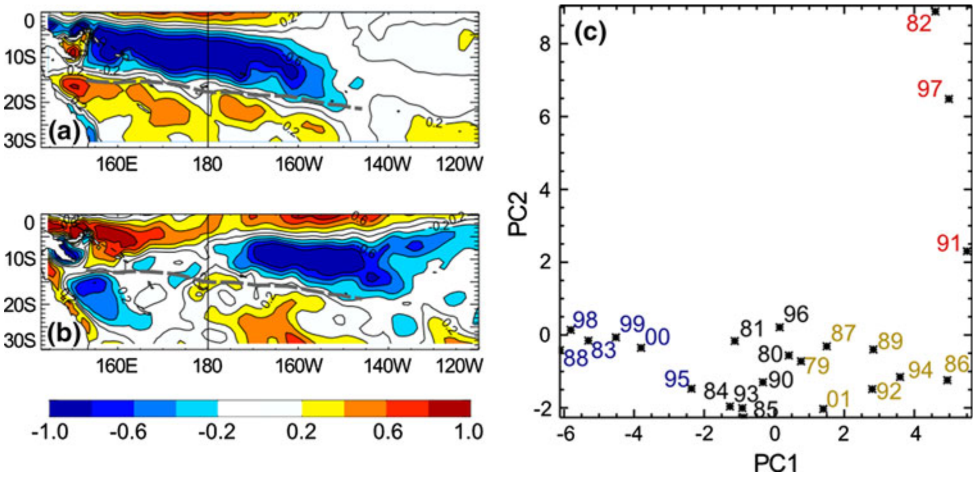

Fig. 9 **a**, **b** First two EOFs of ERA40 DJF vorticity on the period 1979–2002, and **c** coordinates of each year on the two-first modes (*colors* remind the class to which each season belongs, see Sect. 3.1 and Fig. 4). The *dashed line marks* the mean maximum vorticity axis

the maximum precipitation that is collocated with the zero of the vorticity field (Table 5; Fig. 10). This dynamical organisation described from climatological fields is also valid in interannual variations. The displacement of the zero and maximum vorticity axes are strongly tied to the interannual evolution of the SPCZ on its western and eastern part (Table 5) showing that the MSL variability is closely related to the SPCZ variability. From "negative" to "asymmetric", the MSL increases in strength while the CP is displaced north-eastward. During "asymmetric" years, the SPCZ is almost entirely defined by a monsoon type convergence zone, and low-level vorticity within the monsoon trough increases considerably east of the dateline (Fig. 10a).

4 Importance of the position of the SPCZ for tropical cyclogenesis

In the previous section, surface wind variability has been shown to be strongly connected to the displacement of the SPCZ. TC genesis is known to be dependent on large scale dynamical and thermodynamical fields and surface cyclonic vorticity is one of the variables that favour the genesis of TCs (Gray 1979). In this section, we will investigate the relationship between the interannual variability of the SPCZ and the interannual variability of TC genesis geography.

4.1 TC genesis variability in the South Pacific

The mean position of TC genesis[2] for each season derived from the Joint Typhoon Warning Center (JTWC) dataset provides a first look at the interannual variability of the genesis location in the South Pacific (Fig. 11). It appears that the 3 years forming the SPCZ "asymmetric" cluster defined in the previous section \are neatly separated from the rest as their mean longitude of genesis is located east of the dateline. In addition, "negative" years display a more southern location in their mean genesis latitude than do the other years. In contrast, no clear difference in the mean genesis location is observed between "neutral" and "positive" years with regard to their mean genesis position.

This first observation is extended by analysing composites of genesis density maps of the Southern Hemisphere cyclonic seasons (July year n to June year $n + 1$). Note that most TCs form during the December–March period and very similar results are obtained when considering only the TCs formed during this period instead of the full cyclonic season. Density maps of genesis are obtained by generating Probability Density Functions computed from anisotropic Gaussian functions, with an associated standard deviation in zonal and meridional directions, respectively, of 1.5° and 3° following the method used by Ramsay et al. (2008). Each genesis point is spatially extended following this Gaussian shape and density maps for each cyclonic season are obtained by summing the contribution of each Gaussian on a 2.5° × 2.5° grid. On average, the TC genesis distribution is almost zonal (between 10°S and 15°S) and extends from the northern coast of Australia to 160°W (Fig. 12c). For each SPCZ class, the genesis region (black dashed line) is located just south of the SPCZ position. "Asymmetric" and "positive" years both display increased cyclogenesis in the Tuvalu region and decreased cyclogenesis in the Coral Sea. Opposite variations are found for "negative" years in these regions. If the genesis patterns are similar west of the dateline for the "positive" and "asymmetric" classes, they strongly differ east of it. A large positive anomaly of

---

[2] Genesis is defined as the first position of a Tropical Depression in the JTWC database that will develop 1-min averaged winds >17 m/s.

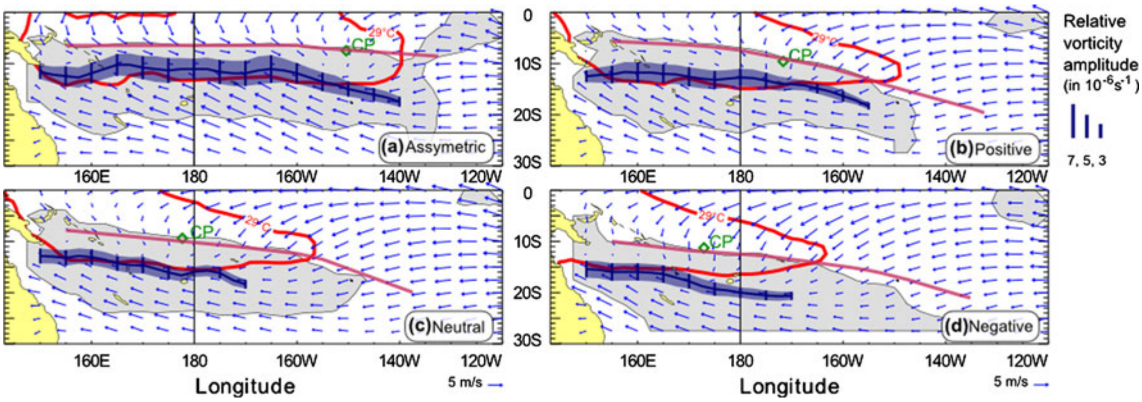

Fig. 10 Composite DJF surface fields related to the SPCZ for the four classes: **a** "asymmetric", **b** "positive", **c** "neutral" and **d** "negative" class. The *purple line* is the SPCZ composite position; *blue vectors* represent the surface wind field; region of cyclonic relative vorticity of surface winds is *shaded in grey*, the *blue line* points the maximum vorticity axis and its *thickness* represents the magnitude of the vorticity along the monsoon shear line (*MSL*); *red line* is the 29°C isotherm of SST; *diamond* indicates the location of the confluence point (*CP*) defined as "the point of the SPCZ where winds change from an eastward component to a westward component". Note that for consistency all fields on this figure are from ERA40 (except SST from HadISST)

cyclogenesis in the central Pacific (Polynesia region), is indeed observed during "asymmetric" years and contrasts with the weak anomaly found in the "positive" class (Fig. 12b).

4.2 Interannual variability of TC genesis favourable parameters

Tropical cyclones have a tendency to form in regions with favourable large-scale environmental parameters: high oceanic heat content (OHC), low-level cyclonic vorticity, high humidity in the mid-troposphere and low vertical wind shear within the troposphere. Several empirical indices have been developed to understand how these dynamical and thermodynamical variables are coupled together to define regions where TCs will be allowed to form. Gray (1979) first developed a seasonal genesis potential index (SGP) followed by Emanuel and Nolan (2004) who developed another genesis potential index (GPI). Both indices are constructed as an empirical combination of all favourable variables fitted to the observed numbers of genesis globally. Royer et al. (1998) simplified the thermal potential of the SGP index by considering only convective precipitation (to allow its use in climate change runs of general circulation models) and named it the convective seasonal genesis potential index (CSGP, see "Appendix"). Compared to the GPI and SGP, the CSGP was found to best reproduce both the climatological patterns and the interannual variations of TC genesis in the South Pacific (Menkes et al. 2009). In particular, it is almost able to reproduce the observed location of maximum cyclogenesis to the south of the SPCZ (Fig. 13c) while other indices locate the maximum of genesis right on the SPCZ (not shown). The CSGP is also able to reproduce the broad features of genesis anomaly patterns associated to the four classes of SPCZ variability (compare Figs. 12a, b, d, 13a, b, d): during the "negative" class, the negative (positive) anomaly north (south) of the SPCZ is well reproduced, positive anomalies for the "positive" and "asymmetric" classes are also quite well reproduced, the main shortcoming comes from the representation of the negative anomaly of genesis in the "Coral Sea" for the two latter classes that is not reproduced by the CSGP with sufficient intensity (and neither by SGP and GPI).

Here we build on the terms involved in the calculation of the CSGP to understand the link observed between TC genesis and SPCZ position interannually. Three terms are involved in the CSGP calculation: the "dynamic potential" is composed of (1) I_S, the calculation of which involves the vertical shear of winds between 950 and 200 hPa, and (2) I_ζ, which involves the relative vorticity at 950 hPa. The "convective potential" C_{pot} is only represented by (3) the convective precipitation term as a measure of the enthalpy available for the cyclone (see "Appendix" for details on these three terms calculation). In the "neutral" years composite of Fig. 14, we note that: (1) the region of minimum vertical shear (shear <16 m s^{-1}/750 hPa) is observed along the SPCZ (10°S/180°–25°S/120°W) and west of the CP a broader region of very low vertical shear (lower than 9 m s^{-1}/750 hPa) is observed in the 7°S–15°S/145°E–180° region. (2) The SPCZ marks the north-eastern limit of the region where favourable cyclonic vorticity can be found. (3) High convective precipitation is localised around the SPCZ position. The organisation of favourable parameters with respect to the SPCZ position described for the "neutral" class is also valid for the three other

Table 5 Mean distance and correlation between the zero and maximum vorticity axes to the SPCZ position in latW and latE regions

	In lat W	In lat E
SPCZ and zero vorticity axis		
Mean distance (° lat)	0.7	−0.6
Correlation	0.93	0.91
SPCZ and max vorticity axis (MSL)		
Mean distance (° lat)	−5.7	−6.2
Correlation	0.88	0.82

All correlations significant at the 95% level with respect to a two-tailed Student's *t* test

composites (Fig. 14a, b, d). Figure 14 shows that the overlap area of positive vorticity, shear values lower than 9 m s^{-1}/750 hPa and convective precipitation >4 mm/day is always found just south of the SPCZ position and west of the CP. The region of observed TC genesis (thick black dashed line) is shown to match this overlap region, with 67% of observed TCs in the South Pacific forming inside this region. The proportion increases to 87% when considering the 16 m s^{-1}/750 hPa vertical shear isoline instead of the 9 m s^{-1}/750 hPa. Chand and Walsh (2009) note that "TC genesis over the Fiji region is highly favoured for environmental vertical wind shear <8 m/s" (calculated between 850 and 200 hPa levels); this value compares to our value of 9 m/s (calculated between 950 and 200 hPa levels) even if our calculation is based on DJF means while their calculation is based on daily composites.

The regions of greater variability for cyclogenesis in the different SPCZ classes are identified in Fig. 12. These are the "Polynesia" (165°W–130°W/5°S–20°S), "Tuvalu" (165°E–165°W/5°S–13°S), "Fiji" (165°E–165°W/13°S–25°S) and "Coral Sea" (143°E–165°E/10°S–20°S) regions. To identify the large scale parameters associated with genesis variability, we compare the TC genesis number per region with the CSGP and the three terms composing it averaged over each of the four regions (Fig. 15). The latter three terms are normalised by their mean magnitude over the South Pacific domain (143°E–120°W/0–30°S) to allow for comparison both between terms and between regions. We first note that the "Polynesia" region is affected by cyclogenesis only during the three "asymmetric" years. This observation is reasonably well reproduced by the CSGP and main variability appears to be due to the vorticity and thermal potential terms (Fig. 15). The zonal orientation of the SPCZ during "asymmetric" years brings deep convection to the central Pacific and allows the eastward extension of background cyclonic vorticity in the "Polynesia" region (Fig. 14).

In the "Tuvalu" region, no cyclones are formed during "negative" years despite favourable shear and thermodynamical conditions. In this case, the background anticyclonic vorticity due to the southward SPCZ shift has produced locally unfavourable conditions responsible for this absence of genesis (Fig. 15b). From "neutral" to "asymmetric" years, an increase of TC genesis number is observed; the CSGP catches an increase of favourable conditions but overestimates the observed variability for the "positive" and "asymmetric" classes. All CSGP terms vary accordingly with the observed increase of cyclogenesis but the vorticity term appears to be the primary driver of the CSGP increase for the "positive" and "asymmetric" classes. We remark that the 1996/1997 season is outside of the "neutral" group with regards to TC genesis number and degrades the relationship (Fig. 15a). During this year, TCs are formed late in the season (2 in March, 2 in April, 1 in May and 1 in June 1997). These late geneses with respect to a standard season are probably related to the onset of the 1997/1998 strong El Niño event in March 1997 and are responsible for the peculiar behaviour of this cyclonic season.

In the "Coral Sea" region, vorticity is always favourable for TC genesis. Indeed the region lies at the heart of the monsoon trough eastern portion that experiences a persistent horizontal shear between monsoon and trade winds. The genesis density difference between "negative"–"neutral" and "positive"–"asymmetric" years observed in Fig. 12 seems to be mostly sensitive to the thermodynamical potential that shows the greatest relative modification. However, little confidence can be given to this result as all three indices show poor skill in reproducing the interannual variability of TC genesis in this region.

Fig. 11 Mean position of cyclogenesis for each year in the South Pacific region (143°E–80°W/0–30°S): year *n* stands for the Southern Hemisphere cyclonic season from July year *n* to June year *n* + 1). Overall mean longitude and latitude given by the *dashed lines*

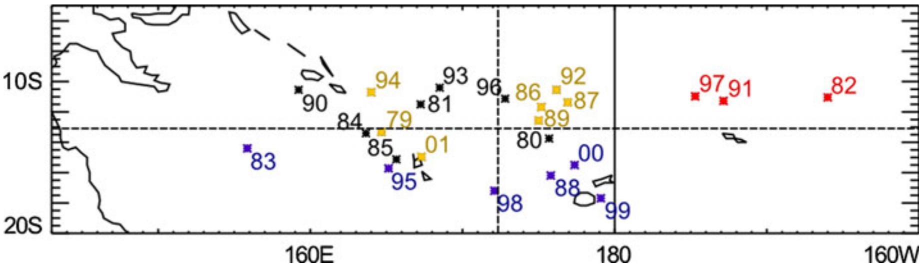

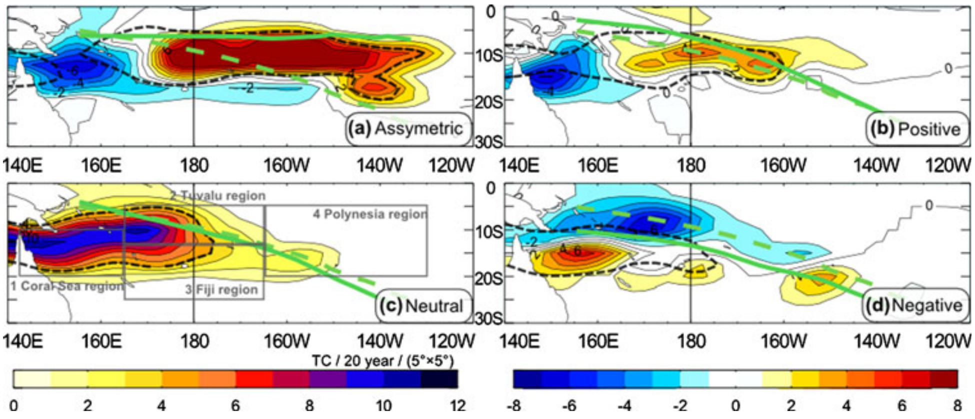

Fig. 12 **c** "Neutral" class TC genesis density (in number of genesis per 20 years and per 5° × 5° boxes); *rectangles* delimitate the different regions discussed in the text: *1* Coral Sea, *2* Tuvalu, *3* Fiji and *4* Polynesia. **a** "Asymmetric", **b** "positive", **d** "negative" composites of TC genesis density anomaly with respect to the "neutral" case; the *thick dashed contour* is the isoline four TC/20 years/(5° × 5°) of TC genesis density. Climatological GPCP SPCZ (*green dashed line*) and composite SPCZ (*green line*) are reported on each map

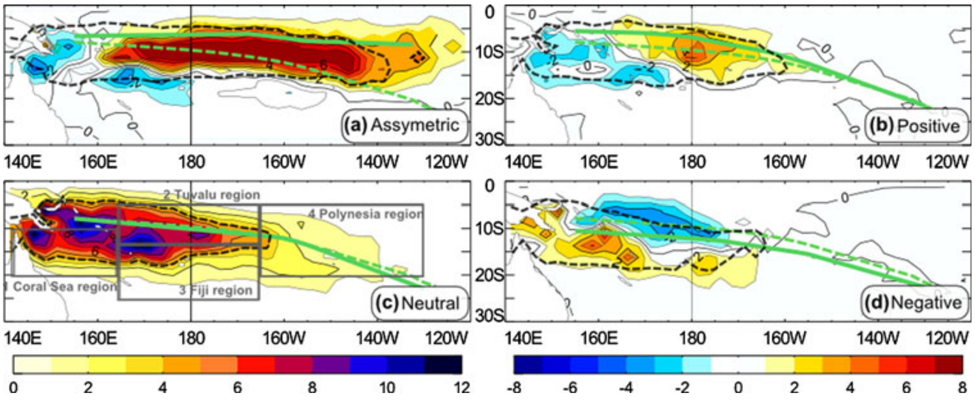

Fig. 13 Same as Fig. 12 but for the composites of the convective seasonal genesis potential index (*CSGP*) for the four classes. Units of the index are fitted to the global TC number and can be read as formation of TC per 5° lon–lat boxes per 20 year. **c** "Neutral" class genesis density, **a** "asymmetric", **b** "positive", **d** "negative" years composites of genesis density anomaly with respect to the "neutral" case; the *thick dashed contour* is the four TC/20 years/(5° × 5°) composite isoline. Climatological ERA40 SPCZ (*green dashed line*) and composite SPCZ (*green line*) are reported on each map

In the "Fiji" region, vorticity is also always favourable and even if increasing from "negative" to "asymmetric" years, the genesis of TCs follows an inverse tendency which is to be related to the thermal potential (and to a lesser extent to wind shear) which decreases from "negative" to "asymmetric" years (Fig. 15). We remark that relatively to other regions, the CSGP always tends to overestimate the number of genesis in "Fiji" and "Coral Sea" regions.

Conducting a similar analysis on the different terms composing the GPI of Emanuel and Nolan (2004) yields very similar results (not shown) about the relative importance of dynamical and thermodynamical terms to constrain the interannual variability of cyclogenesis.

5 Summary and conclusions

This study investigates the interannual variability of the SPCZ and its influence on TC genesis using satellite data and ERA40 reanalysis over the 1979–2002 period.

An AHC method allows four characteristic structures of the interannual position of the SPCZ in austral summer to be identified. A "neutral" class gathers years when the SPCZ is close to the climatological position, while a "negative" ("positive") class gathers years when the SPCZ is displaced by about 3° south (north) of its climatological position. These three classes displace a similar diagonal orientation of the SPCZ position. In contrast, the fourth class (the "asymmetric" class), that only contains 3 years

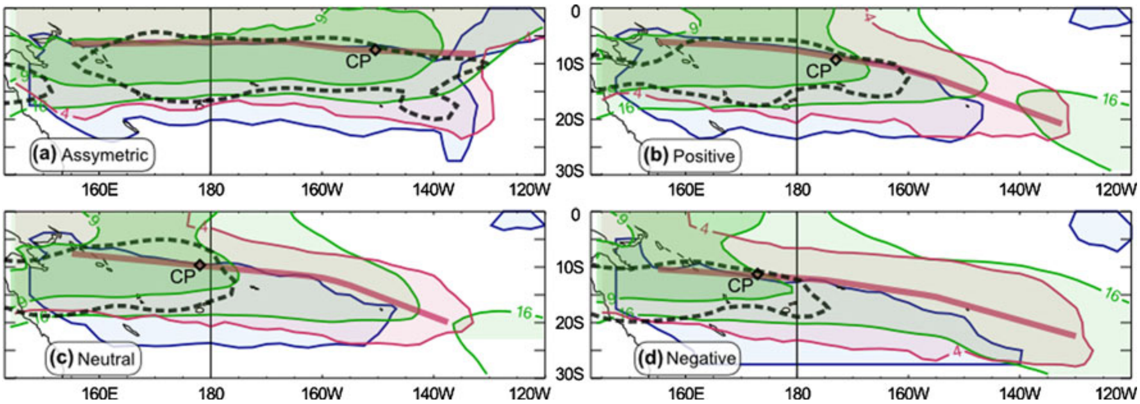

Fig. 14 Composites of ERA40 terms involved in the calculation of the CSGP; *green* 9 and 16 m s^{-1}/750 hPa contours of vertical wind shear (between 950 and 200 hPa), *blue* 0 s^{-1} contour of surface relative vorticity and *purple* 4 mm/day contour of convective precipitation; *purple line* SPCZ composite position and the thick dashed contour reproduces the four TC/20 years/5° isoline of TC genesis density of Fig. 12

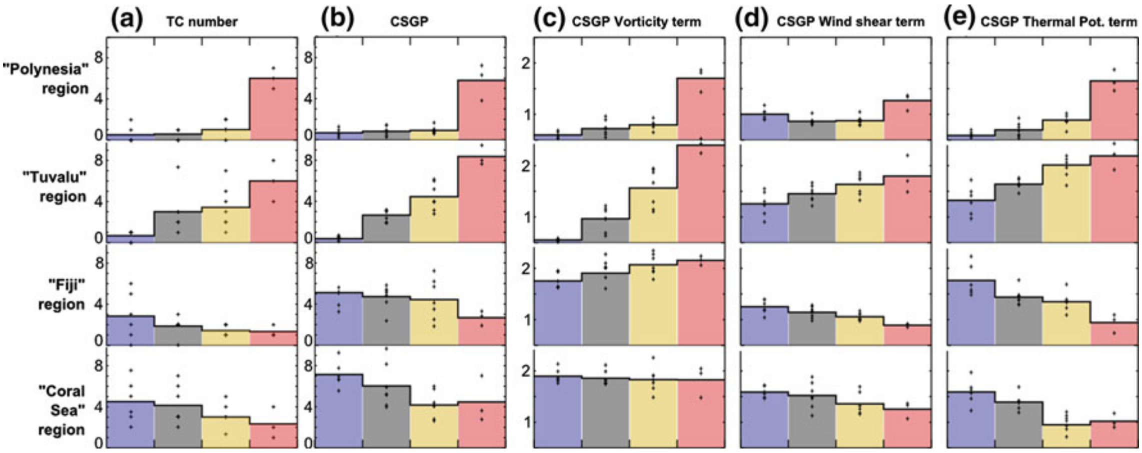

Fig. 15 **a** Averaged TC genesis number and **b** value reconstructed from the CSGP per region and per class [from left to right: "negative" (*blue*), "neutral" (*black*), "positive" (*yellow*) and "asymmetric" (*red*)] and comparison with the terms involved in the calculation of the CSGP (non-dimensional units): **c** vorticity term I_ζ, **d** wind shear term I_S and **e** thermodynamical term C_{pot}. Each term is normalised by its average magnitude in the South Pacific domain (143°E–120°W/0–30°S) to allow comparison between terms and between regions. *Each plus marks* the value of an individual year forming the class for an evaluation of its homogeneity

(the extremes 1982/1983 and 1997/1998 El Niño events and the moderate 1991/1992 El Niño event) displays an SPCZ that is zonally oriented located around 6°S.

This study confirms that ENSO phenomenon strongly modulates the SPCZ movement, as first discussed by Trenberth (1976) and in agreement with Folland et al. (2002). More precisely, the SPCZ location east (west) of the dateline is strongly related to the variability of the equatorial SST in the central Pacific (near the dateline). SST rise (drop) in these equatorial regions increase (decrease) low-level moisture transport just south of the equator and the vertical instability of the atmosphere, allowing deep convection to occur north (south) of its mean position. This mechanism is particularly effective during the two extreme 1982/1983 and 1997/1998 El Niños, as well as during the moderate 1991/1992 El Niño, when the eastern edge of the equatorial warm-pool is displaced east of 160°W. This considerably increases the moisture transport south of the equator, shifting the SPCZ location east of the dateline by more than 10° north of its climatological position. Moreover, the western part of the SPCZ is displaced to the south mainly due to a cold SST anomaly and a surface divergence in the north-western Pacific suppressing the ITCZ here during "asymmetric" years while SPCZ and ITCZ are merged along the equator during "positive" years.

The SPCZ location is found to be a good indicator of the changes to atmospheric circulation in the South Pacific. From year-to-year, the SPCZ location is collocated with the zero relative vorticity axis at low levels, while the MSL (i.e., the maximum vorticity axis) lies 6° south of the SPCZ position. In addition, both the eastward extension of monsoon wind and the intensity of the MSL increase as the SPCZ is displaced northward. During "asymmetric" years, the SPCZ can even be almost entirely defined by a monsoon type convergence regime and the vorticity increases considerably east of the dateline. Because the SPCZ position summarizes large scale dynamic and thermodynamic fields, it is also shown to be a good indicator of the geography of cyclogenesis in the South Pacific. Genesis indices such as the CSGP allow to study the main factors favouring or limiting cyclogenesis. Based on analysis of these factors, we conclude that the anticyclonic vorticity of low-level winds just north of the SPCZ prevents cyclogenesis in this region while low wind shear within the troposphere, vertical instability of the troposphere (depicted as deep convective precipitations) and cyclonic vorticity of low-level wind combine just south of the SPCZ to allow TCs to develop. Cyclogenesis interannual variability in the region is shown to follow SPCZ movement in its north–south displacement and to preferentially occur within 10° south of the SPCZ location. Four distinct spatial patterns are depicted in the TC observations in relation to the SPCZ classes. These patterns are also correctly reproduced by the CSGP (but also by the GPI and SGP indices). Even if the actual TC genesis numbers cannot be reproduced by these indices due to the intrinsic high level of stochasticity in TC genesis in that region (see Jourdain et al. 2009; Menkes et al. 2009 for a detailed discussion), indices do reproduce the "asymmetric" and "negative" patterns pretty well, but do not reproduce the decrease of cyclogenesis in the Coral Sea during "positive" and "asymmetric" phases.

Our approach provides a means of demonstrating that cyclogenesis east of the dateline (in the vicinity of French Polynesia) is only likely to occur when the SPCZ displays a zonal orientation while this observation was previously attributed to El Niño years in general. During the years of "asymmetric" SPCZ, the strong northward displacement of the SPCZ east of the dateline generates a strong positive cyclonic vorticity in this region, favouring cyclogenesis. This zonal orientation of the SPCZ and its associated increased cyclogenesis in the central Pacific depends more strongly on the west–east displacement of the eastern edge of the warm pool than on the SST anomaly magnitude depicted by the Niño 3 SST index. While the 1991/1992 El Niño is considered as a moderate El Niño based on the Niño 3 SST index, our results show that its SPCZ evolution behaves similarly to the extreme 1982/1983 and 1997/1998 El Niño events because these three events display the largest SST anomalies east of the dateline and hence the largest eastward shift of the equatorial warm pool. While Kim et al. (2009) show that the characteristics of the boreal summer equatorial Pacific warming leads to different impacts on the cyclogenesis in the Atlantic basin, we here show that similar characteristics of the austral summer equatorial Pacific warming have to be taken into account when addressing the interannual variability of cyclogenesis in the south-west Pacific. This sensitivity of SPCZ variations and related cyclogenesis in the central Pacific to the equatorial warm pool extent suggests the possibility of additional predictability of cyclogenesis in this region beyond that associated with just predicting the occurrence of El Niño. However, predictions of the details of the pattern of the SST anomalies during El Niño have not yet been demonstrated.

The clarification between cyclogenesis and SPCZ organisation brought by this study may also bring light to the large discrepancies found in the SPCZ region of projected cyclogenesis modifications under climate change scenarios (Caron and Jones 2008; Royer and Chauvin 2009). In this vein, future investigations will require taking into account the modifications in the organisation and interannual variability of the SPCZ simulated by GCMs for future climate.

Acknowledgments This work was supported by the French "Agence Nationale de la Recherche" (ANR) through the programme Cyclones&Climat ANR-06-VULN-002-01. The authors would like to thank ECMWF for making the ERA40 reanalyses available, the Joint Typhoon Warning Center (JTWC) and the National Hurricane Center for the use of their TC best track data as well as the U.K. Met. Office for use of the HadISST dataset. We acknowledge three anonymous reviewers and Daniel Nethery for their useful comments, which lead to improvements to the present manuscript.

Appendix

Details on the calculation of the convective seasonal genesis parameter

Royer et al. (1998) modified the gray convective seasonal parameter index (Gray 1979) to avoid the use of fixed threshold of SST, which prevented it from being used in GCM climate simulations. They suggested replacing the thermal potential with a convective potential C_{pot} directly linked to the convective precipitation of the model:

$$\mathrm{CSGP} = \underbrace{(|f| \times I_{\varsigma} \times I_{\mathrm{S}})}_{\mathrm{DynamicPot}} \times \underbrace{(k \times P_{\mathrm{c}})}_{\mathrm{ConvectivePot}}$$

Here:

- f is the Coriolis parameter (in 10^{-5} m s^{-1}),
- $I_{\varsigma} = \varsigma_{\mathrm{r}} \cdot \frac{f}{|f|} + 5$ where ζ_{r} is the low level relative vorticity at 950 hPa (in 10^{-6} s^{-1}),
- $I_{\mathrm{S}} = \left(\frac{\delta V}{\delta P} + 3\right)^{-1}$ is the inverse of the vertical shear of the horizontal wind between 950 and 200 hPa, (in m s^{-1}/750 hPa),

- P_c is the convective precipitation term of the model,
- k is a constant dependent on the model.

References

Adler RF, Huffman GJ, Chang A, Ferraro R, Xie P, Janowiak J, Rudolf B, Schneider U, Curtis S, Bolvin D, Gruber A, Susskind J, Arkin P (2003) The version 2 Global Precipitation Climatology Project (GPCP) monthly precipitation analysis (1979-present). J Hydrometeor 4:1147–1167

Ashok K, Behera SK, Rao SA, Weng H, Yamagata T (2007) El Niño Modoki and its possible teleconnection. J Geophys Res 112:C11007. doi:10.1029/2006JC003798

Basher RE, Zheng X (1995) Tropical cyclones in the Southwest Pacific: spatial patterns and relationships to southern oscillation and sea surface temperature. J Clim 8:1249–1260

Caron LP, Jones CG (2008) Analysing present, past and future tropical cyclone activity as inferred from an ensemble of coupled global climate models. Tellus 60A:80–96

Chan SC, Evans JL (2002) Comparison of the structure of the ITCZ in the west Pacific during the boreal summers of 1989–93 using AMIP simulations and ECMWF reanalysis. J Clim 15:3549–3568

Chand SS, Walsh KJ (2009) Tropical cyclone activity in the Fiji region: spatial patterns and relationship to large scale circulation. J Clim 22:3877–3893. doi:10.1175/2009JCLI2880.1

Chu PS (2004) ENSO and tropical cyclone activity. Hurricanes and typhoons, past, present and future. Columbia University Press, New York, pp 297–332

Emanuel KA, Nolan DS (2004) Tropical cyclone activity and global climate. In: Proceedings of the 26th conference on hurricanes and tropical meteorology. American Meteorological Society, Miami, FL, pp 240–241

Evans JL, Allan RJ (1992) El Niño/southern oscillation modification to the structure of the monsoon and tropical cyclone activity in the Australasian region. Int J Clim 12:611–623

Folland CK, Renwick JA, Salinger MJ, Mullan AB (2002) Relative influence of the interdecadal Pacific oscillation and ENSO on the South Pacific Convergence Zone. Geophys Res Lett 29:1643. doi:10.1029/2001GL014201

Gouriou Y, Delcroix T (2002) Seasonnal and ENSO variations of sea surface salinity and temperature in the South Pacific Convergence Zone during 1976–2000. J Geophys Res 107:8011. doi:10.1029/2001JC000830

Gray WM (1979) Hurricanes: their formation, structure and likely role in the tropical circulation. In: Shaw DB (ed) Meteorology over the tropical oceans. Roy Meteor Soc, London, pp 155–218

Harrison DE, Vecchi GA (1999) On the termination of El Niño. Geophys Res Lett 26(11):1593–1596

Hastings PA (1990) Southern Oscillation influence on tropical cyclone activity in the Australian/south-west Pacific region. Int J Climatol 10:291–298

Holland GJ, McBride JL, Nicholls N (1988) Australian region tropical cyclones and the greenhouse effect. In: Greenhouse planning for climate change, pp 438–455

Jourdain NC, Marchesiello P, Menkes CE, Lefevre J, Vincent EM, Lengaigne M, Chauvin F, Royer JF (2009) Mesoscale simulation of tropical cyclones in the South Pacific: climatology and interannual variability. J Clim (submitted)

Kiladis GN, Storch HV, Loon HV (1989) Origin of the South Pacific Convergence Zone. J Clim 2:1185–1195

Kim HM, Webster PJ, Curry JA (2009) Impact of shifting patterns of pacific ocean warming on north Atlantic tropical cyclones. Science 325:77–80. doi:10.1126/science.1174062

Kuleshov Y, Qi L, Fawcett R, Jones D (2008) On tropical cyclone activity in the Southern Hemisphere: trends and the ENSO connection. Geophys Res Lett 35:L14S08. doi:10.1029/2007GL032983

Larkin NK, Harrison DE (2002) ENSO warm (El Niño) and cold (La Niña) event life cycles: ocean surface anomaly patterns, their symmetries, asymmetries, and implications. J Clim 15:1118–1140

Lengaigne M, Vecchi GA (2009) Contrasting the termination of moderate and extreme El Niño events in coupled GCM. Clim Dyn. doi:10.1007/s00382-009-0562-3

Lengaigne M, Boulanger JP, Menkes C, Spencer H (2006) Influence of the seasonal cycle on the termination of El Niño events in a coupled general circulation model. J Clim 19:1850–1868. doi:10.1175/JCLI3706.1

Lintner BR, Neelin JD (2008) Eastern margin variability of the South Pacific Convergence Zone. Geophys Res Lett 35:L16701. doi:10.1029/2008GL034298

Menkes C, Lengaigne M, Marchesiello P, Jourdain NC, Vincent EM, Lefevre J, Chauvin F, Royer JF (2009) Comparison of cyclogenesis indices on seasonal to interannual time scales (in preparation)

Nicholls N (1985) Predictability of interannual variations of Australian seasonal tropical cyclone activity. Mon Weather Rev 113:1144–1149

Ramsay HA, Leslie LM, Lamb PJ, Richman MB, Leplastrier M (2008) Interannual variability of tropical cyclones in the Australian region: role of large-scale environment. J Clim 21:1083–1103. doi:10.1175/2007JCLI1970.1

Revell CG, Goulter SW (1986) South Pacific tropical cyclones and the southern oscillation. Mon Weather Rev 114:1138–1145

Reyment RA, Jörekog KG (1993) Applied factor analysis in the earth sciences, 2nd edn. Cambridge University Press, London, p 371

Royer JF, Chauvin F (2009) Response of tropical cyclogenesis to global warming in an IPCC AR-4 scenario assessed by a modified yearly genesis parameter. In: Elsner JB, Jagger TH (eds) Hurricanes and climate change. Springer, Berlin, pp 213–234

Royer JF, Chauvin F, Timbal B, Araspin P, Grimal D (1998) A GCM study of the impact of greenhouse gas increase on the frequency of occurrence of tropical cyclones. Clim Change 38:307–343

Spencer H (2004) Role of the atmosphere in seasonal phase locking of El Niño. Geophys Res Lett 31:L24104. doi:10.1029/2004GL021619

Takahashi K, Battisti DS (2007) Processes controlling the mean tropical Pacific precipitation pattern. Part II: the SPCZ and the southeast Pacific dry zone. J Clim 20:5696–5706. doi:10.1175/2007JCLI1656.1

Trenberth KE (1976) Spatial and temporal variations of the southern oscillation. Q J R Meteorol Soc 102:639–653

Trenberth KE, Smith L (2006) The vertical structure of temperature in the tropics: different flavors of El Niño. J Clim 19:4956–4970

Vecchi GA (2006) The termination of the 1997–98 El Niño. Part II: mechanisms of atmospheric change. J Clim 19:2647–2664

Vincent DG (1994) The south Pacific convergence zone (SPCZ): a review. Mon Weather Rev 122:1949–1970

Wang G, Hendon HH (2007) Sensitivity of Australian rainfall to inter-El Niño variations. J Clim 20:4211–4226

Ward JH (1963) Hierarchical grouping to optimize an objective function. J Am Stat Assoc 58(301):236–244

Xie P, Arkin PA (1997) Global precipitation: a 17-year monthly analysis based on gauge observations, satellite estimates, and numerical model outputs. Bull Am Meteorol Soc 78:2539–2558

Yin X, Gruber A, Arkin PA (2004) Comparison of the GPCP and CMAP merged gauge-satellite monthly precipitation products for the period 1979–2001. J Hydrometeorol 5:1207–1222

Résultats complémentaires

• Articles liés

Des études complémentaires sur la SPCZ et l'activité cyclonique dans le Pacifique Sud–Ouest réalisées en collaboration avec l'équipe IRD de Nouméa ont abouti à la rédaction de deux articles. Les principales conclusions sont résumées ci–après et l'intégralité est fournie en Annexe.

Sensibilité à l'indice de cyclogenèse utilisé (Annexe E) Pour comprendre les mécanismes modulant la cyclogenèse dans le Pacifique Sud–Ouest, j'ai utilisé un indice de cyclogenèse (le CYGP). Il existe pourtant plusieurs indices de cyclogenèse utilisant des formulations ainsi que des poids relatifs différents entre les variables dynamiques et thermodynamiques. Cela pose donc la question de la robustesse de l'interprétation physique des modifications de la cyclogenèse issue de l'analyse d'un seul indice.

Notre article [Menkes *et al.* 2011] compare les quatre principaux indices de cyclogenèse utilisé dans la littérature et explore la sensibilité des mécanismes de cyclogenèse à l'indice et la réanalyse utilisée pour le calculer. La sensibilité à la réanalyse utilisée est faible. Bien que les indices sous–estiment tous l'amplitude de la variabilité interannuelle du nombre de genèse, ils reproduisent de manière acceptable le phasage de la variabilité associée à ENSO. De plus les variables impliquées dans la variabilité interannuelle sont cohérentes entre les indices dans la région de la SPCZ, confirmant la description qualitative du rôle des différents termes impliqués dans la variabilité de la cyclogenèse présentée dans ce chapitre.

Rôles respectifs des processus stochastiques et du climat dans la variation interannuelle de la cyclogenèse (Annexe F) Ce chapitre a mis en évidence un lien entre la variabilité de l'activité cyclonique et des variables grande–échelle, mais quelle est la part maximale de la variabilité cyclonique que l'on peut prétendre expliquer par ce type d'approches ? Notre article [Jourdain *et al.* 2011] s'intéresse à la part de la variabilité interannuelle du nombre de cyclogenèse de la région Pacifique Sud–Ouest qui peut être expliquée par les variables grande–échelle par rapport à la part due à des processus stochastiques (*i.e.* associés à la variabilité intrinsèque de l'atmosphère et non au climat).

Un modèle atmosphérique régional du Pacifique Sud–Ouest à relativement haute résolution (WRF 1/3°) est utilisé pour simuler l'activité cyclonique dans le Pacifique Sud–Ouest. Ce modèle à été forcé aux frontières i) avec un forçage climatologique (identique d'une année sur l'autre) et ii) avec un forçage présentant des variations interannuelles. Alors que la seconde expérience prend en compte à la fois l'influence des processus stochastiques et de la variabilité climatique sur la variabilité de l'activité cyclonique, la seconde ne prend en compte que la variabilité interne atmosphérique. [Jourdain *et al.* 2011] montrent que la variabilité liée aux processus stochastiques est de l'ordre de 1.7 TC/an dans le bassin pour une variabilité interannuelle totale de 3.5 TC/an. On ne peut donc espérer expliquer plus de 50% de la variabilité observée à partir des variables grande–échelle.

Une étude similaire réalisée avec un modèle régional sur l'Atlantique révèle une contribution beaucoup plus faible de la stochasticité sur la variabilité totale de la cyclogenèse [Done *et al.* 2011]. Ce résultat pourrait expliquer le fait que l'activité cyclonique dans l'Atlantique est largement prévisible [Knutson *et al.* 2007].

- **Projets en cours**

Les résultats présentés dans ce chapitre ouvrent des perspectives dans la compréhension des contrôles climatiques de la cyclogenèse. Les analyses que j'ai débutées sur l'importance de la variabilité océanique et du changement climatique sur l'activité cyclonique sont présentées en Annexe ; ces thèmes de recherche sont introduits ci–dessous.

Influence du changement climatique La structure spatiale du réchauffement associé aux évènements *El Niño* est susceptible de changer dans le futur en réponse au changement climatique [Yeh *et al.* 2009]. Une telle modification pourrait affecter la variabilité de la SPCZ et ainsi moduler la géographie de la cyclogenèse dans le Pacifique Sud–Ouest. Des analyses réalisées au cours de ma thèse sur les sorties de modèles couplés de la base CMIP3 (*Coupled Model Intercomparison Projet Phase* 3) utilisé au cours du dernier exercice du GIEC (Groupe d'experts intergouvernemental sur l'évolution du climat) suggèrent que la fréquence des évènements où la SPCZ présente une orientation zonale pourrait augmenter dans un climat plus chaud.

Les résultats principaux de ce travail sont présentés en annexe B et ont donné lieu à la présentation d'un poster lors de la conférence *2$^{\text{nd}}$ International Summit on Hurricanes and Climate Change* [Vincent *et al.* 2009b] ainsi qu'à la publication d'un article dans la revue Nature [Cai *et al.* 2012].

Influences de la SPCZ sur l'océan [Singh *et al.* 2011] ont réalisé une étude des variations interannuelles de salinité de surface du Pacifique Sud–Ouest. Leur classification des années en fonction des caractéristiques du champ de salinité recoupe en grande partie la classification proposée dans ce chapitre. Ils soulignent notamment la particularité des 3 années où la SPCZ se zonalise. La salinité de surface est largement contrôlée par les précipitations de la SPCZ. Pendant les évènements de zonalisation, l'advection horizontale joue aussi un rôle. Le pompage d'Ekman, largement accru au Sud de la SPCZ, peut aussi influencer le budget de salinité de surface en remontant la langue d'eau salée sub–tropicale (maximum de salinité ∼150 m sous la surface à 15°S/170°W) [Vincent *et al.* 2010b].

Influences de la stratification thermique de l'océan L'amplitude de la variabilité du pompage associée à la position de la SPCZ est-elle suffisante pour modifier la stratification thermique de l'océan et ainsi moduler l'amplitude des CWs et donc l'activité cyclonique ? Les analyses effectuées dans ce chapitre, ainsi que la plupart des études sur la variabilité interannuelle des TCs en lien avec les variables grande–échelle, ne permettent pas de mettre en évidence le rôle de la variabilité océanique dans le contrôle des TCs. Une étude a pourtant suggéré que la profondeur de la thermocline dans l'Ouest de l'Océan Indien (TRIO) influence l'activité cyclonique [Xie *et al.* 2002]. Les analyses que j'ai effectuée suggèrent que leur conclusion ne peut être démontrée par une simple approche composite de l'activité cyclonique en fonction de la profondeur de la TRIO (voir Annexe C). En effet, la variabilité de la TRIO est aussi associée à des modifications de variables atmosphériques impliquées dans la modulation des caractéristiques des TCs. La vorticité grande–échelle par exemple influence le pompage et donc la profondeur de la TRIO mais aussi la cyclogenèse. Une approche adéquate pour démontrer clairement un éventuel contrôle de l'activité cyclonique par la variabilité océanique reste à imaginer. Une voie ouverte par cette thèse consiste à étudier la sensibilité des refroidissements de surface à un mélange donné en fonction des modifications interannuelles des propriétés de l'océan de sub–surface.

CHAPITRE 7
Conclusion générale

7.1 Synthèse des principaux résultats

7.1.1 Refroidissement de surface induit par les TCs

Le cyclone tropical (TC) est une machine thermique qui extraie activement de l'énergie de la surface de l'océan sous forme de vapeur d'eau et la convertit en énergie cinétique dans l'atmosphère. Son intensité dépend largement de son environnement atmosphérique et océanique. L'influence que peut avoir l'océan sur le TC s'exprime exclusivement par sa température de surface (SST), or le cyclone a pour effet de refroidir la SST à son passage, ce qui constitue une rétroaction négative sur son intensité. La clé du couplage cyclone–océan est donc ce refroidissement induit par le TC : le « sillage froid » ou *Cold Wake* (CW). Mieux comprendre l'influence de l'océan sur les TCs nécessite donc d'identifier les facteurs contrôlant les caractéristiques de la CW. La première partie de ma thèse s'attache à décrire les processus du refroidissement afin de comprendre la dépendance de son amplitude aux caractéristiques du TC et de l'océan.

• **Contrôles de la rétroaction de la CW** Différents processus interviennent dans le refroidissement de surface. Les flux de chaleur mer-air qui refroidissent principalement par évaporation, l'advection horizontale des courants qui fait diverger les eaux chaudes en surface sous l'œil et le mélange vertical qui brasse les eaux chaudes de surface avec les eaux froides sous–jacentes, refroidissant la surface tout en réchauffant la sub–surface. Ces processus n'ont pas la même importance relative en fonction de la distance au centre du TC. La région clé de la rétroaction de la CW sur le cyclone se situe dans un rayon de 100 à 200 km autour de son centre, où l'extraction de chaleur dont se nourrit le TC est maximale. Le mélange vertical dominant le refroidissement près de la trajectoire (chapitre 3) ; les métriques décrivant les contrôles de la CW doivent être basées principalement sur ce processus de mélange.

La CW augmente avec la puissance du vent La principale caractéristique du vent qui permet d'expliquer l'amplitude du refroidissement sous le TC est la quantité d'énergie cinétique qu'il transmet à l'océan. Intégrer la quantité d'énergie dissipée par le cyclone en un point d'océan permet donc de décrire l'amplitude de la CW. Dans cette thèse, je définis un indice de puissance des vents (WPi pour *Wind Power index*) et montre que l'amplitude du refroidissement augmente linéairement avec WPi. Par contraste, la vitesse maximale du vent $V_{\max}$, souvent utilisée pour caractériser l'intensité d'un TC, n'a pas une telle capacité explicative car le refroidissement sature rapidement pour des $V_{\max}$ croissants.

La CW est modulée par la stratification océanique Le contenu thermique de l'océan (OHC) est communément utilisé pour décrire l'influence de l'océan sur les TCs. Si le cyclone extrayait passivement la chaleur de l'océan, le refroidissement superficiel serait simplement dû à ses flux de chaleur mer–air. Cependant, le cyclone extrait seulement quelques pourcents de l'énergie mesurée par l'OHC, et le refroidissement est principalement dû au mélange vertical. Une mesure pertinente de la caractéristique de l'océan dont dépend le refroidissement de surface doit donc s'appuyer sur ce processus. Le chapitre 4 propose un indice d'interaction cyclone–océan basé sur la résistance mécanique de l'océan superficiel à un refroidissement de surface induit par mélange. Je définis un indice (CI pour *Cooling Inhibition*) mesurant l'inhibition au refroidissement que représente l'énergie potentielle de la stratification de sub–surface. L'importance de l'océan de sub–surface pour les TCs a été évoquée dans plusieurs études auparavant, mais cette thèse réalise la première quantification à l'échelle globale de l'influence de l'océan sur l'amplitude de la CW. La découverte de l'ampleur de cette modulation a probablement été la plus grande surprise de ma thèse. En effet, pour une puissance de vent donné (un WPi), le refroidissement engendré peut varier de 1 à 10, et la quasi–totalité de cette dispersion est expliquée par l'état de l'océan de sub–surface tel que décrit par le CI. Ce résultat démontre que l'océan de sub–surface joue un rôle majeur pour le couplage cyclone–océan.

• **Importance des divers processus de la CW** L'amplitude de la CW peut ainsi être décrite en grande partie par 2 indices simples mesurant les caractéristiques du cyclone et de l'océan. Le chapitre 3 explique ces dépendances en étudiant les processus régissant l'évolution de la température dans la couche mélangée (ML). L'amplitude de la CW augmente avec WPi du fait de l'augmentation du transfert d'énergie cinétique qui intensifie le mélange vertical. La stratification de sub–surface module cette dépendance en modifiant l'efficacité de refroidissement du mélange. Un CI faible est associé à une ML fine et/ou une importante stratification verticale en température à sa base. Le mélange entraînera un refroidissement de surface d'autant plus marqué que la ML est fine (de capacité thermique moindre) et que la stratification thermique est forte, ce qui permet au mélange d'incorporer des eaux plus froides dans la ML.

Du fait de son importance pour la rétroaction de la CW, le processus de mélange vertical a attiré beaucoup d'attention. Mes résultats démontrent pourtant que les deux autres processus principaux (advection et flux de surface) jouent aussi un rôle non–négligeable. La part des flux de surface dans le refroidissement total peut ainsi atteindre 50% pour les vents faibles à modérés. Les cyclones d'intensité modérée représentent une part importante des tempêtes tropicales et les vents modérés, loin de l'œil, affectent de très larges surfaces. Les flux de chaleur de surface ont donc une importance relative croissante à mesure que l'on s'intéresse à des échelles spatiales plus grandes.

Un résultat original de la thèse est de montrer que l'advection horizontale joue un rôle dans l'asymétrie de la CW pour les TCs les plus puissants alors que l'asymétrie est en général attribuée à l'accroissement du mélange associé à la résonance inertielle. L'advection verticale joue aussi un rôle indirect en augmentant la stratification thermique en sub–surface, permettant un effet refroidissant accru du mélange.

• **Méthode de modélisation d'un grand nombre de CWs** L'obtention des résultats commentés ci–dessus est rendu possible par l'analyse des caractéristiques d'un grand nombre de CW. C'est la méthode de modélisation développée au cours de ma thèse qui m'a permis de simuler de manière réaliste la réponse océanique à plus de 3 000 TCs sur les 30 dernières années.

Dans une optique opérationnelle ou de recherche, les simulations d'océan forcé par des cyclones ont toujours été réalisées avec les résolutions les plus élevées possibles en fonction des capacités de calcul de l'époque. Ces modèles, d'une résolution typique de 10 km aujourd'hui, permettent de reproduire de manière très réaliste la réponse de l'océan à un TC. Le chapitre 2 montre cependant qu'il est possible de modéliser de manière réaliste la réponse en SST avec un modèle de résolution modérée. En effet, un point déterminant dans la méthodologie de forçage est de transmettre à l'océan une quantité correcte d'énergie cinétique. Cette condition a été atteinte en appliquant un forçage en vent à haute fréquence (36 minutes) provenant d'une formulation paramétrique des vortex cycloniques. Cette formulation, ajustée aux caractéristiques observées de chaque cyclone, permet de décrire correctement la structure du vent près de l'œil. L'utilisation d'un modèle au $1/2°$ (résolution d'environ 50 km) permet de diviser le coût de calcul par 625 (5^3)[1] par rapport à une résolution de 10 km, tout en capturant correctement l'apport en énergie des cyclones, et raisonnablement bien leur pompage d'Ekman.

L'utilisation d'un modèle relativement peu coûteux présente deux avantages notables :
i) La simulation des CWs induites par plusieurs milliers de cyclones permet de comprendre la dépendance des CWs aux caractéristiques des TCs et de l'océan, chose impossible à partir d'études de cas.
ii) La possibilité de simuler la réponse océanique aux TCs directement dans un

---

[1] facteur 5 pour les résolutions spatiales (dans les 2 directions) et temporelles, sans compter les durées de post–traitement.

modèle de l'océan mondial donne l'opportunité de faire le lien entre les processus ayant lieu à l'échelle du cyclone et leurs conséquences à l'échelle globale.

7.1.2 Interactions entre les TCs et le climat

• **Influence du climat sur l'activité cyclonique** Le chapitre 6 illustre la dépendance de l'activité cyclonique à la variabilité du climat. Cette dépendance s'exprime par des téléconnexions associées aux modes de variabilité (tels que le phénomène *El Niño* / Oscillation Australe ; ENSO) qui modifient régionalement les variables favorables à la genèse et au développement des TCs. L'influence de la variabilité climatique sur l'activité cyclonique a été largement étudiée dans les bassins Atlantique et Pacifique Nord mais peu étudiée dans l'Océan Indien et le Pacifique Sud. Je me suis plus particulièrement intéressé à ce dernier bassin. Ainsi le chapitre 6 montre que la position de la Zone de Convergence du Pacifique Sud (SPCZ) est un bon résumé des conditions grande–échelle favorisant la cyclogenèse dans le Pacifique Sud–Ouest. La région de cyclogenèse est bornée au Nord par la position de la SPCZ et suit ses déplacements interannuels Sud–Ouest/Nord–Est qui sont contrôlés par ENSO. Certains événements *El Niño* sont caractérisés par un déplacement particulier de la SPCZ dont l'orientation devient zonale. Pendant ces années, les TCs peuvent se former dans le centre–Est du bassin et ainsi affecter la Polynésie française.

• **Influence des TCs sur le climat** Il a été suggéré que le mélange océanique associé aux cyclones induit un flux de chaleur vers l'océan intérieur du même ordre de grandeur que le flux de chaleur transporté par l'océan vers les pôles (∼1 PW ou 1 000 TW). De là à supposer que les cyclones influencent ou même dominent le transport méridien de chaleur par l'océan (MHT), il n'y avait qu'un pas.

Une méthode permettant la modélisation explicite de l'effet des TCs sur l'océan Les études précédentes qui ont tenté d'étudier la question ont représenté l'effet des TCs dans des modèles de circulation océanique par l'augmentation du coefficient de mélange vertical. L'hypothèse de l'importance des TCs sur le MHT repose pourtant sur plusieurs approximations concernant : i) les hypothèses faites pour évaluer la valeur du coefficient de mélange ; ii) les modalités d'application de ce coefficient de mélange additionnel dans les simulations numériques ; iii) la prise en compte exclusivement du processus de mélange induit par les TCs ; iv)...

Finalement ces paramétrisations consistent simplement en l'ajout d'un coefficient de mélange qui ne se soucie pas de la stratification verticale où elle est appliquée et ne permet donc aucun contrôle de l'énergie injectée dans le système. L'application d'une énergie de mélange serait physiquement plus correct.

Les simulations réalisées dans cette thèse sont utilisées pour étudier l'influence du forçage par les TCs sur l'océan. Elles présentent l'avantage de ne pas paramétriser l'effet induit par le mélange des TCs mais de le reproduire explicitement. De plus, d'autres processus induits par les TCs sont aussi représentés alors qu'ils ont été systématiquement ignorés dans les études précédentes.

Les flux de chaleur et l'advection ont une importance climatique Jusqu'à présent, l'attention a été focalisée sur le mélange vertical qui est le processus dominant du refroidissement sous l'œil des TCs. Nos analyses démontrent pourtant que les flux de chaleur accrus au moment du passage des TCs contribuent à refroidir les bassins cycloniques de manière significative en été (jusqu'à 1°C en moyenne mensuelle dans le Pacifique Nord–Ouest). D'autre part, l'advection verticale a des conséquences à grande échelle qui n'ont pas été commentées auparavant. L'*upwelling* induit par le TC le long de sa trajectoire peut être équilibré par une circulation géostrophique et générer des ondes de Rossby qui propagent les déplacements verticaux de la thermocline au sein du bassin. Les processus advectifs induits par les TCs conduisent donc à modifier la structure tri–dimensionnelle des températures dans l'océan et participent à modifier le transport océanique de chaleur.

L'influence du cycle saisonnier et sa modification par les TCs Dans nos simulations, le mélange participe à injecter des anomalies chaudes en sub–surface pendant les saisons cycloniques. La quantité de chaleur transmise à l'océan dans le sillage des TCs est de l'ordre de 500 TW, en accord avec les dernières estimations publiées. Cependant, cette énergie transmise n'est pas entièrement disponible pour modifier le transport océanique de chaleur (OHT) pour deux raisons principales.

Premièrement, la chaleur transmise à l'océan dans le sillage des TCs est en partie utilisée pour combler la perte de chaleur due à l'évaporation accrue des vents cycloniques, et en partie pour combler le refroidissement superficiel associé au mélange vertical. Seule cette dernière fraction constitue réellement un gain d'énergie net pour l'océan. Dans notre simulation, la chaleur extraite à l'océan par les vents des TCs lors de leur passage est évaluée à environ 200 TW. Le flux net de chaleur effectivement injecté en sub–surface (noté net OHU pour *net Ocean Heat Uptake*) est donc d'environ 300 TW.

Deuxièmement, nos analyses démontrent que les anomalies chaudes placées en sub–surface pendant la saison cyclonique sont en grande partie rétrocédées à l'atmosphère au cours de l'hiver qui suit du fait de l'approfondissement de la couche de mélange. Ce mécanisme, proposé par [Jansen *et al.* 2010] sur la base d'arguments théoriques, est ici confirmé expérimentalement. Environ $^3/_5{}^{e}$ de l'OHU net est perdue par ce mécanisme, ne laissant que ∼120 TW potentiellement disponible pour modifier l'OHT. Les anomalies chaudes localisées dans la thermocline saisonnière sont remises en contact de l'atmosphère proche de l'endroit où elles ont été injectées ; elles ne participent que faiblement à modifier l'OHT. Seules celles, nettement moins nombreuses, injectées dans la thermocline principale peuvent être transportées par la circulation océanique sur plus d'une année et changer significativement l'OHT. De plus, la chaleur transportée l'est pour un tiers vers l'équateur et elle est partiellement compensée en moyenne zonale, de sorte que l'export de chaleur vers les pôles n'atteint que difficilement les 20 TW vers 25°N et 20°S. On a là un transport méridien de chaleur négligeable pour le climat terrestre.

En revanche, l'entraînement des anomalies chaudes dans la ML restitue en hiver l'énergie stockée en été. Associé au fait que les TCs refroidissent les bassins cycloniques en été, ceci résulte en une réduction de l'amplitude du cycle saisonnier de SST de l'ordre de ∼10% dans les bassins cycloniques. Ces résultats ne signifient donc pas que l'influence des TCs sur le climat est nulle mais que les flux d'énergie associés sont principalement circonscrits au cycle saisonnier. Les conséquences sur le climat tropical de cette modification du cycle saisonnier restent à explorer.

7.2 Perspectives

Les perspectives de recherches et d'applications qu'offre cette thèse sont nombreuses. Elles se déclinent en deux thématiques principales : une meilleure compréhension i) de l'influence de l'océan sur les TCs (à l'échelle du cyclone et à l'échelle climatique) et ii) de l'influence des TCs sur le climat global.

7.2.1 L'influence de l'océan sur les TCs

• **Améliorer les prévisions opérationnelles en intégrant la rétroaction de la CW** Depuis ∼20 ans, les capacités de prévision opérationnelle de l'intensité des TCs se sont peu améliorées. Cette thèse défend l'idée qu'il est envisageable d'améliorer ces prévisions en prenant mieux en compte l'effet de l'océan.

Concernant les méthodes de prévision dynamiques par modélisation 3D, cette idée se traduit par l'utilisation de modèles couplés océan–atmosphère. Un modèle atmosphérique forcé par une SST fixe ne peut représenter la rétroaction de la CW sur l'intensité du cyclone. Améliorer la capacité de simulation des CWs ne peut se faire simplement en augmentant la résolution de ces modèles. Les incertitudes sur l'expression des coefficients de transfert ou les difficultés d'initialisation de l'état du modèle d'océan (faute d'observations) constituent encore des limites importantes.

Concernant les méthodes statistiques, une amélioration potentielle nécessite la prise en compte explicite du refroidissement de surface induit par les TCs. La SST pré–cyclonique est utilisée dans la plupart des méthodes statistiques de prévision et en est une variable centrale. Remplacer cette variable par la SST sous l'œil du TC donnera sûrement des prévisions plus précises. Cependant la différence de SST pré–cyclone − sous l'œil contient une information complémentaire. Dans les tropiques, le différentiel d'énergie (enthalpie) entre l'eau et l'air est tel que le flux de chaleur est dirigé de l'océan vers l'atmosphère. C'est ce déséquilibre d'enthalpie air–mer que la

CW détruit et qui explique l'importance de prévoir le refroidissement (ΔSST). Les méthodes statistiques de prévision devraient donc faire intervenir deux variables de température océanique : la SST pré–cyclonique et la différence de SST par rapport à l'état non–perturbé (ΔSST).

L'amplitude de la CW étant en grande partie contrôlée par deux indices simples (WPi et CI ; 61% de la variance expliquée avec un simple *fit* d'ordre 1), il est envisageable de prévoir simplement ΔSST en améliorant encore ces indices [2]. Le refroidissement prévu sous l'œil pourrait être utilisé comme prédicteur statistique supplémentaire de l'intensité. Le simple ajout de l'OHC en tant que prédicteur supplémentaire dans le modèle statistique SHIPS a permis d'améliorer les prévisions de 5 à 10% pour certains cyclones forts et de 1 à 2% dans le cas général. Une méthodologie plus réfléchie devrait entraîner des améliorations plus importantes. Une thèse menée par S. Neetu et encadrée par M.M. Ali et M. Lengaigne au NIO [3] débute sur ce sujet. Une première étude montre que le CI permet de quantifier l'influence de la stratification haline sur l'amplitude des CWs dans la Baie du Bengale (Fig. 7.1).

Extrait de [Neetu *et al.* 2012]

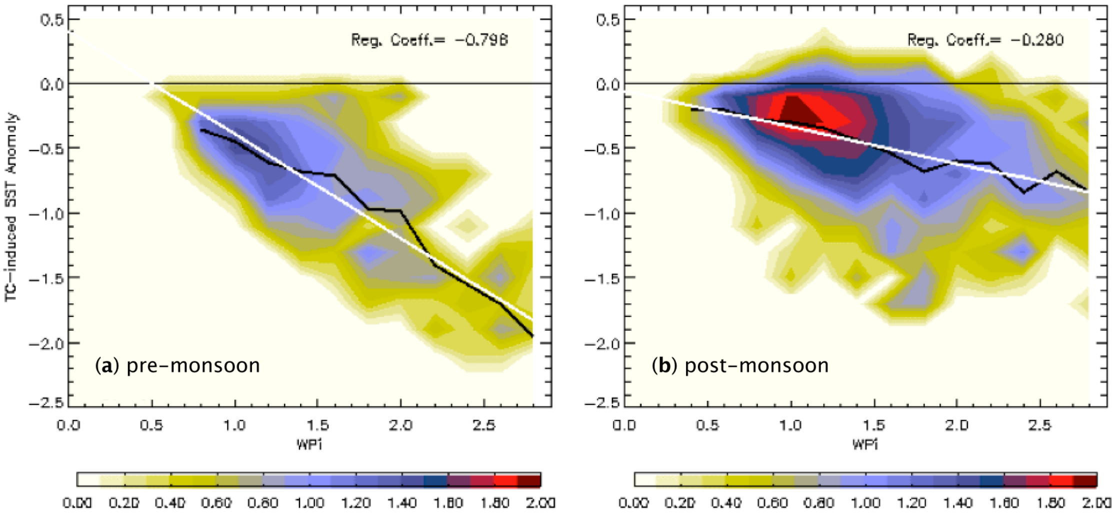

Figure 7.1 – Densité de probabilité du refroidissement induit par les TCs de la Baie du Bengale en fonction de leur puissance (WPi) dans la simulation CYCL : (**a**) avant la mousson et (**b**) après la mousson. La couche barrière d'eau douce formée en post–mousson augmente la stabilité de la colonne d'eau et diminue l'amplitude des refroidissements pour une puissance donnée.

---

[2] Par la prise en compte de la résonance inertielle dans WPi par exemple, ou encore par la prise en compte de l'effet indirect de l'*upwelling* sur le refroidissement dû au mélange.

[3] *National Institute of Oceanography*, Goa, Inde

• **Influence de la variabilité climatique de l'océan sur les TCs** Cette thèse souligne la faiblesse des études passées concernant le contrôle de l'activité cyclonique par l'océan, particulièrement en ce qui concerne le rôle potentiel de la sub–surface.

Variabilité interannuelle Il serait intéressant d'identifier les régions où la variabilité interannuelle de l'océan de sub–surface est susceptible de modifier notablement l'activité cyclonique via une modification de la rétroaction de la CW. L'importante variabilité de la profondeur de la thermocline dans l'Océan Indien Sud (TRIO) en fait une région potentiellement sensible à ce mécanisme. Dans un premier temps, on pourra analyser la variabilité interannuelle du CI. L'investigation pourra être approfondie au moyen de simulations d'ensemble où un même forçage cyclonique est appliqué sur des conditions océaniques variées correspondant à la variabilité interannuelle naturelle de l'océan. La sensibilité des CWs à la variabilité naturelle de l'océan peut ainsi être analysée. Les premiers tests utilisant une telle stratégie ont été réalisés avec la configuration ORCA2° de NEMO. Ils révèlent que l'amplitude de la CW peut varier du simple au double en réponse à un même cyclone en fonction de l'année où le TC se produit (Fig. 7.2).

Changement climatique Le changement climatique en cours est susceptible d'influencer l'activité cyclonique en modifiant les variables favorables à la cyclogenèse. C'est le cas, entre autres, des caractéristiques de sub–surface de l'océan, mais cet effet reste pour le moment inconnu. L'influence des modifications futures de l'océan sur les TCs s'articule en deux problèmatiques distinctes concernant l'influence i) des changements de température de surface et ii) d'une éventuelle modification de la rétroaction de la CW.

Actuellement le lien entre l'augmentation des SSTs et l'activité cyclonique n'apparaît clairement qu'en Atlantique. L'intensité dépend de la différence de température entre le bas et le haut de la troposphère. Or l'effet de serre additionnel induit un réchauffement en basse couche et un refroidissement au niveau de la tropopause. Cet effet peut augmenter l'efficacité thermodynamique du "cycle de Carnot" et donc l'intensité des TCs de manière modérée (1.5.4, p 43).

Le réchauffement climatique actuel a également pour effet d'augmenter la température de l'océan sur les 50–100 premiers mètres de l'océan [Barnett *et al.* 2005]. Etant donné que la couche de surface se réchauffe plus que la sub–surface, le gradient vertical de température augmente. Les TCs suffisamment puissants pour mélanger l'océan sur une profondeur plus importante que le réchauffement superficiel génèreront alors une CW plus importante qu'aujourd'hui ce qui pourrait rétroagir négativement sur leur intensité. Ceci n'est évidemment qu'une hypothèse qu'il convient de valider. Une étude de la modification de la stratification thermique verticale associée au changement climatique futur est donc une piste à explorer. Il convient de rappeler qu'il existe de nombreux autres facteurs influençant les TCs, seuls ceux

Figure réalisée par M. Bador durant son stage de Mastère sous la direction de J. Vialard

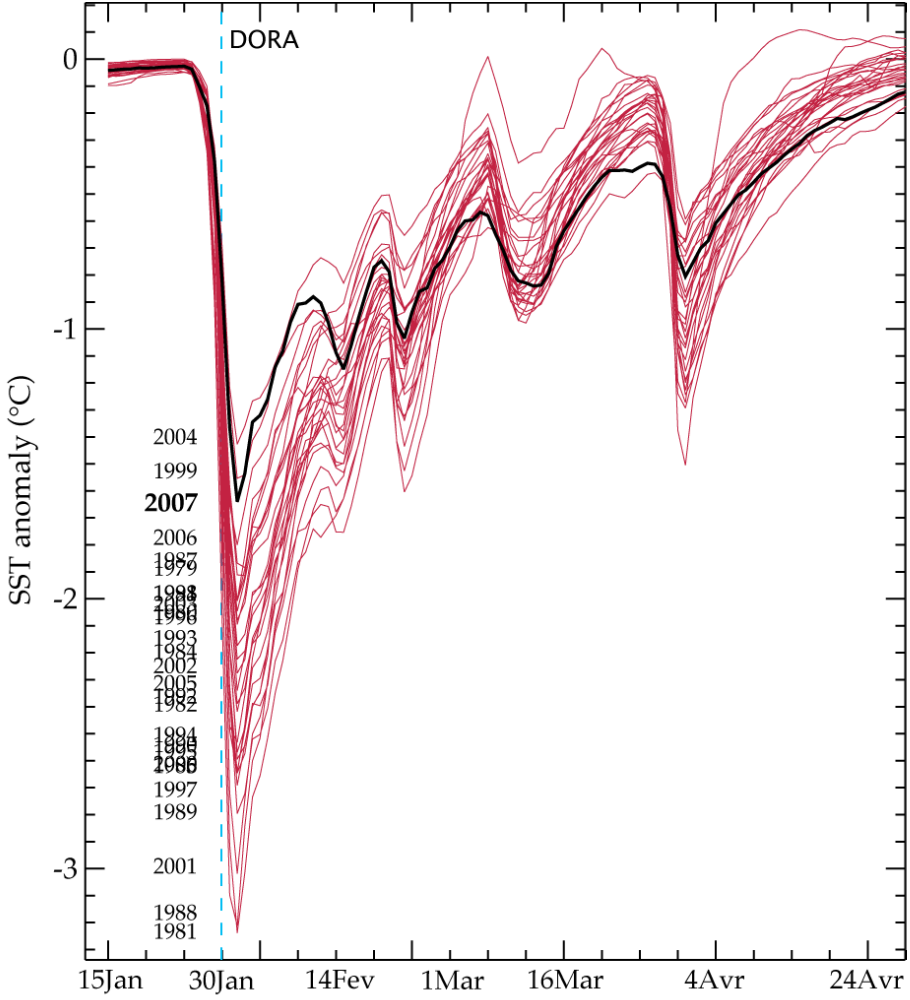

Figure 7.2 – Ensemble de séries temporelles de SST dans la région 65°E–68°E / 7°S–10°S au–dessus de laquelle est passé le TC DORA le 30 Janvier 2007 (*ligne bleue*). Chaque courbe représente un membre de l'expérience d'ensemble correspondant à l'état de l'océan d'une des 30 années entre 1978 et 2007. La *courbe noire* correspond à l'année 2007 lors de laquelle le TC DORA a effectivement été observé ; le faible refroidissement de cette année peut s'expliquer par l'événement IOD qui a eu lieu fin 2006 résultant en une thermocline profonde dans la TRIO. Le refroidissement maximal varie de 1.5°C à plus de 3°C indiquant l'importance de la variabilité interannuelle de l'océan de sub–surface dans le contrôle des CWs dans cette région.
Les épisodes de refroidissement suivants sont associés au passage des TCs Enok, Favio, Gamède et Humba près de la région considérée.

concernant l'océan sont discutés ici, ce qui ne pré–suppose pas que ces effets soient plus importants que les autres.

7.2.2 L'influence des TCs sur le climat

• **Modélisation de processus supplémentaires** Notre méthodologie permet de faire le pont entre l'échelle locale et l'échelle globale et ainsi de décrire l'effet des TCs sur l'océan à l'échelle climatique dans un modèle de résolution modérée ($^1/_2$°). Une étude similaire utilisant un modèle à plus haute résolution serait néanmoins souhaitable pour vérifier la robustesse des résultats. De plus, certains processus, comme par exemple la propagation vers le fond des ondes proche–inertielles, ne sont pas résolus correctement au $^1/_2$°. Or ces ondes participent à propager l'énergie de la surface vers l'océan intérieur où le cisaillement qu'elles génèrent peut contribuer au mélange [Le Vaillant *et al.* 2012]. Des expériences utilisant NEMO au $^1/_{12}$° forcé en surface par des TCs sont en cours d'élaboration dans une configuration régionale afin d'explorer ces aspects.

Les études précédentes se sont focalisées sur le mélange de sub–surface, mais les cyclones sont aussi potentiellement une source de mélange profond. La dépression de surface au cœur du TC est associée à une circulation barotrope qui crée des courants sur l'ensemble de la colonne d'eau. L'interaction des courants profonds avec la bathymétrie peut créer des mouvements verticaux, générer des ondes internes et *in fine* du mélange en profondeur. La question est donc de quantifier la part des TCs comme source du mélange profond, notamment par rapports à la marée.

• **Effet des TCs dans le système couplé océan–atmosphère** Dans cette thèse, l'influence climatique des TCs a été déterminée à l'aide d'un modèle d'océan forcé. Certains impacts océaniques observés dans cette configuration forcée sont toutefois susceptibles d'être modulés par des rétroactions impliquant l'atmosphère. Ainsi, le refroidissement des bassins de l'Ouest du Pacifique en été pourrait diminuer l'intensité des alizés et donc l'amplitude de l'upwelling équatorial dans l'Est. La rétroaction de Bjerkness pourrait ainsi amplifier le réchauffement de la langue d'eau froide du Pacifique Est observé dans le modèle.

Tester ces hypothèses nécessite d'incorporer le forçage en vent associé aux TCs dans un modèle couplé et de disposer de simulations avec et sans cyclones. Les modèles atmosphériques actuels n'ayant pas une résolution suffisante pour les simuler de manière réaliste, il est nécessaire de paramétriser leur effet. L'utilisation d'un coefficient additionnel de mélange vertical n'a pas donné de résultats convaincants et robustes. Une représentation paramétrique du vent des TCs, similaire à celle utilisée dans ma thèse, a été ajoutée dans le modèle couplé de Météo France (NEMO–CNRM). Les simulations, réalisées par E. Maisonnave, sont en cours d'analyse par C. Cassou et M. Lengaigne entre autres.

Une question encore ouverte découle de mes travaux. Les flux de chaleur air–mer contribuent fortement aux changement de cycle saisonnier de SST dans le modèle forcé. Introduire les flux de chaleur à la surface de l'océan dans un système couplé pose le problème de leur transmission à l'atmosphère : comment les introduire de manière à assurer une cohérence énergétique entre les deux milieux ?

Parmi les perspectives évoquées dans cette conclusion, celles que je souhaite poursuivre dans un futur proche sont : (i) de mettre en évidence et de quantifier l'éventuel contrôle de l'activité cyclonique par la variabilité océanique (dans les climats présent et futur) et (ii) de tenter d'améliorer les prévisions opérationnelles de l'intensité des TCs en intégrant correctement la rétroaction de la CW.

Bibliographie

[Andreas 2011] E.L. Andreas. *Fallacies of the Enthalpy Transfer Coefficient over the Ocean in High Winds.* Journal of the Atmospheric Sciences, vol. 68, pages 1435–1445, 2011.

[Axell 2002] L. Axell. *Wind-driven internal waves and Langmuir circulations in a numerical ocean model of the southern Baltic Sea.* Journal of Geophysical Research, vol. 107, pages 25–1, 2002.

[Barnett *et al.* 2005] T.P. Barnett, D.W. Pierce, K.M. AchutaRao, P.J. Gleckler, B.D. Santer, J.M. Gregory et W.M. Washington. *Penetration of human-induced warming into the world's oceans.* Science, vol. 309, no. 5732, page 284, 2005.

[Basher & Zheng 1995] R.E. Basher et X. Zheng. *Tropical Cyclones in the SoutWest Pacific - Spatial patterns and relationships to Southern-Oscillation and Sea-Surface Temperature.* Journal of Climate, vol. 8, no. 5, pages 1249–1260, 5 1995.

[Bates *et al.* 1998] N.R. Bates, A.H. Knap et A.F. Michaels. *Contribution of hurricanes to local and global estimates of air–sea exchange of CO2.* Nature, vol. 395, no. 6697, pages 58–61, 1998.

[Bengtsson *et al.* 2007] L. Bengtsson, K.I. Hodges, M. Esch, N. Keenlyside, L. Kornblueh, J.J.I.A. LUO et T. Yamagata. *How may tropical cyclones change in a warmer climate ?* Tellus A, vol. 59, no. 4, pages 539–561, 2007.

[Beucher 2010] F. Beucher. Météorologie tropicale : des alizés au cyclone. Météo-France, 2010.

[Bister & Emanuel 1998] M. Bister et K.A. Emanuel. *Dissipative heating and hurricane intensity.* Meteorology and Atmospheric Physics, vol. 65, no. 3, pages 233–240, 1998.

[Black *et al.* 2007] P.G. Black, E.A. DAsaro, W.M. Drennan, J.R. French, PP Niller, T.B. Sanford, E.J. Terrill, E.J. Walsh et J.A. Zhang. *Air-sea exchange in hurricanes.* Bulletin of the American Meteorological Society, vol. 88, pages 357–374, 2007.

[Blanke & Delecluse 1993] B. Blanke et P. Delecluse. *Variability of the tropical Atlantic Ocean simulated by a general circulation model with two different mixed-layer physics.* Journal of Physical Oceanography, vol. 23, no. 7, pages 1363–1388, 1993.

[Bougeault & Lacarrere 1989] P. Bougeault et P. Lacarrere. *Parameterization of orography–induced turbulence in a mesobeta–scale model.* Monthly Weather Review, vol. 117, no. 8, pages 1872–1890, 1989.

[Burchard 2002] H. Burchard. *Energy-conserving discretisation of turbulent shear and buoyancy production.* Ocean Modelling, vol. 4, no. 3-4, pages 347–361, 2002.

[Cai *et al.* 2012] W. Cai, M. Lengaigne, S. Borlace, M. Collins, E.M. Vincent*et al.* *More extreme swings of the South Pacific Convergence Zone due to greenhouse warming.* Nature, in press 2012.

[Canuto *et al.* 2001] V.M. Canuto, A. Howard, Y. Cheng et M.S. Dubovikov. *Ocean turbulence. Part I : One-point closure model-momentum and heat vertical diffusivities.* Journal of Physical Oceanography, vol. 31, no. 6, pages 1413–1426, 2001.

[Caron & Jones 2008] L.P. Caron et C.G. Jones. *Analysing present, past and future tropical cyclone activity as inferred from an ensemble of Coupled Global Climate Models.* Tellus A, vol. 60, no. 1, pages 80–96, 2008.

[Chand & Walsh 2009] S.S. Chand et K.J.E. Walsh. *Tropical Cyclone Activity in the Fiji Region : Spatial Patterns and Relationship to Large-Scale Circulation.* Journal of Climate, vol. 22, pages 3877–3893, 2009.

[Charney & Eliassen 1964] J.G. Charney et A. Eliassen. *On the growth of the hurricane depression.* Journal of Atmospheric Sciences, vol. 21, pages 68–75, 1964.

[Cione & Uhlhorn 2003] J.J. Cione et E.W. Uhlhorn. *Sea surface temperature variability in hurricanes : Implications with respect to intensity change.* Monthly Weather Review, vol. 131, no. 8, 2003.

[Cione *et al.* 2000] J.J. Cione, P.G. Black et S.H. Houston. *Surface Observations in the Hurricane Environment.* Monthly Weather Review, vol. 128, pages 1550–1561, 2000.

[Craig & Gray 1996] G.C. Craig et S.L. Gray. *CISK or WISHE as the mechanism for tropical cyclone intensification.* Journal of Atmospheric Sciences, vol. 53, no. 23, pages 3528–3540, 1996.

[D'Asaro *et al.* 2007] E.A. D'Asaro, T.B. Sanford, P.P. Niiler et E.J. Terrill. *Cold wake of Hurricane Frances.* Geophysical Research Letters, vol. 34, no. L15609, 2007.

[DeMaria & Kaplan 1994] M. DeMaria et J. Kaplan. *A statistical hurricane intensity prediction scheme (SHIPS) for the Atlantic basin.* Weather and Forecasting, vol. 9, pages 209–220, 1994.

[DeMaria *et al.* 2005] M. DeMaria, M. Mainelli, L.K. Shay, J.A. Knaff et J. Kaplan. *Further improvements to the statistical hurricane intensity prediction scheme (SHIPS).* Weather and Forecasting, vol. 20, no. 4, pages 531–543, 2005.

[DeMaria 2009] M. DeMaria. *A simplified dynamical system for tropical cyclone intensity prediction.* Monthly Weather Review, vol. 137, no. 1, pages 68–82, 2009.

[Done *et al.* 2011] J. Done, C. Bruyere, G. Holland et A. Suzuki-Parker. *Uncertainty in dynamical model predictions of future hurricane activity.* In 3rd International Summit on Hurricanes and Climate Change, 2011.

[Donelan *et al.* 2004] M.A. Donelan, B.K. Haus, N. Reul, W.J. Plant, M. Stiassnie, H.C. Graber, O.B. Brown et E.S. Saltzman. *On the limiting aerodynamic roughness of the ocean in very strong winds.* Geophysical Research Letters, vol. 31, no. L18306, 2004.

[Duvel *et al.* 2008] J.P. Duvel, C. Basdevant, H. Bellenger, G. Reverdin, A. Vargas et J. Vialard. *The Aeroclipper : A new device to explore convective systems and cyclones.* Bulletin of the American Meteorological Society, 2008.

[Dvorak 1975] V.F. Dvorak. *Tropical cyclone intensity analysis and forecasting from satellite imagery.* Mariners Weather Log., vol. 19, no. 4, pages 199–206, 1975.

[Elsner *et al.* 2008] J.B. Elsner, J.P. Kossin et T.H. Jagger. *The increasing intensity of the strongest tropical cyclones.* Nature, vol. 455, no. 7209, pages 92–95, 2008.

[Emanuel & Khairoutdinov 2011] K.A. Emanuel et M. Khairoutdinov. *Aggregation, Tropical Cyclones, and Climate.* In 3rd International Summit on Hurricanes and Climate Change, 2011.

[Emanuel & Nolan 2004] K.A. Emanuel et D.S. Nolan. *Tropical cyclone activity and global climate.* Bulletin of the American Meteorological Society, vol. 85, no. 5, pages 666–667, 5 2004.

[Emanuel *et al.* 1994] K.A. Emanuel, J.D. Neelin et C.S. Bretherton. *On large-scale circulations in convecting atmospheres.* Quarterly Journal of the Royal Meteorological Society, vol. 120, no. 519, pages 1111–1143, 1994.

[Emanuel *et al.* 2004] K.A. Emanuel, C. DesAutels, C. Holloway et R. Korty. *Environmental control of tropical cyclone intensity.* Journal of Atmospheric Sciences, vol. 61, pages 843–858, 2004.

[Emanuel 1986] K.A. Emanuel. *An air-sea interaction theory for tropical cyclones. Part 1 : Steady-state maintenance.* Journal of the Atmospheric Sciences, vol. 43, no. 6, pages 585–604, 1986.

[Emanuel 1995] K.A. Emanuel. *Sensitivity of tropical cyclones to surface exchange coefficients and a revised steady-state model incorporating eye dynamics.* Journal of the Atmospheric Sciences, vol. 52, pages 3969–3976, 1995.

[Emanuel 1999] K.A. Emanuel. *Thermodynamic control of hurricane intensity.* Nature, vol. 401, no. 6754, pages 665–669, 1999.

[Emanuel 2000] K.A. Emanuel. *A statistical analysis of hurricane intensity.* Monthly Weather Review, vol. 128, pages 1139–1152, 2000.

[Emanuel 2001] K.A. Emanuel. *Contribution of tropical cyclones to meridional heat transport by the oceans.* Journal of Geophysical Research, vol. 106, page 14, 2001.

[Emanuel 2005] K.A. Emanuel. *Increasing destructiveness of tropical cyclones over the past 30 years.* Nature, vol. 436, no. 7051, pages 686–688, 2005.

[Emanuel 2006] K.A. Emanuel. *Climate and tropical cyclone activity : A new model downscaling approach.* Journal of Climate, vol. 19, no. 19, pages 4797–4802, 2006.

[Emanuel 2008] K.A. Emanuel. *The hurricane-climate connection.* Bulletin of the American Meteorological Society, vol. 89, no. 5, 2008.

[Evans & Allan 1992] J.L. Evans et R.J. Allan. *El Niño/Southern Oscillation modification to the structure of the monsoon and tropical cyclone activity in the Australasian region.* International Journal of Climatology, vol. 12, pages 611–623, 1992.

[Fedorov *et al.* 2010] A.V. Fedorov, C.M. Brierley et K.A. Emanuel. *Tropical cyclones and permanent El Niño in the early Pliocene epoch.* Nature, vol. 463, pages 1066–1071, 2010.

[Folland *et al.* 2002] C.K. Folland, J. Renwick, M.J. Salinger et A.B. Mullan. *Relative influences of the Interdecadal Pacific Oscillation and ENSO on the South Pacific Convergence Zone.* Geophysical Research Letters, vol. 29, pages 21–1, 2002.

[Frappier *et al.* 2007] A.B. Frappier, D. Sahagian, S.J. Carpenter, L.A. González et B.R. Frappier. *Stalagmite stable isotope record of recent tropical cyclone events.* Geology, vol. 35, no. 2, page 111, 2007.

[Gaspar *et al.* 1990] P. Gaspar, Y. Grégoris et J.M. Lefevre. *A simple eddy kinetic energy model for simulations of the oceanic vertical mixing : Tests at station Papa and long-term upper ocean study site.* Journal of Geophysical Research, vol. 95, no. C9, pages 16179–16, 1990.

[Gaspar 1988] P. Gaspar. *Modeling the seasonal cycle of the upper ocean.* Journal of Physical Oceanography, vol. 18, no. 2, pages 161–180, 1988.

[Goldenberg & Shapiro 1996] S.B. Goldenberg et L.J. Shapiro. *Physical mechanisms for the association of El Niño and West African rainfall with Atlantic major hurricane activity.* Journal of Climate, vol. 9, no. 6, pages 1169–1187, 1996.

[Goldenberg *et al.* 2001] S.B. Goldenberg, C.W. Landsea, A.M. Mestas-Nuñez et W.M. Gray. *The recent increase in Atlantic hurricane activity : Causes and implications.* Science, vol. 293, no. 5529, page 474, 2001.

[Goni *et al.* 2009] G. Goni, M.A. DeMaria, J. Knaff, C. Sampson, I. Ginis, F. Bringas, A. Mavume, C. Lauer, I.I. Lin et M.M. Ali. *Applications of satellite-derived ocean measurements to tropical cyclone intensity forecasting.* Oceanography, vol. 22, no. 3, page 190, 2009.

[Gray & Emanuel 2010] W.M. Gray et K.A. Emanuel. Introduction to tropical meteorology. COMET, 2010.

[Gray 1968] W. Gray. *Global view of the origin of tropical disturbances and storms.* Monthly Weather Review, 1 1968.

[Gray 1984] W.M. Gray. *Atlantic seasonal hurricane frequency. Part I : El Niño and 30 mb quasi-biennial oscillation influences.* Monthly Weather Review, vol. 112, no. 9, pages 1649–1668, 1984.

[Greatbatch 1983] R.J. Greatbatch. *On the response of the ocean to a moving storm : The nonlinear dynamics.* Journal of Physical Oceanography, vol. 13, pages 357–367, 1983.

[Greatbatch 1984] R.J. Greatbatch. *On the response of the ocean to a moving storm : Parameters and scales.* Journal of Physical Oceanography, vol. 14, pages 59–78, 1984.

[Grossmann & Morgan 2008] I. Grossmann et M.G. Morgan. *Tropical cyclones, climate change, and scientific uncertainty : what do we know, what does it mean, and what should be done ?* Climatic Change, pages 1–37, 2008.

[Halliwell Jr *et al.* 2010] G.R. Halliwell Jr, L.K. Shay, J.K. Brewster et W.J. Teague. *Evaluation and Sensitivity Analysis of an Ocean Model Response to Hurricane Ivan.* Monthly Weather Review, vol. 139, pages 921–945, 2010.

[Hanshaw *et al.* 2008] M.N. Hanshaw, M.S. Lozier et J.B. Palter. *Integrated impact of tropical cyclones on sea surface chlorophyll in the North Atlantic.* Geophysical Research Letters, vol. 35, no. L01601, 2008.

[Hawkins & Imbembo 1976] H.F. Hawkins et S.M. Imbembo. *The Structure of a Small, Intense Hurricane—Inez 1966.* Monthly Weather Review, vol. 104, page 418, 1976.

[Ho *et al.* 2006] C.H. Ho, J.H. Kim, J.H. Jeong, H.S. Kim et D. Chen. *Variation of tropical cyclone activity in the South Indian Ocean : El Niño–Southern Oscillation and Madden-Julian Oscillation effects.* Journal of Geophysical Research, vol. 111, no. D22101, 2006.

[Holland 1980] G.J. Holland. *An analytic model of the wind and pressure profiles in hurricanes.* Monthly Weather Review, vol. 108, pages 1212–1218, 1980.

[Holland 1997] G.J. Holland. *The maximum potential intensity of tropical cyclones.* Journal of the Atmospheric Sciences, vol. 54, no. 21, pages 2519–2541, 1997.

[Hu & Meehl 2009] A. Hu et G.A. Meehl. *Effect of the Atlantic hurricanes on the oceanic meridional overturning circulation and heat transport.* Geophysical Research Letters, vol. 36, 2009.

[Huang & Imberger 2010] P. Huang et J. Imberger. *Variation of pCO_2 in ocean surface water in response to the passage of a hurricane.* Journal of Geophysical Research, vol. 115, no. C10024, 2010.

[Huang *et al.* 2009] P. Huang, T.B. Sanford et J. Imberger. *Heat and turbulent kinetic energy budgets for surface layer cooling induced by the passage of Hurricane Frances (2004).* Journal of Geophysical Research, vol. 114, no. C12023, 12 2009.

[Izumo *et al.* 2010] T. Izumo, J. Vialard, M. Lengaigne, C. de Boyer Montegut, S.K. Behera, J.J. Luo, S. Cravatte, S. Masson et T. Yamagata. *Influence of the state of the Indian Ocean Dipole on the following year's El Niño.* Nature Geoscience, vol. 3, pages 168–172, 2010.

[Jacob & Koblinsky 2007] S.D. Jacob et C.J. Koblinsky. *Effects of precipitation on the upper-ocean response to a hurricane.* Monthly Weather Review, vol. 135, pages 2207–2225, 2007.

[Jacob & Shay 2003] S.D. Jacob et L.K. Shay. *The role of oceanic mesoscale features on the tropical cyclone–induced mixed layer response : A case study.* Journal of Physical Oceanography, vol. 33, pages 649–676, 2003.

[Jansen & Ferrari 2009] M.F. Jansen et R. Ferrari. *Impact of the latitudinal distribution of tropical cyclones on ocean heat transport.* Geophysical Research Letters, vol. 36, no. L06604, 2009.

[Jansen *et al.* 2010] M.F. Jansen, R. Ferrari et T.A. Mooring. *Seasonal versus permanent thermocline warming by tropical cyclones.* Geophysical Research Letters, vol. 37, no. L03602, 2010.

[Jarosz *et al.* 2007] E. Jarosz, D.A. Mitchell, D.W. Wang et W.J. Teague. *Bottom-up determination of air-sea momentum exchange under a major tropical cyclone.* Science, vol. 315, page 1707, 2007.

[Jourdain *et al.* 2011] N.C. Jourdain, P. Marchesiello, C.E. Menkes, J. Lefèvre, E.M. Vincent, M. Lengaigne et F. Chauvin. *Mesoscale Simulation of Tropical Cyclones in the South Pacific : Climatology and Interannual Variability.* Journal of Climate, vol. 24, pages 3–25, 2011.

[Jourdain *et al.* 2012] N.C. Jourdain, M. Lengaigne, G. Madec, J. Vialard, C.E. Menkes, E.M. Vincent et G. Samson. *Observationally based estimates of ocean mixing inhibition by heavy rainfall under tropical cyclones.* Journal of Physical Oceanography, submitted 2012.

[Jullien *et al.* 2012] S. Jullien, P. Marchesiello, C.E. Menkes, A. Koch-Larrouy, M. Lengaigne, N.C. Jourdain, V. Faure, J. Lefèvre, G. Samson et E.M. Vincent. *Impact of tropical cyclones on the heat budget of the South Pacific Ocean.* Journal of Physical Oceanography, 2012.

[Kim *et al.* 2009] H.M Kim, P.J. Webster et J.A. Curry. *Impact of shifting patterns of Pacific Ocean warming on North Atlantic tropical cyclones.* Science, vol. 325, pages 77–80, 2009.

[Knutson *et al.* 2007] T.R. Knutson, J.J. Sirutis, S.T. Garner, I.M. Held et R.E. Tuleya. *Simulation of the recent multidecadal increase of Atlantic hurricane activity using an 18-km-grid regional model.* Bulletin of the American Meteorological Society, vol. 88, no. 10, pages 1549–1565, 2007.

[Knutson *et al.* 2008] T.R. Knutson, J.J. Sirutis, S.T. Garner, G.A. Vecchi et I.M. Held. *Simulated reduction in Atlantic hurricane frequency under twenty-first-century warming conditions.* Nature Geoscience, vol. 1, no. 6, pages 359–364, 2008.

[Korty *et al.* 2008] R.L. Korty, K.A. Emanuel et J.R. Scott. *Tropical cyclone-induced upper-ocean mixing and climate : Application to equable climates.* Journal of Climate, vol. 21, no. 4, pages 638–654, 2008.

[Kossin & Vimont 2007] J.P. Kossin et D.J. Vimont. *A more general framework for understanding Atlantic hurricane variability and trends.* Bulletin of the American Meteorological Society, vol. 88, no. 11, pages 1767–1782, 2007.

[Kossin *et al.* 2007] J.P. Kossin, K.R. Knapp, D.J. Vimont, R.J. Murnane et B.A. Harper. *A globally consistent reanalysis of hurricane variability and trends.* Geophysical Research Letters, vol. 34, no. L04815, 2007.

[Kuleshov *et al.* 2008] Y. Kuleshov, L. Qi, R. Fawcett et D. Jones. *On tropical cyclone activity in the Southern Hemisphere : trends and the ENSO connection.* Geophysical Research Letters, vol. 35, no. L14S08, 2008.

[Kuleshov *et al.* 2009] Y. Kuleshov, C.F. Ming, L. Qi, I. Chouaibou, C. Hoareau et F. Roux. *Tropical cyclone genesis in the Southern Hemisphere and its relationship with the ENSO.* Annales Geophysicae, vol. 27, pages 2523–2538, 2009.

[Landsea 2005] C.W. Landsea. *Meteorology : Hurricanes and global warming.* Nature, vol. 438, no. 7071, pages E11–E12, 2005.

[Large & Yeager 2009] W.G. Large et S.G. Yeager. *The global climatology of an interannually varying air–sea flux data set.* Climate Dynamics, vol. 33, pages 341–364, 2009.

[Large *et al.* 1994] W.G. Large, J.C. McWilliams et S.C. Doney. *Oceanic vertical mixing : A review and a model with a nonlocal boundary layer parameterization.* Reviews of Geophysics, vol. 32, pages 363–403, 1994.

[Le Vaillant *et al.* 2012] X. Le Vaillant, Y. Cuypers, P. Bouruet-Aubertot, J. Vialard et M.J. McPhaden. *Tropical storm-induced near-inertial internal waves during the Cirene experiment : energy fluxes and impact on vertical mixing.* Journal of Geophysical Research, submitted 2012.

[Leipper & Volgenau 1972] D.F. Leipper et D. Volgenau. *Hurricane heat potential of the Gulf of Mexico.* Journal of Physical Oceanography, vol. 2, no. 3, pages 218–224, 1972.

[Leipper 1967] D.F. Leipper. *Observed ocean conditions and Hurricane Hilda, 1964.* Journal of Atmospheric Sciences, vol. 24, pages 182–186, 1967.

[Leroy & Wheeler 2008] A. Leroy et M.C. Wheeler. *Statistical Prediction of Weekly Tropical Cyclone Activity in the Southern Hemisphere.* Monthly Weather Review, vol. 136, page 3637, 2008.

[Levy *et al.* 2012] M. Levy, M. Lengaigne, L. Bopp, E.M. Vincent, G. Madec et C. Ethe. *Contribution of hurricanes to the air-sea CO_2 flux : a global view.* Global Biogeochemical Cycles, vol. 26, no. GB2001, 2012.

[Lin *et al.* 2008] I.I. Lin, C.C. Wu, I.F. Pun et D.S. Ko. *Upper-ocean thermal structure and the western North Pacific category 5 typhoons. Part I : Ocean features and the category 5 typhoons intensification.* Monthly Weather Review, vol. 136, pages 3288–3306, 2008.

[Lin 2007] J.L. Lin. *The double-ITCZ problem in IPCC AR4 coupled GCMs : Ocean-atmosphere feedback analysis.* Journal of Climate, vol. 20, no. 18, pages 4497–4525, 2007.

[Liu & Fearn 2000] K. Liu et M.L. Fearn. *Reconstruction of prehistoric landfall frequencies of catastrophic hurricanes in northwestern Florida from lake sediment records.* Quaternary Research, vol. 54, no. 2, pages 238–245, 2000.

[Liu *et al.* 2008] L.L. Liu, W. Wang et R.X. Huang. *The mechanical energy input to the ocean induced by tropical cyclones.* Journal of Physical Oceanography, vol. 38, pages 1253–1266, 2008.

[Lloyd & Vecchi 2010] I.D. Lloyd et G.A. Vecchi. *Observational Evidence for Oceanic Controls on Hurricane Intensity.* Journal of Climate, vol. 24, pages 1138–1153, 2010.

[Madec 2008] G. Madec. Nemo ocean engine. Institut Pierre-Simon Laplace (IPSL), 2008.

[Mainelli *et al.* 2008] M. Mainelli, M. DeMaria, L. K. Shay et G. Goni. *Application of oceanic heat content estimation to operational forecasting of recent Atlantic category 5 hurricanes.* Wea. Forecasting, vol. 23, no. 1, pages 3–16, 2008.

[Mann & Emanuel 2006] M.E. Mann et K.A. Emanuel. *Atlantic hurricane trends linked to climate change.* Eos, vol. 87, no. 24, pages 233–244, 2006.

[Marks & Shay 1998] F.D. Marks et L.K. Shay. *Landfalling tropical cyclones : Forecast problems and associated research opportunities.* Bulletin of the American Meteorological Society, vol. 79, no. 2, pages 305–323, 1998.

[Marsaleix *et al.* 2008] P. Marsaleix, F. Auclair, J.W. Floor, M.J. Herrmann, C. Estournel, I. Pairaud et C. Ulses. *Energy conservation issues in sigma-coordinate free-surface ocean models.* Ocean Modelling, vol. 20, no. 1, pages 61–89, 2008.

[Mellor & Blumberg 2004] G. Mellor et A. Blumberg. *Wave breaking and ocean surface layer thermal response.* Journal of Physical Oceanography, vol. 34, pages 693–698, 2004.

[Mellor & Yamada 1982] G.L. Mellor et T. Yamada. *Development of a turbulence closure model for geophysical fluid problems.* Reviews of Geophysics and Space Physics, vol. 20, pages 851–875, 1982.

[Menkes *et al.* 2011] C.E. Menkes, M. Lengaigne, P. Marchesiello, N.C. Jourdain, E.M. Vincent, J. Lefèvre, F. Chauvin et J.F. Royer. *Comparison of tropical cyclogenesis indices on seasonal to interannual timescales.* Climate Dynamics, pages 1–21, 2011.

[Miller 1958] B.I. Miller. *On the Maximum Intensity of Hurricanes.* Journal of Atmospheric Sciences, vol. 15, pages 184–195, 1958.

[Neetu *et al.* 2012] S. Neetu, M. Lengaigne, E.M. Vincent, J. Vialard, S. Masson, R. Kumar et G. Madec. *Influence of oceanic stratification on tropical cyclones-induced surface cooling in the Bay of Bengal.* Journal of Geophysical Research, in revision 2012.

[Pielke & Pielke Jr 1997] R.A. Pielke et R.A. Pielke Jr. Hurricanes : Their nature and impacts on society. Wiley, 1997.

[Powell & Reinhold 2007] M.D. Powell et T.A. Reinhold. *Tropical cyclone destructive potential by integrated kinetic energy.* Bulletin of the American Meteorological Society, vol. 88, no. 4, pages 513–526, 2007.

[Powell *et al.* 1998] M.D. Powell, S.H. Houston, L.R. Amat et N. Morisseau-Leroy. *The HRD real-time hurricane wind analysis system.* Journal of Wind Engineering and Industrial Aerodynamics, vol. 77, pages 53–64, 1998.

[Price *et al.* 1986] J.F. Price, R.A. Weller et R. Pinkel. *Diurnal cycling : Observations and models of the upper ocean response to diurnal heating, cooling, and wind mixing.* Journal of Geophysical Research, vol. 91, no. C7, pages 8411–8427, 1986.

[Price 1981] J.F. Price. *Upper ocean response to a hurricane.* Journal of Physical Oceanography, vol. 11, no. 2, pages 153–175, 1981.

[Price 2009] J.F. Price. *Metrics of hurricane-ocean interaction : vertically-integrated or vertically-averaged ocean temperature ?* Ocean Science, vol. 5, pages 351–368, 2009.

[Ramsay & Sobel 2010] H.A. Ramsay et A.H. Sobel. *The effects of relative and absolute sea surface temperature on tropical cyclone potential intensity using a single-column model.* Journal of Climate, vol. 24, pages 183–193, 2010.

[Ramsay *et al.* 2008] H.A. Ramsay, L.M. Leslie, P.J. Lamb, M.B. Richman et M. Leplastrier. *Interannual variability of tropical cyclones in the Australian region : role of large-scale environment.* Journal of Climate, vol. 21, no. 5, pages 1083–1103, 2008.

[Revell & Goulter 1986] C. G. Revell et S. W. Goulter. *South Pacific tropical cyclones and the Southern Oscillation.* Monthly Weather Review, vol. 114, no. 6, pages 1138–1145, 1986.

[Royer *et al.* 1998] J.F. Royer, F. Chauvin, B. Timbal, P. Araspin et D. Grimal. *A GCM study of the impact of greenhouse gas increase on the frequency of occurrence of tropical cyclones.* Climatic Change, vol. 38, no. 3, pages 307–343, 1998.

[Saji & Yamagata 2003] N.H. Saji et T. Yamagata. *Structure of SST and Surface Wind Variability during Indian Ocean Dipole Mode Events : COADS Observations.* Journal of Climate, vol. 16, pages 2735–2751, 2003.

[Saji *et al.* 1999] N.H. Saji, B.N. Goswami, P.N. Vinayachandran et T. Yamagata. *A dipole mode in the tropical Indian Ocean.* Nature, vol. 401, no. 6751, pages 360–363, 1999.

[Samson *et al.* 2009] G. Samson, H. Giordani, G. Caniaux et F. Roux. *Numerical investigation of an oceanic resonant regime induced by hurricane winds.* Ocean Dynamics, vol. 59, no. 4, pages 565–586, 2009.

[Samson 2009] G. Samson. *Titre.* PhD thesis, Université de Toulouse, 2009.

[Sanford *et al.* 2007] T.B. Sanford, J.F. Price, J.B. Girton et D.C. Webb. *Highly resolved observations and simulations of the ocean response to a hurricane.* Geophysical Research Letters, vol. 34, no. L13604, 2007.

[Shay & Brewster 2010] L.K. Shay et J.K. Brewster. *Oceanic Heat Content Variability in the Eastern Pacific Ocean for Hurricane Intensity Forecasting.* Monthly Weather Review, vol. 138, pages 2110–2131, 2010.

[Shay 2010] L.K. Shay. *Air-Sea Interactions in Tropical Cyclones.* Global Perspectives on Tropical Cyclones : From Science to Mitigation, vol. 4, pages 93–131, 2010.

[Singh *et al.* 2000] O.P. Singh, T.M. Ali Khan et M.S. Rahman. *Changes in the frequency of tropical cyclones over the North Indian Ocean.* Meteorology and Atmospheric Physics, vol. 75, pages 11–20, 2000. 10.1007/s007030070011.

[Singh *et al.* 2011] A. Singh, T. Delcroix et S. Cravatte. *Contrasting the flavors of El Niño-Southern Oscillation using sea surface salinity observations.* Journal of Geophysical Research, vol. 116, 2011.

[Sriver & Huber 2010] R.L. Sriver et M. Huber. *Modeled sensitivity of upper thermocline properties to tropical cyclone winds and possible feedbacks on the Hadley circulation.* Geophysical Research Letters, vol. 37, no. L08704, 2010.

[Sriver *et al.* 2008] R. L. Sriver, M. Huber et J. Nusbaumer. *Investigating tropical cyclone-climate feedbacks using the TRMM Microwave Imager and the Quick Scatterometer.* Geochemistry, Geophysics, Geosystems, vol. 9, 2008.

[Sriver *et al.* 2010] R.L. Sriver, M. Goes, M.E. Mann et K. Keller. *Climate response to tropical cyclone-induced ocean mixing in an Earth system model of intermediate complexity.* Journal of Geophysical Research, vol. 115, 2010.

[Terry 2007] J.P. Terry. Tropical cyclones : climatology and impacts in the south pacific. Springer Verlag, 2007.

[Tippett *et al.* 2010] M.K. Tippett, S.J. Camargo et A.H. Sobel. *A Poisson regression index for tropical cyclone genesis and the role of large-scale vorticity in genesis.* Journal of Climate, vol. 24, pages 2335–2357, 2010.

[Trenberth & Fasullo 2007] K.E. Trenberth et J. Fasullo. *Water and energy budgets of hurricanes and implications for climate change.* Journal of Geophysical Research, vol. 112, no. D23107, 2007.

[Vecchi & Knutson 2008] G.A. Vecchi et T.R. Knutson. *On estimates of historical North Atlantic tropical cyclone activity.* Journal of Climate, vol. 21, pages 3580–3600, 2008.

[Vecchi & Soden 2007a] G.A. Vecchi et B.J. Soden. *Effect of remote sea surface temperature change on tropical cyclone potential intensity.* Nature, vol. 450, no. 7172, pages 1066–1070, 2007.

[Vecchi & Soden 2007b] G.A. Vecchi et B.J. Soden. *Increased tropical Atlantic wind shear in model projections of global warming.* Geophysical Research Letters, vol. 34, no. 10.1029, 2007.

[Vialard *et al.* 2009] J. Vialard, J.P. Duvel, M.J. McPhaden, P. Bouruet-Aubertot, B. Ward*et al.* *Cirene : air-sea interactions in the Seychelles-Chagos thermocline ridge region.* Bulletin of the American Meteorological Society, vol. 3179, 2009.

[Vimont & Kossin 2007] D.J. Vimont et J.P. Kossin. *The Atlantic meridional mode and hurricane activity.* Geophysical Research Letters, vol. 34, no. L07709, 2007.

[Vincent *et al.* 2009a] E.M. Vincent, M. Lengaigne, C.E. Menkes, N.C. Jourdain, P. Marchesiello et G. Madec. *Interannual variability of the South Pacific Convergence Zone and implications for tropical cyclone genesis.* Climate Dynamics, vol. 36, pages 1881–1896, 2009.

[Vincent *et al.* 2009b] E.M. Vincent, M. Lengaigne, C.E. Menkes, P. Marchesiello, N.C. Jourdain*et al.* *SPCZ interannual variability and implications for TC genesis in present and future climate.* In 2nd International Summit on Hurricanes and Climate Change, 2009.

[Vincent *et al.* 2010a] E.M. Vincent, M. Lengaigne, R. Kumar, J. Vialard et G. Madec. *Importance of Ocean-Atmosphere coupling for Tropical Cyclones activity in the South Indian Ocean.* In Ocean Sciences Meeting, Portland USA, 2010.

[Vincent *et al.* 2010b] E.M. Vincent, M. Lengaigne, C.E. Menkes, P. Marchesiello et G. Madec. *Interannual variability of the South Pacific Convergence Zone and implications for the southwest Pacific Ocean region.* In Ocean Sciences Meeting, Portland USA, 2010.

[Vincent *et al.* 2012a] E.M. Vincent, M. Lengaigne, G. Madec, J. Vialard, G. Samson*et al.* *Processes setting the characteristics of sea surface cooling induced by Tropical Cyclones.* Journal of Geophysical Research, vol. 117, no. C02020, 2012.

[Vincent *et al.* 2012b] E.M. Vincent, G. Madec, A. Koch-Larrouy, M. Lengaigne et J. Vialard. *Influence of Tropical Cyclones on sea surface temperature seasonal cycle and ocean heat transport.* Climate Dynamics, submitted 2012.

[Vincent *et al.* 2012c] E.M. Vincent, J. Vialard, M. Lengaigne, G. Madec, S. Masson*et al.* *Assessing the oceanic control on the amplitude of sea surface cooling induced by Tropical Cyclones.* Journal of Geophysical Research, vol. 117, no. C05023, 2012.

[Vincent 1994] D.G. Vincent. *The South Pacific convergence zone (SPCZ) : A review.* Monthly Weather Review, vol. 122, no. 9, pages 1949–1970, 1994.

[Wada & Chan 2008] A. Wada et J.C.L. Chan. *Relationship between typhoon activity and upper ocean heat content.* Geophysical Research Letters, vol. 35, no. L17603, 2008.

[Walker *et al.* 2005] N.D. Walker, R.R. Leben et S. Balasubramanian. *Hurricane-forced upwelling and chlorophyll a enhancement within cold-core cyclones in the Gulf of Mexico.* Geophysical Research Letters, vol. 32, pages 1–5, 2005.

[Walsh *et al.* 2004] K.J.E. Walsh, K.C. Nguyen et J.L. McGregor. *Fine-resolution regional climate model simulations of the impact of climate change on tropical cyclones near Australia.* Climate Dynamics, vol. 22, no. 1, pages 47–56, 2004.

[Webster *et al.* 2005] P.J. Webster, G.J. Holland, J.A. Curry et H.R. Chang. *Changes in tropical cyclone number, duration, and intensity in a warming environment.* Science, vol. 309, no. 5742, page 1844, 2005.

[Wheeler & Hendon 2004] M.C. Wheeler et H.H. Hendon. *An all-season real-time multivariate MJO index : Development of an index for monitoring and prediction.* Monthly Weather Review, vol. 132, no. 8, pages 1917–1932, 2004.

[Willoughby *et al.* 2006] H.E. Willoughby, R.W.R. Darling et M.E. Rahn. *Parametric representation of the primary hurricane vortex. Part II : A new family of sectionally continuous profiles.* Monthly Weather Review, vol. 134, no. 4, pages 1102–1120, 2006.

[Xie *et al.* 2002] S.P. Xie, H. Annamalai, F.A. Schott et J.P. McCreary. *Structure and mechanisms of South Indian Ocean climate variability.* Journal of Climate, vol. 15, no. 8, pages 864–878, 2002.

[Yablonsky & Ginis 2009] R.M. Yablonsky et I. Ginis. *Limitation of One-Dimensional Ocean Models for Coupled Hurricane–Ocean Model Forecasts.* Monthly Weather Review, vol. 137, no. 4410-4419, 2009.

[Yeh *et al.* 2009] S.W. Yeh, J.S. Kug, B. Dewitte, M.H. Kwon, B.P. Kirtman et F.F. Jin. *El Niño in a changing climate.* Nature, vol. 461, no. 7263, pages 511–514, 2009.

[Zhang *et al.* 2007] X. Zhang, W. Lin et M. Zhang. *Toward understanding the double Intertropical Convergence Zone pathology in coupled ocean-atmosphere general circulation models.* Journal of Geophysical Research, vol. 112, no. D12102, 2007.

[Zhang 2007] J. Zhang. *An airborne investigation of the atmospheric boundary layer structure in the hurricane force wind regime.* PhD thesis, Univ. of Miami, 2007.

Annexes

Chapitre 8
Annexes

A Impact climatologique des TCs dans ORCA2 vs ORCA05

La figure 1 illustre la faible sensibilité de l'influence des TCs sur les anomalies moyennes de températures tri–dimensionnelles engendrées dans une configuration à 2° de résolution (ORCA2) par rapport à une configuration au $1/2°$ (ORCA05). De manière générale les anomalies observées dans ORCA2 sont 15–20% plus faibles que celles observées dans ORCA05, mais les structures sont respectées. ORCA2 a donc été utilisé pour réaliser la plupart des tests de sensibilité : application du vortex de [Holland 1980] vs [Willoughby *et al.* 2006], simulations d'ensemble, expériences de sensibilité isolant l'effet des processus de mélange / dynamiques / flux de chaleur. Ces trois dernières expériences ont ensuite été réalisées dans des simulations au $1/2°$ au chapitre 5.

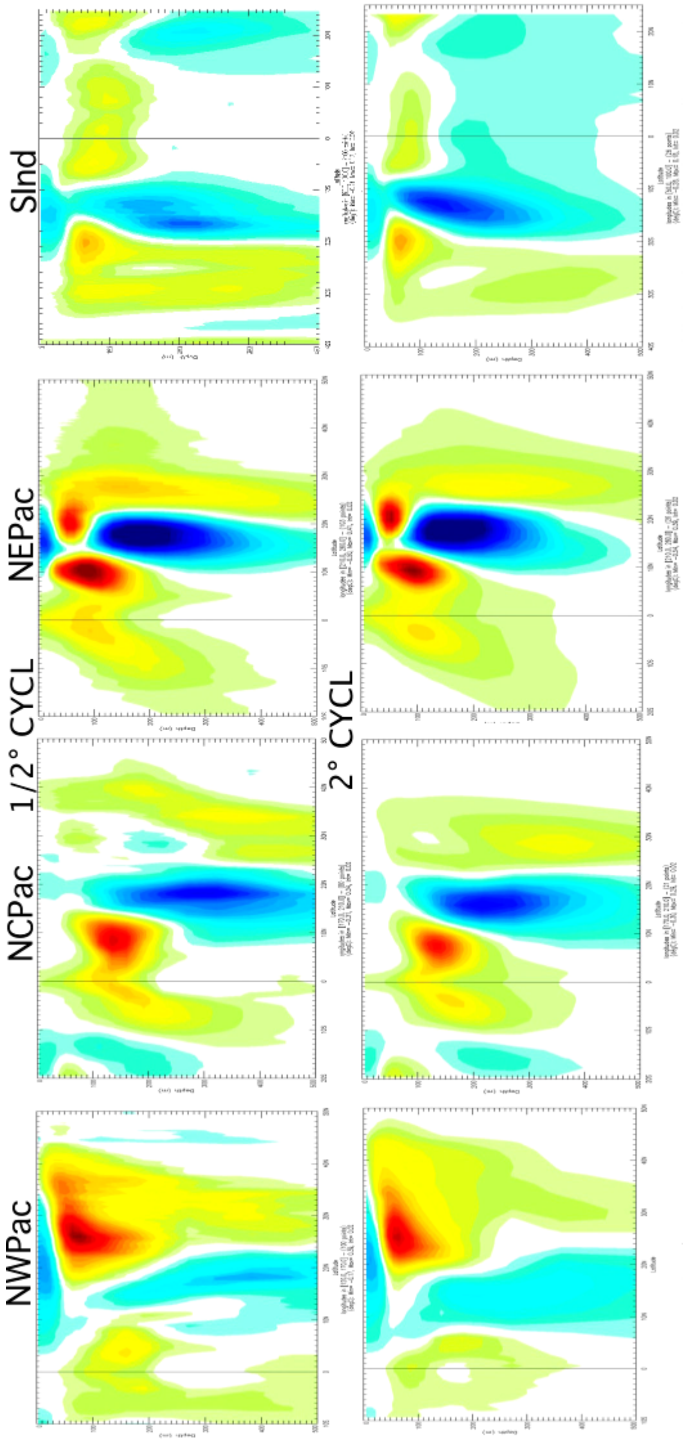

Figure 1 – Coupes latitude–profondeur des anomalies de température entre le run CYCL et FILT pour les simulations à 2° de résolution (ORCA2) et au $^{1}/_{2}$° (ORCA05) dans les bassins Pacifique Nord–Ouest (NWPac : 120-170°E/10°S-50°N), Pacifique Nord–Central (NCPac : 170°E-150°W/10°S-50°N), Pacifique Nord–Est (NEPac : 150°W-100°W/10°S-50°N) et l'Océan Indien (SInd : 50°E-100°E/40°S-25°N).

B Implications du changement climatique pour la cyclogenèse de la région SPCZ

Cette annexe s'appuie sur les travaux présentés sous forme de poster au 2^{nd} *International Summit on Hurricanes and Climate Change* [Vincent *et al.* 2009b]. Le résultat principal a par la suite été publié dans la revue Nature [Cai *et al.* 2012].

B.1 Introduction

L'activité cyclonique est susceptible d'être modifiée en réponse au changement climatique (1.5.4). Les modèles couplés de circulation générale (CGCMs pour *Coupled Global Circulation Models*) de la base de données CMIP3 (*Coupled Model Intercomparion Project Phase 3*) forcés par différents scénarios de changements climatiques permettent de suggérer les modifications régionales de l'environnement favorables à la cyclogenèse. Dans le Pacifique Sud–Ouest, nous avons vu que la variabilité de la position de la SPCZ résume la variabilité de l'activité cyclonique. Etudier les modifications de la position moyenne et de la variabilité de la SPCZ est donc une entrée pour comprendre l'influence du changement climatique sur les caractéristiques de l'activité cyclonique dans la région.

L'approche suivie a consisté à analyser dans un premier temps les capacités des CGCMs à reproduire l'organisation dynamique de la SPCZ, puis à sélectionner les modèles les plus réalistes pour étudier les modifications de la SPCZ qu'ils simulent en changement climatique. La capacité des 22 modèles de la base de données CMIP3 à représenter les caractéristiques de la SPCZ du climat présent est premièrement évaluée en utilisant les simulations au taux de CO_2 pré–industriel. Les simulations avec un taux de CO_2 doublé ($2\times CO_2$) et quadruplé ($4\times CO_2$) par rapport aux concentrations pré–industrielles sont ensuite utilisées pour étudier la SPCZ dans un climat plus chaud.

B.2 Représentation de la SPCZ dans les modèles couplés pour le climat présent

Dans cette sous–section, nous commentons la capacité des modèles à simuler i) la position de la SPCZ en été austral (DJF), ii) la variabilité interannuelle de la position de la SPCZ et iii) l'organisation des variables favorables à la cyclogenèse autour de la SPCZ. La méthodologie utilisée est similaire à celle du chapitre 6.

Position de la SPCZ La figure 2 illustre la représentation de la SPCZ pour deux modèles particuliers. Le modèle du MRI est représentatif des modèles qui ont une position relativement réaliste de la SPCZ ainsi que son orientation diagonale. Le modèle de l'INM est lui représentatif du comportement de la plupart des modèles actuels, qui ne représentent pas correctement la SPCZ. Les précipitations y sont

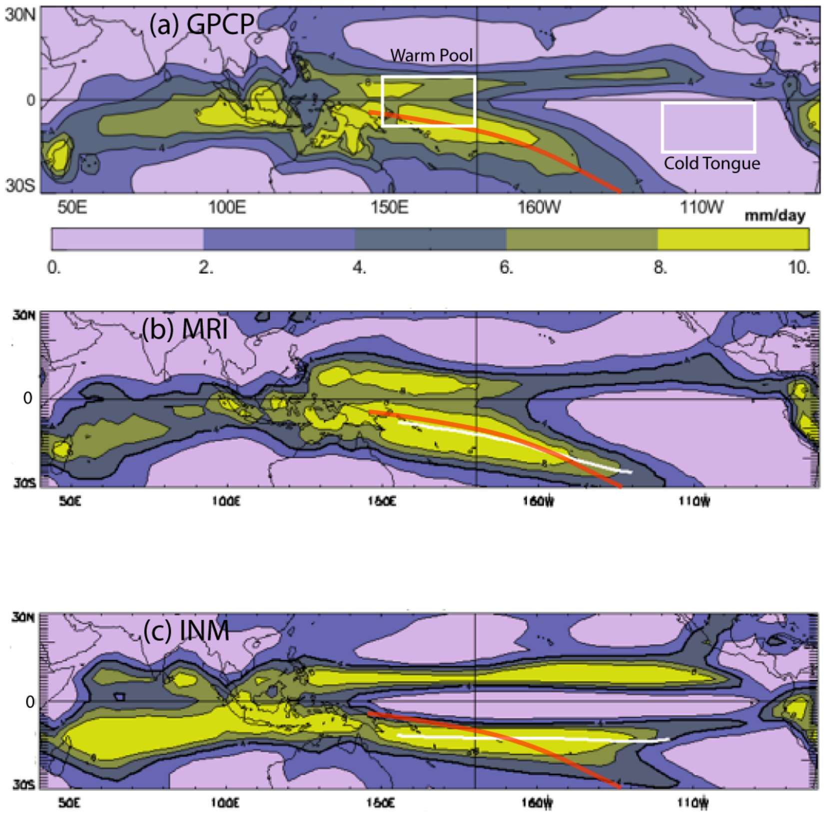

Figure 2 – Illustration du champ de précipitation moyen de l'Indo–Pacifique sur DJF pour deux modèles ((**b**) MRI et (**c**) INM) par rapport aux observations (**a** GPCP). Les *lignes blanches* sont les positions moyennes de la SPCZ des modèles, la *ligne rouge* est celle des observations.
Les *rectangles blancs* indiquent les régions utilisées dans la figure suivante.

sur–estimées, l'orientation de la SPCZ est trop zonale et s'étend trop à l'Est dans le Pacifique Sud. Ce biais caractéristique est connu sous le nom de « *double–ITCZ pathology* » ([Lin 2007], [Zhang *et al.* 2007]).

La figure 3 caractérise le biais de double–ITCZ pour les 22 modèles étudiés. Ce biais est marqué par des précipitations anormalement élevées dans le Pacifique Est, dans la région de l'upwelling (*Cold Tongue*) et anormalement faibles dans la région équatoriale du Pacifique Ouest (*Warm Pool*). Plus un modèle se trouve en bas à droite et plus il présente un problème de double–ITCZ marqué. A peu près tous les modèles sont concernés par ce biais, de manière plus (*e.g.* INM, GISS_EH) ou moins marquée (*e.g.* MIUB, MRI, GFDL).

Variabilité interannuelle et lien avec ENSO L'amplitude des variations interannuelles de la position de la SPCZ à l'Est et à l'Ouest de la ligne de change-

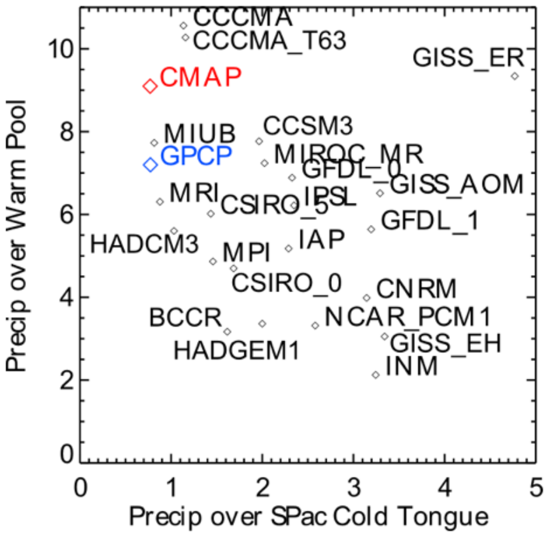

Figure 3 – Diagramme représentant l'intensité des précipitations (en mm/jour) dans le Pacifique Ouest (150°E–180°E / 7°S–7°N) en fonction de l'intensité des précipitations dans le Pacifique Sud–Est (90°W–120°W / 15°S–0°S) pour chacun des 22 modèles analysés. Les valeurs des observations CMAP et GPCP sont indiquées en couleur.

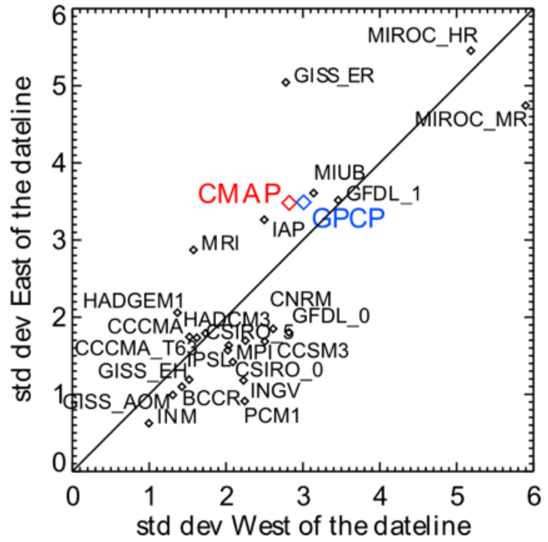

Figure 4 – Déviation standard de la latitude de la SPCZ à l'Est (155°W–175°W) et à l'Ouest (155°E–175°E) de la ligne de changement de date dans la simulation pré–industrielle. La déviation standard est calculée sur l'ensemble des positions moyennes sur Déc–Fév.

ment de date est illustrée pour chacun des modèles sur la figure 4. La plupart des modèles sont caractérisés par une variabilité trop faible en comparaison des observations. Quelques modèles seulement ont une amplitude réaliste (MRI, IAP, MIUB, GFDL).

Seuls quelques modèles représentent la zonalisation de la SPCZ et son lien avec ENSO. Dans le modèle GFDL-1, par exemple, les deux caractéristiques de la zonalisation sont bien représentées (Fig. 5) :

i le mouvement vers le Nord particulièrement marquée de la partie Est de la SPCZ pour les années où les anomalies de température dans le Pacifique central sont particulièrement fortes ;

ii la saturation du mouvement vers le Nord dans l'Ouest de la SPCZ pendant ces mêmes années.

La variabilité de la position de la SPCZ peut être représentée par une analyse en

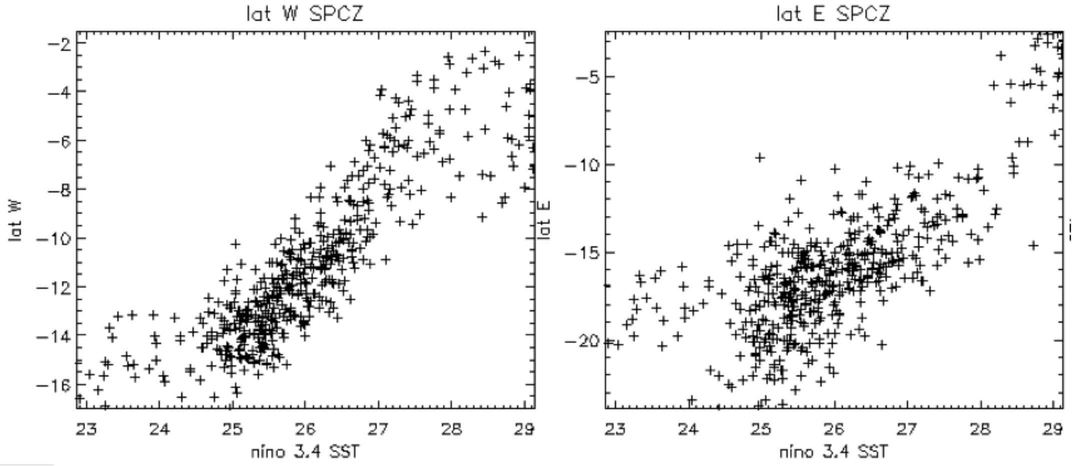

Figure 5 – Latitude moyenne de la SPCZ sur Déc.–Fév. (**a**) à l'Ouest et (**b**) à l'Est de la ligne de changement de date en fonction de la température dans le Pacifique équatorial central (région *niño 3.4*) dans le modèle GFDL-1. La latitude de la SPCZ à l'Ouest augmente avec le réchauffement équatorial mais sature pour les plus forts réchauffements alors qu'à l'Est le mouvement vers le Nord est particulièrement marqué pendant les forts *El Niño* : ces deux caractéristiques définissent l'orientation zonale de la SPCZ.

composante principale (EOF pour *Empirical Orthogonal Functions*), comme nous l'avons fait pour les observations dans le chapitre 6. Le modèle GFDL-1 reproduit de manière réaliste les modes de variabilité principaux décrits dans les observations (Fig. 6, à comparer avec la Fig. 6.3). Le premier mode de variabilité (EOF1) est caractérisé par un dipôle de précipitation de part et d'autre de la position moyenne de la SPCZ associé à son déplacement Nord–Sud. Le second mode est caractérisé par une forte anomalie de précipitation dans le centre du bassin et une diminution le long de la position moyenne de la SPCZ en lien avec les événements asymétriques. En utilisant une méthode de classification des années en fonction de leur latitude à l'Ouest et à l'Est de la ligne de changement de date (comme dans le chapitre 6), il est possible d'identifier 4 types d'années. Cette classification apparaît sur la figure 6.c. Les années positives / négatives s'opposent sur le premier axe (PC1) alors que les années asymétriques sont caractérisées par une contribution non–nulle à la 2^{e} EOF (PC2).

La figure 7 illustre la position de la SPCZ pour les 4 classes identifiées. Alors que la plupart des modèles reproduisent des évènements ENSO stéréotypés (tous identiques), certains simulent des évènements *El Niño* de différents types [Lengaigne *et al.* 2009]. Ces modèles correspondent à ceux capables de reproduire une zonalisation de la SPCZ en plus de son mouvement Nord–Sud.

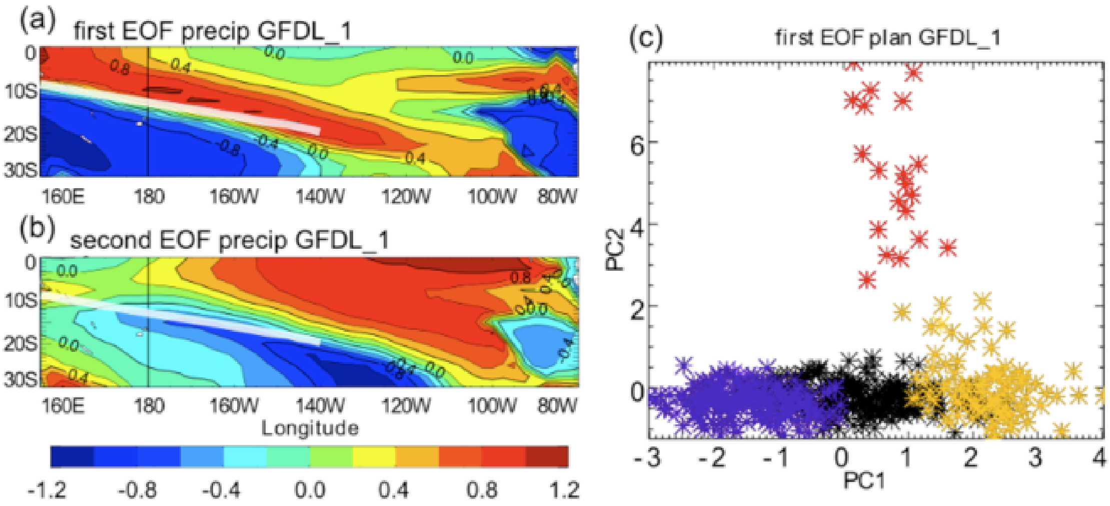

Figure 6 – Premier (**a**) et deuxième (**b**) modes spatiaux d'une analyse en composante principale (EOF) des précipitations dans le Pacifique Sud–Ouest en DJF dans la simulation pré–industrielle du modèle GFDL-1. Le panneau (**c**) représente les valeurs de la série temporelle (PC) associée au deuxième mode en fonction du premier.

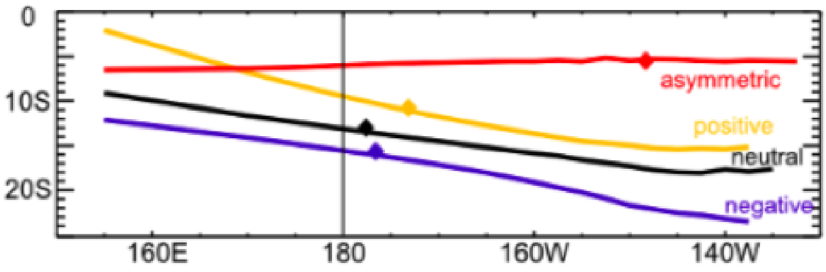

Figure 7 – Position moyenne de la SPCZ pour les saisons DJF des 4 classes identifiées dans la simulation pré–industrielle du GFDL-1.

(a) pre-industrial CO_2run

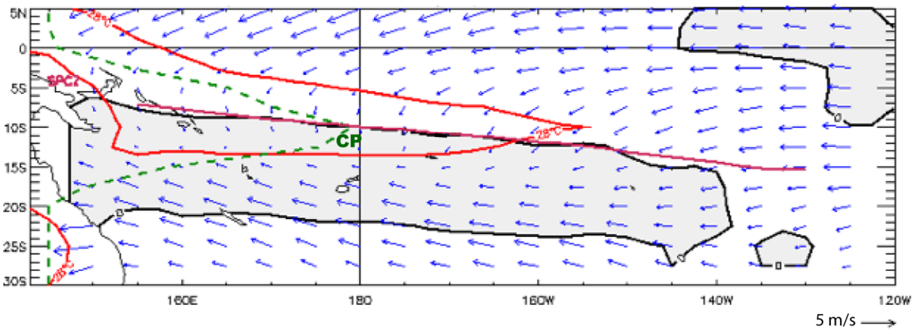

(b) double CO_2run

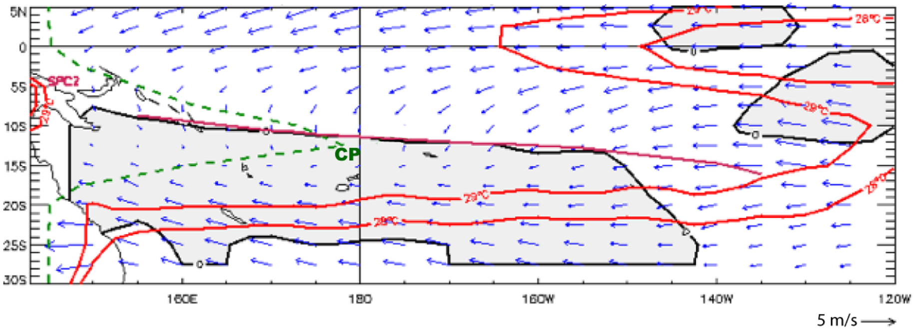

Figure 8 – Composites des champs moyens sur DJF dans les simulations (**a**) pré–industrielle et (**b**) 2×CO_2 du MIUB. La *ligne violette* marque la position de la SPCZ, les *isolignes rouges* sont les isothermes 28°C et 29°C, la région de vorticité cyclonique est *grisée*, les *flèches bleues* représentent les vents à 10 m et CP marque la position du point de confluence.

Organisation dynamique autour de la SPCZ Comme illustré pour le modèle du MIUB sur la figure 8.a, la plupart des modèles présentent une organisation dynamique similaire à celle décrite dans la réanalyse ERA40. La SPCZ est située au–dessus d'une langue d'eau chaude de la *Warm Pool*. La position du point de confluence (CP), marquant l'extension du régime de mousson, illustre que le lien entre la SPCZ et la mousson est réaliste. Le cisaillement horizontal entre les vents de mousson et les alizés crée une zone de vorticité cyclonique au Sud de la SPCZ. Enfin, la SPCZ est associée à une zone de minimum de cisaillement vertical de vent (non–illustré sur la figure).

Le tableau 1 résume les principales caractéristiques de la SPCZ pour les différents modèles. 9 modèles reproduisent correctement les caractéristiques climatologiques de la SPCZ et 6 présentent une variabilité interannuelle comparable à celle des observations.

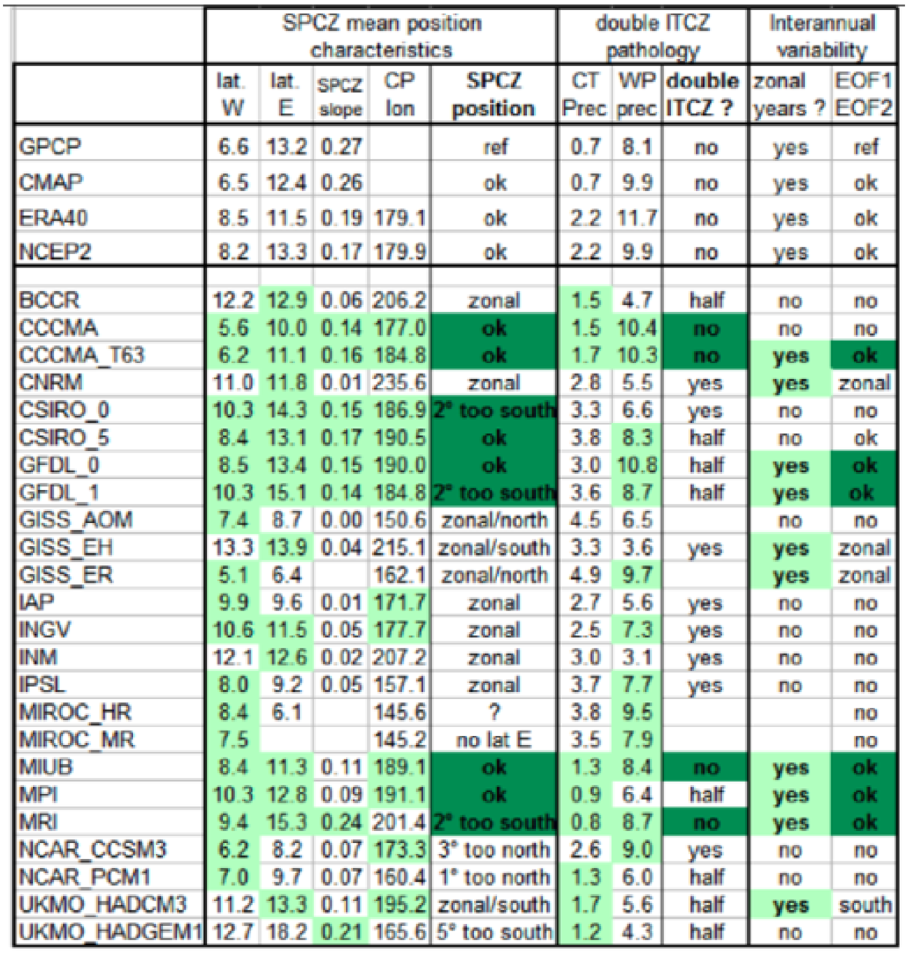

	SPCZ mean position characteristics					double ITCZ pathology			Interannual variability	
	lat. W	lat. E	SPCZ slope	CP lon	**SPCZ position**	CT Prec	WP prec	**double ITCZ ?**	zonal years ?	EOF1 EOF2
GPCP	6.6	13.2	0.27		ref	0.7	8.1	no	yes	ref
CMAP	6.5	12.4	0.26		ok	0.7	9.9	no	yes	ok
ERA40	8.5	11.5	0.19	179.1	ok	2.2	11.7	no	yes	ok
NCEP2	8.2	13.3	0.17	179.9	ok	2.2	9.9	no	yes	ok
BCCR	12.2	12.9	0.06	206.2	zonal	1.5	4.7	half	no	no
CCCMA	5.6	10.0	0.14	177.0	ok	1.5	10.4	no	no	no
CCCMA_T63	6.2	11.1	0.16	184.8	ok	1.7	10.3	no	yes	ok
CNRM	11.0	11.8	0.01	235.6	zonal	2.8	5.5	yes	yes	zonal
CSIRO_0	10.3	14.3	0.15	186.9	2° too south	3.3	6.6	yes	no	no
CSIRO_5	8.4	13.1	0.17	190.5	ok	3.8	8.3	half	no	ok
GFDL_0	8.5	13.4	0.15	190.0	ok	3.0	10.8	half	yes	ok
GFDL_1	10.3	15.1	0.14	184.8	2° too south	3.6	8.7	half	yes	ok
GISS_AOM	7.4	8.7	0.00	150.6	zonal/north	4.5	6.5		no	no
GISS_EH	13.3	13.9	0.04	215.1	zonal/south	3.3	3.6	yes	yes	zonal
GISS_ER	5.1	6.4		162.1	zonal/north	4.9	9.7		yes	zonal
IAP	9.9	9.6	0.01	171.7	zonal	2.7	5.6	yes	no	no
INGV	10.6	11.5	0.05	177.7	zonal	2.5	7.3	yes	no	no
INM	12.1	12.6	0.02	207.2	zonal	3.0	3.1	yes	no	no
IPSL	8.0	9.2	0.05	157.1	zonal	3.7	7.7	yes	no	no
MIROC_HR	8.4	6.1		145.6	?	3.8	9.5			no
MIROC_MR	7.5			145.2	no lat E	3.5	7.9			no
MIUB	8.4	11.3	0.11	189.1	ok	1.3	8.4	no	yes	ok
MPI	10.3	12.8	0.09	191.1	ok	0.9	6.4	half	yes	ok
MRI	9.4	15.3	0.24	201.4	2° too south	0.8	8.7	no	yes	ok
NCAR_CCSM3	6.2	8.2	0.07	173.3	3° too north	2.6	9.0	yes	no	no
NCAR_PCM1	7.0	9.7	0.07	160.4	1° too north	1.3	6.0	half	no	no
UKMO_HADCM3	11.2	13.3	0.11	195.2	zonal/south	1.7	5.6	half	yes	south
UKMO_HADGEM1	12.7	18.2	0.21	165.6	5° too south	1.2	4.3	half	no	no

Table 1 – Comparaison des caractéristiques de la SPCZ et de sa variabilité pour les observations et les modèles. Les valeurs des réanalyses sont données conjointement à celles des observations pour illustrer le degré de ressemblance maximum que l'on peut exiger des modèles. *lat.W* et *lat.E* sont les latitudes de la SPCZ à l'Ouest et à l'Est de la ligne de changement de date ; *SPCZ slope* est la pente moyenne de la SPCZ évaluée par un *fit* linéaire sur la position moyenne ; *CP lon* est la longitude du point de confluence ; *CT prec* et *WP prec* sont les précipitations moyennes dans les régions *Cold Tongue* et *Warm Pool* respectivement ; *zonal years* signale la capacité à représenter l'orientation zonale de la SPCZ et *EOF 1 EOF 2* indique si la variabilité interannuelle capturée par les 2 premières EOFs est similaire aux observations.

B.3 L'augmentation de la fréquence de zonalisation de la SPCZ en changement climatique

Les 6 modèles représentant une variabilité réaliste de la SPCZ pour la simulation pré–industrielle ont ensuite été analysés pour déterminer les modifications attendues des caractéristiques de la SPCZ dans un climat plus chaud.

Etat moyen La plupart des modèles ne présentent pas de modifications significatives de la position climatologique de la SPCZ, comme illustré sur la figure 8.b dans le cas du MIUB.

L'organisation des variables favorables à la cyclogenèse n'est pas fondamentalement modifiée dans un climat plus chaud figure 8.b. La SST est largement augmentée, avec une extension importante de la surface incluse dans l'isotherme 28°C, cependant plusieurs études suggèrent que ce sont les variations de SST relatives (*i.e.* les variations d'une région par rapport au reste des tropiques) et non absolues qui importent pour l'activité cyclonique ([Vecchi & Soden 2007a], [Ramsay & Sobel 2010]). D'après ces observations, il est probable que la région de cyclogenèse ne soit pas profondément modifiée en moyenne et conserve sa position au Sud de la SPCZ.

Variabilité interannuelle L'analyse de la variabilité interannuelle des précipitations dans le Pacifique Sud est répétée dans les simulations $2\times CO_2$ et $4\times CO_2$ disponibles. La figure 9 présente la proportion d'années où une SPCZ zonale est observée dans les modèles représentant correctement la distinction des années zonales dans la simulation pré–industrielle. 5 des 6 modèles présentent une augmentation de la fréquence des évènements de zonalisation de la SPCZ dans les simulations $2\times CO_2$ et $4\times CO_2$ par rapport à la situation pré–industrielle. Ce résultat préliminaire suggère que la variabilité interannuelle de la SPCZ est susceptible d'être modifiée en lien avec le changement climatique. Plusieurs études ont suggéré que l'état moyen des tropiques se rapproche de l'état *El Niño* dans un climat plus chaud. Une perspective intéressante serait d'étudier plus en détail le lien entre les modifications d'ENSO, la SPCZ et la cyclogenèse dans le Pacifique Sud–Ouest en lien avec le changement climatique.

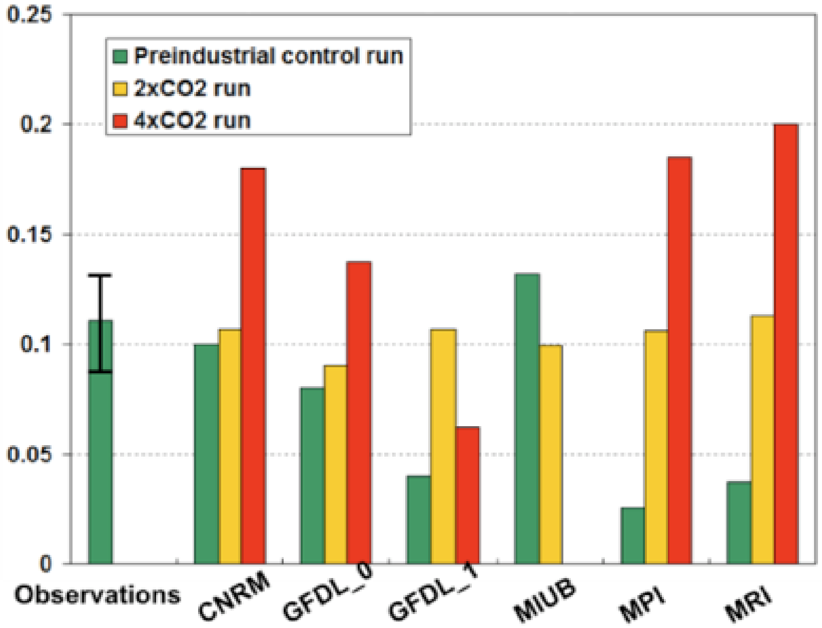

Figure 9 – Proportion d'années présentant une orientation zonale de la SPCZ dans les simulations pré–industrielles (*en vert*), 2×CO_2 (*en orange*) et 4×CO_2 (*en rouge*) pour 6 modèles de la base CMIP3. L'estimation provenant des observations est donnée pour référence.

C Variabilité océanique et activité cyclonique dans l'Océan Indien Sud

Cette annexe s'appuie sur les travaux présentés sous forme de poster à la conférence *Ocean Science* de l'*American Geophysical Union* [Vincent *et al.* 2010a].

C.1 Introduction

Peu d'études se sont intéressées au contrôle de l'activité cyclonique par la variabilité interannuelle des caractéristiques de l'océan au–delà de la SST (1.5.5, p 51). [Xie *et al.* 2002] ont suggéré que la profondeur du dôme de thermocline (TRIO *Thermocline Ridge of the Indian Ocean*) module l'activité cyclonique dans l'Ouest de l'Océan Indien Sud (SIO) (Fig. 1.41). Le mécanisme implicitement invoqué est que l'amplitude des CWs est modulée par la profondeur de la stratification thermique en sub–surface (thermocline). Cette observation peut s'avérer importante car la profondeur de la TRIO est prédictible plusieurs mois en avance, en particulier du fait de sa modulation par ENSO. Les années *El Niño* génèrent des anomalies de vents anticycloniques et donc un *downwelling* dans l'Est du SIO qui se propage vers l'Ouest sous forme d'ondes de Rossby.

D'autre part, plusieurs études ont montré que l'activité cyclonique dans le SIO est modulée par ENSO. Le nombre de TCs observés est accru/diminué dans l'Ouest/l'Est du SIO pendant les années *El Niño* et l'inverse pendant les années *La Niña* ([Ho *et al.* 2006], [Kuleshov *et al.* 2009]). Ces deux études mettent en avant la modification de vorticité par les téléconnexions d'ENSO comme explication principale de cette observation.

Enfin, l'Océan Indien possède aussi un mode de variabilité propre (le dipôle indien ; IOD) qui est susceptible de moduler les variables favorables à la cyclogenèse [Saji & Yamagata 2003]. Aucune étude à ce jour ne s'est intéressée à son influence sur les TCs dans le SIO.

La variabilité interannuelle du nombre de TCs dans l'Ouest du SIO a donc été interprétée de différentes manières par le passé. La motivation de cette étude a été de synthétiser les différentes observations concernant l'influence de la variabilité interannuelle (ENSO, IOD) sur l'activité cyclonique de la région et de mettre en évidence l'importance éventuelle de la profondeur de la thermocline dans la région (TRIO).

C.2 Données et Méthodes

Les données de genèse et trajectoires de TCs proviennent de la base de données IBTrACS sur la période 1978–2007. Chaque saison cyclonique de l'année notée n est caractérisée par le nombre total de genèse entre Juillet de l'année n et Juin de l'année $n+1$.

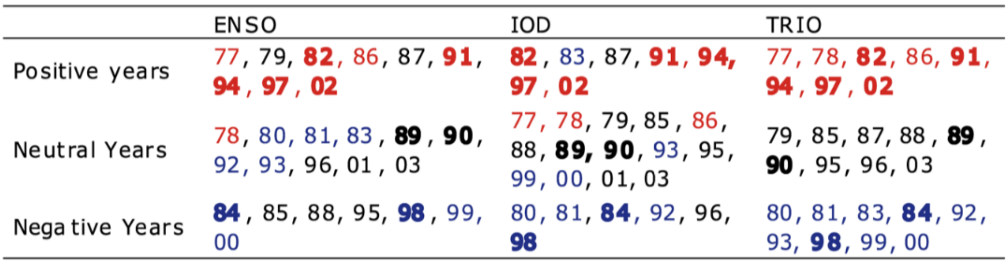

	ENSO	IOD	TRIO
Positive years	77, 79, **82**, 86, 87, **91**, **94** , **97** , **02**	**82** , 83, 87, **91**, **94,** **97** , **02**	77, 78, **82**, 86, **91**, **94** , **97** , **02**
Neutral Years	78, 80, 81, 83 , **89** , **90**, 92, 93, 96, 01 , 03	77, 78, 79, 85 , 86, 88, **89, 90**, 93, 95, 99, 00, 01, 03	79, 85, 87, 88 , **89** , **90** , 95, 96, 03
Negative Years	**84** , 85, 88, 95, **98** , 99, 00	80, 81, **84**, 92, 96, **98**	80, 81, 83, **84**, 92, 93, **98**, 99, 00

Table 2 – Classification des années en phases positives, neutres et négatives vis–à–vis de la variabilité TRIO, ENSO et IOD. Les années TRIO+ sont *en rouge* et les années TRIO− sont *en bleu* ; les années redondantes pour les 3 classifications sont indiquéees*en gras*.

La variabilité de la profondeur moyenne de la thermocline dans la région TRIO (50°E-75°E / 5°S-10°S) est caractérisée dans une simulation ORCA-0.25° forcée par DFS4.

ENSO est caractérisé par l'anomalie de SST dans la région *niño 3.4*.

L'IOD est caractérisé en soustrayant la SST dans la région 90°E-110°E/0-10°S à celle dans 50°E-70°E/5°N-5°S, après retrait du cycle saisonnier [Saji *et al.* 1999].

Les années sont qualifiées de "TRIO+" / "ENSO+" / "IOD+" lorsque l'anomalie de profondeur de thermocline / d'indice *niño 3.4* / d'indice IOD dépasse $^1/_2$ déviation standard, et de "TRIO−" / "ENSO−" / "IOD−" lorsque l'indice est inférieur à -$^1/_2$ déviation standard.

C.3 Résultats

Variabilité interannuelle de l'activité cyclonique

La figure 10.a présente les anomalies de cyclogenèse associées à la variabilité de la profondeur de la thermocline. Un dipôle Ouest–Est est observé avec une cyclogenèse accrue dans la région de la TRIO pendant les années où la thermocline est profonde. La figure 10.bc présente la même analyse en fonction des phases ENSO et IOD. Les anomalies associées à la variabilité de la TRIO sont très similaires à celles associées à ENSO et à l'IOD.

Cette observation est en grande partie due au fait que les classifications en fonction de ces différents indices regroupent en grande partie les mêmes années (Tab. 2).

Lien avec les variables favorables à la cyclogenèse

Comme dans le Pacifique Sud–Ouest, la région de cyclogenèse est localisée au Sud de l'ITCZ. Cette région correspond à un maximum de précipitations convectives, un minimum de cisaillement vertical du vent et une vorticité grande–échelle cyclonique (Fig. 11.a). Le cœur du dôme de thermocline (marquée par l'isoligne

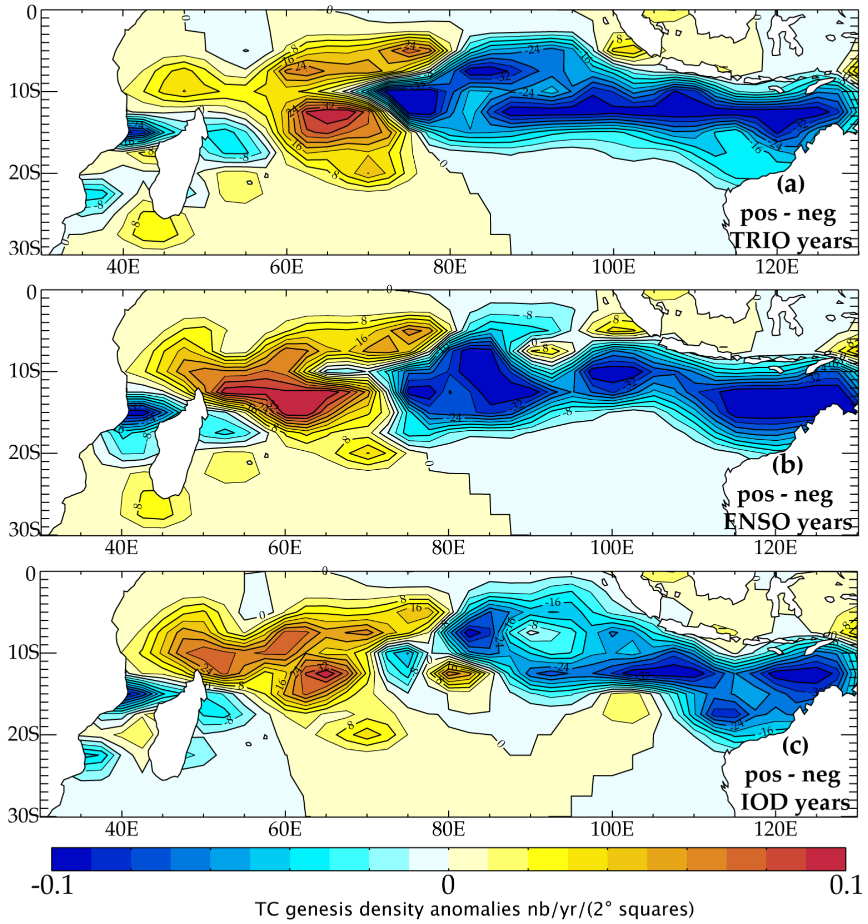

Figure 10 – Cartes composites de la différence de densité de cyclogenèse entre les années "+" et les années "−" concernant les classifications (**a**) TRIO, (**b**) ENSO et (**c**) IOD.

rouge) recoupe partiellement la région de cyclogenèse à l'Ouest du bassin.
Remarque : Contrairement au Pacifique Sud–Ouest, la variabilité de la position de l'ITCZ est faible dans le SIO ; l'étude des variations interannuelles de sa position n'est pas une entrée intéressante pour étudier la variabilité de la cyclogenèse.

Si les variations interannuelles de la vorticité et de la profondeur de la thermocline sont en accord avec la variabilité de la cyclogenèse, ce n'est pas le cas du cisaillement troposphérique (Fig. 11.bc). La thermocline est plus/moins profonde à l'Ouest/à l'Est du SIO pendant les années TRIO+ (l'inverse en TRIO−), ce qui est cohérent avec l'activité cyclonique. De même la vorticité est anticyclonique/cyclonique à l'Est du SIO en années TRIO+/TRIO−, ce qui est aussi cohérent avec les anomalies négatives/positives de cyclogenèse pendant ces années. Par contre, les variations du cisaillement de vent troposphérique ne sont pas cohérentes avec l'activité cyclonique : les années TRIO− sont associées à une anomalie de fort cisaillement dans l'Est alors que la cyclogenèse y est renforcée, par exemple.

Contrairement aux bassins Atlantique et Pacifique Sud–Ouest, les variabilités interannuelles de la vorticité est du cisaillement ne varient pas de manière cohérente dans le SIO. Une telle approche qualitative ne permet pas de distinguer l'influence respective de l'océan et de la vorticité sur l'activité cyclonique. L'utilisation des indices de cyclogenèse est une voie possible pour isoler l'effet de chacune de leurs variables constitutives.

Indice de cyclogenèse

La figure 12 illustre la manière dont chaque indice représente la variabilité des conditions de cyclogenèse en lien avec la variabilité du climat dans le SIO. Alors que le dipôle de cyclogenèse observé sur la figure 10.a n'est pas reproduit par l'indice MYGP, il est correctement reproduit par l'indice YGP et dans une moindre mesure par le GPi (Fig. 12).

Le YGP étant le seul indice incluant une variable océanique (sous la forme de l'OHC), nous avons cherché à tester l'apport que représente cette variable. La figure 12.d révèle que lorsque la variabilité interannuelle de l'OHC est supprimée, l'indice s'éloigne des observations dans l'Ouest. La variabilité de l'OHC est donc partiellement responsable de la capacité de l'indice YGP à reproduire la variabilité de la cyclogenèse dans l'Ouest du bassin SIO.

C.4 Discussion

Cette courte étude suggère que la variabilité interannuelle de l'océan de sub–surface importe pour expliquer la variabilité interannuelle de l'activité cyclonique dans l'Océan Indien Sud. Cependant, l'attribution d'une part de variabilité de l'activité cyclonique aux caractéristiques de l'océan est incertaine lorsque l'on utilise une simple approche composite. La variabilité de l'activité cyclonique dans l'Océan

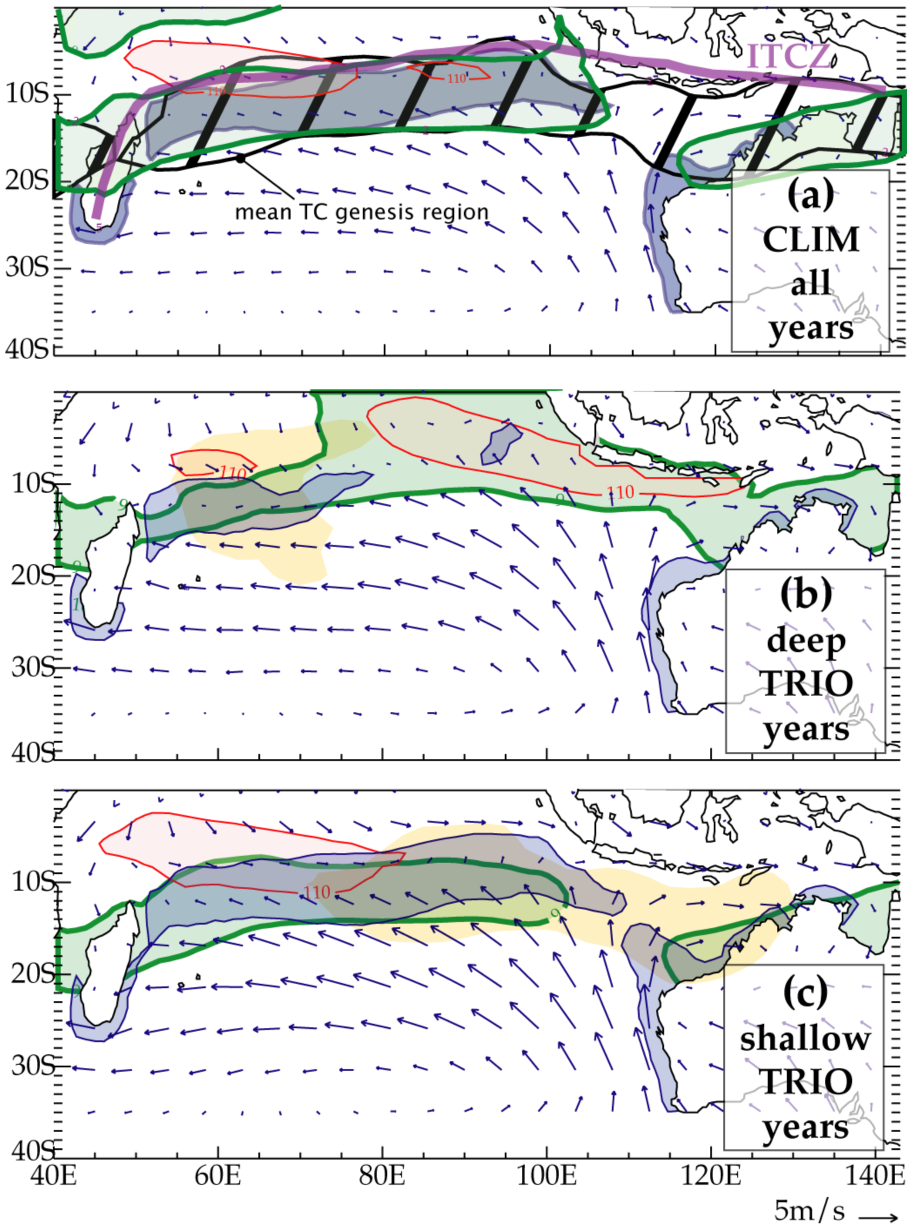

Figure 11 – Cartes composites de variables influençant potentiellement l'activité cyclonique (**a**) en moyenne sur toutes les années, (**b**) pour les années TRIO+ et (**c**) pour les années TRIO−. *En vert*, les régions de faible cisaillement vertical dans la troposphère (<9m/s entre 850 et 200 hPa) ; *En bleu*, les régions de forte vorticité cyclonique ($< -6\times10^{-6}\ s^{-1}$) ; *En rouge*, les régions où l'isobathe 20°C est <110 m. Sur le panneau (**a**), la *ligne violette* marque la position moyenne de l'ITCZ et la région *hachurée noire* marque la région moyenne de cyclogenèse. Sur les panneaux (**b**) et (**c**), les *surfaces jaunes* indiquent la région où la cyclogenèse est accrue.
Les panneaux (**b**) et (**c**) sont très similaires lorsque les composites sont réalisés en fonction des phases d'ENSO ou de l'IOD.

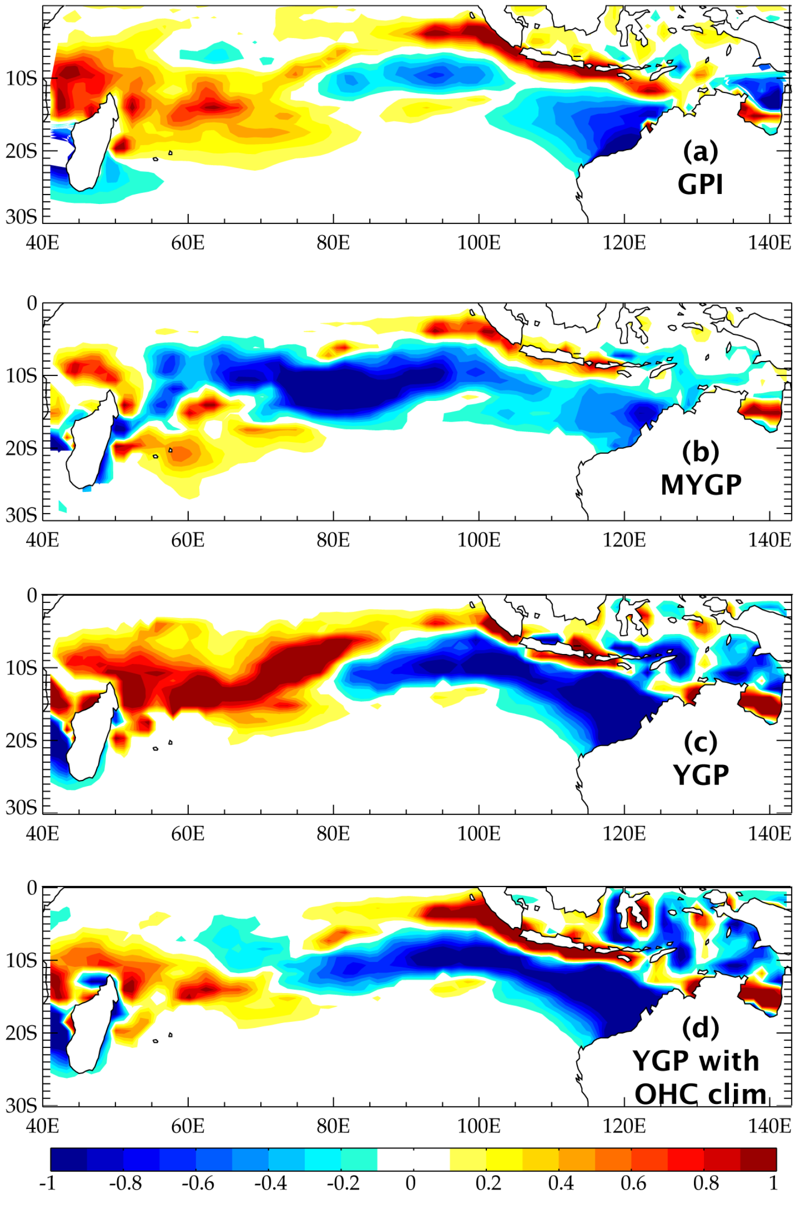

Figure 12 – Régressions spatiales sur l'indice TRIO des différents indices de cyclogenèse (**a**) GPi, (**b**) MYGP, (**c**) YGP. Sur le panneau (**d**) l'indice YGP a été modifié supprimant la variabilité interannuelle de l'OHC (maintenu à sa valeur climatologique).

Indien Sud ne peut être attribuée simplement à ENSO ou à l'IOD dont la variabilité est largement redondante.

Une perspective importante de cette thèse consiste à imaginer une méthode pertinente pour évaluer la part de variabilité de l'activité cyclonique qui peut être attribuée aux caractéristiques de l'océan de sub–surface.

D Contribution des TCs aux flux air–mer de CO_2

GLOBAL BIOGEOCHEMICAL CYCLES, VOL. 26, GB2001, doi:10.1029/2011GB004145, 2012

Contribution of tropical cyclones to the air-sea CO_2 flux: A global view

M. Lévy,[1] M. Lengaigne,[1,2] L. Bopp,[3] E. M. Vincent,[1] G. Madec,[1,4] C. Ethé,[5] D. Kumar,[2] and V. V. S. S. Sarma[6]

Received 16 June 2011; revised 16 December 2011; accepted 27 January 2012; published 7 April 2012.

[1] Previous case studies have illustrated the strong local influence of tropical cyclones (TCs) on CO_2 air-sea flux (F_{CO_2}), suggesting that they can significantly contribute to the global F_{CO_2}. In this study, we use a state-of-the art global ocean biochemical model driven by TCs wind forcing derived from a historical TCs database, allowing to sample the F_{CO_2} response under 1663 TCs. Our results evidence a very weak contribution of TCs to global F_{CO_2}, one or two order of magnitude smaller than previous estimates extrapolated from case studies. This result arises from several competing effects involved in the F_{CO_2} response to TCs, not accounted for in previous studies. While previous estimates have hypothesized the ocean to be systematically oversaturated in CO_2 under TCs, our results reveal that a similar proportion of TCs occur over oversaturated regions (i.e. the North Atlantic, Northeast Pacific and the Arabian Sea) and undersaturated regions (i.e. Westernmost North Pacific, South Indian and Pacific Ocean). Consequently, by increasing the gas exchange coefficient, TCs can generate either instantaneous CO_2 flux directed from the ocean to the atmosphere (efflux) or the opposite (influx), depending on the CO_2 conditions at the time of the TC passage. A large portion of TCs also occurs over regions where the ocean and the atmosphere are in near equilibrium, resulting in very weak instantaneous fluxes. Previous estimates also did not account for any asynchronous effect of TCs on F_{CO_2}: during several weeks after the storm, oceanic pCO_2 is reduced in response to vertical mixing, which systematically causes an influx anomaly. This implies that, contrary to previous estimates, TCs weakly affect the CO_2 efflux when they blow over supersaturated areas because the instantaneous storm *wind effect* and post-storm *mixing effect* oppose with each other. In contrast, TCs increase the CO_2 influx in undersaturated conditions because the two effects add up. These compensating effects result in a very weak contribution to global F_{CO_2} and a very modest contribution to regional interannual variations (up to 10%).

Citation: Lévy, M., M. Lengaigne, L. Bopp, E. M. Vincent, G. Madec, C. Ethé, D. Kumar, and V. V. S. S. Sarma (2012), Contribution of tropical cyclones to the air-sea CO_2 flux: A global view, *Global Biogeochem. Cycles*, *26*, GB2001, doi:10.1029/2011GB004145.

1. Introduction

[2] Tropical cyclones (TCs), also often called typhoons in the Northwest Pacific or hurricanes on the eastern side of the dateline, are recurring extreme summertime weather events which strongly affect the thermal and physical structure of the upper ocean along their wake [e.g., *D'Asaro*, 2003; *Cione and Uhlhorn*, 2003]. One of the strong oceanic response commonly observed in the wake of TCs is the intense cooling of the surface layer that can reach up to 10°C [*Chiang et al.*, 2011]. This cooling mainly ensues from the wind-driven vertical entrainment of cold subsurface waters [*Price*, 1981; *Vincent et al.*, 2012].

[3] A few previous case studies have illustrated that TCs can cause enormous effluxes of CO_2 between the ocean and atmosphere (hereafter F_{CO_2}), large enough to influence the annual local efflux [*Bates et al.*, 1998; *Perrie*, 2004; *Nemoto et al.*, 2009]. Although TCs are short-lived and travel at considerable speed (typically 4–6 m/s), they affect a significant area of the tropical ocean each year, because of their large spatial extent (several ~100 km) [*Willoughby et al.*, 2006] and frequent occurrence (~100 TCs each year). It was thus hypothesized that they exert a significant influence on the global air-sea flux of CO_2 [*Bates et al.*, 1998]. However, the limited availability of pCO_2 data under TCs

---

[1] LOCEAN-IPSL, CNRS/IRD/UPMC/MNHN, Paris, France.
[2] National Institute of Oceanography, Goa, India.
[3] LSCE-IPSL, CNRS/CEA/UVSQ, Gif-sur-Yvette, France.
[4] NOCS, Southampton, UK.
[5] IPSL, CNRS/IRD/UPMC/UVSQ/CEA/Ecole Polytechnique/ENS/CNES/UDD/UPEC, Guyancourt, France.
[6] National Institute of Oceanography, Visakhapatnam, India.

0886-6236/12/2011GB004145

(due to the severe weather conditions) has so far restricted the global quantification of the F_{CO_2} response to TCs to qualitative extrapolations [*Bates et al.*, 1998; *Bates*, 2007; *Huang and Imberger*, 2010].

[4] The F_{CO_2} response to a hurricane passage depends on various factors. F_{CO_2} is a function of piston velocity and of the difference in the partial pressure of CO_2 (pCO_2) between the atmosphere and sea surface. Oceanic pCO_2 depends on total dissolved inorganic carbon (DIC), total alkalinity (TA), temperature (T) and salinity (S) [*Takahashi et al.*, 1993]. TCs increase the magnitude of the F_{CO_2} because the piston velocity strongly increases at high wind speed [*Liss and Merlivat*, 1986; *Wanninkhof*, 1992; *D'Asaro and McNeil*, 2007; *McNeil and D'Asaro*, 2007]. TCs also impact F_{CO_2} because their intense surface winds increase vertical entrainment of subsurface waters (hereafter referred to as mixing) and thereby change the surface properties of T, S, DIC and TA and thus surface oceanic pCO_2. In addition, the net F_{CO_2} response to TCs is complicated by the fact that the TC-induced mixing (affecting the pCO_2) and TC-winds (affecting the piston velocity) are not synchronous [*Nemoto et al.*, 2009]: cooling, the manifestation of vertical mixing, is observed to be maximum between one and three days after the TC-passage [*Vincent et al.*, 2012] because it largely results from shear mixing driven by near-inertial currents which persist for a few days in the wake of TCs, and its intensity depends on the local vertical structure of the upper ocean (E. M. Vincent et al., Assessing the oceanic control on the amplitude of sea surface cooling induced by tropical cyclones, submitted to *Journal of Geophysical Research*, 2011).

[5] These considerations highlight the difficulty in generalizing the F_{CO_2} response to TCs from individual cases and illustrate why the few global TC-induced F_{CO_2} estimates [*Bates et al.*, 1998; *Bates*, 2007; *Huang and Imberger*, 2010] are so disparate: from ~0.5 PgC to ~0.05 PgC per year. This paper proposes an original methodology and a model framework for accurately quantifying the TC-induced F_{CO_2} and the various processes into play. We use a global Ocean General Circulation Model (NEMO) [*Madec*, 2008] coupled with a biogeochemical model (PISCES) [*Aumont and Bopp*, 2006] with a modified version of CORE forcing [*Large and Yeager*, 2009] that includes an analytic formulation of 2-dimensional TC winds along observed TC tracks [*Vincent et al.*, 2012]. We compare two model simulations, with and without TCs, and provide quantitative diagnostics averaged along the tracks of TCs. This enables us to provide a global picture of the effects of hurricanes on air-sea CO_2 transfers.

2. Model and Methods

2.1. Coupled Hydrodynamic and Carbon Model

[6] The hydrodynamical model used here is the global configuration (ORCA2) of Nucleus for European Modelling of the Ocean (NEMO, v3.2) [*Madec*, 2008]. The quasi-isotropic grid has a nominal resolution of 2° with increased 0.5° latitudinal resolution at the equator. In the vertical, 31 levels are used, with 10 levels in the upper 100 m. The mixed layer dynamics is parameterized using an improved Turbulent Kinetic Energy (TKE) closure scheme with a Langmuir cell, a surface wave breaking parameterization and an energetically consistent time and space discretization [*Madec*, 2008]. Additional subgrid-scale mixing parameterizations include a Laplacian viscosity, an iso-neutral Laplacian diffusivity and the use of a GM-scheme to mimic the effect of subgrid-scale eddy processes [*Gent and McWilliams*, 1990]. Complete description of ORCA2 can be found in *Cravatte et al.* [2007].

[7] The Pelagic Interaction Scheme for Carbon and Ecosystem Studies (PISCES, *Aumont and Bopp*, 2006) is coupled to ORCA2. PISCES includes a simple representation of the marine ecosystem and describes the cycles of carbon and of the main marine nutrients (N, P, Fe and Si). The model has 24 compartments. Four living pools are represented: two phytoplankton size classes/ groups (nanophytoplankton and diatoms) and two zooplankton size classes (microzooplankton and mesozooplankton). Fixed Redfield ratios are employed for N and P, while the ratios of both Si, and Fe, to C vary dynamically as a function of the phytoplankton functional group and environmental variables. The carbonate chemistry follows the Ocean Carbon-Cycle Model Intercomparison Project (OCEMIP) protocols (http://www.ipsl.jussieu.fr/OCMIP). The air-sea CO_2 exchange is calculated with the bulk exchange formula:

$$F_{CO_2} = k\,s DpCO_2 \tag{1}$$

where F_{CO_2} is the air-sea CO_2 flux with positive values indicating CO_2 goes within the ocean, *k* is the gas transfer velocity, *s* is the CO_2 solubility and $DpCO_2 = pCO_2^{atm} - pCO_2^{sea}$ is the difference of pCO_2 between the ocean and atmosphere. In the following, we will use the notation pCO_2 for pCO_2^{sea}. There is still large uncertainty in *k*, particularly under hurricane winds [*McNeil and D'Asaro*, 2007; *D'Asaro and McNeil*, 2007]. Following the discussion by *McNeil and D'Asaro* [2007], we used the relationship of *Wanninkhof* [1992] to calculate *k*, which provides a lower limit for *k* under extreme winds compared to other recent formulations [*Perrie*, 2004].

2.2. Model Setup and Experimental Design

[8] The surface boundary conditions used for the present ORCA2-PISCES simulations are based on the version 2 of the atmospheric data sets and formulations developed by *Large and Yeager* [2009] for global ocean-ice models and are referred to as Coordinated Ocean-ice Reference Experiments (CORE) forcing [*Griffies et al.*, 2009]. The forcing data sets are based on a combination of NCEP/NCAR reanalysis products for the years 1958–2007 with various satellite data sets, and involve adjustments that correct global imbalances (e.g., produce near zero global mean heat and freshwater fluxes when used in combination with observed SSTs). Turbulent fluxes are computed from the CORE bulk formulae as a function of the prescribed atmospheric state and the simulated ocean surface state (SST and surface currents). A bound to 33 m s^{-1} has been introduced to the CORE dimensionless surface drag coefficient (C_D) to account for its observed saturation at strong winds following *Donelan* [2004]. Data are prescribed at six-hourly (wind speed, humidity and atmospheric temperature), daily (short- and long-wave radiation) and monthly (rain and snow) resolution, with inter-annual variability over the time range 1958 to 2007 except for runoff which are kept climatological. To avoid an artificial model drift due to a freshwater imbalance, the sea surface salinity is damped towards

monthly-mean climatological values with a piston velocity of 50 m per 300 days [*Griffies et al.*, 2009].

[9] Boundary conditions for the biogeochemical model include atmospheric dust (Fe) deposition, rivers (Fe, N, P, Si and C) and sediment (Fe) mobilization. These sources are described by *Aumont and Bopp* [2006] and kept constant for the duration of the simulation.

[10] Our simulations start in 1978. For the initial state, we used physical and biogeochemical tracers initialized from previous ORCA2-PISCES experiments: the spun-up physical state was obtained by running a 120-year simulation, starting from Levitus and forced by repeating the 50-year CORE forcing; the biogeochemical state was obtained by running a transient 1870–1977 simulation with increasing pCO_2^{atm} levels following historical records.

[11] From 1978 onwards, we performed two simulations: one with the full strength of TCs (Cyclone or C run) and one without TCs (No cyclone or N run). For these simulations, the 10-m wind forcing from CORE has been modified following *Vincent et al.* [2012]: In the N run, the effect of the weaker than observed TC-like vortices seen in the original CORE forcing has been filtered out by applying a 11-day running mean to the wind components within 600 km of each cyclone. In the C run, analytical TCs have been superimposed to the filtered CORE winds. To do so, TC winds are parameterized using the idealized *Willoughby and Rahn* [2004] TC wind spatial pattern, which is based on a statistical fit to the observed TC winds [*Willoughby et al.*, 2006]. Note that the translation speed of the storm is not accounted for in this idealized wind pattern. Although the translation speed is known to affect the wind asymmetry, the study by *Samson et al.* [2009] indeed suggests that it has a limited effect on the cold wake asymmetry and can be neglected. This idealized wind pattern is interpolated in time at each model time step using the position and maximum wind speed of each cyclone in the IBTrACs database (http://www.ncdc.noaa.gov/oa/ibtracks). This analytical formulation enables to correct for the underestimation of the strength of TC-winds in CORE. An illustration of the different wind forcings (CORE, N and C) under a TC is provided by *Vincent et al.* [2012, Figure 1].

[12] Daily model outputs were saved from 1993 onward. Our analysis are thus based on the 1993–2007 period, and sample the ocean's response to 1663 TCs.

2.3. Observational Data Set

[13] We use a blend of Tropical Rainfall Measuring Mission (TRMM) Microwave Imager (TMI) and Advanced Microwave Scanning Radiometer AMSR-E SST daily data set (http://www.ssmi.com/sst) at a 1/4° horizontal resolution to evaluate the modeled SST response under TCs over the 1998–2007 period. Despite its inability to retrieve SST data under heavy precipitation [*Wentz et al.*, 2000], TMI and AMSR-E offer the advantage of being insensitive to atmospheric water vapor and provide accurate observations of SST beneath clouds, a few days before and after TC passage. The inner-core cooling (i.e. cooling under the eye) cannot be assessed confidently with TMI-AMSR; data are most of the time missing in a 400 km radius around the current TC position. This data set however provides a reliable estimate of the cooling in the TCs wake, data being typically available 1 to 2 days after TC passage. It has however to be noted that the cooling amplitude in the TCs' wake may not be fully captured by this data set, especially for slow moving TCs.

[14] For pCO2, we use the unique concomitant, open-ocean SST and pCO2 observations before and after the passage of a TC that were reported at the BATS site in the north Atlantic (31°50′ N, 64°10′ W) by *Bates et al.* [1998].

2.4. Diagnostics of Oceanic Anomalies Generated by TCs Along Their Tracks

[15] The anomalies of a given oceanic variable V (where V is for instance the SST or pCO_2) ensuing from the passage of TCs, noted ΔV, are computed under each TC track. To compute ΔV, the seasonal cycle of V is first removed from V, leading to a seasonally "de-meaned" V. TC track locations, available at 6h intervals, are used to retrieve V at the surface of the ocean. To characterize the amplitude of the ocean response around each TC-track position, we compute $\mathcal{V}$, the average of seasonally "de-meaned" V over a fixed radius of 200 km (about 3–4 radius of maximum wind) around the track position. We do this averaging because the impact of TCs on sea-surface properties is not restricted to a narrow path along the storm's center but rather can occur in a swath hundreds of kilometers wide, as reported for instance by *Bond et al.* [2011]. The reference unperturbed pre-storm conditions ($\mathcal{V}_{before}$) is defined as the average of $\mathcal{V}$ over 10 to 3 days prior to TC passage. The evolution of the ocean response anomaly at time t to a TC is then defined as $\Delta V(t) = \mathcal{V}(t) - \mathcal{V}_{before}$. The post-storm anomalies $\Delta V(t)$ are generally maximum within 1 to 4 days after the TC passage (section 3.1). We define $\mathcal{V}_{after}$ as the mean value of $\mathcal{V}$ over days 1 to 4 after TC passage, and the wake anomaly as $\overline{\Delta} V = \mathcal{V}_{after} - \mathcal{V}_{before}$ (dashed vertical lines in Figure 1).

[16] This methodology is applied to the model runs and to satellite observations of SST. In the N-run, where TCs have been smoothed out, ΔV_N is close to zero but is not strictly equal to zero because of the presence of variability not due to TCs. This background variability is present in both the C and N runs. To remove it from our estimates of ΔV, for model variables we define $\widetilde{\Delta} V$ as $\widetilde{\Delta} V = \Delta V_C - \Delta V_N$, where subscripts N and C refer to the model solutions of the N and C runs, respectively. Removing ΔV_N does not change our main results and reduces the dispersion (not shown).

2.5. Air-Sea Flux Anomaly Diagnostics

[17] Anomalies in F_{CO_2} in response to TCs (ΔF_{CO_2}) can result either from changes in the wind (and thus in gas transfer velocity Δk) or from changes in mixing (and thus in $\Delta(sDpCO_2)$):

$$\Delta F_{CO_2} = \underbrace{\Delta k \times sDpCO_2}_{\text{wind effect}} + \underbrace{k \times \Delta(sDpCO_2)}_{\text{mixing effect}} \tag{2}$$

[18] Using the results from the C and N runs, the wind and mixing effects are approximated as :

$$\Delta k \times sDpCO_2 \simeq (k_C - k_N) \times s_N (DpCO_2)_N \tag{3}$$

and

$$k \times \Delta(sDpCO_2) \simeq k_N \times (s_C (DpCO_2)_C - s_N (DpCO_2)_N) \tag{4}$$

where subscripts N and C refer to the model solutions of the N and C runs, respectively. Note that the second order terms

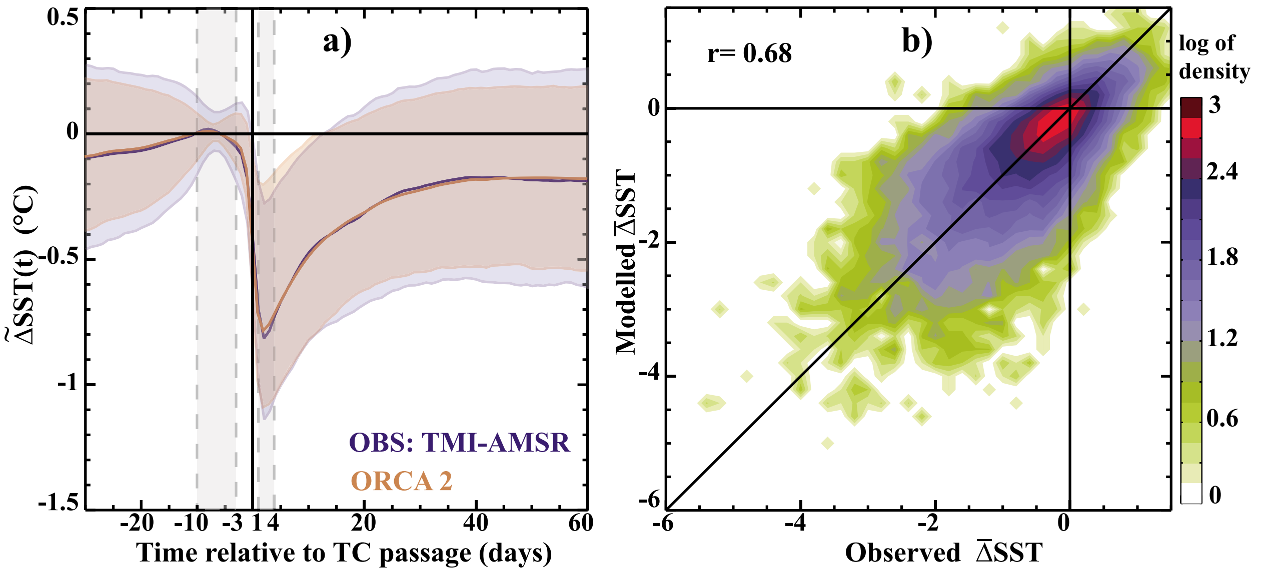

Figure 1. Evaluation of the timing and amplitude of surface temperature response to TCs (a) Temporal evolution of the mean TC-induced cooling along TC tracks for model and observations over the period 1998–2007. Shading indicates the spread around the mean value, calculated as ±1/2 quartile. (b) Scatter-plot (shown as a probability density function) of the amplitude of modeled (C-run minus N-run) against observed (TMI-AMSR) TC-induced cold wake amplitude (computed as explained in section 2.4) at individual locations in the wake of TCs.

have been omitted in this approximation; a posteriori, our results show that they are smaller than the first order terms.

3. Model Evaluation

3.1. Evaluation of TC-Induced Cooling

[19] The C run accurately captures the temporal evolution of the average observed TC-induced cooling (Figure 1a). In both model and observation, SST, averaged over a 200 km radius, starts decreasing a few days before the TC reaches a given location (Day 0) and maximum cooling occurs after the TC passage. Although maximum cooling appears to occur 1 to 3 days after the TC passage on Figure 1a for both model and observations, the exact timing of the maximum cooling after the TC passage cannot be confidently validated due to numerous missing satellite SST data around the time of TC passage. However, the fact that maximum cooling is reached a few days after the passage of the storm agrees with previous observations from buoy measurements [*Dickey*, 2008; *Cione and Uhlhorn*, 2003] and models [*Samson et al.*, 2009; *Jullien et al.*, 2012]. The reason is that the cooling largely results from shear mixing driven by near-inertial currents.

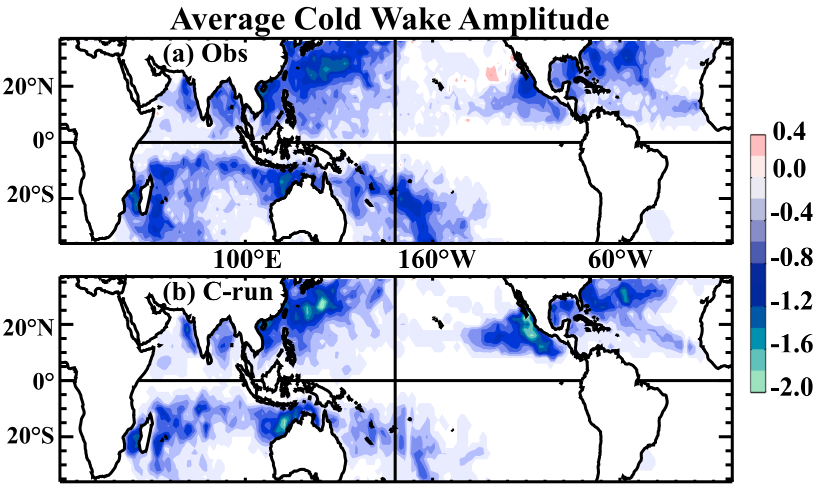

Figure 2. Evaluation of the spatial distribution of the surface temperature response to TCs. Spatial map of averaged cold wake anomaly amplitude (in °C) during the cyclonic season over the 1998–2007 period for (a) TMI-AMSR observations and (b) C-run.

These currents have a period of about a day and last for a few days in the wake of the tropical cyclones so that mixing is still acting to cool the mixed layer a few days after its passage. Figure 1a also illustrates that the decaying time scale of the cooling is accurately simulated, with about 40 days for the SST signal to disappear. The persistence of the cold anomaly for several weeks after the TC passage reflects the time needed for surface heat fluxes to restore the SST to pre-storm values. We can also note that, after 40 days, SST remains on average 0.2°C colder than during pre-storm conditions, in agreement with previous observational analysis [*Price et al.*, 2008; *Lloyd and Vecchi*, 2011; *Vincent et al.*, 2012].

[20] Based on this composite picture, the average value of the e-folding time (time for the cold anomaly to be reduced by a factor e) is 15 days. Moreover, there is a 0.68 correlation between modeled and observed TC-induced cooling magnitudes ($\overline{\Delta}$T) in the wake of TCs at individual locations (Figure 1b), indicating that our simulation realistically samples the ocean response to the wide spectrum of TC characteristics. Because the analytic cyclone wind field formulation is fitted to an average of observed cyclone wind radial profiles [*Willoughby and Rahn*, 2004], and because the underlying ocean state does not exactly match the observed one (biases, missing oceanic eddies), we however do not expect each simulated cold wake to perfectly match the corresponding observed one, as illustrated by the spread on Figure 1b. The model also successfully reproduces the observed spatial distribution of the TC-induced cooling (Figure 2): the average cooling within TC-active regions is about 1°C in all basins, with maximum amplitude of about 2°C in the north-west Pacific region where amongst the most intense TCs occur. The main model deficiency lies in the North-East Pacific basin where modeled coolings are overestimated by almost 1°C. This bias can be tracked back to a shallower than observed thermocline in this region. The use of a coarse horizontal resolution (2°) in our simulation does not hinder the realism of the ocean response to TCs: similar comparisons to observations have indeed been obtained with a simulation of higher (0.5°) resolution using similar boundary conditions and forcing strategy [*Vincent et al.*, 2012, Figure 5].

3.2. Evaluation of the DpCO$_2$

[21] Simulated DpCO$_2$ has been evaluated against observations-based climatologies in *Aumont and Bopp* [2006] both in terms of annual-mean, seasonal amplitude and phasing. Here, we focus on the mean DpCO$_2$ during the TC-season, i.e. from November to April in the southern hemisphere and from May to October in the northern hemisphere (Figure 3). The TC-season DpCO$_2$ displays regions both with positive and negative values qualitatively well reproduced by the model. Regions with negative DpCO$_2$ (oceanic sources of CO$_2$ to the atmosphere) are in the tropical eastern Pacific, the tropical Atlantic, the Arabian sea. Regions with positive DpCO$_2$ (oceanic sinks for atmospheric CO$_2$) are found off the west coast of Australia, in the Southwest Pacific and in the mid-latitudes of all oceanic basins.

4. Results

4.1. Case of TC Felix at Station BATS

[22] The observations of *Bates et al.* [1998] at station BATS (31°10′N, 64°10′W) in the Western North Atlantic before and after the passage of TC Felix provide a unique opportunity to evaluate the response in pCO$_2$ predicted by our model. Around BATS, typical summertime conditions are characterized by weak winds and seawater pCO$_2$ larger than atmospheric pCO$_2^{atm}$ levels, causing a small flux from ocean to atmosphere. Felix passed over the station on 14–15 August 1995. It was quite large (350 km in diameter) and had sustained winds of 40–45 m s^{-1}. For several weeks before the storm, the SST was close to 28°C and pCO$_2$ ranged from 400–420 μatm. A sharp decrease of SST and pCO$_2$ occurred following the TC passage, with similar amplitudes in both model and observations (resp. -3C and -45 μatm). The SST and pCO$_2$ rebounded after passage of Felix, but did not return to pre-storm values (data from *Bates et al.* [1998], reproduced in Figures 4a and 4b). The oceanic response to Felix is hence successfully captured by our simulation. We should note however that the absolute pCO$_2$ values display a systematic ~ 10 μatm shift compared to observations (Figure 4b). This shift could be due to the coarse model resolution (2°) used here. This resolution implies that model data represent an average over a 2° region around station BATS, which is characterized by large horizontal gradients of all fields.

[23] The TC passage results in significant changes of the modeled F_{CO_2} (Figure 4c). In the C-run, the F_{CO_2} peaks very abruptly during the 2-days corresponding to the TC passage (August 14–15) reaching 58 mmole/m^2/day, then nearly vanishes (from August 16–29) until three other storms hit the area (in September). In the N-run, the F_{CO_2} do not experience any large variations during the passage of the main TC and of the subsequent storms compared to the C-run, but is larger during the more quiet periods (Figures 4c and 4d).

[24] To interpret the differences of F_{CO_2} between the 2 runs, the wind and mixing effects have been separated according to equations (2), (3), and (4) applied at the fixed location of BATS (Figure 4d). This diagnostics clearly reveals that the wind effect is the driver of the strong increase of F_{CO_2} during the 2 days of the TC-passage and of the three subsequent storms (green curve in Figure 4d). On the other hand, the mixing effect (blue curve in Figure 4c) acts to increase the pCO$_2$ and thus to reduce the DpCO$_2$, which reduces the F_{CO_2}; moreover, the mixing effect is lagged and lasts longer compared to the wind effect, reducing F_{CO_2} for more than 2 weeks reaching a maximum 2–3 days after the passage of Felix.

[25] The F_{CO_2} caused by Felix has been previously estimated by *Bates et al.* [1998], by assuming that the oceanic pCO$_2$ was constant in the lead up of the storm, then decreased linearly to the end of the hurricane. This led to a total flux of 40 mmoleC m^{-2} during the two-days passage of the storm; this estimate did not account for the flux reduction during post-hurricane conditions. With our model, we predict a $\tilde{\Delta} F_{CO_2}$ of 62 mmoleC m^{-2} during the storm. This larger number compared with to *Bates et al.* [1998] is due to the slower decrease of the oceanic pCO$_2$ in the model compared to the linear decrease hypothetized by *Bates et al.* [1998]. *Koch et al.* [2009] also estimated the $\tilde{\Delta} F_{CO_2}$ caused by Felix during the two-days of the storm with a regional model, forced with daily NCEP winds. They found a lower value than *Bates et al.* [1998] of 32 mmoleC m^{-2}, which they attribute to the underestimation of their model wind forcing. In a second step, to account for the post-storm effect, we integrate the impact of TC Felix over two weeks. In this case, the increase of the

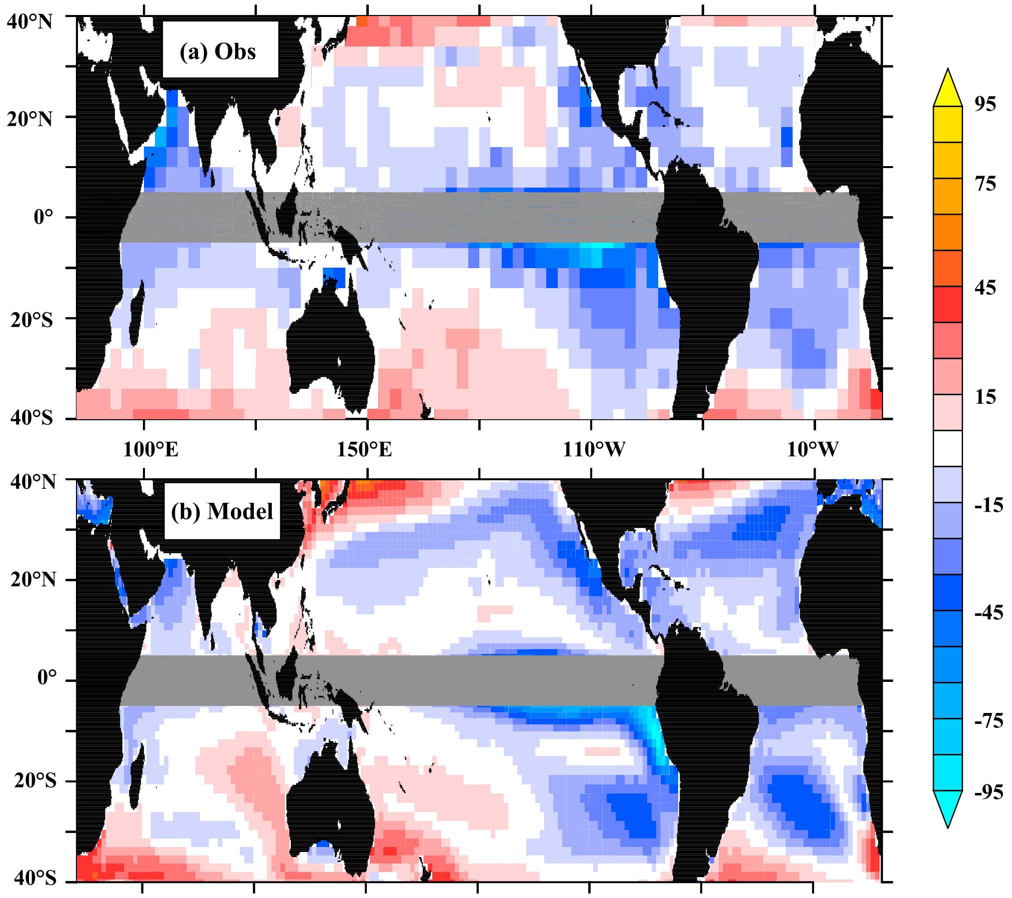

Figure 3. Evaluation of $DpCO_2$ during cyclonic season. $DpCO_2$ climatology (in μatm) during the cyclonic season (MJJASO in the northern hemisphere and NDJFMA in the southern hemisphere) from (a) Observed estimates [*Takahashi et al.*, 2009] and (b) the model (C run) over the 1993–2007 period. The grey band is to mark the time discontinuity between the two hemispheres.

$\tilde{\Delta} F_{CO_2}$ during the TC passage is counter-balanced by an the increased during post-TC conditions by approximately half, which leads to the final estimate of 30 mmoleC m^{-2}. This post-storm effect was not accounted for in the estimates of *Bates et al.* [1998] and *Koch et al.* [2009].

[26] A situation similar to that observed at BATS by *Bates et al.* [1998] was reported by *Nemoto et al.* [2009] in the coastal East China Sea, from continuous temperature and pCO_2 measurements at a moored buoy. Because their buoy was located in a coastal area, we cannot directly compare their observations with our 2° model results. However, *Nemoto et al.* [2009] examined how the variations in wind and in pCO_2 affected the F_{CO_2}. They found, in agreement with our analysis at BATS, that the F_{CO_2} efflux is increased during the passage of the storm, because of the increase in wind speed, and is decreased after the storm has passed, because of the decrease of pCO_2. Nevertheless, their estimate of the impact of TCs on the F_{CO_2}, approximately 30 mmoleC m^{-2} per typhoon, only accounts for the wind effect.

4.2. Sign of $DpCO_2$ Under TCs

[27] The efflux observed at BATS during TC Felix results from the negative $DpCO_2$ at the time t_0 of the TC passage. Previous studies that attempted to estimate the global impact of TC on F_{CO_2} have generalized this observation, hypothesizing that $DpCO_2$ at t_0 was negative for all TCs. Our numerical experiment allows to check this hypothesis (Figure 5): we found almost as many occurrences of negative and positive $DpCO_2$ at t_0 (25773 versus 21178 cases). The immediate consequence is that TCs do not systematically cause CO_2 effluxes at t_0 (as in BATS) but are also be responsible for influxes, in similar proportion (Figure 5b). Moreover, $|DpCO_2|$ at t_0 is larger than 10 μatm in ~50% of the cases, and cause the largest F_{CO_2} anomalies (tails of the distribution in Figure 5b). In the other ~50% cases, the impact of TC on the F_{CO_2} is small because $DpCO_2$ is close to zero.

[28] The spatial distribution of the positive and negative $DpCO_2$ cases under TCs in the C-run is displayed in Figures 6a and 6b. Areas with negative $DpCO_2$ during the cyclonic seasons are found mostly in the Western North Atlantic, Western and Eastern North Pacific, Arabian Sea and South West Indian Ocean, while areas of positive $DpCO_2$ are mostly in the Westernmost North Pacific, central south Indian Ocean, Bay of Bengal and South western Pacific, in broad agreement with the pCO_2 distribution during the cyclonic season (Figure 3). The same diagnostic applied to the climatology of *Takahashi et al.* [2009]

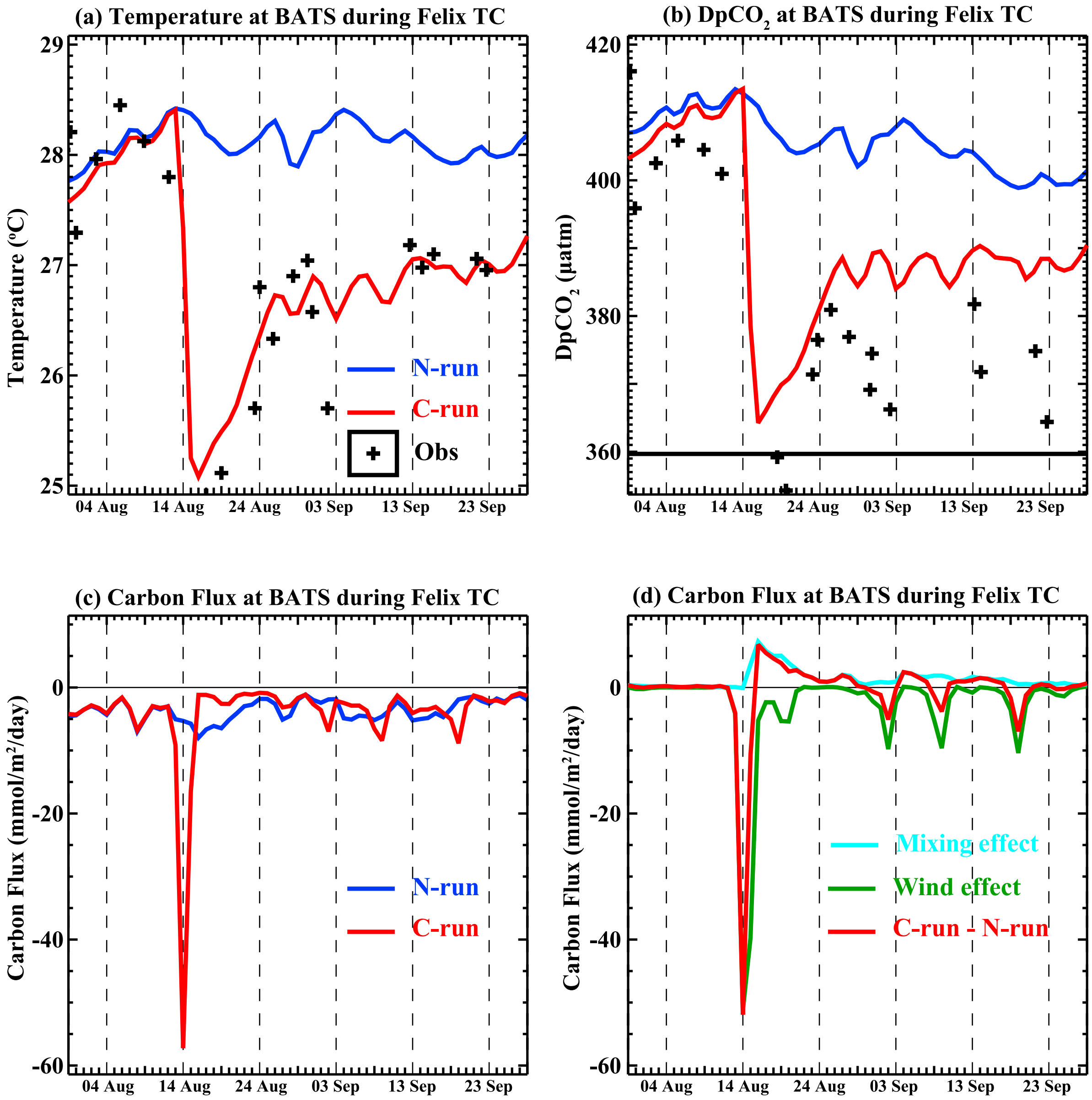

Figure 4. Hurricane Felix test case (BATS, August 1995). Temporal evolution of (a) SST and (b) oceanic pCO2 (in μatm) in the C run (red), the N run (blue) and shipboard measurements from *Bates et al.* [1998] (dots) during the passage of Hurricane Felix in the Sargasso Sea near Bermuda in August 1995. (c) Temporal evolution of the air-sea CO_2 flux (negative when oriented from the ocean to the atmosphere in mmole/m^2/day) for the C run (red) and the N run (blue) (d) Temporal evolution of the flux difference between the C and N runs (red), flux anomaly related to the TC wind effect (green), flux anomaly related to the TC mixing effect (blue) (computed according to section 2.4).

interpolated in time reveals similar regional patterns (Figures 6c and 6d). The differences are due both to model imperfections and to the absence of interannual variations in the climatology.

4.3. TCs Induced $DpCO_2$ and F_{CO_2} Anomalies

[29] Since the F_{CO_2} response differ depending on the sign of the $DpCO_2$ background conditions at the time of TCs passage, two different cases are considered in the following: the case where $DpCO_2$ is negative at t_0, causing an efflux to the atmosphere (case of BATS), and the opposite case, where $DpCO_2$ is positive at t_0, causing an influx to the ocean. Figure 7 shows the composite evolution of wind speed, SST, $DpCO_2$ and F_{CO_2} anomalies associated with the passage of all TCs falling in each category, and computed following section 2.4.

[30] In the two cases, the composite time-evolution of the wind, SST and $DpCO_2$ TC-induced anomalies are consistent

(a) $DpCO_2$ under TC

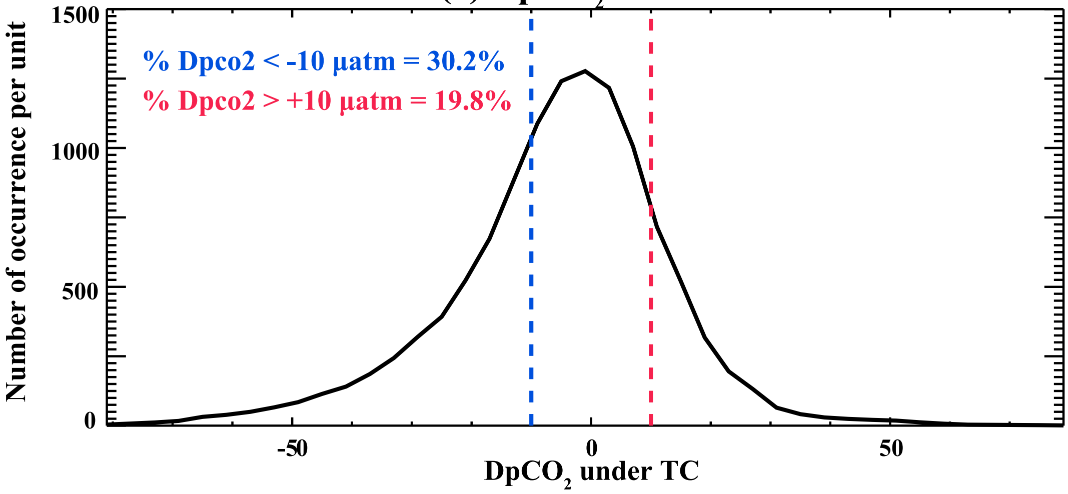

(b) TC-related Carbon Flux anomaly

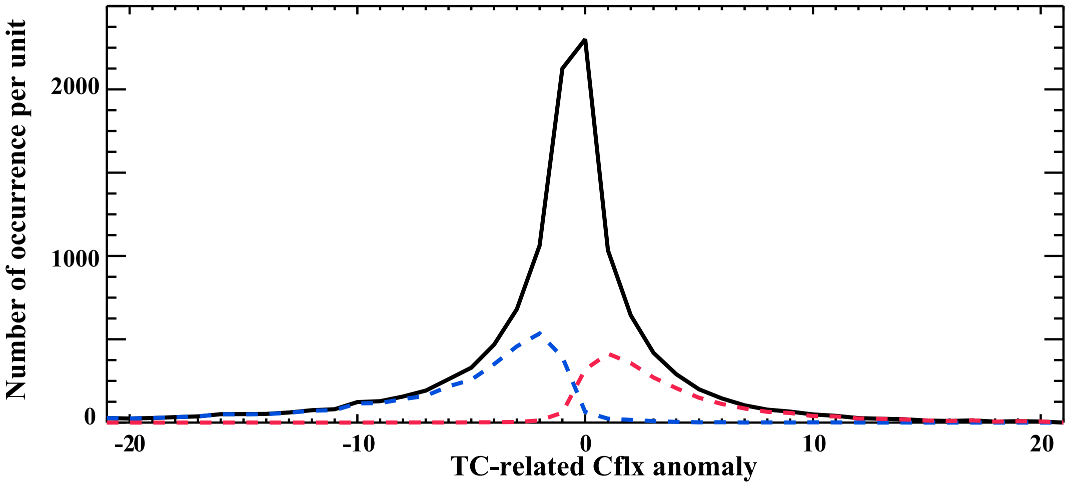

Figure 5. Distribution of $DpCO_2$ under TCs. Histograms of (a) $DpCO_2$ (in μatm) and (b) TC-related air-sea flux anomaly (in mmole/m^2/day) under TCs at time of maximum wind intensity for 46951 TC locations along 1663 TC tracks over the 1993–2007 period. Blue (red) curve on Figure 5b correspond to the histogram of TC-related air-sea flux anomaly under cyclones where $DpCO_2 < 10$ μatm ($DpCO_2 > 10$ μatm) corresponding to 30.2% (19,8%) of the cases.

with the results obtained in the case of TC Felix at BATS: TCs induce a cooling of the SST (Figure 7b), which reaches its maximum amplitude two to three days after the maximum wind speed intensity and slowly returns to its pre-storm value during the month that follows the passage of the TC. In our simulation, the maximum coolings reach 4°C, and the mean cooling when averaged over all TCs is less than 1°C. In agreement with [*Vincent et al.*, 2012], this cooling mainly results from the entrainment of cold sub-surface waters driven by the storm, especially for the strongest wind forcing. The mean cooling is larger in the negative $DpCO_2$ case, because the most intense TCs (and most intense coolings) occur over the NE Pacific (between 20–30°N) and NW Pacific (between 20–30°N), where the $DpCO_2$ is negative. Vertical mixing not only decreases SST but also, in agreement with the theoretical pCO_2 change with temperature [*Sarmiento and Gruber*, 2006], decreases pCO_2 and thus increases $DpCO_2$ (Figure 7c). The DpCO2 anomaly thus has the same sign in the undersaturated and supersaturated case (Figure 7c). Note that, rather counter intuitively, in the undersaturated case, the post-storm pCO2 decreases despite an influx of CO2 during and after the storm. This is because the temperature effect largely prevails over the increase of total inorganic carbon associated to the air-sea flux. Moreover, as for SST, the maximum magnitude of the pCO_2 drawdown is reached 2 to 3 days after the passage of the storm (Figure 7c), and the change is larger in the negative $DpCO_2$ case.

[31] Because the pre-storm air-sea fluxes have different signs in the two cases, the direct impact of TC winds on the air-sea CO_2 fluxes are opposite. At t_0, TC winds acts to increase the amplitude of the flux in either direction, thus

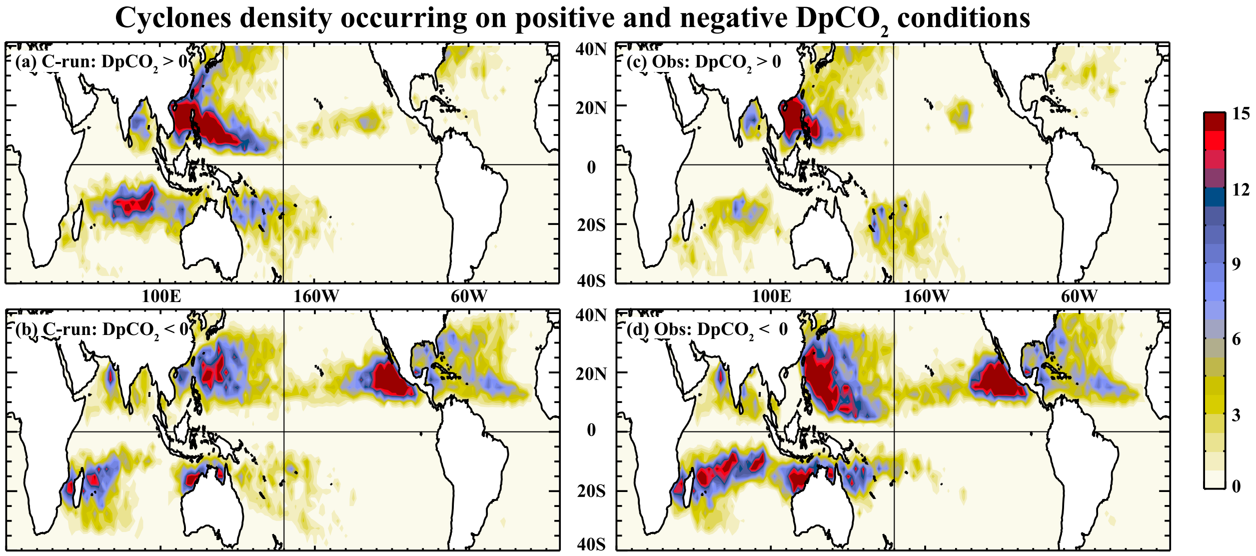

Figure 6. Locations where $DpCO_2$ is positive and negative under TCs. Density distribution (in cyclone-day/year) for TCs where (a) $DpCO_2 > 0$ and (b) $DpCO_2 < 0$ at $t = t_0$, t_0 being the time of maximum wind intensity. Densities are computed over the 1993–2007 period. (c and d) Same diagnostics applied to the $DpCO_2$ climatology of *Takahashi et al.* [2009] interpolated in time.

enhancing effluxes in the case of negative $DpCO_2$, and enhancing influxes in the case of positive $DpCO_2$ (Figure 7). After the storm, the decrease of pCO_2 causes $|DpCO_2|$ to decrease in the negative $DpCO_2$ (undersaturated) case (and eventually change sign), and to increase in the positive $DpCO_2$ (oversaturated) case (Figure 8); consequently, the amplitude of the flux is reduced in the oversaturated case (and eventually reverses), and is increased in the undersaturated case, in comparison with pre-storm conditions (Figures 7 and 8).

4.4. Respective Influence of TCs Wind and Induced Mixing on F_{CO_2}

[32] To assess and quantify the impact of TCs on F_{CO_2}, the wind and mixing effects have been separated according to equations (2), (3), and (4) for each TC, and averaged out for all oversaturated (resp. undersaturated) cases (Figure 9). In both cases, the wind effect explains most of the increase of the flux in either direction during the TC-passage, while the mixing effect explains the modifications of the flux after the storm, in opposite sign in the case of oversaturation, and in same sign in the case of undersaturation.

[33] In the oversaturated case, when integrated over 30 days, the time integral of the TC-induced flux anomaly is 1.1 mmole/m^2 and is positive. This means that, on average over all TCs, the negative wind-driven flux anomaly during the storm is more than offset by the post-storm, positive, mixing-driven flux anomaly. In the undersaturated case, the time integral of the TC-induced flux anomaly is 10.1 mmole/m^2; in this case, the wind-driven and mixing-driven anomalies are both positive and add up.

4.5. Regional and Global Impact of TC on F_{CO_2}

[34] In Figure 10, the storm and post-storm impacts of TCs on F_{CO_2} are evaluated regionally. This is done by integrating ΔF_{CO_2} over two time periods.

[35] During the storm peak intensity (t_0 − 1.5d to t_0 + 1.5d, Figure 10b), the averaged TC-driven flux anomaly is negative in the North West Atlantic, North West Pacific, North East Pacific, Arabian Sea and South West Indian, and is positive in the Westernmost North Pacific, central south Indian Ocean, Bay of Bengal and South western Pacific. These patterns are due to the first (resp. second) regions being predominantly supersaturated (resp. undersaturated) during the cyclonic season (Figure 3). After the storm (t_0 + 1.5d to t_0 + 30d, Figure 10c), the flux anomaly is systematically positive (except for a small region in the north eastern Pacific, where pCO_2 is enhanced by vertical mixing) and its pattern is that of the TC density. When considering the whole period (t_0 − 1.5d to t_0 + 30d, Figure 10a), the storm and post-storm effects often balance when they are of opposite signs.

[36] In consequence, in the North West Atlantic and Arabian Sea, which are mostly supersaturated during the cyclonic season, the net effect of TC on F_{CO_2} during the cyclonic season is very weak because the storm and post-storm effects almost compensate. The situation is different in the North West Pacific, where the strongest SST anomalies occur (Figure 2); because of these strong SST anomalies, the post-storm effect prevails over the storm effect, with the consequence of a net TC-induced CO_2 influx anomaly. In regions which are predominantly undersaturated during the cyclonic season, the storm and post-storm effects reinforce each other. Consequently, the mean effect of TC in the Westernmost North Pacific, central south Indian Ocean, Bay of Bengal and South western Pacific is to increase the uptake of CO_2 by the ocean during the cyclonic season.

[37] Tables 1 and 2 provide more quantitative numbers of the impact of TCs on F_{CO_2} over the large regions delimited in Figure 10a. Except in the North West Pacific and in the Bay of Bengal, the flux due to TC is generally less than

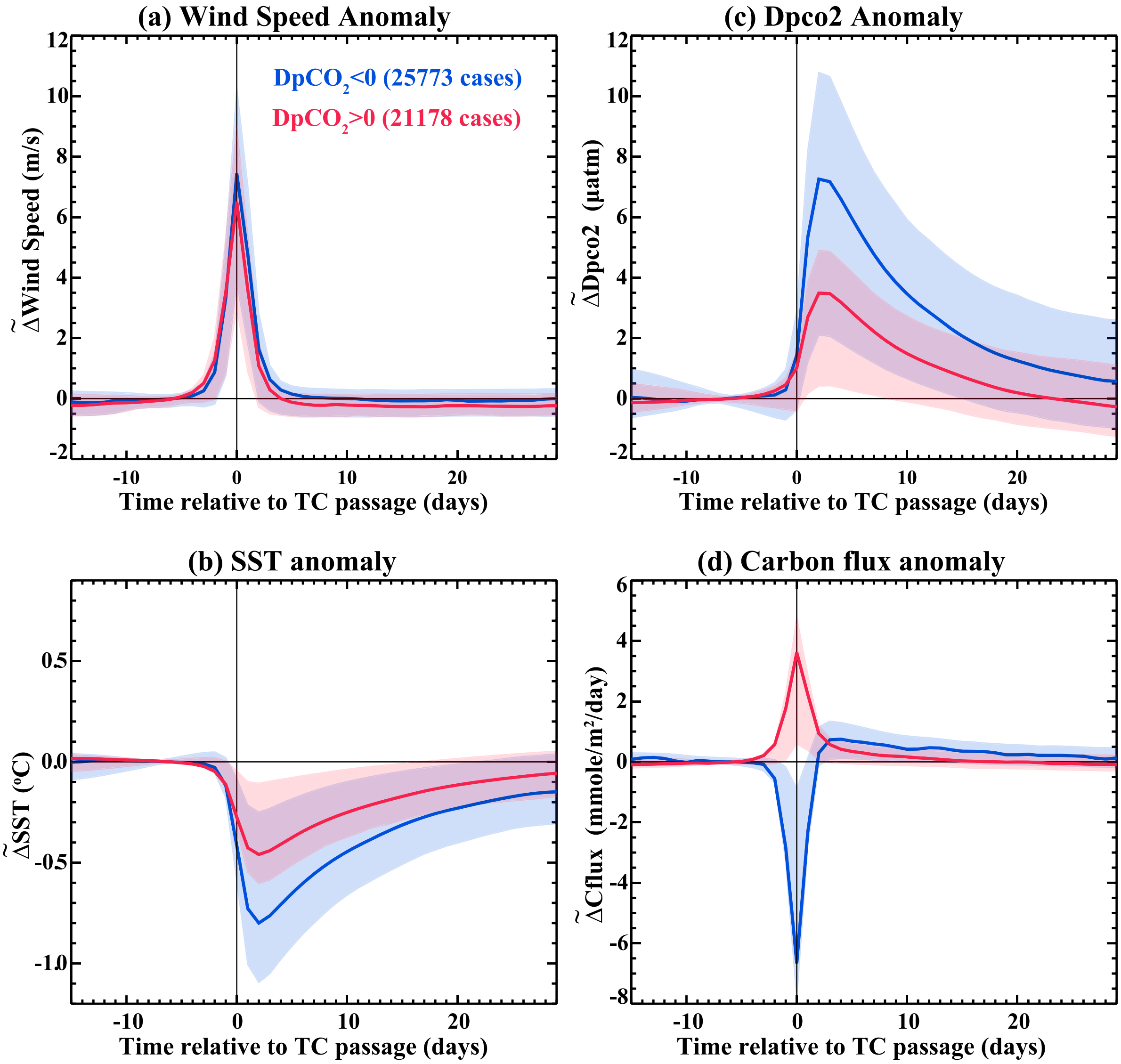

Figure 7. Composite time evolution of wind speed, SST, $DpCO_2$ and air-sea flux anomalies generated by the passage of TCs. Blue color: Mean composite of all cases (25773) where $DpCO_2 < 0$ at $t = t_0$, with t_0 the time of maximum wind intensity. Red color: Mean composite of all cases (21,178) where $DpCO_2 > 0$ at $t = t_0$. Shading show the ±1/2 standard deviation around the mean composite value. Composites are computed over the 1993–2007 period. Anomalies are computed according to section 2.4.

±3% of the total flux. In the North West Pacific and Bay of Bengal the percentage is larger (+33.4% and −13.6%, respectively) but they concern regions which weakly (15.5 and −0.6 TgC, respectively) contribute to the total F_{CO_2} during the cyclonic season (−305 TgC). Note also that in most regions, the flux due to TCs is not systematically in the same direction (Table 2); for instance, the North Atlantic is submitted to an average of 80 TC-days over supersaturated conditions, contributing to a TC efflux of −1.6 TgC, but also to 16 TC-days over undersaturated regions, which cause an influx of +1 TgC. Under undersaturated conditions, the TC induced flux is always positive, while it can be either positive or negative under supersaturated conditions (depending on the relative strength of the storm and post-storm effects) (Table 2). The North West Pacific and Bay of Bengal are predominantly undersaturated, which explains the larger % of the TC-flux to the total flux.

5. Discussion

5.1. Comparison With Previous Estimates

[38] The global impact of TCs on air-sea CO_2 fluxes estimated in this study (0.007 $Pg\,C\,y^{-1}$, i.e. 2% of the mean, subtropical flux during the cyclonic season, Table 1) is one order of magnitude less than the lowest previous estimates [*Perrie*, 2004; *Bates*, 2007; *Koch et al.*, 2009; *Huang and Imberger*, 2010] and is in opposite direction (influx anomaly). This is because previous estimates did not account for

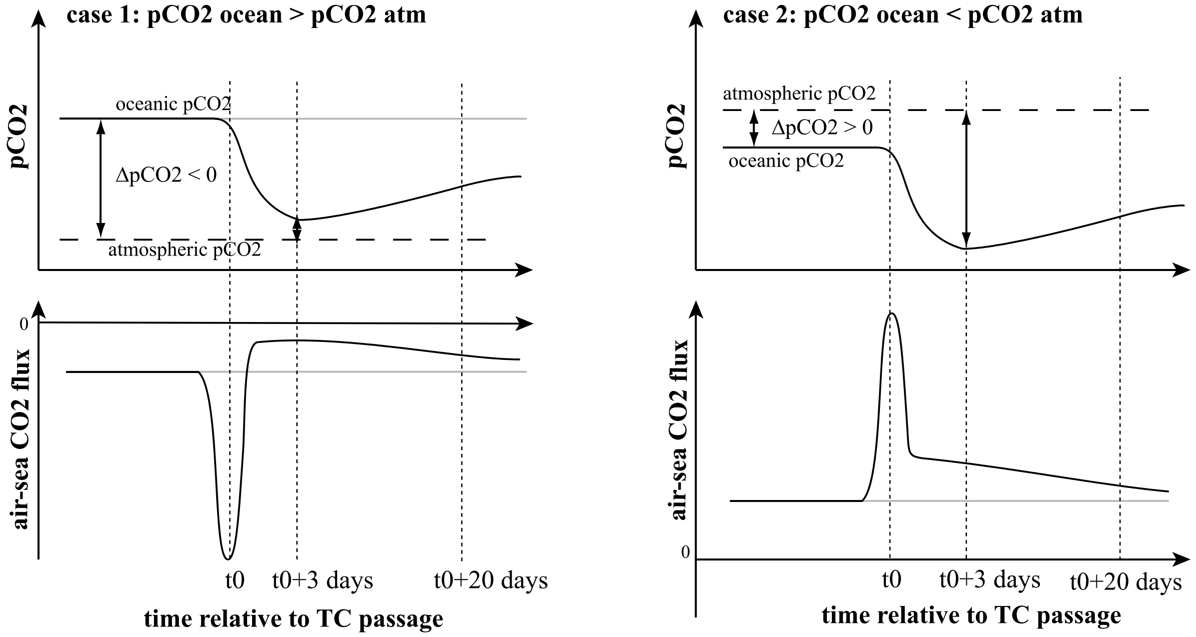

Figure 8. Schematic representation of the impact of TCs on pCO_2 and air sea flux. Schematic time evolution of oceanic pCO_2 and air-sea CO_2 flux associated with the passage of a TC (black curves). For reference, the grey curves show the stationary situation in the absence of TC. Day t_0 is the time of maximum wind intensity during the passage of TC. The left column is the case where the oceanic pCO_2 is initially larger than the atmospheric pCO_2 and the air-sea flux is directed from the ocean to the atmosphere (case of BATS). The right column is when the atmospheric pCO_2 is initially larger than the oceanic pCO_2 and the air-sea flux is directed from the atmosphere to the ocean.

two important aspects: first, in supersaturated regions, they did not account for the post-storm mixing-effect, which balances the storm wind-effect; second, they did not consider the impact of TCs over undersaturated regions.

[39] Previous estimates of air-sea CO_2 fluxes under TCs mainly focused on hurricanes in the North West Atlantic [*Bates et al.*, 1998; *Perrie*, 2004; *Bates*, 2007; *Koch et al.*, 2009; *Huang and Imberger*, 2010], with the exception of one study in the East China Sea [*Nemoto et al.*, 2009]. These

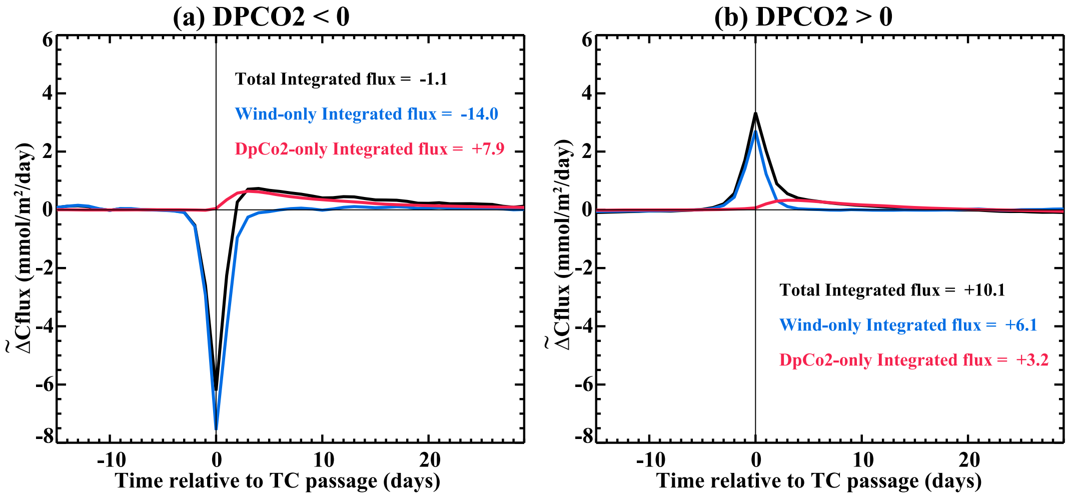

Figure 9. Composite time evolution of TC-induced air-sea flux anomalies: controlling mechanisms. Mean of all cases where (a) $DpCO_2 < 0$ at $t = t_0$ and (b) $DpCO_2 > 0$ at $t = t_0$, t_0 being the time of maximum wind intensity. Anomalies are computed over the 1993–2007 period. The black curve is the total TC-induced flux anomaly, the blue curve is the wind effect on the flux (section 2.4, equation (2)), the red curve is the mixing effect on the flux (section 2.4, equation (3)).

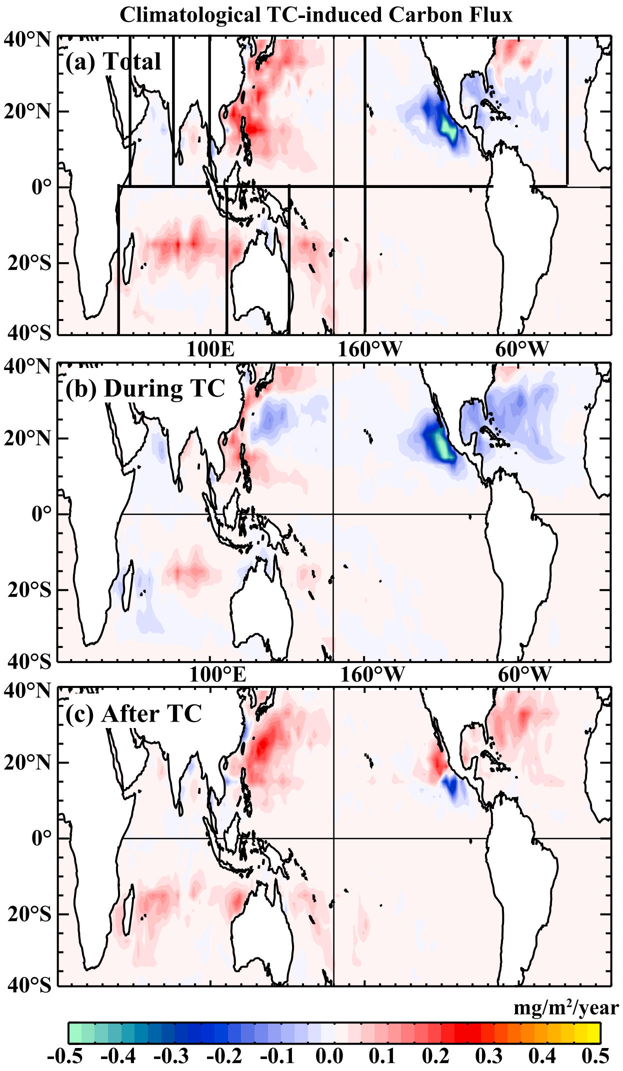

Figure 10. Climatological TC-induced air-sea flux. Climatological average of seasonally cumulated air-sea flux (in mmol/m^2/season) induced by cyclones along their tracks in the C-run between (a) $t_0 - 1.5d$ and $t_0 + 30d$ (b) $t_0 - 1.5d$ and $t_0 + 1.5d$ (c) $t_0 + 1.5d$ and $t_0 + 30d$. Dashed lines on Figure 10a indicate the boundaries of the regions discussed in Tables 1 and 2.

Table 1. Regional and Global CO_2 Fluxes and Contribution of TCs[a]

	Total Flux	TC-Flux	% TC/Total	STD (Total/TC)
North Atlantic	−65.7 (−2699)	−0.6	+1%	11.1/1.8
North East Pacific	−130.0 (−4988)	−3.0	+2.3%	24.3/2.9
North West Pacific	+15.5 (+384)	+5.2	+33.4 %	21.8/2.3
Bay of Bengal	−0.6 (−117)	+0.1	−13.6 %	4.3/0.3
Arabian Sea	−43.4 (−2727)	−0.1	+0.2 %	6.1/0.2
South Indian	+93.1 (+2838)	+2.7	+2.9 %	26.8/1.2
Australia	+ 18.1 (+2017)	+0.5	+2.5 %	5.0/0.4
South Pacific	+53.3 (+2492)	+1.7	+3.2%	18.2/ 1.0
Total	−305.0 (−1258)	+6.7	−2.2%	85.0/5.0

[a] Mean and standard deviation of total and TC-induced carbon flux cumulated over the cyclonic season and over different oceanic basins (delimited in Figure 10a), in Tera gC/cyclonic season. The STD represents interannual variations. The Total flux is computed over the region 40S-40N for the cyclonic season (NDJFMA for Southern Hemisphere and MJJASO for Northern Hemisphere). Value in parenthesis in the first column are in mgC/m^2.

studies took place in undersaturated regions. In most of them, it was attempted to extrapolate the results from a few TCs (one to three TCs, typically) to the global ocean, by using TCs database and making assumptions about storm area, wind speed and oceanic pCO_2 values. Moreover, it was generally assumed that the oceanic conditions at the time and location of TC passage did not significantly deviate from the case study that was examined. The different assumptions and methods used led to a wide range of estimates. The first annual, global estimate by *Bates et al.* [1998] was a TC-induced efflux of up to 0.51 Pg C. Later, *Bates* [2007] estimated a smaller efflux of 0.04–0.08 Pg C, but no details on the method were provided. The method of *Huang and Imberger* [2010], with different extrapolation assumptions, lead to an efflux of 0.047–0.141 Pg C. *Nemoto et al.* [2009] restricted their extrapolation to the western subtropical North Pacific, and found a contribution of TCs equal to 76% of the summer efflux, a value even larger than the 20–54% estimate of *Bates et al.* [1998]. Our estimate in for North West Atlantic is close to zero (1%, Table 1), because the wind and mixing effect are in balance. In the North West Pacific, we found a larger impact (−37%, Table 1) but with opposite sign, because the mixing effect is larger than the wind effect. In that respect, our results are thus significantly different from the previous estimates.

[40] Moreover, it was hypothetized that the year-to year differences in TC frequency and intensity might be an important mechanism for controlling interannual variability in F_{CO_2} [*Bates et al.*, 1998; *Bates*, 2007], although this hypothesis was not supported by the model result of *Koch et al.* [2009] in the subtropical North Atlantic. To examine this question over different ocean sub-basins, we compared the standard deviation of the year-to-year regional F_{CO_2} budget to the standard deviation of the year-to-year regional TC-induced F_{CO_2} flux (Table 1). Our result extend the conclusion of *Koch et al.* [2009]: over the different sub-basins, TC explain between 0 and 10% of the interannual flux changes, with a global mean of ~5 %.

Table 2. Global and Regional CO_2 Fluxes due TCs Depending on Oceanic State[a]

	TC-Flux $\Delta pCO_2 > 0$	TC-Flux $\Delta pCO_2 < 0$	Days $\Delta pCO_2 > 0$	Days $\Delta pCO_2 < 0$
North Atlantic	+1.0	−1.6	16	80
North East Pacific	+0.3	−3.3	14	93
North West Pacific	+5.2	0.0	168	119
Bay of Bengal	+0.1	0.0	15	8
Arabian Sea	0.0	−0.1	0	13
South Indian	+2.5	+0.2	77	66
Australia	+0.5	0	19	27
South Pacific	+1.5	+0.2	45	24
Total	11.3	−4.6	354	430

[a] Mean TC-induced carbon flux cumulated over the cyclonic season (NDJFMA for Southern Hemisphere and MJJASO for Northern Hemisphere) and over different oceanic basins (delimited in Figure 10a). For each region, we count the number of TCs occurrences (In days/cyclonic season) and associated carbon flux (in Tera gC/cyclonic season) over undersaturated (versus oversaturated) oceanic state.

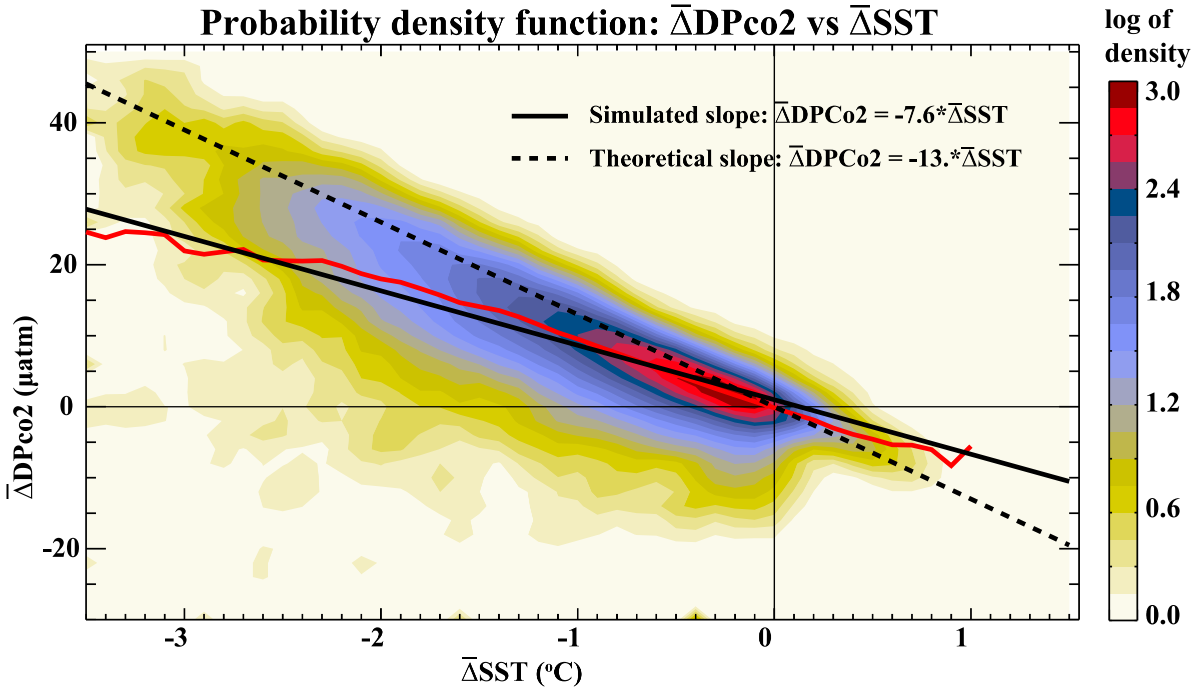

Figure 11. TC-induced $DpCO_2$ anomaly versus SST anomaly. Probability Density function of TC-induced $DpCO_2$ wake anomaly versus SST wake anomaly simulated in the model. Thick black line indicates the theoretical relationship of Gruber and Sarmiento, with a slope of −13. The blue line is the mean $\overline{\Delta}$SST per bin of $\overline{\Delta}DpCO_2$. The black line is the linear fit to the blue line and as a slope of −7.6. Anomalies are computed over the 1993–2007 period along TC tracks for run C.

5.2. The Post-Storm, Mixing Effect

[41] One of the important process highlighted in this study is the impact of TC-induced vertical mixing with thermocline waters, which occurs essentially after the storm, cools the SST and reduces the pCO_2. The importance of this processes is revealed by the persistence of the cold SST anomaly after the passage of the storm that can last from a few days to over a month. This persistence is accurately reproduced by our model when compared with satellite AMSR observations. The link between the cooling and the change in pCO_2 is however not straightforward. Figure 11 shows the distribution of the change in pCO2 after the passage of TC, against the change in SST (computed following section 2.4 as $\overline{\Delta}pCO_2$ versus $\overline{\Delta}T$). It confirms that in most cases, pCO_2 decreases after the passage of TCs; the average decrease (−7.6 μatm per °C) is however smaller than the theoretical decrease due to the temperature effect alone (−13 μatm per °C, *Sarmiento and Gruber* [2006]). This feature can be explained by the entrainment of higher DIC water from the thermocline into the surface mixed-layer which increases the pCO_2 and partly offsets the temperature effect; TC can also alleviate nutrient limitation and promote phytoplankton blooms [*Babin et al.*, 2004; *Walker et al.*, 2005; *Son et al.*, 2006; *Patra et al.*, 2007; *Liu et al.*, 2009; *Hanshaw et al.*, 2008; *Gierach and Subrahmanyam*, 2008], thus decreasing the pCO2. How mixing of these different elements impact pCO_2 depends on their respective vertical gradients and is spatially and temporally variable [*Mahadevan et al.*, 2011]. Our model results are in that respect consistent with the analysis of *Mahadevan et al.* [2011], based on climatological distributions of T, S, DIC, nutrients and TA, which suggest that the temperature impact on pCO_2 prevails upon the change of the other variables (S, TA, DIC) in the tropical oceans and during the summer cyclonic season. However, a sharp rise in pCO_2 has recently been reported after the passage of typhoon Choi-Wan in 2009 in the North West Pacific, which preceded the drop in temperature by about 6 h [*Bond et al.*, 2011]. Such short-term sequence could not be examined with the daily resolution of our model outputs and deserves further investigation.

5.3. Caveats

[42] Our results rely on an number of assumptions that were made to build the model. An inherent limitation of our modeling strategy is that the analytical formulation of TC winds derived from *Willoughby et al.* [2006] does not account for the vast variety of wind structures associated with TCs. The latest version of the IBTrACS database provides radius estimations for some TCs, which could be a first step in better defining the geometry of the wind. The wind forcing asymmetry due to the translation speed of TCs has also not been accounted for in our modeling strategy: including this effect may also improve characteristics of the simulated TC-induced cooling, in particular for fast cyclones. Another factor that was not accounted for is the intense rain falls that often come with TCs, and can dilute the salinity and DIC, with possible modifications of the surface pCO_2. A more precise estimate of the TC induced F_{CO_2} would certainly require to examine this aspect.

[43] Regarding model resolution, as shown by *Vincent et al.* [2012], a 2° resolution reasonably captures the transfer of cyclone kinetic energy to the upper ocean (their Figure 2), which is the main driver of mixing, a dominant process in the cold wake formation. However, their analysis also suggests that the maximum amplitude of Ekman pumping near the eye, a process which is also involved in the cold wake formation but is less dominant [*Greatbatch*, 1985; *Yablonsky and Ginis*, 2009; *Jullien et al.*, 2012], is strongly underestimated with a resolution of 2°. Moreover, a resolution of 2° is not sufficient to explicitly resolve oceanic mesoscale eddies, which, as discussed in previous studies [e.g., *Shay et al.*, 1992; *Jaimes et al.*, 2011], can modulate the SST response to TCs. Although we have shown that our 2° resolution model reasonably captures the magnitude of the TC-induced cooling, a main factor affecting the FCO_2, further studies at higher resolution would be needed to strengthen our results and evaluate the role of the small scale oceanic processes that were not accounted for in the present study.

[44] Decreasing atmospheric pCO_2 during the passage of TCs, associated with the decrease atmospheric pressure, have been reported [*Bates et al.*, 1998; *Huang and Imberger*, 2010], with values up to 20 μatm (V.V.S.S. Sarma, unpublished data, 2011). In our model, the atmospheric pCO_2 is increased from year to year but is not impacted by TCs. The model study of *Huang and Imberger* [2010], which accounts for that effect, suggest that it is very short-lived (<12 h) and limited to the core of the TC (in a 50 km radius); we thus expect this effect to be weak when averaged over the large oceanic area influenced by TCs.

[45] Our results are also certainly dependent on the choice of the parameterization of the gas transfer velocity at hight wind speed, as suggested by the sensitivity analysis of *Perrie* [2004]. A different choice might imply larger absolute values of the fluxes, and modulate the strengths of the compensations.

6. Conclusion

[46] In this study, we used a state-of-the-art global ocean biogeochemical model driven by TC wind forcing derived from a historical TC database. This allows us to examine the ocean response along 1,663 TC tracks over the 1993–2007 period. The resulting modeled SST response to TCs compares very well with satellite estimates during the same period. The model also accurately reproduces the sharp pCO_2 drawdown recorded after the passage of Hurricane Felix in 1995 in the NW Atlantic.

[47] Previous case studies have illustrated the strong influence of TCs on ocean-atmosphere CO_2 fluxes by increasing the gas exchange coefficient and decreasing the SST and oceanic pCO_2. Moreover, it was generally assumed that the ocean is oversaturated in CO_2 under TCs, because TCs blow essentially in the tropics during the summer season. Thus, based on a these few observations, it has been suggested that TCs significantly increase the CO_2 efflux from the ocean to the atmosphere. However, limited availability of pCO_2 observations under TCs harsh conditions has so far restricted global quantification of the TC-induced F_{CO_2} to hazardous extrapolations.

[48] We found a similar proportion of TCs over undersaturated regions (~20% of TC locations are over regions where $DpCO_2 < -10$ μatm) and oversaturated regions (~30% for $DpCO_2 > 10$ μatm), with a large proportion (~50%) of TCs over regions where the ocean and atmosphere are in near equilibrium. This estimation, based on our model outputs, is consistent with a similar estimation from observed climatological pCO_2 variations. The consequence is that TCs can generate instantaneous CO_2 fluxes directed from the ocean to the atmosphere (efflux) or vise-versa (influx), depending on the oceanic condition at the time of the TC passage; this instantaneous flux is very weak in ~50% of the cases.

[49] Moreover, we identify two competing effects of TCs on F_{CO_2} that are not synchronous. During the storm and depending on the sign of the difference of pCO_2 between the ocean and atmosphere, TCs are responsible for large efflux or influx anomalies due to the strong winds. During several weeks after the storm, oceanic pCO_2 is reduced in response to vertical mixing, which systematically causes an influx anomaly. Generally, the storm wind-effect and post-storm mixing effect have the same order of magnitude. This implies that, contrary to previous estimates, TCs weakly impacts the CO_2 efflux because the two effects oppose with each other when they blow over supersaturated areas (typically in the North Atlantic, North-East Pacific, Arabian Sea). In contrast, TCs increase the CO_2 influx because the two effects add up under undersaturated conditions (e.g. in the Westernmost North Pacific, Bay of Bengal, South Indian and Pacific Ocean). In total, we find that TCs account for ~2% of the F_{CO_2} during the cyclonic season over the tropical ocean (40°N-40°S). This is an order of magnitude less than the lowest previous estimates. Moreover, we find that regionally, TC account for 0 to 10% of the year-to-year variations of the F_{CO_2}.

[50] **Acknowledgments.** This study was supported by IRD, CNRS, INSU (LEFE project CYCLOCEAN AO2010-538863), CNES (project CPUMP) and through EU FP7 project CARBOCHANGE (Changes in carbon uptake and emissions by oceans in a changing climate) which received funding from the European Community's Seventh Framework Programme under grant agreement 264879. This is NIO contribution 5131. Model development was supported by the NEMO system team. The study was initiated during M. Lévy, M. M. Lengaigne, and E. M. Vincent's stay at the NIO.

References

Aumont, O., and L. Bopp (2006), Globalizing results from ocean in situ iron fertilization studies, *Global Biogeochem. Cycles*, *20*, GB2017, doi:10.1029/2005GB002591.

Babin, S., J. Carton, T. Dickey, and J. Wiggert (2004), Satellite evidence of hurricane-induced phytoplankton blooms in an oceanic desert, *J. Geophys. Res.*, *109*, C03043, doi:10.1029/2003JC001938.

Bates, N. R. (2007), Interannual variability of the oceanic CO_2 sink in the subtropical gyre of the North Atlantic Ocean over the last 2 decades, *J. Geophys. Res.*, *112*, C09013, doi:10.1029/2006JC003759.

Bates, N. R., A. Knap, and A. Michaels (1998), Contribution of hurricanes to local and global estimates of air-sea exchange of CO_2, *Nature*, *395*(6697), 58–61.

Bond, N., M. Cronin, C. Sabine, Y. Kawai, H. Ichikawa, P. Freitag, and K. Ronnholm (2011), Upper ocean response to typhoon Choi-Wan as measured by the Kuroshio Extension Observatory mooring, *J. Geophys. Res.*, *116*, C02031, doi:10.1029/2010JC006548.

Chiang, T.-L., C.-R. Wu, and L.-Y. Oey (2011), Typhoon Kai-Tak: An ocean's perfect storm, *J. Phys. Oceanogr.*, *41*(1), 221–233, doi:10.1175/2010JPO4518.1.

Cione, J., and E. Uhlhorn (2003), Sea surface temperature variability in hurricanes: Implications with respect to intensity change, *Monthly Weather Rev.*, *131*, 1783–1796.

Cravatte, S., G. Madec, T. Izumo, C. Menkes, and A. Bozec (2007), Progress in the 3-D circulation of the eastern equatorial Pacific in a climate ocean model, *Ocean Modell.*, *17*(1), 28–48, doi:10.1016/i.ocemod.2006.11.003.

D'Asaro, E. (2003), The ocean boundary layer below hurricane Dennis, *J. Phys. Oceanogr.*, *33*(3), 561–579.

D'Asaro, E., and C. McNeil (2007), Air-sea gas exchange at extreme wind speeds measured by autonomous oceanographic floats, *J. Mar. Syst.*, *66*(1–4), 92–109.

Dickey, W. J. B. T. D. (2008), Observations and analyses of the upper ocean responses to tropical storms and hurricanes in the vicinity of Bermuda, *J. Geophys. Res.*, *113*, C08009, doi:10.1029/2007JC004358.

Donelan, M. A. (2004), On the limiting aerodynamic roughness of the ocean in very strong winds, *Geophys. Res. Lett.*, *31*, L18306, doi:10.1029/2004GL019460.

Gent, P. R., and J. C. McWilliams (1990), Isopycnal mixing in ocean circulation models, *J. Phys. Oceanogr.*, *20*, 150–155.

Gierach, M. M., and B. Subrahmanyam (2008), Biophysical responses of the upper ocean to major Gulf of Mexico hurricanes in 2005, *J. Geophys. Res.*, *113*, C04029, doi:10.1029/2007JC004419.

Greatbatch, R. J. (1985), On the role played by upwelling of water in lowering sea surface temperatures during the passage of a storm, *J. Geophys. Res.*, *90*, 11,751–11,755, doi:10.1029/JC090iC06p11751.

Griffies, S. M., et al. (2009), Coordinated ocean-ice reference experiments (cores), *Ocean Modell.*, *26*(1), 1–46, doi:10.1016/j.ocemod.2008.08.007.

Hanshaw, M. N., M. S. Lozier, and J. B. Palter (2008), Integrated impact of tropical cyclones on sea surface chlorophyll in the North Atlantic, *Geophys. Res. Lett.*, *35*, L01601, doi:10.1029/2007GL031862.

Huang, P., and J. Imberger (2010), Variation of pCO$_2$ in ocean surface water in response to the passage of a hurricane, *J. Geophys. Res.*, *115*, C10024, doi:10.1029/2010JC006185.

Jaimes, B., L. K. Shay, and G. R. Halliwell (2011), The response of quasigeostrphic oceanic vortices to tropical cyclone forcing, *J. Phys. Ocean.*, *41*, 1965–1985.

Jullien, S., C. E. Menkes, P. Marchesiello, N. C. Jourdain, M. Lengaigne, A. Koch-Larrouy, J. Lefevre, E. M. Vincent, and V. Faure (2012), Impact of tropical cyclones on the south pacific ocean heat budget, *J. Phys. Oceanogr.*, in press.

Koch, J., G. A. Mckinley, V. Bennington, and D. Ullman (2009), Do hurricanes cause significant interannual variability in the air-sea CO$_2$ flux of the subtropical North Atlantic?, *Geophys. Res. Lett.*, *36*, L07606, doi:10.1029/2009GL037553.

Large, W. G., and S. G. Yeager (2009), The global climatology of an interannually varying air-sea flux data set, *Clim. Dyn.*, *33*(2–3), 341–364, doi:10.1007/s00382-008-0441-3.

Liss, P. S., and L. Merlivat (1986), Air-sea gas exchange rates: Introduction and synthesis, in *The Role of Sea-Air Exchange in Geochemical Cycling*, *NATO/ASI Ser.*, vol. 185, edited by P. Buat-Ménard, pp. 113–127, D. Reidel, Dordrecht, Netherlands.

Liu, X., M. Wang, and W. Shi (2009), A study of a Hurricane Katrina–induced phytoplankton bloom using satellite observations and model simulations, *J. Geophys. Res.*, *114*, C03023, doi:10.1029/2008JC004934.

Lloyd, I. D., and G. A. Vecchi (2011), Observational evidence for oceanic controls on hurricane intensity, *J. Clim.*, *24*(4), 1138–1153, doi:10.1175/2010JCLI3763.1.

Madec, G. (2008), Nemo ocean engine, *Note du Pole de modelisation de l'Institut Pierre-Simon Laplace*, *27*, 1–217, doi:ISSN:1288-1619.

Mahadevan, A., A. Tagliabue, L. Bopp, A. Lenton, L. Memery, and M. Lévy (2011), Impact of episodic vertical fluxes on sea surface pCO$_2$, *Philos. Trans. R. Soc. A*, *369*(1943), 2009–2025, doi:10.1098/rsta.2010.0340.

McNeil, C., and E. D'Asaro (2007), Parameterization of air-sea gas fluxes at extreme wind speeds, *J. Mar. Syst.*, *66*(1–4), 110–121.

Nemoto, K., T. Midorikawa, A. Wada, K. Ogawa, S. Takatani, H. Kimoto, M. Ishii, and H. Inoue (2009), Continuous observations of atmospheric and oceanic CO$_2$ using a moored buoy in the East China Sea: Variations during the passage of typhoons, *Deep Sea Res., Part II*, *56*(8–10), 542–553.

Patra, P. K., M. D. Kumar, N. Mahowald, and V. V. S. S. Sarma (2007), Atmospheric deposition and surface stratification as controls of contrasting chlorophyll abundance in the North Indian Ocean, *J. Geophys. Res.*, *112*, C05029, doi:10.1029/2006JC003885.

Perrie, W. (2004), The role of midlatitude storms on air-sea exchange of CO$_2$, *Geophys. Res. Lett.*, *31*, L09306, doi:10.1029/2003GL019212.

Price, J. (1981), Upper ocean response to a hurricane, *J. Phys. Oceanogr.*, *11*, 153–175.

Price, J. F., J. Morzel, and P. P. Niiler (2008), Warming of SST in the cool wake of a moving hurricane, *J. Geophys. Res.*, *113*, C07010, doi:10.1029/2007JC004393.

Samson, G., H. Giordani, G. Caniaux, and F. Roux (2009), Numerical investigation of an oceanic resonant regime induced by hurricane winds, *Ocean Dyn.*, *59*, 565–586.

Sarmiento, J., and N. Gruber (2006), *Ocean Biogeochemical Dynamics*, 564 pp., Princeton Univ. Press, Princeton, N. J.

Shay, L. K., P. Black, A. Mariano, J. Hawkins, and R. Elsberry (1992), Upper ocean response to hurricane gilbert, *J. Geophys. Res.*, *97*(20), 227–248.

Son, S., T. Platt, H. Bouman, D. Lee, and S. Sathyendranath (2006), Satellite observation of chlorophyll and nutrients increase induced by Typhoon Megi in the Japan/East Sea, *Geophys. Res. Lett.*, *33*, L05607, doi:10.1029/2005GL025065.

Takahashi, T., J. Olafsson, J. G. Goddard, D. W. Chipman, and S. C. Sutherland (1993), Seasonal variation of CO2 and nutrients in the high-latitude surface oceans: A comparative study, *Global Biogeochem. Cycles*, *7*(4), 843–878, doi:10.1029/93GB02263.

Takahashi, T., et al. (2009), Climatological mean and decadal change in surface ocean pCO$_2$, and net sea-air CO$_2$ flux over the global oceans, *Deep Sea Res., Part II*, *56*(8–10), 554–577.

Vincent, E. M., M. Lengaigne, G. Madec, J. Vialard, G. Samson, N. C. Jourdain, C. E. Menkes, and S. Julien (2012), Processes setting the characteristics of sea surface cooling induced by tropical cyclones, *J. Geophys. Res.*, *117*, C02020, doi:10.1029/2011JC007396.

Walker, N., R. Leben, and S. Balasubramanian (2005), Hurricane-forced upwelling and chlorophyll a enhancement within cold-core cyclones in the Gulf of Mexico, *Geophys. Res. Lett.*, *32*, L18610, doi:10.1029/2005GL023716.

Wanninkhof, R. (1992), Relationship between wind speed and gas exchange over the ocean, *J. Geophys. Res.*, *97*(C5), 7373–7382.

Wentz, F. J., C. Gentemann, D. Smith, and D. Chelton (2000), Satellite measurements of sea surface temperature through clouds, *Science*, *288*, 847–850.

Willoughby, H., and M. Rahn (2004), Parametric representation of the primary hurricane vortex. part I: Observations and evaluation of the Holland (1980) model, *Monthly Weather Rev.*, *132*, 3033–3048.

Willoughby, H., R. Darling, and M. Rahn (2006), Parametric representation of the primary hurricane vortex. part II: A new family of sectionally continuous profiles, *Monthly Weather Rev.*, *134*(4), 1102–1120.

Yablonsky, R. M., and I. Ginis (2009), Limitation of one-dimensional ocean models for coupled hurricane-ocean model forecasts, *Monthly Weather Rev.*, *137*, 4410–4419.

L. Bopp, LSCE-IPSL, Orme des Merisiers, CEA Saclay, F-91191 Gif Sur Yvette, France.

C. Ethé, M. Lengaigne, M. Lévy, G. Madec, and E. Vincent, LOCEAN-IPSL, UPMC, BC 100, 4 pl. Jussieu, F-75252 Paris CEDEX 05, France. (marina@locean-ipsl.upmc.fr)

D. Kumar, NIO, Dona Paula, Goa 403004, India.

V. V. S. S. Sarma, NIO, Visakhapatnam 530017, India.

E Comparaison des indices de cyclogenèse des échelles saisonnières à interannuelles

Clim Dyn
DOI 10.1007/s00382-011-1126-x

Comparison of tropical cyclogenesis indices on seasonal to interannual timescales

Christophe E. Menkes · Matthieu Lengaigne · Patrick Marchesiello · Nicolas C. Jourdain · Emmanuel M. Vincent · Jérôme Lefèvre · Fabrice Chauvin · Jean-Francois Royer

Received: 7 July 2010 / Accepted: 15 June 2011

Abstract This paper evaluates the performances of four cyclogenesis indices against observed tropical cyclone genesis on a global scale over the period 1979–2001. These indices are: the Genesis Potential Index; the Yearly Genesis Parameter; the Modified Yearly Convective Genesis Potential Index; and the Tippett et al. Index (J Clim, 2011), hereafter referred to as TCS. Choosing ERA40, NCEP2, NCEP or JRA25 reanalysis to calculate these indices can yield regional differences but overall does not change the main conclusions arising from this study. By contrast, differences between indices are large and vary depending on the regions and on the timescales considered. All indices except the TCS show an equatorward bias in mean cyclogenesis, especially in the northern hemisphere where this bias can reach 5°. Mean simulated genesis numbers for all indices exhibit large regional discrepancies, which can commonly reach up to ±50%. For the seasonal timescales on which the indices are historically fitted, performances also vary widely in terms of amplitude although in general they all reproduce the cyclogenesis seasonality adequately. At the seasonal scale, the TCS seems to be the best fitted index overall. The most striking feature at interannual scales is the inability of all indices to reproduce the observed cyclogenesis amplitude. The indices also lack the ability to reproduce the general interannual phase variability, but they do, however, acceptably reproduce the phase variability linked to El Niño/Southern Oscillation (ENSO)—a major driver of tropical cyclones interannual variations. In terms of cyclogenesis mechanisms that can be inferred from the analysis of the index terms, there are wide variations from one index to

C. E. Menkes · M. Lengaigne · E. M. Vincent
IRD, Laboratoire d'Océanographie et du Climat: Expérimentation et Approches Numériques (LOCEAN), IRD/UPMC/CNRS/MNHN, Paris, France

M. Lengaigne
e-mail: matthieu.lengaigne@ird.fr

E. M. Vincent
e-mail: emmanuel.vincent@locean-ipsl.upmc.fr

M. Lengaigne
IRD, National Institute of Oceanography, Goa, India

C. E. Menkes · N. C. Jourdain · J. Lefèvre
IRD, BP A5, Nouméa Cedex 98848, New Caledonia

N. C. Jourdain
e-mail: Nicolas.Jourdain@hmg.inpg.fr

J. Lefèvre
e-mail: jerome.lefevre@ird.fr

P. Marchesiello · J. Lefèvre
IRD, Laboratoire d'Etudes en Géophysique et Océanographie Spatiale (LEGOS), 14 Av Edouard Belin,
31400 Toulouse, France
e-mail: patrick.marchesiello@ird.fr

F. Chauvin · J.-F. Royer
Météo-France, CNRM/GAME (Météo-France/CNRS),
42, Avenue Coriolis, 31057 Toulouse Cedex 01, France
e-mail: fabrice.chauvin@meteo.fr

J.-F. Royer
e-mail: jean-francois.royer@meteo.fr

C. E. Menkes (✉)
LOCEAN, IRD/UPMC/MNHN/CNRS,
Institut de Recherche Pour le Développement,
BP A5 Boîte 100, 98848 Nouméa Cedex, New Caledonia
e-mail: christophe.menkes@ird.fr

another at seasonal and interannual timescales and caution is advised when using these terms from one index only. They do, however, show a very good coherence at ENSO scale thus inspiring confidence in the mechanism interpretations that can be obtained by the use of any index. Finally, part of the gap between the observed and simulated cyclogenesis amplitudes may be attributable to stochastic processes, which cannot be inferred from environmental indices that only represent a potential for cyclogenesis.

Keywords Cyclogenesis indices · Atmospheric reanalyses · ENSO · Cyclone stochasticity

1 Introduction

Understanding the generation, development and fate of tropical cyclones is a major challenge for scientists and is of great importance to society. Tropical cyclones occur in specific large-scale environments and to improve understanding of how that environment favours cyclogenesis, Gray (1968, 1975, 1979) first developed an empirical cyclogenesis index referred to as the Yearly Genesis Parameter (YGP). This first index was followed by the construction of two other well known indices: the Modified Yearly Convective Genesis Potential Index (CYGP) developed by Royer et al. (1998) which is a variant of the YGP, and the Genesis Potential Index (GPI) developed by Emanuel and Nolan (2004). Tippett et al. (2011) have recently proposed improvements to the GPI. These improvements are referred to as 'TCS' (Tippett, Camargo, Sobel) in this paper. The TCS allows a better representation of off-equatorial cyclogenesis maxima and of cyclogenesis during unfavourable seasons Murakami and Wang (2010) discuss another variant of the GPI for the western North Pacific and Emanuel (2010) has also proposed a more general modification of the GPI which has particular importance in relation to issues of climate change.

The advantages of these empirical indices are that they can be applied to observed or simulated low resolution datasets for the current climate (e.g. Gray 1979; Watterson et al. 1995; Camargo et al. 2007a, b; Royer et al. 1998; Tippett et al. 2011; Yokoi et al. 2009 etc.) and future climates (e.g. Caron and Jones 2008; Royer and Chauvin 2009; McDonald et al. 2005; Kim et al. 2010). They can also be used to study cyclogenesis frequencies on a number of timescales ranging from intraseasonal (Camargo et al. 2009) to interannual timescales (Camargo et al. 2007a, b; Watterson et al. 1995; Lyon and Camargo 2009; Vincent et al. 2009; Tippett et al. 2011). These indices may also inherently reveal the main large-scale factors influencing cyclogenesis on mean, seasonal or specific event levels, such as El Niño/Southern Oscillation (ENSO, Camargo et al. 2007a; Watterson et al. 1995; Chand and Walsh 2009; Vincent et al. 2009) or during the Madden Julian Oscillation (MJO, Camargo et al. 2009).

The four indices are all based on the same principle: that the large-scale environment favourable to cyclogenesis is a product of thermal and dynamical potential, which themselves are combinations of similar ingredients but with different formulations. It is important to stress that the formulations entering these indices are empirically fitted onto a global and seasonal scale designed to provide values as realistic as possible within these scales. Thus, the constants and the exact formulations by which the individual terms enter the final index can differ significantly from one index to the other. Furthermore, the indices represent a potential for cyclogenesis controlled by large scale climatic variations but do not take into account other processes important for actual tropical cyclones (TCs) generation such as stochastic processes (Simpson et al. 1997; Jourdain et al. 2010) or small-scale triggers (Gray 1998) which may lower the expected index performances on different scales (Camargo et al. 2009; Jourdain et al. 2010).

Another source of uncertainty in evaluating TC numbers from these indices arises from the climate datasets used for their calculation. For example, Kim et al. (2010) have used four different reanalyses, ERA40 (Uppala and Co-authors 2005), JRA25 (Onogi et al. 2007), NCEP1 (Kalnay et al. 1996) and NCEP2 (Kanamitsu et al. 2002) reanalyses to compare the CYGP performances on seasonal scales. They conclude that no particular reanalysis outperforms the others, although their individual performances can vary significantly from one region to another. A similar conclusion was reached by Tippett et al. (2011), using the TCS with ERA40 and NCEP1, and also by Camargo et al. (2009), using the GPI at the MJO scale where the ERA40 indices showed a higher variability due to larger mid-tropospheric humidity. Because the functional forms of terms entering the index formulation vary from one index to the other, it is not a priori obvious to translate the information from different studies into a clear message. Even when only one index were used, difficulties arose which compelled Kim et al. (2010) to conclude that "these results illustrate that ConvGP" (the CYGP) "identifies many aspects in seasonal TC genesis but with some deficiencies, indicating that it has both useful information and limitations".

However, there is still a need to understand how these four indices compare on different scales. When examining results from previously published work (Royer et al. 1998; Royer and Chauvin 2009; McDonald et al. 2005, for the YGP and CYGP, Camargo et al. 2007a, b for the GPI and Tippett et al. 2011 for the TCS), it appears that these indices give roughly similar geographical distributions and seasonal variability in most cyclogenesis regions. Additional quantitative comparisons between the YGP and CYGP have been described in

Caron and Jones (2008) who concluded that the CYGP is more appropriate than the YGP to study cyclogenesis in the context of global warming. Watterson et al. (1995) also concluded that the YGP is not an accurate index to grasp interannual variability of cyclogenesis in the Pacific Ocean. The CYGP also shows some biases: it globally underestimates cyclogenesis in the northern Hemisphere (e.g. McDonald et al. 2005; Kim et al. 2010) but so far it has not been evaluated in terms of its accuracy on interannual timescales. On the other hand, Camargo et al. (2007a, b) and Tippett et al. (2011) have explored the relationship between ENSO and the GPI/TCS response and show that the GPI and TCS have some skills in representing the phase relationship between ENSO and tropical cyclogenesis. However, they do not report the simulated TC genesis numbers on ENSO timescales, which creates difficulties in making comparisons between the YGP index types (YGP/CYGP) and the GPI types (GPI, TCS). Because individual terms entering the index may help to understand the main factors involved in cyclogenesis, Tippett et al. (2011) have explored the relative contribution of these components to cyclogenesis. Camargo et al. (2009) have investigated the role of these terms during MJOs and Camargo et al. (2007a) have described their evolution during ENSO. The latter study has shown that a combination of vorticity, relative humidity, and vertical wind shear can explain most of the GPI behaviour during ENSO. They have also demonstrated that the contribution of each term in the final index also has regional variations thus suggesting that different mechanisms may be at work (in reality) in different regions (Camargo and Sobel 2007).

Interannual variability can be high in many regions of the world, some (but not all) of which can be linked to ENSO (see Landsea 2000; Chu 2004 for reviews). Therefore, it is important to have a better understanding of how effective the indices are in simulating observed phase and amplitude of TC formation on interannual timescales. Whether the indices are in agreement and can bring coherent insights about the possible dynamics of TC formation through their contributing terms also needs to be investigated. The main purpose of this study is to understand and evaluate the common features of these four indices calculated with four reanalyses with regards to observations on seasonal and interannual scales and also to understand how the terms composing these indices contribute to cyclogenesis on these scales.

2 Data and cyclogenesis indices

2.1 Tropical cyclone, reanalyses data and indices

For the tropical cyclone genesis data, we use the global datasets gathered and kindly provided by Dr. Emanuel and freely available online at (ftp://texmex.mit.edu/pub/emanuel/HURR/tracks_netcdf/) which are derived from a compilation of the best track datasets from diverse centres. Because our interest lies in characterizing the performances of cyclogenesis indices, we define cyclogenesis location as the first position of a storm in the dataset, provided the storm reaches 17 m/s at some point along its trajectory; a definition identical to McDonald et al. (2005) and very similar to that of Watterson et al. (1995). The definition is somewhat arbitrary and may vary from study to study. For instance, other studies have defined cyclogenesis location as the first point in which a storm reaches 17 m/s (e.g. Caron and Jones 2008). The difference between the two definitions is illustrated in Fig. 1 which demonstrates that the latter distribution has a poleward offset of about 2.5°, when compared to our definition. We then use a formalism similar to that described by Ramsay et al. (2008) to convert discrete cyclone data into smooth gridded dataset. To generate this, we affiliate to each cyclone point an anisotropic Gaussian function, with an associated standard deviation of 1° and 3° in meridional and zonal directions respectively (Jourdain et al. 2010) and regrid it on a regular 2.5° × 2.5° grid. All other data are similarly gridded when necessary. In the following, the gridded dataset is used when spatial patterns are examined and the original data is made use of when time series or cyclone counting are involved.

Four sets of reanalyses are used to calculate the indices. NCEP-NCAR reanalyses starting in 1948 (NCEP: http://nomad1.ncep.noaa.gov/dods/reanalyses/reanalysis-1) and an "improved" NCEP–DOE AMIP-II reanalysis dataset (NCEP2: http://nomad1.ncep.noaa.gov/dods/reanalyses/reanalysis-2) starting in 1979. ERA-40 reanalyses are provided by ECMWF and the Japan Meteorological Agency. The Central Research Institute of Electric Power Industry (JRA25) reanalysis is also utilised. It is not the primary purpose of this paper to discuss the differences in these datasets and the reader is referred to Grotjahn (2008) for a thorough comparison between NCEP2 and ERA40. Our datasets are averaged into monthly means for the index comparisons. For coherence, all fields used in the index calculations are interpolated onto the NCEP 2.5° × 2.5° grid. Fields from January 1979 to December 2001 are used when comparing the differential influence of each reanalysis (as ERA40 finishes in August 2002 and NCEP2 starts in 1979).

Equations for the indices are described in the "Appendix" and are reproductions of otherwise published indices, namely the YGP index by Gray (1975), the CYGP by Royer et al. (1998), the GPI by Emanuel and Nolan (2004) and the TCS by Tippett et al. (2011). If they are to be used as assessive or predictive tools it is important that indices yield reasonable quantitative numbers. As mentioned in

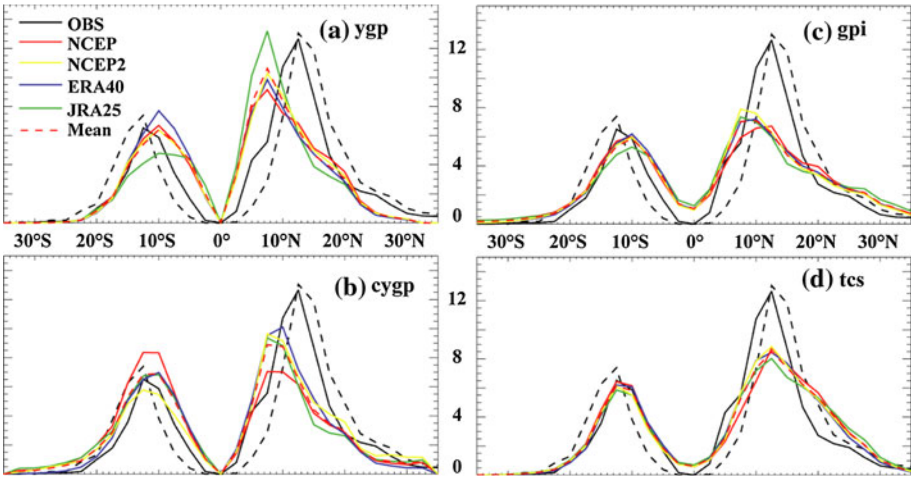

Fig. 1 Meridional distribution of zonally and time averaged observed and modelled cyclogenesis. In *black*, observed cyclogenesis defined by the first point in the dataset of storms that will reach 17 m/s along their track. In *dashed lines* observed cyclogenesis defined as the first position when storms reach 17 m/s. In *colours* mean cyclogenesis index distribution for the YGP (*top panel*), the CYGP (*second panel*), the GPI (*third panel*) and the TCS (*last panel*) using the four atmospheric reanalyses, NCEP (*red curve*), NCEP2 (*yellow curve*), ERA40 (*blue curve*) and JRA25 (*green curve*). The REM index (*see text*) is added on each panel as a *dashed red curve*

several studies, the "proportionality" constants (e.g. the 50 and 70 in the GPI, or the k in the CYGP, see "Appendix") are somewhat arbitrary and result from fit to the global and seasonal observed cyclogenesis data (Camargo et al. 2007a; McDonald et al. 2005; Caron and Jones 2008; Royer et al. 1998; Chauvin et al. 2006). Because these indices are all a priori dependent on the data sets used for their construction and the periods on which they are fitted to observations, the constants must necessarily be adjusted to match observed values. In order to compare all the indices on a common basis, it was decided to scale the indices calculated for each reanalysis by calculating the yearly number of tropical cyclones in the 30°S–30°N region for the 1979–2001 period amounting to ~85 cyclones/year in the range of previously published studies (Gray 1975, 1979; Tsutsui and Kasahara 1996; Royer et al. 1998; Royer and Chauvin 2009; Caron and Jones 2008; Kim et al. 2010). Kim et al. (2010) have also used a similar scaling in their analyses in order to compare all reanalyses and model outputs on common grounds. Discussion about such scaling can be found alongside the study and in the conclusion.

3 Results

3.1 Mean distributions

Figures 1, 2 and 3 present results for the mean distribution of modelled cyclogenesis. The indices have some skills in reproducing the first order meridional distribution of observations (Fig. 1). These distributions are consistent with previous studies (e.g. Watterson et al. 1995; Caron and Jones 2008; Royer et al. 1998, Tippett et al. 2011). Aside from the TCS, the other indices show too broad a distribution with simulated maxima that are too close to the equator by at least 2.5° independently of the reanalysis considered, especially in the northern hemisphere. By contrast, the TCS simulates the right maxima locations and the strong equatorial genesis decrease. Compared to the GPI, the accurate TCS behaviour is related to the use of "clipped" vorticity (see "Appendix") as discussed in Tippett et al. (2011).

The GPI shows particularly weak maxima in the northern hemisphere (Fig. 1) compared to the other indices but its interhemispheric balance (number of [30°S–0] cyclones over number of [0–30°N] cyclones) is the best among the indices (see Fig. 3). The GPI "weak" maxima (compared to the others) are partly due to the normalisation chosen. In fact, Figs. 1 and 2 show that the GPI has a tendency to overestimate cyclogenesis in regions outside the main cyclogenesis areas (e.g. off 20°N and within 10°S–10°N) (Camargo et al. 2007a). Therefore, normalising the GPI by a constant to ensure that the global count within (30°S–30°N) is 85 necessarily gives lower maxima amplitude in the main cyclogenesis regions compared to normalisation in a smaller latitudinal band. If another normalisation was chosen so that the number of modelled and observed cyclones agrees to within 20°S/20°N, the result would be that both the northern and southern maxima would be higher. Regardless, the southern maxima of GPI would not be well represented. In principle, the global indices could be adjusted to produce the right numbers in a given region but with the result that other regions would not agree with observations, as discussed further in the text.

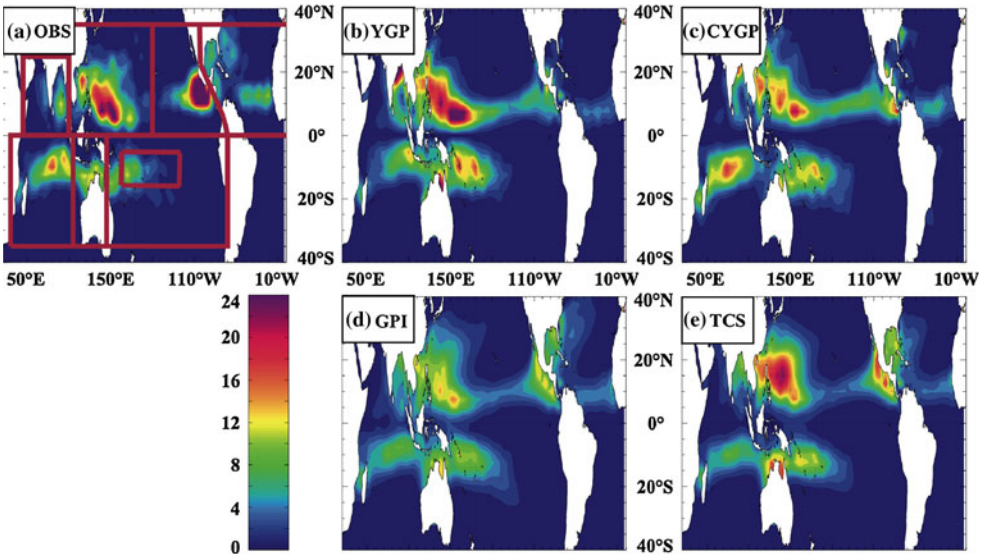

Fig. 2 1979–2001 mean cyclogenesis numbers per 5° and per 20 years for the observations (*panel a*) and all REM indices (*panel b* YGP, *panel c* CYGP, *panel d* GPI and *panel e* TCS). *Red boxes* noted on panel mark the regions used in the remainder of the paper and are defined in Table 1

Dispersion due to the choice of reanalysis is higher in the CYGP and the YGP than in the GPI and TCS where the reanalysis choice makes little difference. Except for the NCEP2-YGP, and NCEP-CYGP, all reanalyses produce coherent modelled cyclogenesis distributions. For the YGP, the use of NCEP2 leads to an underestimation of cyclogenesis in the southern hemisphere and overestimation in the northern hemisphere, when compared to other reanalyses. Such is not the case for the CYGP, thus pointing to the thermal term in NCEP2-YGP being responsible for its difference with NCEP2-CYGP (since the dynamical terms are identical). It appears that it is the strong north–south asymmetry of the shear temperature term (see "Appendix") calculated with NCEP2 that produces the north/south asymmetry compared with ERA40 or NCEP. A similar argument holds for the peculiar behaviour of NCEP-CYGP where, for instance, the ratio of north/south convective precipitation is weaker in NCEP than in NCEP2. Apart from these examples, there is better coherence for one index calculated using different reanalyses than between different indices sharing the same reanalysis. Hence, in the following, a "mean" index calculated as the average of that index with the four reanalyses, referred to as the "REM" index is often presented for clarity purposes (see dashed red line in Fig. 1), and the impact of specific reanalysis is only emphasized when needed.

Figure 2 provides the mean spatial distribution of cyclogenesis in observations and for the different REM indices. Figure 3 provides comparisons in the box-averaged regions drawn in Fig. 2 where the impact of the use of specific reanalysis is detailed. Large differences appear in the mean simulated cyclogenesis when compared to observations. For example, none of the indices are able to properly capture the cyclogenesis areas of the northeastern Pacific (see bottom panels on Fig. 3 and also Caron and Jones 2008 for a discussion on the YGP and CYGP using ERA40) even though the GPI and TCS show better spatial structures than the YGP and CYGP (Fig. 2). The YGP and CYGP simulate weak cyclogenesis in the western Atlantic compared to observations and to the GPI and TCS. On the other hand, the GPI overestimates cyclogenesis within 10°S–10°N and off 25°N. All indices also produce an unrealistic continuous cyclogenesis band along the ITCZ (Inter Tropical Convergence Zone) in the central Pacific. The genesis locations in the Bay of Bengal are also poorly reproduced in all indices (e.g. Caron and Jones 2008; Tippett et al. 2011). However, the TCS is in general the best-fitted index for such mean pictures.

This finding is also confirmed quantitatively in Fig. 3 when considering global northern and southern hemispheric averages (note that the boxes chosen and described in Table 1 are close to those of Caron and Jones 2008; also note that our results are very close to their Table 2 when calculated over the same time period and when taking into account the normalisation differences between the two studies). The relative error of the TCS on mean hemispheric numbers is less than 10% while the CYGP is shown to be the worst index based on that metric with a 50% overestimation in the southern hemisphere (Royer et al. 1998; McDonald et al. 2005; Caron and Jones 2008), mostly due to an overestimation of the southern Indian Ocean cyclogenesis; the GPI and YGP yield similar medium-quality results. Yet, these hemispheric figures hide large regional discrepancies that may compensate each other in the total hemispheric count. For example, the positive bias in the northwestern Pacific for TCS nearly

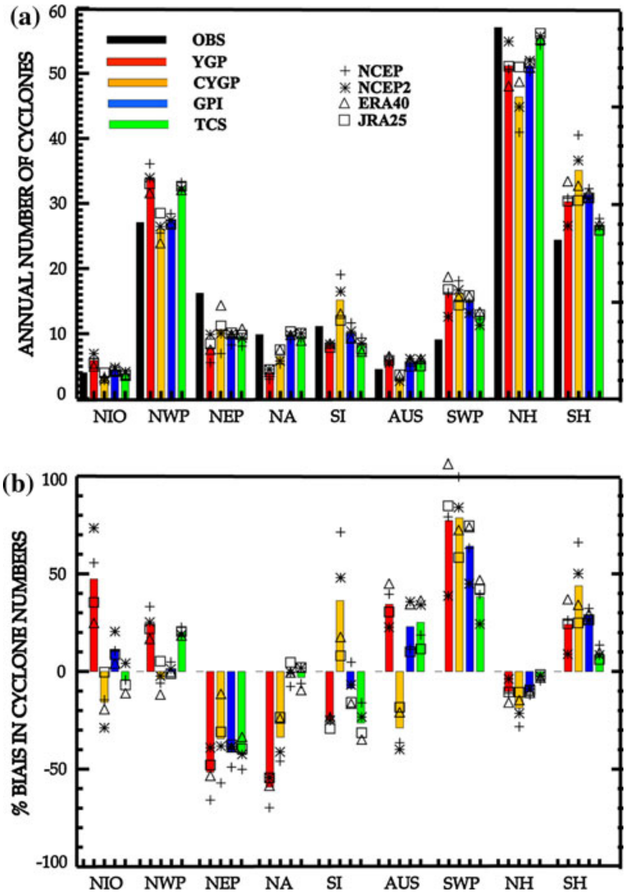

Fig. 3 Histograms of **a** annual mean number of cyclones in regions defined in Table 1 and shown in Fig. 2. In addition to the 7 boxes, total numbers for the northern hemisphere (NH) and southern hemisphere (SH) are shown for all indexes. These are labelled as *Y* YGP, *C* CYGP, *G* GPI, *T* TCS and *O* denotes the observations. The *colourbars* represent the numbers for the REM indices and each reanalysis result is added on each *colourbar* as follows: + NCEP, *open triangle* ERA40, *star* NCEP2, *open square* JRA25. **b** same as **a** but for the normalized differences to observations: (index-observation)/observations in percentage

Table 1 Definition of the geographical limits used in Fig. 2

Acronym	Longitudes	Latitudes
NIO North Indian region	45°E–100°E	EQ-35°N
NWP North Western Pacific	100°E–160°W	EQ-35°N
NEP North Eastern Pacific	160°W–90°W	EQ-35°N
NA North Atlantic	Atlantic domain	EQ-35°N
SI South Indian region	30°E–105°E	35°S-EQ
AUS Australian region	105°E–145°E	35°S-EQ
SP South Pacific region	145°E–70°W	35°S-EQ
SWP South Western Pacific	170°E–120°W	16°S–5°S

cancels out the negative bias in the northeastern Pacific so that the overall best agreement shown in integrated numbers using TCS is less apparent when looking regionally.

Hence, this quantitative comparison highlights the poor ability of the indices to reproduce the observed cyclogenesis numbers regionally, especially in the South Pacific (resp. Northeast Pacific) where cyclogenesis is overestimated (resp. underestimated) by more than 50% in all indices. The North Atlantic is poorly represented by the YGP and the CYGP while the GPI and TCS have good skills in that area. When examining the results as a function of reanalyses, the picture becomes more complicated. No dataset clearly outperforms any other in terms of all indices and regions, although using JRA25 seems to result in a relatively better estimation of mean cyclogenesis overall.

It is of interest to compare the respective contribution of each term to the total index. Because the index is a product of the partial terms, the most convenient way to quantitatively compare the term contributions is to examine the index logarithm, thereby expressing it as a sum of components. This method is used by Tippett et al. (2011) for the seasonal decomposition. Here we use the same method for mean patterns. Figure 4 shows the contribution of mean logarithms of the dynamical term for the different REM indices in percentages (thermal contributions are the complement to 100% of the dynamical component). The contribution of this term produces spatial variation that has no similarity in the indices. In terms of processes, the GPI and YGP compare relatively well, although with higher influence of the dynamics in the YGP. In the YGP, cyclogenesis is mostly dominated by the dynamical component everywhere, while in the GPI the thermal and dynamical terms are more equilibrated (however, when returning to the index itself, the contribution differences are necessarily enhanced). The CYGP has more spatially uniform dynamical contribution than the other indices while the TCS displays the largest meridional gradients. In pursuing this analysis, we focus on a specific region where dynamical terms are contrasted. Figure 5 presents the comparison for the North Atlantic region where all log terms entering the index composition are evaluated in percentage.

Firstly, Fig. 5 shows that the choice of reanalysis is globally unimportant when examining the mechanisms at work in the index constructions with concern to mean estimations (this is also true for other regions). Secondly, the relative contribution of all terms varies from one REM index to another. For example, the total dynamical (and thus inversely for the total thermal) terms vary from 40% in the TCS to 65% in the CYGP and the vorticity term varies from 10% (TCS) to 40% in the YGP. Note that the ocean content (HE) dominates the thermal term in the YGP as recorded by Royer et al. (1998). Obviously, the TCS and GPI have better skills at reproducing the observed numbers in the Atlantic (Fig. 3) and the YGP is by far the worst. With regards to the term partition, it is difficult to find an

Fig. 4 Percentage of contribution of the dynamical term in the mean of each log index (see text for additional information)

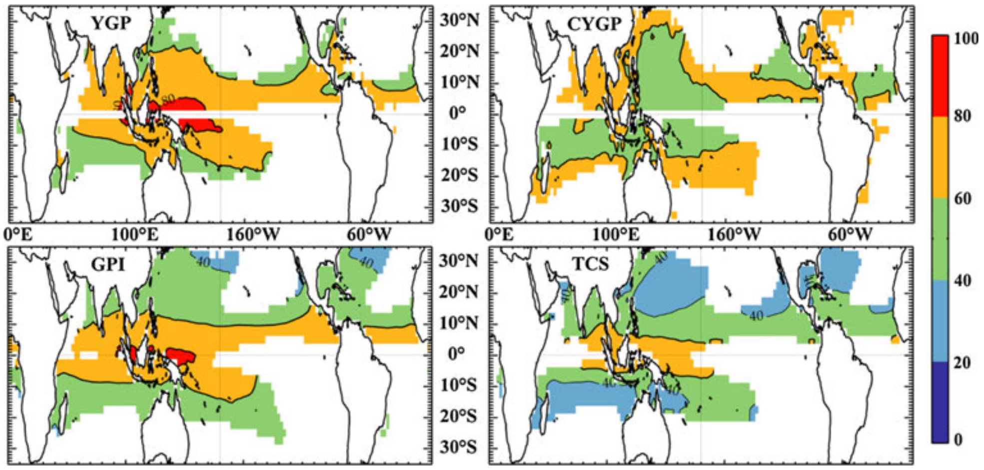

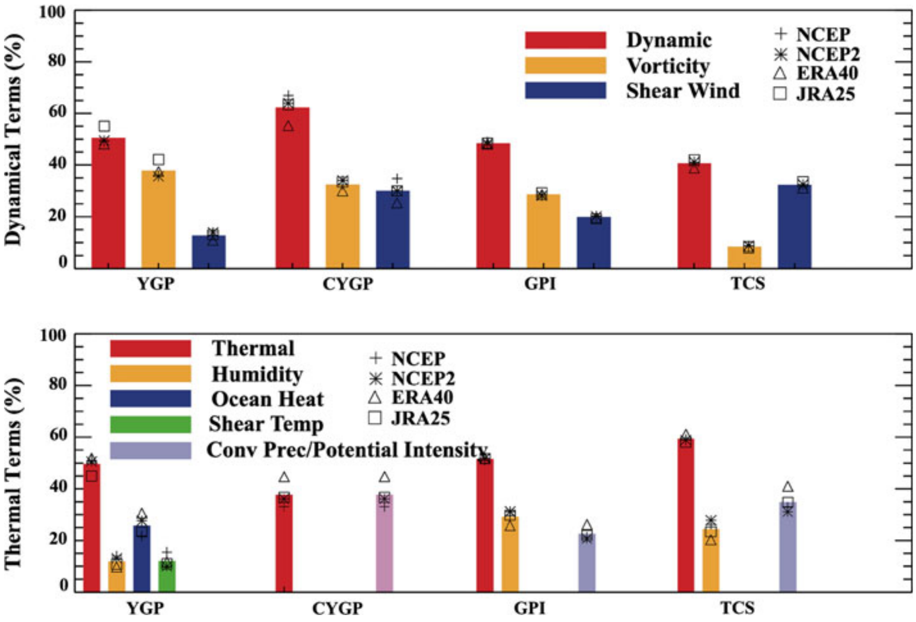

Fig. 5 Same as Fig. 4 but for all terms entering the REM index construction in the North Atlantic box (NA). *Y* YGP, *C* CYGP, *G* GPI and *T* TCS. For the individual term definitions, see "Appendix". The *first panel* represents the contribution of the dynamical terms: dynamical term (*red*), vorticity term (*orange*), wind shear term (*blue*). The *second panel* represents the thermal contribution. Thermal term (*red*), humidity term (*orange*), ocean heat term in the YGP (*blue*); temperature shear contribution in the YGP (*green*), convective precipitation term in the CYGP (*gray*). Potential intensity term in the GPI (*gray*) and SST term contribution in the TCS (*gray*). *Colour bars* are results for the REM indices and *symbols* on each *bar* present the results for individual reanalysis. These *symbols* are the same as those of Fig. 3

obvious bias that would point to any discrepancies or malfunction in the YPG. Interaction between the terms are complex and it may be that vorticity is too dominant in the YGP compared to GPI or that the wind shear and relative humidity terms do not have enough weight in the YGP, but going beyond these basic considerations would be difficult.

From these mean comparisons, it can be concluded that the indices are somewhat successful in globally reproducing the observed mean cyclogenesis at zeroth order independently of the reanalysis used. However, some unrealistic features also prevail. One instance of this can be seen in the northern hemisphere where an equatorward offset of modelled cyclogenesis by 2.5°–5° can be seen in all the indices except the TCS. They can reproduce cyclogenesis numbers in some specific regions using a constant global scaling (Kim et al. 2010) but not everywhere. The indices can always be adjusted to give the best reproduction of a specific mean number regionally but this is at the expense of degrading another region because the biases are not homogeneous. Alternatively, an *ad hoc* correction can be designed to adjust mean simulated data to mean observations everywhere but this does not actually enhance index performances on other timescales (see "Discussion"). Finally, it is difficult to estimate the actual quantitative contribution of a given mechanism in the indices because the relative contributions can vary significantly from one index to another.

Overall, the TCS seems better adjusted to simulate the mean cyclogenesis but detailed regional comparisons show that regional biases may still be important and that they depend on the chosen reanalysis.

3.2 Seasonal variations

In this section we assume that the indices are best fitted to the observed climatology. Box averaged times series are shown in Fig. 6. The boxes chosen are also close to those presented on Fig. 4 of Camargo et al. (2007a) and on Fig. 7 of Tippett et al. (2011). As earlier, the indices agree and disagree with observations in various ways. All indices have a correct seasonal cycle except for the YGP and, to a lesser extent, the CYGP in the north Indian region (see following discussions on the individual terms). The results presented here are coherent with other studies. The TCS is the best fitted for the global seasonal cycle especially in the northern hemisphere, although not everywhere (e.g., the northwestern Pacific during the peak season). This is another illustration of the need for individual regional examinations to properly evaluate any index. The TCS is also the only index that minimises the discrepancy with observations during the unfavourable season. Variations between indices are huge in the North Atlantic where the CYGP and YGP seasonal variations are too weak. Bruyere et al. (2010) also emphasized that the GPI showed biases in the Gulf of Mexico regions to the extent that little confidence could be given to the spatial structure of that index. Note also that the dispersion between indices is relatively important at peak seasons, except for the South Pacific box. Again, the northeastern Pacific region is systematically underestimated. Such a seasonal picture given by the REM indices, is quite similar to that using individual reanalyses (not shown). The dispersion of one index using different reanalyses is far weaker than that of the indices using the same reanalysis.

Attention is now turned to the mean contributions where all indices are now examined to discover how the different terms contribute to the seasonal cycle of the index logarithm. A similar analysis can be found for the TCS in Tippett et al. (2011). Although this is only an analysis of the log contribution, their variations reflect those of the actual terms since exponential is a monotonically increasing function. The method consists of calculating the seasonal anomalies of the individual term logarithms so that the seasonal anomaly of the total index logarithm is the sum of all individual seasonal logarithmic anomaly terms. Figure 7 presents the cases of the northern hemisphere and the North Indian Ocean where TCS and GPI are the best-adjusted indices and the YGP does not perform well. In order to compare the relative influence of terms between indices, all curves for a given index are normalised by the maximum value of the seasonal index logarithm in each box so that all terms vary within ±1. Behaviour in the

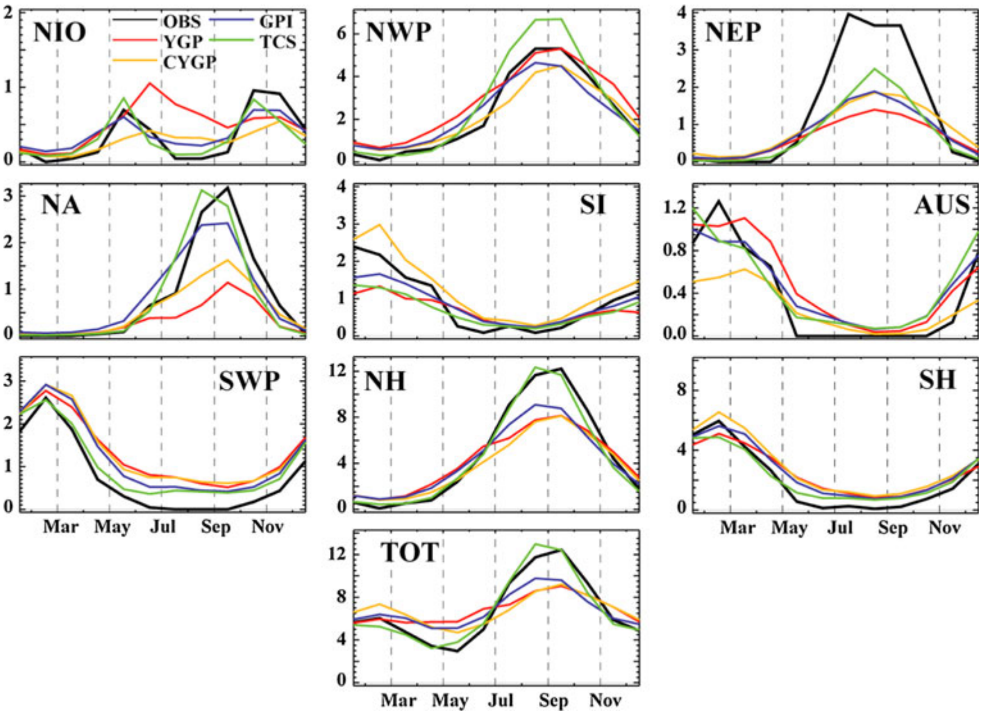

Fig. 6 Seasonal variations of observed cyclogenesis (*black*) and REM indices in all *boxes* of Fig. 2. This goes for the northern and southern hemispheres as well as for the globe which are all labelled in the titles. Observations are in *black*, YGP is in *red*, CYGP in *orange*, GPI in *blue* and TCS is in *green*

northern hemisphere is representative of all other regions (not shown) except the north Indian Ocean region. The (logarithmic) YGP seasonal cycle is always dominated at 80% by seasonal variation of the thermal potential, itself dominated by the ocean heat content (Royer et al. 1998). The remaining 20% can be explained by variations in wind shear and surface vorticity. By contrast, the CYGP is strongly dominated by the dynamical term (see previous section) with an almost equal interplay between vorticity and vertical wind shear terms. In retrospect this is surprising as the CYGP thermal potential was designed to simplify the YGP thermal potential. The GPI offers a more delicate balance where the thermal potential dominates the seasonal variations (~60%) but where all terms (except vorticity) play an equivalent role. Note that the thermal potential variations are in fact due to the interplay of the PI and relative humidity terms. In the TCS, the partition between dynamical and thermal is almost identical with the thermal term being slightly dominant. Again vorticity plays a minor role in explaining the seasonal variations but when compared to the GPI, relative humidity plays a weaker role in the thermal term, which instead is dominated by variations of the SST index (Tippett et al. 2011).

The north Indian Ocean cyclogenesis (enhanced in the Bay of Bengal) is unique in that it shows two peaks. The phasing of these peaks is best reproduced by the GPI and TCS (Fig. 6). The YGP picture is more complex with all terms coming into play at one moment or another. During the first season, the index peaks with a 1-month delay (Fig. 6) when compared to the other indices and observations. This can also be seen in the log index. The 1 month delay is explained by the existence of a delay in the thermal component related to humidity. This humidity effect dominates the thermal component in June-July. The delay is further explained by noting that the dynamical term decreases during the observed period and does not compensate for the thermal component increase. By contrast, in the other indices the dynamical component dominates the index decrease. It seems clear that the overall parameterisation of the YGP is at fault, but as the interplay between the terms is quite intricate and interdependent, which specific term is to blame (if any) could be difficult to explain. It is of interest to also note that in the CYGP, the dynamical terms can vary in opposition, contrary to the TCS and GPI, and even to the YGP (compare the vorticity terms—blue dash in all panels). The TCS and GPI exhibit similar behaviours but the respective term balances vary significantly between the two indices, although both reproduce the observed peaks with some success. Tippett et al. (2011) also analyse cyclogenesis variations in this region via the individual TCS terms. Our analysis with the CYGP and GPI support their findings: that pre-monsoon reduction in wind vertical shear creates the pre-monsoon maximum and that its increase leads to the decrease of the first genesis peak. Our analysis also suggests that the mechanisms at work quantitatively differ according to the index.

Overall, even if the indices have been historically adjusted to simulate seasonal cyclogenesis, it can be seen that for the annual mean and seasonal cycle, caution is still needed in reference to their ability in explaining observed regional cyclogenesis. Index performances differ globally and regionally and one conclusion drawn using a single index may not hold for the others. This is also true when seeking cyclogenesis mechanisms from these indices. At best, they can only give qualitative indications regionally and we advise caution in drawing firm conclusions. The complex interplay between individual terms prevents an easy understanding of the parameterization flaws that lead to misrepresentation of cyclogenesis. Eventually, it might be possible to pin point index defaults in one basin by readjusting the index parameterisation in a given region and comparing that new parameterisation to the global one, thus allowing a characterisation of the distance between the global and the regional parameterisation. However, this is beyond the scope of the present paper.

3.3 Interannual variations

There have been relatively few studies that explore the pertinence of cyclogenesis indices on interannual timescales in the present climate. Watterson et al. (1995) used the YGP to describe and understand how is cyclogenesis influenced by large scale forcing, using ECMWF analysed fields (1979–1988). After exploring the YGP's ability to reproduce observed interannual variability with particular emphasis on ENSO they concluded that the index has limited success in terms of observed variability reproduction. They particularly noted that the amplitude of simulated cyclogenesis is much weaker than that observed. Camargo et al. (2007a) detailed the GPI patterns associated with ENSO and concluded that the index "successfully reproduces the most well known ENSO signals in the best-observed basin". Camargo et al. (2007b) went into further details by looking at sub-basin interannual variability and emphasized the need to investigate ENSO impact on regional rather than basin-wide scales. To evaluate the interannual skill of the GPI, the focal point of the research focussed on correlation patterns with limited quantitative estimates of interannual cyclogenesis numbers. Lyon and Camargo (2009) used the GPI to understand ENSO impact on TC genesis in the Philippine region, which was shown to qualitatively agree with patterns of observed cyclogenesis. Vincent et al. (2009) used the CYGP to understand the differential impact of ENSO phases on TCs in the South Pacific Convergence Zone (SPCZ) region. These studies

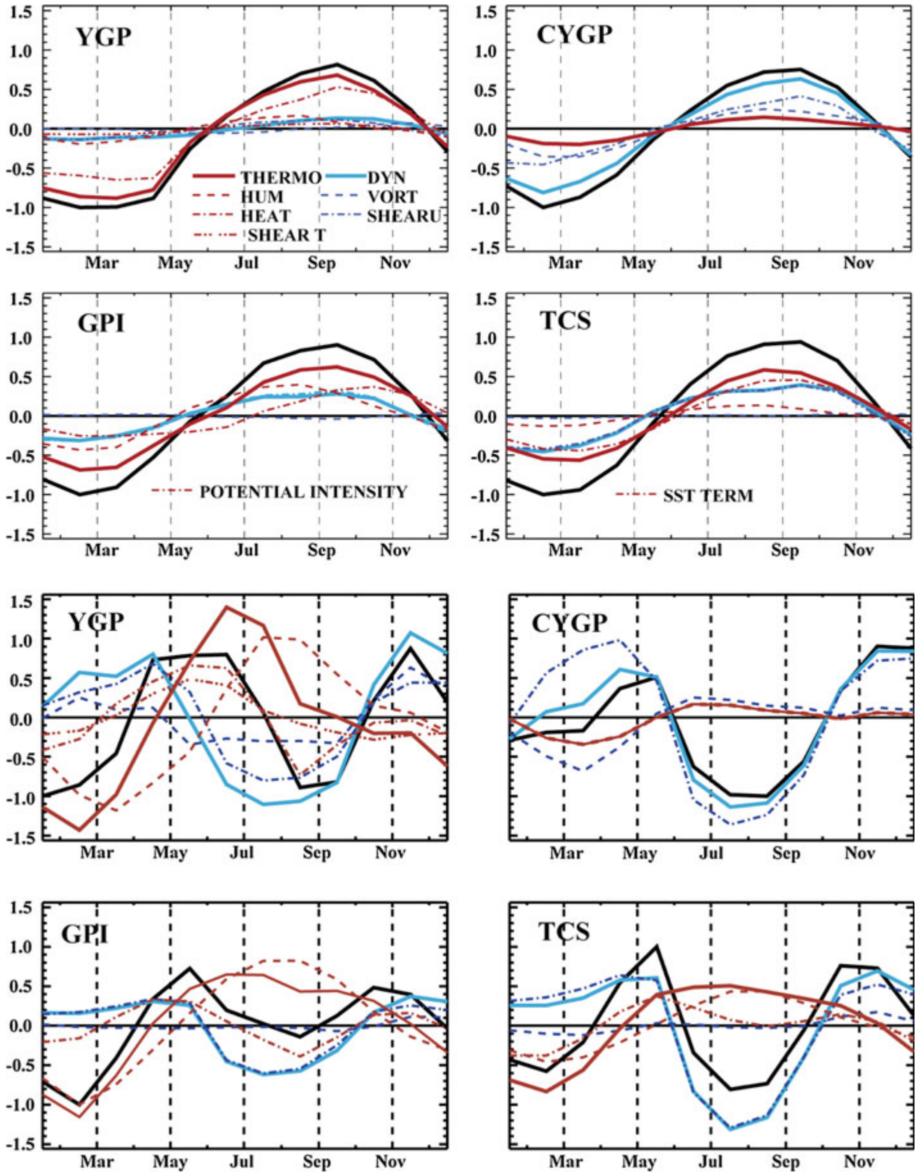

Fig. 7 Contribution of all terms in the seasonal variations of log index for each REM index. The northern hemisphere box is illustrated in the *first four panels* and the north Indian Ocean is shown in the *last 4 panels*. In *black* the total variations of the log index is represented. In *blue* dynamical terms with the total dynamical term being represented as a plain *blue curve*. In *red* thermal terms: total thermal term in plain *red curve*. *Dashed red* is the humidity term, *dashed-dotted red* is the ocean heat contribution for the YGP, *dashed-doubled dotted red* is the temperature shear term. For the GPI, *dashed-dotted red* is the potential intensity contribution and for the TCS, *dashed dotted red* is the SST index contribution. For the dynamical terms (*plain blue*), *dashed blue* is the vorticity term and *dashed-dotted blue* is the wind shear term contribution

also agreed on the usefulness of the indices in understanding certain underlying physics of cyclogenesis on interannual timescales. Finally, Tippett et al. (2011) also examined interannual variability and showed that results using the ERA40 reanalysis were significantly different from those using NCEP and that ERA40-TCS showed considerably more variability than NCEP-TCS. They also concluded that the correlation levels of TCS versus observations were “roughly” similar to those found in Camargo et al. (2007a).

In this paper, we build upon these studies by exploring, at the global scale, the skills of all indices and reanalyses in reproducing interannual variability. Figure 8 presents the interannual standard deviation of all REM indices and observations. The most striking feature of this figure is that it shows systematic failure of all indices to reproduce observed interannual amplitudes. Such low variability indicates that there is little chance that these indices can be used to simulate accurate interannual variations in worldwide TC numbers.

For a more precise illustration, box-averaged time series are presented in Fig. 9 with corresponding statistics in Fig. 10. These figures show that all the indices tend to agree on their regional discrepancies with observed variability. The failure to reproduce the north Indian Ocean interannual cyclogenesis is coherent with previous studies (e.g. Tippett et al. 2011). None of the indices are able to produce significant correlation with observations in the South Indian region, except for the CYGP using NCEP and ERA40. The NCEP2-CYGP and JRA25-CYGP were examined to understand why they did not produce acceptable cyclogenesis compared to NCEP-CYGP and

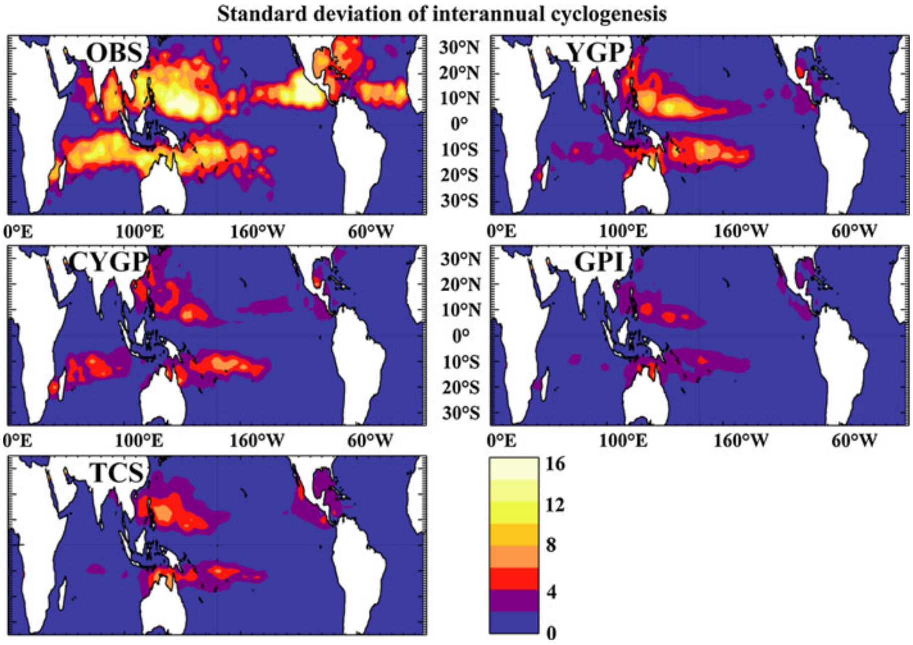

Fig. 8 Standard deviation of interannual cyclogenesis from observations (*top*, *left panel*), and REM indices. Units are numbers per 5° and per 20 years

ERA40-CYGP but a clear conclusion could not be reached. Moreover, with the exception of the CYGP, the north-western Pacific variability is not reproduced by the indices. It seems clear that the success of the CYGP there is linked to its parameterisation of the thermal potential. That stated, it is still unclear what changes need to be made in the other indices to reach the correct variability. When looking at the time series (Fig. 9, panel B), the CYGP is not obviously better than the other indices and a few peaks in phase with the observations probably make the correlation significant for the CYGP, in contrast to the other indices.

Phase relationships in other regions are globally reproduced by all indices but with varying performances. The usual correlation of indices to observations is about 0.5 and does not exceed 0.7. It also varies from one index to another and depends on the region under consideration. With a few exceptions, the choice of reanalysis has relatively little effect on performances. Also note that ERA40 is the only reanalysis that produces significant correlation with the YGP, CYGP and GPI in the northwestern Pacific. Again, the reasons for this are not obvious. Figure 9 also shows that on interannual timescales, the GPI and the TCS usually exhibit similar performances except in the north-west Pacific where all indices differ, with bad performances as depicted above. Strikingly enough, in Figs. 9 and 10 the bottom panel shows that for region-wide averages the interannual indices generally do poorly at representing the amplitude of interannual cyclogenesis and that there are wide variations within regions, indices and reanalyses. It must be noted that these results are (only) a more detailed confirmation of those inferred from Fig. 8. The only region where interannual standard deviation may be in relative agreement with observations for all indices is the north-western Pacific but, again, phase variability is poor when compared to observations (Fig. 9).

As in the previous section, the influence of each term entering the indices is evaluated. Unlike the previous section, here it is possible to isolate each term's influence in the total interannual index using a Taylor expansion of the total indices with respect to their seasonal cycle. A similar method applied to climate change evaluation is used in Kim et al. (2010) (see their Eq. 2). Hypothesizing that the interannual deviations are small compared to the seasonal cycle, the index interannual signal can be written as:

$$I_{\text{total}}^{\text{INTER}} \approx I_{\text{total}}^{\text{SAIS}} \left(\sum_{z=\text{terms}} \left(I_z^{\text{INTER}} - I_z^{\text{SAIS}} \right) \Big/ I_z^{\text{SAIS}} \right)$$

It was verified that such approximation is valid with less than 5% error except off 20°N in the CYGP and YGP indices. The advantage of this method is that it allows estimating the real contribution of any term in the total index at interannual timescales. Once each term contribution has been calculated for all indices, these terms are then regressed to the total interannual signal at each grid point. Results in Fig. 11 are only displayed when the significance of the correlation between the interannual index and each term exceeds 90%. Some of the terms have been omitted in this figure for clarity, but, for instance, the contribution of the wind shear to the total signal can be deduced from the difference between the dynamical and the vorticity contributions. Similarly, the thermal contribution to the total index is the complement to 1 of the dynamical contribution. Figure 11 shows that the

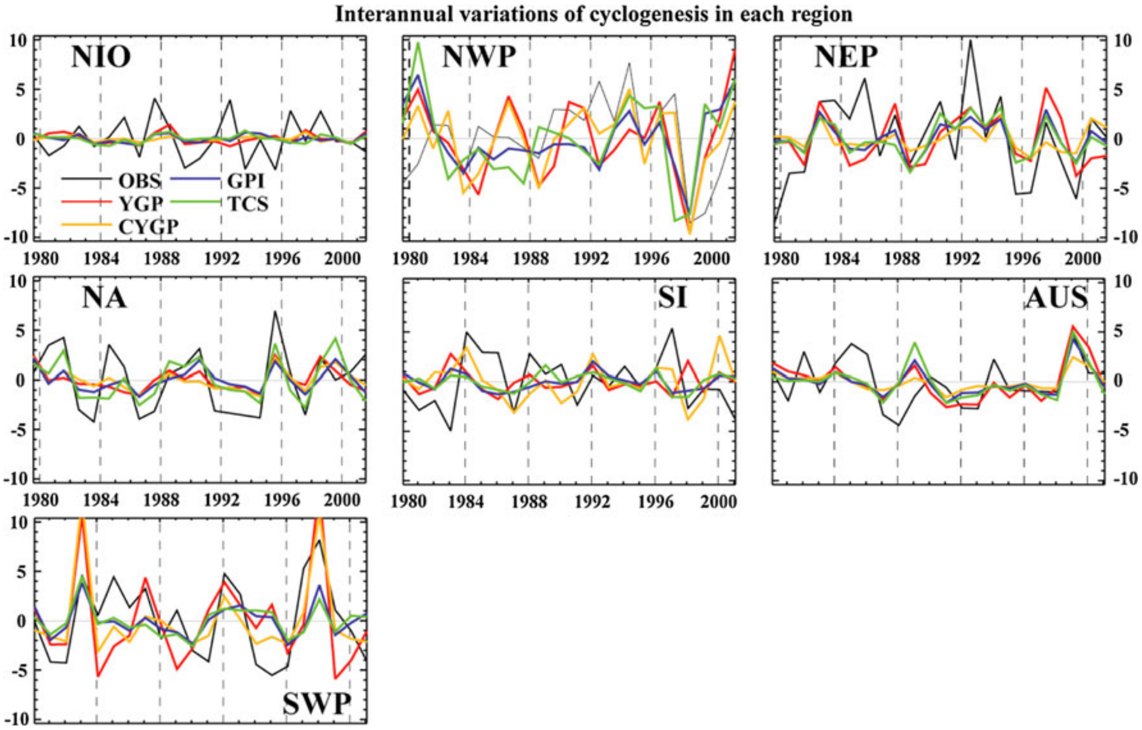

Fig. 9 Time series of yearly observed and REM interannual cyclogenesis anomalies in boxes depicted in Fig. 2. Observations are in *black*, YGP in *red*, CYGP in *orange* and GPI in *blue* and TCS is *green*

dynamical contribution to the total index strongly depends on the index and the region considered. On the global scale, this contribution is larger in the CYGP than in the other indices. Overall, the CYGP and YGP term partitions are closer than for the TCS and GPI. North of 20°N, our separation method shows large errors for the CYGP and YGP which cannot be significantly separated into terms. In this region, interannual cyclogenesis from TCS and GPI are dominated by thermal terms. Because the previous figures have shown the inability of these indices to reproduce observed interannual variability in the northwest Pacific, we maintain that the partition shown in the TCS and GPI may not be appropriate. The partition between vorticity and shear also differs among indices (and regionally).

Strikingly, the interannual variability of cyclogenesis in the SPCZ region (denoted by the black line, see legend) is strongly dominated by vorticity in the YGP and CYGP (Vincent et al. 2009) but far less so in the TCS and GPI. At the same time all indices yield similar performances in terms of phase variability (Figs. 9, 10). The CYGP and YGP are however in better agreement with observations in terms of amplitude (Figs. 9, 10). In light of the term partitions, it may thus be that a stronger dynamical influence on the final index is required in the TCS and GPI formulation to yield the most realistic amplitude. South of the SPCZ and around Australia, interannual cyclogenesis is dominated by the thermal influence but the partition between the thermal terms varies significantly among indices. In the North Atlantic, where TCS yields the best interannual cyclogenesis, the partition between SST and relative humidity effects is almost equal in contrast to the GPI where humidity dominates.

The major flaw of all the indices at interannual timescales is their weak simulated amplitude of interannual variability. Evidently, the index amplitudes are directly connected to the normalisation chosen. In this study we used a global normalization, but a regional amplitude correction may yield improvements on interannual variability (see Kim et al. 2010 for a discussion as well as our concluding remarks). Finally, it appears from analysing the genesis index components that there are significant differences between the working mechanisms of each index. Index partitioning may be used on occasions for future index diagnostic improvements, but, to a limited extent, as the simulated effect of an environmental variable (i.e., humidity or vorticity…) is subject to the somewhat arbitrary choice of its functional form. Nevertheless, one outcome of such analysis is that the respective effect of each term appears to vary at a lower scale than that used for box-average quantification. For instance, cyclogenesis mechanisms around Australia differ from those involved in the SPCZ region. Therefore, analysing cyclogenesis in a large inhomogeneous region may be inappropriate (e.g. Camargo et al. 2007b and the following discussion).

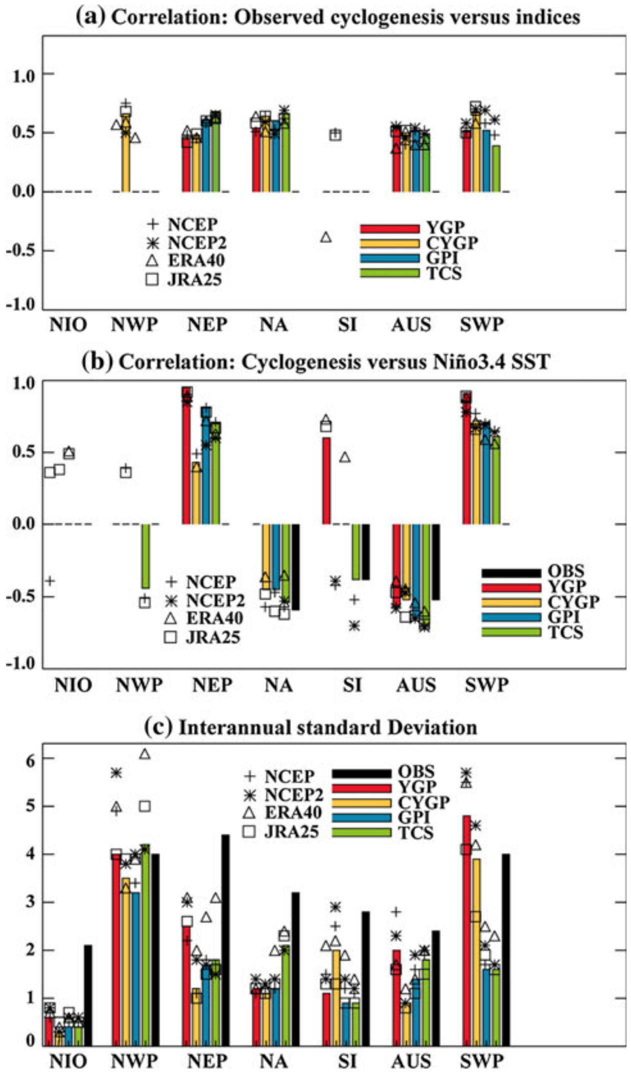

Fig. 10 Histograms of **a** correlation of box-averaged interannual observed cyclogenesis and REM indices. **b** correlation between box-averaged interannual cyclogenesis from REM indices and NINO3.4 (*red* for YGP-NINO3.4, *orange* for CYGP-NINO3.4, *blue* for GPI-NINO3.4 and *green* for TCS-NINO3.4) and between observed cyclogenesis and NINO3.4 (*black*). **c** Interannual standard deviation of box averaged time series of REM indices (*colours*) and of observed cyclogenesis (*black*). Other *symbols* and *labels* in the figure are identical to those of previous figures. Individual reanalysis results are labeled with + NCEP, *open triangle* ERA40, *star* NCEP2, *open square* JRA25; only >90% significant correlation are shown. NINO3.4 is calculated as the SST anomaly time series in the 120°W–170°W and 5°S–5°N region (e.g. Trenberth 1997)

3.4 Interannual variations: ENSO

As widely discussed (e.g. Chu 2004; Camargo et al. 2007a, b; Tippett et al. 2011 and references therein), ENSO is a major contributor to the interannual variability of cyclogenesis and induces regional cyclogenesis differences. Typically, ENSO induces large-scale cyclogenesis displacements that result in dipole patterns in observed cyclogenesis anomalies as well as in indices such as the GPI (e.g. Camargo et al. 2007a; Lyon and Camargo 2009). Such dipole patterns in the SPCZ region are detailed in Vincent et al. (2009), Jourdain et al. (2010) using observations, high-resolution model simulations and the CYGP. Figure 12 shows the correlation between ENSO, observed cyclogenesis, and index simulation. It should be used along with Fig. 13 that presents the actual Niño-Niña composites over the time period (see legend for the years over which the composite is calculated). The first panel of Fig. 12 shows that all regions of high-observed interannual variability exhibit a phase relationship to ENSO but with varying significance and correlation level. It is of interest that maximum correlation rarely exceeds 0.7 locally and the largest coherent patterns of correlations between ENSO and observed cyclogenesis are located in the southern hemisphere and in the central North Pacific.

The proximity of positive and negative correlations in Panel 1 of Fig. 12 primarily indicates spatial shifts in cyclogenesis activity from Niño to Niña phases, which can be seen in Panel 1 of Fig. 13. As an example, the northwestern Pacific region shows a significant dipole pattern that corresponds to a southeastward shift of cyclogenesis during El Niño years. With the exception of its southern edge, the northeastern Pacific shows a poor correlation with ENSO while its interannual variability is large (Figs. 8, 9, 10). In this example, ENSO does not seem to be a major driver of interannual cyclogenesis. However, other interannual processes seem to be at work (see Chu 2004 for additional discussion). Nevertheless, ENSO mainly has a tendency to decrease cyclones off the coast of Mexico (Fig. 13). Similarly, in the North Atlantic Ocean, ENSO influence on cyclogenesis is limited to the Gulf of Mexico, and the ITCZ, with a tendency for weaker cyclogenesis during El Niño and stronger during La Niña. The South Pacific shows the largest regions of significant correlation The Australian region is coherently and negatively correlated to El Niño in agreement with numerous other studies (see Ramsay et al. 2008, for a recent and exhaustive review of that region). From ∼160°E to the eastern Pacific, a large pattern of positive correlation is visible and bordered to an extent by negative correlation in the south. Positive and negative patterns are established along a northwest/southeast axis (see Fig. 15) that corresponds to the maximum cyclonic relative vorticity associated with the SPCZ (Vincent et al. 2009). Cyclogenesis changes on ENSO timescales (as detailed in Vincent et al. 2009) have strong constraints imposed by the SPCZ dynamics and its north/south and east/west movements. In the South Indian Ocean, negative correlations with ENSO are consistently found in observations from western Australia to about 70°E and correspond to decreased cyclogenesis (Fig. 13). Because of the dipole patterns discussed above, box averaged

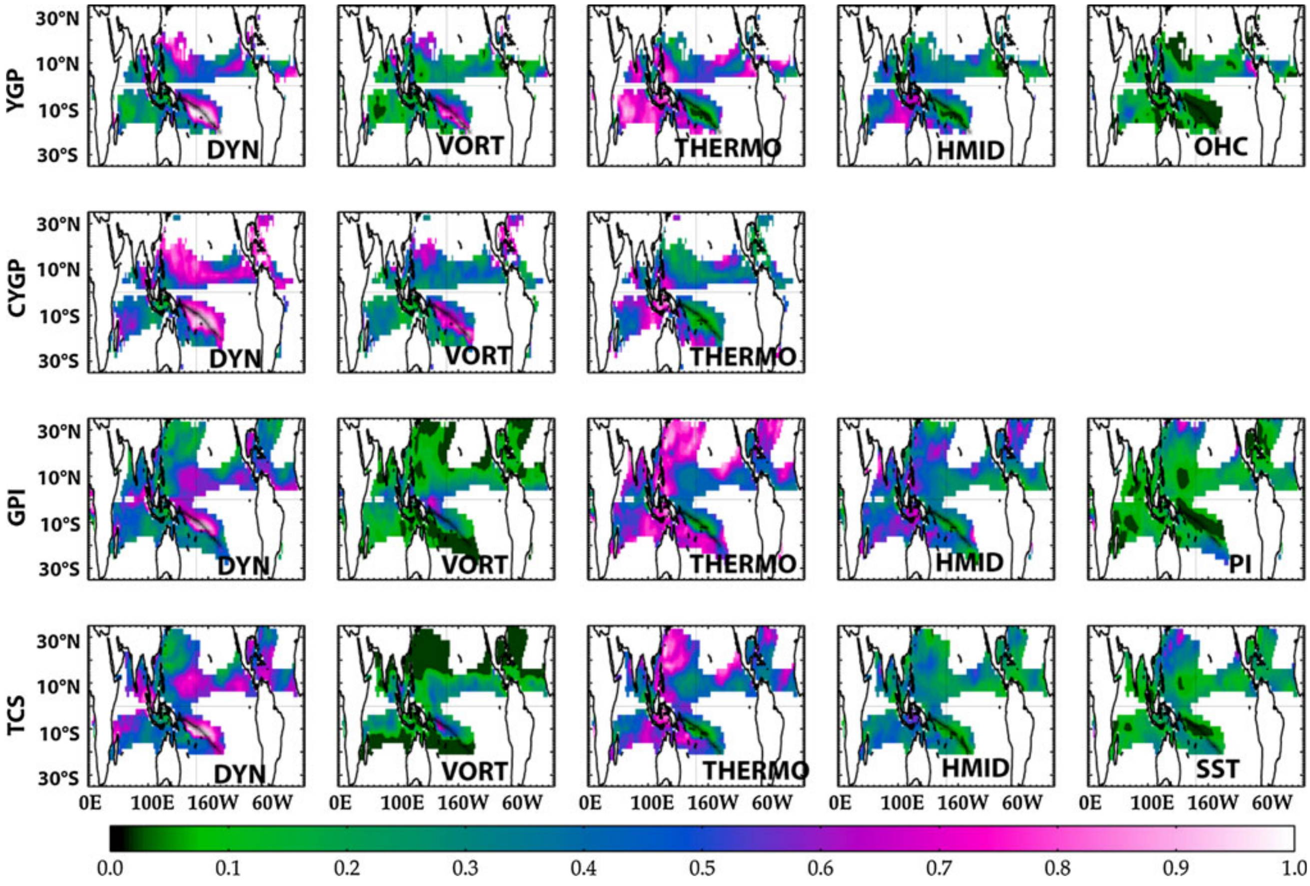

Fig. 11 Regressions between selected terms of the REM index and the REM index for each index. *First line panels* the YGP analysis, *second line* the CYGP, *third line* the GPI and *fourth line* the TCS. A *black line* on each panel in the southwest Pacific represents the mean SPCZ position as calculated by the maximum precipitation from CMAP (Vincent et al. 2009)

correlation of ENSO with TC genesis in large regions such as those presented in the boxes of Fig. 2 should be weak, as mentioned by Camargo et al. (2007b). Indeed, as seen in the middle panel of Fig. 10 (see black bars), it is striking that it is only in those regions where ENSO has a coherent impact on TC (see first panels of Figs. 12, 13) that box-averaged correlations are significant.

By contrast, box-averaged indices can exhibit significant correlations with ENSO whereas the observations do not (middle panel in Fig. 10) This can be seen in the South Pacific or in the northeastern Pacific. This seems to suggest that the indices can occasionally overestimate the cyclogenesis impact of ENSO. This is confirmed in Fig. 12 where ENSO dipole patterns are clearly depicted by all indices but with more coherent spatial structures and higher correlation numbers than in the observations (compare the top left panels with the others). Again in Fig. 12, we have limited the index-ENSO correlation to the regions where the observed inter-annual standard deviation is greater than 1 (see Fig. 8) but the pattern of index-ENSO correlation is much wider than in the observations. Therefore, it can be seen that on the one hand all the indices have obvious skills in characterising the typical TC genesis shifts under ENSO conditions, yet based on the present dataset, they also tend to overestimate the influence of ENSO onto TC genesis. This latter point is not very surprising as the indices represent *the potential* for cyclogenesis which cannot be reached in reality as stochastic effects may be important (Jourdain et al. 2010). This point is further discussed in the conclusion. Figure 13 provides another way of more precisely validating the ENSO effect on TCs. With reference to the correlation patterns of Figs. 12, 13 shows that the indices are globally successful in reproducing the observed Niño-Nina patterns, even if quantitatively in certain areas the general tendency is to underestimate the numbers almost everywhere (as discussed before). Again, this general statement does not always hold true. For example, in the eastern Pacific, the Atlantic ITCZ, and in the south Indian Ocean, ENSO impacts on cyclogenesis are not reproduced by the indices. In the northwestern Pacific, the TCS shows the best skills (see the middle panel of Fig. 10) while the CYGP is strongly biased. Referring back to the South Pacific and with the exception of the YGP, the composites from all the indices are coherent with observations, albeit with weaker amplitude.

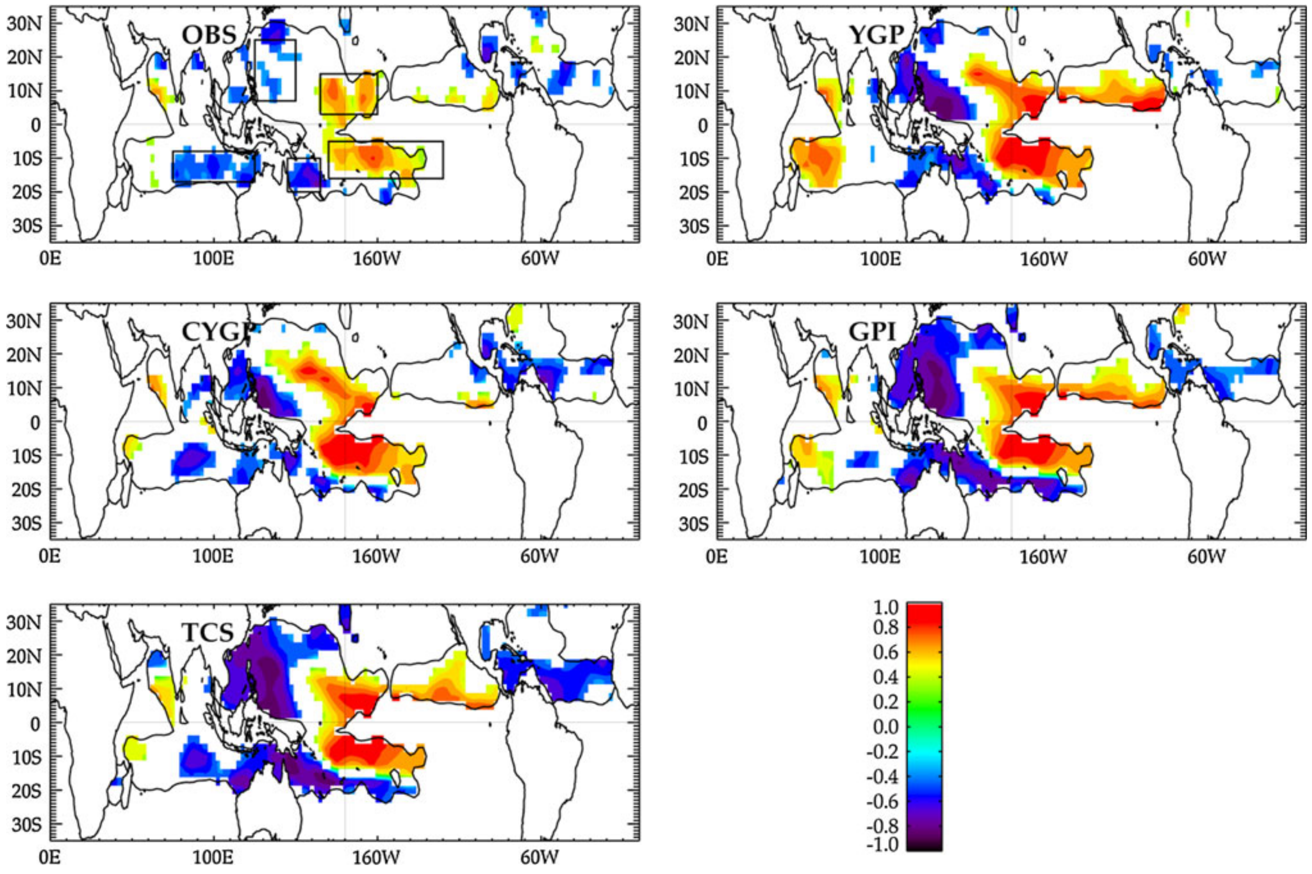

Fig. 12 Correlation maps between the interannual cyclogenesis anomaly and Niño 3.4 index. *Top left panel* correlation between observed cyclogenesis and Niño 3.4. Only >90% significant correlation is shown. Correlation patterns are limited to the region where interannual standard deviation numbers are greater than 1 (Fig. 8), as depicted by a *thin black* contour. *Other panels* same as the first except for all REM indices calculated. On the *top left panel black boxes* used in Fig. 14

Kim et al. (2009) have shown that not all El Niño types impact cyclogenesis identically in the North Atlantic (see their discussion on the differential impacts of eastern Pacific versus central Pacific warming). Similarly, Vincent et al. (2009) have shown that a strong asymmetrical El Niño mode exists with a distinct impact on cyclogenesis as discussed above. Hence, it may be that Figs. 12 and 13 would change when the influence of the El Niño types are considered separately. This is of great interest, yet the limited length of data used here does not allow a quantitative exploration and is left for future investigation.

It is of interest to evaluate the index performances at their best within the regions of coherent patterns rather than in large boxes averaging dipole patterns. Thus, Fig. 10 is reproduced, except in coherent correlation and pattern regions depicted in Figs. 12 and 13 (see black boxes). These results are presented in Fig. 14. As expected, choosing coherent sub regions yields higher and more significant correlation numbers both between indices and observed cyclogenesis (compare top panels, Figs. 10, 14) but also between indices and ENSO (second panels, Figs. 10, 14). Correlations to ENSO are usually higher than those with observed cyclogenesis, suggesting again that the indices have better skills at simulating the cyclogenesis impact of ENSO than at simulating the interannual TC variability in general. Figure 14 also confirms that the indices can overestimate the TC genesis impact of ENSO compared with observations (for example, see the north-western Pacific box where the correlation between observed cyclogenesis and ENSO is lower than that computed with the indices). Yet, the bottom panel of Fig. 14 clearly shows that in most cases (with the exception of the SPCZ region for the CYGP and YGP and the northwestern Pacific for the YGP and TCS), the amplitude and the interannual indices are usually much lower than that observed (Fig. 8).

Finally, we have performed a similar analysis as presented in Fig. 11 for the terms dominating the interannual indices during ENSO. This is done by regressing all the interannual index terms to ENSO. Figure 15 shows that, unlike the diversity discussed in Fig. 11, all indices have good agreement on the dominant mechanisms modifying the index cyclogenesis during ENSO. Retrospectively, this gives additional support and credibility to the conclusions

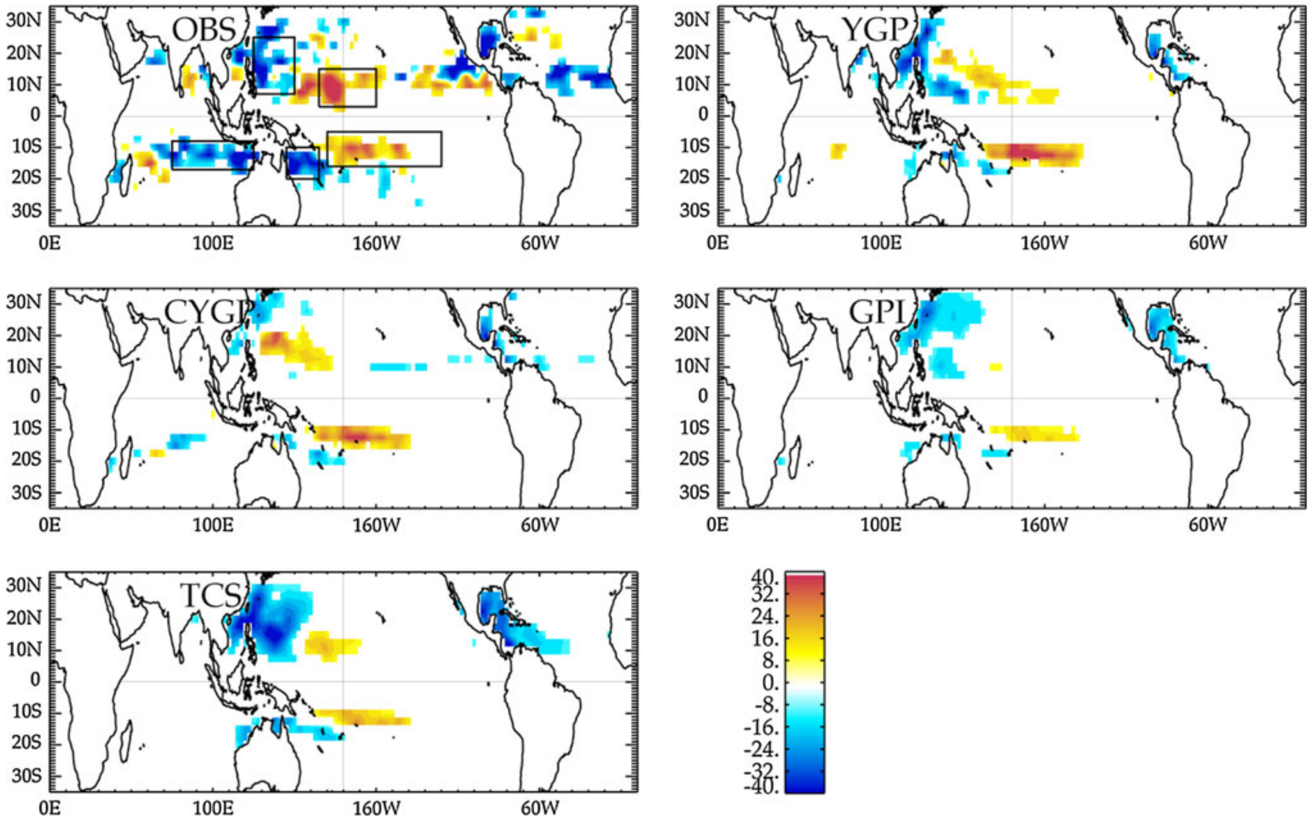

Fig. 13 Composites of cyclogenesis number differences between Niños and Niñas for the observations (*top left*) and the REM indices. Units are in cyclones/20 years/5°. The southern hemisphere shows the signal for the January–March composites while the northern hemisphere shows the signal for the August–October composites. Years entering Niño composite are for the southern hemisphere: 1983, 1987, 1992, 1995, 1998 and for the northern hemisphere: 1982, 1986, 1987, 1991, 1994, 1997. Years of Niñas composites, are for the southern hemisphere: 1985, 1986, 1996, 1999 and for the northern hemisphere: 1988, 1998, 1999

reached by Camargo et al. (2007a), Vincent et al. (2009) and other studies using one index and one reanalysis. To concentrate in regions where ENSO correlates significantly with observed cyclogenesis (black boxes in Fig. 12) and in regions where these regressions are significant, strong conclusions about the mechanisms at work can be drawn. An example of this is in the north central Pacific box where TC genesis increases during El Niño primarily in response to increased vorticity, followed by decreased wind shear, and to a lesser extent, by increased humidity. In the southern hemisphere and north of the mean SPCZ position, mechanisms are identical at first order although with an even stronger dominance of the vorticity increase. This is due to the peculiar asymmetric mode that occurs in the SPCZ on ENSO timescales (Vincent et al. 2009). To the south of the SPCZ and in the Australian region, cyclogenesis decrease during El Niño is mainly driven by thermal changes, such as decrease of mid-tropospheric relative humidity and other thermal terms (e.g. the SST index in the TCS, the PI index in the GPI etc…). To a lesser extent, it is driven by the wind shear term (increased wind shear; see Ramsay et al. 2008) but vorticity does not play a major role. This role of mid-tropospheric humidity agrees with the findings of Camargo et al. (2007a) but seems to disagree with the dominant mechanisms evoked in the analyses of Ramsay et al. (2008) who examined direct correlation between TCs and environmental variables such as vorticity and vertical wind shear during ENSO. In particular, they suggest that the causal relationship between vorticity and TC numbers over northern Australia is a main driver for TC variability. The existence of such a correlation is proven in their study and its existence is not argued here. However, correlation does not imply causation and the use of cyclogenesis indices support the idea that the decrease of mid-tropospheric humidity, not the decrease of vorticity, may be the dominant driving mechanism involved in TC decrease over Australia.

4 Discussion and conclusions

In this study, we have attempted to compare the annual mean and seasonal to interannual variability of four cyclogenesis indices: the GPI, CYGP, YGP and TCS

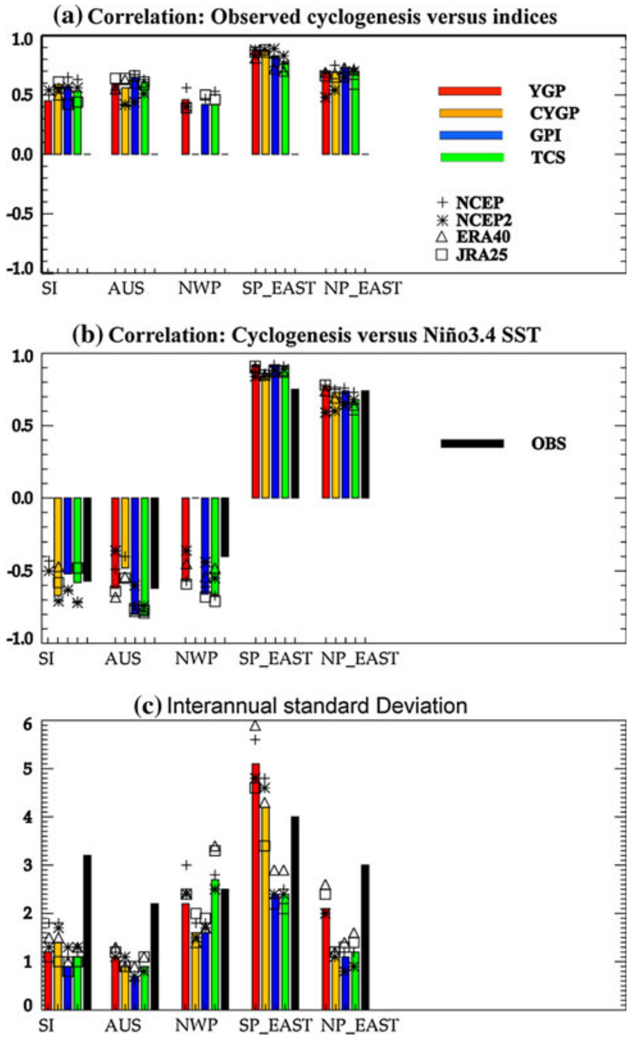

Fig. 14 Same as Fig. 10 but for the *boxes* of Fig. 12

(Tippett et al. 2011) for the period 1979–2001. We have also tested how the index performances vary with the four reanalyses ERA40, NCEP, NCEP2 and JRA25. There are usually more differences between indices for a given forcing than between one index calculated using different reanalyses. Considering the climatology, one obvious flaw of the YGP, GYGP and GPI is a ~2.5°–5° equatorward bias of the main cyclogenesis areas, especially visible in the northern hemisphere. This bias does not exist in the TCS index where the use of a "clipped" vorticity is the key for suppressing such offset (Tippett et al. 2011). The spatial distributions of the biases are not homogeneous with regions of positive and negative biases. Errors in the mean numbers can reach up to 50% positively or negatively in large regions.

On seasonal timescales, another flaw found in all indices—although to a lesser extent in the TCS—is the overestimation of simulated cyclogenesis during unfavourable seasons. The index response variety in different regions also renders making a general conclusion difficult. Again, the mechanisms explaining the seasonal variations as deduced from individual terms that compose the indices do, in fact, differ from one index to another significantly. This result leads us to advise caution when deducing specific mechanisms from (only) one index as is sometimes done (e.g. Yokoi et al. 2009). Overall, however, we feel that the TCS is perhaps the best-adjusted index on seasonal timescales.

When examining the interannual scales, we have distinguished the effect of ENSO from the interannual variability. In general, the indices do not accurately represent the observed interannual cyclogenesis as significant regional correlation rarely exceeds 0.6 on annual averages. Furthermore, all the indices strikingly underestimate the observed amplitudes almost everywhere and when they do not, their correlation to observations is often weak or insignificant on sub-basin scales. However, it seems evident that estimating index performances on large regions blurs their performances because sub-regional patterns may vary oppositely within one large region. These sub regional variations are usually linked to ENSO.

ENSO is a major contributor to interannual genesis. It usually induces patterns of dipole anomalies where enhanced cyclogenesis lies next to weakened cyclogenesis. Thus, a sub regional analysis on areas of coherent ENSO impact is preferable. Unlike our previous conclusions, cyclogenesis phase changes linked to ENSO are coherently simulated by the indices and compare acceptably with observations on most occasions. However, correlation of indices to ENSO is often higher than correlation of actual cyclogenesis to ENSO. This suggests that the indices overestimate the actual cyclogenesis variability responding to ENSO. The indices still usually exhibit large discrepancies to observations on ENSO timescales in terms of variability amplitude even in regions like the South Pacific Convergence Zone where interannual correlation to ENSO can reach 0.8 both in observations and in the indices.

When considering the mechanisms (thermal and dynamical terms) explaining the distributions, we have shown that they can differ significantly between indices at all timescales (except ENSO), which renders the understanding of the individual mechanisms involved in actual cyclogenesis somewhat speculative. This is especially true when using a single index (e.g. Yokoi et al. 2009). On most occasions, there has been a failure to understand the main faults leading to obvious misrepresentation of cyclogenesis variations in specific basins and specific indices. This is mostly due to the complexity of interplay between the individual terms for each index. Another reason is because the overall index performances vary from basin to basin. However, all the indices basically agree on the mechanisms controlling ENSO-related cyclogenesis variations,

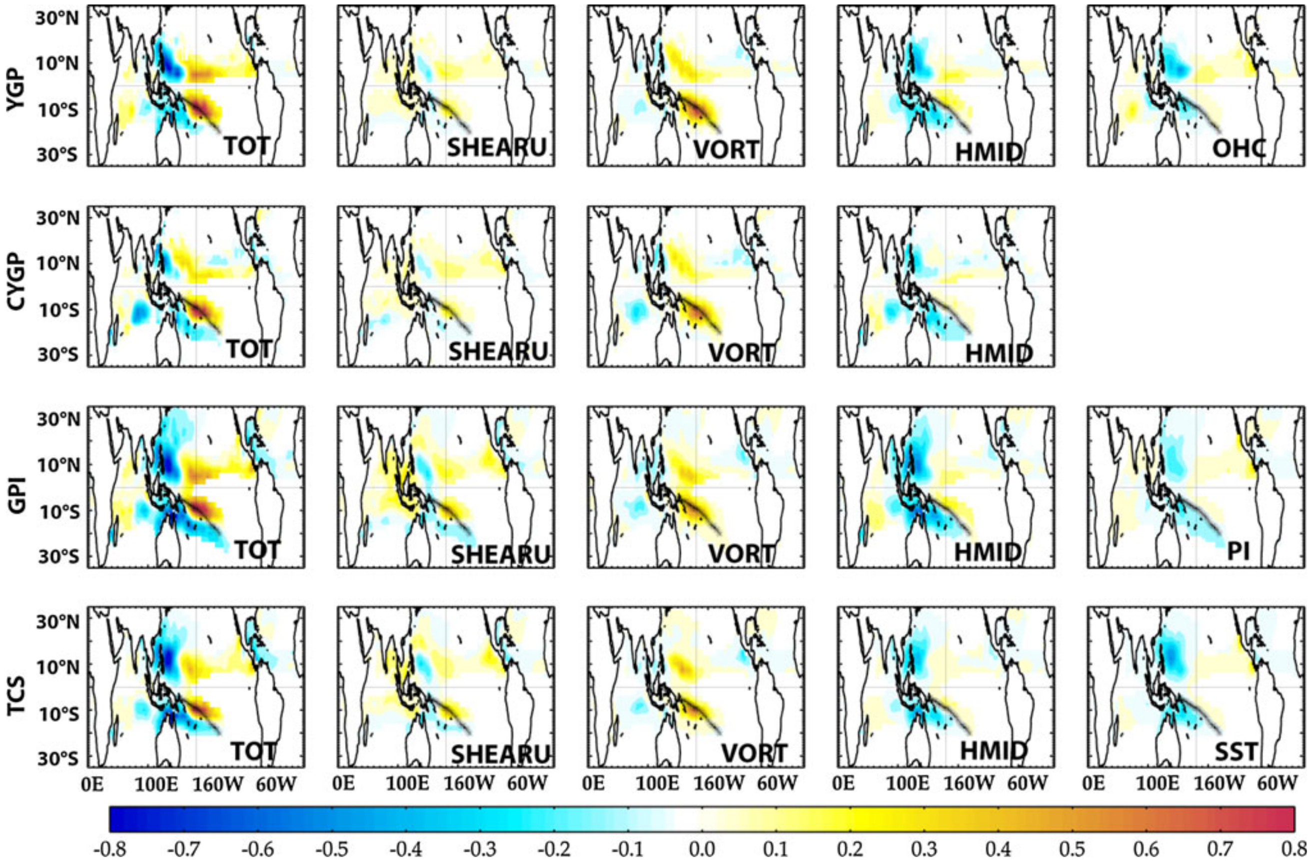

Fig. 15 Standardized regressions of selected (dominant) terms on the ENSO index. Note that the first column is the regression of the total index to the ENSO index, the second is the regression of the wind shear to ENSO, third is the regression of vorticity term to the ENSO index; fourth is the humidity term and fifth is the ocean heat term for the YGP, potential intensity for the GPI, and SST index for the TCS

suggesting that the conclusions reached on the basis of a single index are valid.

The global discrepancies found in the mean, seasonal and interannual amplitudes simulated by all the indices cannot be corrected by the simple use of a global constant that fits the mean yearly-observed cyclogenesis. Kim et al. (2010) discuss this point and conclude that it may be better to use regionally adjusted constants even if their justification would remain unclear. We have tried to apply such spatially dependent correction by fitting the mean indices to observations at each point. While the use of such *ad hoc* correction improves the seasonal variations, it has globally no effect on reducing the biases found in the interannual variations. Eventually, we believe that regional improvements can only come from a new adjustment of the functional forms or of the type of variable entering the index. Along these lines, Murakami and Wang (2010) have added a new term to the GPI to improve the index performances in the northwestern Pacific. Similarly, Emanuel (2010) has proposed a modified version of the GPI, which seems to be more suited for climate projections. The analyses conducted in the present study, although not exhaustive, present a benchmark with which to test these new indices and other future indices.

The question arises as to what extent genesis indices can be expected to reproduce observed cyclogenesis. These indices are only indications of the large-scale conditions favourable to cyclogenesis. Hence, while large-scale conditions may be favourable, actual cyclogenesis may not necessarily occur. This may explain why indices can be better correlated to ENSO than to actual cyclogenesis. One important mechanism controlling cyclogenesis in a favourable environment relies on stochastic processes. These are not represented by the indices but have been shown to be potentially important for cyclogenesis (Simpson et al. 1997). For example, Jourdain et al. (2010) have specifically shown using a high resolution model of the SPCZ region that roughly half of the South Pacific cyclogenesis may be due to stochasticity while the large-scale forcing represented by the indices explains the remaining variability. This may also explain why the global high-resolution simulations of Zhao et al. (2009) poorly simulate the variability of the South Pacific region (see their Fig. 11a) while the North Atlantic variability is much better simulated. It is interesting to note that Camargo et al. (2009) invoke a similar argument to explain some discrepancies between the GPI and the observations at MJO timescales.

Compared to large-scale forcing that may be predictable, especially if dominated by ENSO, stochasticity limits predictability of cyclogenesis on intraseasonal to interannual timescales. Stochasticity has, however, no effect on long-term estimations. Yet, given the large regional biases of climatological indices and the failure of GCMs to capture a number of observed atmospheric trends (Emanuel 2010), the evaluation of the long-term regional cyclogenesis changes associated with climate change using these indices (Caron and Jones 2008; Royer and Chauvin 2009; Chauvin and Royer 2011; Kim et al. 2010) remains an issue to be addressed with caution., Finally, in this study, no attempt was made to compare the interannual variability of the indices within the framework of climate models such as those used in the IPCC-AR4 database. Given the divergence of our results to observations, and the vast diversity of ENSO response in these models (Collins et al. 2010), we believe that the indices are not equipped to give quantitative regional estimates of interannual cyclogenesis in the future climate. This should be addressed more precisely in future work.

Acknowledgments The authors wish to thank K. Emanuel for sharing the cyclone netcdf data as well as the GPI routines. We would like to thank our two anonymous reviewers for their fruitful comments. Thanks also goes to Michael Tippett for insightful discussions and for sharing his results prior to publication. This work was supported by the Institut de Recherche pour le Développement (IRD) and ANR grant ANR-VULN-002-01. The JRA25 datasets are from the JRA-25 long-term reanalysis cooperative research project carried out by the JMA and the CRIEPI.

Appendix: cyclogenesis index definition

In the text, we use the label “reanalysis-index” (e.g., NCEP-YGP, ERA40-GPI etc…) for an index calculated with a given reanalysis. The definitions that follow are exact replications of those found in the original papers. They are:-

1. GPI

The GPI monthly index is constructed as in Camargo et al. (Camargo et al. 2007a, b) and Emanuel and Nolan (2004) as $\mathrm{GPI} = \underbrace{|10^5\eta|^{3/2}(1+0.1V_{\mathrm{shear}})^{-2}}_{\text{dynamic}}\underbrace{\left(\frac{H}{50}\right)^3\left(\frac{V_{\mathrm{pot}}}{70}\right)^3}_{\text{thermal}}$

with η is the absolute vorticity at 850 hPa in s^{-1}, H is the relative humidity at 600 hPa, V_{pot} is the potential intensity calculated using a routine provided by Dr. Emanuel (http://wind.mit.edu/~emanuel/home.html). V_{shear} is the magnitude of the vertical wind shear between 850 and 200 hPa in ms^{-1}. For consistency with the other indices below, we sometimes refer to thermal and dynamical potentials (see equation).

2. TCS (Tippett et al. 2011)

This index uses the same variables as the previous one except for the V_{pot} which is replaced by an SST index:

$$\begin{aligned}\mathrm{TCS} &= \exp(b + b_\eta\eta + b_{V_{\mathrm{shear}}}V_{\mathrm{shear}} + b_H H + b_T T + \log(\cos\phi))\\ &= \cos\phi * \exp b * \underbrace{\exp(b_\eta\eta + b_{V_{\mathrm{shear}}}V_{\mathrm{shear}})}_{\text{dynamic}} * \underbrace{\exp(b_H H + b_T T)}_{\text{thermal}},\end{aligned}$$

with $T = \mathrm{SST} - \overline{\mathrm{SST}}^{[20^\circ\mathrm{S}-20^\circ\mathrm{N}]}$ and $\eta = \min(\eta, 3.7)$ is referred to as the “clipped vorticity”, φ is the latitude. The constant used in the calculation is that given by Tippett et al. (2011)’s Table 1 line 6, namely: $b = 5.8$; $b_\eta = 1.03$; $b_H = 0.05$; $b_T = 0.56$; $b_V = -0.15$.

3. YGP

For consistency with the GPI, we have constructed monthly YGP and CYGP indices rather than seasonal indices as initially proposed by Gray (1979), Watterson et al. (1995), Royer et al. (1998). The monthly YGP is calculated as $\mathrm{YGP} = \underbrace{|f|I_\zeta I_s}_{\text{dynamic}}\underbrace{EI_\theta I_{\mathrm{RH}}}_{\text{thermal}}$ where f is the Coriolis parameter in $10^{-5}\mathrm{s}^{-1}$, $I_\zeta = \zeta_r\frac{f}{|f|} + 5$ with ζ_r the relative vorticity at 925 hPa in 10^{-6} s^{-1}, $I_s = \left(\left|\frac{\delta V}{\delta P}\right| + 3\right)^{-1}$ where $\frac{\delta V}{\delta P}$ is the vertical shear of the horizontal wind between 925 and 200 hPa in m s^{-1}/750 hPa, $I_\theta = \left(\frac{\delta\theta_e}{\delta P} + 5\right)$ where $\frac{\delta\theta_e}{\delta P}$ is the vertical gradient of the equivalent potential temperature between 925 and 500 hPa in K/500 hPa, $I_{\mathrm{RH}} = \max\left(\min\left(\frac{\mathrm{RH}-40}{30}, 1\right), 0\right)$ with RH is the average relative humidity in percent between 700 and 500 hPa. More simply put, if RH is greater than 70% then $I_{\mathrm{RH}} = 1$ and if RH lower than 40%, $I_{\mathrm{RH}} = 0$. $E = \int_0^{60m}\rho_w c_w(T-26)dz$ is the thermal energy of water above 26°C in the top 60 m of the ocean. ρ_w and c_w are the density and specific ocean heat capacity taken as constant. We have access to two OGCMs (Ocean General Circulation Model) outputs forced by NCEP and ERA40 reanalyses from the OPA model (Rodgers et al. 2008) with which to calculate E but we do not have similar outputs for the NCEP2 reanalyses. However, the averaged E over 25°S–25°N, 0–360° and for the 1970–2001 time period yields 7.6 10^3 cal cm^{-2} for NCEP-OPA (referring to the OPA output forced by NCEP) and 7.9 for ERA40-OPA outputs. The two time series correlate at 0.98 and their respective standard deviation are 0.92 and 0.99. Thus, despite differences in the two wind fields, the OGCM thermal energy E yields very similar quantities. Hence, it is reasonable to think that NCEP2-OPA, if it existed, would have also given a very similar E. Thus, we have confidently used E from NCEP-OPA in the calculation of the NCEP2 YGP.

4. CYGP

The CYGP replaces the thermal potential of the YGP by a convective potential $k(P_c - P_0)$where k is an arbitrary constant to be adjusted depending on the reanalysis or data set used. P_c is the convective precipitation in mm day^{-1} and P_0 is a threshold below which the convective potential is set to zero to avoid spurious cyclogenesis off the tropics. We chose $P_0 = 3$ from previous studies (Chauvin and Royer 2011; Royer and Chauvin 2009) but tests on this threshold do not change the analyses performed in that paper. k was adjusted for each reanalysis in order to yield a ~85 cyclone/year global mean, as observed (see also main text).

For consistency with the GPI, we have constructed monthly YGP and CYGP indices rather than seasonal indices as initially proposed by Gray (1979), Watterson et al. (1995), Royer et al. (1998). It was checked that introducing monthly variations rather than 3-month seasons does not induce significant differences in the seasonal index estimates.

References

Bruyere C, Holland G, Done J, Suzuki-Parker A (2010) Genesis potential index for tropical cyclones in the nested regional climate model (NRCM) experiments. In: Proceedings of 29th conference on hurricanes and tropical meteorology, Tucson, Arizona, 10–14 May 2010, 7A.2

Camargo SJ, Sobel AH (2007) Workshop on tropical cyclones and climate. Bull Metorol Soc 88(3):389–391. doi: 10.1175/BAMS-88-3-389

Camargo SJ, Emanuel KA, Sobel AH (2007a) Use of a genesis potential index to diagnose ENSO effects on tropical cyclone genesis. J Clim 20:4819–4834

Camargo SJ, Sobel AH, Barnston AG, Emanuel KA (2007b) Tropical cyclone genesis potential index in climate models. Tellus 59A:428–443

Camargo SJ, Wheeler MC, Sobel AH (2009) Diagnosis of the MJO modulation of tropical cyclogenesis using an empirical index. J Atmos Sci 66:3061–3074

Caron LP, Jones CG (2008) Analysing present, past and future tropical cyclone activity as inferred from an ensemble of coupled global climate models. Tellus 60A:80–96

Chand SS, Walsh KJE (2009) Tropical cyclone activity in the Fiji region: spatial patterns and relationship to large-scale circulation. J Clim 22:3877–3893

Chauvin F, Royer J-F (2011) Role of the SST anomaly structures in response of cyclogenesis to global warming. In: Elsner JB et al (eds) Hurricanes and climate change, vol 2. Springer Science, Berlin. doi:10.1007/978-90-481-9510-7_3

Chauvin F, Royer J-F, Déqué M (2006) Response of hurricane-type vortices to global warming as simulated by ARPEGE-Climat at high resolution. Clim Dyn 27:377–399

Chu PS (2004) ENSO and tropical cyclone activity. In: Murnane RJ, Liu K-B (eds) Hurricanes and typhoons, past, present and future. Columbia University Press, Columbia, pp 297–332

Collins M, An S-I, Cai W, Ganachaud A, Guilyardi E, Jin F-F, Jochum M, Lengaigne M, Power S, Timmermann A, Vecchi G, Wittenberg A (2010) The impact of global warming on the tropical Pacific and El Niño. Nat Geosci 3:391–397. doi: 10.1038/ngeo868

Emanuel K (2010) Tropical cyclone activity downscaled from NOAA-CIRES reanalysis, 1908–1958. J Adv Model Earth Syst 2:1–12. doi:10.3894/JAMES.2010.2.1

Emanuel KA, Nolan DS (2004) Tropical cyclone activity and global climate. In: Proceedings of 26th conference on hurricanes and tropical meteorology. American Meteorological Society, Miami, FL, pp 240–241

Gray WM (1968) Global view of the origin of tropical disturbances and storms. Mon Weather Rev 96:669–700

Gray WM (1975) Tropical cyclone genesis. Colorado State University, Colorado

Gray WM (1979). Hurricanes: their formation, structure and likely role in the tropical circulation. Meteorology over the Tropical Oceans. Ed R Meteor Soc 155–218

Gray WM (1998) The formation of tropical cyclones. Meteorol Atmos Phys 67:37–69. doi:10.1007/BF01277501

Grotjahn R (2008) A comparison of selected fields in NCEP/DOE AMIP-II and ECMWF ERA-40 reanalyses. Dyn Ocean Atmos 44:108–142

Jourdain NC, Marchesiello P, Menkes CE, Lefèvre J, Vincent EM, Lengaigne M and Chauvin F (2010) Mesoscale simulation of tropical cyclones in the South Pacific: climatology and interannual variability. J Clim. doi: 10.1175/2010JCLI3559.1

Kalnay EC et al (1996) The NCEP/NCAR reanalysis project. Bull Am Meteorol Soc 77:437–471

Kanamitsu M, Ebisuzaki W, Woollen J, Yang S-K, Hnilo JJ, Fiorino M, Potter GL (2002) NCEP-DOE AMIP-II reanalysis (R-2). Bull Am Meteor Soc 83:1631–1643

Kim J-H, Brown S, McDonald RE (2010) Future changes in tropical cyclone genesis in fully dynamic ocean- and mixed layer ocean-coupled climate models: a low-resolution model study. Clim Dyn. doi:10.1007/s00382-010-0855-6

Kim HM, Webster PJ, Curry JA (2009) Impact of shifting patterns of Pacific Ocean warming on North Atlantic tropical cyclones. Science 325:77–80. doi:10.1126/science.1174062

Landsea CW (2000) El Niño–Southern oscillation and the seasonal predictability of tropical cyclones. In: Díaz HF, Markgraf V (eds) El Niño: impacts of multiscale variability on natural ecosystems and society. Cambridge University Press, Cambridge, pp 149–181

Lyon B, Camargo SJ (2009) The seasonally-varying influence of ENSO on rainfall and tropical cyclone activity in the Philippines. Clim Dyn 32:125–141. doi:10.1007/s00382-008-0380-z

McDonald RE, Bleaken DG, Cresswell DR, Pope VD, Senior CA (2005) Tropical storms: representation and diagnosis in climate models and the impacts of climate change. Clim Dyn 25:19–36

Murakami H, Wang B (2010) Future change of North Atlantic tropical cyclone tracks: projection by a 20-km-mesh global atmospheric model. J Clim 23:2699–2721

Onogi K, Tsutsui J, Koide H, Sakamoto M, Kobayashi S, Hatsushika H, Matsumoto T, Yamazaki N, Kamahori H, Takahashi K, Kadokura S, Wada K, Kato K, Oyama R, Ose T, Mannoji N, Taira R (2007) The JRA-25 reanalysis. J Meteorol Soc Jpn 85:369–432. doi:10.2151/jmsj.85.369

Ramsay HA, Leslie LM, Lamb PJ, Richman MB, Leplastrier M (2008) Interannual variability of tropical cyclones in the Australian region: role of large-scale environment. J Clim 21:1083–1103. doi:10.1175/2007JCLI1970.1

Rodgers KB, Aumont O, Menkès C, Gorgues T (2008) Decadal variations in equatorial Pacific ecosystems and ferrocline/pycnocline decoupling. Glob Biogeochem Cycles 22(2):17–32

Royer J-F, Chauvin F (2009) Response of tropical cyclogenesis to global warming in an IPCC AR-4 scenario assessed by a modified yearly genesis parameter. In: Elsner JB, Jagger TH (eds) Hurricanes and climate change. Springer, Berlin, pp 213–234

Royer J-F, Chauvin F, Timbal B, Araspin P, Grimal D (1998) A GCM study of the impact of greenhouse gas increase on the frequency of occurrence of tropical cyclones. Clim Chang 38:307–343

Simpson J, Ritchie E, Holland G, Halverson J, Stewart S (1997) Mesoscale interactions in tropical cyclone genesis. Mon Weather Rev 125(10):2643–2661

Tippett MK, Camargo SJ, Sobel A (2011) A poisson regression index for tropical cyclone genesis and the role of large-scale vorticity in genesis. J clim. doi:10.1175/2010JCLI3811.1, accepted

Trenberth KE (1997) The Definition of El Niño. Bull Am Meteorol Soc 78:2771–2777

Tsutsui JI, Kasahara A (1996) Simulated tropical cyclones using the National center for atmospheric research community climate model. J Geophys Res Atmos 101:15013–15032

Uppala SM, Co-authors (2005) The ERA-40 re-analysis. Q J R Meteorol Soc 131(612 Part B):2961–3012

Vincent E, Lengaigne M, Menkes CE, Jourdain NC, Marchesiello P, Madec G (2009) Interannual variability of the South Pacific convergence zone and implications for tropical cyclone genesis. Clim Dyn. doi:10.1007/s00382-009-0716-3

Watterson IG, Evans JL, Ryan BF (1995) Seasonal and interannual variability of tropical cyclogenesis: diagnostics from large-scale fields. J Clim 8:3052–3066

Yokoi S, Takayabu YN, Chan JCL (2009) Tropical cyclone genesis frequency over the western North Pacific simulated in medium-resolution coupled general circulation models. Clim Dyn 33:665–683. doi:10.1007/s00382-009-0593-9

Zhao M, Held IM, Lin S-J, Vecchi GA (2009) Simulations of global hurricane climatology, interannual variability, and response to global warming using a 50 km resolution GCM. J Clim. doi:10.1175/2009JCLI3049.1

F Simulation méso–échelle des TCs du Pacifique Sud : climatologie et variabilité interannuelle

VOLUME 24 JOURNAL OF CLIMATE 1 JANUARY 2011

Mesoscale Simulation of Tropical Cyclones in the South Pacific: Climatology and Interannual Variability

NICOLAS C. JOURDAIN,* PATRICK MARCHESIELLO,*,+ CHRISTOPHE E. MENKES,*,# JÉROME LEFÈVRE,*
EMMANUEL M. VINCENT,# MATTHIEU LENGAIGNE,#,@ AND FABRICE CHAUVIN&

** Institut de Recherche pour le Développement, Nouméa, New Caledonia*
+ Laboratoire d'Etudes en Géophysique et Océanographie Spatiale, Toulouse, France
 # Laboratoire d'Océanographie et du Climat: Expérimentation et Approches Numériques, Paris, France
@ National Institute of Oceanography, Goa, India
& Centre National de Recherches Météorologiques, Toulouse, France

(Manuscript received 9 December 2009, in final form 4 August 2010)

ABSTRACT

The Weather Research and Forecast model at ⅓° resolution is used to simulate the statistics of tropical cyclone (TC) activity in the present climate of the South Pacific. In addition to the large-scale conditions, the model is shown to reproduce a wide range of mesoscale convective systems. Tropical cyclones grow from the most intense of these systems formed along the South Pacific convergence zone (SPCZ) and sometimes develop into hurricanes. The three-dimensional structure of simulated tropical cyclones is in excellent agreement with dropsondes and satellite observations. The mean seasonal and spatial distributions of TC genesis and occurrence are also in good agreement with the Joint Typhoon Warning Center (JTWC) data. It is noted, however, that the spatial pattern of TC activity is shifted to the northeast because of a similar bias in the environmental forcing. Over the whole genesis area, 8.2 ± 3.5 cyclones are produced seasonally in the model, compared with 6.6 ± 3.0 in the JTWC data. Part of the interannual variability is associated with El Niño–Southern Oscillation (ENSO). ENSO-driven displacement of the SPCZ position produces a dipole pattern of correlation and results in a weaker correlation when the opposing correlations of the dipole are amalgamated over the entire South Pacific region. As a result, environmentally forced variability at the regional scale is relatively weak, that is, of comparable order to stochastic variability (±1.7 cyclones yr^{-1}), which is estimated from a 10-yr climatological simulation. Stochastic variability appears essentially related to mesoscale interactions, which also affect TC tracks and the resulting occurrence.

1. Introduction

Thirty years ago, Gray (1979) showed that the seasonal frequency of tropical cyclone (TC) genesis at any location is closely related to large-scale environmental parameters. Based on this study, genesis indices were developed for seasonal predictions (Watterson et al. 1995; Camargo et al. 2007a) and climate projections (Royer et al. 1998). However, as noted by Ooyama (1982), the synoptic conditions do not directly determine the genesis process, but only affect the probability of its happening. Suitable environmental conditions are generally present in monsoonal genesis regions, such as the western South Pacific, but are not sufficient. Triggering mechanisms are also needed to overcome the obstacle of relatively low midtropospheric humidity. They appear in the form of externally forced convergence, such as wind surges in the trade winds or monsoon flow, or/and mesoscale interactions (Gray 1998; Simpson et al. 1997). Simpson et al. (1997) use the few available observations in the western South Pacific to suggest that interactions of mesoscale convective systems (MCSs) play a crucial role in TC genesis once favorable large-scale conditions have been established [large scales refer to structures larger than about 2000 km, following the subdivision of Orlanski (1975)]. These mesoscale interactions are essentially stochastic in nature, although the degree of stochasticity may be reduced by environmental influences. In the Atlantic region, tropical cyclones often form from tropical waves moving off of Africa (Landsea 1993). In this case, TC genesis appears to rely less on mesoscale stochastic processes and more on forced background conditions, so that predictability seems higher in

---

Corresponding author address: Nicolas Jourdain, IRD, Nouméa Center, BP A5, Nouméa CEDEX, New Caledonia.
E-mail: nicolas_jourdain@yahoo.fr

DOI: 10.1175/2010JCLI3559.1

the Atlantic than in the Pacific (Vitart et al. 1997; Knutson et al. 2007; Zhao et al. 2009). Specifically, Zhao et al. (2009) found correlations greater than 0.8 between observed and simulated yearly hurricane counts in the North Atlantic, but only 0.3 in the South Pacific.

Many climatological studies do not consider mesoscale interactions because they rely on atmospheric general circulation models (AGCMs) of coarse horizontal resolution that simulate cyclone-like vortices, that is, vortices that have some characteristics of tropical cyclones but much lower intensities (e.g., Wu and Lau 1992; Bengtsson et al. 1996; Vitart et al. 1997; Sugi et al. 2002; Camargo et al. 2005; Yoshimura et al. 2006). Their relevance to actual TC activity remains difficult to assess (Gray 1998; Camargo et al. 2007b). More recent studies have shown that increasing AGCM resolution to around 50 km improves the representation of simulated cyclones (Oouchi et al. 2006; Chauvin et al. 2006; Bengtsson et al. 2007; Zhao et al. 2009). However, global simulations have a high computational cost, limiting the number of sensitivity experiments that are much needed for calibrating convection parameterizations. Consequently, they generally show variable performances in the TC genesis regions, with poor results in the South Pacific.

Regional atmospheric models represent a cost-effective alternative for simulating multiple seasons of TC activity. They also benefit from a geographical focus that allows better adjustments of parameterizations, and from the opportunity of controlling lateral inputs. Despite these advantages, few attempts have been made at running long-term regional TC simulations (Nguyen and Walsh 2001; Walsh et al. 2004; Knutson et al. 2007). To date, only one fine-resolution application by Walsh et al. (2004) is reported for the South Pacific, using a 30-km-mesh version of the Commonwealth Scientific and Industrial Research Organisation (CSIRO) Division of Atmospheric Research model. High-resolution atmospheric models appear to generate intense tropical cyclones, with structures that are often in remarkably good agreement with dropsonde data. However, the intensity distribution is generally distorted, with the number of both weak and extreme TCs underestimated. The climatological location of TC genesis and tracks are reasonably well simulated, although there are always some significant regional discrepancies. In particular, the South Pacific environmental conditions present a difficult task for regional TC models (Walsh et al. 2004). To improve the representation of large-scale conditions, various methods related to data assimilation can be found. While these methods may be useful to control the environmental conditions, they affect the development of intense vortices in the simulations (Bengtsson et al. 2007). A spectral nudging technique was developed by von Storch et al. (2000) to improve on this problem and constrain the large scales while allowing the model to generate smaller-scale disturbances. However, TCs are mixed synoptic-scale–mesoscale phenomena with relatively long life spans, and selective control of their environmental conditions is difficult. Knutson et al. (2007) only use this nudging technique as a means of controlling the excessive storminess of their regional model of Atlantic TCs, not for selectively constraining the large-scale conditions.

A major objective of long-term TC simulations is to quantify the interannual variability of TC activity, identify the forcing mechanisms (whether external or internal), and estimate the degree of predictability that can be used to build cyclone warning systems. Zhao et al. (2009), when modeling the global atmosphere at 50-km resolution, find much lower correlations between the seasonal number of observed and simulated TCs in the Pacific compared to that in the North Atlantic. Part of the discrepancy between the model and data is statistical, that is, resulting from the stochastic nature of the triggering mechanisms of TC genesis. This implies that ensemble simulations can greatly improve these correlations, especially in the North Atlantic (Vitart et al. 1997; Knutson et al. 2007; Zhao et al. 2009), even with a two-member ensemble. However, the improvements are regionally variable, and the South Pacific (as a whole) presents weak correlations even in ensemble simulations (Vitart et al. 1997; Zhao et al. 2009). Nevertheless, when subregions are considered, observational studies tend to relate cyclonic interannual variability in this region to El Niño–Southern Oscillation (ENSO). For example, significant correlations are found between the seasonal number of TCs around Australia and ENSO signals (Nicholls 1984; Evans and Allan 1992). Basher and Zheng (1995) and Kuleshov et al. (2008) also note a greater number of cyclones in the Coral Sea during La Niña than during El Niño. They also show an eastward and northward shift of cyclonic activity associated with a shift of the monsoon trough [or, equivalently, the South Pacific convergence zone (SPCZ)] during El Niño phases (see also Camargo et al. 2007a; Vincent et al. 2009).

In this paper, the Weather Research and Forecast model (WRF; Skamarock et al. 2005) is used to simulate the South Pacific TC activity and its interannual variability. Scales ranging from synoptic to mesoscale are considered so that both the environmental forcing and the mesoscale interactions needed for genesis are simulated. No assimilation or relaxation technique is used to avoid the artificial damping of storminess. We rely instead on the choice of a convective parameterization (needed for resolution larger than 5 km) selected from a sensitivity experiment (section 3). The results from a 25-yr present-climate experiment are investigated and the climatology of the simulated cyclonic activity is evaluated (section 4). The role of ENSO as an environmental forcing to the interannual variability of TC activity is analyzed in section 5. Finally, the degree of stochasticity in cyclogenesis is estimated using a climatological simulation to produce a 10-member ensemble of the same average season.

2. Materials and methods

a. Model and configuration

In this study, WRF version 2.2 (Skamarock et al. 2005), based on compressible, nonhydrostatic Euler equations, is used with the dynamic solver, the Advanced Research WRF (ARWRF; Skamarock and Klemp 2008). The physical parameterizations include the WRF single-moment three-class microphysics scheme (WSM3; Hong et al. 2004), a simple cloud-interactive shortwave radiation scheme (Dudhia 1989), the Rapid Radiation Transfer Model (RRTM) for longwave radiation (Mlawer et al. 1997), the Yonsei University planetary boundary layer (YSU; Noh et al. 2003) with Monin–Obukhov surface layer parameterization, and the WRF simple five-layer (thermal diffusion) land surface model. The drag parameterization over the ocean is based on the work of Charnock (1955) and has the caveat of overestimating surface roughness at wind speed over 30–40 m s^{-1}, with debated consequences on TC maturation (Powell et al. 2003; Moon et al. 2004). The parameterization of subgrid-scale convection is from the Betts–Miller–Janjic (BMJ) scheme (Janjić 1994) and was selected from a comparison with two other schemes [the Kain–Fritsch (KF) and Grell–Devenyi (GD) schemes; see section 3].

The 25-yr, present-climate simulation of TC activity in the South Pacific is designed as a dynamical downscaling product of the National Centers for Environmental Prediction (NCEP)/Department of Energy Global Reanalysis 2 (GR2; Kanamitsu et al. 2002) for the period of 1979–2004. A two-way nesting approach was chosen to extend the lateral boundaries of the model because attempts to position them near the SPCZ or intertropical convergence zone (ITCZ) introduced strong biases in the simulations (not shown). The domain is represented in Fig. 1: the coarser grid resolution is 105 km, the inner grid resolution is 35 km (about ⅓°), and 31 vertical levels are used in both grids. The meteorological and oceanographic data used for model initialization and boundary forcing [preprocessed with the WRF preprocessing system (WPS) package] are from the 6-hourly 1979–2004 GR2. For surface forcing, GR2 includes an optimal interpolation of daily sea surface temperature (SST) analysis on a coarse 1° grid, while lateral boundary forcing is imposed on the outer domain through a five-point relaxation zone.

b. Effective model resolution

The effective resolution of a model can be defined as the scale at which the model kinetic energy spectrum decays relative to the expected spectrum (Errico 1985; Skamarock 2004). The simulated January–March (JFM) mean spectrum for the 1981 model year is plotted in Fig. 2, together with the energy spectrum derived from GR2 and the $k^{-5/3}$ Kolmogorov scaling law, describing motions at scales below 1000 km. The break in the model slope indicates an effective resolution estimate of 155 km, that is, about 5 Δx. Effective resolution can be expected to evolve as a function of Δx, because the model filters scale with the mesh size and the ratio of effective resolution to mesh size is model dependent. The low ratio found for WRF results from its highly scale-selective implicit and explicit model filters; otherwise, that ratio is larger in most community models (Skamarock 2004).

Figure 2 shows that the GR2 forcing conditions are properly passed down to WRF because the spectra obtained for WRF and GR2 are very similar for scales larger than 3000 km, and then small differences down to 1250 km are presented, which appears to be the effective resolution of GR2 in that area. The mesoscale dynamics are thus entirely handled through regional downscaling. The effective resolution of 155 km is finer than most mesoscale vortices formed in the SPCZ (Gray 1998) and is of the order of the smallest tropical cyclones (midget typhoons).

c. Tracking methodology

The method used here was developed by Chauvin et al. (2006) for a 50-km-resolution model. The following several criteria are used to distinguish tropical cyclones from intense midlatitude systems at each time step:

- mean sea level pressure is a local minimum;
- 850-hPa vorticity > VOR;
- maximum 850-hPa wind speed > WT;
- mean 700–300-hPa temperature anomaly > TT;
- 300-hPa temperature anomaly > 850-hPa temperature anomaly; and
- 850-hPa tangential wind > 300-hPa tangential wind.

VOR, WT, and TT are threshold parameters for vorticity, wind speed and temperature anomaly respectively. Anomalies are defined as the difference between the system and its environment [both areas are defined using the radius of the maximum radial pressure gradient; see Chauvin et al. (2006)]. The tracks are then constructed by an iterative process that links the points where the criteria are satisfied; tracks shorter than 1.5 day are eliminated. As a final step, all selection criteria except the 850-hPa vorticity > VOR are removed so that the tracks are

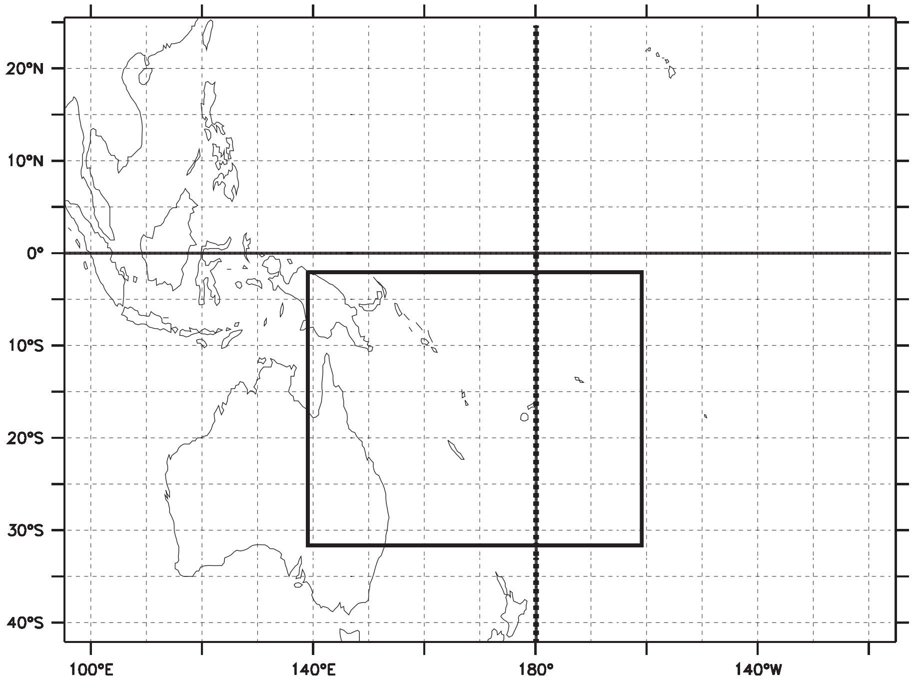

FIG. 1. Domain of integration. The black box represents the inner domain, and the map boundaries are those of the outer domain. Date line, equator, and coasts are indicated (thick black lines).

completed both backward and forward. This procedure prevents a cyclonic system whose intensity decreases below the threshold value and then increases again from being counted twice (Camargo and Zebiak 2002).

The WT threshold can be objectively determined following Walsh et al. (2007). An empirical choice of the two other thresholds was made by analyzing the first year of simulation step by step. The aim of this choice was to detect all of the significant simulated TCs (eliminating intense midlatitude vortices) rather than adjusting favorably to the real world. The analysis gives

$$\mathrm{VOR} = 30.10^{-5}\,\mathrm{s}^{-1}, \quad \mathrm{WT} = 17\,\mathrm{m\,s}^{-1} \quad \text{and} \quad \mathrm{TT} = 3\,\mathrm{K}.$$

The VOR and WT thresholds are higher than those of Chauvin et al. (2006), which is due to the higher resolution used in our analysis. VOR and TT are not chosen independently of WT because the fields of temperature anomaly, vorticity, and maximum wind speed are tightly related in TCs. However, because VOR and TT are mostly empirical values, the sensitivity of the tracking method to their choice must be checked. In Fig. 3, the surface wind speed distribution (in cyclone days) is plotted for different values of the thresholds. When removing the TT criteria (i.e., TT = 0 K), there is a large increase of detected systems with low 10-m maximum wind speed, whereas the number of systems with high 10-m maximum wind speed remains almost unchanged. The opposite sensitivity is found when shifting TT to 4 K. The vorticity threshold also has a significant impact on cyclone days for storms with low wind speed. Therefore, the strongest storms reach a stable number of detections for various threshold values (all intense TCs likely have a midtropospheric warm core and vorticity values that exceed the thresholds). On the other hand, a sufficient amount of TCs is needed to produce reliable statistical analyses. A good compromise is to only consider TCs whose surface wind speeds reach 22 m s^{-1} at least once (an additional criteria

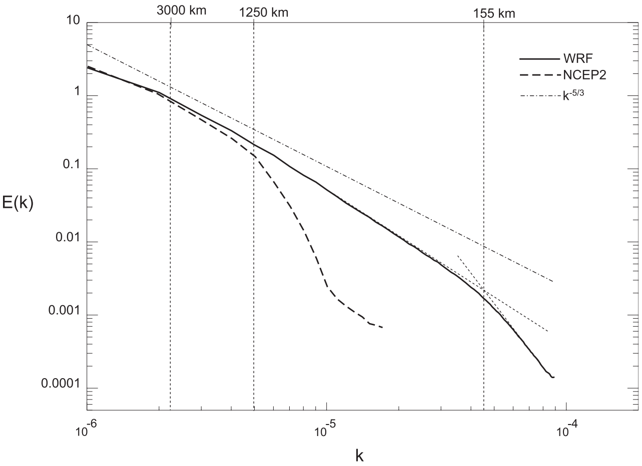

FIG. 2. JFM 1981 wavenumber spectra of simulated surface air (10 m) kinetic energy. E is in Joules, k is in m^{-1}.

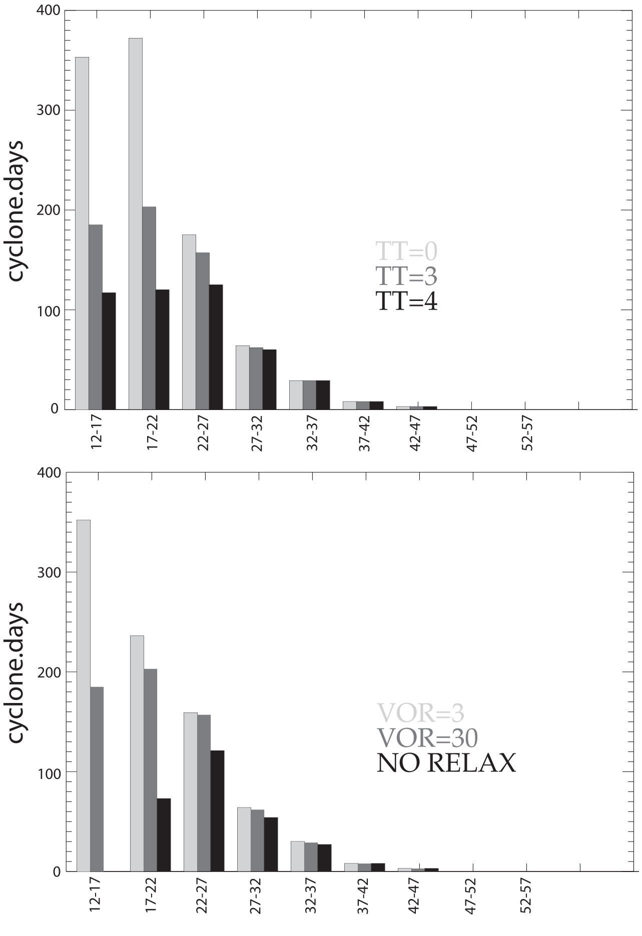

FIG. 3. Simulated 10-m wind speed distribution for the period of 1979–86 (in cyclone days versus m s^{-1}) according to different values of detection thresholds for temperature anomaly TT and vorticity VOR (see text for definitions). The wind speed threshold is held constant: WT = 17 m s^{-1}. (top) TT is variable and VOR = 30.10^{-5} s^{-1}; (bottom) VOR is variable and TT = 3 K.

to WT); genesis location is defined as the first point along their tracks where TCs reach 17 m s^{-1}.

3. Convective parameterization: A sensitivity study

MCSs found in the tropics represent 250-km areas of concentrated deep convection organized in broad mesoscale cloud clusters. Within MCSs, 50-km areas of extreme convection can be activated and very occasionally initiate TC formation (Gray 1998). Whether they develop intense precipitation or not, MCSs are all triggered by small-scale mechanical forcings that are unresolved by our present model at 155-km effective resolution. Therefore, we rely on parameterization of convection to produce both the large-scale heat and moisture conditions of the SPCZ and the mesoscale conditions of TC genesis.

All sensitivity tests to convection schemes are generally concerned with the evolution of individual TC events over synoptic periods; to our knowledge, none have been reported on statistical properties of free-running long-term simulations. In this section, we propose such an experiment, comparing three WRF implementations of widely used convective precipitation (CP) schemes: BMJ (Janjić 1994), KF (Kain 2004), and GD (Grell and Dévényi 2002). The BMJ scheme is a convective adjustment scheme that initially had been developed for tropical areas (Betts 1986) and successfully tested in mesoscale TC simulations (Baik et al. 1990b). Its success owes to realistic heating and moistening in the vertical resulting from a simple relaxation to observation-based reference profiles (Janjić 2000). The last two CP schemes are mass flux–type schemes, which attempt to represent updrafts/downdrafts and entrainment/detrainment processes; they where initially developed to improve precipitation forecasts of synoptic events. The GD scheme, which uses a mass flux formulation based on averages from various closure assumptions and entrainment/detrainment rates, shows the worst results in our sensitivity tests, showing weak and patchy convection activity, numerical instability, and almost no TC formation. These results will not be overly commented on here because it is presently unclear whether its faulty behavior is a result of wrong implementation or an actual inability to handle tropical dynamics in long-term simulations.

a. *SPCZ sensitivity*

Simulated precipitation in the SPCZ is mainly produced by the CP scheme (see following section). It is also a good proxy for the thermal structure of the whole troposphere (Royer et al. 1998), that is, of the thermal environment of TC activity. It is therefore a natural choice for our model–data comparison. The modeled large-scale dynamics are less sensitive to the choice of CP scheme. In particular, the surface winds are reasonably close to the Quick Scatterometer (QuikSCAT) estimations, although slightly weaker (Chelton and Freilich 2005, and references therein).

The three CP schemes are evaluated against high-resolution precipitation data, which are only available from January 1999 to June 2004, thereby restricting the experimental window. The main precipitation dataset is the 0.25° Tropical Rainfall Measuring Mission (TRMM) product 3B-43, which combines estimates of precipitation generated from satellite-calibrated instruments (3B-42) and globally gridded rain gauge data (Adler et al. 2000). We have also used for comparison the 2.5° Global Precipitation Climatology Project (GPCP) dataset (Huffman et al. 1997) because it has been more widely used in recent studies (both datasets are monthly fields). Comparing measurements of west Pacific atoll precipitation rates to TRMM and GPCP, Adler et al. (2003) found a negative bias of approximately 10% for the two datasets. They also noted that differences between TRMM products computed with different algorithms (based on radar and radiance measurements) can reach 30% in the heavy precipitation areas of the SPCZ.

Figure 4 shows the mean precipitation patterns observed and simulated in the western Pacific. Locations of the austral summer (JFM) ITCZ and SPCZ are represented as the meridional maximum precipitation in the Northern and Southern Hemisphere, respectively (Vincent et al. 2009). The position of the ITCZ is very similar in each model run, whereas there are large discrepancies in the SPCZ location and intensity. TRMM is very similar to GPCP in this region, but offers a better resolution, as expected. Compared with observations, the simulated SPCZ using KF extends too far south (by 5°–10°) and has a zonal orientation east of 170°E rather than the classical northwest–southeast tilt. The location of the SPCZ in the BMJ experiment is much better. Regional mean SPCZ rain rates of BMJ are very similar to those of TRMM, but there are local discrepancies. Precipitation is overestimated east of the date line (by 2–4 mm day^{-1}), there is a bias in the SPCZ tilt east of 160°W, and the SPCZ is located about 3° too far north near the date line. Simulated precipitation over Papua New Guinea is also 2–3 times greater than in TRMM and GPCP, which can be attributed to the difficult treatment of high orography in models. Finally, precipitation is underestimated over northern Australia in all of the experiments.

We now compare the CP schemes for their impact on seasonal and interannual SPCZ variability. As shown in Lefevre et al. (2010), the migration of SPCZ location is a good indicator of seasonal variations as well as ENSO impacts on the southwest Pacific climate (through the longitudinal extension of the monsoon winds). Vincent et al. (2009) show that the main modes of SPCZ variability differ in the western and eastern parts of the SPCZ. Following this study, we define two indices to characterize the SPCZ location on either side of the date line. The western SPCZ index (SPCZ-$\mathrm{I_W}$) is constructed using the SPCZ latitude zonally averaged over 155°–175°E, while the eastern index (SPCZ-$\mathrm{I_E}$) is an average over 155°–175°W. In this section, we use monthly values of SPCZ-$\mathrm{I_W}$, while both indices are used in section 5 (with JFM rather than monthly mean values because the eastern SPCZ is not well defined in austral winter). The comparisons between SPCZ-$\mathrm{I_W}$ built from precipitation data and from WRF simulations using the three CP schemes are summarized in Table 1. The standard deviations of SPCZ-$\mathrm{I_W}$ from BMJ and KF are both very close to the observed ones. However, model–data correlations are much stronger using BMJ (0.64) than using KF (0.36). Note that these two correlation values would possibly be higher if the model could accurately simulate Madden–Julian oscillation (MJO). The latter indeed form the other important external forcing driving SPCZ variations at the intraseasonal time scale (section 5), but for reasons yet unknown the western boundary between GR2 and WRF solutions is not transparent to the propagation of this signal (section 5).

b. TC sensitivity

In addition to a better representation of large-scale conditions, the BMJ scheme provides the only realistic experiment in terms of TC counts: 6.6 TC yr^{-1} are observed [Joint Typhoon Warning Center (JTWC) data], while 8.2 TC $\mathrm{yr}^{-1}$are produced using BMJ compared to a much too large value of 25.6 TC yr^{-1} using the KF scheme (and only 0.2 TC yr^{-1} using the GD scheme). Because CP schemes have such a widespread impact on the preconditioning, genesis, and intensification of TCs, it is difficult at this point to interpret their various responses. Such an interpretation would require a better understanding of the schemes' trigger mechanisms and the interplay between subgrid-scale and grid-scale convection in mesoscale models. Here we can merely advance some suggestions.

Parameterization of convective transports is required in conditionally unstable situations where only intense, subgrid-scale motion and instability can trigger deep convection. However, when the air becomes saturated and grid-scale vortex motion has intensified, the resolved motion is able to sustain extreme convection, dominating the parameterization work along the eyewall (see section 4b). This model behavior, also described in Baik et al. (1990a) using the BMJ scheme, is consistent with observations that radial eddy fluxes are only dominant in the early stages of TC formation, while frictionally forced convergence would dominate later stages (see Gray 1998 for a review). The KF scheme is designed to allow more interaction between grid-scale and subgrid-scale convection, first by basing the trigger function on resolved vertical motion, and then by feeding back parameterized vertical motion to the resolved scales. As a result, this scheme is more sensitive to horizontal resolution (Gallus 1999) and may overstimulate the grid-scale contribution to deep convection at the present resolution, especially in the early stages of TC evolution. This would explain the large production of cyclones and the shift in TC distribution, from storm level to intense TCs (not shown). Note that our suggestion is reminiscent of Gray's remark (Gray 1998) that the most recent CP schemes are probably too preoccupied with catching the full intensity of TC properties in the later formation stages, because this represents the most important task for event forecasters who bypass the earlier stages using data assimilation. On the other hand, a tuning of the KF trigger function and mass flux

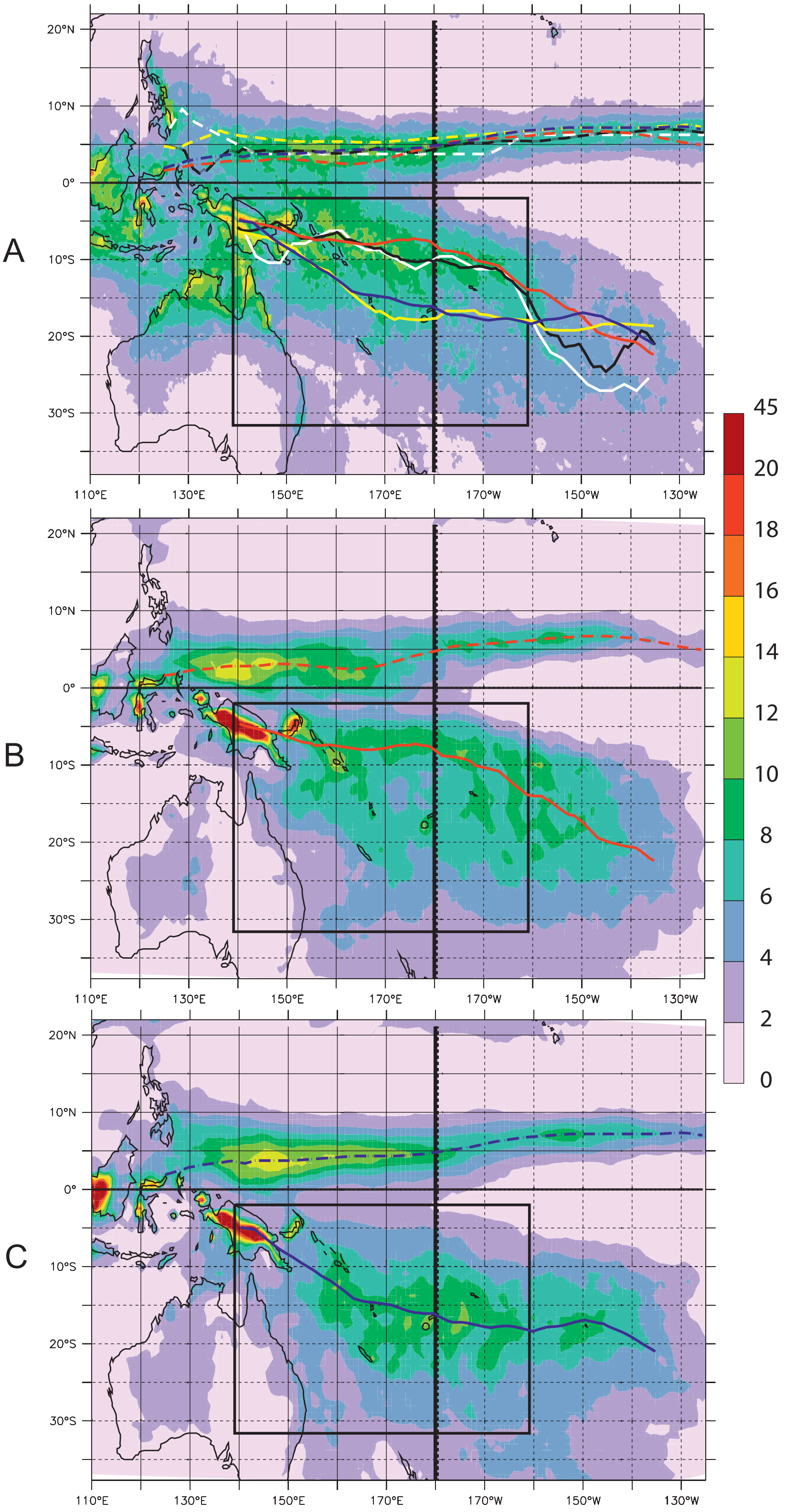

FIG. 4. Mean JFM precipitation from 2000 to 2004 (mm day^{-1}). (a) TRMM precipitation, with position of ITCZ (dashed) and SPCZ from different datasets: TRMM (black), GPCP (white), BMJ (red), KF (dark blue), and GD (yellow). (b) WRF–BMJ precipitation. (c) WRF–KF precipitation. The inner domain of integration is delimited (black box). The lines representing the SPCZ are defined as maxima of the meridionally smoothed precipitation field.

TABLE 1. Variability of the monthly western SPCZ index; σ is standard deviation, and r(GPCP) and r(TRMM) are correlation coefficients comparing each series with GPCP and TRMM, respectively. The values inside the parentheses are correlations are not significant at 95% according to the Student's t test.

Index	Data	σ	r(GPCP)	r(TRMM)
SPCZ-I_W	GPCP	4.1	1	0.89
	TRMM	3.6	0.89	1
	BMJ	3.6	0.63	0.64
	KF	3.5	0.36	0.34
	GD	2.8	(0.20)	(0.23)

formulation could probably improve the representation of transition between subgrid-scale and grid-scale convection in our experiment (Hong and Pan 1998).

It is interesting that, by shifting the pattern of large-scale convergence lines with numerous mesoscale disturbances to frequent intense vortices, the excess of the intense grid-scale convection would also affect the large-scale SPCZ conditions. In our BMJ experiment, parameterized convection appears to be closely linked to the resolved low-level moisture convergence, an expected relation on which earlier CP schemes were entirely based. In turn, convection areas produce low pressure conditions that tend to drive convergent flows. In the KF experiment, there is a shift of convection activity from the broad areas of convergence to cyclonic vortices further south, possibly explaining the southward SPCZ shift. However, a thorough investigation of SPCZ and TC sensitivity to CP schemes is left to further research, which should also consider the response of parameterized convection to changing resolution and ocean feedback. We conclude for now that the BMJ scheme is an obvious choice for our study and the next sections will describe in more detail the TC simulation using this parameterization.

4. TC climatology

The climatology of TC activity in a 25-yr, present-climate simulation of the South Pacific is evaluated and analyzed in this section using the available observations. Statistical analyses are performed using the tracking method described in section 2 and compared with the JTWC best tracks (Chu et al. 2002). Short-lived tracks (shorter than 1.5 days) are removed from JTWC data to be consistent with the tracking method, and because the detection of short-lived TCs in satellite data is sensitive to changes in observational systems and analysis technics (Landsea et al. 2010).

a. Structural properties

We first describe the vertical structure of simulated tropical cyclones to assess the model's ability to accurately reproduce the structural properties of actual systems. Several cyclonic events have been analyzed in the experiment, and a three-dimensional plot of a representative modeled TC is given in Fig. 5. This example presents a maximum 10-m wind speed of 32 m s^{-1}, and a maximum 700-hPa wind speed of 45 m s^{-1}. The maximum vertical wind speed is 1.7 m s^{-1} in this case and is always below 2 m s^{-1} in all of the other simulated cyclones. It appears to be at the lower end of the range given by airplane observations, although the latter generally concerns TCs that are more intense than those of our simulation. For example, Marks (1981) has recorded a sustained updraft velocity above 3 m s^{-1} over a distance of 40 km (about the resolution of the model), in a TC reaching a maximum wind speed $V_{\max}$ of 80 m s^{-1}; Black et al. (1996) have observed updrafts of 4–8 m s^{-1} over shorter distances of 10 km in a TC with $V_{\max} \simeq 75$ m s^{-1}. The maximum simulated vertical ascent velocity is found between 600 and 400 hPa, which is in agreement with Jorgensen et al. (1985). There is a well-developed eye, with a maximum subsident velocity of 0.3 m s^{-1} between 600 and 400 hPa, which is 3 times the typical value mentioned by Emanuel (2003). Possible misrepresentation of extreme vertical velocities in the model may be

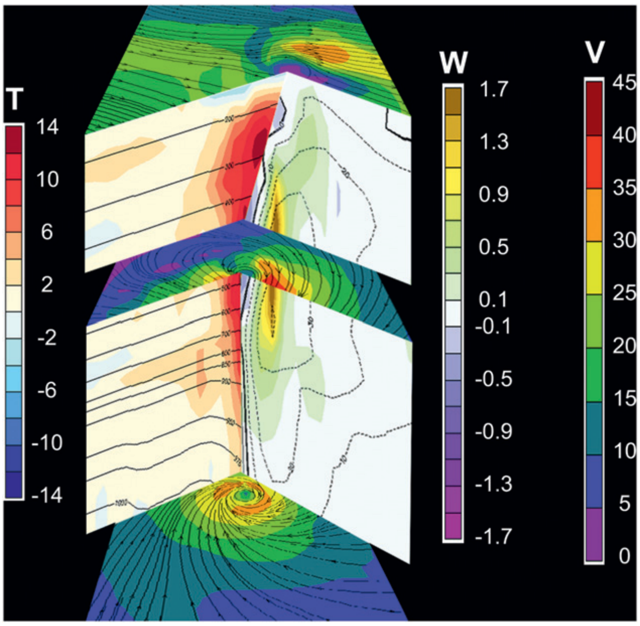

FIG. 5. Three-dimensional presentation of a modeled tropical cyclone (model date: 1800 UTC 8 Apr 1983). Horizontal maps present the horizontal wind speed (V, m s^{-1}), with streamlines at 10 m, 510 hPa, and 220 hPa. (left) Warm core temperature anomalies (T, K) with respect to the mean temperature found 20° away from the cyclone eye are shown; black contours indicate pressure (every 100 hPa above 900 hPa, and every 25 hPa below 950 hPa). (right) Vertical wind speed (W, m s^{-1}) and tangential wind speed (dashed contours, contours every 10 m s^{-1}) are presented.

due to missing subgrid-scale updraft velocity along the underresolved eyewall. However, we conclude that in view of observational studies, TCs vertical motions are well captured by our mesoscale model.

The maximum warm core anomaly is found between 300 and 200 hPa, where it reaches 14 K. This value is similar to those from the literature [e.g., 16 K at 250 hPa observed with dropsondes by Hawkins and Imbembo (1976) in a TC reaching $V_{\max} \simeq 65$ m s^{-1}; 11 K at 400 hPa observed with dropsondes by Halverson et al. (2006) in a TC reaching $V_{\max} \simeq 54$ m s^{-1}; 8 K in the upper troposphere of a simple hurricane model with $V_{\max} \simeq 60$ m s^{-1} (Emanuel 1995, 2003)]. Moreover, the vertical structure of temperature anomalies (seen from the vertical cross section in Fig. 5) is very similar to that derived from satellite imagery by Kidder et al. (2000) and from aircraft dropsondes by Hawkins and Imbembo (1976).

b. *Precipitation*

As mentioned before, the convection in MCSs is not explicitly resolved by the model whose effective resolution is about 155 km. It appears, however, that the parameterization of convection within these systems is able to initiate cyclogenesis. All of the model TCs are initiated by intense convective events and the mean maximum precipitation rate at genesis time (found by the tracking method) is 5.9 mm h^{-1} (standard deviation $\sigma = 1.5$ mm h^{-1}). The highest values are observed at the mature stage of TC formation after tangential winds have strongly intensified and triggered intense updraft from frictionally forced convergence. At this stage, the spatial maximum of mean TC precipitation is 20 mm h^{-1} ($\sigma =$ 10 mm h^{-1}), with the highest values in the whole experiment exceeding 50 mm h^{-1}. As a comparison, Kelley et al. (2004) note that rainfall adjacent to the TC eye is higher than 10 mm h^{-1} most of the time and is up to 100 mm h^{-1} in small areas (from 163 precipitation radar overflights of TCs with intensity greater than 33 m s^{-1}). At the intensifying stage in the model, there is a transition from subgrid-scale convective precipitation to grid-scale precipitation, which takes off to extreme values, consistently with idealized mesoscale simulations (Baik et al. 1990a). A typical example of TC development is illustrated in Fig. 6. After the transition period between subgrid-scale and grid-scale precipitation (characterized by oscillations of grid-scale precipitation that are described in Baik et al. 1990a), grid-scale rain rate shows a sharp increase and closely follows the time evolution of low-level wind speed and vorticity. Even though parameterized convection is an absolute requirement for cyclogenesis at this resolution, extreme precipitation results from resolved updrafts, with subgrid-scale rain rates representing only one-quarter of grid-scale peak values.

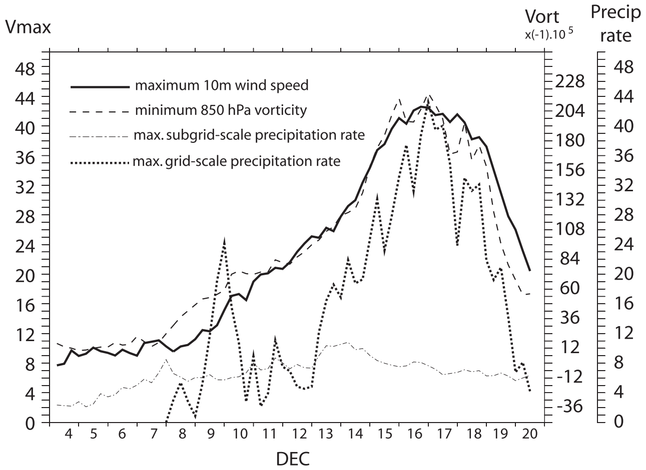

FIG. 6. Example of the evolution of a modeled tropical cyclone detected by automatic tracking in December of model year 1981 (thin dashed line). Wind speed (m s^{-1}), relative vorticity (s^{-1}), and precipitation rate (mm h^{-1}) are shown.

A question of interest is whether extreme TC rain rates contribute to a substantial part of tropical precipitation, that is, within the SPCZ. The SPCZ is defined here as the area where JFM 25-yr mean precipitation is higher than 6 mm day^{-1} (Vincent et al. 2009). Results for various precipitation classes are shown in Table 2. The classification first separates grid-scale precipitation resolved by the model from subgrid-scale precipitation parameterized in the CP scheme. Precipitation classes are further defined according to rain rates at each time step. Each convective precipitation intensity is related to a typical cloud cluster size. Cluster size in each class is given by the maximum width of a rectangle covering the largest cluster of a given class at each time step (the rectangular shape enables one to measure width rather than length of cloud bands). It shows that simulated climatological precipitation is mostly a result of broad mesoscale clusters, with 68% of JFM precipitation originating from systems with rates lower than 3 mm h^{-1}. TCs are responsible for nearly 10%

TABLE 2. Classification of modeled SPCZ precipitation in JFM, according to identified clusters of precipitation rates. Size statistics are constructed from size values estimated at each time step. The SPCZ is defined as the zone with climatological precipitation rates larger than 6 mm day^{-1}, with Papua New Guinea being excluded. Here, σ is standard deviation.

Precipitation class	Size	σ	SPCZ %
Grid scale	>1000 km		1.8%
Subgrid scale 0–1 mm h^{-1}	1010 km	230 km	25.1%
Subgrid scale 1–3 mm h^{-1}	500 km	110 km	42.8%
Subgrid scale 3–5 mm h^{-1}	280 km	80 km	17.6%
Subgrid scale >5 mm h^{-1}	200 km	40 km	3.2%
Subgrid scale cyclonic	520 km	120 km	9.5%

of the total amount of precipitation in the climatological summer SPCZ, with a small fraction being contributed by grid-scale precipitation. This is comparable to the value of the 5% contribution of TCs to the 1999–2006 JFM rainfall in the South Pacific basin (0°–40°S, 135°E–150°W) found by Jiang and Zipser (2010) from TRMM data. The grid-scale precipitation is thus responsible for the modeled TC peak values but is restricted to the eyewall region, while subgrid-scale precipitation is active over a much larger area with a classical spiral pattern. Note that TC displacements to higher latitudes (out of the cyclogenesis area) may contribute to extending the edges of the SPCZ. For example, the mean contribution of TC precipitation to simulated climatological precipitation around 20°S can reach 20% (not shown).

c. *Intensity distribution*

The distribution of 10-m wind speed of simulated cyclones is compared to the values from JTWC best tracks. The JTWC wind speed data are 1-min-average sustained wind speed, which needs to be compared with the 3-min-average values of the model (corresponding to the model time step). Note that JTWC wind speeds are estimated from satellite imagery following Dvorak (1975, 1984) and that the method contains some uncertainty. In addition, wind speed data are often missing before 1983, and we thus limit our comparison to the period from 1983 to 2004. Figure 7 shows that WRF is able to generate intense tropical cyclones of up to 47 m s^{-1}. This is approximately the maximum wind speed obtained by recent modeling studies (Knutson et al. 2007; LaRow et al. 2008; Zhao et al. 2009). This upper limit and the speed distribution are sensitive to model resolution and parameterizations. In our case, the simulated distribution exhibits too few very intense TCs and too many weaker ones (between 17 and 27 m s^{-1}). The shift in distribution toward the lower end is probably due to insufficient model resolution. As reported by Emanuel and Nolan (2004), there is a nontrivial dependence of model storm intensity on horizontal resolution, even at grid spacing as small as 1 km, because maximum wind speed near the eyewall results from both internal instability processes and external forcing. Additionally, the lack of oceanic feedback in the atmospheric model may produce a positive intensification effect on tropical storms, thus enhancing (from the lower end of the distribution) the intensity category of named cyclones.

d. *Seasonal cycle*

For robustness, we now only consider in both model and observations TCs whose 10-m wind speed exceeds 22 m s^{-1} at least once along the track. The period considered for comparison here is also 1983 to 2004.

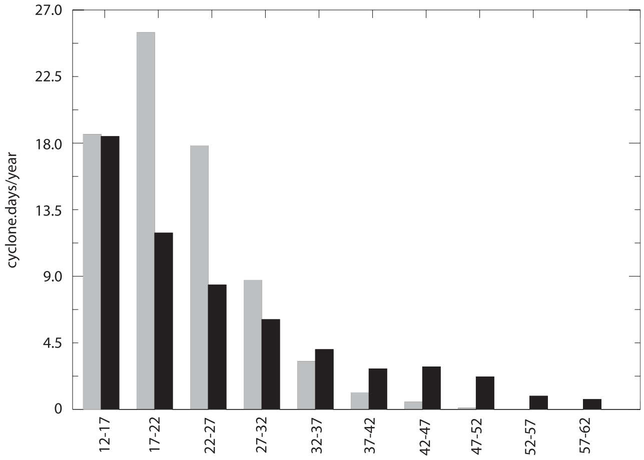

FIG. 7. Distribution of the maximum 10-m wind speed in observed cyclones (black) and in simulated cyclones (gray) between 1983 and 2004 (cyclone days versus m s^{-1}).

First, seasonal distribution of TC genesis and occurrence for the period 1983–2004 are plotted in Fig. 8. The general aspect of the distribution is similar in the model and observations, with most of the cyclones appearing in JFM. There are, however, some differences: 54% of the TC genesis occur in JFM in the experiment against 70% in the JTWC data. There is even a small background level of cyclogenesis persisting in the cold season [July–September (JAS)], which has never been observed (in the 1979–2004 period). To understand this peculiar result, we note that most of the JAS tropical cyclones are simulated near the northern boundary of the inner domain (not shown). An interesting feature is that among the 13 cyclones simulated in JAS between 1979 and 2004, 7 are generated in 2002 and 2003, that is, when the mean JAS SST was significantly higher than the mean 1979–2004 JAS SST in the cyclogenesis sector (i.e., 50% more than the standard deviation in the JAS time series). The mean 2002–03 JAS vertical wind shear (between 950 and 200 hPa) is also lower than the mean 1979–2004 JAS value (i.e., 10% less than the standard deviation). These large-scale anomalies, known as El Niño Modoki (Ashok et al. 2007), may have favored the simulated winter cyclogenesis (by increasing enthalpy fluxes to the atmosphere and midtropospheric humidity levels). According to the JTWC data however, the observed SST positive anomaly in winter of 2002/03 did not lead to cyclogenesis. However, the mean 2002–03 JAS precipitation rate from GPCP was higher than the 1979–2004 JAS mean (40% higher than the standard deviation). This suggests that the model may be overly responsive to favorable large-scale conditions, by overrepresenting either the required trigger mechanisms of TC genesis or the convective instability processes of first and second kinds (Gray 1998). Nevertheless, this model bias remains small compared to seasonal and interannual variability.

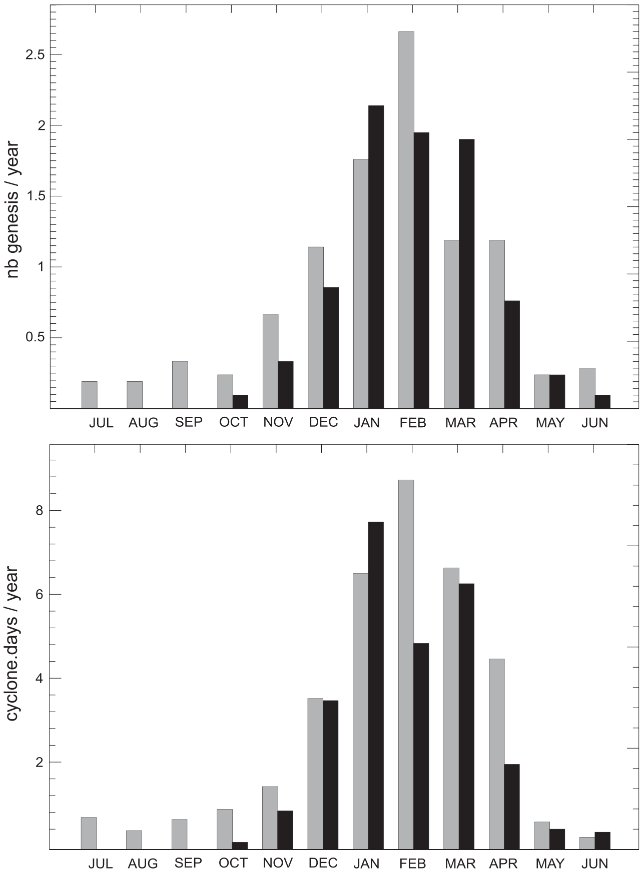

FIG. 8. Seasonal statistics of model TCs for the period between July 1983 and June 2004. (top) Model TC genesis number (cyclones reaching 22 m s^{-1}). (bottom) Number of cyclone days with 10-m wind speed higher than 22 m s^{-1}. JTWC data (black) and simulations (gray) are shown.

e. *Spatial distribution*

As in Ramsay et al. (2008), probability density functions (PDFs) are used to describe the spatial distribution of both genesis and occurrence in the model and JWTC data. To generate PDFs, we compute anisotropic Gaussian functions, with an associated standard deviation in meridional and zonal directions respectively of 1° and 2° for occurrence, and 1.5°and 3° for genesis. The PDF is the normalized sum of these individual Gaussian functions associated with TC genesis or occurrence steps. This gives

$$\int\int_{\text{domain}} \text{PDF}(x, y, t)\, dx\, dy = N(t), \qquad (1)$$

where $N(t)$ is the total number of either TC genesis or occurrence at time t. Figure 9 represents the 1983–2004 mean PDF for genesis and occurrence, respectively. Only tracks whose 10-m wind speed reaches 22 m s^{-1} at least once are considered (see section 2c). Simulated TC genesis is defined as the first point where wind speed reaches 17 m s^{-1} along those tracks, while observed genesis is given by the JTWC best-track data.

The area of high TC genesis probability in the model shows notable differences with JTWC data. It appears too close to the equator (the maximum of zonal mean PDF is at 9.5°S in the model, but at 14.5°S in the observations), and there is an excess of cyclogenesis east of 170°W and a lack near Australia. These discrepancies are explained in the next section. The simulated occurrence is more accurate, being centered near 16°S both in the JTWC data and in the model, although the latter appears more dispersed with more cyclone days east of the date line. The model results in terms of intensity, and spatial and seasonal distributions of cyclonic activity are good when compared to previous modeling studies in this region (Walsh et al. 2004; Zhao et al. 2009).

f. *Environmental forcing*

Chauvin et al. (2006) estimate a seasonal genesis index, the convective yearly genesis parameter (CYGP; Royer et al. 1998), from the climatological conditions simulated by their high-resolution model of the North Atlantic region. They show that, despite local discrepancies, the genesis index matches the general distribution pattern of TC genesis explicitly simulated by the model. This comparison is reproduced here, and mean CYGP for the period of 1983–2004 is presented in Fig. 10. Note that our genesis index is constructed using 5-day averages of atmospheric conditions immediately prior to every genesis event. This filtering procedure is made to avoid the signature of mature TCs and highlight the large-scale environment favorable to cyclogenesis, although the difference is small from the original unfiltered CYGP.

Figure 10 shows that small areas of strong genesis index values are apparent near the Solomon and New Britain islands but these are artifacts of the high-resolution data (small-scale, high relative vorticity values should be filtered out). At larger scales, the genesis index is very similar to the PDF of genesis derived from the model (black contours in Fig. 10), with two main relative maxima at the same locations. This confirms the statement of Chauvin et al. (2006) that CYGP is a good indicator of statistical locations of simulated genesis in a high-resolution model. It also shows that the spatial distribution of cyclogenesis is controlled by the large-scale environment. Therefore, the differences with observed cyclogenesis distribution exposed in the previous section can be attributed to misrepresentation of the large-scale atmospheric conditions.

5. TC interannual variability

The model mean seasonal TC genesis and interannual standard deviation σ_N are very comparable to the

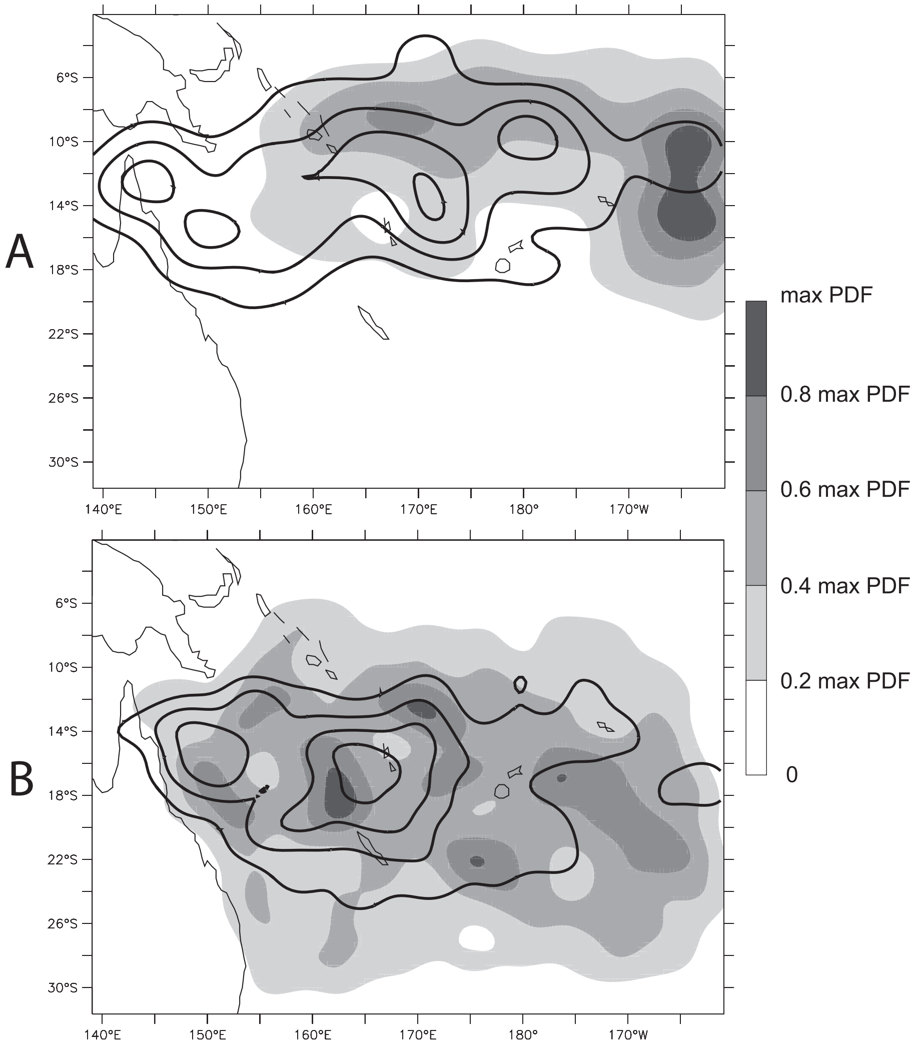

FIG. 9. PDF of TC (a) genesis and (b) occurrence for the period between July 1983 and June 2004 (cyclones reaching 22 m s^{-1}). The model PDF is shown in gray and the corresponding PDF of the JTWC data is represented with black contours (interval: 0.2 max PDF).

observations: 8.2 ± 3.5 cyclones are produced seasonally in the model, compared with 6.6 ± 3.0 in the observations. Figure 11 presents the interannual variability of seasonal TC genesis averaged over the domain of integration. Interestingly, while the standard deviations are similar in the model and observations, there is no correlation between the two time series within the whole South Pacific area. In addition, the variability of TC genesis resulting from environmental control, as estimated from the CYGP genesis index ($\sigma_f = 1.8$), is only about half of the total value σ_N (Fig. 11; note that CYGP is normalized so that the mean number of cyclogenesis estimated from the index equals the explicitly resolved genesis number). This result is insensitive to the choice of genesis index [CYGP, Gray's index (Gray 1979), or genesis potential index, GPI, from Emanuel and Nolan (2004)], as shown by Menkes et al. (2010, manuscript submitted to *Climate Dyn.*) using reanalysis data. We argue in this section that the lack of global correlation can be interpreted partly as compensating forced variability between southwestern and northeastern regions and partly as a product of stochasticity.

a. Forced variability

The genesis index that was previously used (CYGP) shows favorable environmental conditions in areas of deep convection. It would be expected to be maximum at the SPCZ line where convective available potential energy is maximum, but background low-level cyclonic vorticity tends to shift the most favorable conditions to the south (Fig. 10, see also Vincent et al. 2009).[1]

---

[1] The literature has not settled the question of whether the background low-level vorticity is a truly large-scale dynamical structure or a residual of the numerous mesoscale vortices stemming from the southern edge of the SPCZ. We leave this question open for further research.

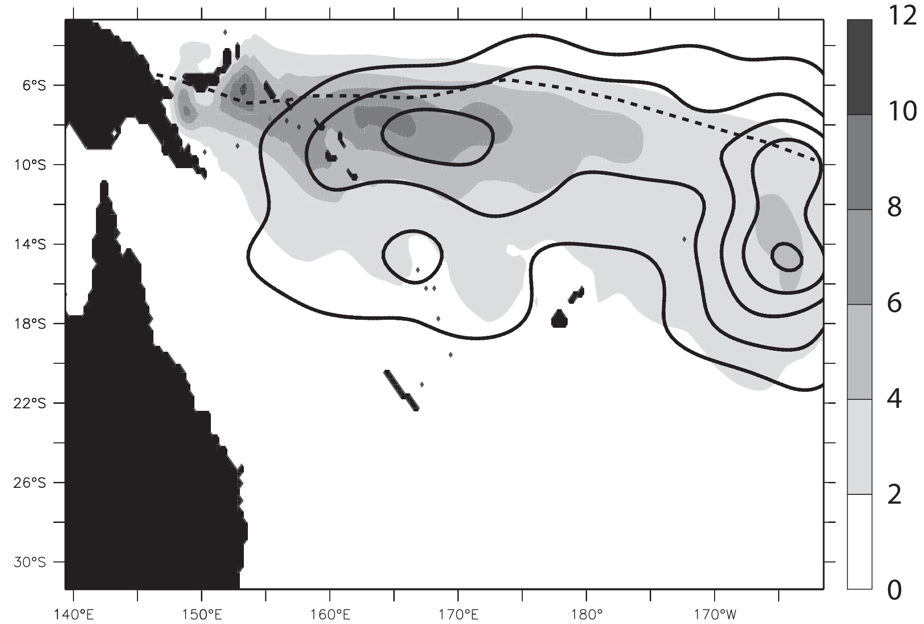

FIG. 10. Mean 1983–2004 CYGP. Land is black. The corresponding mean PDF of TC genesis is represented (thick contours, interval: 0.2 max PDF), as is the mean 1983–2004 SPCZ location (dashed thick line).

Nevertheless, the variability of the genesis index is tightly related to the SPCZ position, which therefore represents a simpler index for genesis variability in the South Pacific than CYGP (Vincent et al. 2009). The simulated SPCZ position is analyzed through a latitude index, as in section 3, but now considers both the western and eastern indices (SPCZ-I_W and SPCZ- I_E for regions west and east of 175°E, respectively) computed using JFM mean precipitation; seasonal and intraseasonal variations are excluded from this analysis. The simulation is again compared with GPCP precipitation data. Table 3 shows that the model SPCZ indices have significant correlations to GPCP data (a correlation of 0.71 for SPCZ-I_E and 0.63 for SPCZ-I_W, both of which are significant at 99%). As in Vincent et al. (2009), four classes are defined to represent yearly changes of the SPCZ position (Fig. 12, which are closely related to ENSO phases):

- strong El Niño years,
- ‘‘positive’’ years (including moderate El Niño and some neutral ENSO years),
- ‘‘negative’’ years (including La Niña and some neutral ENSO years), and
- neutral years.

Table 4 shows error statistics (bias and root-mean-square error) of the simulated SPCZ position in the four regimes. It confirms that the modeled SPCZ in neutral and negative conditions is too zonal (with a positive bias of SPCZ-I_E). A zonal orientation of the SPCZ in nature is characteristic of strong El Niño conditions and is shown to favor TC genesis in the central Pacific (Vincent et al. 2009). This may explain our model bias toward excessive eastern cyclogenesis. In the eastern regions, the largest correlations and lowest RMSE are associated with strong El Niño conditions, that is, zonalization of the SPCZ, which occurs clearly in both the model and data.

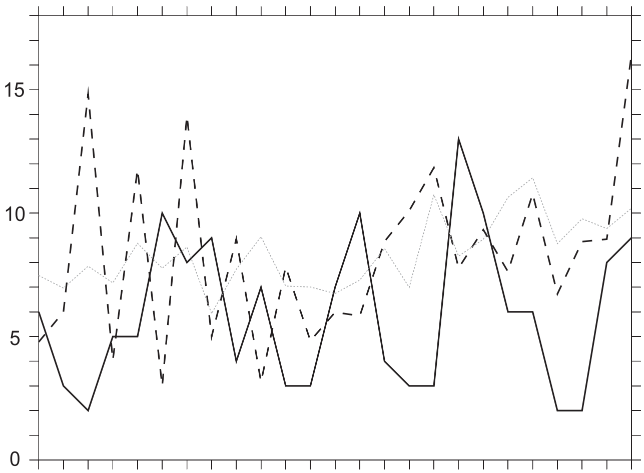

FIG. 11. Number of South Pacific TCs per season (July–June) in the JTWC data (solid line) and in the 25-yr standard experiment (dashed line). Only TCs reaching 22 m s^{-1} are counted. An estimation of TC genesis by the CYGP genesis index applied to the model variables is represented (dotted line). Pearson’s correlation between JTWC and WRF genesis number is $r = 0.30$ (not significant at the 90% level), and the correlation between WRF genesis number and CYGP is $r = 0.48$ (significant at the 95% level).

TABLE 3. Statistics of JFM SPCZ indices from 1979 to 2003; σ is standard deviation, and r (GPCP) is the correlation coefficient comparing GPCP and model (with associated significance according to the Student's t test).

Index	Data	σ	r (GPCP)
SPCZ-I_W	GPCP	3.6	1
(JFM)	WRF	4.4	0.63 (99%)
SPCZ-I_E	GPCP	6.1	1
(JFM)	WRF	4.6	0.71 (99%)

The spatial pattern of correlation with ENSO is given by maps of correlation coefficients between PDFs of cyclogenesis (for both the model and JTWC data) and mean November–April Niño-3.4 index (Fig. 13). These maps should be analyzed in parallel with Fig. 9, which presents model–data comparisons. The pattern of ENSO correlation for the JTWC data is consistent with a northeast shift of cyclonic activity during El Niño phases and a southwest shift (nearer to Australia) during La Niña phases (see the introduction). In the WRF experiment, there is the same pattern of correlation (with strong and significant local values), although the line separating positive and negative correlations appears to be shifted to the northeast, which is consistent with a similar bias in the SPCZ lines (Fig. 13). In both the model and data, positive correlations are located between SPCZ lines representing, respectively, strong El Niño conditions and La Niña conditions, while negative correlations are south of the SPCZ position during La Niña.

The strong interrelation between cyclogenesis and the SPCZ position may partly explain that cyclogenesis variability in the South Pacific is often poorly simulated (Zhao et al. 2009), because proper SPCZ representation is a difficult task for atmospheric models. A Newtonian nudging approach, as used by Knutson et al. (2007) in the North Atlantic, would be a way to circumvent the problem, but it would also impact the TC formation process. It has been suggested (Matthews et al. 1996) that one particular source of error in the representation of SPCZ variability may be associated with the role of the MJO, which is not captured by our model. Matthews et al. (1996) even suggest that the existence of the mean SPCZ itself may be related to the MJO. The fact that our regional model captures the mean SPCZ characteristics tends to invalidate this idea, but some of the model–data discrepancy in the interannual variability can still be attributable to missing MJO in the model. Nevertheless, in the next section, we show that the largest part of the discrepancy is due to stochasticity.

In summary, the model is able to reproduce the observed variability of TC genesis by the measure of standard deviations. The forced component of this variability is essentially associated with ENSO events (particularly strong El Niño phases) that impact the SPCZ position through meridional translation and zonalization. Displacement of the SPCZ position produces a corresponding displacement of cyclogenesis, which is expressed

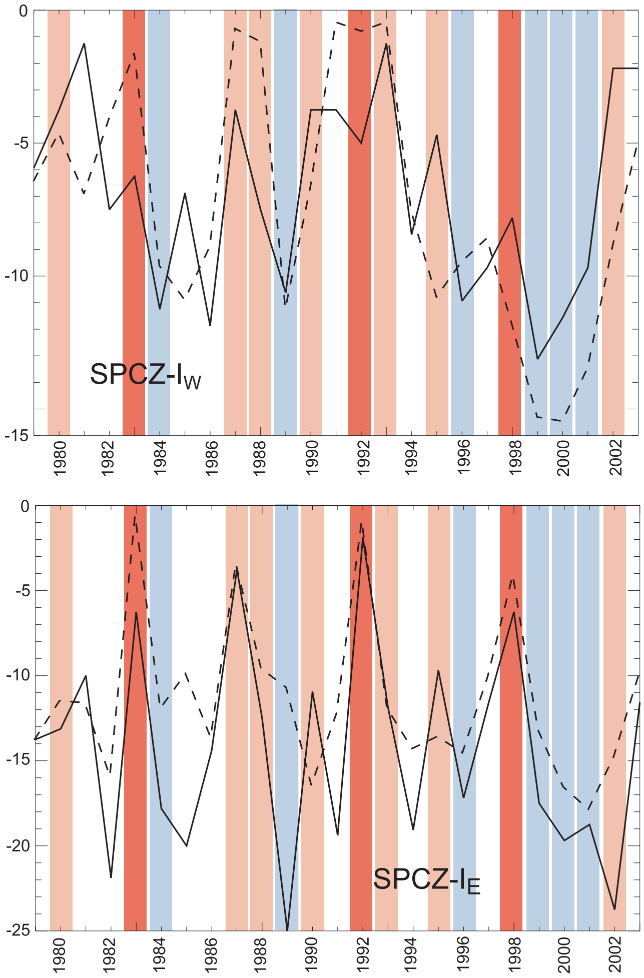

FIG. 12. SPCZ indices time series. Values are JFM means for each year; the indices computed from GPCP precipitation data (solid lines) and the 25-yr WRF experiment (dashed lines) are represented; "positive" (light red), "negative" (light blue), and strong El Niño (dark red) years are indicated.

TABLE 4. Mean bias and RMSE of the model JFM SPCZ indices compared with GPCP estimations (° latitude). A positive (negative) bias indicates that the SPCZ line is too far north (south) in the model. The categories "negative," "positive," and "strong El Niño" are shown in Fig. 12 and correspond to definitions given in Vincent et al. (2009).

Index		Neutral	Negative	Positive	Strong El Niño
SPCZ-I_W	Mean bias	0.2	−0.5	−0.6	1.9
	RMSE	3.1	2.2	4.2	4.1
SPCZ-I_E	Mean bias	3.3	5.1	0.6	2.8
	RMSE	4.9	6.7	4.4	3.5

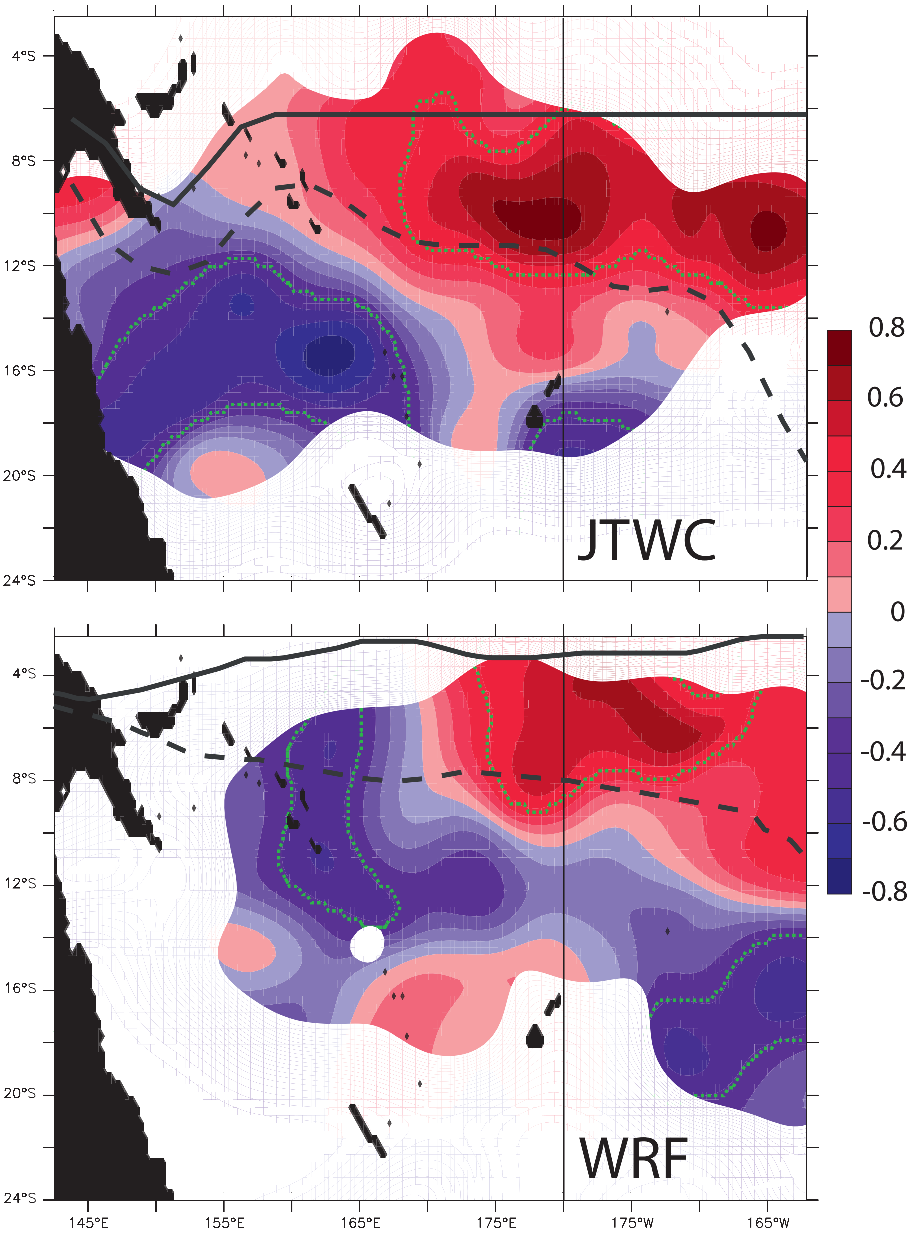

FIG. 13. Correlation coefficients between the annual mean PDF of cyclogenesis and the Niño-3.4 index averaged from November to April, for the (top) JTWC data and (bottom) WRF interannual simulation. Correlation significances of 90% according to the Student's *t* test are represented (green dotted contours). SPCZ lines are superimposed and represent strong El Niños conditions (solid line) and La Niña conditions (dashed line).

in genesis–ENSO correlation maps as a dipole pattern. Therefore, even though local correlations can be strong, the dipole pattern results in compensating variability over the whole cyclonic activity area. The reason that the broader scale is important to consider is that TC occurrence, and hence tropical cyclone hazard, results from dispersion of TCs around the genesis location. Figure 14 shows that the dipole pattern of correlation is lost for TC occurrence as positive genesis anomalies travel southwestward (with TCs advected by the mean tropospheric flow) and mix with negative anomalies generated in the Coral Sea.

b. Stochasticity estimation

Any regional model exhibits internal (intrinsic) variability that mostly depends on synoptic conditions, season, region, and model configuration (e.g., Giorgi and Bi 2000; Lucas-Picher et al. 2008). Intrinsic variability is produced by nonlinear interactions occurring at the mesoscale and synoptic scales when the domain of integration is wide

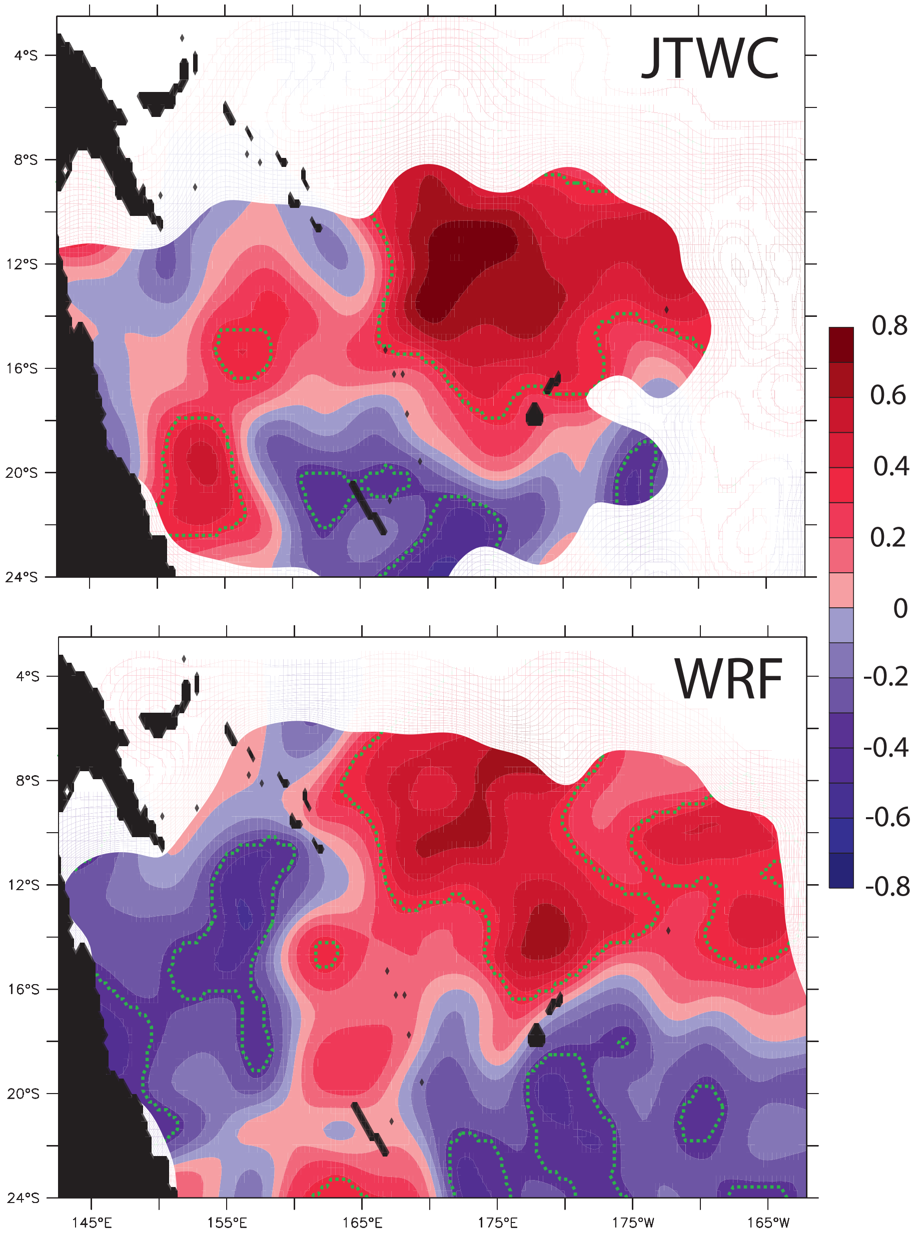

FIG. 14. Correlation coefficients between the annual mean PDF of occurrence and the Niño-3.4 index averaged from November to April, for the (top) JTWC data and (bottom) WRF interannual simulation. A correlation significance of 90% according to the Student's *t* test are represented (dotted green contours).

enough to allow for the interior dynamics to depart from the solution imposed by the lateral boundary forcing. Our objective in this section is to estimate the internal part of variability in TC activity. Error propagation rules will also provide an estimation of the part that is only forced by environmental conditions. This study thus provides a measure of seasonal predictability, that is, a measure of the stochastic error made in attempting seasonal predictions using environmental indices.

We have devised a new experiment where the regional model is forced by climatological fields. Climatological lateral and surface forcings, derived from GR2 1979–2004 means, are repeated for 10 yr. This experiment constitutes an ensemble simulation, with exactly the same forcing but different initial states every year. As shown by Alexandru et al. (2007), a 10-member ensemble is sufficient to investigate the internal variability of the model. In the climatological simulation, the mean number of TC genesis exceeding 22 m s^{-1} (in the inner domain) is 7.6 cyclones $season^{-1}$, that is, close to that of the standard experiment described in the previous section. The standard deviation around the mean is 1.7 cyclones $season^{-1}$

while the number of genesis remains within the range of 5–10 cyclones season^{-1}.

The modeled internal variability of TC genesis may be related to both mesoscale and synoptic events. To set apart those two possibilities, the genesis index can be applied to the climatological simulation. Here again, CYGP is integrated over the domain and normalized so that the mean number of cyclogenesis estimated from the index equals the explicitly resolved genesis number. The variability of the normalized genesis index is much lower ($\sigma_f = 0.4$) than the variability of the number of detected cyclones ($\sigma = 1.7$) with no significant correlation between the two time series. In addition, the spatial pattern of the genesis index variance (not shown) suggests that the index variability is weak near its mean maximum, which confirms that the area of large genesis probability is the same every repeated year. We conclude that the stochastic variability of model cyclogenesis in the climatological experiment is essentially related to mesoscale processes rather than synoptic variations of environmental conditions. This result is consistent with the stochastic nature of mesoscale interactions and its suggested importance in TC genesis (Simpson et al. 1997).

Our simulations further allow description of the uncertainty propagation associated with random processes by considering the yearly TC genesis count as a product of forced and stochastic variability functions (von Storch and Zwiers 2001),

$$\begin{cases} N(t) = \phi_s(t).\mathrm{GI}(t) \\ \overline{N}^t = \overline{\mathrm{GI}}^t \end{cases}, \qquad (2)$$

where $\phi_s(t)$ is a stochastic function; $N(t)$ is the annual cyclogenesis count; and $\mathrm{GI}(t)$ is annual, spatially integrated, and normalized CYGP. We find that the values of $\ln[N(t)/\mathrm{GI}(t)]$ follow a normal distribution in both climatological and interannual experiments [using a Shapiro–Wilk test of normality with $p = 0.10$; Shapiro and Wilk (1965)]. In the 25-yr interannual experiment, $\phi_s(t)$ follows the lognormal distribution Log-$N(\mu = -0.05; \sigma = 0.35)$ with mean and standard deviation $\overline{\phi_s}^t = 0.96$ and $\sigma_s = 0.36$. To test the usefulness of this law, 10 000 realizations of the interannual experiment were generated using random values of ϕ_s in Eq. (2). The resulting statistics of the reconstructed TC genesis number give 8.0 ± 3.3 cyclones season^{-1}, which is very close to the simulated values (8.2 ± 3.5). Because GI and ϕ_s are uncorrelated variables ($r = 0.01$), the rules of uncertainty propagation suggest the following statistical relations between forced and stochastic variability:

$$\left(\frac{\sigma_N}{\overline{N}^t}\right)^2 \simeq \left(\frac{\sigma_f}{\overline{\mathrm{GI}}^t}\right)^2 + \left(\frac{\sigma_s}{\overline{\phi_s}^t}\right)^2, \qquad (3)$$

where σ_N, σ_f, and σ_s are the standard deviations of genesis number, genesis index (lowerscript f stands for forcing), and stochastic distribution, respectively. It is a direct relation between the variance of genesis counts and the mean genesis number $\overline{N}^t$. If validated, it may be applied (in the South Pacific) to correct estimations that are based on the sole use of a genesis index. A first validation is provided by comparing in Table 5 the values of the three relative variance terms of Eq. (3). This comparison also shows that stochasticity may play a larger role (70% of total variance) than forcing in the interannual variability of cyclogenesis, although this partition is dependent on the averaging region of interest. We checked that Eq. (3) remains valid in subregions of the southwest Pacific and that interannual forcing has a larger comparative effect in regions of strong positive or negative correlations with ENSO.

However, these estimations are affected by a degree of uncertainty associated with the capacity of the genesis index formulation to accurately represent the environmental forcing. If CYGP is accurate, we would expect to find the same stochastic distribution ϕ_s in the climatological and interannual experiments, but the standard deviation σ_s is 0.22 in the climatological experiment instead of 0.36. Even though these values are not significantly different given the small number of simulated seasons (an F test does not reject the hypothesis of equal variance at the 10% level), they may suggest that stochasticity is overestimated in the interannual experiment analysis (as a result of uncertainties in the CYGP formulation), or alternatively that the climatological experiment underestimates interactions between forced and stochastic processes. In any case, we can safely conclude that stochastic variability resulting from mesoscale interactions in the South Pacific is never negligible and may even be very large.

TABLE 5. Statistics of averaged TC genesis in the South Pacific (143°–200°E) in JTWC observations, WRF simulations, and CYGP genesis index (applied to the model variables). Here, $\overline{N}^t$ and σ_N are the annual mean and standard deviation of the number of cyclogenesis events. $\overline{\mathrm{GI}}^t$ and σ_f are the mean and standard deviation of the estimated number of events resulting from large-scale forcing (CYGP is computed, averaged, and normalized to verify $\overline{\mathrm{GI}}^t = \overline{N}^t$); $\overline{\phi_s}$ and σ_s are the mean and standard deviation of the stochastic distribution estimated from Eq. (2).

TC statistics	$\overline{N}^t$	σ_N	σ_f	σ_s	$(\sigma_N/\overline{N}^t)^2$	$(\sigma_f/\overline{\mathrm{GI}}^t)^2$	$(\sigma_s/\overline{\phi_s}^t)^2$
Observations	6.6	3.0			0.21		
Present-climate experiment	8.2	3.5	1.8	0.36	0.18	0.05	0.13
Climatological experiment	7.6	1.7	0.4	0.22	0.05	0.00	0.05

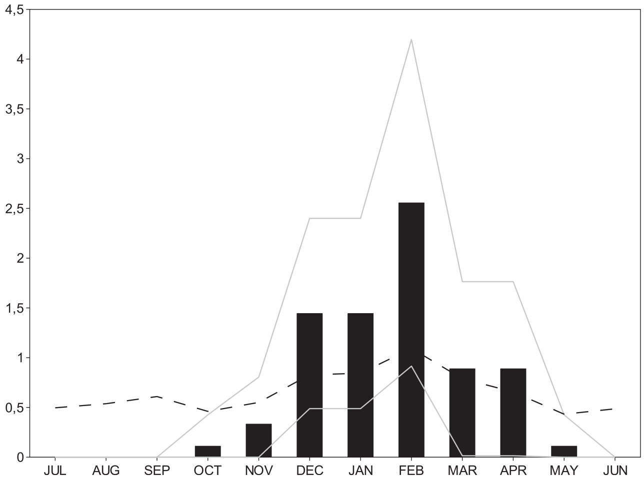

FIG. 15. Mean monthly number N of model TC genesis in the 10-yr climatological experiment. Gray curves indicate $N + \sigma$ and $N - \sigma$, where σ is the standard deviation for each month. Monthly values of CYGP computed using the 10-yr climatological experiment are shown (dashed curve).

Note finally that the seasonal distribution of cyclogenesis in the climatological experiment (shown in Fig. 15) presents no genesis in winter, as opposed to the 25-yr interannual experiment (Fig. 8). This confirms that winter genesis in the interannual experiment only results from anomalous seasonal conditions, not from stochastic behavior under mean forcing conditions (section 4d). In addition, Fig. 15 shows that the monthly ratio σ_N/N is almost constant during the months of strong cyclonic activity [December–February (DJF) here], which is consistent with Eq. (3) using monthly rather than annual parameters (σ_f is small). However, during the months with fewer cyclogenesis, Eq. (3) is not satisfied. This analysis thus suggests that Eq. (2) cannot be straightforwardly applied to describe seasonal variations of cyclogenesis resulting from the poor representation of the seasonal cycle of genesis indices (Fig. 15; see also Menkes et al. 2010, manuscript submitted to *Climate Dyn.*).

c. *Mesoscale interactions*

We now suggest some mechanisms by which mesoscale interactions in the model can produce stochasticity in TC activity. These simulated mesoscale interactions are compared to some observations reported in the literature.

A step-by-step examination of individual TC formations along all seasons of both the interannual and climatological simulations shows that mesoscale interactions are ubiquitous in the cyclogenesis area. These interactions are various but appear to follow a pattern. Multiple mesoscale vortices and associated cloud clusters are first produced along SPCZ lines of strengthened convergence (mostly around 10°S). Interaction then occurs, involving two or even three vortices of various intensities. Our modeled vortex interactions appear to span the different regimes of known classification (Dritschel 1995), from elastic interaction to partial/complete straining and partial/complete merger. On the occasions of complete mergers, two vortices of unequal sizes can merge into one larger vortex and form an intense TC, as illustrated in Fig. 16. The process apparent in this example seems to be in good agreement with potential vorticity theories of vortex interaction and formation of spiral bands in TCs (Guinn and Schubert 1993). It includes mutual cyclonic rotation, followed by the weaker vortex being elongated (by shearing strain) and wrapped cyclonically around the stronger one to become a spiral band. During this process, the weaker vortex provides additional latent heat to the stronger one, fueling it at its own expense (it is destroyed by the intense middle-level flow of the stronger vortex). The merger takes about 3 days to proceed and the final merger occurs at a distance of about 500 km, closely resembling the merger, described in Kuo et al. (2000), of TCs Zeb and Alex (October 1998 in the North Pacific). Note that not all vortex interactions in the model lead to vortex growth, and most cyclones do not appear to result from merger, but at some point they are almost all interacting with the mesoscale flow.

The interaction of formed TCs with mesoscale features is also responsible for the significant variability in TC tracks (Holland and Lander 1993). Combined with random variations of genesis location, it may increase the dispersion effect on TC occurrence. This is illustrated in Fig. 17, showing TC tracks in different years of the climatological simulation. This argument reiterates the point previously made in section 5a that the relation between ENSO and cyclonic activity is degraded when considering TC occurrence rather than genesis.

6. Conclusions

In this paper, we have examined the ability of a regional mesoscale model (WRF) at 1⁄3° resolution to simulate the statistics of tropical cyclone activity in the present climate of the South Pacific. A preliminary objective was to properly simulate the climatological conditions of TC genesis, in particular the characteristics defining the South Pacific convergence zone. The results found were mostly sensitive to the choice of cumulus parameterization, because the largest part of precipitable convection is still subgrid scale at this resolution. The Betts–Miller–Janjic convective adjustment scheme was selected because it clearly shows the best ability to represent the SPCZ position and associated precipitation rates compared with two mass flux convection schemes. The interannual variability of the SPCZ is also mostly

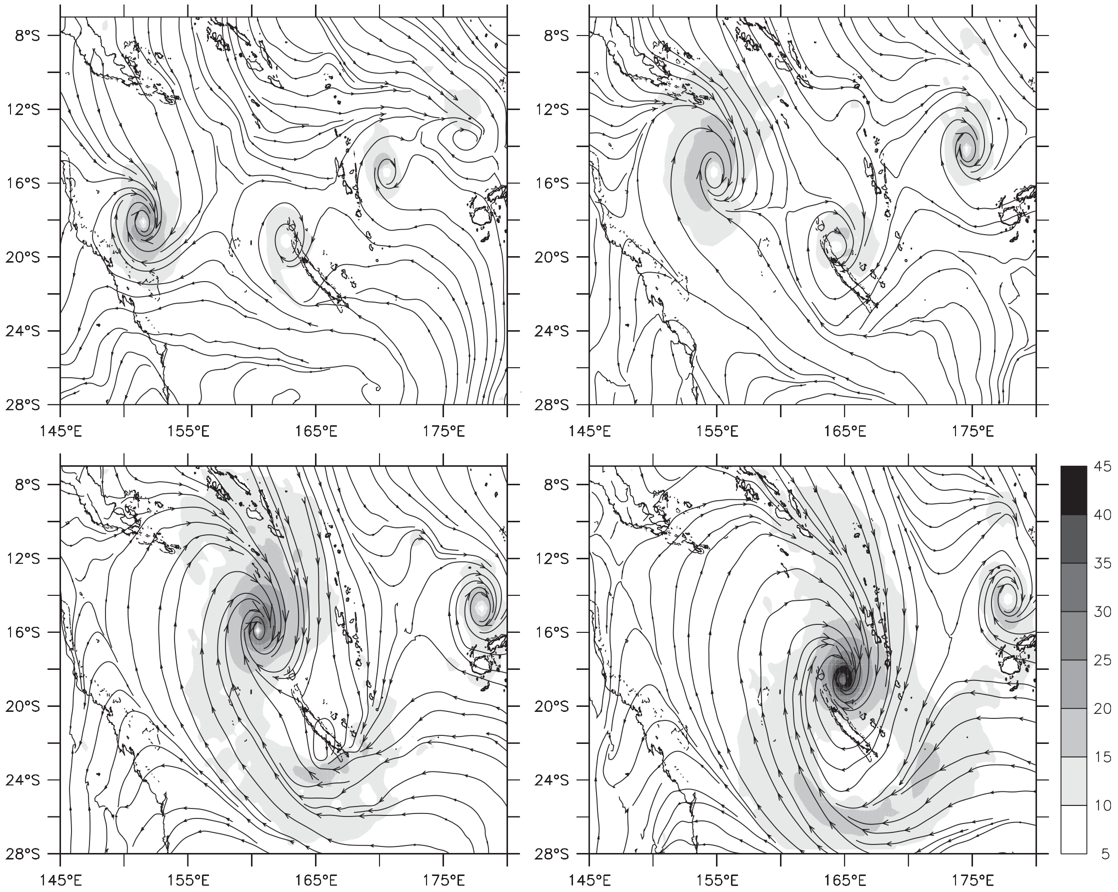

FIG. 16. Simulated TC formation by vortex merging in the Coral Sea. A 4-day event of the model year 1986, on 8, 9, 11, and 12 February, respectively, is shown. Low-level wind (at 925 hPa) is shown as streamlines and colors (m s^{-1}).

captured by the model, particularly its zonalization during strong El Niño events.

With a grid scale of 35 km (155-km effective resolution), we have shown that WRF is able to reproduce a wide range of mesoscale convective systems. Cloud clusters with horizontal scales around 500 km constitute the bulk of precipitation in the SPCZ, but the most intense precipitation systems have only small residual effects. Tropical cyclones in particular represent only 10% of the mean SPCZ precipitation. Yet they grow from the most intense systems formed along SPCZ lines of strengthened convergence (generally around 10°S) and sometimes develop into hurricanes of up to 45 m s^{-1} (maximum 10-m wind speed). As in previous numerical studies (e.g., Knutson et al. 2007; LaRow et al. 2008; Zhao et al. 2009), the maximum intensity of observed hurricanes is not captured by the model (Saffir–Simpson category 5 includes TCs of over 70 m s^{-1} sustained wind speed). This can be partly explained by the known relation between TC intensity and model resolution, but also by the approximations of physical parameterizations. The three-dimensional structure of simulated tropical cyclones is nevertheless in remarkable agreement with dropsondes and satellite observations. The mean seasonal and spatial distributions of TC genesis and occurrence are in reasonably good agreement with the JTWC data. We note, however, that the spatial pattern of TC genesis is shifted to the northeast due to a similar bias in the environmental forcing. Over the whole genesis area, the annual TC count and interannual standard deviation are also very comparable to observations: 8.2 ± 3.5 cyclones are produced seasonally in the model, compared with 6.6 ± 3.0 in the JTWC observations. The model is thus able to reproduce the observed range of variability, some of it associated with ENSO forcing (particularly strong El Niño phases). ENSO events impact the SPCZ position through meridional translation and zonalization. Displacement of the SPCZ position leads to a corresponding displacement of cyclogenesis, which is expressed in correlation maps as a dipole pattern. Therefore, even though local correlations can be strong, the dipole pattern results in weaker regional correlations resulting from compensating variability.

Large-scale forcing is not the only process driving interannual variations of TC genesis in the South Pacific; more than half of it may be due to stochastic processes.

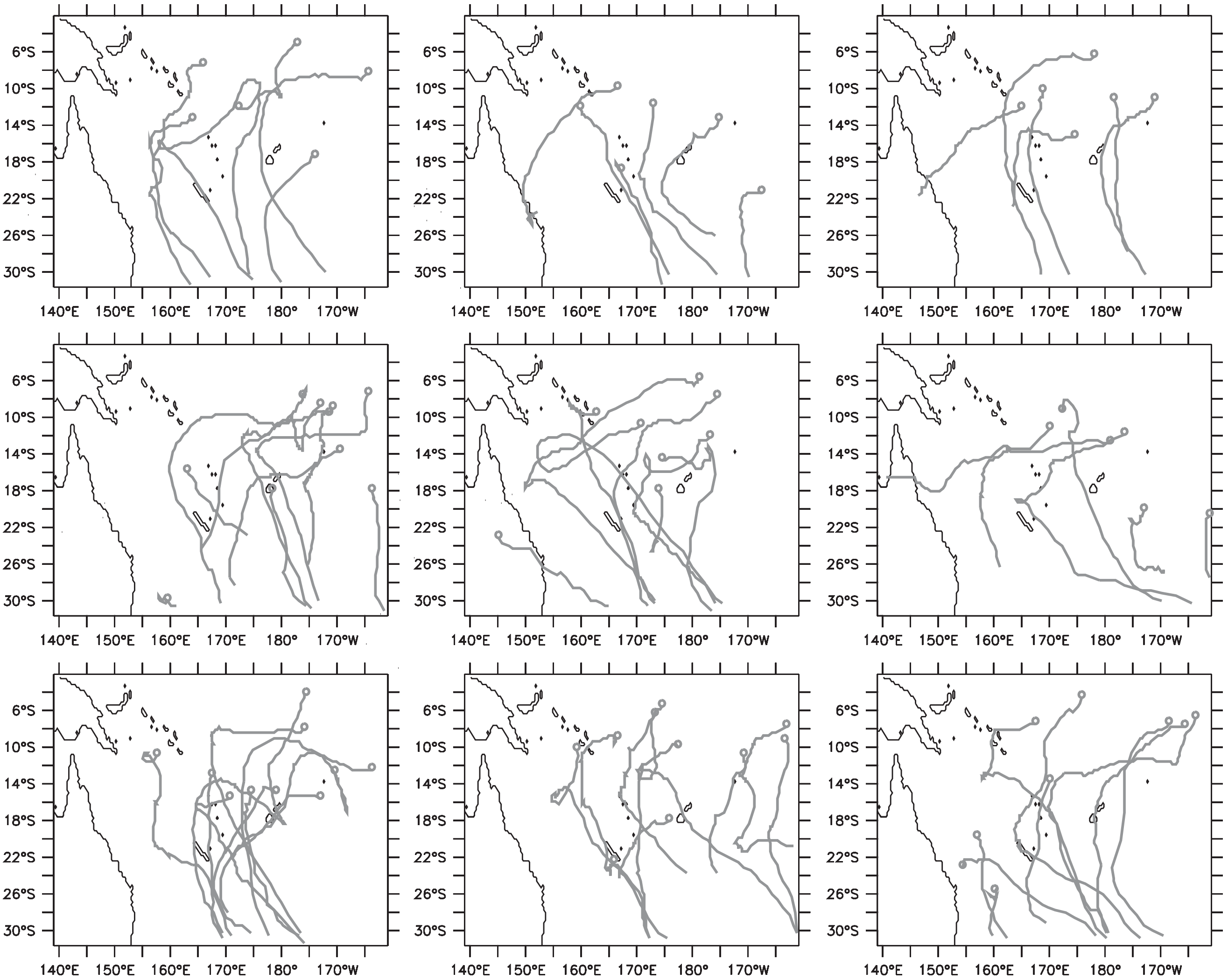

FIG. 17. TC tracks (thick gray lines, the circles represent the beginning of the tracks) computed for each year (from July to June) of the 10-yr climatological experiment. Coastlines are in black.

This estimation of intrinsic variability was permitted by a 10-yr climatological simulation that operated as a 10-member ensemble simulation of an averaged year with differing initialization values. It shows that a standard deviation of 1.7 cyclones yr^{-1} emerges from the internal variability of the model (compared to the total of 3.5 cyclones yr^{-1}). Because the internal variability of the regional environment (not transmitted through the lateral boundaries) is low, the internal variability of cyclogenesis in the ensemble simulation appears essentially related to mesoscale interactions. We are aware that the use of subgrid-scale convective parameterization may lead to misrepresentation (over- or underrepresentation depending on the CP scheme) of small-scale random processes needed for triggering TC genesis. As an example of overrepresentation, our model appears excessively sensitive to favorable winter anomalies of environmental conditions, producing occasional winter TC events. Nevertheless, assuming that mesoscale vortex interactions (at scales larger than 200 km) constitute a large source of internal variability (Simpson et al. 1997), our explicit resolution of these ubiquitous stochastic processes, from elastic interactions to merger, gives us some confidence that the model has captured an interesting part of reality.

A possible way to cope with intrinsic variability and the associated loss of predictability is to perform ensemble simulations, although the efficiency of ensemble predictions depends on the region of application. Using a four-member ensemble simulation with a 50-km resolution model, Zhao et al. (2009) find a correlation with observed TC genesis of 0.8 in the North Atlantic, but only 0.6 in the east Pacific, 0.5 in the west Pacific, and even 0.3 in the South Pacific. Estimation of interannual variability from genesis indices are consistent with these results, showing the best predictability in the Atlantic basin (Camargo and Sobel 2004; Menkes et al. 2010, manuscript submitted to

Climate Dyn.), where forced variability seems to be dominant. In our study, comparison of TC genesis from direct TC counts and from estimates using a genesis index (Table 5) shows that the low standard deviation of yearly genesis index in the South Pacific may be due to comparatively large stochastic variability and less so to index failure. In this case, a correction to genesis indices can be applied using stochastic distributions estimated from mesoscale models. However, the limit of this method is dependent on the genesis index accuracy to represent the environmental forcing.

Finally, we can make three concluding remarks concerning the benefit of ensemble simulations for improving predictability in the South Pacific:

- If stochastic variability in the real world is similar to that of the model, then it also constitutes a large part of its interannual variability. Ensemble simulations can only reduce the model uncertainties, not the observed ones. Therefore, the latter will form a limit to predictability, independent from model improvements.
- Correlations are greater in local rather than regional areas. Therefore, the efficiency of ensemble simulations may well be locally high but regionally low. The reason that the broader scale is important to consider is because TC occurrence, and hence landing and population vulnerability, results from dispersion of TCs around genesis location. TCs move approximately with the barotropic background airflow and their tracks are affected by a number of phenomena, including synoptic variability and chaotic advection, in which mesoscale interactions can act as a trigger mechanism. The dispersion of TC tracks, amplifying the uncertainty of genesis location, can thus explain the degraded relation between ENSO and TC activity when considering occurrence rather than genesis. Nevertheless, TC occurrence remains correlated to the interannual forcing at some locations, especially in eastern regions, that is, away from high cyclonic activity (Basher and Zheng 1995; Kuleshov et al. 2008).
- Model errors constitute another source of uncertainty and are difficult to assess. Ensemble simulations with varying model parameters may lower the model error, but cannot account for missing physics. Sensitivity to convective parameterization, model resolution, ocean feedback, and the wave interface under extreme events are all important areas of future research. However, we were able to reduce a major component of model errors by selecting the configuration and parameterizations that allowed a more realistic representation of SPCZ forcing and statistical TC counts than thatpreviously shown (Vitart et al. 1997; Walsh et al. 2004; Zhao et al. 2009). This result and indications that mesoscale interactions are realistic in the model gives us confidence that the present work contributes new and robust elements to the understanding of TC activity in the region.

Acknowledgments. We acknowledge support from the French Agence Nationale de la Recherche (ANR Project Cyclones and Climate). The authors wish to thank Jean-François Royer and three anonymous reviewers for their careful review.

REFERENCES

Adler, R. F., G. J. Huffman, D. T. Bolvin, S. Curtis, and E. J. Nelkin, 2000: Tropical rainfall distributions determined using TRMM combined with other satellite and rain gauge information. *J. Appl. Meteor.,* **39,** 2007–2023.

——, C. Kummerow, D. Bolvin, S. Curtis, and C. Kidd, 2003: *Status of TRMM Monthly Estimates of Tropical Precipitation. Meteor. Monogr.,* No. 51, Amer. Meteor. Soc., 223 pp.

Alexandru, A., R. de Elia, and R. Laprise, 2007: Internal variability in regional climate downscaling at the seasonal scale. *Mon. Wea. Rev.,* **135,** 3221–3238.

Ashok, K., S. K. Behera, S. A. Rao, H. Weng, and T. Yamagata, 2007: El Niño Modoki and its possible teleconnection. *J. Geophys. Res.,* **112,** C11007, doi:10.1029/2006JC003798.

Baik, J.-J., M. DeMaria, and S. Raman, 1990a: Tropical cyclone simulations with the Betts convective adjustment scheme. Part I: Model description and control simulation. *Mon. Wea. Rev.,* **118,** 513–528.

——, ——, and ——, 1990b: Tropical cyclone simulations with the Betts convective adjustment scheme. Part II: Sensitivity experiments. *Mon. Wea. Rev.,* **118,** 529–541.

Basher, R. E., and X. Zheng, 1995: Tropical cyclones in the southwest Pacific: Spatial patterns and relationships to Southern Oscillation and sea surface temperature. *J. Climate,* **8,** 1249–1260.

Bengtsson, L., M. Botzet, and M. Esch, 1996: Will greenhouse gas-induced warming over the next 50 years lead to higher frequency and greater intensity of hurricanes? *Tellus,* **48A,** 57–73.

——, K. I. Hodges, and M. Esch, 2007: Tropical cyclones in a T159 resolution global climate model: Comparison with observations and re-analyses. *Tellus,* **59A,** 396–416.

Betts, A. K., 1986: A new convective adjustment scheme. Part I: Observational and theoretical basis. *Quart. J. Roy. Meteor. Soc.,* **112,** 677–691.

Black, M. L., R. W. Burpee, and F. D. Marks Jr., 1996: Vertical motion characteristics of tropical cyclones determined with airborne Doppler radial velocities. *J. Atmos. Sci.,* **53,** 1183–1197.

Camargo, S. J., and S. E. Zebiak, 2002: Improving the detection and tracking of tropical cyclones in atmospheric general circulation models. *Wea. Forecasting,* **17,** 1152–1162.

——, and A. H. Sobel, 2004: Formation of tropical storms in an atmospheric general circulation model. *Tellus,* **56A,** 56–67.

——, A. G. Barnston, and S. E. Zebiak, 2005: A statistical assessment of tropical cyclone activity in atmospheric general circulation models. *Tellus,* **57A,** 589–604.

——, K. A. Emanuel, and A. H. Sobel, 2007a: Use of a genesis potential index to diagnose ENSO effects on tropical cyclone genesis. *J. Climate,* **20,** 4819–4834.

——, A. H. Sobel, A. G. Barnston, and K. A. Emanuel, 2007b: Tropical cyclone genesis potential index in climate models. *Tellus,* **59A,** 428–443.

Charnock, M., 1955: Wind stress on a water surface. *Quart. J. Roy. Meteor. Soc.,* **1,** 639–640.

Chauvin, F., J.-F. Royer, and D. Deque, 2006: Response of hurricane-type vortices to global warming as simulated by ARPEGE-Climat at high resolution. *Climate Dyn.,* **27,** 377–399.

Chelton, D., and M. Freilich, 2005: Scatterometer-based assessment of 10-m wind analyses from the operational ECMWF and NCEP numerical weather prediction models. *Mon. Wea. Rev.,* **133,** 409–429.

Chu, J. H., C. R. Sampson, A. S. Levine, and E. Fukada, 2002: The Joint Typhoon Warning Center tropical cyclone best-tracks, 1945–2000. Naval Research Laboratory Rep. NRL/MR/7540-02-16. [Available online at http://www.usno.navy.mil/NOOC/nmfc-ph/RSS/jtwc/best_tracks/TC_bt_report.html.]

Dritschel, D. G., 1995: A general theory for two-dimensional vortex interactions. *J. Fluid Mech.,* **293,** 269–303.

Dudhia, J., 1989: Numerical study of convection observed during the Winter Monsoon Experiment using a mesoscale two-dimensional model. *J. Atmos. Sci.,* **46,** 3077–3107.

Dvorak, V. F., 1975: Tropical cyclone intensity analysis and forecasting from satellite imagery. *Mon. Wea. Rev.,* **103,** 420–430.

——, 1984: Tropical cyclone intensity analysis using satellite data. NESDIS Tech. Rep. 11, NOAA Tech. Memo., 47 pp. [Available from National Environmental Satellite, Data, and Information Service, Washington, DC 20233; online at ftp://satepsanone.nesdis.noaa.gov/Publications/Tropical/Dvorak_1984.pdf.]

Emanuel, K., 1995: The behavior of a simple hurricane model using a convective scheme based on subcloud-layer entropy equilibrium. *J. Atmos. Sci.,* **52,** 3959–3968.

——, 2003: Tropical cyclones. *Annu. Rev. Earth Planet. Sci.,* **31,** 75–104.

——, and D. S. Nolan, 2004: Tropical cyclone activity and global climate. Preprints, *26th Conf. on Hurricanes and Tropical Meteorology,* Miami, FL, Amer. Meteor. Soc., 10A.2. [Available online at http://ams.confex.com/ams/pdfpapers/75463.pdf.]

Errico, R. M., 1985: Spectra computed from a limited area grid. *Mon. Wea. Rev.,* **113,** 1554–1562.

Evans, J. L., and R. J. Allan, 1992: El Niño/Southern Oscillation modification to the structure of the monsoon and tropical cyclone activity in the Australasian region. *Int. J. Climatol.,* **12,** 611–623.

Gallus, W. A., 1999: Eta simulations of three extreme precipitation events: Sensitivity to resolution and convective parameterization. *Wea. Forecasting,* **14,** 405–426.

Giorgi, F., and X. Bi, 2000: A study of internal variability of a regional climate model. *J. Geophys. Res.,* **105** (D24), 29 503–29 521.

Gray, W. M., 1979: Hurricanes: Their function, structure and likely role in the tropical circulation. *Supplement of Meteorology over the Tropical Oceans,* D. B. Shaw, Ed., Royal Meteorological Society, 155–218.

——, 1998: The formation of tropical cyclones. *Meteor. Atmos. Phys.,* **67,** 37–69.

Grell, G., and D. Dévényi, 2002: A generalized approach to parameterizing convection combining ensemble and data assimilation techniques. *Geophys. Res. Lett.,* **29,** 1693, doi:10.1029/2002GL015311.

Guinn, T. A., and W. H. Schubert, 1993: Hurricane spiral bands. *J. Atmos. Sci.,* **50,** 3380–3403.

Halverson, J. B., J. Simpson, G. Heymsfield, H. Pierce, T. Hock, and L. Ritchie, 2006: Warm core structure of Hurricane Erin diagnosed from high altitude dropsondes during CAMEX-4. *J. Atmos. Sci.,* **63,** 309–324.

Hawkins, H. F., and S. M. Imbembo, 1976: The structure of a small, intense hurricane—Inez 1966. *Mon. Wea. Rev.,* **104,** 418–442.

Holland, G. J., and M. Lander, 1993: The meandering nature of tropical cyclone tracks. *J. Atmos. Sci.,* **50,** 1254–1266.

Hong, S. Y., and H. L. Pan, 1998: Convective trigger function for a mass-flux cumulus parameterization scheme. *Mon. Wea. Rev.,* **126,** 2599–2620.

——, J. Dudhia, and S. H. Chen, 2004: A revised approach to ice microphysical processes for the bulk parameterization of clouds and precipitation. *Mon. Wea. Rev.,* **132,** 103–120.

Huffman, G. J., and Coauthors, 1997: The Global Precipitation Climatology Project (GPCP) Combined Precipitation Dataset. *Bull. Amer. Meteor. Soc.,* **78,** 5–20.

Janjić, Z. I., 1994: The step-mountain eta coordinate model: Further developments of the convection, viscous sublayer, and turbulence closure schemes. *Mon. Wea. Rev.,* **122,** 927–945.

——, 2000: Comments on "Development and evaluation of a convection scheme for use in climate models." *J. Atmos. Sci.,* **57,** 3686.

Jiang, H., and E. J. Zipser, 2010: Contribution of tropical cyclones to the global precipitation from eight seasons of TRMM data: Regional, seasonal, and interannual variations. *J. Climate,* **23,** 1526–1543.

Jorgensen, D. P., E. J. Zipser, and M. A. Le Mone, 1985: Vertical motions in intense hurricanes. *J. Atmos. Sci.,* **42,** 839–856.

Kain, J. S., 2004: The Kain–Fritsch convective parameterization: An update. *J. Appl. Meteor.,* **43,** 170–181.

Kanamitsu, M., W. Ebisuzaki, J. Woollen, S.-K. Yang, J. J. Hnilo, M. Fiorino, and G. L. Potter, 2002: NCEP–DOE AMIP-II Reanalysis (R-2). *Bull. Amer. Meteor. Soc.,* **83,** 1631–1643.

Kelley, O. A., J. Stout, and J. B. Halverson, 2004: Tall precipitation cells in tropical cyclone eyewalls are associated with tropical cyclone intensification. *Geophys. Res. Lett.,* **31,** L24112, doi:10.1029/2004GL021616.

Kidder, S. Q., M. D. Goldberg, R. M. Zehr, M. DeMaria, J. F. W. Purdom, C. S. Velden, N. C. Grody, and S. J. Kusselson, 2000: Satellite analysis of tropical cyclones using the Advanced Microwave Sounding Unit (AMSU). *Bull. Amer. Meteor. Soc.,* **81,** 1241–1259.

Knutson, T. R., J. J. Sirutis, S. T. Garner, I. M. Held, and R. E. Tuleya, 2007: Simulation of the recent multidecadal increase of Atlantic hurricane activity using an 18-km-grid regional model. *Bull. Amer. Meteor. Soc.,* **88,** 1549–1565.

Kuleshov, Y., L. Qi, R. Fawcett, and D. Jones, 2008: On tropical cyclone activity in the Southern Hemisphere: Trends and the ENSO connection. *Geophys. Res. Lett.,* **35,** L14S08, doi:10.1029/2007GL032983.

Kuo, H.-C., G. T.-J. Chen, and C.-H. Lin, 2000: Merger of Tropical Cyclones Zeb and Alex. *Mon. Wea. Rev.,* **128,** 2967–2975.

Landsea, C. W., 1993: A climatology of intense (or major) Atlantic hurricanes. *Mon. Wea. Rev.,* **121,** 1703–1713.

——, G. A. Vecchi, L. Bengtsson, and T. R. Knutson, 2010: Impact of duration thresholds on Atlantic tropical cyclone counts. *J. Climate,* **23,** 2508–2519.

LaRow, T. E., Y. K. Lim, D. W. Shin, E. P. Chassignet, and S. Cocke, 2008: Atlantic basin seasonal hurricane simulations. *J. Climate,* **21,** 3191–3206.

Lefevre, J., P. Marchesiello, N. C. Jourdain, C. E. Menkes, and A. Leroy, 2010: Weather regimes and orographic circulation around New Caledonia. *Mar. Pollut. Bull.,* **61,** 413–431.

Lucas-Picher, P., D. Caya, R. de Elìa, and R. Laprise, 2008: Investigation of regional climate models' internal variability with a ten-member ensemble of 10-year simulations over a large domain. *Climate Dyn.,* **31,** 927–940.

Marks, F. D., 1981: Evolution of the structure of precipitating convection in Hurricane Allen. Preprints, *20th Conf. on Radar Meteorology,* Boston, MA, Amer. Meteor. Soc., 720–725.

Matthews, A. J., B. J. Hoskins, J. M. Slingo, and M. Blackburn, 1996: Development of convection along the SPCZ within a Madden-Julian oscillation. *Quart. J. Roy. Meteor. Soc.,* **122,** 669–688.

Mlawer, E. J., S. J. Taubman, P. D. Brown, M. J. Iacono, and S. A. Clough, 1997: Radiative transfer for inhomogeneous atmospheres: RRTM, a validated correlated-k model for the longwave. *J. Geophys. Res.,* **102,** 16 663–16 682.

Moon, I. J., I. Ginis, and T. Hara, 2004: Effect of surface waves on air–sea momentum exchange. Part II: Behavior of drag coefficient under tropical cyclones. *J. Atmos. Sci.,* **61,** 2334–2348.

Nguyen, K. C., and K. J. E. Walsh, 2001: Interannual, decadal, and transient greenhouse simulation of tropical cyclone–like vortices in a regional climate model of the South Pacific. *J. Climate,* **14,** 3043–3054.

Nicholls, N., 1984: The Southern Oscillation, sea surface temperature, and interannual fluctuations in Australian tropical cyclone activity. *Int. J. Climatol.,* **4,** 661–670.

Noh, Y., W. G. Cheon, S. Y. Hong, and S. Raasch, 2003: Improvement of the K-profile model for the planetary boundary layer based on large eddy simulation data. *Bound.-Layer Meteor.,* **107,** 401–427.

Oouchi, K., J. Yoshimura, H. Yoshimura, R. Mizuta, S. Kusunoki, and A. Noda, 2006: Tropical cyclone climatology in a global-warming climate as simulated in a 20 km- mesh global atmospheric model: Frequency and wind intensity analyses. *J. Meteor. Soc. Japan,* **84,** 259–276.

Ooyama, K. V., 1982: Conceptual evolution of the theory and modeling of the tropical cyclone. *J. Meteor. Soc. Japan,* **60,** 369–379.

Orlanski, I., 1975: A rational subdivision of scales for atmospheric processes. *Bull. Amer. Meteor. Soc.,* **56,** 527–530.

Powell, M. D., P. J. Vickery, and T. A. Reinhold, 2003: Reduced drag coefficient for high wind speeds in tropical cyclones. *Nature,* **422,** 279–283.

Ramsay, H. A., L. M. Leslie, P. J. Lamb, M. B. Richman, and M. Leplastrier, 2008: Interannual variability of tropical cyclones in the Australian region: Role of large-scale environment. *J. Climate,* **21,** 1083–1103.

Royer, J.-F., F. Chauvin, B. Timbal, P. Araspin, and D. Grimal, 1998: A GCM study of the impact of greenhouse gas increase on the frequency of occurrence of tropical cyclones. *Climatic Change,* **38,** 307–343.

Shapiro, S. S., and M. B. Wilk, 1965: An analysis of variance test for normality (complete samples). *Biometrika,* **52** (3–4), 591–611.

Simpson, J., E. Ritchie, G. J. Holland, J. Halverson, and S. Stewart, 1997: Mesoscale interactions in tropical cyclone genesis. *Mon. Wea. Rev.,* **125,** 2643–2661.

Skamarock, W. C., 2004: Evaluating mesoscale NWP models using kinetic energy spectra. *Mon. Wea. Rev.,* **132,** 3019–3032.

——, and J. B. Klemp, 2008: A time-split nonhydrostatic atmospheric model for weather research and forecasting applications. *J. Comput. Phys.,* **227,** 3465–3485.

——, ——, J. Dudhia, D. O. Gill, D. M. Barker, W. Wang, and J. G. Powers, 2005: A description of the Advanced Research WRF version 2. NCAR Tech. Notes-468+ STR, 100 pp. [Available online at http://www.mmm.ucar.edu/wrf/users/docs/arw_v2.pdf.]

Sugi, M., A. Noda, and N. Sato, 2002: Influence of the global warming on tropical cyclone climatology: An experiment with the JMA global model. *J. Meteor. Soc. Japan,* **80,** 249–272.

Vincent, E. M., M. Lengaigne, C. E. Menkes, N. C. Jourdain, P. Marchesiello, and G. Madec, 2009: Interannual variability of the South Pacific convergence zone and implications for tropical cyclone genesis. *Climate Dyn.,* doi:10.1007/s00382-009-0716-3, in press.

Vitart, F., J. L. Anderson, and W. F. Stern, 1997: Simulation of interannual variability of tropical storm frequency in an ensemble of GCM integrations. *J. Climate,* **10,** 745–760.

von Storch, H., and F. W. Zwiers, 2001: *Statistical Analysis in Climate Research.* Cambridge University Press, 484 pp.

——, H. Langenberg, and F. Feser, 2000: A spectral nudging technique for dynamical downscaling purposes. *Mon. Wea. Rev.,* **128,** 3664–3673.

Walsh, K. J. E., K.-C. Nguyen, and J. L. McGregor, 2004: Fine-resolution regional climate model simulations of the impact of climate change on tropical cyclones near Australia. *Climate Dyn.,* **22,** 47–56.

——, M. Fiorino, C. W. Landsea, and K. L. McInnes, 2007: Objectively determined resolution-dependent threshold criteria for the detection of tropical cyclones in climate models and reanalyses. *J. Climate,* **20,** 2307–2314.

Watterson, I. G., J. L. Evans, and B. F. Ryan, 1995: Seasonal and interannual variability of tropical cyclogenesis: Diagnostics from large scale fields. *J. Climate,* **8,** 3052–3065.

Wu, G., and N. C. Lau, 1992: A GCM simulation of the relationship between tropical-storm formation and ENSO. *Mon. Wea. Rev.,* **120,** 958–977.

Yoshimura, J., M. Sugi, and A. Noda, 2006: Influence of greenhouse warming on tropical cyclone frequency. *J. Meteor. Soc. Japan,* **84,** 405–428.

Zhao, M., I. M. Held, S. J. Lin, and G. A. Vecchi, 2009: Simulations of global hurricane climatology, interannual variability, and response to global warming using a 50-km resolution GCM. *J. Climate,* **22,** 6653–6678.

Abstract :

Tropical Cyclones' (TCs) intensity heavily depends on the processes occurring at the air–sea interface. TCs draw their energy from the warmth of the ocean surface but they induce a sea surface cooling (Cold Wake CW) that negatively feeds back on their intensity.

This dissertation first describes the processes explaining the surface cooling along with the characteristics of the TC and of the ocean that control its magnitude. Three main processes participate in the CW : vertical mixing, surface heat fluxes (mainly evaporation) and advection. By mixing together warm water from the surface and cold water from below, the first process cools the surface while warming the sub–surface. Mixing is responsible for the major part of the cooling right under the TC and is thus the key process of the CW feedback. By contrast, surface heat fluxes poorly contribute to the cooling right under the TC but they cool the ocean surface over very large regions. Horizontal advection participates in cooling by surface divergence of warm water and modifies the shape of the CW. In this thesis, I define an index integrating the wind power during the TC passage (Wind Power index ; WPi) and show that the CW magnitude increases with WPi. However, for a given wind power, the state of the ocean sub–surface modulates the magnitude of the CW by a factor of 10 ! To account for this control of the CW by the ocean sub–surface, I propose an index measuring the potential energy of the oceanic stratification (Cooling Inhibition index ; CI).

These results have been made possible thanks to an experimental setup allowing the simulation of oceanic response to TCs for a moderate numerical cost. It allows a statistical analysis of the CW characteristics induced by more than 3,000 TCs over the last 30 years. By directly simulating the ocean response to TCs within a global ocean model, it also allows to link the processes occurring at the event scale to their effect on the ocean at climatic scale.

Warm water injected in the sub–surface by mixing under TCs has been suggested to modify the global ocean heat transport (OHT). However, warm anomalies injected in the sub–surface during the cyclonic season (local summer) hardly reach depth below the seasonal thermocline. Mixed layer deepening in winter reabsorb these warm anomalies, hence considerably reducing the potential effect of TCs on the OHT. On the other hand, enhanced surface heat fluxes by TCs act to significantly cool cyclonic basins during summer. Adding this to the winter surface warming evoked above, this process leads to a 10% reduction of surface temperature seasonal cycle within TC basins.

Finally, this thesis open perspectives for a better understanding of how TCs' activity may be affected by the natural and anthropogenic variability of ocean characteristics.

Keywords Tropical Cyclone, Hurricane, Wind Power, Air–sea interaction, Cold Wake, Cooling Inhibition, Ocean stratification, Ocean modelling, NEMO

Résumé :

Les processus qui se déroulent à l'interface air–mer ont une importance cruciale pour les cyclones tropicaux (TCs). Les TCs tirent leur énergie de la chaleur de l'océan superficiel mais induisent aussi un refroidissement en surface : le sillage froid (ou *Cold Wake* CW) qui exerce une rétroaction négative sur leur intensité.

Cette thèse détaille tout d'abord les processus impliqués dans le refroidissement de surface ainsi que les caractéristiques du cyclone et de l'océan qui en contrôlent l'amplitude. Trois processus principaux participent à la CW : le mélange vertical, les flux de chaleur en surface (dominés par l'évaporation) et l'advection. Le mélange vertical homogénéise les eaux chaudes de surface et les eaux froides sous–jacentes, refroidissant la surface tout en réchauffant la sub–surface. Il est responsable de la majeure partie du refroidissement sous le TC et est donc le processus clé de la rétroaction de la CW. Les flux de chaleur contribuent peu au refroidissement sous le TC, mais ils refroidissent sur de larges régions. Enfin, l'advection horizontale fait diverger les eaux chaudes en surface et participe à modifier la forme de la CW. Dans cette thèse, je définis un indice de puissance du vent intégré pendant le passage du TC (WPi pour *Wind Power index*) et montre que l'amplitude de la CW augmente linéairement en fonction du WPi. Cependant, pour une puissance de TC donnée, l'état de l'océan de sub–surface module l'amplitude de la CW d'un facteur 10 ! Afin de décrire le contrôle de la CW par l'océan de sub–surface, je propose un indice mesurant l'énergie potentielle associée à la stratification océanique (CI pour *Cooling Inhibition index*).

Ces résultats sur le contrôle de la CW ont été obtenus grâce à un dispositif expérimental simulant la réponse océanique aux TCs à un coût numérique modéré. Cette approche permet une analyse statistique des caractéristiques des CWs induites par les ∼3,000 TCs observés sur les 30 dernières années. En modélisant la réponse océanique aux TCs directement dans un modèle de circulation océanique mondiale, ce dispositif expérimental permet aussi de faire le lien entre les processus océaniques à l'échelle des TCs et leur effet sur l'océan à l'échelle climatique.

Il a été suggéré que la chaleur injectée en sub–surface par le mélange vertical sous les TCs peut modifier le transport de chaleur océanique global (OHT). Cependant, les anomalies chaudes injectées en sub–surface par les TCs en été ne pénètrent guère au–delà de la thermocline saisonnière. L'approfondissement de la couche mélangée en hiver a pour effet de réinjecter ces anomalies dans l'atmosphère, ce qui limite considérablement l'influence des TCs sur l'OHT. En revanche, les flux de chaleur sous les TCs refroidissent significativement les bassins cycloniques en été. Associé au réchauffement hivernal évoqué ci–dessus, ce processus réduit d'environ 10% l'amplitude du cycle saisonnier de température dans les bassins cycloniques.

Finalement, la thèse ouvre des perspectives pour comprendre comment les modifications océaniques liées à la variabilité climatique naturelle et anthropique peut moduler l'activité cyclonique.

Mots–clés Cyclones Tropicaux, Puissance des vents, couplage air–mer, Sillage froid, Inhibition au refroidissement, Stratification océanique, Modélisation océanique, NEMO